

Tomorrow's Earth
pp. 1051, 1066, & 1079

Climate clues from Puerto Rico's
storm-damaged forest *p. 1064*

The weekly bird
migration report *p. 1115*

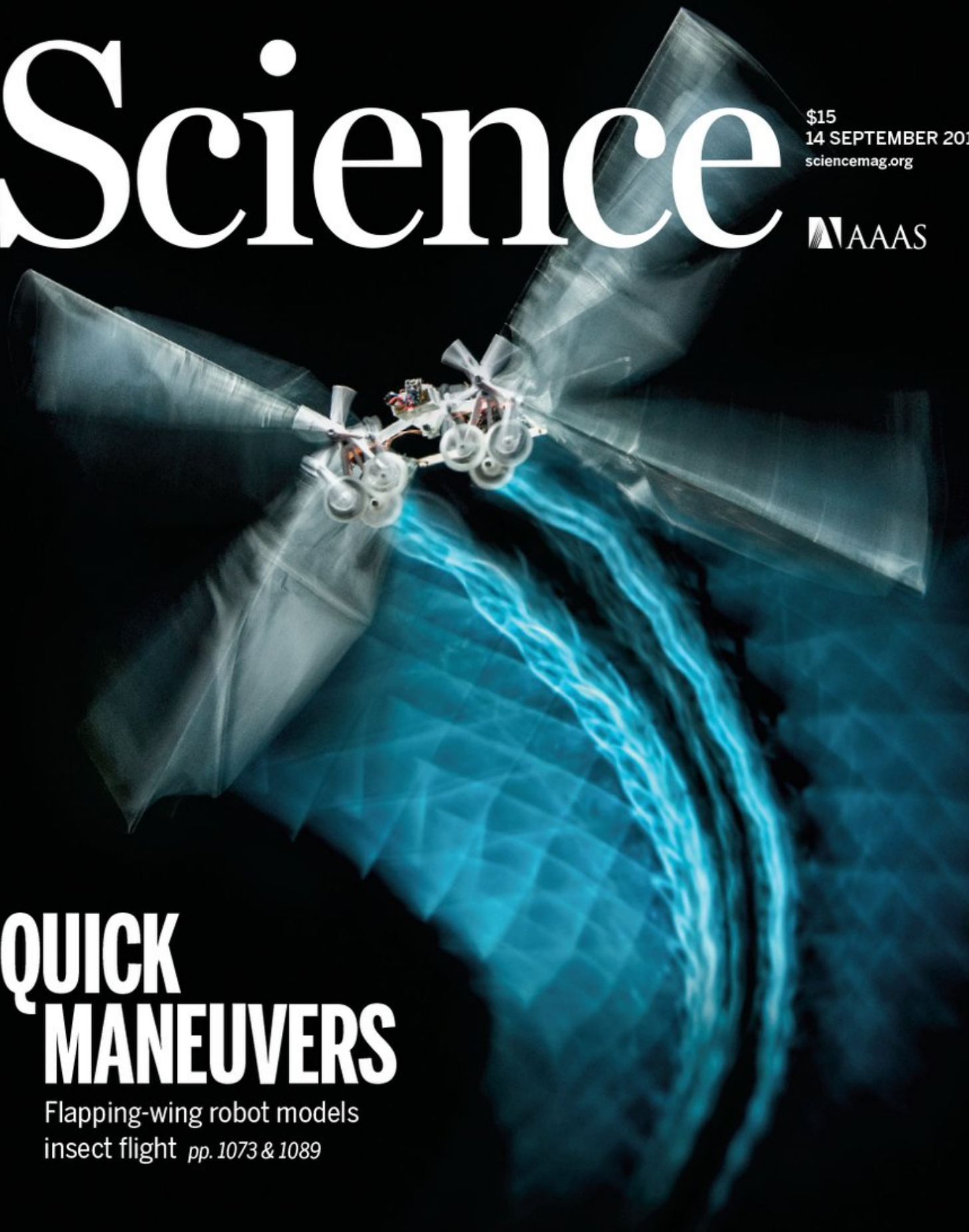
Science

\$15
14 SEPTEMBER 2018
sciencemag.org

AAAS

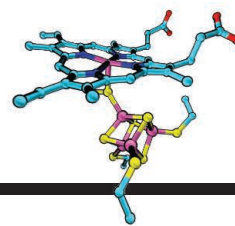
QUICK MANEUVERS

Flapping-wing robot models
insect flight *pp. 1073 & 1089*



CONTENTS

14 SEPTEMBER 2018 • VOLUME 361 • ISSUE 6407



1071 & 1098

Metals power
designed enzyme



Forest resilience after Hurricane Maria

NEWS

IN BRIEF

1052 News at a glance

IN DEPTH

1054 PHYSICISTS PLAN HUNT FOR HIGGS BOSON PAIRS

Rare double-Higgs events at the Large Hadron Collider could point to new physics *By A. Cho*

1055 STEEP DROP IN ZIKA CASES UNDERMINES VACCINE TRIAL

Controversial strategy of intentionally infecting volunteers to test vaccine candidates is now back on the agenda *By J. Cohen*

► PODCAST

1056 NEW CANCER-FIGHTING CELLS ENTER TRIALS

Engineered natural killer cells and macrophages may be next immunotherapies *By M. Leslie*

1058 NASA SPACE LASER TARGETS MELTING POLES

ICESat-2 is set to reveal disappearing sea ice and retreating glacier beds *By P. Voosen*

1059 SCARRED BIRD BONES REVEAL EARLY SETTLEMENT ON MADAGASCAR

Find reignites debate about megafauna extinctions *By A. Lawler*

► RESEARCH ARTICLE BY J. HANSFORD ET AL.
10.1126/SCIADV.AAT6925

FEATURES

1060 PIERCING THE HAZE

Ammonia, a poorly understood smog ingredient, could be key to limiting deadly particulate pollution

By J. Plautz

1064 WINDFALL

A catastrophic hurricane gave scientists a rare chance to study how tropical forests will fare in a warmer, stormier future

By S. Amandolare

INSIGHTS

PERSPECTIVES

1066 GAIA 2.0

Could humans add some level of self-awareness to Earth's self-regulation?

By T. M. Lenton and B. Latour

► EDITORIAL P. 1051; BOOK REVIEW P. 1079

1068 NERVOUS SYSTEM-LIKE SIGNALING IN PLANT DEFENSE

Herbivory induces rapid long-distance calcium signals through glutamate-like receptors *By G. K. Muday and H. Brown-Harding*

► REPORT P. 1112

1069 A PINCH OF RNA SPICES UP DNA REPAIR

Transient incorporation of RNA precursors helps fix broken DNA *By M. Modesti*

► REPORT P. 1126

1071 REVVING UP AN ARTIFICIAL METALLOENZYME

An engineered metalloenzyme shows promising catalytic activity for sulfite reduction

By K. M. Lancaster

► REPORT P. 1098

1072 ENANTIOSELECTIVE FOUR-COMPONENT UGI REACTIONS

A chiral organocatalyst condenses four reactants with stereochemical control *By R. Riva*

► RESEARCH ARTICLE P. 1087

1073 ROBOTIC-FLAPPER MANEUVERS AND FRUITFLY TURNS

Studies of an aerial robot help explain rapid banked turns in the fruitfly

By F. Ruffier

► REPORT P. 1089

POLICY FORUM

1075 A "TECHNOLOGY-SMART" BATTERY POLICY STRATEGY FOR EUROPE

Batteries' inherent characteristics should inform policies

By M. Beuse et al.

BOOKS ET AL.

1078 SMARTER, STRONGER, LONGER

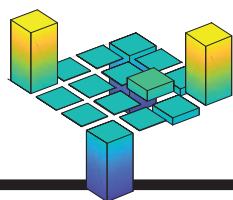
From extreme longevity to photographic memory, unusual individuals push the boundaries of human ability

By C. Kemp

1079 LOOKING AHEAD

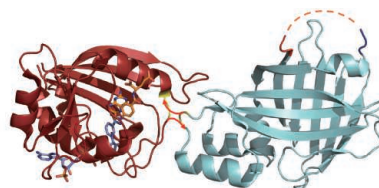
A cosmologist advocates thoughtful deployment of science and technology to address the challenges facing humanity *By A. Robinson*

► EDITORIAL P. 1051; PERSPECTIVE P. 1066



1101 & 1104

Metamaterials go quantum



1122

Sensor proteins monitor metabolites

LETTERS

1081 GRAZING LIMITS BENEFITED BRIDGE CREEK

By R. Demmer and R. L. Beschta

1081 U.S. FAST TEST REACTOR WILL PAY DIVIDENDS

By P. B. Lyons and J. F. Kotek

1082 ONLINE BUZZ PRIORITIZING POPULATION POLICIES

By K. R. Smith et al.

1082 TECHNICAL COMMENT ABSTRACTS

1082 ERRATA

RESEARCH

IN BRIEF

1083 From *Science* and other journals

RESEARCH ARTICLES

1086 IMMUNOLOGY

Differential IL-2 expression defines developmental fates of follicular versus nonfollicular helper T cells
D. DiToro et al.

RESEARCH ARTICLE SUMMARY; FOR FULL TEXT:
[dx.doi.org/10.1126/science.aao2933](https://doi.org/10.1126/science.aao2933)

1087 ORGANIC CHEMISTRY

Asymmetric phosphoric acid-catalyzed four-component Ugi reaction
J. Zhang et al.

RESEARCH ARTICLE SUMMARY; FOR FULL TEXT:
[dx.doi.org/10.1126/science.aas8707](https://doi.org/10.1126/science.aas8707)

► PERSPECTIVE P. 1072

1088 NEUROSCIENCE

Recurrent cortical circuits implement concentration-invariant odor coding
K. A. Bolding and K. M. Franks

RESEARCH ARTICLE SUMMARY; FOR FULL TEXT:
[dx.doi.org/10.1126/science.aat6904](https://doi.org/10.1126/science.aat6904)

REPORTS

1089 ROBOTICS

A tailless aerial robotic flapper reveals that flies use torque coupling in rapid banked turns
M. Karásek et al.

► PERSPECTIVE P. 1073

1094 SOLAR CELLS

Organic and solution-processed tandem solar cells with 17.3% efficiency
L. Meng et al.

1098 ENZYME DESIGN

A designed heme-[4Fe-4S] metalloenzyme catalyzes sulfite reduction like the native enzyme
E. N. Mirts et al.

► PERSPECTIVE P. 1071

METAMATERIALS

1101 Quantum entanglement of the spin and orbital angular momentum of photons using metamaterials
T. Stav et al.

1104 Quantum metasurface for multiphoton interference and state reconstruction
K. Wang et al.

1108 FOREST ECOLOGY

Classifying drivers of global forest loss
P. G. Curtis et al.

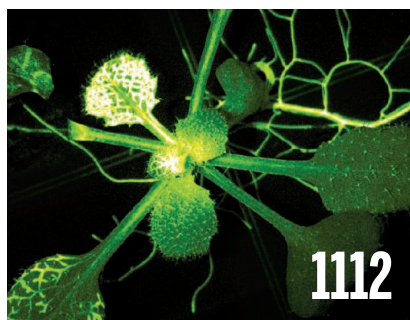
1112 BOTANY

Glutamate triggers long-distance, calcium-based plant defense signaling
M. Toyota et al.

► VIDEO

1115 MIGRATION

A continental system for forecasting bird migration
B. M. Van Doren and K. G. Horton



1118 PROTEIN TARGETING

An ER surface retrieval pathway safeguards the import of mitochondrial membrane proteins in yeast
K. G. Hansen et al.

1122 BIOCHEMISTRY

Semisynthetic sensor proteins enable metabolic assays at the point of care
Q. Yu et al.

1126 MOLECULAR BIOLOGY

Ribonucleotide incorporation enables repair of chromosome breaks by nonhomologous end joining
J. M. Pryor et al.

► PERSPECTIVE P. 1069

DEPARTMENTS

1051 EDITORIAL

Space for nature

By Jonathan Baillie and Ya-Ping Zhang

► PERSPECTIVE P. 1066; BOOK REVIEW P. 1079

1158 WORKING LIFE

Learning to lead
By Lucka Bibic

ON THE COVER



An agile, tailless untethered robot with four flapping wings performs a fruitfly-inspired turning maneuver. The image combines the robot in flight with a time exposure of its flight path. This robot

offers a fresh perspective on insect flight, revealing a passive aerodynamic mechanism that helps fruitflies perform rapid banked turns to avoid dangers. See pages 1073 and 1089. For more on the process behind the cover image, see <https://scim.ag/2N1bdl>.

Image: Skopei Films/©TU Delft

Science Staff	1050
New Products	1130
Science Careers	1131

SCIENCE (ISSN 0036-8075) is published weekly on Friday, except last week in December, by the American Association for the Advancement of Science, 1200 New York Avenue, NW, Washington, DC 20005. Periodicals mail postage (publication No. 484460) paid at Washington, DC, and additional mailing offices. Copyright © 2018 by the American Association for the Advancement of Science. The title SCIENCE is a registered trademark of the AAAS. Domestic individual membership, including subscription (12 months): \$165 (\$74 allocated to subscription). Domestic institutional subscription (51 issues): \$1808; Foreign postage extra: Mexico, Caribbean (surface mail) \$55; other countries (air assist delivery): \$89. First class, airmail, student, and emeritus rates on request. Canadian rates with GST available upon request. GST #125488122. Publications Mail Agreement Number 1069624. Printed in the U.S.A. Change of address: Allow 4 weeks, giving old and new addresses and 8-digit account number. Postmaster: Send change of address to AAAS, P.O. Box 96178, Washington, DC 20090-6178. Single-copy sales: \$15 each plus shipping and handling; bulk rate on request. Authorization to reproduce material for internal or personal use under circumstances not falling within the fair use provisions of the Copyright Act is granted by AAAS to libraries and others who use Copyright Clearance Center (CCC) Pay-Per-Use services provided that \$35.00 per article is paid directly to CCC, 222 Rosewood Drive, Danvers, MA 01923. The identification code for Science is 0036-8075. Science is indexed in the Reader's Guide to Periodical Literature and in several specialized indexes.

Editor-in-Chief Jeremy Berg

Executive Editor Monica M. Bradford **News Editor** Tim Appenzeller

Editor, Insights Lisa D. Chong **Editors, Research** Valda Vinson, Jake S. Yeston

Research and Insights

DEPUTY EDITORS Julia Fahrenkamp-Uppenbrink(UK), Stella M. Hurlley(UK), Phillip D. Szurmi, Sacha Vignieri **DEPUTY EDITOR, EMERITUS** Barbara R. Jasny **SR. EDITORIAL FELLOW** Andrew M. Sugden(UK) **SR. EDITORS** Gemma Alderton(UK), Caroline Ash(UK), Pamela J. Hines, Paula A. Kiberstis, Marc S. Lavine(Canada), Steve Mao, Ian S. Osborne(UK), Beverly A. Purnell, L. Bryan Ray, H. Jesse Smith, Jelena Stajic, Peter Stern(UK), Brad Wible, Laura M. Zahn **ASSOCIATE EDITORS** Michael A. Funk, Brent Grocholski, Priscilla N. Kelly, Tage S. Rai, Seth Thomas Scanlon(UK), Keith T. Smith(UK) **ASSOCIATE BOOK REVIEW EDITOR** Valerie B. Thompson **LETTERS EDITOR** Jennifer Sills **LEAD CONTENT PRODUCTION EDITORS** Harry Jach, Lauren Kmec **CONTENT PRODUCTION EDITORS** Amelia Beyna, Jeffrey E. Cook, Amber Esplin, Chris Filiatreau, Cynthia Howe **SR. EDITORIAL COORDINATORS** Carolyn Kyle, Beverly Shields **EDITORIAL COORDINATORS** Aneera Dobbins, Joi S. Granger, Jeffrey Hearn, Lisa Johnson, Maryrose Madrid, Shannon McMahon, Jerry Richardson, Alice Whaley(UK), Anita Wynn **PUBLICATIONS ASSISTANTS** Ope Martins, Nida Masulius, Dona Mathieu, Ronnel Navas, Hilary Stewart(UK), Alana Warnke, Brian White **EXECUTIVE ASSISTANT** Jessica Slater **ASI DIRECTOR, OPERATIONS** Janet Clements(UK), **ASI SR. OFFICE ADMINISTRATOR** Jessica Waldo(UK)

News

NEWS MANAGING EDITOR John Travis **INTERNATIONAL EDITOR** Martin Enserink **DEPUTY NEWS EDITORS** Elizabeth Culotta, Lila Guterman, David Grimm, Eric Hand, David Malakoff, Leslie Roberts **SR. CORRESPONDENTS** Daniel Clery(UK), Jon Cohen Jeffrey Mervis, Elizabeth Pennisi **ASSOCIATE EDITORS** Jeffrey Brainard, Catherine Maticic **NEWS WRITERS** Adrian Cho, Jennifer Couzin-Frankel, Jocelyn Kaiser, Kelly Servick, Robert F. Service, Erik Stokstad(Cambridge, UK), Paul Voosen, Meredith Wadman **INTERNS** Frankie Schembri **CONTRIBUTING CORRESPONDENTS** Warren Cornwall, Ann Gibbons, Mara Hvistendahl, Sam Kean, Eli Kintisch, Kai Kupferschmidt(Berlin), Andrew Lawler, Mitch Leslie, Eliot Marshall, Virginia Morell, Dennis Normile(Shanghai), Charles Piller, Tania Rabesandratana(London), Emily Underwood, Gretchen Vogel(Berlin), Lizzie Wade(Mexico City) **CAREERS** Donisha Adams, Rachel Bernstein(Editor), Katie Langin **COPY EDITORS** Julia Cole (Senior Copy Editor), Cyra Master (Copy Chief) **ADMINISTRATIVE SUPPORT** Meagan Weiland

Executive Publisher Rush D. Holt

Publisher Bill Moran **Chief Digital Media Officer** Josh Freeman

DIRECTOR, BUSINESS STRATEGY AND PORTFOLIO MANAGEMENT Sarah Whalen **DIRECTOR, PRODUCT AND CUSTOM PUBLISHING** Will Schweitzer **MANAGER, PRODUCT DEVELOPMENT** Hannah Heckner **BUSINESS SYSTEMS AND FINANCIAL ANALYSIS DIRECTOR** Randy Yi **DIRECTOR, BUSINESS OPERATIONS & ANALYST** Eric Knott **ASSOCIATE DIRECTOR, PRODUCT MANAGEMENT** Kris Bishop **SENIOR SYSTEMS ANALYST** Nicole Mehmedovich **SENIOR BUSINESS ANALYST** Cory Lipman **MANAGER, BUSINESS OPERATIONS** Jessica Tierney **BUSINESS ANALYSTS** Meron Kebede, Sandy Kim, Jourdan Stewart **FINANCIAL ANALYST** Julian Inari **ADVERTISING SYSTEM ADMINISTRATOR** Tina Burks **SALES COORDINATOR** Shirley Young **DIRECTOR, COPYRIGHT, LICENSING, SPECIAL PROJECTS** Emilie David **DIGITAL PRODUCT ASSOCIATE** Michael Hardesty **RIGHTS AND PERMISSIONS ASSOCIATE** Elizabeth Sandler **RIGHTS, CONTRACTS, AND LICENSING ASSOCIATE** Lili Catlett **RIGHTS & PERMISSIONS ASSISTANT** Alexander Lee

DIRECTOR, INSTITUTIONAL LICENSING Iquo Edim **ASSOCIATE DIRECTOR, RESEARCH & DEVELOPMENT** Elisabeth Leonard **SENIOR INSTITUTIONAL LICENSING MANAGER** Ryan Rexroth **INSTITUTIONAL LICENSING MANAGERS** Marco Castellani, Chris Murawski **SENIOR OPERATIONS ANALYST** Lana Guz **MANAGER, AGENT RELATIONS & CUSTOMER SUCCESS** Judy Lillibridge

WEB TECHNOLOGIES TECHNICAL DIRECTOR David Levy **PORTFOLIO MANAGER** Trista Smith **PROJECT MANAGER** Dean Robbins **DEVELOPERS** Liana Birke, Ryan Jensen

DIGITAL MEDIA DIRECTOR OF ANALYTICS Enrique Gonzales **MULTIMEDIA MANAGER** Sarah Crespi **MANAGING WEB PRODUCER** Kara Estelle-Powers **DIGITAL PRODUCER** Jessica Hubbard **VIDEO PRODUCER** Chris Burns **SOCIAL MEDIA PRODUCER** Brice Russ

DIGITAL/PRINT STRATEGY MANAGER Jason Hillman **QUALITY TECHNICAL MANAGER** Marcus Spiegel **DIGITAL PRODUCTION MANAGER** Lisa Stanford **ASSISTANT MANAGER DIGITAL/PRINT** Rebecca Doshi **SENIOR CONTENT SPECIALISTS** Steve Forrester, Antoinette Hodal, Lori Murphy **CONTENT SPECIALISTS** Jacob Hedrick, Kimberley Oster

DESIGN DIRECTOR Beth Rakouskas **DESIGN MANAGING EDITOR** Marcy Atarod **SENIOR DESIGNER** Chrystal Smith **DESIGNER** Christina Aycock **GRAPHICS MANAGING EDITOR** Alberto Cuadra **GRAPHICS EDITOR** Nirja Desai **SENIOR SCIENTIFIC ILLUSTRATORS** Valerie Altounian, Chris Bickel **SCIENTIFIC ILLUSTRATOR** Alice Kitterman **INTERACTIVE GRAPHICS EDITOR** Jia You **SENIOR GRAPHICS SPECIALISTS** Holly Bishop, Nathalie Cary **PHOTOGRAPHY MANAGING EDITOR** William Douthitt **PHOTO EDITOR** Emily Petersen **IMAGE RIGHTS AND FINANCIAL MANAGER** Jessica Adams

SENIOR EDITOR, CUSTOM PUBLISHING Sean Sanders: 202-326-6430 **ASSISTANT EDITOR, CUSTOM PUBLISHING** Jackie Oberst: 202-326-6463 **ADVERTISING PRODUCTION OPERATIONS MANAGER** Deborah Tompkins **SR. PRODUCTION SPECIALIST/GRAPHIC DESIGNER** Amy Hardcastle **SR. TRAFFIC ASSOCIATE** Christine Hall **DIRECTOR OF BUSINESS DEVELOPMENT AND ACADEMIC PUBLISHING RELATIONS**, ASIA Xiaoying Chu: +86-131 6136 3212, xchu@aaas.org **COLLABORATION/CUSTOM PUBLICATIONS/JAPAN** Adarsh Sandhu + 81532-81-5142 asandhu@aaas.org **EAST COAST/E. CANADA** Laurie Faraday: 508-747-9395, FAX 617-507-8189 **WEST COAST/W. CANADA** Lynne Stickrod: 415-931-9782, FAX 415-520-6940 **MIDWEST** Jeffrey Dembski: 847-498-4520 x3005, Steven Loerch: 847-498-4520 x3006 **UK EUROPE/ASIA** Roger Gonçalves: TEL/FAX +41 43 243 1358 **JAPAN** Kaoru Sasaki (Tokyo): +81 (3) 6459 4174 ksasaki@aaas.org

ASSOCIATE DIRECTOR, BUSINESS DEVELOPMENT Justin Jaworsky **GLOBAL MARKETING MANAGER** Allison Pritchard **DIGITAL MARKETING ASSOCIATE** Aimee Aponte **MARKETING MANAGER, JOURNALS** Shawana Arnold **MARKETING ASSOCIATES** Mike Romano, Tori Velasquez **SENIOR DESIGNER** Kim Huynh **TRADE SHOW COORDINATOR** Andrew Clamp

GLOBAL SALES DIRECTOR ADVERTISING AND CUSTOM PUBLISHING Tracy Holmes: +44 (0) 1223 326525 **CLASSIFIED** advertise@sciencecareers.org **SALES MANAGER, US, CANADA AND LATIN AMERICA** SALES CAREERS Claudia Paulsen-Young: 202-326-6577 **EUROPE/ROW SALES** Sarah Lelarge **SALES ADMIN ASSISTANT** Kelly Grace +44 (0)1223 326528 **JAPAN** Miyuki Tani(Osaka): +81 (6) 6202 6272 mtani@aaas.org **CHINA/TAIWAN** Xiaoying Chu: +86-131 6136 3212, xchu@aaas.org

AAAS BOARD OF DIRECTORS, CHAIR Susan Hockfield **PRESIDENT** Margaret A. Hamburg **PRESIDENT-ELECT** Steven Chu **TREASURER** Carolyn N. Ainslie **CHIEF EXECUTIVE OFFICER** Rush D. Holt **BOARD** Cynthia M. Beall, May R. Berenbaum, Rosina M. Bierbaum, Kaye Husbands Fealing, Stephen P.A. Fodor, S. James Gates, Jr., Michael S. Gazzaniga, Laura H. Greene, Robert B. Millard, Mercedes Pascual, William D. Provine

SUBSCRIPTION SERVICES For change of address, missing issues, new orders and renewals, and payment questions: 866-434-AAAS (2227) or 202-326-6417, FAX 202-842-1065. Mailing addresses: AAAS, P.O. Box 96178, Washington, DC 20090-6178 or AAAS Member Services, 1200 New York Avenue, NW, Washington, DC 20005

INSTITUTIONAL SITE LICENSES 202-326-6730 **REPRINTS:** Author Inquiries 800-635-7181 **COMMERCIAL INQUIRIES** 803-359-4578 **PERMISSIONS** 202-326-6765, permissions@aaas.org **AAAS Member Central Support** 866-434-2227 www.aaas.org/membercentral

Science serves as a forum for discussion of important issues related to the advancement of science by publishing material on which a consensus has been reached as well as including the presentation of minority or conflicting points of view. Accordingly, all articles published in Science—including editorials, news and comment, and book reviews—are signed and reflect the individual views of the authors and not official points of view adopted by AAAS or the institutions with which the authors are affiliated.

INFORMATION FOR AUTHORS See www.sciencemag.org/authors/science-information-authors

BOARD OF REVIEWING EDITORS (Statistics board members indicated with \$)

Adriano Aguzzi, *U. Hospital Zürich*
Takuzo Aida, *U. of Tokyo*
Leslie Aiello, *Wenner-Gren Foundation*
Judith Allen, *U. of Manchester*
Sebastian Amigorena, *Institut Curie*
Meinrat O. Andrae, *Max Planck Inst. Mainz*
Paola Ariotti, *Harvard U.*
Johan Auwerx, *EPFL*
David Awschalom, *U. of Chicago*
Clare Baker, *U. of Cambridge*
Nenad Ban, *ETH Zürich*
Franz Bauer, *Pontificia Universidad Católica de Chile*
Ray H. Baughman, *U. of Texas at Dallas*
Carlo Beenakker, *Leiden U.*
Kamran Behnia, *ESPCI*
Yasmine Belkaid, *NIAD, NIH*
Philip Benfey, *Duke U.*
Gabriele Bergers, *VIB*
Bradley Bernstein, *Massachusetts General Hospital*
Peer Bork, *EMBL*
Chris Bowler, *Ecole Normale Supérieure*
Ian Boyd, *U. of St. Andrews*
Emily Brodsky, *U. of California, Santa Cruz*
Ron Brookmeyer, *U. of California, Los Angeles (\$)*
Christian Büchel, *UKE Hamburg*
Dennis Burton, *Scripps Research*
Carter Tribley Butts, *U. of California, Irvine*
Gyorgy Buzsaki, *New York U. School of Medicine*
Blanche Capel, *Duke U.*
Mats Carlsson, *U. of Oslo*
Ib Chorkendorff, *Denmark TU*
James J. Collins, *MIT*
Robert Cook-Deegan, *Arizona State U.*
Lisa Coussens, *Oregon Health & Science U.*
Alan Cowman, *Walter & Eliza Hall Inst.*
Roberta Croce, *VU Amsterdam*
Jeff L. Dangl, *U. of North Carolina*
Tom Daniel, *U. of Washington*
Chiara Daraio, *Caltech*
Nicolas Dauphas, *U. of Chicago*
Frans de Waal, *Emory U.*
Stanislas Dehaene, *Collège de France*
Robert Desimone, *MIT*
Claude Desplan, *New York U.*
Sandra Diaz, *Universidad Nacional de Córdoba*
Dennis Discher, *U. of Penn.*
Gerald W. Dorn II, *Washington U. in St. Louis*
Jennifer A. Doudna, *U. of California, Berkeley*
Bruce Dunn, *U. of California, Los Angeles*
William Dunphy, *Caltech*
Christopher Dye, *U. of Oxford*
Todd Ehlers, *U. of Tübingen*
Jennifer Elisseeff, *Johns Hopkins U.*
Tim Elston, *U. of North Carolina at Chapel Hill*
Nader Engheta, *U. of Pennsylvania*
Barry Everitt, *U. of Cambridge*
Vanessa Ezenwa, *U. of Georgia*
Ernst Fehr, *U. of Zürich*
Michael Feuer, *The George Washington U.*
Toren Finkel, *U. of Pittsburgh Medical Ctr.*
Kate Fitzgerald, *U. of Massachusetts*
Peter Fratzl, *Max Planck Inst. Potsdam*
Elaine Fuchs, *Rockefeller U.*
Eileen Furlong, *EMBL*
Jay Gallagher, *U. of Wisconsin*
Daniel Geschwind, *U. of California, Los Angeles*
Karl-Heinz Glassmeier, *TU Braunschweig*
Marta Gonzalez, *U. of California, Berkeley*
Ramon Gonzalez, *Rice U.*
Elizabeth Grove, *U. of Chicago*
Nicolas Gruber, *ETH Zürich*
Kip Guy, *U. of Kentucky College of Pharmacy*
Taekjip Ha, *Johns Hopkins U.*
Christian Haass, *Ludwig Maximilians U.*
Sharon Hammes-Schiffer, *U. of Illinois at Urbana-Champaign*
Wolf-Dietrich Hardt, *ETH Zürich*
Louise Harra, *U. College London*
Michael Hasselmo, *Boston U.*
Jian He, *Clemson U.*
Martin Heimann, *Max Planck Inst. Jena*
Carl-Philipp Heisenberg, *IST Austria*
Ykä Helariutta, *U. of Cambridge*
Janet G. Hering, *Eawag*
Kai-Uwe Hinrichs, *U. of Bremen*
David Hodell, *U. of Cambridge*
Lora Hooper, *UT Southwestern Medical Ctr. at Dallas*
Fred Hughson, *Princeton U.*
Randall Hulet, *Rice U.*
Auke Ijspeert, *EPFL*
Akiko Iwasaki, *Yale U.*
Stephen Jackson, *USGS and U. of Arizona*
Seema Jayachandran, *Northwestern U.*
Kai Johnsson, *EPFL*
Peter Jonas, *Inst. of Science & Technology Austria*
Matt Kaebberlein, *U. of Washington*
William Kaelin Jr., *Dana-Farber Cancer Inst.*
Daniel Kammen, *U. of California, Berkeley*
Abby Kavner, *U. of California, Los Angeles*
Masashi Kawasaki, *U. of Tokyo*
V. Narry Kim, *Seoul Nat. U.*
Robert Kingston, *Harvard Medical School*
Etienne Kochlin, *Ecole Normale Supérieure*
Alexander Kolodkin, *Johns Hopkins U.*
Thomas Langer, *U. of Cologne*
Mitchell A. Lazar, *U. of Penn.*
David Lazer, *Harvard U.*
Stanley Lemon, *U. of North Carolina at Chapel Hill*
Ottoline Leyser, *U. of Cambridge*
Wendell Lim, *U. of California, San Francisco*
Marcia C. Linn, *U. of California, Berkeley*
Jianguo Liu, *Michigan State U.*
Luis Liz-Marzán, *CIC biomaGUNE*
Jonathan Losos, *Harvard U.*
Ke Lu, *Chinese Acad. of Sciences*
Christian Lüscher, *U. of Geneva*
Fabienne Mackay, *U. of Melbourne*
Anne Magurran, *U. of St. Andrews*
Oscar Marin, *King's College London*
Charles Marshall, *U. of California, Berkeley*
Christopher Marx, *U. of Idaho*
C. Robertson McClung, *Dartmouth College*
Rodrigo Medellín, *U. of Mexico*
Graham Medley, *London School of Hygiene & Tropical Med.*
Jane Memmott, *U. of Bristol*
Tom Misteli, *NCI, NIH*
Yasushi Miyashita, *U. of Tokyo*
Richard Morris, *U. of Edinburgh*
Alison Motsinger-Reif, *NC State U. (\$)*
Daniel Neumark, *U. of California, Berkeley*
Kitty Nijmeijer, *TU Eindhoven*
Helga Nowotny, *Austrian Council*
Rachel O'Reilly, *U. of Warwick*
Harry Orr, *U. of Minnesota*
Pilar Ossorio, *U. of Wisconsin*
Andrew Oswald, *U. of Warwick*
Isabella Pagano, *Istituto Nazionale di Astrofisica*
Margaret Palmer, *U. of Maryland*
Steve Palumbi, *Stanford U.*
Jane Parker, *Max Planck Inst. Cologne*
Giovanni Parmigiani, *Dana-Farber Cancer Inst. (\$)*
Samuel Pfaff, *Salk Inst. for Biological Studies*
Matthieu Piel, *Institut Curie*
Kathrin Plath, *U. of California, Los Angeles*
Martin Plenio, *Ulm U.*
Albert Polman, *FOM Institute for AMOLF*
Elvira Poloczanska, *Alfred-Wegener-Inst.*
Philippe Poulin, *CNRS*
Jonathan Pritchard, *Stanford U.*
David Randall, *Colorado State U.*
Sarah Reisman, *Caltech*
Félix A. Rey, *Institut Pasteur*
Trevor Robbins, *U. of Cambridge*
Amy Rosenzweig, *Northwestern U.*
Mike Ryan, *U. of Texas at Austin*
Mitsunori Saitou, *Kyoto U.*
Shimon Sakaguchi, *Osaka U.*
Niquel Salmeron, *Lawrence Berkeley Nat. Lab*
Nitin Samarth, *Penn. State U.*
Jürgen Sandkühner, *Medical U. of Vienna*
Alexander Schier, *Harvard U.*
Wolfram Schlenker, *Columbia U.*
Susannah Scott, *U. of California, Santa Barbara*
Vladimir Shaleev, *Purdue U.*
Beth Shapiro, *U. of California, Santa Cruz*
Jay Shendure, *U. of Washington*
Brian Shoichet, *U. of California, San Francisco*
Robert Siliciano, *Johns Hopkins U. School of Medicine*
Uri Simonsohn, *U. of Penn.*
Lucia Sivilotti, *U. College London*
Alison Smith, *John Innes Centre*
Richard Smith, *U. of North Carolina at Chapel Hill (\$)*
Mark Smyth, *QIMR Berghofer*
Pam Soltis, *U. of Florida*
John Speakman, *U. of Aberdeen*
Tara Spire-Jones, *U. of Edinburgh*
Allan C. Spradling, *Carnegie Institution for Science*
Eric Steig, *U. of Washington*
Marka Stephan, *Georgia State U.*
V. S. Subrahmanian, *U. of Maryland*
Ira Tabas, *Columbia U.*
Sarah Teichmann, *U. of Cambridge*
Shubha Tole, *Tata Inst. of Fundamental Research*
Wim van der Putten, *Netherlands Inst. of Ecology*
Bert Vogelstein, *Johns Hopkins U.*
David Wallach, *Weizmann Inst. of Science*
Jane-Ling Wang, *U. of California, Davis (\$)*
David Waxman, *Fudan U.*
Jonathan Weissman, *U. of California, San Francisco*
Chris Wikle, *U. of Missouri (\$)*
Terrie Williams, *U. of California, Santa Cruz*
Ian A. Wilson, *Sciparis Research (\$)*
Timothy D. Wilson, *U. of Virginia*
Yu Xie, *Princeton U.*
Jan Zaenen, *Leiden U.*
Kenneth Zaret, *U. of Penn. School of Medicine*
Jonathan Zehr, *U. of California, Santa Cruz*
Maria Zuber, *MIT*

Space for nature

How much of the planet should we leave for other forms of life? This is a question humanity must now grapple with. The global human population is 7.6 billion and anticipated to increase to around 10 billion by the middle of the century. Consumption is also projected to increase, with demands for food and water more than doubling by 2050. Simply put, there is finite space and energy on the planet, and we must decide how much of it we're willing to share. This question requires deep consideration as it will determine the fate of millions of species and the health and well-being of future generations.

About 20% of the world's vertebrates and plants are threatened with extinction, mostly because humans have degraded or converted more than half of the terrestrial natural habitat. Moreover, we are harnessing biomass from other forms of life and converting it into crops and animals that are more useful to us. Livestock now constitute 60% of the mammalian biomass and humans another 36%. Only 4% remains for the more than 5000 species of wild mammals. This ratio is not surprising: Wild vertebrate populations have declined by more than 50% since 1970. Both from an ethical and a utilitarian viewpoint, this depletion of natural ecosystems is extremely troubling.

Most scientific estimates of the amount of space needed to safeguard biodiversity and preserve ecosystem benefits suggest that 25 to 75% of regions or major ecosystems must be protected. But estimating how much space is required to protect current levels of biodiversity and secure existing ecosystem benefits is challenging because of limited knowledge of the number of species on this planet, poor understanding of how ecosystems function or the benefits they provide, and growing threats such as climate change. Thus, spatial targets will be associated with great uncertainty. However, targets set too low could have major negative implications for future generations and all life. Any estimate must therefore err on the side of caution.



Spix's macaw, native to Brazil, is critically endangered.

“Current levels of protection do not even come close to the required levels.”

Current levels of protection do not even come close to the required levels. Just less than half of Earth's surface remains relatively intact, but this land tends to be much less productive. Only 3.6% of the oceans and 14.7% of land are formally protected. Many of these protected areas are “paper parks,” meaning they are not effectively managed, and one-third of the terrestrial protected lands are under intense human pressure.

At the 2010 Nagoya Conference of the Convention on Biological Diversity, the world's governments convened to agree on an ambitious “strategic plan for biodiversity” and adopted 20 Biodiversity Targets, widely referred to as the Aichi Targets. The 11th Target states that by 2020, at least 17% of the terrestrial and inland water, and 10% of coastal and marine areas, should be conserved. Target 12 advocates for preventing extinction of known species, and Target 14 advocates for the safeguarding of ecosystems that provide essential services. These goals beg the question: Would achieving Target 11 be sufficient to allow the achievement of Target 12 or 14? Current scientific evidence suggests that it would be woefully inadequate for the task.

If we truly want to protect biodiversity and secure critical ecosystem benefits, the world's governments must set a much more ambitious protected area agenda and ensure it is resourced. In 2020, the world's governments will meet at the Convention on Biological Diversity in Beijing, China, to set biodiversity targets for the future. Given the evidence to date and the implications of an underestimate, we encourage governments to set minimum targets of 30% of the oceans and land protected by 2030, with a focus on areas of high biodiversity and/or productivity, and to aim to secure 50% by 2050. This will be extremely challenging, but it is possible, and anything less will likely result in a major extinction crisis and jeopardize the health and well-being of future generations.

–Jonathan Baillie and Ya-Ping Zhang



Jonathan Baillie
is executive vice president and chief scientist at the National Geographic Society, Washington, DC, USA. jbaillie@ngs.org



Ya-Ping Zhang
is a biologist at the Kunming Institute of Zoology, Chinese Academy of Sciences, Beijing, China. zhangyp@mail.kiz.ac.cn



TOMORROW'S EARTH

Read more articles online at scim.ag/TomorrowsEarth

IN BRIEF

Edited by Lila Guterman

GEOLOGY

Slippery layer raised Japan quake deaths



Landslides peppered the area near the earthquake's epicenter.

The 6 September 6.6-magnitude earthquake that struck Hokkaido, Japan's northernmost main island, caused extensive landslides that surprised both residents and scientists. Most of the 41 people who died as a result of the quake were buried by the landslides, which occurred close to the epicenter, 65 kilometers southeast of Sapporo. Some researchers suspect several unusual factors came together to create disaster. First, a typhoon that passed through Japan just 2 days before the quake soaked the soil, making it heavy. A few meters deep at the quake site are layers of structurally weak volcanic deposits from long-past eruptions. The material is porous and gets slippery when wet. The earthquake stress caused the volcanic layer to split, allowing the rain-laden soil to slip down the slope. At least one other researcher says on-the-ground investigations are needed to verify this scenario.

Trump taps climate doubter

SCIENCE POLICY | Physicist William Happer, an emeritus professor at Princeton University and critic of mainstream climate science, has joined the White House. Happer, who was a Department of Energy official under former President George H.W. Bush, will focus on emerging technologies on President Donald Trump's National Security Council, according to media reports. Happer has accused federal research agencies of manipulating climate data and asserted that the planet could benefit from higher atmospheric concentrations of carbon dioxide (CO₂), because the warming gas fuels plant growth. Happer said in January that he supported Trump's decision to pull the United States out of the Paris climate accord. "There is no problem from CO₂," he said.

Vertebrate genomes unveiled

BIOLOGY | This week, marking a fresh start for a project that began in 2009, researchers released high-quality genomes of 14 species from across the vertebrate family tree. Thanks to the adoption of new sequencing technologies and software, the Vertebrate Genomes Project says it can generate additional genomes for about \$15,000 per 1 billion bases. They will be at least as complete as the best human genome, says project head Erich Jarvis, a neuroscientist at The Rockefeller University in New York City. The newly released genomes include a kakapo—an endangered New Zealand parrot—named Jane, a Canadian lynx, a newly discovered turtle species from Mexico, a legless amphibian called a caecilian, and two cichlids—one that's a popular aquarium fish and another that's the object of extensive evolutionary studies. Next, the scientists hope to sequence a representative of each of the 266 major branches of the vertebrate family tree. To reach the goal of all 66,000 vertebrates will require about \$600 million.

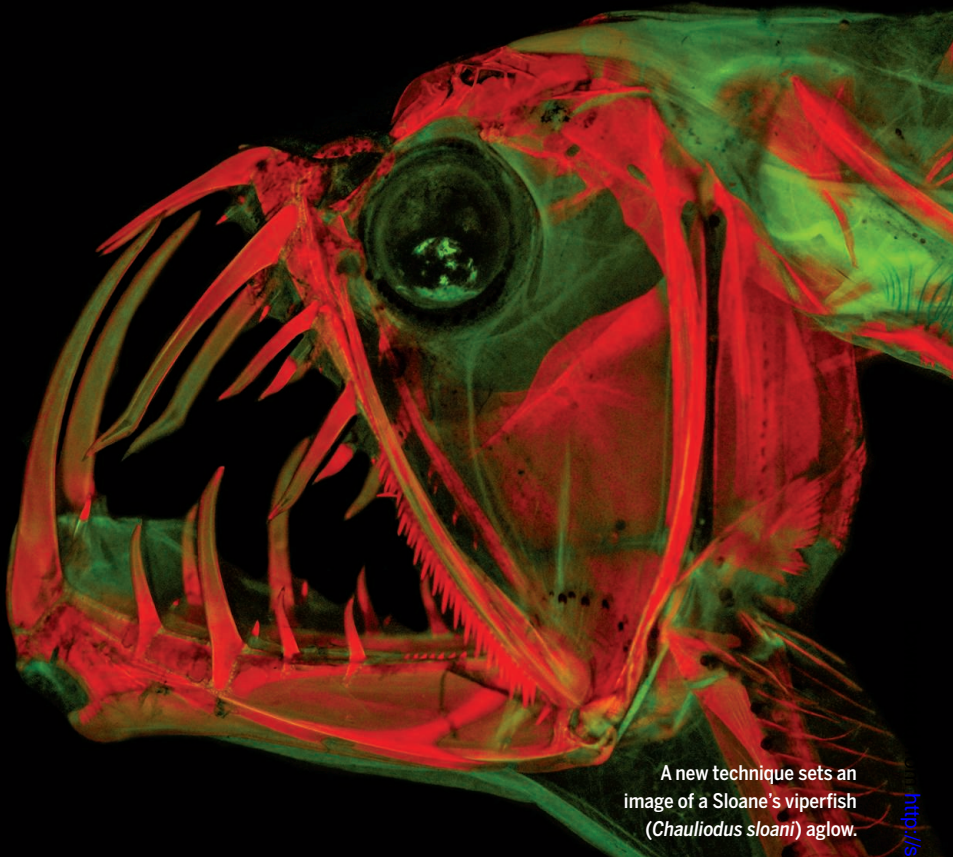
Google adds data searches

INFORMATION SCIENCE | Google is now doing for data what it's done for news articles, movie times, academic papers, and cat photos: It is providing a search

IMAGING

Scans light up anatomy

A new version of a decades-old technique makes anatomical images pop like never before. In the technique, called clearing and staining, scientists dip fish, amphibian, reptile, and mammal specimens in chemical baths that make the flesh transparent. Several more baths dye cartilage bright blue and bones bright red. But some detail gets lost. To enhance the method's images, researchers at the University of Kansas in Lawrence and St. Cloud State University in Minnesota shined specific wavelengths of light on the dyed specimens and then filtered out all colors except red or green. The resulting images—in which the bones are still red, but soft tissues appear green—help differentiate between tissues, the team reports in the September issue of *Copeia*. The technique might prove useful for imaging fossils because scientists could use it to “delete” the surrounding rock from scans to focus on the bones. Another improvement: The scientists figured out a way to get floppy specimens to sit up straight. By adding a little gelatin to a bath of 40% glycerin in water, the researchers had just enough time to pose their creatures before they hardened into place.



A new technique sets an image of a Sloane's viperfish (*Chauliodus sloani*) aglow.

tool for convenient access. Last week, the Mountain View, California-based company launched Dataset Search. Type in a phrase such as “sea surface temperature” or “social vulnerability,” and it will point to data sets stored online in repository sites such as figshare, and on university and government web pages. Users can also access information about the data set authors, publication dates, and descriptions. The search now focuses on environmental and social sciences, but as more disciplines push for open data, the tool's results should expand, Google says.

Study results go undisclosed

CLINICAL TRIALS | Nearly nine in 10 university clinical studies fail to report results within the 1-year time frame set by the European Union, says a study in *The BMJ* from the University of Oxford in the United Kingdom. The rules, which apply to studies done in the European Union, went into effect in late 2016, but there is no punishment for those who haven't complied, the authors say. About half of 7274 completed trials met the requirement, the Oxford team found. Only 11% of noncommercial trials in the study complied, compared with 68% of commercial ones. The worst offenders include the Karolinska Institute in Stockholm and the Charité University Hospital in Berlin, which together owe results on 84 trials and have reported none.

Pulsar discoverer to donate prize

NEWSMAKER | Jocelyn Bell Burnell, an astrophysicist at the University of Oxford in the United Kingdom, last week won a Breakthrough Prize for her role in the discovery 50 years ago of pulsars, rapidly spinning neutron stars. She says she will use the \$3 million that comes with the award to establish a scholarship for women and ethnic minority students in physics. In 1967, as a graduate student, Bell Burnell used a radio telescope she helped build to detect regular signals from what turned out to be pulsars, the remains of collapsed stars. The clocklike signals have since been used to test Albert Einstein's theory of relativity, observe the first exoplanets, and infer the existence of gravitational waves. Her thesis adviser, Antony Hewish, shared the 1974 Nobel Prize in Physics for the discovery, but Bell Burnell was overlooked.

Gene-editing tool shows promise

BIOMEDICINE | The first test of a gene-editing tool in people has yielded hints that it could help treat a rare, inherited metabolic disorder. The disorder, Hunter syndrome, results from the lack of an enzyme to break down certain sugars. The experimental treatment was developed by biotech company Sangamo Therapeutics of Richmond, California. It uses a harmless virus to deliver DNA for zinc finger nucleases to the liver,

where they snip the genome at a specific spot. The virus also carries a gene for the missing enzyme, which fills the break. After 4 months, two patients' urine levels of the excess sugars dropped by 39% and 63%. But their bodies weren't making detectable blood levels of the missing enzyme. Results for two patients who received a higher dose are expected early next year.

Report calls for exoplanet imager

ASTRONOMY | To search for life on other worlds, NASA should build a large space telescope to directly image Earth-like planets around other sunlike stars, according to a 5 September report from the National Academies of Sciences, Engineering, and Medicine (NASEM). The telescope should have a starshade or a coronagraph, two ways of blocking starlight to reveal faint reflected light from the planet. The report says giant ground-based telescopes would also aid in characterizing Earth-like exoplanets, and it calls on the National Science Foundation (NSF) to support both the Giant Magellan Telescope and the Thirty Meter Telescope, two rival projects (*Science*, 25 May, p. 839). Astronomers will soon begin the 2020 decadal survey, a separate NASEM effort to prioritize future NASA and NSF projects. Two of four proposed space telescopes that the survey will consider would satisfy many of the science requirements in the exoplanet report.



PARTICLE PHYSICS

Physicists plan hunt for Higgs boson pairs

Rare double-Higgs events at the Large Hadron Collider could point to new physics

By **Adrian Cho**

For particle physicists eager to explore new frontiers, spotting the Higgs boson has become a bittersweet triumph. Detected in 2012 at the world's biggest atom smasher, the Large Hadron Collider (LHC), the long-sought particle filled the last gap in the standard model of fundamental particles and forces. But since then, the standard model has stood up to every test, yielding no hints of new physics. Now, the Higgs itself may offer a way out of the impasse. Experimenters at the LHC, located at CERN, the European particle physics laboratory near Geneva, Switzerland, plan to hunt for collisions that produce not just one Higgs boson, but two. Finding more of these rare double-Higgs events than expected could point to particles or forces beyond the standard model and might even help explain the imbalance of matter and antimatter in the universe.

"This is the next big thing," says Sally Dawson, a theorist at Brookhaven National Laboratory in Upton, New York, and an organizer of a workshop last week at the Fermi National Accelerator Laboratory (Fermilab) in Batavia, Illinois, where more than 100 physicists gathered to hone the conceptual tools needed for the long search.

The Higgs boson plays a special role in the standard model, which describes how a dozen types of particles interact through

three forces: electromagnetism and the weak and strong nuclear forces. (The theory does not include gravity, a major failing.) The forces in the model arise from certain mathematical symmetries. But that math works only so long as the particles do not start out with mass. So mass must somehow emerge through interactions among the otherwise massless particles themselves.

That's where the Higgs comes in. Physicists assume that space contains a Higgs field—a bit like an electric field—generated by Higgs bosons lurking in the vacuum. Particles interact with the field to gain energy and, through Albert Einstein's famous equation, $E=mc^2$, mass.

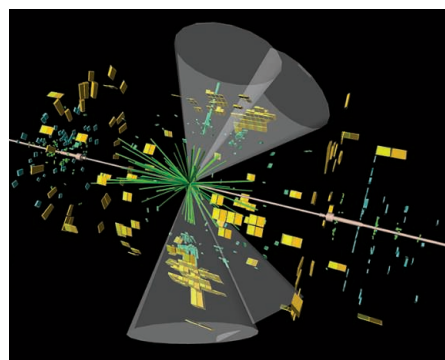
This Higgs mechanism received resounding support 6 years ago, when experimental-

ists working with the two biggest particle detectors fed by the LHC, A Toroidal LHC Apparatus (ATLAS) and the Compact Muon Solenoid (CMS), blasted into existence a fleeting particle weighing 133 times as much as a proton. It decays in the ways that the Higgs is supposed to—for example, into a pair of photons. But physicists aren't sure whether they've observed the standard model Higgs boson or something subtly different.

Double-Higgs events promise a way to tell for sure, by revealing how strongly the Higgs field interacts with itself. An electric field vanishes if there's no charge around, but the Higgs field must always linger in the vacuum—or else it wouldn't be able to impart mass to other particles. The standard model presumes this happens with a Higgs field that interacts with itself and minimizes its energy not by vanishing, but by taking a nonzero strength.

Mathematically, there are many ways to cook up such a scheme, and the standard model employs the simplest one, controlled by just one parameter. That parameter, in turn, predicts the rate at which Higgs pairs should emerge in particle collisions—giving physicists a way to test the standard model.

The challenge is finding the extremely rare decays. The standard model predicts that for every 10,000 proton-proton collisions at the LHC that produce a single Higgs boson, roughly six will produce a pair. Those double-Higgs events should generate messy showers



Two Higgs bosons may have decayed into bottom quarks in this 2016 collision in the ATLAS detector.

The giant CMS detector at the Large Hadron Collider will search for double-Higgs events.

of other particles, making them even harder to identify. The LHC has already probably produced about 1000 double-Higgs events, but ATLAS and the CMS cannot yet come close to sifting a signal from the background.

However, LHC experimenters say they're optimistic about their chances, especially because their techniques for spotting Higgs bosons are improving. Last month, they announced proof they had detected a particularly messy decay mode in which a Higgs spawns a pair of massive particles called bottom quarks, as it should in nearly 60% of all decays. That bodes well for double-Higgs searches because they rely on at least one Higgs in the pair decaying in this most probable way.

The LHC experiments may need years to see a signal. Later this year, the LHC will idle for 2 years for upgrades. In 2026 it will undergo another 2-year hiatus to boost its collision rate. The so-called High-Luminosity LHC would then run until 2034. On paper, only the full run will yield enough data to validate the standard model prediction. However, some physicists think they can beat that timetable as their Higgs-spotting algorithms continue to improve. "Even before the High-Luminosity LHC, I think we could get close to the standard model prediction," says Caterina Vernieri, a CMS member at Fermilab.

Of course, all LHC experimenters hope the rate for double-Higgs events will exceed the standard model prediction. It cannot be sky high or it would run into indirect constraints from the observed Higgs decays, says Eleni Vryonidou, a theorist at CERN. Still, the double-Higgs rate could be as much as six times as big as the standard model prediction, she estimates.

Such an enhancement would indicate a strongly self-interacting Higgs field. It could also signal fleeting new particles that tend to decay into Higgses, such as heavier Higgs partners predicted by many standard model extensions. And it might have implications far beyond particle physics, says Marcela Carena, a theorist at Fermilab. Physicists don't know why the infant universe ended up with more matter than antimatter. But Carena says the sudden emergence of a strongly self-interacting Higgs field might have locked in the imbalance.

Even if the rate of double-Higgs events doesn't defy standard model predictions, the quest to count them will pay off handsomely, says Katharine Leney, an ATLAS experimentalist at University College London. "What's driving a lot of people, including myself, is being able to say once and for all, by God, it is or isn't the standard model Higgs." ■

INFECTIOUS DISEASE

Steep drop in Zika cases undermines vaccine trial

Controversial strategy of intentionally infecting volunteers to test vaccine candidates is now back on the agenda

By Jon Cohen

In 2016, as the mosquito-borne Zika virus spread through the Americas and cases of infected women having brain-damaged babies mounted, investigators raced to develop a vaccine. Now, a \$110 million vaccine trial is underway at 17 sites in nine countries, but it faces an unexpected, and ironic, challenge. Cases of Zika have plummeted to levels so low that most people vaccinated in the trial likely will never be exposed to the virus, which could make it impossible to tell whether the vaccine works.

"Right now, there are no infections, and certainly not enough to even think about an efficacy signal at this point," says Anthony Fauci, director of the U.S. National Institute of Allergy and Infectious Diseases (NIAID) in Bethesda, Maryland, which launched the trial. Human trials of other Zika vaccine candidates at earlier stages are also in limbo, and last year one large vaccinemaker pulled the plug on development of its candidate. But NIAID and others are pressing ahead, saying a vaccine might someday be needed. To make up for the lack of new cases, other investigators are turning to an unusual, and ethically complex, strategy. Starting next year, *Science* has learned, they plan to test a vaccine by deliberately infecting people with Zika.

Launched in March 2017, NIAID's placebo-controlled vaccine trial includes two sites in

Brazil, where Zika hit hardest and where the brain damage known as microcephaly first surfaced. From the beginning of the outbreak in 2015 until the start of this year, Brazil had about half of all 800,000 suspected and confirmed Zika cases in the Americas, according to the Pan American Health Organization in Washington, D.C. But from January through June, Brazil's Ministry of Health reported fewer than 7000 probable cases, in a nation of 200 million people. "It's a good dilemma because we don't have Zika anymore," says Esper Kallás of the University of São Paulo in São Paulo, Brazil, principal investigator for the local NIAID site. "But it's a dilemma. Everybody is concerned about it. It's a lot of investment."

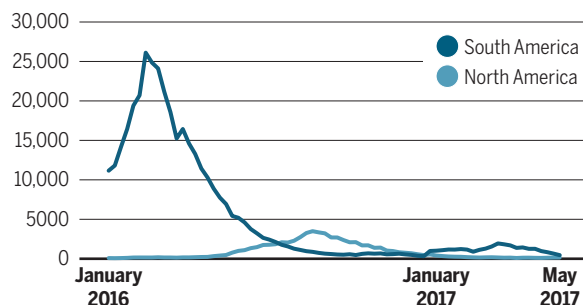
To date, 1380 participants have enrolled in the trial, which tests a vaccine containing a small circular piece of DNA that holds two Zika genes. From the outset, the researchers had planned to open new trial sites at infection hot spots, if needed. But new cases have dropped to a trickle throughout the Americas (see graph, below).

Further complicating the trial, many people throughout Latin America and the Caribbean have already been infected with Zika and recovered, which has left them immune to the virus and hence ineligible for vaccine trials. "We have problems finding people to participate," Kallás says. Indeed, nearly 50% of 2147 Nicaraguans studied in Managua—which is not a site in the NIAID trial—tested positive for antibodies to the Zika virus between January and September 2016, a group reported 27 August in the *Proceedings of the National Academy of Sciences*.

Kallás says evidence of efficacy could still emerge from areas of São Paulo that, inexplicably, have had little Zika. Those pockets, where less than 5% of the people test positive for Zika antibodies, remain susceptible to the outbreaks that could give the vaccine a real test. "There's this sense the epidemic

Zika's vanishing act

Weekly counts of new Zika cases, suspected and confirmed, have plummeted in North and South American countries hosting a vaccine trial.



will hit our region, but we don't know when," Kallás says. "We don't understand why it didn't happen already."

Given the drop in cases, a surer way to test any vaccine against Zika is to deliberately expose inoculated subjects to the virus. Researchers have used this strategy, known as a human challenge trial, for decades to test vaccines against diseases that either can be effectively treated or, like Zika, typically cause mild symptoms.

But in 2017, an ethics committee convened by NIAID and the Walter Reed Army Institute of Research in Silver Spring, Maryland, called it "premature" for Zika. They worried that people intentionally infected with the virus might transmit it to their sexual partners, primarily through infected semen. And they were confident that traditional field trials could test the efficacy of the leading vaccine candidates.

The report froze plans for a human challenge study, which NIAID had agreed to fund. "It was a great setback," says the study's leader, Anna Durbin of the Johns Hopkins University Bloomberg School of Public Health in Baltimore, Maryland. "If we had been allowed to go forward, we'd know today which vaccine candidates look good."

Now, the study is being considered again, as Zika disappears from the region and industry loses interest in bringing a vaccine to market. In a major blow, Sanofi Pasteur halted work on its vaccine, licensed from Walter Reed, in September 2017. "There's a compelling reason to conduct a human challenge trial now," says bioethicist Seema Shah of Northwestern University's Feinberg School of Medicine in Chicago, Illinois, who chaired the 2017 ethics com-

mittee. But, she adds, "The details are complicated and it's important to have a rigorous review."

"If they're careful, we have no problems supporting it," Fauci says. Durbin plans to submit her new protocol for review in about a month, and in early 2019 hopes to start injecting Zika virus into people immunized with a vaccine containing live, but weakened Zika virus made by NIAID's Stephen Whitehead. As a precaution, she plans to enroll only women at first, to avoid semen transmission from infected males. The volunteers will receive a low dose of Zika virus, and they will remain in clinics for the 2 weeks it typically takes to clear the infection. Any vaccine that works in the challenge study theoretically could then be evaluated in a real-world outbreak—just as is occurring now with an unlicensed but promising Ebola vaccine.

The much larger NIAID trial could also pay off, even if it doesn't show whether the Zika vaccine is effective. It will yield data on safety and immune responses; combined with animal data on efficacy, the results might be enough for the U.S. Food and Drug Administration to license the vaccine, Fauci says.

But regardless of whether the trial leads to an approved vaccine, he has no regrets about launching it. "Zika was a very ominous threat just a couple of years ago, and there is certainly the possibility that it is going to come back," Fauci says. "It's a risk that you'll spend this money and never use the vaccine, but balancing the importance of this infection and the impact it could have, we felt it was a good decision to move ahead. And I would be happy to defend that anywhere." ■

BIOMEDICINE

New cancer-fighting cells enter trials

Engineered natural killer cells and macrophages may be next immunotherapies

By Mitch Leslie

The cancer fighters known as CAR T cells have proved their prowess in recent years. Three therapies using the altered T cells against lymphoma or leukemia have won U.S. Food and Drug Administration approval, and hundreds of trials are now unleashing them on other malignancies, including solid tumors. But the cells may soon have company. Researchers have equipped other immune guardians—natural killer cells and macrophages—with the same type of cancer-homing receptor, and the natural killer cells have made their debut in clinical trials.

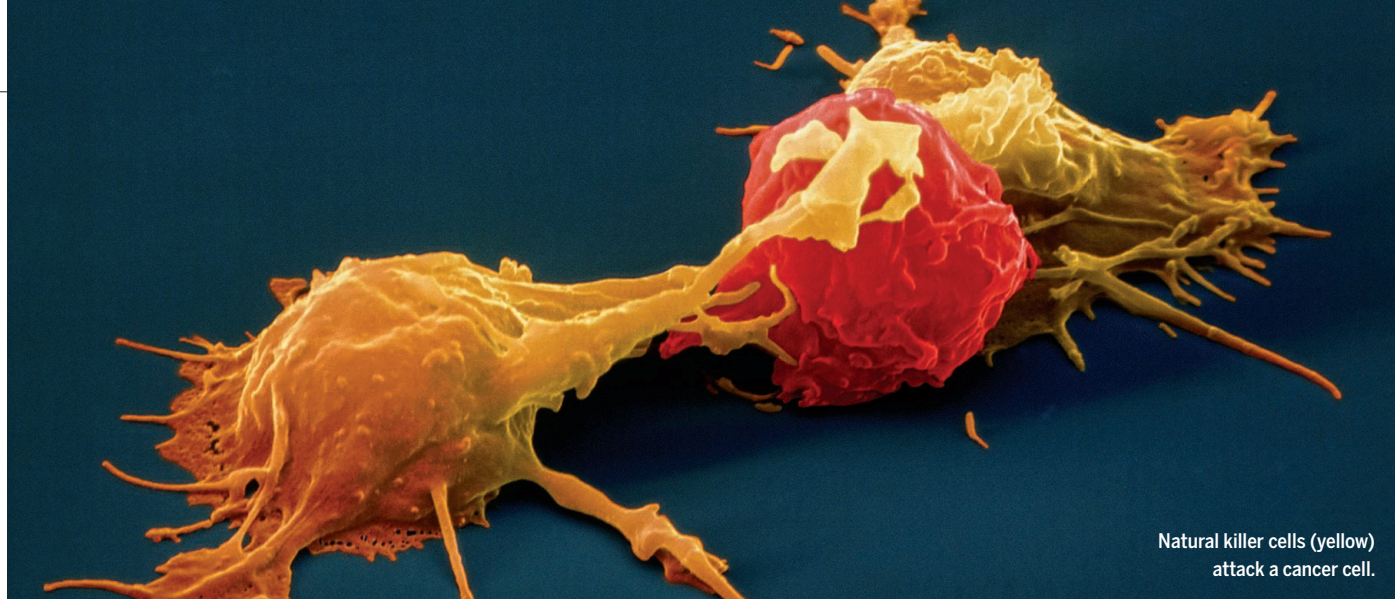
CAR T cells—their name comes from the chimeric antigen receptor, or CAR, added to help the immune cells target cancer cells—inspired the new work. CAR natural killer (CAR NK) cells could be safer, faster to produce, and cheaper, and they may work in situations where T cells falter. CAR-carrying macrophages also have potential advantages, and one firm plans to launch the first clinical trials of these cells next year.

Although they aren't likely to replace CAR T cells, these alternative cancer fighters "could be an addition to the armamentarium of cell therapies," says hematologist and oncologist Katy Rezvani of the University of Texas MD Anderson Cancer Center in Houston. She is leading the first trial of CAR NK cells in the United States, which began in 2017, and organizing another that is due to start this year.

Making CAR T cells involves removing patients' own T cells and genetically altering them to attack cancer cells that carry a specific immune-stimulating molecule, or antigen. (All of the CAR T treatments approved so far target the CD19 protein on cancerous B cells, a type of immune cell.) The cells have produced impressive results in clinical trials—in one study, they triggered remissions in 83% of children with previously untreatable acute lymphoblastic leukemia. But some patients who have



A Brazilian mother holds her daughter, who was born in 2016 with microcephaly, a Zika-caused birth defect.



Natural killer cells (yellow)
attack a cancer cell.

already undergone chemotherapy or radiation treatment may not have enough T cells left to donate. And these powerful immune warriors can trigger a potentially fatal flood of the immune system molecules known as cytokines or turn against normal body cells.

Perhaps the biggest shortcoming of CAR T cells, though, is they don't work well against solid tumors, says hematologist and oncologist Saar Gill of the University of Pennsylvania. Tumors rebuff T cells that try to enter, inhibit immune cells that do make it inside, and can curb production of antigens targeted by CAR T cells. Researchers are trying several approaches to improve CAR T cells' performance against solid tumors. But NK cells are a tempting alternative, scientists say.

"Natural killer cells are our first line of defense against cancer cells," Rezvani says. They scan other cells in the body and destroy any that are infected or otherwise abnormal, including tumor cells. Researchers have been trying to harness the cancer-fighting activity of NK cells that don't carry CARs for more than 20 years, notes translational immunologist Jeffrey Miller of the University of Minnesota in Minneapolis. But upgrading them by adding CARs seems to boost their potency.

Earlier this year, for instance, stem cell biologist Dan Kaufman of the University of California (UC), San Diego, and colleagues reported that in mice, CAR NK cells perform about as well against ovarian tumors as CAR T cells do—and substantially better than unaltered NK cells. Mouse trials also suggest CAR NK cells may not cause some of the side effects of CAR T cells, such as excess cytokine release and neurological damage. CAR NK cells might also be less vulnerable to some of tumors' tricks for avoiding attacks. Because NK cells rely on other receptors to recognize tumor cells, not just the CAR, they may be able to detect a tumor even if it alters its antigens. In addition, Kaufman points out, it may be feasible to give patients multiple doses of CAR NK cells and hammer away at

tumors, whereas the cost of CAR T cells limits patients to a single dose.

The first trials of CAR NK cells started in China in 2016 in patients with several kinds of cancers—early results from one suggest the cells are safe. Rezvani and colleagues' initial trial is pitting the cells against several varieties of lymphoma and leukemia. A European trial, which is testing CAR NK cells in patients with the brain cancer glioblastoma, launched this year. In the upcoming MD Anderson trial, patients with B cell lymphoma, a type of blood cancer, will receive stem cell transplants and chemotherapy before CAR NK cells, which the researchers hope will mop up any remaining cancer cells.

"I think the future is bright for CAR NK cells, but we are at the very beginning," says hematologist Mitchell Cairo of the New York Medical College in Hawthorne. One unknown is the best source for the cells. T cells from someone other than the patient can trigger a potentially fatal immune complication known as graft-versus-host disease, in which the transplanted cells attack the recipient's own tissues. But NK cells from a donor do not appear to cause that response, which opens a range of options. Although sieving NK cells from donors' blood is a possibility, the procedure is expensive and can harm the donors. Both MD Anderson trials instead rely on NK cells isolated from umbilical cord blood and then implanted with CARs. Donated umbilical cord blood is abundant and plenty of NK cells can be grown from it.

In contrast, the Chinese and European trials generated enough NK cells by turning to a cell line derived from a person with a type of lymphoma. These cells are staples of clinical trials, and despite their cancerous origin, they appear to be safe, says immunologist Torsten Tonn of the Technical University of Dresden in Germany, one of the researchers participating in the glioblastoma trial. Kaufman and colleagues are also exploring another possible source of NK

cells: induced pluripotent stem cells, which are produced by nudging adult body cells to return to an unspecialized state.

All these approaches could lead to off-the-shelf CAR NK cells that avoid the need to extract and modify a cancer patient's own cells. The patient's immune system will eventually reject any foreign NK cells, Miller notes. But before that happens, Rezvani and other researchers think the donor NK cells will have a window of time during which they can combat cancer cells. The question, she says, is whether they will persist long enough to benefit patients.

Like NK cells, macrophages can destroy cancer cells, but the catch is that most macrophages inside a tumor are traitors, which help the tumor by quashing immune attacks against it, for example. "Tumors acquire macrophages to support their own growth and turn them into their minions," Gill says. But he and graduate student Michael Klichinsky have discovered that the procedure for equipping macrophages with a CAR prevents them from switching sides. The duo helped found a company, Carisma Therapeutics in Philadelphia, Pennsylvania, that expects to begin clinical trials of CAR macrophages next year.

At least in the lab, adding a CAR to macrophages boosts their tumor-fighting abilities, just as it does for other immune cells, postdoc Meghan Morrissey of UC San Francisco and colleagues have also reported. But tumor immunologist Kim O'Neill of Brigham Young University in Provo, Utah, who leads another group trying to improve the cells' tumor-killing abilities, suggests macrophages could do the most good by recruiting other immune cells. T cells, for example, respond to the cellular debris left over when a macrophage digests a tumor cell, so he envisions that patients would receive CAR macrophages along with CAR T cells. Like great detectives, even the most powerful cancer-fighting cells might benefit from a talented sidekick. ■

EARTH SCIENCE

NASA space laser targets melting poles

ICESat-2 is set to reveal disappearing sea ice and retreating glacier beds

By Paul Voosen

Nowhere are the realities of human-driven climate change more apparent than at Earth's thawing poles. Arctic sea ice is vanishing, while melting ice sheets in Greenland and Antarctica are driving an acceleration in sea level rise. Yet for nearly a decade, NASA has lacked a dedicated satellite to measure how high the polar ice is piled—and how it is subsiding as ice melts or slides into the oceans.

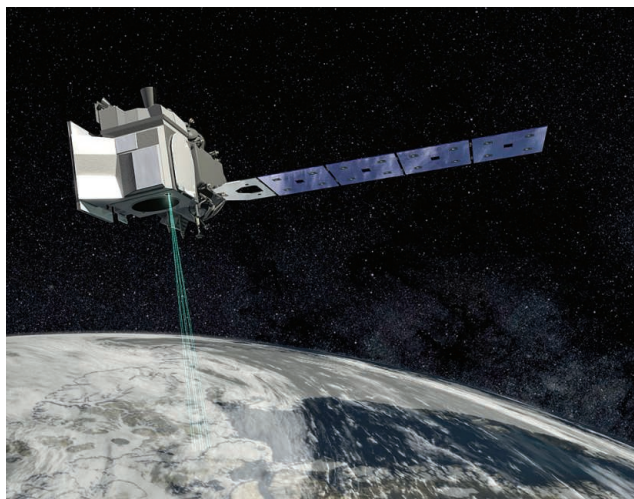
That gap is set to close with the 15 September launch of the \$1 billion Ice, Cloud and land Elevation Satellite (ICESat-2) from Vandenberg Air Force Base in California. ICESat-2 will bounce laser light off Earth's surface, gauging changes in its elevation as small as the diameter of a pencil. Although the mission is a successor in name to ICESat-1, which ended in 2010, its multibeam laser instrument puts it in a different class, says Ted Scambos, a glaciologist at the National Snow & Ice Data Center in Boulder, Colorado. "Every season we'll get a better map than ICESat-1 ever made."

Whereas ICESat-1 wielded a single laser beam, ICESat-2 has three pairs of parallel beams, enabling it to scan along multiple paths at once. (The pairings are needed to calculate slopes across a given track, which will help avoid misinterpretations of ice loss when a slightly offset return pass identifies changes in elevation.) Its resolution is also far higher: Where ICESat-1 took readings once every 150 meters along its track, ICESat-2 will record elevations every 70 centimeters, firing its lasers 10,000 times a second. The frequent firing means each pulse is relatively weak; to capture the faint reflections, the satellite uses a small telescope to funnel light to sensitive vacuum tubes that can detect single photons. "I'm a physicist, and I'm still shocked it works," says Thorsten Markus, the mission's project scientist at NASA's Goddard Space Flight Center in Greenbelt, Maryland.

ICESat-2's advances didn't come cheap. Crystals used to amplify its lasers cracked when their metallic mounts expanded unexpectedly. Repairing them and addressing other complications delayed the original

2016 launch date and caused costs to balloon by hundreds of millions of dollars.

During the long wait scientists kept an eye on polar ice with the European Space Agency's (ESA's) CryoSat-2, which uses radar to detect height. But its readings have lower resolution because of its wider radar beam. NASA also mounted an annual airplane-based campaign called IceBridge, which worked well for Greenland but could not cope with the vast expanse of Antarctica, says Beata Csatho, a remote-sensing glaciologist at the University at Buffalo, part of the State University of New York sys-



ICESat-2's three paired laser beams will cover the poles more quickly than its predecessor, and at higher resolution.

tem. "For Antarctica this gap is really huge. We really don't know what's happened."

A first task for ICESat-2 will be to assess the blank white mystery that is the East Antarctic Ice Sheet, Earth's most massive. Extreme cold and high elevation are thought to protect it from major ice loss, but scientists want to understand how snowfall, melting ice, and shifting bedrock contribute to tiny changes in elevation. The satellite will also be able to peer into the crags of the Antarctic Peninsula, which, despite its small size, is responsible for a quarter of the continent's ice loss. "That will certainly be the first place I look," says Andrew Shepherd, a glaciologist at the University of Leeds in the United Kingdom and principal scientific adviser for CryoSat-2. He notes that CryoSat-2's radar beam is too wide to deliver precise ice measurements within the peninsula's rugged mountain peaks.

Scientists will also use ICESat-2 to monitor ice sheets' grounding lines, where glaciers draining to the ocean first float free of the bedrock and become ice shelves. These shelves are vulnerable to melting from below by warm ocean waters, causing grounding lines to retreat inland. Because of the bowl-shaped topography of Antarctica's bedrock, glaciologists worry the retreat could accelerate and expose ice to ever more water in a feedback process that could cause rapid ice collapse.

Grounding lines reveal themselves at the surface of a glacier by subtle changes in the slope of the ice at the point where the ice starts to rise and fall with the tides. ICESat-1 could detect grounding lines, but only a few, and only for part of the year; ICESat-2 will check on them every 3 months. "We're going to get a much better idea where warmer water is coming in underneath the ice," says glaciologist Helen Fricker at the Scripps Institution of Oceanography in San Diego, California.

If an ice shelf is about to collapse into the sea, scientists will want to put together an observing campaign right away. Csatho is exploring how to use ICESat-2 data in an early warning system that would detect sudden melting events in near-real time, rather than a year or two afterward.

When ICESat-2 is not watching ice sheets, it will measure the canopy height of high-latitude forests, providing climate scientists with a proxy measure for the carbon stored in trees. It will also join forces with CryoSat-2 to measure the snow that blankets land and sea ice. Because laser light bounces off the snow, while radar reflects from the ice below, combining the two satellites' measurements could help investigators separate the snow from the ice. In Antarctica, where drifts can stand nearly 2 meters tall, that could sharpen measurements of changes in ice thickness. NASA and ESA are already discussing whether to shift CryoSat-2's orbit to create more overlaps, Shepherd says. The European satellite has enough fuel to make the move, he adds.

But first, ICESat-2 has to reach orbit and show that its eye on the ice is as sharp as promised. ■



Giant elephant birds may have coexisted with people for millennia.

ARCHAEOLOGY

Scarred bird bones reveal early settlement on Madagascar

Find reignites debate about megafauna extinctions

By **Andrew Lawler**

Lying about 425 kilometers off the African coast, Madagascar was long thought to be one of the last corners of Earth to be settled. This week in *Science Advances*, however, researchers report that ancient butchered bones show people made their home on the lush island 10,500 years ago, an astonishing 8 millennia earlier than once thought.

The discovery, by a team led by James Hansford of the Zoological Society of London, rekindles a contentious debate over whether humans are responsible for the extinction of Madagascar's unique megafauna, including giant lemurs and the world's largest bird. All flourished after the island broke away from the Indian subcontinent 88 million years ago, then died out centuries ago, seemingly not long after people arrived. But the blade-scarred bones from the massive elephant bird *Aepyornis maximus* suggest a long coexistence between humans and megafauna—challenging the belief that people inevitably kill off large mammals and flightless birds when they arrive in a new land.

David Burney, a paleobiologist at the National Tropical Botanical Garden in Koloa, Hawaii, who was not involved in the study, says the results “fly in the face of all that we thought we knew about human arrival in Madagascar.” The discovery, along with a few other new finds that also point to early settling, “is big news,” he says, although he and others question whether it is enough to resolve the megafauna debates.

Pinning down the arrival date of humans

on Madagascar has been difficult, says Ian Tattersall, an anthropologist at New York City's American Museum of Natural History (AMNH), because “archaeological evidence for early human presence ... is scarce at best.” East Africans and Indonesians are known to have established farming settlements by 500 C.E., but butchered bones of now-extinct lemurs and hippos hinted that humans were present a half-dozen centuries earlier. And on the northeast coast, archaeologists recently found small stone blades that appeared to date to before 2000 B.C.E., although the claim is not widely accepted.

In 2008, anthropologist Patricia Wright of the State University of New York in Stony Brook heard from a colleague's aunt that a man looking for sapphires had unearthed dinosaur bones near Ilakaka, in the south central part of the island. “I didn't believe the aunt, but eventually went to visit,” Wright says. With Armand Rasoamiamanana of the University of Antananarivo, she found the “dinosaurs” were actually the remains of massive lemurs, hippos, giant tortoises, and crocodiles. The trove also included bones



Grooves on 10,500-year-old elephant bird bones appear to have been left by humans.

from the elephant bird, an ostrichlike creature that stood more than 3 meters high and weighed more than 350 kilograms.

The bones were stored at a nearby field center, where Hansford examined them in 2016. On 2-meter-long leg bones from the elephant bird, he noticed deep grooves, evidently made by humans butchering their prey with sharp stone tools. By measuring carbon-14, the team dated the bones to 10,500 years ago. The find “represents the earliest known evidence of human presence in Madagascar,” Hansford and colleagues note.

The date does more than push back humans' arrival. Many archaeologists accept the idea proposed more than 4 decades ago by archaeologist Paul Martin of the University of Arizona in Tucson that megafauna such as mammoths and other giant mammals on northern continents died off because of a “blitzkrieg” by human hunters entering new territory, not because of factors like climate change. Madagascar has since emerged as a key testing ground for the theory.

Hansford argues that his group's results, by showing that humans coexisted with megafauna for as long as 9 millennia, “eliminate the rapid extinction hypothesis or blitzkrieg for Madagascar.” Only after farming populations had expanded across the island, altering the environment and increasing hunting pressure, did creatures like the elephant bird finally go extinct, he proposes. Ross MacPhee, an anthropologist at AMNH, says the paper's conclusion is “highly consequential,” because such extinctions “are frequently held up as proof of humanity's consistent record of destruction, past, present, and future.”

Tattersall, however, says it's “premature” to make generalizations about human impact. He and Burney, a longtime advocate of the blitzkrieg theory, both note that the Madagascar find could be a sign of a small group of humans who sojourned only briefly on the island, with little effect on the fauna. And the blitzkrieg hypothesis remains viable elsewhere: New Zealand's moa—another large flightless bird—went extinct less than 2 centuries after the arrival of the first Polynesians. The Madagascar example may show there is no one-size-fits-all explanation for the extinctions, says Henry Wright, an archaeologist at the University of Michigan in Ann Arbor.

So far, the archaeologists searching through the ancient bones have not found stone tools, which might shed light on the early settlers' way of life and how long they persisted on the island. Resolving the twin debates about Madagascar's settlement and the demise of its megafauna will take more digging and dating, Hansford concedes. He and his team hope to return to the bone pit in the near future, “now that we understand the incredible significance of the site.” ■

FEATURES

PIERCING THE HAZE

Ammonia, a poorly understood smog ingredient, could be key to limiting deadly particulate pollution

By Jason Plautz, in Salt Lake City

Downloaded from <http://science.sciencemag.org> on September 17, 2018

Winters can be toxic here. For days or even weeks, a thick haze settles over this city of skiers and hikers, as polluted air becomes trapped in a basin ringed by mountains. It can be hard to see the next car on the road. Hospital visits for pneumonia and asthma spike, schools suspend outdoor recess, and even healthy residents complain of scratchy throats and coughing fits.

Meteorologists say the phenomenon, known as an inversion, is easy to explain: A high-pressure system traps cold air in the basin, placing a lid over the pollution. But the smog's specific ingredients, and how they interact in the atmosphere, have been something of a mystery. And there is growing pressure to solve it: The U.S. Environmental Protection Agency (EPA) has judged the city to be in "serious" violation of clean air standards for part of each year, obligating state officials to come up with a plan for reducing the threat—something they've so far been unable to do.

Last year, in an effort to help develop that plan, researchers from six universities and several state and federal agencies launched an unprecedented effort to better understand the precise chemical makeup and sources of the pollution. During two inversions that lasted a total of 17 days, they gathered data from aircraft, balloons, and ground stations.

The broad strokes of what they found came as little surprise. The haze was mostly composed of tiny particles, less than 2.5 microns in diameter (PM_{2.5}), which can lodge in the lungs and contribute to premature death. Some of the particles were dust, smoke, or soot, but about three-quarters were made up of ammonium nitrate. It forms when nitrogen oxides produced by vehicles, furnaces, and industrial equipment combine with ammonia, which typically wafts from farms that use ammonia-based liquid fertilizers or produce heaps of animal manure.

The researchers were startled, however, by the levels of pure ammonia they measured, given that Utah's farms are mostly idle in winter. "We don't typically think of the winter months as being big months for ammonia," says chemist Jennifer Murphy of the University of Toronto in Canada, who participated in the study. Researchers and regulators are now trying to nail down exactly why those levels were so high, and whether cutting those emissions could help clear the air

Surprisingly high levels of ammonia appear to play a role in fueling the smog that envelops Salt Lake City in the winter.

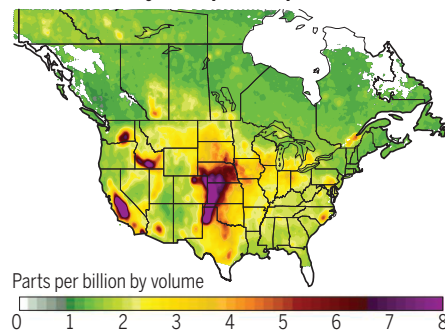
over what some residents have come to call "Smog Lake City."

Despite its abundance, the role of the colorless, sharp-smelling, and eye-watering gas in deadly air pollution is poorly understood. In part, that's because it is notoriously difficult to track. Ammonia molecules are "sticky" and eagerly combine with other compounds, making it difficult for monitoring instruments to capture them. And the gas can have a very short life span—sometimes just a few days. "Ammonia is awful," says environmental engineer

Fresh off the farm

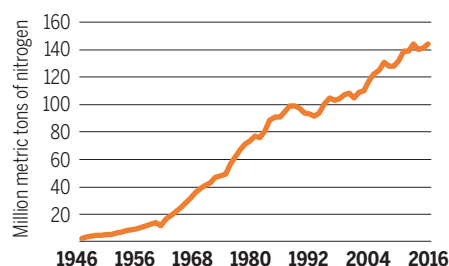
Agricultural regions can be major sources of ammonia (NH₃, dark areas), especially during the growing season when use of liquid fertilizers is high. Wildfires (some yellow areas near top of map) can also produce plumes of the compound.

Ground-level NH₃ from April to September 2013



Fertile market

Growing demand for chemical fertilizers has caused global NH₃ production to rise dramatically.



Mark Zondlo of Princeton University. "It's truly one of the worst gases to measure in the atmosphere."

Around the world, new ground-, air-, and space-based sensors are helping bring the sources, movements, and fate of ammonia into clearer focus. The improved monitoring comes as some nations, including the United Kingdom, are moving to slash ammonia emissions. But others, including the United States, have not made limiting ammonia a priority, in part because of uncertainty surrounding sources, as well as concerns that costly controls might do little

to improve air quality. Instead, regulators have often opted to target other key smog ingredients, including oxides of nitrogen and sulfur created by combustion.

But the focus on ammonia is likely to intensify. Global emissions of the gas have doubled over the past 70 years and are forecast to continue to rise, in large part because of growing demand for chemical fertilizers. That has put pressure on researchers and regulators to better understand the implications for air quality.

THIS SUMMER, atmospheric scientist Jeff Collett of Colorado State University in Fort Collins stood in a clearing in Rocky Mountain National Park surrounded by instruments that highlighted just how challenging it is to track ammonia. Other air pollutants, such as ozone and carbon monoxide, are generally monitored by networks of automated instruments that collect and relay data in real time. But to track ammonia, Collett's team must make an hourlong trip from campus to the field several times a week to manually collect samples from their instruments.

One is a simple bucket that collects rainwater, which researchers analyze to see how much ammonia has become trapped in water vapor. Another relies on a sponge coated with an acid to absorb the gas. (Ammonia, a base, eagerly reacts with acids.) There is also an acid-coated glass spiral, which strips the sticky ammonia molecules out of air samples before separating out other components of particulate matter.

It's a finicky process, but the samples are vital to Collett's effort to document how ammonia drifts from farms about 80 kilometers away in Greeley, Colorado, into the park, where the nutrient can damage sensitive ecosystems, and into Denver, where it contributes to smog. The work, underway since 2011, has helped sharpen the picture of the region's ammonia sources and movements. For example, when Colorado farm groups argued that golf courses were playing an outsized role in ammonia emissions because of their liberal fertilizer use, Collett stuck a monitor near a local golf course and showed that wasn't correct; farms were the bigger source. The monitoring has also enabled the state to establish a system that warns farmers when weather conditions are predicted to push ammonia toward Denver, encouraging them to voluntarily limit fertilizer applications and cover manure piles.

Elsewhere, other monitoring efforts—including a 66-site national networking run by EPA that reports readings every 2 weeks—have painted a bigger, continent-wide picture, including how ammonia emissions can vary by weather and season (see map, left).

Advances in mobile monitoring have made it possible to more quickly collect measurements like Collett's. And since 2008, NASA satellites have provided a global look at ammonia's signature in the atmosphere. Such tools are helping scientists assemble a more complete picture of ammonia sources, including wildfires, which are estimated to produce 10% of global ammonia emissions by releasing the compound from plants.

"A decade ago, we had maybe a dozen long-term measurements around the country, and only one or two aircraft measurements ever," says atmospheric chemist Daven Henze of the University of Colorado in Boulder. "Now, we're able to regularly get information about timing, magnitude, variability, and sources."

working to understand that variation and figure out where the ammonia is coming from. The team is using a network of ground monitors, combined with aerial measurements, to map ammonia concentrations within the city. They are examining wind patterns to see how ammonia might drift in from nearby agricultural areas. And they are looking for sources that may have been overlooked.

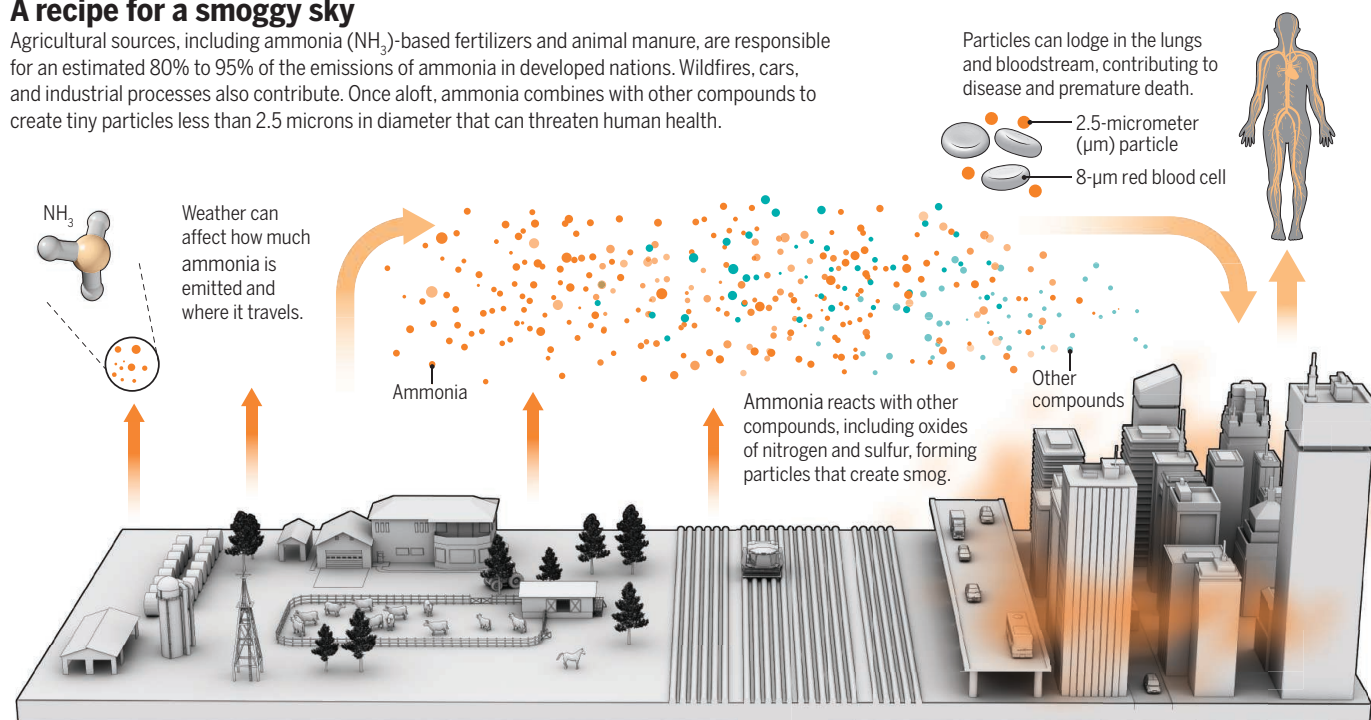
Cars in urban areas, for example, may be contributing more ammonia than previously understood. In one recent study, Zondlo deployed mobile instruments that use lasers to measure ammonia plumes released by vehicles in cities in the United States and China. He found that vehicles—which produce ammonia as a byproduct of their emissions—

boring valleys, the state could try to curb those sources—perhaps by asking farmers to limit fertilizer use—when the weather is ripe for inversions. But that strategy might not make sense if urban ammonia sources like cars turn out to be playing a bigger role in driving the chemistry that produces smog. "With so many factors, we need to understand the full picture," Murphy says.

Regulators also want to be sure that potentially costly controls on farms or other ammonia sources will produce a benefit, which means cracking the chemical makeup of the smog. In the United States, for example, existing air pollution regulations have sharply reduced atmospheric concentrations of nitrogen oxides, meaning fewer molecules of those compounds are available to combine with

A recipe for a smoggy sky

Agricultural sources, including ammonia (NH_3)-based fertilizers and animal manure, are responsible for an estimated 80% to 95% of the emissions of ammonia in developed nations. Wildfires, cars, and industrial processes also contribute. Once aloft, ammonia combines with other compounds to create tiny particles less than 2.5 microns in diameter that can threaten human health.



FEW EFFORTS to inventory ammonia, however, have been as thorough as the one undertaken in the Salt Lake City region in the winter of 2017. The two inversion events documented by the ground and air campaign each lasted more than a week, and the researchers were able to gather observations in each of the area's three major valleys: Salt Lake, Cache, and Utah.

Existing tallies of Utah's ammonia sources suggested ammonia levels would be similar in each of the three valleys. In fact, the researchers found that levels varied by geography—and that the readings were higher than they expected.

Now, Murphy and allied researchers are

cleaning catalytic converters—were emitting about twice as much ammonia as assumed. "In the grand scheme of things, vehicles were a fairly small source," he notes. Still, the emissions could play an important role in particulate pollution in cities, he says, because the ammonia is being produced in close proximity to other combustion compounds that fuel the creation of PM2.5.

In Utah, state regulators hope a better understanding of Salt Lake City's ammonia sources will help them build improved computer simulations of air pollution events, which can be key to identifying solutions. For example, if it turns out that ammonia is drifting into the city from farms in neigh-

borhoods and form particulates. So, reducing ammonia emissions might not make much of a difference in areas where other smog ingredients are already in short supply. In other areas, however, choking off ammonia plumes could be key to reducing particulates. "We're still not in a place," says Murphy, "where we can even say that difficult measures are going to [have] an impact."

THE SITUATION is very different in Europe, where environmental regulators have long put a spotlight on ammonia, in part because of concerns about its impact on ecosystems. (Ammonia can leach into streams and rivers, for instance, where it can be toxic to



aquatic organisms.) The Economic Commission for Europe, a United Nations offshoot, set ammonia limits in 2012, and European countries have used a variety of strategies to reduce overall agriculture emissions by 24% since 1990. Germany, for example, placed per-hectare limits on the use of certain kinds of fertilizers, and the Netherlands created financial incentives for more efficient fertilizer use.

Earlier this year, the United Kingdom unveiled a sweeping air quality plan that includes plans to cut the nation's ammonia emissions from agriculture by 16% by 2030. The move came in the wake of a U.K. Environment Agency finding that ammonia was the nation's only major air pollutant to increase since 2013, and that emissions from farms would continue to rise without "urgent action." That trend threatened the government's bid to halve, by 2025, the number of people breathing air with PM_{2.5} levels deemed unsafe by the World Health Organization (WHO). (The WHO particulate standard is 10 micrograms [μg] of PM_{2.5} per cubic meter of air, averaged over a year; the U.S. annual standard is 12 $\mu\text{g}/\text{m}^3$.)

To achieve the ammonia cut, the government plans to require farmers to limit fertilizer applications and cover manure piles, and it will impose stricter controls on dairy

operations. The agriculture industry, which was consulted on the plan, has been largely receptive. Farmers have already voluntarily taken similar steps, industry officials noted, and they welcomed government plans to help fund the deployment of ammonia-control technologies.

OTHER NATIONS with hefty ammonia emissions aren't yet ready to follow the United Kingdom's lead. China, which is known to be a global ammonia emissions hot spot but doesn't have a reliable inventory of sources, does not regulate the compound. Neither does the United States, although EPA does consider ammonia to be a precursor to PM_{2.5}.

One big issue facing U.S. regulators is a lack of comprehensive data on ammonia sources. "It's hard to regulate something if you're not measuring it," Collett says. U.S. farm groups have, to date, rebuffed efforts to require farmers to report ammonia emissions, arguing the effort would be needlessly burdensome. In 2013, EPA did launch a 2-year ammonia monitoring study, in concert with the pork, dairy, and poultry industries, involving 24 sites in nine states. But the project was halted after agency science advisers criticized the quality of data that were being collected.

If EPA did pursue ammonia regulations, politics would likely pose a stum-

Managing ammonia sources on farms, such as this heap of chicken manure in Maryland, could be key to limiting emissions.

bling block. Farm groups have argued that, because the gas has many sources and can drift long distances, any controls would have to be carefully designed; a fix would not be as straightforward as, for instance, installing a chemical scrubber on a power plant. They also note farmers have already taken voluntary steps to limit emissions, such as reducing the amount of ammonia precursors used in animal feed and changing manure management practices.

Still, U.S. regulators could face pressure to act if studies from Salt Lake City and elsewhere provide evidence that ammonia has become an important driver of particulate pollution. And at least one scientist believes answers could come sooner than later—in "years, not decades," predicts Henze, who sits on the EPA advisory panel considering the issue. "EPA has not been willing to push the ball forward because of the uncertainty" surrounding ammonia, he says. "Now we're pushing past the uncertainty." ■

Jason Plautz is a journalist in Denver.



WINDFALL

A catastrophic hurricane gave scientists a rare chance to study how tropical forests will fare in a warmer, stormier future

By Sarah Amandolare, in Puerto Rico's El Yunque National Forest

A year after Hurricane Maria raked Puerto Rico with winds of 250 kilometers per hour and a meter of rain, the island is still struggling to recover. Estimated deaths have risen to shocking levels—nearly 3000—and although power has been almost completely restored, blackouts occur regularly. The wind and flooding also devastated ecosystems as diverse as mangrove swamps and rainforest. As they mend, scientists are watching closely.

A major focus is this rainforest in the Luquillo Mountains of northeastern Puerto Rico that scientists have been monitoring since the 1940s. The only tropical forest in the U.S. Forest Service's (USFS's) National Forest System, it has endured several major hurricanes. But Maria and Irma—a hurricane that struck the island a glancing blow just 2 weeks earlier—were the strongest in a century, turning lush forest into ranks of skeletal trees and piles of sticks. Maria also destroyed research infrastructure and blocked access

to some experiments for weeks.

As scientists get back to work, the devastated forest presents a rare opportunity to explore how tropical forests—and their ability to store carbon—recover from the extreme weather that is becoming more common as the world warms. The wealth of ongoing research in the forest “has positioned us really well to tackle this question of how tropical forests are going to respond,” says Grizelle Gonzalez, an ecologist at the International Institute of Tropical Forestry, run by USFS in San Juan. Tana Wood, a biogeochemist and ecologist at the institute, says she was trapped in her house for 2 days after Maria, and her research site was hit hard. “But scientifically, it's incredibly exciting,” she says. “It's a unique chance to look ahead.”

Already the researchers have seen hints that as temperatures warm, forests may be slower to recover from damage. Other findings, from a long-term effort here to simulate hurricane damage, suggest more frequent major disturbances could also

make forest ecosystems less resilient, in part by causing the downed trees and branches to release their carbon into the air rather than the soil. That could fuel further climate change and extreme weather.

STEPPING INTO EL YUNQUE used to offer relief from the ferocious sun. But now, Wood shades her eyes from the glare as she surveys new understory vegetation. Hurricane Maria destroyed the canopy that once blanketed the forest in cool darkness and shielded the experiment that Wood began in 2016, a year before the storms. Her project, the Tropical Responses to Altered Climate Experiment (TRACE), tracks how increasing temperatures affect wet tropical forests. Because the world doesn't warm much during the time scale of a research project, TRACE features an infrared heating system that warms understory plants and soils by 4°C, fast-forwarding climate change.

For Wood, El Yunque serves as a proxy for tropical forests worldwide, which account

PHOTO: G. GONZALEZ
<http://science.sciencemag.org/> on September 13, 2018

Research sites in El Yunque National Forest were off-limits for days after Maria hit on 20 September 2017.

for more than two-thirds of the planet's terrestrial plant biomass and store about a third of the world's soil carbon. Wood's original goal for TRACE was to understand how warming might affect that storage capacity. In tropical forests, she says, "Any small change in the uptake or release of carbon dioxide can have disproportionately large effects on the concentration in the atmosphere." Now, she and her team have a new opportunity: to evaluate whether the artificial warming is affecting recovery from Irma and Maria's damage. What the group finds could be an omen for Earth's warmer future.

Wood is monitoring multiple actors in the forest, including the fine roots that supply trees with water and nutrients. Although roots are protected from the wind, a hurricane can shred them, she notes. "In these huge gusts of wind, the trees are moving and twisting," pulling away from their roots. Roots also may suffer, she says, when a tree loses its leaves, where photosynthesis produces sugars and starch. Because the roots don't photosynthesize, they depend on leaves to nourish them.

To see how well the fine roots are recovering from hurricane damage, the TRACE team lowers cameras through clear plastic pipes driven a meter into the soil. The researchers also measure the infiltration of new roots into fresh soil packed into boreholes in the forest floor. "Our preliminary results are that we saw less root production in the warmed plots," Wood says.

She speculates that a scarcity of stored carbohydrate in thicker, intact roots could be a factor. When a hurricane strips foliage and interrupts photosynthesis, trees can draw on that stored food to regenerate fine roots. But Wood and her colleagues have seen hints that before Maria, photosynthesis was slower in the warmed plots, possibly leaving the trees with a smaller reserve to fuel recovery. The idea, she says, is that "warming can stress vegetation, but it may not be observable until you have another stress on top of that"—namely, a hurricane.

Either way, lagging root regrowth could mean the trees in warmed plots will recover more slowly and, as a result, will capture less carbon dioxide. And because root growth and die-off pumps carbon into the soil, lasting damage could mean a loss of soil carbon.

Other researchers have studied how warming affects rainforest plants in the laboratory. What is unusual about TRACE, says tropical ecologist Jennifer Powers of the University of Minnesota in St. Paul, is that it tracks the effects of warming amid the "full complexity of the coupled soil-plant ecosystem."

ABOVE GROUND IN EL YUNQUE, trees that survived the hurricane resemble bottle brushes, with new leaves sprouting from their trunks. The lush understory now reaches shoulder height in places and is "thicker and more dense than I have ever seen," Wood says. Ongoing measurements will show whether the amount of foliage and the thickness of individual leaves have risen since the storm, perhaps for protection from drying or scorching under the storm-damaged canopy. More foliage could boost carbon uptake—and perhaps counteract any reduction in carbon storage resulting from damaged roots.

Wood's team, which is funded to continue its work for another 3 years, is also tracking another possible legacy of the storms: changes in species composition. By counting and identifying as many as 600 new seed-

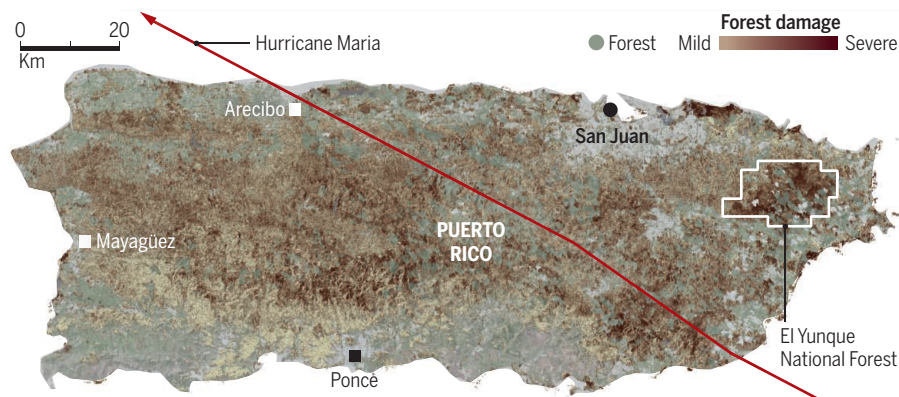
exposed it helped speed decomposition.

The CTE team is dissecting the process. In some plots, the scientists deposited debris but left the canopy intact; in others, they used chain saws and shears to trim the canopy but hauled away all the branches and foliage. Still other plots got both treatments, mimicking the effects of a major storm. After a decade, plots that only received debris deposits showed a significant increase in soil organic matter. Fungi and minuscule animals took up nutrients from the debris and returned them to the soil for plants to use. "That's how the system kind of jump-starts and recovers," Gonzalez says.

But on plots that experienced the hurricane-like treatment of both debris and canopy opening, intense sunshine and pelting rains disrupted the community of fungi and ani-

A storm's swath

Landsat data sensitive to debris and exposed wood traced forest damage after Hurricane Maria swept across Puerto Rico on 20 September 2017. The storm destroyed or severely damaged as many as 31 million trees.



lings in a single 4-meter plot, the researchers are monitoring the fate of slow-growing, shade-tolerant plants, which could struggle to survive, and watching for nonnative species, which could decrease overall diversity. A shift in species could ultimately change the canopy structure, allowing more heat and light to reach the understory and exacerbating climate warming.

At an experimental site farther west, meanwhile, Gonzalez is studying the fate of the carbon and other nutrients locked up in the hurricane debris. Here, backyard-size plots are carpeted with browned leaves, sticks, and decaying palm fronds—a mess left not just by Maria, but also by the Canopy Trimming Experiment (CTE), underway since 2004. The project was sparked by a striking observation after hurricanes Hugo and Georges in 1989 and 1998, respectively: All the organic debris that the storms dumped onto the forest floor had decomposed within a year or two. Scientists suspected that the more intense sun and rain reaching the soil after the storms

imals. Microbes stepped in, sending much of the carbon back to the atmosphere.

The results suggest "it's kind of a race between the microbes and the physical processes that move that material down to the soil," says Whendee Silver, an ecologist and biogeochemist at the University of California, Berkeley, whose CTE work indicates that the same carbon-stealing microbes might attack organic matter deeper in the soil. If the pace of disturbances accelerates, researchers note, the canopy would have less time to recover, and organic matter in the soil could dwindle along with the health of the forest.

"One of our really big concerns is that, if hurricane frequency and intensity increase, it will slowly deplete these ecosystems of what they need to grow and survive," Silver says. That could be bad news—not just for this lush corner of Puerto Rico, but for the planet as a whole. ■

Sarah Amandolare is a journalist based in New Paltz, New York.

INSIGHTS

PERSPECTIVES

SUSTAINABILITY

Gaia 2.0

Could humans add some level of self-awareness to Earth's self-regulation?

By Timothy M. Lenton¹ and Bruno Latour²

According to Lovelock and Margulis's Gaia hypothesis, living things are part of a planetary-scale self-regulating system that has maintained habitable conditions for the past 3.5 billion years (1, 2). Gaia has operated without foresight or planning on the part of organisms, but the evolution of humans and their technology are changing that. Earth has now entered a new epoch

called the Anthropocene (3), and humans are beginning to become aware of the global consequences of their actions. As a result, deliberate self-regulation—from personal action to global geoengineering schemes—is either happening or imminently possible. Making such conscious choices to operate within Gaia constitutes a fundamental new state of Gaia, which we call Gaia 2.0. By emphasizing the agency of life-forms and their ability to set goals, Gaia 2.0 may be an effective framework for fostering global sustainability.

At first sight, the potential for a successful Gaia 2.0 does not seem promising. Despite large-scale mobilization of scientists, activists, and citizens, large parts of the human population are indifferent to the Anthropocene, and many deny anthropogenic climate change (4). In addition, there is no proof that consciousness in this context is anything but the belated and retrospective realization that mistakes had been made and might be partially redressed. Indeed, the first formulation of the Gaia hypothesis (1) is almost exactly contemporary with

The commercial Earth observation satellite WorldView-4 has been providing high-resolution imagery since its launch in 2016 from Vandenberg Air Force Base in California.

what is now seen as the start of the Anthropocene (3). Furthermore, the examples of social Darwinism, sociobiology, and dialectical materialism suggest that drawing political lessons from nature is problematic.

Nevertheless, it is important to have a second look at the connection between the original Gaia concept and a possible Gaia 2.0, because the original Gaia has many traits that were not detectable in earlier notions of nature associated with the development of Western civilization. Before the Anthropocene, Western societies saw themselves as the only conscious agents in a passive material environment. Today, they must cope with the brutal reactions of living organisms that are continually reshaping their surroundings, creating in part their own conditions for survival (4, 5). Gaia thus establishes a new continuity between humans and nonhumans that was not visible before—a relation

¹Global Systems Institute, University of Exeter, Exeter EX4 4QE, UK. ²Sciences Po, 75337 Paris Cedex 07, France. Email: t.m.lenton@exeter.ac.uk

between free agents (4). This understanding offers the potential to learn from features of Gaia to create a Gaia 2.0. We focus here on three of these features: autotrophy, networks, and heterarchy.

AUTOTROPHY

Autotrophs use free energy to continually remake themselves out of simple substances that are present in their surroundings. Earth's surface, where most of the biosphere resides, is a very nearly materially closed system. Hence, like an autotroph, the collective flourishing of life for the past 3.5 billion years has depended on the internal recycling of materials, powered by solar energy (6). The origin of these material recycling loops is at least partially understood (7). There needs to be a source of free energy to support recycling, which usually comes from the Sun and enters the system via photosynthetic primary producers. Recycling is built on metabolic by-products, with one organism's waste becoming another's food. Closure of a recycling loop triggers a self-perpetuating feedback process: The participants in the recycling loop are no longer limited by what comes into their world, but rather by how efficiently they can recycle resources. For example, coral reefs and the Amazon rainforest thrive on recycling in otherwise low-nutrient conditions.

If, by contrast, we consider the state of the technosphere in the Anthropocene (5), an audit made by Gaia would question the purported quality of many innovations and note that from an engineering standpoint, they perform poorly. Humans currently extract fossil energy, rock phosphate, and other raw materials from Earth's crust far faster than they would normally come to the surface, and then dump the waste products on land, in the atmosphere, and in the ocean. Compared to Gaia, this is a very poorly coupled and unsustainable set of inventions.

This does not mean that humans should stop inventing, but rather that engineering should shift attention to become as smart as Gaia in achieving nearly closed material cycling powered by sustainable energy. The input of solar energy has the potential to far outstrip current fossil energy consumption, and renewables are rapidly becoming cost-competitive with fossil fuel energy for electricity generation (8). There should thus be no long-term shortage of energy. The challenge is to design and incentivize a transition to a circular economy. As in the original Gaia, this must be built on waste products becoming useful resources to make new products. Despite practical obstacles and thermodynamic constraints, there is huge potential to increase material recycling in Gaia 2.0 (9).

NETWORKS

Gaia was built by adaptive networks of microbial actors that exchanged materials, electrons, and information (10), the latter through ubiquitous horizontal gene transfer. These microbial networks form the basis of the recycling loops that make up global biogeochemical cycles. Functional roles in these networks have been retained even when the taxa performing them were replaced (11). Therefore, sufficient biodiversity to provide functional redundancy contributes to the robust self-regulation of Gaia.

Microbial networks also created long-lived products that sometimes accumulated globally—notably oxygen in the atmosphere. This in turn facilitated an increase in the diversity of life and metabolisms and enabled the evolution of new levels of biological organization and connectedness (6), with new mechanisms of coordination. Humans and our adaptive social networks are the latest realization of this process.

In Gaia 2.0, horizontal transfer of information, functional diversity with redundancy, and distributed control will likely be important to a successful circular economy. The challenge is to support diverse, autocatalytic networks of human agents that can propel transformations toward goals such as sustainable energy, fueling the efficient cycling of resources. This is particularly challenging given a social and economic paradigm of short-term localized gain and relatively weak global, unifying, long-term structures to counteract this paradigm.

HETERARCHY

Depending on the scale and time span considered, completely different mechanisms are at work within Gaia (7). This heterarchy is particularly visible in the climate regulation that has received so much political attention of late. Some of Earth's climate self-regulation mechanisms (6) are purely physical and chemical, but many involve biology. On time scales of hundreds of thousands of years, changes in global temperature are counteracted by biologically amplified changes in the removal of CO₂ by silicate weathering. On intermediate time scales of millennia, the dissolution of carbonate sediments on land and the ocean floor increases CO₂ storage in the ocean. On even shorter time scales of years to centuries, land and ocean carbon sinks roughly halve the rate of CO₂ rise and climate change.

Thus, each mechanism in Gaia has its own capacity for resistance and expansion. Natural selection can only help to explain environmental regulation at small scales of space and time (7). At large space and time scales, simpler dynamical mechanisms are at play (7): Systems that find self-stabilizing configura-

tions tend to persist (12), and systems that persist have a greater likelihood of acquiring further persistence-enhancing properties (11, 13). Through these cruder selection mechanisms, Earth may have acquired and accumulated stabilizing feedback mechanisms involving life (7).

The upshot is that Gaia's self-regulation of climate is probably fairly crude compared to its efficient recycling of resources. The recent glacial-interglacial cycles indicate that the climate system can be quite unstable and thus vulnerable to human interference, which has already increased atmospheric CO₂ to levels last seen 3 to 5 million years ago. This heterarchy of mechanisms of different reliability

makes the task of Gaia 2.0 to restabilize the climate especially daunting. Simultaneously, humans are altering nutrient cycles relatively more than the carbon cycle, posing an additional challenge for Gaia 2.0 to restabilize nutrient cycling.

Implementation of alternative forms of climate control to reduce production of CO₂ or augment existing feedbacks (14) depends on who is in charge of such voluntary activity. The results would clearly be different if the Intergovernmental Panel on Climate Change, President Putin, the California legislature, or President Trump had their finger on the proverbial thermostat. In reality, all these agents and many others have some grip on the thermostat, and their combined effect is not simple to predict.

POLITICS

Drawing a parallel between the original Gaia concept and a possible Gaia 2.0 gives an occasion to reevaluate our collective goals, as well as the means of achieving them. A central goal for this century is surely to achieve a flourishing future for all life on this planet, including a projected 9 to 11 billion people. Human flourishing is not possible without a biodiverse, life-sustaining Earth system. This is recognized in the United Nations' 17 Sustainable Development Goals. But achieving those goals requires that human societies exercise self-aware self-regulation (14).

Yet, maintaining a self-regulating, human life-supporting planet is not the primary goal of some dominant modes of collective human activity today. Despite a flood of monitoring information, present industrial societies seem less able to track changes in their environment than the life-forms that compose Gaia, because that information is often ignored where it matters by those in power. It's as if purposelessness had shifted from the natural to the social domain.

There is clearly at this point a political question of orientation toward or away



Read more articles
online at scim.ag/TomorrowsEarth

from the lessons to be drawn from Gaia. The resulting conflict takes precedence over all others. The climate science controversies demonstrate that scientists are now drawn into knowledge and power struggles for which they are not well prepared. Yet, people inspired by Gaia will not necessarily be endowed with deeper foresight. In matters of politics, it is prudent to follow John Dewey's advice (15) that we cannot expect to know the best solution in advance, but only that we can improve the quality of the sensors—both instruments and people—that detect shortcomings and the speed with which we rectify the course. If in politics the blind lead the blind, then hope rests on finding the best way to activate the white cane to fumble in the dark.

This is where the scientific establishment will play a crucial role in multiplying the sensors, improving their qualities, speeding the dissemination of their results, improving models, and proposing alternative explanations to phenomena. Such an infrastructure cannot, however, be limited to scientists: They must collaborate with citizens, activists, and politicians to quickly realize where things are going wrong.

Creating an infrastructure of sensors that allows tracking the lag time between environmental changes and reactions of societies is the only practical way in which we can hope to add some self-awareness to Gaia's self-regulation. This framing of the problem gives a clear ethical direction: Any attempt to tamper with the sensors or slow down the reaction to errors jeopardizes the chance to learn from Gaia how to close the loops that would enable Gaia 2.0 to better sustain the human population than the present world. ■

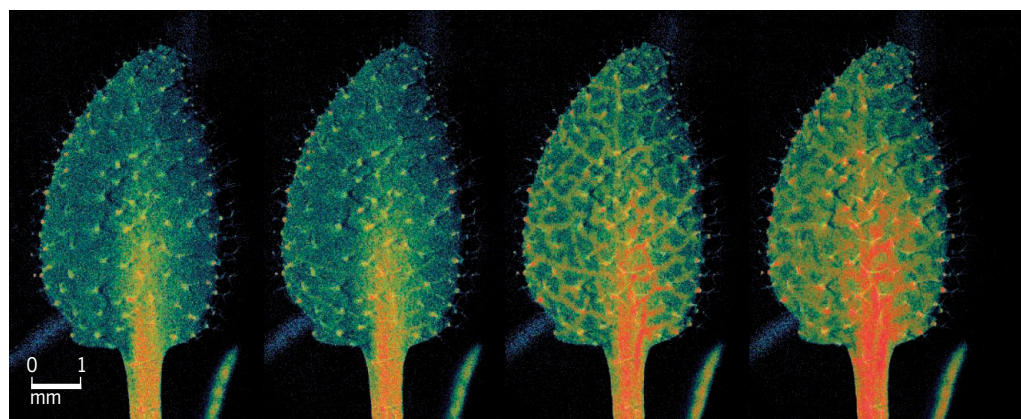
REFERENCES AND NOTES

1. J. E. Lovelock, *Atmos. Environ.* **6**, 579 (1972).
2. J. E. Lovelock, L. Margulis, *Tellus* **26**, 2 (1974).
3. C. N. Waters *et al.*, *Science* **351**, aad2622 (2016).
4. B. Latour, *Facing Gaia: Eight Lectures on the New Climatic Regime* (Polity, 2017).
5. P. K. Haff, *Geol. Soc. Lond. Spec. Publ.* **395**, 301 (2013).
6. T. Lenton, A. Watson, *Revolutions That Made the Earth* (Oxford Univ. Press, 2011).
7. T. M. Lenton *et al.*, *Trends Ecol. Evol.* **33**, 633 (2018).
8. IRENA, Renewable Power Generation Costs in 2017 (International Renewable Energy Agency, Abu Dhabi, 2018).
9. L. Ciaccietti *et al.*, *Environ. Sci. Technol.* **50**, 11394 (2016).
10. P. G. Falkowski, T. Fenchel, E. F. DeLong, *Science* **320**, 1034 (2008).
11. W. F. Doolittle, *J. Theor. Biol.* **434**, 11 (2017).
12. A. Wagner, *Robustness and Evolvability in Living Systems*, S. A. Levin, S. H. Strogatz, Eds., Princeton Studies in Complexity (Princeton Univ. Press, 2007).
13. W. F. Doolittle, *Biol. Philos.* **29**, 415 (2014).
14. O. Morton, *The Planet Remade: How Geoengineering Could Change the World* (Princeton Univ. Press, 2015).
15. J. Dewey, *The Public and its Problems* (Holt, 1927).

ACKNOWLEDGMENTS

We thank the Giorgio Cini Foundation for bringing us together, the two reviewers, S. Dutreuil, and participants in the dialogue "What's the Body of the Body Politic? Sovereignty, Identity, Ecology" for valuable feedback, and the Zentrum für Media Kuntz Karlsruhe for support.

10.1126/science.aau0427



PLANT BIOLOGY

Nervous system-like signaling in plant defense

Herbivory induces rapid long-distance calcium signals through glutamate-like receptors

By Gloria K. Muday and Heather Brown-Harding

The ability to initiate a rapid defense against biotic attacks and mechanical damage is critical for all organisms. Multicellular organisms have developed mechanisms to systematically communicate the occurrence of a wound to help them escape or defend themselves from predators. Because plants are stationary and cannot escape herbivory, they must respond with chemical defenses to deter herbivores and repair damaged tissue. On page 1112 of this issue, Toyota *et al.* (1) report long-distance calcium ion signaling in the model plant *Arabidopsis thaliana* in response to caterpillar herbivory or mechanical wounding (see the image). They uncover long-distance calcium signals that require glutamate-like receptor (GLR) channels for signal propagation. These channels are activated by extracellular glutamate, a well-known mammalian neurotransmitter and a more recently uncovered developmental signal in plants (2). In mammals, glutamate receptors are central to fast excitatory neurotransmission, which is an intriguing parallel to their role as long-distance signals in wounding and defense in plants.

This study combines genetic and imaging approaches to reveal a rapid and long-dis-

tance signaling pathway that communicates leaf damage to intact leaves that are spatially and developmentally distant from the wounded leaf. Toyota *et al.* detect increased calcium signals at the site of both herbivory and mechanical wounding within 2 s and in distant leaves within 2 min after damage. This signal moves through the plant vasculature at rates of ~1 mm/s, which is faster than can be explained by diffusion. This systemic calcium response can be induced through application of glutamate, but not with other amino acids, suggesting a role of GLRs. These GLRs are ion channels that open upon binding glutamate to allow calcium influx. Toyota *et al.* demonstrate that this long-distance signaling is lost in plants with mutations in *GLR3.3* and *GLR3.6*. These GLRs have sequence and structural similarity to mammalian ionotropic glutamate receptors (iGRs), which are critical in learning and memory in mammals, suggesting that very different physiological processes can be mediated by related proteins from the plant and animal kingdoms.

This work builds on detailed structural and functional characterization of mammalian iGRs (3). Plant GLRs and animal iGRs have similarities in structure and abundance in genomes (4, 5). The plant GLR genes are classified into three clades: *GLR3.3* and *GLR3.6* are in the third clade and have a "gate" domain, where glutamate is predicted to bind and open the channel, with the highest similarity to mammalian iGRs (4). One member of clade 3, the plasma

Department of Biology and Center for Molecular Signaling, Wake Forest University, 455 Vine Street, Winston Salem, NC 27101, USA. Email: muday@wfu.edu

The rapid wound-induced spread of a calcium signal is visualized using a genetically encoded reporter. Scale bar, 1 mm.

membrane-localized GLR3.4 protein, is the only plant GLR for which ion channel activity and gating by glutamate has been demonstrated (6). Clade 3 GLRs also are the only GLRs to contain a motif found in metabotropic glutamate receptors (mGluRs) (4). mGluRs function in a diversity of processes, including responses to pain and noxious stimuli (7, 8), which are related to wounding responses. Whether these particular features of the GLR3s in plants tie them to their function in wounding or other processes awaits further investigation.

An important question raised by this study is, how does this long-distance calcium signal move through the plant? In the mammalian nervous system, glutamate is a local signal that induces a long-distance ionic response. Glutamate is released into the nerve synapse from synaptic vesicles, where it binds to iGRs on the postsynaptic neuron, opening these ion channels and allowing influx of calcium ions and other cations. The ion influx induces membrane potential changes that lead to signal propagation (3). The results of Toyota *et al.* suggest an endocrine action of glutamate, which is dissimilar from glutamate as a neurotransmitter in mammals and more akin to a hormonal role of glutamate. This mode of action is supported by the observations that the fluorescent calcium ion reporter GCaMP3 localizes to the vasculature and that GLR3.6 is found in the cells that line the vasculature, where other wound-signaling molecules, such as jasmonates, are synthesized (9). A fluorescent glutamate sensor was also used to show that glutamate was increased at the site of wounding; this signal extends along the vasculature and exits the leaf after wounding, which is consistent with a mobile glutamate signal. These results suggest a model in which herbivore and mechanical wounding releases glutamate into the vascular system, where it can travel long distances and activate GLR3 ion channels in the plasma membrane of cells that line the vasculature. This increases the calcium ion influx into these cells. Consistent with this model, GLR3.3 and GLR3.6 were previously shown to be required for systemic wound-activated surface potential changes that are linked to the predicted behavior of these proteins as gated ion channels (10–12). GLR3 activity is required for the increased synthesis of enzymes of the jasmonate biosynthesis pathway

in leaves distant from the wound site (1, 10), leading to the accumulation of jasmonates, which convey host resistance to various invading organisms (9). Additional experiments are needed to determine whether the rate of long-distance glutamate movement is sufficient to drive the rapid long-distance calcium changes.

The findings of Toyota *et al.* are only possible because of the powerful advances in microscopy and biosensors that were used for these observations. The authors used two calcium ion sensors and a glutamate sensor visualized by means of imaging approaches that allow detection of the dynamics of

rapidly transmitted long-distance signals. The availability of a microscope that can capture a large field of view with a highly efficient camera that is sensitive enough to detect relatively weak fluorescence, and that is capable of time-lapse imaging to capture rapid signal transduction, provides insight that was not previously possible.

This combination of approaches has the potential to provide additional evidence for the importance of glutamate and GLRs in plant signaling (2). Future experiments are needed to resolve whether glutamate is moving long distances rather than acting via the localized release and long-distance propagation of ionic signals. In addition to measuring long-distance glutamate biosensor changes, another approach is to use labeled glutamate to show that this amino acid is released at wounds and travels through the vasculature to distant undamaged leaves to initiate defense responses. The possibility that glutamate may participate in systemic signaling to modulate developmental and environmental responses across the plant kingdom is an exciting avenue for future studies. ■

REFERENCES

1. M. Toyota *et al.*, *Science* **361**, 1112 (2018).
2. B. G. Forde, *J. Exp. Bot.* **65**, 779 (2014).
3. S. F. Traynelis *et al.*, *Pharmacol. Rev.* **62**, 405 (2010).
4. M. M. Wudick *et al.*, *J. Exp. Bot.* **10.1093/jxb/ery153** (2018).
5. M. B. Price, J. Jelesko, S. Okumoto, *Front. Plant Sci.* **3**, 235 (2012).
6. E. D. Vincill, A. M. Bieck, E. P. Spalding, *Plant Physiol.* **159**, 40 (2012).
7. S. Chiechio, F. Nicoletti, *Curr. Opin. Pharmacol.* **12**, 28 (2012).
8. G. R. Elliott, S. P. Leys, *J. Exp. Biol.* **213**, 2310 (2010).
9. M. L. Campos, J. H. Kang, G. A. Howe, *J. Chem. Ecol.* **40**, 657 (2014).
10. S. A. Mousavi, A. Chauvin, F. Pascaud, S. Kellenberger, E. E. Farmer, *Nature* **500**, 422 (2013).
11. V. Salvador-Recatalà, W. F. Tjallingii, E. E. Farmer, *New Phytol.* **203**, 674 (2014).
12. V. Salvador-Recatalà, *Plant Signal. Behav.* **11**, e1161879 (2016).

10.1126/science.aau9813

GENETICS

A pinch of RNA spices up DNA repair

Transient incorporation of RNA precursors helps fix broken DNA

By Mauro Modesti

When DNA is replicated by DNA polymerases, deoxyribonucleotides are incorporated, whereas when DNA is transcribed by RNA polymerases, ribonucleotides are used. The misincorporation of ribonucleotides into DNA occurs frequently during DNA replication (1). However, the presence of ribonucleotides in DNA makes it more fragile and threatens genome stability that needs to be maintained for faithful transmission of genetic information. To counteract this, cells have evolved efficient ribonucleotide removal strategies that rely on ribonuclease H2 (RNase H2) (2). On page 1126 of this issue, Pryor *et al.* (3) report the surprising discovery that ribonucleotides are frequently incorporated at broken DNA ends, which enhances repair. This important finding overturns the central dogma of molecular biology by demonstrating that transient incorporation of ribonucleotides in DNA has a biological function.

DNA double-strand breaks (DSBs) in the genome arise through the action of external agents such as exposure to ionizing radiation or clastogenic chemicals. They are also caused endogenously by reactive oxygen species produced during oxidative metabolism or when DNA replication forks collapse. In addition, DSBs initiate programmed genome rearrangements including V(D)J recombination in developing lymphocytes that shuffles antigen and T cell receptor gene segments during the adaptive immune response; or during the process of meiotic recombination in germ cells. DSBs are repaired either by homologous recombination or by nonhomologous end joining (NHEJ) path-

Cancer Research Center of Marseille, CNRS UMR7258; Inserm UMR1068, Aix Marseille Université U105; Institut Paoli Calmettes, 27 Boulevard Lei Roure CS30059, 13273 Marseille, Cedex 09, France. Email: mauro.modesti@inserm.fr

ways. In mammals, the canonical NHEJ (c-NHEJ) pathway primarily repairs DSBs induced by exposure to ionizing radiation or by the endonuclease encoded by the recombination-activating genes 1 and 2 that initiates V(D)J recombination (4). Individuals with deficiencies in c-NHEJ suffer from radiosensitive severe combined immunodeficiency disorders and genome instability that leads to deleterious chromosomal aberrations.

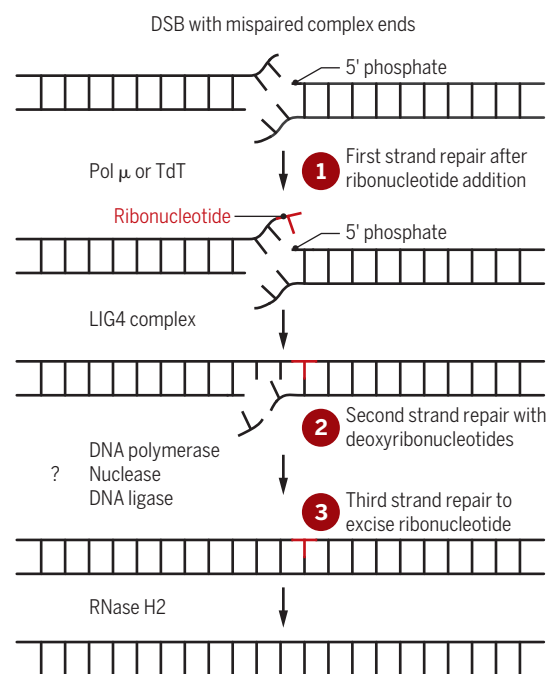
DSBs induced by exposure to ionizing radiation and V(D)J recombination have complex DNA end structures that require processing by nucleases and DNA polymerases to generate suitable substrates for the c-NHEJ pathway component DNA ligase 4 (LIG4), which joins DNA ends by phosphodiester bond catalysis. Among the DNA processing enzymes involved in c-NHEJ, X-family polymerases, including the ubiquitous DNA polymerase μ (Pol μ) and lymphocyte-specific terminal deoxynucleotidyl transferase (TdT), are key for the ability of c-NHEJ to adapt to complex end structures at broken termini (5, 6). However, Pol μ and TdT are special DNA polymerases because they are poor at discriminating the sugar moiety (ribose or deoxyribose) of the nucleotide used during DNA synthesis at broken DNA ends. In vitro, both enzymes can incorporate ribonucleotides almost as efficiently as deoxyribonucleotides into DNA (7, 8). Therefore, Pryor *et al.* examined whether ribonucleotides are incorporated during c-NHEJ in mouse fibroblasts and pre-B cells, and if so, how this affects NHEJ.

The authors found that ribonucleotides are frequently incorporated during c-NHEJ, during V(D)J recombination and DSB repair of simple blunt-ended DSBs induced by CRISPR-Cas9 (which is used for genome editing) but that are extended by TdT. Within 1 minute, up to 60% of DSB junctions contained ribonucleotides, but ribonucleotides were absent at repaired DSBs 30 minutes later. Ribonucleotide incorporation was dependent on Pol μ (one ribonucleotide incorporated per junction) and TdT (average of 2.7 nucleotides incorporated per junction, likely all ribonucleotides), and their removal dependent on RNase H2.

What is the advantage of incorporating ribonucleotides during DSB repair by c-NHEJ? Pryor *et al.* find that the presence of a terminal ribonucleotide favors direct ligation of complex mispaired DNA end structures, which are typically formed by exposure to ionizing radiation and V(D)J

Model of the ribo-NHEJ mechanism

Pryor *et al.* propose that DSBs with complex ends are repaired by a rapid and coordinated triple strand repair mechanism.



recombination. Moreover, a terminal ribonucleotide uniquely stimulates ligation by LIG4. Thus, ribonucleotide addition may help channel repair to the c-NHEJ pathway as opposed to other DSB repair pathways, such as alternative NHEJ (a-NHEJ) or homologous recombination that rely on complementarity base pairing to connect the broken ends. Additionally, c-NHEJ is faster than the other DSB repair pathways (9) and given that ribonucleotides are more abundant than deoxyribonucleotides inside cells, incorporation of ribonucleotides might allow rapid repair kinetics so that interference with DNA replication or transcription is minimized and rejoining unrelated DSB ends is avoided.

What is the mechanism of this ribo-NHEJ pathway? The authors propose a triple strand repair model (see the figure), involving sequential strand repair whereby, after a ribonucleotide is added by Pol μ or TdT to the 3' end of the DSB end, strand continuity is restored by LIG4; this is followed by repair, by undetermined enzymes, of the other strand through addition of deoxyribonucleotides; and finally, the ribonucleotides are excised in an RNase H2-dependent process. The entire pathway is so rapid that the authors suggest that this triple strand repair process is tightly coordinated and may involve interaction between components of different DNA repair pathways. Interestingly, the a-NHEJ DNA repair proteins poly(ADP-

ribose) polymerase 1 (PARP1), LIG3, and XRCC1 (x-ray repair cross-complementing protein 1) interact with c-NHEJ components (10, 11). These factors could be involved in the second strand repair step of ribo-NHEJ. Advanced super-resolution microscopy has enabled direct visualization of NHEJ components at DSBs in cells (12) and should now be used to identify and probe the recruitment of the ribo-NHEJ components. It will also be important to determine how ribo-NHEJ components functionally interact with other DNA repair factors. Pryor *et al.* show that when high levels of deoxyribonucleotides are artificially introduced in cells, c-NHEJ is impaired and thus nucleotide pool imbalances, often detected in cancer cells and regulated during cell cycle progression, could influence DSB repair pathway choice.

Moreover, further detailed analysis of the ribo-NHEJ machinery should help design strategies for genome editing with CRISPR-Cas9. Pryor *et al.* paved the way toward that goal by showing that coexpression of TdT and Cas9 changes the sequence spectra of NHEJ junctions by increasing the frequencies of two nucleotide insertions, which could facilitate gene deletion studies.

Beneficial roles for ribonucleotide incorporation in DNA have been identified previously (13). For example, ribonucleotide incorporation in DNA was implicated in mating-type switching in yeast, and for helping strand discrimination during DNA mismatch repair in eukaryotic cells. It is likely that further studies will unveil other physiological roles for ribonucleotide incorporation in DNA. ■

REFERENCES AND NOTES

1. J. S. Williams *et al.*, *Nat. Rev. Mol. Cell Biol.* **17**, 350 (2016).
2. M. A. M. Reijns *et al.*, *Cell* **149**, 1008 (2012).
3. J. M. Pryor *et al.*, *Science* **361**, 1126 (2018).
4. M. R. Lieber, *Annu. Rev. Biochem.* **79**, 181 (2010).
5. J. Loc'h, M. Delarue, *Curr. Opin. Struct. Biol.* **53**, 22 (2018).
6. M. J. Martin, L. Blanco, *Nucleic Acids Res.* **42**, 7923 (2014).
7. A. F. Moon *et al.*, *Nucleic Acids Res.* **45**, 9138 (2017).
8. J. B. Boulé *et al.*, *J. Biol. Chem.* **276**, 31388 (2001).
9. J. A. Kochan *et al.*, *Nucleic Acids Res.* **45**, 12625 (2017).
10. M. Xing *et al.*, *Nat. Commun.* **6**, 6233 (2015).
11. A. Craxton *et al.*, *Cell Death Differ.* **22**, 890 (2015).
12. D. A. Reid *et al.*, *Proc. Natl. Acad. Sci. U.S.A.* **112**, E2575 (2015).
13. C. J. Potenski, H. L. Klein, *Nucleic Acids Res.* **42**, 10226 (2014).

ACKNOWLEDGMENTS

M.M. thanks K. Meek for critical reading of the manuscript and the French National Research Agency, the French National Cancer Institute, and the French National League Against Cancer for support.

Revving up an artificial metalloenzyme

An engineered metalloenzyme shows promising catalytic activity for sulfite reduction

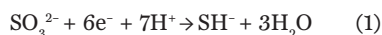
By **Kyle M. Lancaster**

Inorganic oxyanions such as perchlorate, nitrate, and arsenate are aqueous contaminants that are environmentally persistent and easily taken up by biological organisms (1). For example, perchlorate, a common ingredient in products including rocket fuels, munitions, and fertilizers, interferes with human thyroid function when ingested from contaminated drinking water or food (2). Another oxyanion of concern is the fertilizer component nitrate, which leaks from agricultural soil into the water table and promotes eutrophication in aquatic environments (3). Oxyanion decontamination is thus a key challenge facing chemists in the 21st century. On page 1098 of this issue, Mirts *et al.* report a landmark study in protein engineering that affords valuable insights into future solutions for oxyanion remediation (4).

Conversion of oxyanions to more benign species requires selective, multielectron reduction processes. Such processes are mainly driven by redox-active transition metals. However, many oxyanions bind weakly, if at all, to transition metals. Nevertheless, numerous strategies have been

introduced for the sequestration and/or detoxification of harmful oxyanions. These strategies include accumulation in metal-organic frameworks or reduction via homogeneous transition metal catalysts (5, 6). However, these approaches can be stymied when oxyanions occur as mixtures. For example, the relatively environmentally benign sulfite (SO_3^{2-}) ions can interfere with the aforementioned remediation strategies (7), and methods for selective sulfite removal would thus be useful. This is the issue that Mirts *et al.* address.

As with many valuable chemical reactions, biological systems have evolved a solution to sulfite reduction: the metalloenzyme sulfite reductase (SiR), an enzyme that is found in diverse organisms and is a key player in the biogeochemical sulfur cycle. SiR bears a siroheme cofactor at which sulfite is reduced, as well as a four-Fe, four-S ([4Fe-4S]) cluster that provides the electrons needed for the reaction (8). These features enable the enzyme to reduce sulfite all the way to hydrosulfide (SH^-), involving addition of six electrons:



Selectivity for SH^- production varies between assimilatory SiR enzymes (involved in biosynthesis) and dissimilatory SiR enzymes (involved in respiration); the latter yield far broader product distributions that span different sulfur oxidation states (8).

Synthetic models bearing both heme and [4Fe-4S] have been reported, but these systems cannot catalyze sulfite reduction (9). This behavior reflects an often encountered phenomenon in bioinorganic chemistry: Structural reproduction of metalloenzyme active sites is seldom sufficient for promoting the desired reactivity. The metalloprotein matrix has precisely tuned second-sphere motifs with defined electrostatics and medium polarity that enmesh the cofactors and that are vital for effective catalysis (10).

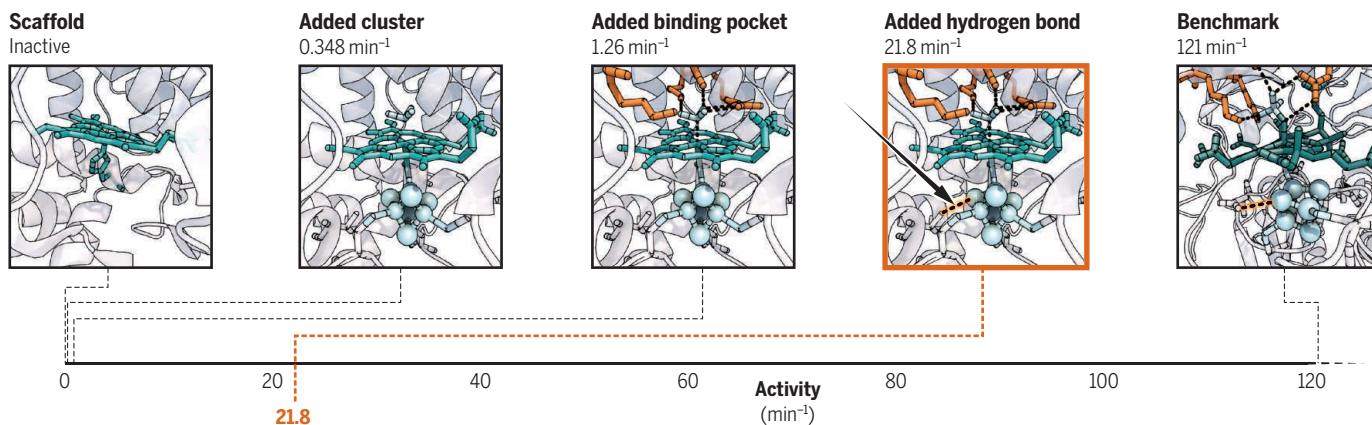
To elucidate the missing ingredients that differentiate a synthetic heme-[4Fe-4S] conjugate from a functional SiR enzyme, Mirts *et al.* took a bottom-up approach (see the figure). The authors first reconstituted metal-locofactors within a surrogate protein matrix. They chose yeast cytochrome c peroxidase (CcP) because it bears a large pocket beneath its heme cofactor that could potentially harbor a [4Fe-4S] cluster. Using protein design software, they engineered a CcP variant with [4Fe-4S]-binding cysteine residues in this pocket. Spectroscopic and other analytical methods verified that this variant, heme-FeS-SiRCcP1, binds both a [4Fe-4S] cluster and a heme b cofactor. Simply adding this [4Fe-4S] to the already heme-containing CcP heme was sufficient to imbue SiR reactivity, albeit poor (see the figure).

To enhance reactivity, the authors expanded their design parameter space be-

Department of Chemistry and Chemical Biology, Baker Laboratory, Cornell University, Ithaca, NY 14853, USA.
Email: kml236@cornell.edu

Protein engineering of metalloenzyme catalytic activity

The enzyme SiR can reduce sulfite all the way to hydrosulfide, a process that involves the addition of six electrons. Mirts *et al.* have engineered a protein that can catalyze this reaction, although the activity remains lower than that of the natural benchmark protein. The engineered protein provides insight into the components that are needed for successful catalysis.



yond the metallocofactors. Native SiR substrate binding pockets contain lysine and arginine residues that are thought to help compensate for the weak binding of sulfite to transition metals. By introducing these substitutions to produce a variant termed K+R-heme-FeS-SiRCcP1, the authors raised the activity somewhat (see the figure). Subsequent variants capitalized on the profound effect of second-sphere hydrogen-bonding and electrostatics over the reduction potentials of metallocofactors (10). Specifically, mutating a native valine to asparagine or cysteine residues, which can form hydrogen bonds to one sulfide of the [4Fe-4S] cluster, markedly increased activity. One such variant, K+R-heme-FeS-SiRCcP3, exhibited the highest activity in the study (see the figure). However, this is still far below the benchmark value for *Escherichia coli* SiR. Furthermore, design features that promote selectivity for full six-electron reduction of sulfite remain to be identified. The influence of heme b substitution for siroheme also merits further investigation.

The study by Mirts *et al.* is a milestone in the use of metalloprotein engineering as a tool to guide catalyst design. It joins other recent achievements such as the use of artificial metalloproteins to elucidate hydrogenase mechanisms (11) or to drive unnatural chemical transformations such as C-Si bond formation (12). This sculpting of protein scaffolds and repurposing of ancient metallocofactors provides key insights that will empower catalyst design toward solving pressing needs, such as oxyanion remediation. ■

REFERENCES AND NOTES

1. H. Rüdel *et al.*, *Environ. Sci. Pollut. Res.* **22**, 7405 (2015).
2. C. M. Steinmaus, *Curr. Environ. Health Rep.* **3**, 136 (2016).
3. G. F. McIsaac, M. B. David, G. Z. Gertner, D. A. Goolsby, *Nature* **414**, 166 (2001).
4. E. N. Mirts, I. D. Petrik, P. Hosseinzadeh, M. J. Nilges, Y. Lu, *Science* **361**, 1098 (2018).
5. A. J. Howarth, Y. Liu, J. T. Hupp, O. K. Farha, *CrystEngComm* **17**, 7245 (2015).
6. C. L. Ford, Y. J. Park, E. M. Matson, Z. Gordon, A. R. Fout, *Science* **354**, 741 (2016).
7. G. T. Townsend, J. M. Suflita, *Appl. Environ. Microbiol.* **63**, 3594 (1997).
8. B. R. Crane, E. D. Getzoff, *Curr. Opin. Struct. Biol.* **6**, 744 (1996).
9. C. Zhou, L. Cai, R. Holm, *Inorg. Chem.* **35**, 2767 (1996).
10. K. M. Lancaster, in *Molecular Electronic Structures of Transition Metal Complexes I* (Springer, 2011), pp. 119–153.
11. J. W. Slater, S. C. Marguet, H. A. Monaco, H. S. Shafaat, *J. Am. Chem. Soc.* **140**, 10250 (2018).
12. S. J. Kan, R. D. Lewis, K. Chen, F. H. Arnold, *Science* **354**, 1048 (2016).

ACKNOWLEDGMENTS

Metalloprotein studies in the author's laboratory are funded by the U.S. Department of Energy Office of Science (DE-SC0013996), the Alfred P. Sloan Foundation, and the National Institute of General Medical Sciences (R35GM124908).

10.1126/science.aau7754

ORGANIC CHEMISTRY

Enantioselective four-component Ugi reactions

A chiral organocatalyst condenses four reactants with stereochemical control

By Renata Riva

In 1921, Passerini (1) reported the reaction that combines an isocyanide with a carbonyl compound (usually an aldehyde) and a carboxylic acid to give a depsipeptide (see the figure). This reaction was the first reported example of a multicomponent reaction (MCR)—one where the product contains essential parts of all of the reactants with the simultaneous generation of several new bonds—based on isocyanides. Such reactions based on isocyanides are called IMCRs. For several years, this reaction received only scant attention; the bad smell of the low-molecular weight isocyanides likely discouraged chemists from exploiting their reactivity. In 1959, the Ugi reaction was reported, in which a fourth component—a primary amine—allows for the formation of a peptide-like structure with the introduction of a new stereogenic center (2). On page 1087 of this issue, Zhang *et al.* (3) now report an enantioselective organocatalytic four-component Ugi reaction.

In MCRs, if a stereogenic center is created, it forms as racemic compounds that must undergo chiral separation. The Ugi reaction, like many other MCRs, has received increasing attention because of the advantages relative to linear syntheses leading to similar scaffolds. First, a one-pot procedure that builds very complex structures in a highly convergent manner ensures atom economy (maximizing the number of reactant atoms that end up in the product) and step economy (minimizing the number of reactions needed to get to the final product). Second, the reaction conditions are very mild; in most cases, the use of protecting groups is unnecessary even if bifunctional reagents are used. Finally, the structure of the fragments bearing the needed functional groups can be varied

at will with the introduction of a high variety of decorations, which allows for a diversity-oriented approach. However, there are also some drawbacks with IMCRs. The scaffold obtained through the MCR is invariably a peptide-like or a depsipeptide skeleton, which limits the structural variety of the new molecules. Also, a stereogenic center is usually generated, so stereochemical issues must be considered, including diastereoselectivity (if at least one reagent is chiral) and enantioselectivity (if all of the reagents are achiral).

Several strategies to increase the scaffold diversity are available. The most versatile is represented by postcondensation transformations that can occur if one or two additional functional groups are present (4). These chemical transformations offer great

opportunities to synthesize new heterocycles that can find applications as possible drugs (5) or as fluorophores (6). In addition, MCRs can be used to generate polymers directly (7). In contrast, an area that is still underexplored in IMCR chemistry is the control of the configuration of the new stereogenic center. In the last half century, extensive studies

on either diastereoselectivity or enantioselectivity control of many organic reactions have been reported, but the solution to these problems within MCRs is more difficult. The complexity of the reaction mechanism plays a crucial role. One possibility is to use chiral, enantiomerically pure reagents to achieve a substrate-controlled diastereoselection. This goal can be realized by using chiral inputs obtained from the chiral pool or by using biocatalytic or organocatalytic procedures, which could yield green MCRs (8).

The Passerini and Ugi reactions can in principle be run with control of the enantioselectivity in the presence of a chiral mediator, possibly a catalyst. However, some intrinsic characteristics of IMCRs hamper this approach. Both reactions can proceed spontaneously under appropriate conditions, and these competing background reactions

“Despite many efforts in the intervening 15 years, the enantioselective four-component Ugi reaction had remained elusive...”

Department of Pharmacy, University of Genova, 16147 Genova, Italy. Email: renata.riva@unige.it

can have an impact on the enantiomeric excess. The activation responsible for the enantioselectivity must occur on the carbonyl (Passerini reaction) or on the imine (the first intermediate, arising from the condensation of the aldehyde with the amine, in the Ugi reaction) before the formation of the new stereogenic center. If a Lewis acid is used, a competition with other basic groups can occur, or, if a Brønsted acidic catalyst is used, the competition with the achiral carboxylic acid can become important. Finally, if a metal surrounded by a chiral ligand is used, the coordination of the isocyanide may negatively influence the reaction pathway.

After some pioneering work published in 2003 by Denmark and Fan (9), several groups studied the catalytic asymmetric approach to IMCRs. Despite many efforts in the intervening 15 years, the enantioselective four-component Ugi reaction had remained elusive, although brilliant solutions were found for the catalytic enantioselective version of some Passerini- or Ugi-type reactions [for a recent review, see (10)]. These reactions are in most cases performed in the absence of the carboxylic acid and different scaffolds are obtained (for example, 5-aminooxazoles).

The previous achievements in the field of IMCRs and the development of very efficient organocatalytic procedures that can activate several electrophilic species, including imines, provided Zhang *et al.* with important groundwork. The catalytic effect was ensured by choosing a Brønsted acid, with a higher acidity than the carboxylic acid reactant. More difficult was the optimization of the structure of the catalyst in order to obtain an efficient control of the enantioselectivity. Only by fine-tuning with the development of a new family of complex chiral phosphoric acids were they able to meet this formidable

challenge. The methodology is robust, as a library of more than 80 α -acylaminoamides was synthesized in good to excellent enantiomeric excess. Moreover, density functional theory calculations were useful for understanding the mechanism of the reaction and the reasons for the enantioselectivity and offered insight into further investigations.

Especially in the field of medicinal chemistry, the need for enantiomerically pure compounds is of paramount importance. A robust and efficient catalytic enantioselective procedure like that demonstrated by Zhang *et al.* is in principle the most helpful approach. Diastereoselective procedures usually suffer from a narrower scope because stereochemical control is sometimes limited only to a specific class of compounds. Finally, the possibility of elaborating these enantiomerically pure products through postcondensation transformation makes this protocol even more valuable, allowing a diversity-oriented approach to a nearly unlimited number of new structures. ■

REFERENCES

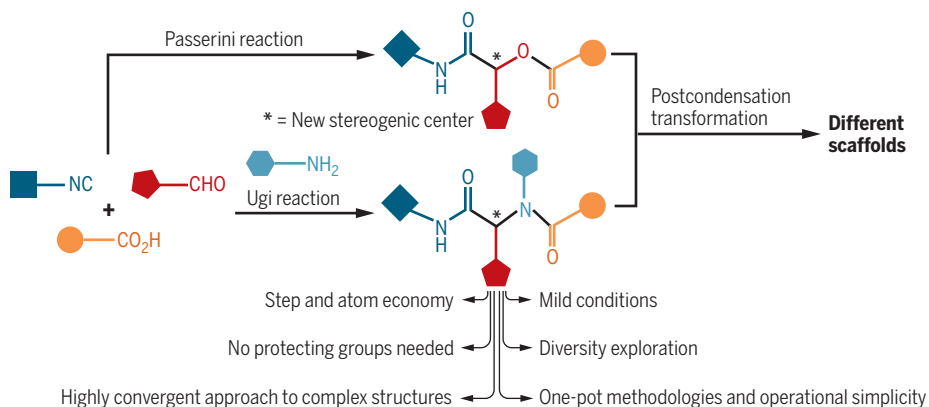
1. M. Passerini, *Gazz. Chim. Ital.* **51**, 126 (1921).
2. I. Ugi, R. Meyr, U. Fetzer, C. Steinbrückner, *Angew. Chem.* **71**, 389 (1959).
3. J. Zhang *et al.*, *Science* **361**, eaas8707 (2018).
4. L. Banfi, A. Basso, R. Riva, in *Synthesis of Heterocycles via Multicomponent Reactions I*, R. V. A. Orru, E. Ruijter, Eds. (Springer, 2010), pp. 1–40.
5. I. Akritopoulou-Zanze, *Curr. Opin. Chem. Biol.* **12**, 324 (2008).
6. R. Riva, L. Moni, T. J. J. Müller, *Targets in Heterocyclic Systems*, vol. 20 (Società Chimica Italiana, 2016), pp. 85–112.
7. O. Kreye, T. Tóth, M. A. R. Meier, *J. Am. Chem. Soc.* **133**, 1790 (2011).
8. L. Banfi, A. Basso, L. Moni, R. Riva, *Eur. J. Org. Chem.* **2014**, 2005 (2014).
9. S. E. Denmark, Y. Fan, *J. Am. Chem. Soc.* **125**, 7825 (2003).
10. Q. Wang, D.-X. Wang, M.-X. Wang, J. Zhu, *Acc. Chem. Res.* **51**, 1290 (2018).

10.1126/science.aau7497

The advantages of multicomponent reactions

The figure highlights the potential and the advantages of multicomponent reactions that include isocyanides, the Passerini and Ugi reactions, with respect to the classical linear synthesis.

Zhang *et al.* now extends these advantages with an organocatalyst that enables the formation of specific enantiomeric products with the Ugi reaction.



ROBOTICS

Robotic-flapper maneuvers and fruitfly turns

Studies of an aerial robot help explain rapid banked turns in the fruitfly

By Franck Ruffier

Winged insects have been a rich source of inspiration for designing flying robots, but robots can also be used to test hypotheses about the mechanisms underlying the control of insect flight (1). Winged insects perform continuously demanding tasks from takeoff to landing that include rapid turns as well as virtuosic chasing behaviors. During evasive maneuvers, the fruitfly executes rotations to achieve banked turns (2). On page 1089 of this issue, Karásek *et al.* (3) show that the accurate control of a new tailless, flapping-wing robot reveals how these insects perform rapid banked turns, even though the robot is much larger than a fruitfly. The similarities between the maneuver dynamics of the robot and that of fruitflies strongly support the hypotheses that rotation around the vertical axis (the “yaw” movement) is passively controlled throughout evasive maneuvers and that fruitflies actively control their heading only after executing these turns.

In addition to mating and food foraging, escaping from dangers such as predators is one of the main challenges of flying animals. Most escapes of flying animals involve rapid banked turns that can occur at different pitch-to-roll rate ratios [for the fruitfly, see (2)], corresponding to either roll-dominated or pitch-dominated maneuvers. Maneuvering an aerial robot that has kinematics similar to that of the fruitfly and that can freely execute any control-command sequences allows testing of hypotheses about the insect’s flight. In particular, adding a yaw command did not make the robot of Karásek *et al.* turn more quickly. Thus, fruitflies may perform such evasive maneuvers as fast as possible without feedback information.

Karásek *et al.* also developed a functional, low-complexity model of aerodynamic yaw

Aix-Marseille Université, CNRS, Institute of Movement Sciences (ISM), Marseille, France. Email: franck.ruffier@univ-amu.fr

torque that explains the rapid banked turn of the robot. Specifically, two new terms were added: the so-called translation-induced coupled yaw torques. Each of the new yaw-torque terms depends on a product between a translational velocity and the torque command around the axis of this same translation. One—the roll command—is the product between the longitudinal velocity (the forward speed) and the angular acceleration around the longitudinal axes (roll rate). The other—the pitch command—is the product between the transverse velocity (the sideways speed) and the angular acceleration around the transverse axes (pitch rate). Such couplings were highly correlated with the biological flight data, so the fruitfly might use these torque couplings to passively induce yaw acceleration and execute rapid banked turns.

Karásek *et al.* used their flapping-wing robot as a tool to better understand the sophisticated control-command system during escape behavior. Their meticulous design enables free flight with four control inputs, which is comparable to the helicopter-like simplified modeling of a winged insect (4). The lift force is produced by two bioinspired clap-and-fling mechanisms of the wings moving at 17 Hz. The yaw torque is produced by changing the wing root angle asymmetrically, the pitch torque is produced by adjusting the dihedral angle, and the roll torque is produced by generating asymmetrical flapping lift. The asymmetrical frequency control of the clap-and-fling mechanisms relies on two independent motors. The independent mechanisms of the roll and pitch torque generation allow for different pitch-to-roll ratios, and the robot can perform 360° roll and pitch flips.

Such increased controllability let the authors test a full range of banked-turn ma-

neuvers. In forward flight, 90° banked turns are dominated by roll commands—low pitch-to-roll ratio. The roll commands rely on different techniques to generate the roll torque across the bioinspired aerial robot (see the figure). In forward flight, the pitch also controls the forward velocity, the yaw controls the heading, and the lift controls the altitude. A slightly smaller flapping-wing robot, the Nano Hummingbird, used a different asymmetrical lift mechanism to generate roll torque and also achieved an autonomous 360° roll flip (5). This robot used an asymmetrical 30-Hz flapping-wing orientation, that combined both wing twist and angle-of-attack modulation.

At the insect scale, a tiny 120-Hz flapping-wing robot, the Robobee, used asymmetrical wing-stroke amplitude (6) to produce roll torque. At larger scales, roll control was achieved by disabling lift on the inside wing toward the desired turn. A 6-Hz flapping-wing, birdlike robot used spoilers (7), and a bird-inspired glider used tip-feather ailerons (8). Recently, a roll-dominated banked-turn maneuver was reproduced with a small drone endowed with a distinctive morphing wing design composed of artificial feathers (9). The folding of these artificial feathers on the inside wing creates asymmetric surface morphing. Such an asymmetrical wing surface lets the drone turn rapidly without using conventional ailerons. Precisely gliding birds can achieve banked turns by flexing the wrist and elbow of their inside wing toward their desired turn, thus substantially reducing the inside wing surface (10).

Gliding is one solution to overcome the main challenge for aerial robots: their high energy consumption during powered flight. At high pitch, the double clap-and-fling

configuration chosen by Karásek *et al.* also benefits from nonnegligible gliding effects that substantially increase its flight range. Indeed, the flight endurance increases with the robot mass in small drones (11), and the wingspan increases with the mass in flapping micro air vehicles (12). In bioinspired aerial robots, when the flapping frequency decreases, the wingspan, mass, flight endurance, and flight range generally increase (see the figure). Biomimetic aerial robotics that will integrate bioplausible perception and bioplausible flight mechanics could lead to further insights into animal behavior, such as puzzling aerial chasing behavior. Indeed, trials have been reported with bioprincipic robots typically equipped with propellers to test free-collision navigation hypotheses, as reviewed in (13, 14). ■

REFERENCES AND NOTES

1. N. Franceschini, *Proc. IEEE* **102**, 751 (2014).
2. F. T. Muijres *et al.*, *Science* **344**, 172 (2014).
3. M. Karásek, F. T. Muijres, C. De Wagter, B. D. W. Remes, G. C. H. E. de Croon, *Science* **361**, 1089 (2018).
4. G. Portelli, J. Serres, F. Ruffier, N. Franceschini, *J. Physiol. Paris* **104**, 27 (2010).
5. M. Keennon, K. Klingebiel, H. Won, in *Proceedings of the 50th American Institute of Aeronautics and Astronautics (AIAA) Aerospace Sciences Meeting Including the New Horizons Forum and Aerospace Exposition* (AIAA, 2012), p. 588.
6. K. Y. Ma *et al.*, *Science* **340**, 603 (2013).
7. G. A. Folkertsma, W. Straatman, N. Nijenhuis, C. H. Venner, S. Stramigoli, *IEEE Robot. Autom. Mag.* **24**, 22 (2017).
8. R. G. Hoey, *Bioinspir. Biomim.* **5**, 045008 (2010).
9. M. Di Luca, S. Mintchev, G. Heitz, F. Noca, D. Floreano, *Interface Focus* **7**, 20160092 (2017).
10. D. R. Warrick, M. W. B. Bundle, K. P. Dial, *Integr. Comp. Biol.* **42**, 141 (2002).
11. D. Floreano, R. J. Wood, *Nature* **521**, 460 (2015).
12. H. Liu, S. Ravi, D. Kolomenskiy, H. Tanaka, *Phil. Trans. R. Soc. B* **371**, 20150390 (2016).
13. M. V. Srinivasan, *Physiol. Rev.* **91**, 413 (2011).
14. J. R. Serres, F. Ruffier, *Arthropod Struct. Dev.* **46**, 703 (2017).

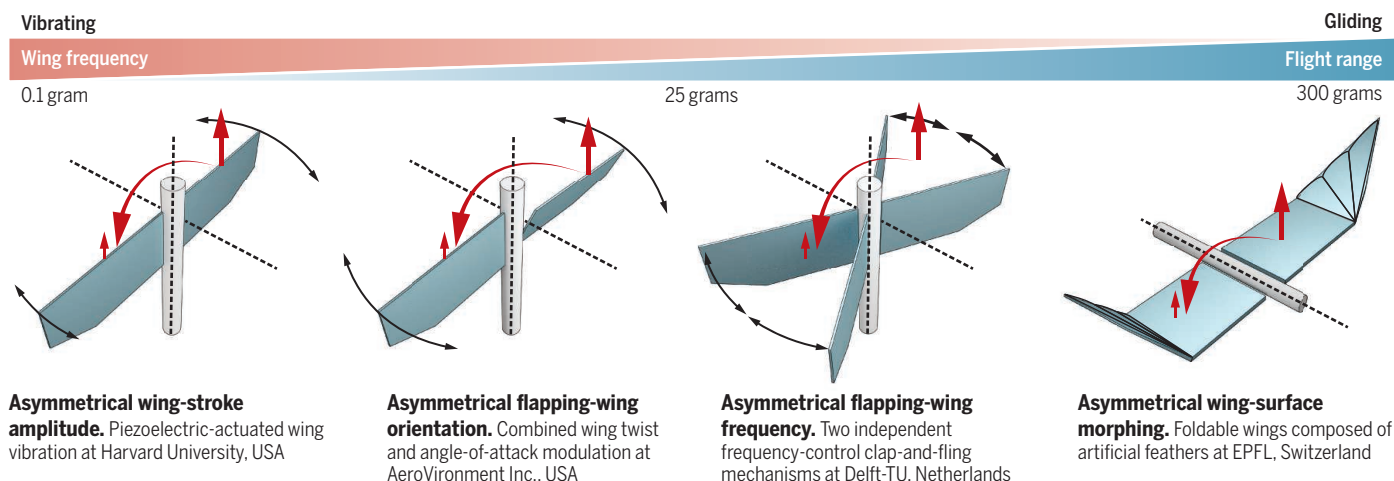
ACKNOWLEDGMENTS

I thank K. Trego-Ruffier for fruitful comments on the manuscript.

10.1126/science.aau7350

Ready to roll

Roll commands have been implemented with wing mechanisms for robots exhibiting various flight ranges. Various mechanisms exist, from powering the flight directly with the vibrating wings in lighter bioinspired robots (left) to relying on gliding in heavier bioinspired robots (right).



A “technology-smart” battery policy strategy for Europe

Batteries’ inherent characteristics should inform policies

By **Martin Beuse¹**, **Tobias S. Schmidt¹**,
Vanessa Wood²

The world market for battery and hybrid electric vehicles (EVs), including passenger cars, buses, and freight trucks, is growing rapidly. Currently, almost all lithium-ion (Li-ion) battery cells for EVs are produced by East Asian (Chinese, Japanese, and Korean) manufacturers. Meanwhile, the European automotive industry, among the largest in the world, generates 4% of European gross domestic product, and 12 million jobs (1); however, Europe houses less than 1% of the global Li-ion battery cell manufacturing capacity, and this production capability largely addresses niche markets. Manufacturing of batteries for EVs is thus at the center of industry policy discussions at the European Commission (EC), with calls for “European sovereignty” in Li-ion battery manufacturing (2). Here, we offer insights from battery research and innovation studies to suggest that catching up with East Asian companies is worthwhile, but can only be achieved step by step, by bringing competences to Europe through strategic global collaborations, supported by creation of an attractive European market for EVs.

EV batteries consist of cells packaged together and controlled by a battery management system. The cell makes up roughly 70% of the cost of an automotive battery, which currently amounts to more than 40% of the cost of a fully electric car (3). Bolstered by national industrial policies and the demands for Li-ion batteries in consumer electronics (with 2 billion cell phone batteries and 350 million tablet and laptop batteries manufactured in 2017), East Asian manufacturers have achieved continual improvements in terms of performance (e.g., lifetime, energy density) and cost of batteries. Recently, several East Asian players announced the construction of gigafactories

in Europe (battery cell manufacturing factories with output capacity in excess of 1 GWh/year; e.g., CATL in Germany, LG Chem in Poland, Samsung and SK Innovation in Hungary).

High-level policy-makers in Europe have expressed the importance of the battery industry in ensuring Europe’s continued competitiveness in the automotive sector and have called for exclusively European-owned cell factories, an “Airbus for batteries.” For example, Maroš Šefčovič, vice-president of the European Commission, stated: “By 2025,...the European battery market could be...as large as the entire Danish economy. Do we want to leave this to our global competitors” (4)?

To seize this opportunity, the EC estimates an investment requirement of €20 billion, or 10 to 20 European gigafactories. To support these ambitions, the EC has developed a Strategic Action Plan together with representatives from industry and academia, outlining potential actions and funding opportunities (potentially up to

several billion €) (2). In line with these ambitions, three consortia (led by Saft, TerraE, and Northvolt) have formed to build European-owned gigafactories, supported by the European Investment Bank (e.g., with a €52.5 million loan for Northvolt’s demonstration cell factory).

However, the European automotive industry is currently not financially invested in these consortia and has not yet indicated if and when they want to enter large-scale cell manufacturing themselves. The industry broadly acknowledges the relevance of understanding battery cells and has invested in various R&D activities; however, their views regarding cell manufacturing differ. Some automotive companies consider battery cells a commodity-like component, sourced from suppliers according to specification. These firms see added value primarily in downstream activities of the supply chain (see the figure). Other companies consider ownership in cell manufacturing worthwhile; however, they have not yet entered the arena and discuss leapfrogging to “next generation” technologies, such as solid-state batteries.

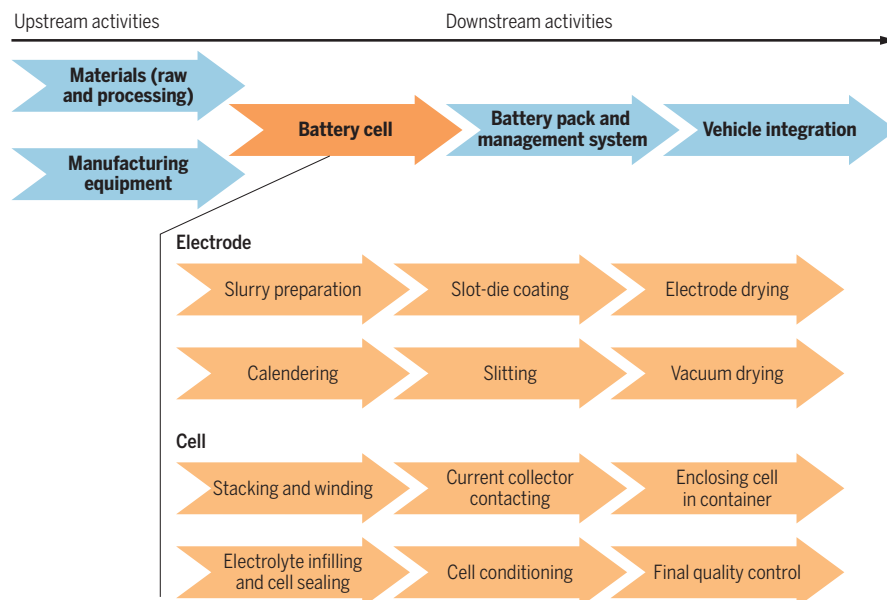
Given this current state of affairs, it is important for policy-makers, the automotive industry, and the cell manufacturing industry to consider three questions in order to determine a common strategy.

BATTERIES: A STRATEGIC COMPONENT?

Is the battery cell a commodity-like part or a core component of strategic value to the European automotive industry? Currently, we consider battery cells as core components

A complex supply chain for Li-ion battery cell manufacturing

A simplified distinction between upstream and downstream activities is shown [adapted from (12) and (13)].



¹Energy Politics Group, ETH Zurich, Haldeneggsteig 4, CH-8092 Zurich, Switzerland. ²Materials and Device Engineering Group, ETH Zurich, Gloriastrasse 35, CH-8092 Zurich, Switzerland. Email: tobias.schmidt@ethz.ch; vwood@ethz.ch



for three reasons. First, they are at the center of an EV's product architecture, meaning that their properties influence many other components (e.g., chassis material choice) and the overall vehicle design (e.g., through changed center of gravity). Second, the development of new cells is highly dynamic. For instance, the performance specifications of battery cells, such as the energy and voltage they can deliver at a certain current, depend on the materials used and their design. Each year, new cell designs evolve (5), providing opportunity for strategic differentiation of products among manufacturers.

Third, cells are complex to design, involving a multitude of trade-off decisions. Cells may be optimized for applications with high energy or power requirements, for cycle life, or for cost. For example, decreasing cost and cobalt dependence through increasing the nickel content in the cathode might enable higher cell voltage but decrease cell life (5, 6). To manage these trade-offs and make smart design decisions, close interaction between the cell manufacturer and automaker is important (7, 8). In other words, manufacturing close to markets fosters innovation (9). Local ownership (e.g., through equity joint ventures) further increases transfer and exchange of tacit knowledge and intellectual property (10). Given the cell's centrality, dynamic development, and complexity, policies that aim at localizing cell manufacturing industry can thus result in a competitive advantage. Conversely, simply sourcing battery cells from foreign players will lead to strong dependence on their performance.

LEAPFROGGING?

Is it possible for the European battery industry to leapfrog East Asian suppliers with the next generation of battery cell technology? Leapfrogging current market leaders is difficult, if not impossible because, even for incumbents, production of high-performing cells at continuous quality levels is challenging (11), largely due to the dually complex nature of battery cell technologies (complex in both design and manufacturing, with interplay between both). Changes in one cell manufacturing step require adjustments in other steps and most likely in the design of the cell as well (12). Likewise, changing cell design requires adjustments not only in other design features, but also to the manufacturing. For example, to obtain a cell that discharges faster, a manufacturer might change the size of the materials that store the Li. This will require reformulation of the slurry and changes to the slurry mixing. In turn, this may require changes to the slurry coating and drying parameters (which are used to get the active materials onto the foils that are stacked or wound into the cell), the additives added into the liquid electrolyte, and the formation protocol (i.e., how the cell is cycled prior to shipping to ensure stability).

The ability to improve upon existing dually complex technology relies heavily on tacit knowledge, which is gained by experience with the product and the manufacturing process and which is not easily copied or transferred (8). In the battery field, the move from laboratory experiments or pilot-

scale demonstrations to full-scale manufacturing requires knowledge gained from direct experience with full-scale production (12). Dual complexity also increases the need for interaction among actors along the supply chain (7), making a technology harder to replicate (13). For batteries, knowledge is spread across multiple domains, from materials processing to manufacturing and integration. Incumbent firms can leverage not only their assets, but also their accumulated tacit knowledge and long-term partnerships across the value chain to evolve with a technology's trajectory.

The last decades of battery research indicate that future cell generations will draw heavily from knowledge gained through designing and manufacturing current-generation cells at large scale. Li-ion batteries are on a clear trajectory, with several future developments already on the horizon (e.g., high-voltage cathodes, high-capacity anodes, and solid electrolytes) (5) that will evolve sequentially, building on existing but often tacit design and manufacturing knowledge. The process of discovering new battery materials to actually commercializing a battery cell with these materials is very time consuming and can take up to 20 years (14). Literature on catching up suggests that technological discontinuities in dually complex technologies, like the emergence of the next-generation battery technology, do not necessarily help new entrants overtake incumbents, but rather strengthen the position of incumbents, who can leverage their cumulative knowledge base (15). High entry barriers are

A Tesla, Inc. gigafactory in Sparks, Nevada, manufactures automotive battery cells.



also exemplified by multiple accounts of battery technology startups failing in the past. Therefore, a leapfrogging strategy does not seem promising. If Europe wants to successfully compete in battery cell manufacturing, it will have to catch up step by step.

REALISTIC?

Is it a realistic policy strategy to build a European battery cell industry? History has shown that catching-up in Li-ion battery manufacturing is possible. Korea caught up to Japan, and China, with the announcement of multiple gigafactories, is set to triple the rest of the world's combined capacity.

To catch up in a dually complex product like batteries, it is necessary to transfer tacit knowledge (in manufacturing equipment integration and product design), as well as enable interactive learning up- and downstream of cell manufacturing (7, 8).

A starting point for transferring capital goods can be to acquire existing equipment or an entire factory from an established player. For example, leading Chinese companies purchase their battery manufacturing lines from Japanese and Korean companies. However, it is not sufficient to focus on individual parts of the value chain, as most tacit knowledge is gained from interactions across the value chain (7).

For successful catching up, it is paramount that the tacit knowledge be accessible and that domestic companies develop the capability to learn (15). Korean firms have leveraged licenses from Japanese producers and hired retired Japanese engineers to transfer their

product design knowledge. Chinese firms entered R&D and production partnerships with Japanese and Korean firms. China's CATL, the world's fastest growing cell manufacturer, evolved from ATL, a subsidiary of Japanese TDK that produces consumer electronics batteries. Tesla cooperates with Panasonic (Japan) for cell manufacturing in a gigafactory in Nevada, USA, and pursues the pack assembly and software design itself. This partnership was enabled, among other factors, by the huge scale envisioned, making the partnership interesting to an incumbent cell manufacturer like Panasonic. In other words, a substantial market is an important factor in catching up.

Europe seems to be an attractive location for cell manufacturing, as demonstrated by the announcements of East Asian firms to build gigafactories. In addition, Europe is not starting from zero. It can build upon strong research facilities and downstream activities, as well as specialized cell manufacturing know-how. If Europe wants to tap this potential and build its own industry, waiting is not an option because the knowledge gap to market leaders is ever widening. The EC has rightfully recognized the need to act. However, policy-makers should not be hung up on the idea of European independence in cell manufacturing from the start. For dually complex technologies, the sensible, theory- and practice-proven approach is to create an attractive home market and learn quickly together with current competitors. This will enable the European industrial players to choose later whether they want to pursue cell manufacturing themselves.

A TECHNOLOGY-SMART POLICY

To support this process, a technology-smart policy strategy, considering battery cells' dual complexity, based on insights from battery research and innovation studies, is needed. The European Union (EU) should put particular emphasis on two elements: First, incentivizing collaborative R&D between companies along the supply chain. Importantly, these incentives should also be available for research consortia that include non-European companies. European companies have already formed such collaborations, predominantly outside Europe (e.g., European BASF and Japanese TODA for a calcination facility in the United States; European Bühler and Chinese Lishen for manufacturing equipment in China). This can be backed up with measures to educate engineers and to secure access to raw materials and capital.

Second, a consistent European EV policy strategy is needed to create an attractive EV market that makes partnerships for current market-leading East Asian firms worth-

while and provides planning security for European firms. Although many European national and subnational governments have already introduced EV support policies, this policy patchwork misses the opportunity to leverage the massive size of the EU's common car market. We therefore recommend an ambitious yet realistic EU-wide EV target. One option would be to mandate a certain market share of EVs or even completely phase out internal combustion engine cars, as China has done. However, such policy is politically hard to sell. A more realistic alternative is to increase the stringency of the EU's emissions standard on car fleets to a level that translates into large market shares of EVs.

Only once the European industry has started to catch up should the EU consider incentivizing differentiation of European cells through novel chemistry, manufacturing approaches, or design. With an established market for European-made EVs that use cells produced in Europe, differentiating features can be introduced gradually, guided by R&D activities that identify the unique opportunities for batteries within the European automotive sector. ■

REFERENCES AND NOTES

1. European Commission, Automotive Industry - Internal Market, Industry, Entrepreneurship, and SMEs (2018); <https://ec.europa.eu/growth/sectors/automotive>.
2. European Commission, "Strategic Action Plan on Batteries" (2018); https://ec.europa.eu/transport/sites/transport/files/3rd-mobility-pack/com20180293-annex2_en.pdf.
3. C. Curry, "Lithium-ion Battery Costs and Market" (2017); <https://data.bloomberglp.com/bnef/sites/14/2017/07/BNEF-Lithium-ion-battery-costs-and-market.pdf>.
4. European Commission, Press Release Database, Speech by Vice-President for Energy Union Maroš Šefčovič at the Industry Days Forum on the Industry-led initiative on batteries / the EU Battery Alliance (2018); http://europa.eu/rapid/press-release_SPEECH-18-1168_en.htm.
5. R. Schmuch, R. Wagner, G. Hörpel, T. Placke, M. Winter, *Nat. Energy* **3**, 267 (2018).
6. M. Ebner, F. Marone, M. Stambanoni, V. Wood, *Science* **342**, 716 (2013).
7. A. Malhotra, T. S. Schmidt, J. Huenteler, "Accelerating low-carbon innovation through policy," AAAS Annual Meeting 2017: Serving Society Through Science Policy, panel together with Jessika Trancik (MIT) and Masaru Yurime (Tokyo Univ.), Boston/USA (T. S. Schmidt) (2017).
8. T. S. Schmidt, J. Huenteler, *Glob. Environ. Change* **38**, 8 (2016).
9. E. R. H. Fuchs, *Science* **345**, 519 (2014).
10. D. C. Mowery, J. E. Oxley, B. S. Silverman, *Strateg. Manage. J.* **17**, 77 (1996).
11. S. J. Harris, D. J. Harris, C. Li, *J. Power Sources* **342**, 589 (2017).
12. A. Kwade et al., *Nat. Energy* **3**, 290 (2018).
13. A. Stephan, T. S. Schmidt, C. R. Bening, V. H. Hoffmann, *Res. Policy* **46**, 709 (2017).
14. G. Crabtree, "The Joint Center for Energy Storage Research (JCESR): A New Paradigm for Energy Storage Research" (2015); <https://anl.app.box.com/v/15-10-11JCESR-ECSPHOENIX>.
15. F. Malerba, R. Nelson, *Ind. Corp. Change* **20**, 1645 (2011).

ACKNOWLEDGMENTS

We acknowledge A. Malhotra for valuable discussions and comments on this manuscript.

10.1126/science.aau2516



Accepted at Oxford University at age 15, polymath John Nunn became a chess grandmaster at age 23.

BOOKS *et al.*

HUMAN PHYSIOLOGY

Smarter, stronger, longer

From extreme longevity to photographic memory, unusual individuals push the boundaries of human ability

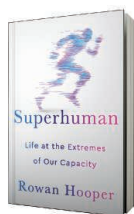
By **Christopher Kemp**

Daniel Tammet dreams in pi. Familiar to most of us, at least in an abstract sort of way, pi is the ratio of a circle's circumference to its diameter. It's an infinitely long number, starting with the digits three-point-one-four and continuing forever. Tammet, an autistic savant, has memorized it to more than 22,000 digits. He also learned to speak Icelandic in a week.

What makes Tammet different from the rest of us? In *Superhuman*, Rowan Hooper sets out to explore the extremes of human ability, traveling the world and meeting a colorful cast of superlative subjects along the way. He meets centenarians, opera singers with extraordinary range, people who don't seem to experience fear, and people with HSAM—highly superior autobiographical memory—who can recall every mundane detail about their life going back decades. Give them a date and they will tell you the weather,

what they were wearing, and what they ate that day. He meets chess grandmasters and people who have taught themselves dozens of languages.

An editor for *New Scientist*, Hooper trained as an evolutionary biologist and is an open-minded and able guide, lucidly explaining the genetic and environmental factors that allow rare individuals to run for days on end, or sleep 3 hours a night long-term, or learn dozens of languages fluently.



Superhuman
Life at the Extremes of
Our Capacity
Rowan Hooper
Simon & Schuster,
2018. 352 pp.

Jeanne Calmet lived to be 122. In the case of longevity, Hooper notes, the science is incredibly complicated and still mostly unresolved. Hoping to find the specific genes responsible for long life, researchers have screened the genomes of inhabitants of Blue Zones—discrete regions such as Okinawa in Japan and Sardinia, near Italy, where inhabitants live longer on average than elsewhere. They have found thousands of candidate genes that might contribute a benefit but not in one's early life. Environmental factors decide whether an individual gets to 80, but complex genetics decide whether that person hits 100.

By contrast, for Alex Mullen, a World Memory Champion who can memorize the

order of a shuffled deck of cards in less than 20 s, the secret lies in specific memory-training regimens that anyone can learn. It's all environmental, all the time.

At times, one feels a little bound by Hooper's prejudices. In his chapter on intelligence, for example, I was waiting for him to address the neuroanatomical abnormalities of Einstein's brain. The physicist's corpus callosum—the nerve fibers that connect the two hemispheres of the brain—was enormously oversized. For decades, neuroscientists have pondered whether those and other structural brain differences allowed Einstein to process information differently from the rest of us. But Hooper doesn't mention it. Instead, he speaks with author Hilary Mantel, who has an innate ability—learned in childhood, she says—to write immersive historical narratives.

In a chapter on singing, I was certain Hooper would explore the fascinating mysteries of overtone singing. Practiced in Mongolia, Tibet, Kazakhstan, and elsewhere, overtone singers can manipulate the resonance of air in their throat to sing two distinctly different notes at once. But instead, he profiles opera singer Matthew Rose. From numerous twin studies, Hooper writes, genetic traits have been shown to have a profound effect on musical skills, determining both how much an individual practices and the subsequent effects of the practice.

In total, Hooper examines 11 different human traits, which are organized into three parts: thinking (including traits such as intelligence, memory, and language); doing (bravery, singing, or running, for example); and being (which includes longevity and happiness). I wouldn't expect a project such as this to be exhaustive by any means. But there are substantial gaps in the human experience.

Why, for instance, is there no chapter on pain, a fascinating and still poorly understood part of life for everyone, except for the rare people who congenitally cannot feel it? This, in particular, seems like an oversight.

Despite this, *Superhuman* is an incredibly readable and endlessly interesting book. Perhaps most importantly, it is an inspiring book. I am clearly not a superhuman. I might be worth a chapter in a book titled *Okay Human*. But Hooper has shown me a multitude of other goals that I could still strive toward—such as altruism through charity or profound happiness in the face of adversity—and for that I am superlatively thankful. ■

The reviewer is the author of *The Lost Species: Great Expeditions in the Collections of Natural History Museums* (University of Chicago Press, 2017). Email: cjkemp@gmail.com

SCIENCE & SOCIETY

Looking ahead

A cosmologist advocates thoughtful deployment of science and technology to address the challenges facing humanity

By **Andrew Robinson**

In 2004, the year before he became president of Britain's Royal Society, Martin Rees memorably remarked that "we are no wiser than Aristotle was more than 2000 years ago." The reason that humankind has made such extraordinary scientific progress since Aristotle's time, Rees argued, is primarily because of technological advances, such as telescopes and space probes in the case of astronomy—his own field of expertise.

Rees's latest book, *On the Future: Prospects for Humanity*, written "as a scientist, as a citizen, and as a worried member of the human species," is really a meditation on this earlier thought, short in extent but wide in range: from redesigning genes, through the likelihood of human-induced climate change, to the possibility of encounters with alien intelligence in the Universe. Its overall theme is that Earth's growing population will flourish only if science and technology are deployed with "wisdom."

Inevitably, much of the interest in this topic derives from the author's predictions about the coming decades, although Rees is mindful of the fact that scientists are "rotten forecasters—almost as bad as economists." As he notes, one of his predecessors as astronomer royal famously announced in 1956 that newspaper predictions of imminent manned space travel were "utter bilge."

On the whole, he is cautionary, sometimes pessimistic, whether speaking of our home planet or deep space. About driverless cars, for example, he notes that in 1930 there were a million vehicles on the roads of Britain and more than 7000 fatalities, whereas in 2017, the number of vehicles had increased 30 times and the number of fatalities had fallen to 1700. In the intervening period, roads had improved, yet the main reason for the fall in deaths was increased safety in cars, brought

about by technological improvements, including electronic satellite navigation.

Most likely, this trend will continue, with better lane discipline on motorways, platooning of goods vehicles, and so on. But can we assume that ever-faster computing will enable a wirelessly connected car to distinguish the nature of an obstacle on the road ahead and respond safely to it with greater reliability than an average human driver? Perhaps—yet only by using an amount of electric power comparable with the power needed to propel the car, according to some experts, notes Rees. And will the car's passengers accept no human driver? Not on the basis of civil aviation, the bulk of which is now done



The electric power required to respond to obstacles with greater reliability than a human driver may mitigate the value of driverless cars, notes Rees.

on autopilot but has yet to reach the point of dispensing with a human pilot.

Regarding climate change, Rees anticipates, realistically, that carbon dioxide concentrations in the atmosphere from burning of fossil fuels will continue to rise steadily for the next 20 years. By then, however, it should be possible to predict future "climate sensitivity"—the effect on the ground of increased water vapor and clouds—from a longer time base of data and better modeling.

If sensitivity is high, and existing climates are at risk, then climate may need to be rapidly controlled through geoengineering, by using solar-reflecting aerosols in the upper atmosphere and even sunshades in space. Because the political problems of geoengineer-

On the Future
Prospects for Humanity
Martin Rees
Princeton University Press,
2018. 272 pp.



ing would be "an utter political nightmare," Rees argues that it would be "prudent" now to explore geoengineering techniques, so as to clarify which of them make sense and also to dampen down any unjustified optimism about a "quick fix" for climate change.

As for space exploration by humans, Rees favors privately sponsored expeditions, despite his admiration for the 1960–1970s NASA Apollo program. But he strongly disagrees with the view, proposed by Elon Musk of Space-X and also Rees's late Cambridge University colleague Stephen Hawking (not to mention some science-fiction writers), that there can be mass emigration from Earth.

"Coping with climate change may seem daunting, but it's a doddle compared to terraforming Mars. Nowhere in our Solar system offers an environment even as clement as the Antarctic or the top of Everest." Better, thinks Rees, to depute exploration and settlement of other planets to robots and artificial intelligence, enabled by Earth-based humans.

Underlying the development and exploitation of technology must be values that science itself cannot provide, Rees concludes, after some interesting discussion of science and society, including religion. "I would describe myself as a practicing but unbelieving Christian," he comments somewhat enigmatically.

"It's salutary and depressing to realize how much of the economy is dedicated to activities and products that would be superfluous if we felt we could trust each other," such as military forces and unhackable computer systems, writes Rees. Ancient thinkers, including Aristotle, expressed a comparable regret about their societies. What has changed over the millennia, of course, is that the impact of our lack of wisdom—amplified by the internet—is now global and requires global, not local, solutions. ■

10.1126/science.aau9686

The reviewer is the author of *Einstein: A Hundred Years of Relativity* (Princeton University Press, 2015), *The Story of Measurement* (Thames & Hudson, 2007), and *Earth-Shattering Events: Earthquakes, Nations and Civilizations* (Thames & Hudson, 2016). Email: andrew@andrew-robinson.org



TOMORROW'S EARTH
Read more articles online
at scim.ag/TomorrowsEarth



LETTERS

In Bridge Creek, Oregon, reduced grazing rejuvenated the ecosystem.

Edited by Jennifer Sills

Grazing limits benefited Bridge Creek

In the News Feature story “Beavers, rebooted” (8 June, p. 1058), B. Goldfarb discusses a field project where beaver dam analogs were constructed for stream restoration along a portion of Bridge Creek in central Oregon. Goldfarb writes that when the project began in 2007, the system was a narrow trench bordered by desiccated pastures, with a lingering population of steelhead and rainbow trout and a “skeleton crew” of beavers that built dams across the sluice-like channel that tended to wash away. However, the area was much more vibrant than Goldfarb suggests.

Between 1989 and 1991, the Bureau of Land Management acquired land along large portions of Bridge Creek (1), and after 1991, there was no grazing in the area for 5 years (2). In the years that followed, only limited winter grazing was permitted (2). As a result, streamside willows and other riparian vegetation flourished (3–5).

In 1988, the Bureau of Land Management began monitoring beaver activity by inventorying dams twice a year along a 25-km reach (2). As streamside vegetation recovered during the 1990s, beaver dams appeared throughout the area (2). Even where dams breached, remnant portions contributed positively to the ongoing riparian and channel recovery—they redirected flows, added local channel complexity, widened the floodplain, and accumulated sand/gravel bars, all of which expanded the riparian community while increasing channel sinuosity and

reducing stream gradient (2). Although this dynamic process of natural recovery had been under way for nearly 2 decades before beaver dam analogs were constructed along 3.4 km of stream, it was not mentioned in the News story.

Because the Bureau of Land Management changed streamside management along Bridge Creek (i.e., protecting it from grazing impacts after 1991), recovered riparian plant communities could handle the high density of beaver dam analogs installed after 2007 (6). Thus, the real success story of Bridge Creek is the reduction in grazing, which allowed vegetation recovery and beaver presence along 25 km of stream, not intensive structuring with beaver dam analogs along the 3.4 km discussed in the News story.

Rick Demmer¹* and Robert L. Beschta²

¹Newport, TN 37821, USA. ²Department of Forest Ecosystems and Society, Oregon State University, Corvallis, OR 97331, USA.

*Corresponding author.

Email: rickdemmer@msn.com

REFERENCES

1. Bureau of Land Management, “Sutton Mountain Coordinated Resource Management Plan (CRMP)” [U.S. Department of the Interior (USDI), Bureau of Land Management, Prineville District, Prineville, OR, 1995].
2. R. Demmer, R. L. Beschta, *Northwest Sci.* **82**, 309 (2008).
3. Bureau of Land Management, “Decision Record Sutton Mountain Coordinated Resource Management Plan (CRMP)” (USDI Bureau of Land Management, Prineville District, Prineville, OR, 1996).
4. H. A. Cooke, S. Zack, “Avian responses to management of riparian habitat in the Prineville District” (Bureau of Land Management, Central Oregon, Report of 1999 and 2000 Field Activities, North American Program, Wildlife Conservation Society, 2000).
5. H. A. Cooke, S. Zack, “Using riparian zone width and height to predict riparian songbird community diversity and distribution in Central Oregon: Implications for assessment and restoration” (North American Program, Wildlife Conservation Society, 2003).
6. J. B. Kauffman, R. L. Beschta, N. Otting, D. Lytjen, *Fisheries* **22**, 12 (1997).

10.1126/science.aau5005

U.S. fast test reactor will pay dividends

In his News story “Congress pushes for multibillion-dollar nuclear reactor that critics call a boondoggle” (3 July, <https://scim.ag/Reactor>), A. Cho discusses the proposed Versatile Fast Neutron Source, a test reactor that many in the research community deem important to build. We agree with the nuclear scientists and engineers who support the fast reactor. Technology advances when the tools are available. The fast reactor will enable potentially groundbreaking advances in nuclear energy technology and materials science.

If the United States does not have a fast test reactor, our nuclear innovators will have no option but to use the dwindling number of fast test reactors available in other countries. For example, TerraPower, a U.S. nuclear reactor design company, has been forced to rely on a test reactor in Russia for essential materials testing (1).

As explained in the News story, some don’t like the idea of a new American fast-neutron test reactor. But today’s commercial reactors, workhorse anchors of the power grid and by far our largest source of emissions-free energy (2), are just the beginning of what nuclear energy can do. New technologies promise higher-quality heat, better use of fuel, more flexible operations, and lower-cost fabrication (3).

Commercialization takes time, and to reap these benefits, we should be working on this now. Building a test reactor takes time, too, and the two most capable

test reactors in the United States are each more than 50 years old (4). Meanwhile, the planet is warming, and a lot of the energy-hungry developing world is choking on the smoke from fossil-fueled generators. In decades past, the United States was the global leader in nuclear exports (5), enabling it to define non-proliferation and safety norms. Now, as the world needs copious amounts of clean, reliable energy, there will be a corresponding global need for a new generation of reactors, whether we develop and export them or leave that to Russia or China.

Peter B. Lyons¹ and John F. Kotek^{2*}

¹Retired Commissioner of the Nuclear Regulatory Commission and Assistant Secretary for Nuclear Energy, U.S. Department of Energy, Washington, DC 20585, USA. ²Nuclear Energy Institute, Washington, DC 20004, USA.

*Corresponding author. Email: jfk@nei.org

REFERENCES

1. J. Conca, "Should the U.S. build a fast nuclear test reactor or continue to be beholden to Russia?," *Forbes* (2018); www.forbes.com/sites/jamesconca/2018/07/26/should-we-build-a-fast-nuclear-test-reactor-or-continue-to-be-beholden-to-russia.
2. Nuclear Energy Institute, "Nuclear by the numbers" (2018); www.nei.org/CorporateSite/media/filefolder/resources/fact-sheets/nuclear-by-the-numbers-20180412.pdf.
3. "Advanced nuclear 101," *Third Way* (2015); www.thirdway.org/report/advanced-nuclear-101.
4. D. Meserve *et al.*, "Assessment of user needs for irradiation testing" (2016); www.energy.gov/sites/prod/files/2016/12/f34/Test%20Reactor%20Charge%20Presentation%2012-9-16_1.pdf.
5. L. S. H. Holgate, S. Saha, "America must lead on nuclear energy to maintain national security," *The Washington Quarterly* (2018); https://twq.elliott.gwu.edu/sites/g/files/zaxdzs2121/f/downloads/TWQ_Summer2018_HolgateSaha.pdf.

10.1126/science.aau7786

TECHNICAL COMMENT ABSTRACTS

Response to Comment on "Unexpected reversal of C₃ versus C₄ grass response to elevated CO₂ during a 20-year field experiment"

Peter B. Reich, Sarah E. Hobbie, Tali D. Lee, Melissa A. Pastore

Nie and colleagues suggest a key role for interannual climate variation as an explanation for the temporal dynamics of an unexpected 20-year reversal of biomass responses of C₃-C₄ grasses to elevated CO₂. However, we had already identified some climate-dependent differences in C₃ and C₄ responses to eCO₂ and shown that these could not fully explain the temporal dynamics we observed.

Full text: [dx.doi.org/10.1126/science.aau8982](https://doi.org/10.1126/science.aau8982)

ERRATA

Erratum for the Report "Degradation of microRNAs by a Family of Exoribonucleases in *Arabidopsis*" by V. Ramachandran, X. Chen, *Science* 361, eaav2481 (2018).

Published online 7 September 2018;

10.1126/science.aav2481

ONLINE BUZZ

Prioritizing population policies

In their Policy Forum "Global warming policy: Is population left out in the cold?" (17 August, p. 650), J. Bongaarts and B. C. O'Neill explore why climate groups such as the Intergovernmental Panel on Climate Change (IPCC) have overlooked the role of population growth. Authors of a recent IPCC report responded that population growth was addressed in their chapter but excluded from the summary for policy-makers. An excerpt of their comment is shown below. Read the full eLetter and add your own at <http://science.sciencemag.org/content/361/6403/650/tab-e-letters>.

"...[T]he Policy Forum deplores the failure to explicitly include population issues in IPCC summaries....Population issues, however, were in fact discussed in the Fifth Assessment....Chapter 11.9.2 [www.ipcc.ch/pdf/assessment-report/ar5/wg2/WGIIAR5-Chap11_FINAL.pdf] specifically [notes] that providing greater access to reproductive health services for those who wish to limit their families will both...mitigate climate-relevant pollutants and protect human health. Unfortunately, this information was not included in the final WGII Summary to Policy-Makers or IPCC Synthesis Report....Indeed, there are a wide range of issues raised in the assessment chapters that never see the 'light of day' in the summaries...[We] should focus...on developing rigorous and transparent guidance on how decisions are made on what, from a vast panorama of analyses in the main chapters, is highlighted for policy attention...."

Kirk R. Smith, Alistair Woodward, Andy Haines, Zoe Chafe

10.1126/science.aav3528

Cite as: P. B. Reich *et al.*, *Science*
10.1126/science.aau8982 (2018).

Response to Comment on “Unexpected reversal of C₃ versus C₄ grass response to elevated CO₂ during a 20-year field experiment”

Peter B. Reich^{1,2*}, Sarah E. Hobbie³, Tali D. Lee⁴, Melissa A. Pastore³

¹Department of Forest Resources, University of Minnesota, St. Paul, MN 55108, USA. ²Hawkesbury Institute for the Environment, Western Sydney University, Penrith, NSW 2753, Australia. ³Department of Ecology, Evolution, and Behavior, University of Minnesota, St. Paul, MN 55108, USA. ⁴Department of Biology, University of Wisconsin, Eau Claire, WI 54701, USA.

*Corresponding author. Email: preich@umn.edu

Nie and colleagues suggest a key role for interannual climate variation as an explanation for the temporal dynamics of an unexpected 20-year reversal of biomass responses of C₃-C₄ grasses to elevated CO₂. However, we had already identified some climate-dependent differences in C₃ and C₄ responses to eCO₂ and shown that these could not fully explain the temporal dynamics we observed.

Using some new analyses, Nie and colleagues (1) suggest that growing season temperature and rainfall can explain much more of the unexpected 20-year reversal of C₃ versus C₄ grass community responses to elevated CO₂ than our analyses and interpretation concluded (2). They based their analyses on statistical models using 3-year running averages of the effect of eCO₂ on total biomass (i.e., the average difference between ambient and enriched CO₂ across all C₃ or C₄ plots), which they compared to the 3-year running average of growing season (May–Sept) rainfall and temperature.

We question whether using 3-year running averages [which we included solely for visualization purposes in (2)] is the best way to test for interannual climate variation interactions with the elevated CO₂ treatment; we believe that at the very least, using annual data makes more sense for such examinations. Moreover, we believe that using all data (i.e., 88 plots for all 20 years, $n = 1760$) in a mixed model [as in (2)] makes the best use of all available information; whereas Nie *et al.* used a data set of $n = 36$, comprising just the 18 values representing the 3-year running averages of effect size for each of the C₃ and C₄ groups. As two-thirds of the data for each 3-year running average of effect size is shared with both the prior and subsequent years, there is considerable lack of independence of such data across years.

Additionally, Nie *et al.* chose to use climate data from the Minneapolis–St. Paul International Airport rather than data available from Cedar Creek. The airport is more than 60 km south of the experimental site, averaged $>1.5^{\circ}\text{C}$ warmer for the growing seasons in question, and most problematic, had only moderate correlations ($R^2 \approx 0.5$) for May–Sept rainfall and temperature with the same metrics at the

experimental site, meaning they share only roughly 50% of the same information. Given that Cedar Creek lies outside of the urban heat island while the airport lies within it (3), the relatively fine-scale spatial variability in rainfall, and the availability of data on site, use of the alternate data from the southern Twin Cities metropolitan area is not warranted, in our view. Note also that Nie *et al.* use growing season temperature and rainfall defined as May–September values (except in their figure 2 where they used MJJ rainfall and unspecified temperature data), whereas in (2) we used summer temperature and rainfall defined as May–July (MJJ); our rationale was that biomass harvests and net nitrogen mineralization assays were completed by very early August each year, such that the three prior months were a reasonable metric for assessing climate sensitivity of CO₂ responses. We also used MMJ rainfall measured at the experimental site, rather than at the Cedar Creek weather station 2 km away, for years when it was available.

Regardless of the appropriateness of the approach used, Nie *et al.* assert that potential collinearity among explanatory variables might have masked the true effects of climate on biomass responses in our analyses and suggest that their analysis with only two independent variables (growing season rainfall and temperature) avoids such potential problems. They found that response of C₄ biomass to eCO₂ was positively correlated with both growing season rainfall and temperature (May–September) and response of C₃ biomass to eCO₂ was negatively correlated with growing season temperature. However, when we ran similar analyses to Nie *et al.* using annual biomass differences (between ambient and elevated CO₂) and rainfall and temperature data from the

experimental site, rather than 3-year running averages of biomass from the experiment and 3-year running average climate data from the Minneapolis–St. Paul International Airport, we did not find any significant ($P < 0.10$) relationship with MJJ or May–September temperature for either functional group (Fig. 1). We also did not find any significant ($P < 0.10$) relationship with MJJ or May–September rainfall for the C_3 grasses (Fig. 1). We did find a marginally significant positive ($P = 0.08$) relationship of C_4 biomass response to eCO_2 with May–September rainfall (Fig. 1). However, the simple bivariate fit of C_4 biomass response to eCO_2 versus May–September rainfall using annual data (and local climate data) was weaker ($R^2 = 0.16$, R^2 adjusted = 0.12) than when using the 3-year running average data used by Nie *et al.* ($R^2 = 0.32$). Thus, annual data do also suggest some degree of dependency of C_4 biomass response to eCO_2 to growing season rainfall (May–Sept), similar to that previously reported in relation to MJJ rainfall in (2), albeit not as strongly as suggested by the analyses of Nie *et al.* However, annual data provide no support for any such dependency for either functional group on summer or growing season temperature.

Moreover, we had tested for collinearity among explanatory variables in our original analyses and found it to be extremely modest; although we did not report these results in (2), we did point out that MJJ rainfall was only weakly correlated with year as a continuous variable (2). Thus, we were able to independently assess the effects of MJJ rainfall and year on the effects of CO_2 on C_4 versus C_3 biomass [table S1 of (2)]. As reported in (2), we noted a significant ($P = 0.0243$) interaction of $CO_2 \times$ functional group \times MJJ rainfall on the biomass response [table S1 of (2)]; C_4 grasses were more responsive to eCO_2 when rainfall was higher, whereas C_3 grasses were more responsive in low rainfall (the same conclusion Nie *et al.* draw from their analysis). However, we also found that the $CO_2 \times$ year \times functional group interaction was significant ($P = 0.0347$) even after accounting for differential responses to rainfall for the two functional groups by including rainfall and rainfall interactions in the model [table S1 of (2)]. Thus, despite differential sensitivity to eCO_2 as a function of summer rainfall, the reversal of responsiveness of C_3 and C_4 plots to eCO_2 over time was not explained by interannual variation in precipitation. Including temperature in the above model [which we had tested for but did not report in (2)] did not alter the results and there were no interactions involving temperature and eCO_2 response for either functional group. Thus, the reversal of responsiveness of C_3 and C_4 plots to eCO_2 over time was not explained by interannual variation in temperature.

In summary, we do not believe that the approach taken by Nie and colleagues is sufficiently robust to overturn our conclusions that C_3 and C_4 group responses to CO_2 were dif-

ferentially sensitive to summer rainfall, but that those differences did not cause the longitudinal shift over time in responses of the two groups. Figure 2 of Nie *et al.* is consistent with our interpretation in (2); C_4 grasses responded more positively to eCO_2 in moist than dry years, and late in the experiment than early in the experiment. Nie *et al.* suggest visually that the average of 1°C warmer summers after 2010 made the C_4 grass response to eCO_2 during those moist 8 years stronger than during the moist 7 years from 1999–2005. In a full model that includes year, local summer temperature, and local summer rainfall, we find no evidence that responses to eCO_2 were greater in C_4 grasses in warmer summers ignoring summer rainfall (i.e., there was no $CO_2 \times$ functional group \times MJJ temperature interaction) or in warmer summers that also had higher summer rainfall (i.e., there was no $CO_2 \times$ functional group \times MJJ temperature \times MJJ rainfall interaction). Thus, although their ideas are intriguing, our analyses do not provide evidence to support them.

REFERENCES

1. M. Nie, J. Zou, X. Xu, C. Liang, C. Fang, B. Li, Comment on "Unexpected reversal of C_3 versus C_4 grass response to elevated CO_2 during a 20-year field experiment". *Science* **361**, eaau3016 (2018).
2. P. B. Reich, S. E. Hobbie, T. D. Lee, M. A. Pastore, Unexpected reversal of C_3 versus C_4 grass response to elevated CO_2 during a 20-year field experiment. *Science* **360**, 317–320 (2018). doi:10.1126/science.aas9313 Medline
3. B. V. Smoliak, P. K. Snyder, T. E. Twine, P. M. Mykleby, W. F. Hertel, Dense network observations of the Twin Cities canopy-layer urban heat island. *J. Appl. Meteorol. Climatol.* **54**, 1899–1917 (2015). doi:10.1175/JAMC-D-14-0239.1

22 August 2018; accepted 23 August 2018
Published online 14 September 2018
10.1126/science.aau8982

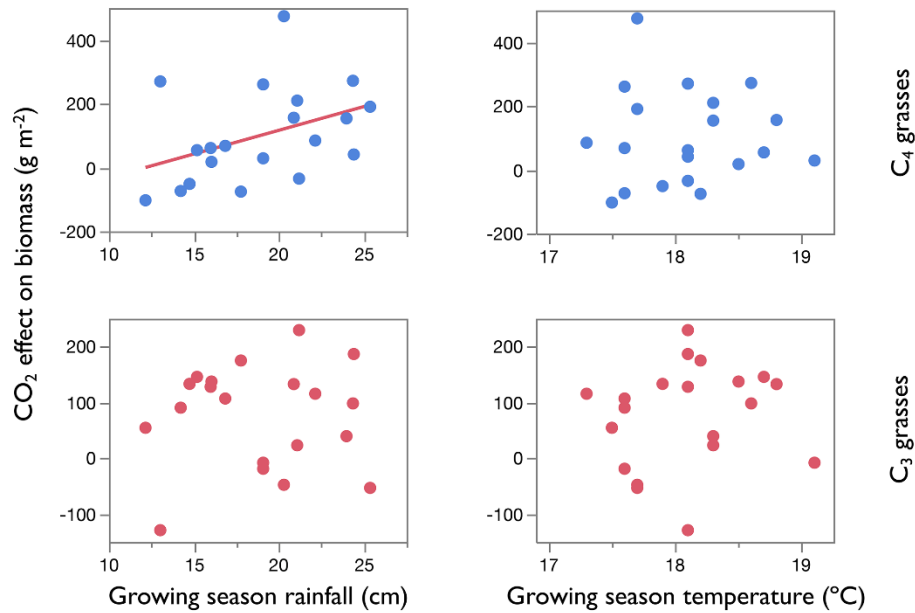
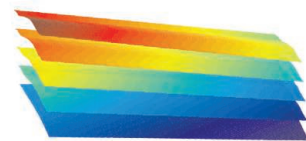


Fig. 1. Bivariate relationships between the CO₂ effect on total C₃ and C₄ biomass and growing season climate using annual biomass and climate data. CO₂ effect size = biomass under eCO₂ – biomass under ambient CO₂. Growing season is defined as May–September. Biomass data match those in figure S1 of (2). Note, unlike in (1), climate data are from Cedar Creek, not the Minneapolis–St. Paul International airport. The relationship between the CO₂ effect size and temperature was not significant for either the C₃ group ($P = 0.55$, $R^2 = 0.02$) or the C₄ group ($P = 0.98$, $R^2 = 0.00$). The relationship between the CO₂ effect size and rainfall was not significant for the C₃ group ($P = 0.88$, $R^2 = 0.00$) and was marginally significant for the C₄ group ($P = 0.076$, $R^2 = 0.16$).

RESEARCH

Solution processing with tandem organic solar cells

Meng et al., p. 1094



IN SCIENCE JOURNALS

Edited by **Stella Hurtley**



MIGRATION

Bird forecast

Billions of birds migrate across the globe each year, and, in our modern environment, many collide with human-made structures and vehicles. The ability to predict peak timing and locations of migratory events could greatly improve our ability to reduce such collisions. Van Doren and Horton used radar and atmospheric-condition data to predict the peaks and flows of migrating birds across North America. Their models predicted, with high accuracy, patterns of bird migration at altitudes between 0 and 3000 meters and as far as 7 days in advance, a time span that will allow for planning and preparation around these important events. —SNV *Science*, this issue p. 1115

A new prediction framework will protect migrating birds like this blue-winged warbler.

ENZYME DESIGN

Metals brought together do more

Enzymatic reduction of oxyanions such as sulfite (SO_3^{2-}) requires the delivery of multiple electrons and protons, a feat accomplished by cofactors tailored for catalysis and electron transport. Replicating this strategy in protein scaffolds may expand the range of enzymes that can be designed de novo. Mirts *et al.* selected a scaffold protein containing a natural heme cofactor and then engineered a cavity suitable for binding a second cofactor—an iron-sulfur cluster (see the Perspective by Lancaster). The resulting designed enzyme was optimized through rational mutation into a catalyst with spectral characteristics and activity similar to that of natural sulfite reductases. —MAF

Science, this issue p. 1098;
see also p. 1071

ROBOTICS

Flying fast and free

Insect flight can be fast and agile, making it hard to study its detailed aerodynamics. Karásek *et al.* designed an untethered, flapping-wing robot with impressive agility that can mimic fruitfly maneuvers (see the Perspective by Ruffier). They studied the robot's motion during rapid banked turns, which revealed that passive motion through the turn generated yaw torque coupling. This correcting yaw rotation propelled the robot toward the escape heading needed for effective turning. —MSL

Science, this issue p. 1089;
see also p. 1073

BIOCHEMISTRY

A protein designed to sense metabolites

Many diseases cause characteristic changes in blood metabolites. Yu *et al.* describe

a paper-based assay in which a chosen metabolite can be oxidized to generate reduced nicotinamide adenine dinucleotide phosphate (NADPH). Color changes in a designed NADPH sensor protein are then quantified by a digital camera. The sensor system successfully generated point-of-care measurements of phenylalanine, glucose, and glutamate. Concentrations of phenylalanine in the blood of phenylketonuria patients were analyzed within minutes with only half a microliter of blood. —VV

Science, this issue p. 1122

FOREST ECOLOGY

Mapping global deforestation patterns

Forest loss is being driven by various factors, including commodity production, forestry, agriculture, wildfire, and urbanization. Curtis *et al.* used high-resolution Google Earth imagery to map

and classify global forest loss since 2001. Just over a quarter of global forest loss is due to deforestation through permanent land use change for the production of commodities, including beef, soy, palm oil, and wood fiber. Despite regional differences and efforts by governments, conservationists, and corporations to stem the losses, the overall rate of commodity-driven deforestation has not declined since 2001. —AMS

Science, this issue p. 1108

MOLECULAR BIOLOGY

RNA takes over DNA repair

Damage to DNA genomes is normally thought to be repaired with DNA. Pryor *et al.* now describe a clear exception (see the Perspective by Modesti). They found that RNA is routinely incorporated during the repair of DNA double-strand breaks through the mammalian nonhomologous end-joining (NHEJ) pathway. In a variety of contexts,

including V(D)J recombination and Cas9-induced genome engineering, two “DNA” polymerases specific to NHEJ preferentially added RNA in cells. These RNA additions facilitated the critical step of ligation and were later replaced by DNA to complete the NHEJ repair process. —SYM

Science, this issue p. 1126;
see also p. 1069

METAMATERIALS

Going quantum with metamaterials

Metasurfaces should allow wafer-thin surfaces to replace bulk optical components. Two reports now demonstrate that metasurfaces can be extended into the quantum optical regime. Wang *et al.* determined the quantum state of multiple photons by simply passing them through a dielectric metasurface, scattering them into single-photon detectors. Stav *et al.* used a dielectric metasurface to generate entanglement between spin and orbital angular momentum of single photons. The results should aid the development of integrated quantum optic circuits operating on a nanophotonic platform. —ISO

Science, this issue p. 1104, p. 1101

ORGANISMAL BIOLOGY

Teasing apart ant venom

Ant venoms are primarily made up of poorly characterized polypeptides. Robinson *et al.*

combined transcriptomics and mass spectrometry-based proteomics to determine the mechanism of action of giant red bull ant venoms. Most of the venom peptides stemmed from a diverse hymenopteran toxin gene superfamily. Two peptides were responsible for causing pain in mammals, but by two different mechanisms. One peptide had both pain-causing activity and incapacitated crickets, a food for these ants, thereby functioning in both defense and predation. —PJB

Sci. Adv. 10.1126/sciadv.aau4640
(2018).

HUNTINGTON'S DISEASE

Improving Huntington's disease detection

Early detection of Huntington's disease (HD) could help the development of therapeutic strategies to block or delay disease progression. Byrne *et al.* found that blood and cerebrospinal fluid concentrations of mutant huntingtin (mHTT) and neurofilament light (NfL) proteins correlated with disease severity in HD patients. Alterations in circulating mHTT and NfL concentrations were among the earliest detectable changes in HD. Thus, concentrations of these proteins in biofluids might be used in combination with other clinical measures for improving the accuracy and efficiency of early HD detection. —MM

Sci. Transl. Med. 10, eaat7108 (2018).

IN OTHER JOURNALS

Edited by **Caroline Ash**
and **Jesse Smith**



CANCER

The benefits of marginal brain therapy

Diffuse gliomas are among the most common brain tumors in adults. Surgery is often successful, but, in many patients, the tumor eventually recurs at the surgical margins. A promising drug targets certain mutationally altered metabolic enzymes in gliomas but is toxic when delivered systemically. Shankar *et al.* hypothesized that both problems could be addressed by applying the drug directly to the surgical margins immediately after tumor resection. They developed a diagnostic tool that can be used in the operating room to determine tumor mutation status and, hence, drug sensitivity. By studying mouse models, they found that when they injected a sustained-release formulation of the drug directly into gliomas of the appropriate genotype, the mice survived

considerably longer than control mice. —PAK

Proc. Natl. Acad. Sci. U.S.A. 115, E8388
(2018).

DEVELOPMENTAL BIOLOGY

Unraveling the mystery of thalidomide

Off-label use of thalidomide became a worldwide trend in the 1950s and early 1960s to alleviate morning sickness. It resulted in a historical tragedy, as thousands of babies were born with severe birth defects. Donovan *et al.* may have found a missing link to explain how the drug affects fetal development. The researchers show that thalidomide and closely related drugs rapidly degrade the transcription factor Sal-like protein 4 (SALL4), which is necessary for fetal limb and organ formation. Adding further weight to their findings, certain individuals with mutations in the *SALL4*



The giant red bull ant has complex multifunctional venom.

PHOTO: KAAREL OLESKY/GETTY IMAGES

ECOLOGY AND CLIMATE

Organic-matter flow in kelp forest

As the global climate warms, there are shifts in the geographical distribution of organisms, which can be accompanied by changes in ecosystem functioning. Pessarrodona *et al.* have been investigating the ecosystem consequences of the climate-driven arrival of warm-temperate kelp forest communities to the northwestern coastlines of Europe. Cycling of organic matter in the ecosystem—through kelp growth, herbivory, and decomposition—was faster in the new communities relative to cycling in native cold-temperate kelp communities. Notably, decomposition of plant detritus occurred 6.5 times faster. The continued northward expansion of warm-temperate kelp can be expected to lead to shifts in the flow of organic matter through these ecosystems and to further changes in associated communities of consumer organisms. —AMS
J. Ecol. 10.1111/1365-2745.13053 (2018).

Laminaria ochroleuca
is moving north
as the climate warms.

gene develop abnormalities that resemble thalidomide-induced birth defects. —PNK
eLife **7**, e38430 (2018).

PHOSPHATASE DRUGS

Drugging the undruggable

The reversible phosphorylation of proteins controls all aspects of life. Targeting phosphorylation offers a broad range of therapeutic opportunities. Although kinases are among the most prevalent drug targets, phosphatases have traditionally been overlooked. Krzyzosiak *et al.* used surface plasmon resonance to develop a method to enable target-based discovery of serine/threonine phosphatases. The method identified Raphin1, a selective inhibitor of the regulatory subunit of protein phosphatase 1, PPP1R15B, a negative regulator of protein quality control. Raphin1 boosted protein quality control in cells and slowed down disease

progression in a mouse model of Huntington's disease. —SMH
Cell **174**, 1216 (2018).

PHYSICS

The entropy of a few

Mesoscopic structures have been predicted to host topologically nontrivial quantum states that could form the basis of

fault-tolerant quantum computing. Distinguishing these states from more mundane ones is tricky; one potentially distinguishing characteristic is the entropy of the state, which would have to be measured to high precision in a system of only a few particles. Hartman *et al.* demonstrate such a technique and validate it using a well-understood GaAs quantum dot system. The method is based on the relationship between changes in the chemical potential and changes in temperature, entropy, and the number of particles residing on the dot. Its precision suggests that it could be used in more exotic settings. —JS

Nat. Phys. 10.1038/s41567-018-0250-5 (2018).

ENVIRONMENT

Following plastic through the economy

Over the past 50 years, plastic production and pollution have surged. Efforts to better handle plastic waste require detailed knowledge of the life cycles of different plastic types. Kawecki *et al.* report a probabilistic study of the life cycles of seven polymers that together make up 80% of the plastics used by manufacturers in Europe. The authors provide a detailed picture of the production, manufacturing, consumption, waste collection, and recycling, including trade flows, for each polymer, with a particular focus

on textiles. The results can be used to predict how much plastic is likely to be released into the environment at different stages of each plastic's life cycle, thus informing strategies for preventing plastic pollution. —JFU

Environ. Sci. Technol. **52**, 9874 (2018).

PROTEIN FOLDING

Specialized chaperones required

Although some proteins can reach a properly folded state without assistance, many require help to adopt the correct topology and avoid kinetic trapping in nonnative states. Chaperones encapsulate guest proteins and use adenosine triphosphate (ATP)–driven conformational changes to help them fold, but not all chaperones work for all substrates. Balchin *et al.* compared the folding pathway of the cytoskeleton protein actin with its proper chaperone, TRiC, to the incorrect folding that occurs with the bacterial chaperone GroEL. TRiC functions by stabilizing an extended form of actin with the proper secondary structure and topology. ATP binding and hydrolysis drives release of this partially folded intermediate into the chaperone where it can successfully fold. GroEL fails to bind the intermediate properly and thus is not able to successfully fold actin, even after ATP binding and hydrolysis. —MAF
Cell **174**, 1507 (2018).



Reducing plastic pollution requires better knowledge of its entire life cycle.

ALSO IN SCIENCE JOURNALS

Edited by Stella Hurtley

IMMUNOLOGY

(IL-2) be or not to be?

Immunological T follicular helper (T_{FH}) cells are a subpopulation of $CD4^+$ T cells that support B cell antibody production and the establishment of B cell memory. By contrast, non- T_{FH} cells orchestrate enhanced innate immune cell functions at sites of pathogen encounter. The factors underlying differentiation into a T_{FH} or non- T_{FH} cell remain poorly understood, though there is evidence to suggest that the T cell growth factor interleukin-2 (IL-2) may play a role. Using IL-2 reporter mice, DiToro *et al.* show that naïve $CD4^+$ T cells that produce IL-2 are fated to become T_{FH} cells, whereas nonproducers, which receive IL-2, become non- T_{FH} cells. The $CD4^+$ T cell–fate decision was linked to T cell receptor strength—only those naïve $CD4^+$ T cells that received the highest T cell receptor signals were able to produce IL-2. —STS

Science, this issue p. 1086

ORGANIC CHEMISTRY

Steering together all four Ugi pieces

The nearly 60-year-old Ugi reaction is a remarkably efficient means of linking together four molecular building blocks: an aldehyde, an amine, a carboxylic acid, and an isocyanide. Because each component is independently tunable, the reaction is especially well suited to the assembly of diverse compound libraries. However, stereoselectivity has been a challenge. Zhang *et al.* now show that chiral phosphoric acids can catalyze the four-component coupling with high enantioselectivity (see the Perspective by Riva). Theory suggests that a hydrogen-bonded complex involving the phosphoric acid and carboxylic acid sets the stereochemistry for isocyanide attack on an imine intermediate. —JSY

Science, this issue p. 1087; see also p. 1072

NEUROSCIENCE

Representing the identity of a smell

We still don't know how odors retain their identities over a range of concentrations. Working in mice, Bolding and Franks simultaneously recorded spiking activity from neurons in the olfactory bulb and piriform cortex, two important brain regions for olfaction. Odor information was transformed from a representation that was highly concentration dependent in the olfactory bulb to a representation that was largely concentration invariant in the piriform cortex. The underlying mechanism involves a “winner-takes-all” lateral inhibition. In the collateral network of the piriform cortex, the principal cells responded promptly to output from the olfactory bulb, and recurrent inhibition curtailed the intensity dependence of the signal. —PRS

Science, this issue p. 1088

SOLAR CELLS

Tailoring tandem organics

Tandem solar cells can boost efficiency by using a wider range of the solar spectrum. The bandgap of organic semiconductors can be tuned over a wide range, but, for a two-terminal device that directly connects the cells, the currents produced must be nearly equal. Meng *et al.* used a semiempirical analysis to choose well-matched top- and bottom-cell active layers. They used solution processing to fabricate an inverted tandem device that has a power conversion efficiency as high as 17.4%. —PDS

Science, this issue p. 1094

PROTEIN TARGETING

ER-SURF protein import into mitochondria

Eukaryotic cells contain membrane-bound organelles, defined by distinct protein compositions. Almost all cellular proteins are

synthesized in the cytosol, and thus, organelle-resident proteins must be directed to their appropriate location after synthesis. Working in yeast, Hansen *et al.* identified a protein-targeting paradigm termed ER-SURF, in which the membrane expanse of the endoplasmic reticulum (ER) serves as a “capture net” for mitochondrial proteins. This process productively redirected mitochondrial precursor proteins for efficient mitochondrial import. Thus, two distinct organelles, once thought to be mutually exclusive protein destinations, can cooperate during protein targeting. —SMH

Science, this issue p. 1118

SUSTAINABILITY

Gaia enters a new state

According to the Gaia hypothesis, living organisms and their inorganic environments form a self-regulating system that helps to maintain the conditions for life on Earth. In a Perspective, Lenton and Latour argue that Gaia is entering a new state—Gaia 2.0—in which humans are becoming aware of their influence on Earth processes and will change their behavior to improve conditions for life on Earth. The authors explore some of the fundamental features of Gaia and how they can inform efforts to maintain a self-regulating, human life–supporting planet. —JFU

Science, this issue p. 1066

CANCER THERAPY

A target for medulloblastoma

Medulloblastoma is an aggressive brain tumor that most often arises in children and lacks targeted therapeutic options. The subtypes driven by the sonic hedgehog (SHH) pathway are particularly resistant to current drugs, such as SMO inhibitors that suppress this pathway. Purzner *et al.* found that the kinase CK2 drove SHH signaling in medulloblastoma. CK2

inhibitors blocked the growth of SMO inhibitor–resistant, SHH-type human and mouse medulloblastoma cells and markedly extended the survival of tumor-bearing mice. A clinical trial is under way to test a CK2 inhibitor in pediatric patients. —LKF

Sci. Signal. **11**, eaau5147 (2018).

ALLERGY

Age matters in allergy

Development of allergy is driven by the type 2 cytokines interleukin-4 (IL-4), IL-5, and IL-13. Type 2 innate lymphoid cells (ILC2s) and T cells can produce these cytokines. Saglani *et al.* studied mouse models of allergic airway inflammation and found that the contributions of T cells and ILC2s were dependent on age. T cells were the predominant source of IL-13 in neonatal mice, whereas ILC2s were mainly responsible for cytokine production in adult mice. Given that neonates have fewer T cells than adults, the results are contrary to expectations and bring to the fore an unappreciated role of neonatal T cells. —AB

Sci. Immunol. **3**, eaan4128 (2018).

PLANT SCIENCE

Rapid, long-distance signaling in plants

A plant injured on one leaf by a nibbling insect can alert its other leaves to begin anticipatory defense responses. Working in the model plant *Arabidopsis*, Toyota *et al.* show that this systemic signal begins with the release of glutamate, which is perceived by glutamate receptor–like ion channels (see the Perspective by Muday and Brown-Harding). The ion channels then set off a cascade of changes in calcium ion concentration that propagate through the phloem vasculature and through intercellular channels called plasmodesmata. This glutamate-based long-distance signaling is rapid: Within minutes, an undamaged leaf can respond to the fate of a distant leaf. —PJH

Science, this issue p. 1112; see also p. 1068

RESEARCH ARTICLE SUMMARY

IMMUNOLOGY

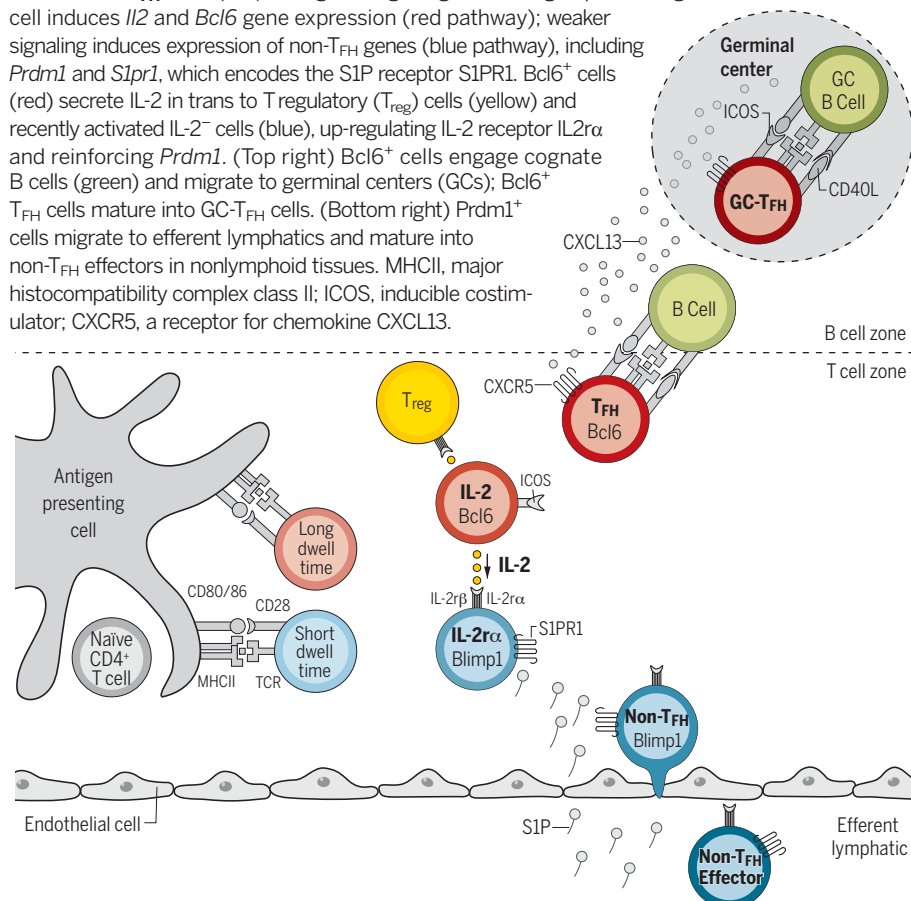
Differential IL-2 expression defines developmental fates of follicular versus nonfollicular helper T cells

Daniel DiToro*, Colleen J. Winstead*, Duy Pham, Steven Witte, Rakieb Andargachew, Jeffrey R. Singer, C. Garrett Wilson, Carlene L. Zindl, Rita J. Luther, Daniel J. Silberger, Benjamin T. Weaver, E. Motunrayo Kolawole, Ryan J. Martinez, Henrietta Turner, Robin D. Hatton, James J. Moon, Sing Sing Way, Brian D. Evavold, Casey T. Weaver†

INTRODUCTION: The adaptive immune system has evolved to mount different types of responses that are matched to the type of invading pathogen. For CD4⁺ T cells, this is predicated on the multipotentiality of clonally restricted naïve T cells, which differentiate into distinct subsets of effector T cells contingent on recognition of cognate antigen and cytokine cues from cells of the innate immune system. There are two broad divisions of effector CD4⁺ T cells: T follicular helper (T_{FH}) cells,

which are programmed to interact with B cells within lymphoid tissues to support production of high-affinity, class-switched antibodies, and non-T_{FH} effector cells, including T helper 1 (T_H1), T_H2, and T_H17 cells, which are programmed to egress from lymphoid tissues to orchestrate heightened innate immune cell function at sites of pathogen entry. The mechanisms controlling bifurcation into T_{FH} versus non-T_{FH} effector cell pathways are incompletely understood.

IL-2–producing CD4⁺ T cells become T_{FH} cells, whereas IL-2 nonproducers become non-T_{FH} cells. (Left) Strong TCR signaling via an antigen presenting cell induces *Il2* and *Bcl6* gene expression (red pathway); weaker signaling induces expression of non-T_{FH} genes (blue pathway), including *Prdm1* and *S1pr1*, which encodes the S1P receptor S1PR1. Bcl6⁺ cells (red) secrete IL-2 in trans to T regulatory (T_{reg}) cells (yellow) and recently activated IL-2[−] cells (blue), up-regulating IL-2 receptor IL2Rα and reinforcing *Prdm1*. (Top right) Bcl6⁺ cells engage cognate B cells (green) and migrate to germinal centers (GCs); Bcl6⁺ T_{FH} cells mature into GC-T_{FH} cells. (Bottom right) *Prdm1*⁺ cells migrate to efferent lymphatics and mature into non-T_{FH} effectors in nonlymphoid tissues. MHCII, major histocompatibility complex class II; ICOS, inducible costimulatory; CXCR5, a receptor for chemokine CXCL13.



RATIONALE: An impediment to understanding mechanisms controlling T_{FH}–non-T_{FH} cell divergence is an absence of early markers to define cells destined for these alternative fates. Unlike effector CD4⁺ T cells, which produce a diversity of cytokines that define their phenotype and function, naïve CD4⁺ T cells are largely limited to the rapid production of interleukin-2 (IL-2) when activated by antigen. IL-2 is only produced by a subset of activated naïve T cells, suggesting a possible relationship between IL-2 production and effector cell fate determination. To explore this, we developed two IL-2 reporter

ON OUR WEBSITE

Read the full article at <http://dx.doi.org/10.1126/science.aao2933>

mice strains with complementary features that enabled the tracking and deletion of T cells on the basis of differential IL-2 expression. This allowed us to determine whether

naïve T cells that do, or do not, produce IL-2 are biased in their developmental programming and, if so, how.

RESULTS: RNA sequencing of naïve T cells sorted on the basis of IL-2 reporter expression identified cosegregation of transcripts encoding IL-2 and Bcl6—the signature transcription factor of T_{FH} cells. Conversely, IL-2–negative (IL-2[−]) cells preferentially expressed the gene *Prdm1*, which encodes the transcriptional repressor Blimp1. Blimp1, in turn, antagonizes Bcl6 and the T_{FH} developmental program. This suggested that IL-2 producers give rise to T_{FH} cells, whereas IL-2 nonproducers give rise to non-T_{FH} effector cells. Moreover, the fact that IL-2 receptor signaling induces expression of *Prdm1* via Stat5 suggested that IL-2 producers resisted IL-2 signaling and activated IL-2 signaling in nonproducers in trans. Indeed, in vivo studies established that IL-2 signaling was mostly paracrine and that depletion of IL-2–producing cells selectively impaired T_{FH} cell development. Finally, IL-2 expression was limited to a subset of naïve T cells that received the strongest T cell receptor (TCR) signals, establishing a link between TCR signal strength, IL-2 production, and T_{FH} versus non-T_{FH} differentiation.

CONCLUSION: This study provides new insights into the mechanisms that control early bifurcation of CD4⁺ T cells into T_{FH} and non-T_{FH} effectors. Naïve T cells that receive differing strengths of TCR signals stratify into those that exceed a threshold predisposing them to IL-2 production and early T_{FH} commitment and those that do not express IL-2 yet receive IL-2 signaling, which reinforces non-T_{FH} effector commitment. ■

The list of author affiliations is available in the full article online.
*These authors contributed equally to this work.
†Corresponding author. Email: cweaver@uab.edu
Cite this article as D. DiToro et al., *Science* 361, eaao2933 (2018). DOI: 10.1126/science.aao2933

RESEARCH ARTICLE

IMMUNOLOGY

Differential IL-2 expression defines developmental fates of follicular versus nonfollicular helper T cells

Daniel DiToro^{1,*}, Colleen J. Winstead^{1,*†}, Duy Pham¹, Steven Witte¹, Rakieb Andargachew², Jeffrey R. Singer¹, C. Garrett Wilson¹, Carlene L. Zindl¹, Rita J. Luther^{1‡}, Daniel J. Silberger¹, Benjamin T. Weaver³, E. Motunrayo Kolawole^{2§}, Ryan J. Martinez², Henrietta Turner¹, Robin D. Hatton¹, James J. Moon⁴, Sing Sing Way⁵, Brian D. Evavold^{2§}, Casey T. Weaver^{1||}

In response to infection, naïve CD4⁺ T cells differentiate into two subpopulations: T follicular helper (T_{FH}) cells, which support B cell antibody production, and non-T_{FH} cells, which enhance innate immune cell functions. Interleukin-2 (IL-2), the major cytokine produced by naïve T cells, plays an important role in the developmental divergence of these populations. However, the relationship between IL-2 production and fate determination remains unclear. Using reporter mice, we found that differential production of IL-2 by naïve CD4⁺ T cells defined precursors fated for different immune functions. IL-2 producers, which were fated to become T_{FH} cells, delivered IL-2 to nonproducers destined to become non-T_{FH} cells. Because IL-2 production was limited to cells receiving the strongest T cell receptor (TCR) signals, a direct link between TCR-signal strength, IL-2 production, and T cell fate determination has been established.

Naïve CD4⁺ T cells are multipotent precursors that differentiate into functionally distinct effector subsets to coordinate different aspects of immunity. T helper 1 (T_H1), T_H2, and T_H17 cells are products of developmental pathways induced by different classes of pathogens. They are programmed to egress from T cell zones of secondary lymphoid tissues soon after induction to orchestrate heightened innate immune cell function at sites of pathogen entry. T follicular helper (T_{FH}) cells develop concurrently with T_H1, T_H2, and T_H17 cells but are programmed to migrate to B cell zones within secondary lymphoid tissues. They provide help to B cells to support the production of high-affinity, class-switched antibodies. T_{FH}- and non-T_{FH} effector cell development diverges early in evolving adaptive responses. However, the type of immune response (type 1, 2, or 3) is linked such that pathogen-clearance mechanisms mediated by innate immune cells are amplified by coordinated

help from non-T_{FH} cell effectors and the antibodies that result from T_{FH} cell-mediated B cell help. Cytokines elicited from innate immune cells by pathogens appear to be dominant in determining the type of adaptive response (1), whereas the intensity of T cell receptor (TCR) signaling appears to contribute to T_{FH}-non-T_{FH} cell specification (2) by mechanisms that are incompletely understood.

An impediment to understanding the mechanisms controlling T_{FH}-non-T_{FH} cell divergence is the absence of reliable early markers to define cells destined for these alternative fates. Unlike effector CD4⁺ T cells, which are distinguished by a diversity of cytokines that define their phenotype and function, naïve CD4⁺ T cells are largely limited to the production of interleukin-2 (IL-2), which is produced rapidly by a subset of antigen-activated cells (3). Through the activation of Stat5 and induction of Blimp1 (4, 5), IL-2 suppresses Bcl6—a central T_{FH} transcription factor—and, consequently, T_{FH} development (6). This implies a direct relationship between the production of IL-2 by naïve CD4⁺ T cells and their development into either non-T_{FH} or T_{FH} effector cells. We explored this relationship using transgenic mice engineered to report the expression of IL-2.

IL-2 and Bcl6 expression cosegregate within hours of naïve T cell activation

IL-2.eGFP reporter mice were generated by the targeted insertion of an IRES-eGFP (internal ribosome entry site-enhanced green fluorescent protein) expression cassette into the fourth exon

of the endogenous *Il2* gene (Fig. 1A). Naïve CD4⁺ T cells from IL-2.eGFP mice stimulated under nonpolarizing conditions in vitro diverged into CD69⁺IL-2⁺ (GFP⁺) and CD69⁺IL-2⁻ (GFP⁻) subpopulations within hours of activation and before cell division (Fig. 1, B to E). Reporter expression was rapidly detectable and peaked at approximately 24 hours before declining. This decline lagged production of IL-2 because of the relatively long half-life of the reporter. To define genes differentially expressed by IL-2 producers and nonproducers, CD69⁺IL-2⁺ and CD69⁺IL-2⁻ cells were analyzed by RNA-sequencing (RNA-seq) (Fig. 1C). Among the 151 genes that were preferentially expressed by IL-2⁺ cells were *Bcl6* and the tumor necrosis factor (TNF) superfamily member *Cd40l*, which are important in T_{FH} cell development or function, respectively. Also enriched in IL-2⁺ cells was *Zbtb32*, which, like *Bcl6*, encodes a member of the POK/ZBTB family of transcription factors and has been shown to restrict the expression of T_H1 and T_H2 cell cytokines (7). By contrast, among the 210 genes preferentially expressed by IL-2⁻ cells were multiple genes characteristic of non-T_{FH} effector cell differentiation, including *Prdm1*, which encodes Blimp1, as well as *S1pr1* and *Klf2*. Similar results were obtained from an analysis of naïve SMARTA TCR-transgenic IL-2.eGFP CD4⁺ T cells stimulated with antigen (fig. S1). *S1pr1* is required for the egress of non-T_{FH} effector CD4⁺ T cells from secondary lymphoid tissues (8), and its expression inhibits T_{FH} development in vivo (9, 10). *Klf2* suppresses T_{FH} differentiation while promoting non-T_{FH} effector cell differentiation, at least in part via the induction of Blimp1 (9). These findings, which were independently validated by quantitative polymerase chain reaction (qPCR) (Fig. 1, D and E), suggested that IL-2 producers may be fated to become T_{FH} cells, whereas IL-2 nonproducers may be fated to become non-T_{FH} effector cells. Akin to findings in CD4⁺ T cells, the differential expression of *Bcl6* and Blimp1 was found in IL-2⁺ and IL-2⁻ subsets isolated from activated naïve CD8⁺ T cells (fig. S2). This suggests that, despite their lower production of IL-2 relative to that of CD4⁺ T cells, early divergence of CD8⁺ T cells destined to become Blimp1⁺ short-lived effector cells or *Bcl6*⁺ memory precursor effector cells (11) may be similarly linked to the differential expression of IL-2.

The differential expression kinetics of *Bcl6* and *Prdm1* by CD4⁺ T cells were discordant (Fig. 1D). *Bcl6* expression tracked with *Il2* expression and decayed to background levels as *Prdm1* expression increased. Indeed, at the peak of differential *Bcl6* expression (8 hours), *Prdm1* expression remained at background levels in both IL-2⁺ and IL-2⁻ cells. Thus, although these transcription factors are believed to be directly antagonistic in the specification of T_{FH} versus non-T_{FH} effectors (12), the rapid, reciprocal expression of *Bcl6* in IL-2⁺ and IL-2⁻ fractions was not controlled by Blimp1. Instead, we found differential expression of the gene encoding *Mxd1* (also known as *Mad1*) (Fig. 1C and fig. S3), which has been

¹Department of Pathology, University of Alabama at Birmingham, Birmingham, AL 35203, USA. ²Department of Microbiology and Immunology, Emory University, Atlanta, GA 30322, USA. ³HudsonAlpha Institute for Biotechnology, Huntsville, AL 35806, USA. ⁴Center for Immunology and Inflammatory Diseases, Massachusetts General Hospital and Harvard Medical School, Boston, MA 02129, USA. ⁵Division of Infectious Diseases and Perinatal Institute, Cincinnati Children's Hospital, Cincinnati, OH 45229, USA.

*These authors contributed equally to this work. †Present address: Merck and Company, Inc., Kenilworth, NJ 07033, USA. ‡Present address: Valencia College, Orlando, FL 32825, USA. §Present address: Department of Pathology, University of Utah, Salt Lake City, UT 35203, USA.

||Corresponding author. Email: cweaver@uab.edu

shown to directly bind and down-regulate *Bcl6* during the differentiation of germinal center B cells into plasma cells (13). The contemporaneous, reciprocal expression of *Mxd1* and *Bcl6* antecedent to the expression of *Prdm1* suggests

that repression of *Bcl6* by *Mxd1*, rather than by Blimp1, may contribute to the early bifurcation of T_{FH} and non-T_{FH} effectors (Fig. 1D and fig. S3).

Although *Bcl6*, like Blimp1, often acts as a transcriptional repressor, the parallel kinetics

of *Il2* and *Bcl6* expression suggested that *Bcl6* may positively regulate *Il2* expression. Thus, we performed chromatin immunoprecipitation (ChIP) analysis of conserved noncoding sequences in the *Il2* promoter and 35 kb upstream that were

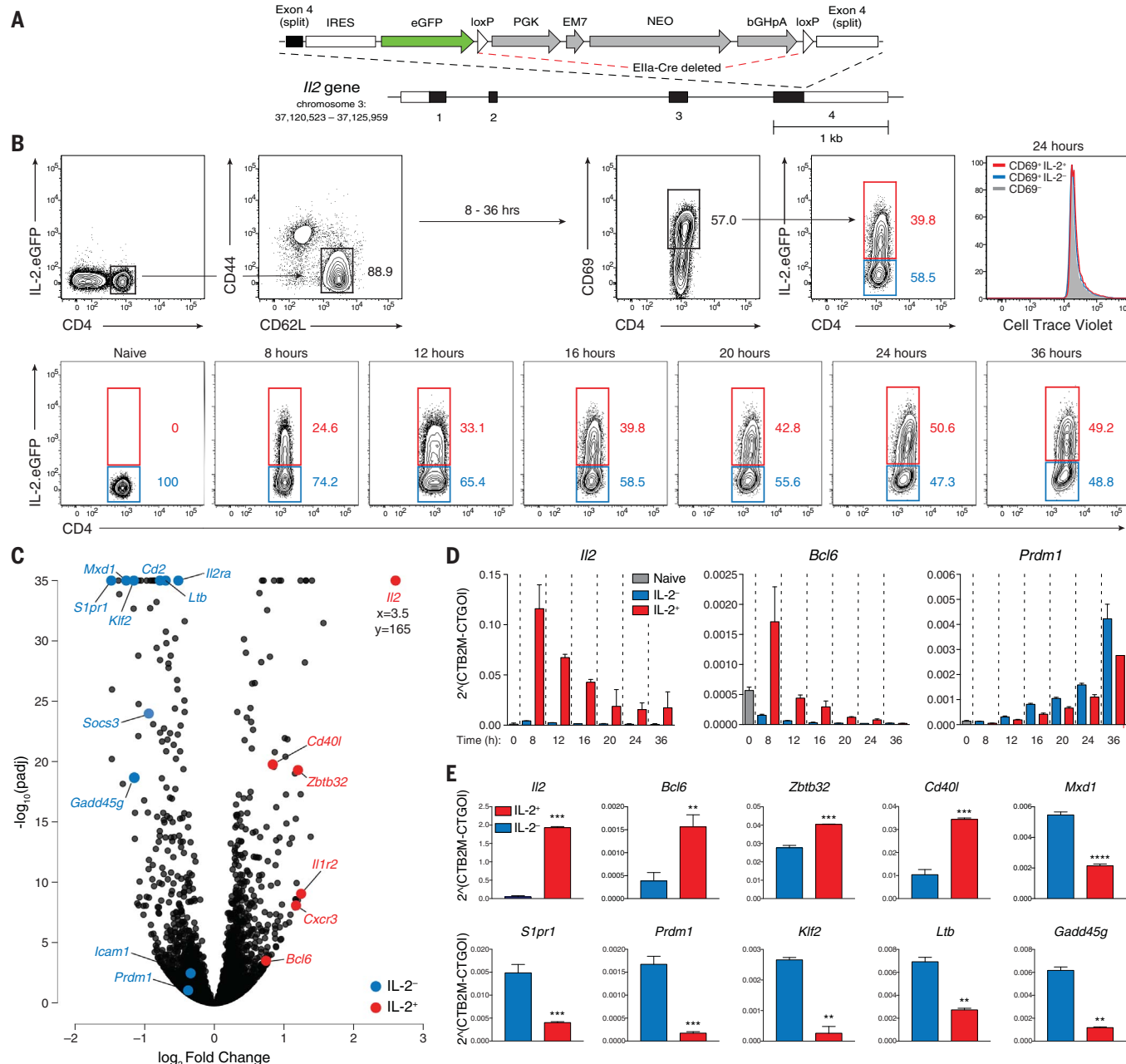


Fig. 1. Differential expression of *Bcl6* and *Blimp1* by IL-2⁺ and IL-2⁻ T cells. (A) Gene-targeting strategy for the generation of IL-2.eGFP knockin reporter mice. The loxP-flanked neomycin resistance cassette was deleted by crossing founders to Ella-Cre transgenic mice. (B) Sorted naïve (GFP⁺CD44⁺CD62L⁺) IL-2.eGFP CD4⁺ T cells were labeled with CellTrace Violet (CTV), stimulated in vitro with soluble anti-CD3 (5 µg/ml) and irradiated CD4-depleted feeder cells, and then examined for expression of CD69 and IL-2.eGFP by flow cytometry at the indicated time points. Data are representative of four experiments with at least three replicates per condition. CTV staining was performed in two of four experiments. (C) Total RNA isolated from naïve IL-2.eGFP CD4⁺ T cells stimulated for 18 to 24 hours as in (B) and fluorescence-activated cell

sorter (FACS)–purified into CD69⁺GFP⁺ (IL-2⁺) or CD69⁺GFP⁻ (IL-2⁻) fractions was analyzed by comparative expression profiling with RNA-seq. Data depict two biological replicates per condition. padj, adjusted *P* value. (D) RNA isolated from IL-2.eGFP CD4⁺ T cells stimulated and FACS-purified as in (C) was analyzed by qPCR for expression of *Il2*, *Bcl6*, and *Prdm1* at the indicated time points. Error bars represent SEM of three technical replicates per sample. Data are representative of four experiments. (E) Validation of selected transcript expression with RNA isolated from IL-2.eGFP CD4⁺ T cells stimulated and FACS-purified as in (C). Three technical replicates per sample are shown. Data were analyzed by using Student's *t* tests and are representative of two experiments. ***P* < 0.01; ****P* < 0.001; *****P* < 0.0001; error bars depict SEM.

identified by ATAC-seq (assay for transposase-accessible chromatin-sequencing) analysis as accessible in IL-2⁺ cells compared with naïve and IL-2⁻ cells (Fig. 2A). Bcl6 preferentially bound these sites in IL-2-producing cells relative to IL-2 nonproducers, at a time point (20 hours) when the expression of Bcl6 and Blimp1 overlapped (Fig. 2B). Blimp1 preferentially bound these sites in IL-2⁻ cells, as did Foxo1, which was recently shown to suppress T_{FH} differentiation (14). The permissive histone modification trimethylated histone H3 lysine 4 (H3K4me3) was significantly enriched in IL-2⁺ cells at the sites of Bcl6 binding, whereas repressive H3K27me3 histone marks were reduced in both IL-2⁺ and IL-2⁻ cells relative to naïve cells. Thus, the expression of *Il2* correlated positively with Bcl6 binding at sites of induced chromatin accessibility in the *Il2* gene locus and negatively with binding of Blimp1 (and Foxo1) at the same sites. Because the expression of *Prdm1* significantly trailed the peak of differential *Il2* expression (Fig. 1D), occupancy of these sites by Blimp1 did not appear to be required for the repression of *Il2* early in IL-2⁻ cells. Rather, Blimp1 appeared to act primarily to reinforce the lack of *Il2* expression in the IL-2⁻ fraction of activated naïve T cells at later time points. This is consistent with Blimp1's reported role as a feedback inhibitor of IL-2 (15, 16). These findings indicate that, in addition to its predictive value in defining early precursors of T_{FH} and non-T_{FH} effector cells, expression of IL-2 may be directly regulated by the antagonistic actions of Bcl6 versus Blimp1 and Foxo1 at conserved cis-regulatory elements in the *Il2* gene locus.

Because T_{FH} cell development occurs concurrently with each of the CD4⁺ T effector cell

pathways, we determined if the correlation between reciprocal expression of Bcl6-Blimp1 and IL-2 occurred under T_H1, T_H2, and T_H17 cell polarizing conditions (Fig. 3A), as it did for T_H0 cells (Figs. 1 and 3). Under each of these activation conditions, the expression of the IL-2.eGFP reporter was limited to a subset of cells expressing the highest amounts of CD69 (Fig. 3A). GFP expression also correlated positively with *Bcl6* expression and negatively with *Prdm1* expression (Fig. 3B). Cells activated under T_H17 cell conditions expressed the highest frequency and single-cell levels of IL-2, despite the reported suppression of T_H17 cell differentiation by IL-2 signaling (17). Thus, *Il2* and *Bcl6* expression mirrored one another under each of the conditions examined (Fig. 3B), and the highest amounts of *Il2* and *Bcl6* were found in IL-2⁺ cells activated under T_H17 cell conditions. This may reflect the shared requirement for IL-6 in both T_H17 and T_{FH} cell developmental programs.

IL-2 signaling is predominantly paracrine

Although the foregoing studies suggested a link between *Il2* gene expression and T_{FH}-non-T_{FH} cell fate determination, the differentiation of physiologic T_{FH} cells ex vivo has not yet been established. Thus, we examined this relationship in vivo, in the context of infection with ActA-deficient *Listeria monocytogenes* (ActA-Lm) (2, 18). This attenuated type 1 bacterial pathogen was engineered to express peptide antigens, which enabled the tracking of endogenous antigen-specific CD4⁺ T cell responses with peptide-loaded major histocompatibility complex class II (MHCII) (p:MHC) tetramers or transferred TCR-transgenic T cells (2, 19). Naïve CD4⁺ T cells

from CD45.2⁺ IL-2.eGFP-SMARTA TCR-transgenic mice were transferred into wild-type (WT) CD45.1⁺ mice and infected with ActA-Lm that express ovalbumin (OVA) peptide and the gp66 peptide recognized by the SMARTA TCR (ActA-Lm-OVA-gp66). Antigen-activated SMARTA T cells were recovered near the peak of IL-2 expression and sorted into IL-2⁺ and IL-2⁻ fractions for differential gene expression analysis by RNA-seq (Fig. 4A). In agreement with our in vitro findings (Fig. 1C), IL-2⁺ cells were significantly enriched for expression of *Il2*, *Bcl6*, *Zbtb32*, and *CD40l*, whereas IL-2⁻ cells were significantly enriched for *Prdm1*, *Slpr1*, and *Klf2*. Multiple T_H1 cell-associated transcripts (e.g., *Ifng*, *Il12rb2*, *Ltb*, and *Gzmb*) were identified in IL-2⁻ cells, consistent with the induction of type 1 immunity by ActA-Lm. Gene set enrichment analysis (GSEA) identified enhanced activity of multiple effector signaling pathways in IL-2⁻ cells. Of these, two of the most significant were interferon- and inflammatory-signaling gene sets (Fig. 4B). By contrast, the most significantly enhanced gene sets in IL-2⁺ cells were those of Myc and the E2F family of transcription factors (Fig. 4B and fig. S4, A and B). Both are involved in cell-cycle regulation and are suppressed by Blimp1 in germinal center B cells (20, 21). Mxd1, the transcript for which was again one of the most highly enriched in IL-2⁻ cells, antagonizes Myc by competing for binding to a shared dimerization partner, Max (22). Myc expression by T cells correlates directly with strength of activation (23, 24), implicating a role for Mxd1 in restraining the actions of Myc in less strongly activated T cells and consistent with expression of IL-2 by more strongly activated naïve CD4⁺ T cells.

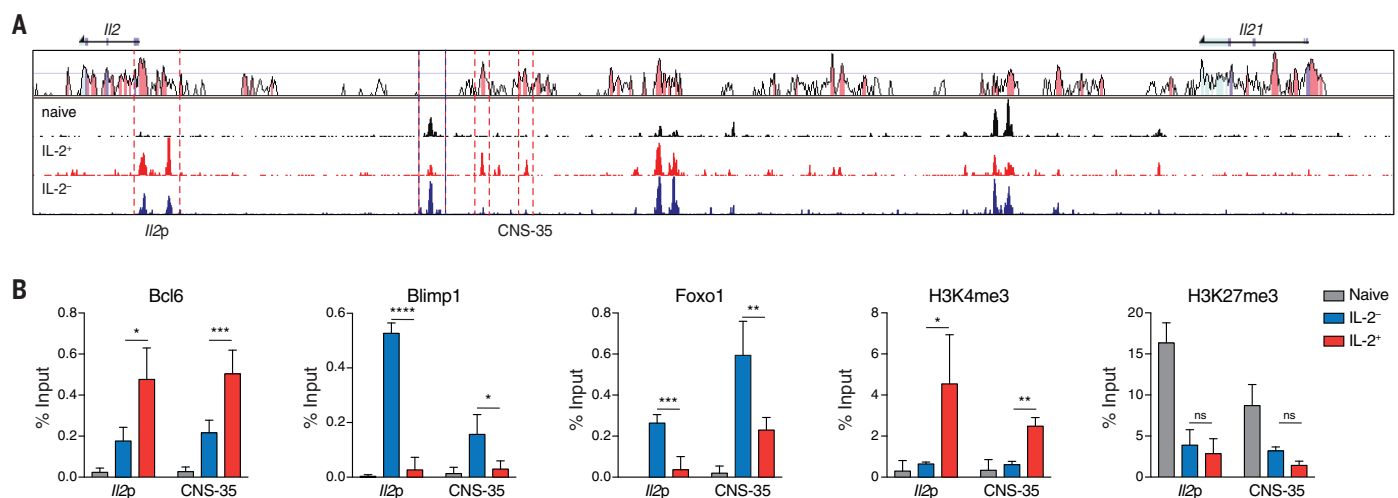


Fig. 2. Differential chromatin accessibility and transcription factor binding at the *Il2* locus in IL-2⁺ and IL-2⁻ T cells. (A) ATAC-seq was performed on nuclei isolated from naïve (GFP⁺CD44⁺CD62L⁺) IL-2.eGFP CD4⁺ T cells and FACS-purified CD69⁺GFP⁺ (IL-2⁺) and CD69⁺GFP⁻ (IL-2⁻) fractions treated as in Fig. 1C. Chromatin accessibility peaks were visualized by using Integrated Genome Browser (IGB) and are shown aligned against a VISTA plot of syntenic regions of mouse and human chromosomes corresponding to *Il2*-*Il21* and *Il2*-*Il21* gene loci, respectively. Data are representative of two experiments. (B) Naïve IL-2.eGFP CD4⁺

T cells were treated as in Fig. 1C, and the IL-2 promoter region (Il2p) and conserved noncoding sequence 35 kb upstream of the *Il2* transcription start site (CNS-35) of CD69⁺GFP⁺ (IL-2⁺) and CD69⁺GFP⁻ (IL-2⁻) fractions were analyzed by quantitative ChIP-PCR for the presence of Bcl6, Blimp1, and Foxo1 binding or H3K4me3 and H3K427me3 histone modifications, normalized to total DNA input. Three technical replicates per group are shown. Data for each region were analyzed separately by one-way analysis of variance (ANOVA). Not significant (ns), $P > 0.05$; * $P < 0.05$; ** $P < 0.01$; *** $P < 0.001$; **** $P < 0.0001$; error bars depict SEM.

Notably, *Il2ra*, which encodes the inducible, high-affinity component of the IL-2 receptor (IL-2 α or CD25) that is up-regulated on activated T cells, was enriched in IL-2 $^{-}$ cells (Fig. 4A). Accordingly, the hallmark IL-2-Stat5 signaling gene set was significantly enriched in IL-2 $^{-}$ cells (Fig. 4B). Among a manually curated consensus list of 23 gene sets modulated by IL-2 signaling (fig. S4C), those up-regulated in response to IL-2 were enriched in IL-2 $^{-}$ cells, many of which include *Il2ra* (fig. S4, D and E). By contrast, genes down-regulated in response to IL-2 were enriched in IL-2 $^{+}$ cells.

Collectively, these findings support a model in which highly activated naïve T cells up-regulate Bcl6, produce IL-2, and are fated to become T_{FH} effectors. IL-2 producers deliver IL-2 to non-producers, inducing the latter's up-regulation of Blimp1 and differentiation into non-T_{FH} effectors. To examine the relationship between IL-2 production and utilization in vivo and directly address the fate of IL-2 producers and non-producers, we generated a second transgenic IL-2 reporter mouse line with features complementary to those of the IL-2.eGFP mice (Fig. 4C). IL-2.BAC-in Thy1.1 (2BiT) reporter mice were engineered to express high amounts of the surface molecule Thy1.1 under control of the *Il2* gene locus to facilitate intracellular costaining by flow cytometry and enable the in vivo deletion of IL-2-producing cells (25). As with T cells from IL-2.eGFP mice, activated (CD69 $^{+}$) 2BiT T cells rapidly bifurcated into Thy1.1 $^{+}$ (IL-2 $^{+}$) and Thy1.1 $^{-}$ (IL-2 $^{-}$) fractions (Fig. 4D and fig. S5). To determine whether IL-2 production and signaling segregate in antigen-activated naïve CD4 $^{+}$ T cells, 2BiT mice were infected with ActA-Lm and analyzed for the expression of IL-2 versus intracellular phospho-Stat5 (p-Stat5) at the peak of IL-2 expression (Fig. 4E). Reciprocal IL-2 expression and IL-2 signaling were observed; Thy1.1 (IL-2) was almost exclusively expressed by p-Stat5 $^{+}$ CD4 $^{+}$ T cells (Fig. 4E), whereas p-Stat5 was limited to Thy1.1 $^{-}$ cells. Consistent with gene expression results (Fig. 4A), nearly all Thy1.1 $^{+}$ cells were CD25 $^{-}$ at this time point, whereas nearly all p-Stat5 $^{+}$ cells were CD25 $^{+}$. Thus, IL-2 signals predominantly in a paracrine, not autocrine, manner (26). Moreover, IL-2 producers are initially resistant to IL-2 signaling, in accord with their lack of CD25 up-regulation.

Most endogenous p-Stat5 $^{+}$ CD4 $^{+}$ T cells immediately after infection are Foxp3 $^{+}$ regulatory T (T_{reg}) cells (26), owing to their constitutive expression of CD25 and relative abundance compared with that of naïve clonal precursors. To examine IL-2-induced Stat5 signaling in naïve pathogen-specific non-T_{reg} cells, naïve CD45.2 $^{+}$ 2BiT-SMARTA T cells were transferred into CD45.1 $^{+}$ WT mice infected with ActA-Lm expressing the gp66 peptide (ActA-Lm-OVA-gp66) (Fig. 4F). Analysis of transferred 2BiT-SMARTA (clonotypic) and endogenous CD4 $^{+}$ T cells showed that the majority of endogenous p-Stat5 $^{+}$ cells were Foxp3 $^{+}$, whereas p-Stat5 $^{+}$ clonotypic T cells were Foxp3 $^{-}$. Thus, the paracrine model of IL-2 signaling applies to both “bystander” T_{reg} cells

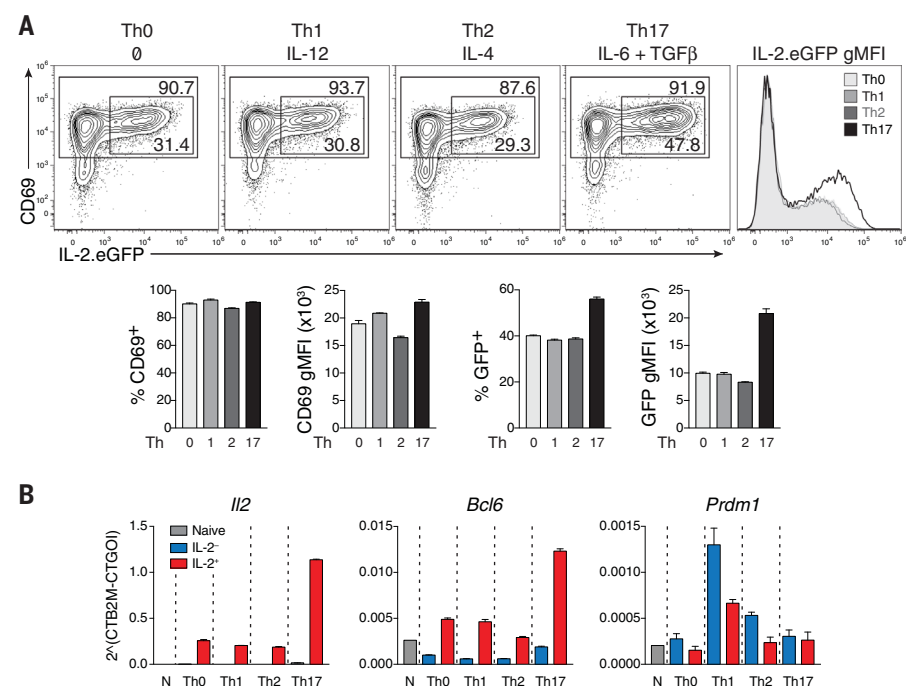


Fig. 3. Bcl6 and IL-2 cosegregate early in each T effector cell developmental program. (A) Naïve (GFP $^{+}$ CD44 $^{+}$ CD62L $^{+}$ CD69 $^{+}$ CD25 $^{-}$) IL-2.eGFP CD4 $^{+}$ T cells were stimulated in vitro under T_H0, T_H1, T_H2, and T_H17 cell conditions for 20 hours and examined by flow cytometry for CD69 and IL-2.eGFP expression. Data are representative of two experiments. Flow plots depict cell number—controlled concatenated averages of three samples per group. Error bars depict SD. gMFI, geometric mean fluorescence intensity. (B) Experiment performed as in (A), with CD69 $^{+}$ IL-2.eGFP $^{+}$ and IL-2.eGFP $^{-}$ CD4 $^{+}$ T cells sorted 20 hours after activation. RNA was isolated and analyzed by qPCR for expression of *Il2*, *Bcl6*, and *Prdm1*. Three technical replicates per condition are shown. N, naïve T cells. Error bars depict SEM. Data for (A) and (B) are representative of two experiments each.

as well as naïve CD4 $^{+}$ T cells responding to infection.

T_{FH} cells are derived from IL-2 producers

To examine the fate of antigen-activated IL-2-producing and -nonproducing T cells in vivo, 2BiT mice were treated with a depleting anti-Thy1.1 or nondepleting control antibody (25) immediately before infection with ActA-Lm co-expressing OVA and the antigenic peptides gp66, 2W1S, Cbirl, or Flc (Fig. 5 and fig. S6). MHCII-tetramer analysis of endogenous CD4 $^{+}$ T cells specific for each of these peptides showed that IL-2 (Thy1.1) expression was restricted to CXCR5 $^{+}$ cells and that the depletion of IL-2-expressing cells preferentially eliminated T_{FH} cells and spared non-T_{FH} (T_H1) effectors, as defined by expression of CXCR5 and PD-1 (Fig. 5A and fig. S6) or CXCR5 and Bcl6 (Fig. 5B). Notably, the number of non-T_{FH} effectors was not compromised by the depletion of IL-2 producers (Fig. 5C). This suggested that IL-2 was not required for the clonal expansion of non-T_{FH} effectors. However, this likely reflects the discordant kinetics of IL-2 secretion relative to reporter expression and antibody-mediated cell depletion, because IL-2 reporter expression and Stat5 phosphorylation were only partially decreased at the peak of IL-2 expression (fig. S7). Thus, T_{FH} effector cells developed from IL-2-expressing precursors, whereas non-T_{FH}

effectors did not. Accordingly, IL-2 was a reliable marker with which to distinguish precursors fated to become T_{FH} or non-T_{FH} effector cells.

Although surface markers define T_{FH} cells capable of providing B cell help, T_{FH} cell function is predicated on a subset of T_{FH} cells that localize to the germinal center after productive interactions with cognate B cells. Referred to as germinal center (GC)-T_{FH} T cells, these cells express high amounts of PD-1, Bcl6, and CXCR5 and support the germinal center response and production of high-affinity, class-switched antibodies (12). To examine the effects of depletion of IL-2-expressing precursors on the development and function of this T_{FH} cell subset, we characterized the effects of anti-Thy1.1 depletion on antibody responses and the generation of GC-T_{FH} cells. 2BiT mice were immunized with heat-killed Lm (HKLm) (Fig. 5, D to F), because infection with live Lm does not induce good antibody responses (27). Anti-Thy1.1 depletion of IL-2-producing T cells reduced the production of Lm-specific immunoglobulin G (IgG) by more than 90% compared with treatment with an isotype control antibody (Fig. 5D). Similarly, anti-Thy1.1 treatment of 2BiT mice immunized with OVA under type 1 conditions markedly impaired the anti-OVA IgG response, in association with the depletion of endogenous OVA-specific T_{FH} cells and reduction of germinal center B cells (fig. S8).

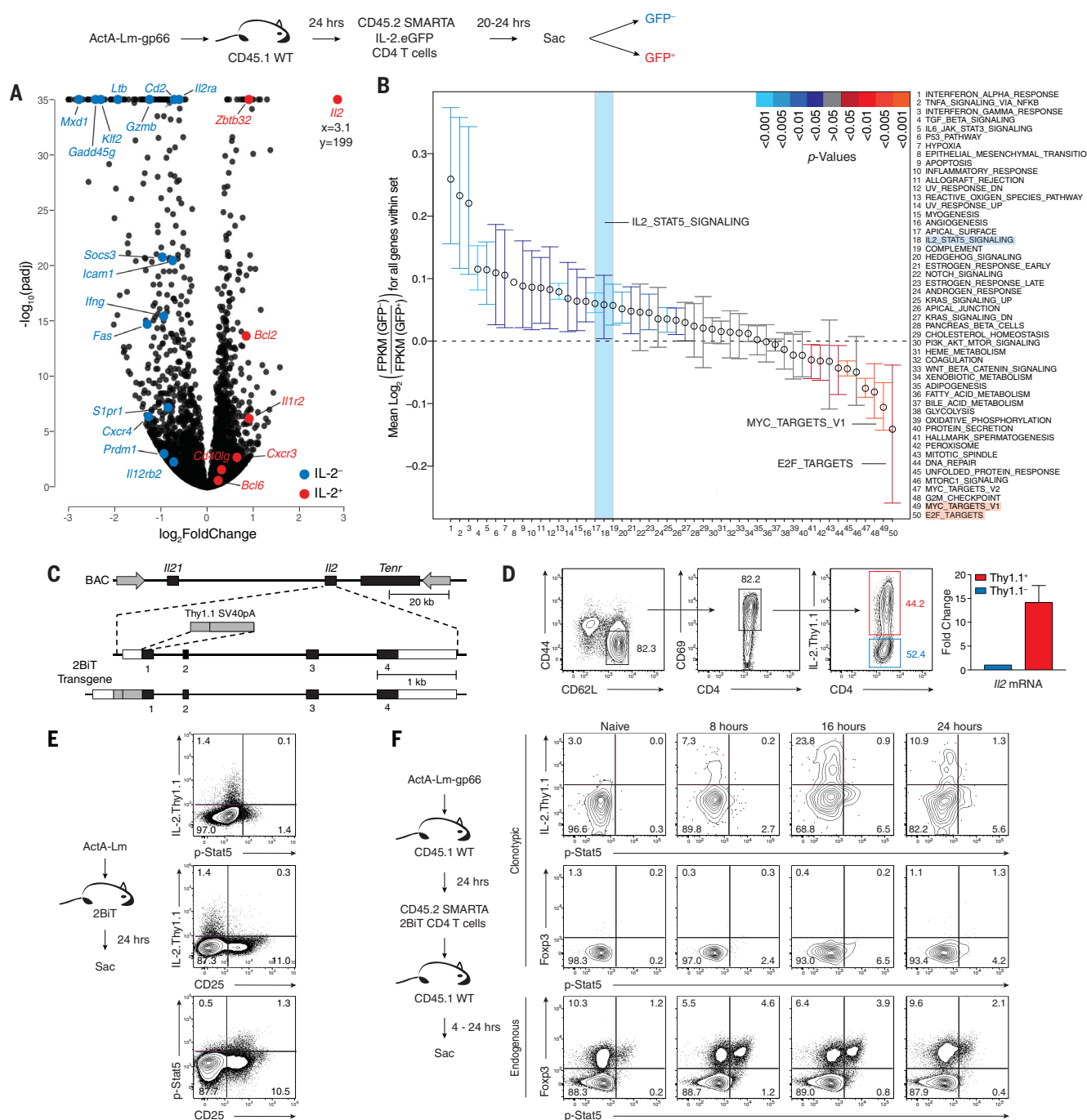


Fig. 4. IL-2⁺ T cells activate IL-2⁻ T cells via paracrine IL-2 signaling to drive differential gene expression in vivo. (A) Sorted naïve (GFP⁻CD44⁺CD62L⁺) IL-2.eGFP CD45.2⁺ SMARTA CD4⁺ T cells were transferred into CD45.1⁺ WT mice infected with ActA-Lm-gp66 24 hours before transfer. Total RNA was isolated by FACS-purified CD45.2⁺ CD69⁺GFP⁺ (IL-2⁺) and CD69⁺GFP⁻ (IL-2⁻) CD4⁺ T cells 20 to 24 hours after transfer and analyzed by RNA-seq. Data depict three biological replicates per condition from three separate experiments. Sac, sacrificed. (B) Hallmark GSEA of IL-2⁺ and IL-2⁻ T cells from (A). For each pathway, mean and 95% confidence intervals are plotted and then color coded to indicate false discovery rate–corrected P values. FPKM, fragments per kilobase million. (C) Schematic of targeting strategy to generate IL-2.BAC-in Thy1.1 (2BIT) transgenic reporter mice. BAC, bacterial artificial chromosome. (D) Sorted naïve (Thy1.1⁺CD44⁺CD62L⁺) 2BIT CD4⁺ T cells were stimulated in vitro

with soluble anti-CD3 (5 μ g/ml) and irradiated CD4-depleted feeder cells for 24 hours and then examined by flow cytometry for expression of CD69 and Thy1.1. RNA isolated from CD69⁺Thy1.1⁺ (IL-2⁺) and CD69⁺Thy1.1⁻ (IL-2⁻) CD4⁺ T cells was analyzed by qPCR for expression of *Il2* mRNA. Error bars represent SEM of three technical replicates per sample. Data are representative of two experiments. (E) 2BIT mice were infected with ActA-Lm. After 18 hours, mice were sacrificed and splenic CD4⁺ T cells were analyzed by flow cytometry for the expression of IL-2, Thy1.1, CD25, and tyrosine phosphorylation of Stat5 (p-Stat5). Data are representative of two experiments. (F) Congenic CD45.1⁺ WT mice were infected with ActA-Lm-gp66. After 24 hours, naïve CD45.2⁺ SMARTA 2BIT CD4⁺ T cells were transferred into infected CD45.1⁺ recipients. Mice were sacrificed at the indicated times, and splenic CD4⁺ T cells were analyzed for expression of Thy1.1, Foxp3, and p-Stat5. Data are representative of two experiments.

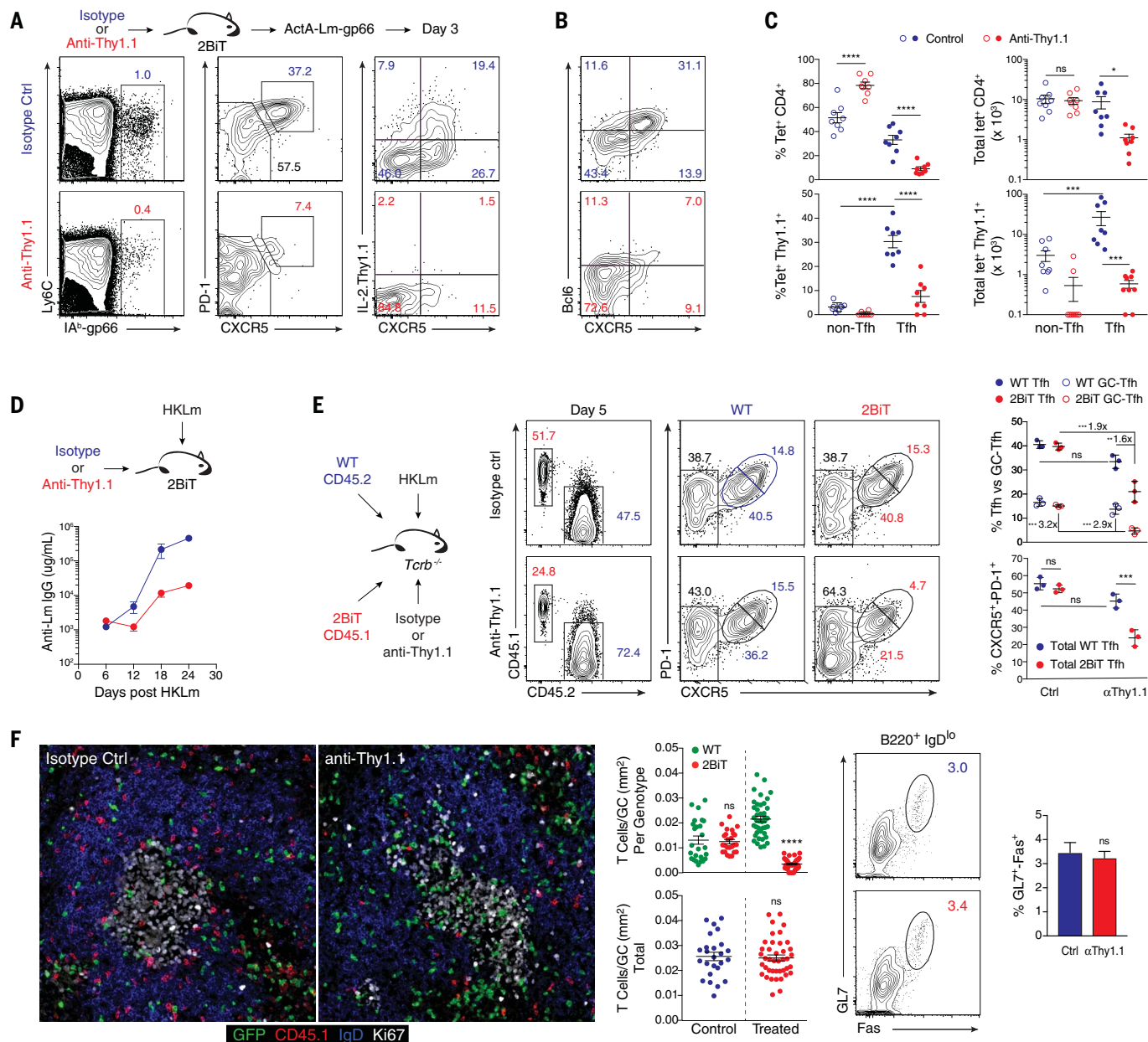


Fig. 5. IL-2 producers are precursors of T_H cells. (A to C) 2BiT mice were injected with 250 μ g of anti-Thy1.1 or isotype control (Ctrl) monoclonal antibody (mAb), then infected 1 day later with ActA-Lm-gp66. Endogenous CD4⁺ T cells specific for IA^b-gp66 were enriched from lymph nodes and spleens 3 days after infection by using tetramer-based magnetic sorting and analyzed by flow cytometry for IA^b-gp66 tetramer binding (tet⁺) and expression of Ly6C, CXCR5, IL-2-Thy1.1, and PD-1 (A) or Bcl6 (B). Flow plots depict cell number-controlled concatenated averages of all samples within a group. Data for (A) and (B) are representative of two experiments each. (C) Data from the experiments depicted in (A) and fig. S6 were analyzed by two-way ANOVA. A total of eight control and eight treatment animals from two separate experiments are shown. (D) 2BiT mice were injected with 250 μ g of anti-Thy1.1 or isotype control mAb and immunized with 2×10^{10} colony-forming units (CFU) of HKLm. Mice were bled every 6 days for 24 days, and serum anti-Lm IgG was measured by enzyme-linked immunosorbent assay (ELISA). $n = 7$ mice per group. Data are representative of two experiments. (E) Magnetically enriched WT CD45.1⁺ and 2BiT CD45.2⁺ CD4⁺ T cells were

transferred into *Tcrb*^{-/-} mice. After 24 hours, mice were immunized with 2×10^{10} CFU HKLm and injected with 250 μ g anti-Thy1.1 or isotype control mAb. Mice were sacrificed 5 days after immunization, and splenic CD4⁺ T cells were analyzed by flow cytometry for expression of CD44, CD45.1, CD45.2, PD-1, and CXCR5. Results were analyzed by two-way ANOVA. $n = 3$ mice per group. Data are representative of three experiments. (F) CD4⁺ T cells magnetically enriched from WT CAG-eGFP (CD45.2) mice and CD45.1⁺ 2BiT mice were adoptively transferred into TCR β -deficient recipients. After 24 hours, the mice were immunized with 2×10^{10} CFU HKLm and injected with 250 μ g of anti-Thy1.1 or isotype control mAb. Two weeks after immunization, spleens were collected and analyzed by confocal microscopy for the expression of GFP (WT), CD45.1 (2BiT), Ki67, and IgD. Quantitation of WT (GFP⁺), 2BiT (CD45.1⁺), and total T cell numbers in germinal centers (GCs) was performed by computer-assisted counting. Splenic B cells were analyzed by flow cytometry for the expression of IgD, B220, GL7, and Fas in an IgD^{lo} B cell gate. $n = 3$ mice per group. Data are representative of three experiments. ns, $P > 0.05$; * $P < 0.05$; ** $P < 0.01$; *** $P < 0.001$; **** $P < 0.0001$; error bars depict SEM.

To examine the effects on GC- T_{FH} cell differentiation, we transferred equivalent numbers of congenically marked 2BiT and GFP-expressing WT $CD4^+$ T cells into T cell-deficient (*Tcrb*^{-/-}) mice, which were immunized with HKLM (Fig. 5, E and F). Anti-Thy1.1 treatment selectively depleted $CD45.1^+$ 2BiT $PD-1^+CXCR5^+$ T cells and had no significant effect on $CD45.2^+$ GFP⁺ control T cells (Fig. 5E). The magnitude of reduction was highest among $PD-1^{hi}CXCR5^{hi}$ cells. Immunohistology revealed that Thy1.1 depletion dramatically reduced the number of 2BiT $CD4^+$ T cells found within germinal centers, with a compensatory increase in the numbers of WT GFP⁺ T cells, resulting in no change in total numbers of germinal center T cells or B cells (Fig. 5F). These data establish that functional T_{FH} effectors that populate germinal centers and provide help for class-switched antibody responses in response to type 1 pathogens develop from IL-2–producing precursors.

To extend these findings, we determined whether the in vivo depletion of IL-2⁺ cells also selectively targeted T_{FH} cells under conditions of type 2 (T_H2) and type 3 (T_H17) immune induction (Fig. 6). Anti-Thy1.1 treatment of 2BiT mice immunized with OVA by using the T_H2 -inducing adjuvant alum resulted in the specific depletion of OVA-specific T_{FH} cells and ablation of germinal center B cell and anti-OVA antibody responses, while sparing OVA-specific non- T_{FH} effectors (Fig. 6A). Similarly, anti-Thy1.1 depletion of 2BiT mice challenged with the T_H17 cell-inducing enteric pathogen *Citrobacter rodentium* (28) resulted in a loss of bacterial clearance, the kinetics of which were characteristic of an impaired anti-*Citrobacter* antibody response (29, 30). This was associated with depletion of T_{FH} cells specific for the immunodominant *Citrobacter* antigen intimin, as well as a markedly impaired germinal center B cell response (Fig. 6B). There was no significant decrease in IL-17A- or interferon- γ (IFN γ)-producing cells in infected spleens (Fig. 6C), both of which are characteristic of the T cell response against *Citrobacter* (28). However, a modest, but significant, decrease in T_H17 cells, but not T_H1 cells, was observed in the mesenteric lymph nodes of mice depleted of IL-2 producers (Fig. 6D). These findings indicate that, in the context of type 3 responses, there is some overlap in the developmental fate of IL-2–producing precursors of T_{FH} and T_H17 effector cells. They also establish that IL-2⁺ T cells are precursors for T_{FH} cells in the context of type 1, type 2, and type 3 effector responses.

IL-2 production and T_{FH} cell differentiation correlate with TCR signal strength

The developmental divergence of T_{FH} and non- T_{FH} cells is influenced by a combination of cell-intrinsic factors, including TCR affinity, and cell-extrinsic factors, such as antigen availability, strength of costimulation, and cytokine milieu. Given its direct correlation with T_{FH} -non- T_{FH} cell fate determination, we examined whether IL-2 expression shared similar mechanistic underpinnings. To

examine the relationship between antigen dose, IL-2 expression, and T_{FH} -non- T_{FH} cell specification on T cells of uniform TCR affinity, naïve $CD45.2^+$ IL-2.eGFP-SMARTA T cells were transferred into WT $CD45.1^+$ recipients, which were infected with various doses of ActA-Lm expressing the gp66 peptide (ActA-Lm-OVA-gp66; condition Lm-gp66). Nonspecific effects of Lm-induced inflammatory signals were excluded by keeping the total dose of ActA-Lm constant via coinfection with ActA-Lm expressing an irrelevant specificity (ActA-Lm-OVA-2W1S; condition Lm-2W1S) (Fig. 7, A and B). Splenic $CD45.2^+$ cells were analyzed for CD69 and GFP (IL-2) expression around the peak of IL-2 expression (Fig. 7A). The frequencies and absolute numbers of endogenous gp66-specific T_{FH} and non- T_{FH} cells were quantified near the peak of the effector T cell response (Fig. 7B). The expression of both CD69 and GFP correlated tightly with pathogen-expressed antigen dose, as did the magnitude of clonal expansion and reciprocal T_{FH} versus non- T_{FH} differentiation. There was a similar correlation over a broader dose range of ActA-Lm-OVA-gp66 administered alone (fig. S9). Thus, the frequencies of $CD69^+$ and IL-2⁺ cells correlated positively with Lm-gp66 dose, as did the generation of T_{FH} cells. This indicates that antigen dose—and consequently TCR signal strength—is a major determinant of the fraction of clonal precursors that express IL-2 and are fated to become T_{FH} cells.

The relative development of T_{FH} and non- T_{FH} effectors is also influenced by TCR affinity, which is invariant on individual T cell clones but varies between different clones within the repertoire (2). In agreement with the strong correlation between differential IL-2 expression and T_{FH} -non- T_{FH} cell bifurcation, we found that two clonal populations of the same precursor frequency, which had differing TCR specificities (OVA versus gp66) and affinities, produced significantly different frequencies of IL-2–expressing T cells in response to the same antigen dose despite no difference in the frequency of cells expressing CD69 (Fig. 7C). Similarly, the relative frequencies of endogenous T_{FH} and non- T_{FH} cells generated by two TCR specificities of differing TCR affinities diverged in response to the same antigen dose (Fig. 7D). In accord with these results, T_{FH} cells were characterized by a significantly greater two-dimensional (2D) TCR affinity than non- T_{FH} cells that developed in a polyclonal T cell response to the same antigen (gp66) (Fig. 7E). Together with our antigen-dose results, these findings support a deterministic function of TCR signal strength in driving T_{FH} versus non- T_{FH} cell development (2), such that higher TCR signaling favors T_{FH} cell development.

To calculate 2D affinity values, normalized adhesion-bond measurements must be adjusted to control for TCR density (31). Although equivalent in terms of cell size, gp66-specific T_{FH} cells expressed more TCR molecules per cell than non- T_{FH} cells (Fig. 7E). Similar results were found for OVA-specific and total T_{FH} cells. Accordingly, the difference in the normalized adhesion bond was accounted for by differences in both TCR affinity

and TCR number per cell. Thus, we examined the influence of variation in TCR number on T cell activation and IL-2 production (fig. S10A). As expected, there was no difference in 2D TCR affinity of $CD69^+IL-2^+$ SMARTA IL-2.eGFP T cells compared with that of $CD69^+IL-2^-$ cells. However, when naïve SMARTA IL-2.eGFP T cells were stimulated with limiting concentrations of gp66 peptide, only cells expressing the highest amounts of the TCR component $V\alpha 2$ up-regulated CD69 and IL-2 (Fig. 7F). Moreover, when naïve T cells were sorted on the basis of high or low TCR β expression and stimulated with a range of anti-CD3 concentrations, cells with higher TCR numbers showed higher CD69 expression across the full range of anti-CD3 concentrations and expressed increased IL-2 (fig. S10B). Thus, in addition to intrinsic TCR affinity differences between T cell clones, variation in TCR number within a clonal population may influence the probability that a given cell will exceed a threshold for activation and expression of IL-2 and, therefore, T_{FH} versus non- T_{FH} cell differentiation.

The expression of CD69 by activated naïve T cells has been shown to correlate linearly with the expression of Myc and Nur77, providing an indicator of graded TCR signal intensity (23, 32). Yet, on the basis of the observed limitation of IL-2 expression to a subset of the highest CD69 expressors (Figs. 3A and 7A), our findings suggested that only those T cells that exceeded a minimum TCR signaling intensity produced IL-2, linking T_{FH} -non- T_{FH} cell bifurcation to a threshold of TCR signaling.

To explore this further, the relative expression of CD69 and IL-2 by naïve T cells was assessed under conditions in vitro for which only the intensity of TCR stimulation was varied (Fig. 8A). The percentage of cells expressing CD69 and IL-2 correlated positively with the dose of anti-CD3, as did expression amounts of CD69 and IL-2, consistent with our in vivo antigen-dose experiments (Fig. 7A and fig. S8A). However, although the distribution and mean expression of CD69 varied with the intensity of TCR stimulation, CD69 expression among IL-2⁺ cells was constant, and only cells that exceeded an invariant, high magnitude of CD69 expressed IL-2. A similar effect was seen with the induction of inducible costimulator (ICOS) expression (fig. S11A), which is a functional marker of T_{FH} cell differentiation (33). ICOS expression was highest among IL-2⁺ cells across a range of stimulation conditions. Although the mean expression of ICOS varied with the intensity of TCR stimulation among IL-2⁺ cells, its expression by IL-2⁺ cells was constant. The expression of ICOS ligand by antigen-presenting cells was not required for the induction of IL-2 (fig. S11B). Thus, under conditions for which only TCR signaling strength is varied, there is a minimum threshold for IL-2 expression and, by extension, T_{FH} cell differentiation.

The expression of Myc, which has been directly correlated with the number of cell divisions that T cells are fated to undergo (24), was tightly correlated with CD69 expression and thus

TCR signal intensity and IL-2 expression (Fig. 8B). The early expression of E2F family members, which are associated with cell-cycle entry, was limited to cells that exceeded a threshold for IL-2 expression. This was consistent with the GSEA data (Fig. 4B and fig. S4), which indicated that E2F family targets are strongly enriched in IL-2⁺ cells compared with IL-2⁻ cells. This suggests

that IL-2⁺ cells enter the cell cycle more rapidly than IL-2⁻ cells and are likely to undergo a greater number of cell divisions before exiting the cell cycle. Accordingly, T_{FH} effectors demonstrated an increase in the average number of cell divisions relative to non-T_{FH} effectors in vivo (Fig. 8C). Thus, although IL-2 has traditionally been viewed as a T cell growth factor, precursors

of T_{FH} cells, which do not respond to IL-2 despite producing it, appear programmed for earlier cell-cycle entry and a greater number of cell divisions than precursors of non-T_{FH} effectors, which do respond to IL-2.

Our results support a model whereby cell-intrinsic and -extrinsic variables that influence TCR signal strength contribute to a threshold

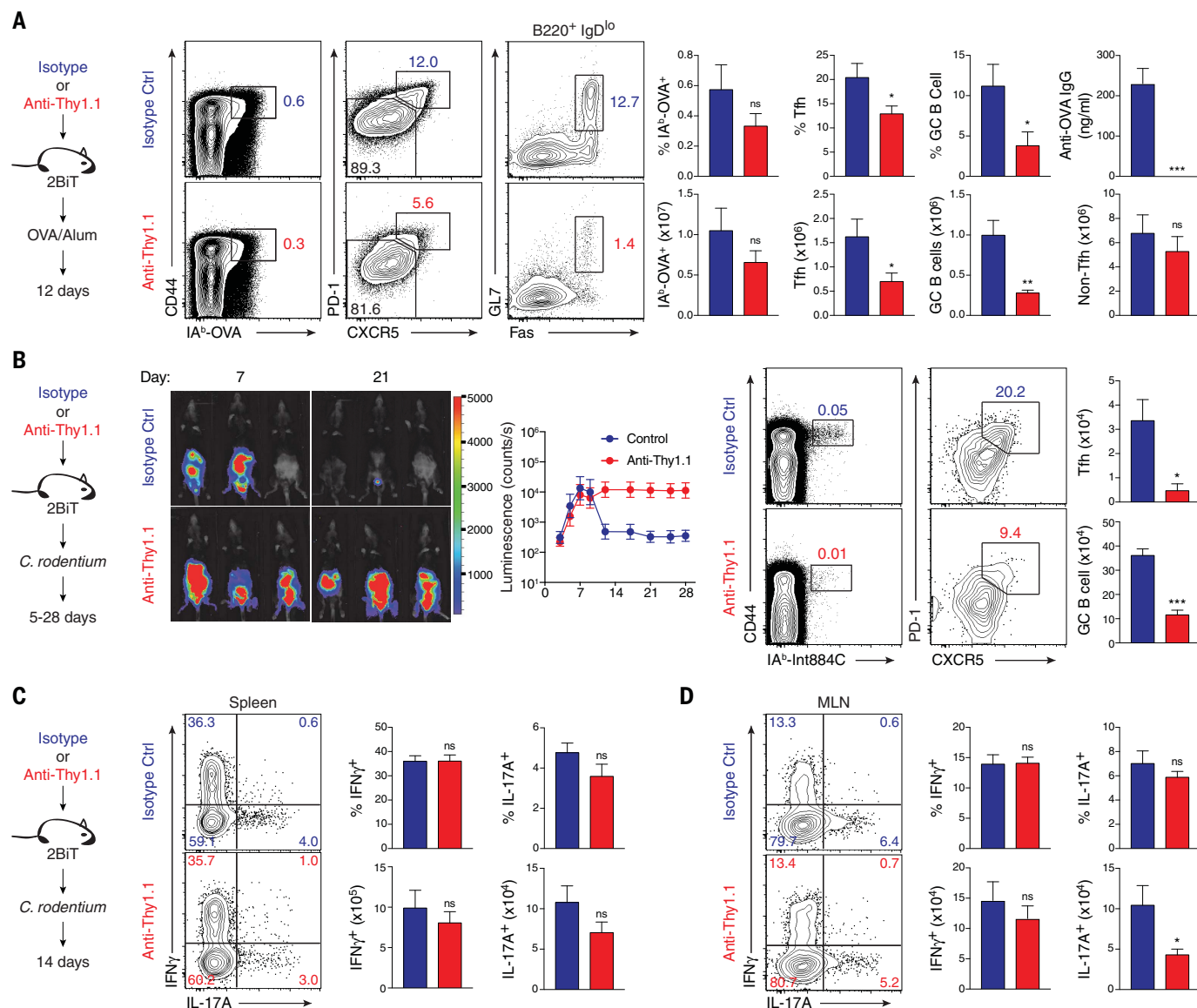


Fig. 6. IL-2 producers are fated to become T_{FH} cells in type 2 and type 3 immune responses. (A) 2BIT mice were injected with 250 μ g of anti-Thy1.1 or isotype control. After 24 hours, they were immunized with OVA emulsified in alum. Mice were bled and sacrificed on day 12. Splenic IA^b-OVA tetramer-specific CD4⁺ T cells were analyzed by flow cytometry for the expression of CD44, PD-1, and CXCR5. Splenic B cells were analyzed for the expression of B220, IgD, GL7, and Fas. Serum anti-OVA IgG was measured by ELISA. *n* = 5 or 6 mice per group. (B) 2BIT mice were injected with 250 μ g of anti-Thy1.1 or isotype control. After 24 hours, they were orally gavaged with 1×10^9 to 2×10^9 CFU *C. rodentium* strain DBS100 (ATCC 51459) or the bioluminescent ICC180 derivative. Whole-body bioluminescence was tracked and quantified after infection. Splenic IA^b-Int884C tetramer-specific CD4⁺ T cells harvested

on day 14 were analyzed by flow cytometry for the expression of CD44, PD-1, and CXCR5. Splenic B cells were analyzed for the expression of B220, IgD, GL7, and Fas. Serum anti-OVA IgG was measured by ELISA. *n* = 5 or 6 mice per group. (C and D) Splenic (C) and mesenteric lymph node (MLN) (D) CD4⁺ T cells harvested from mice treated as in (B) were isolated, restimulated with phorbol myristate acetate (PMA) and ionomycin and then analyzed by flow cytometry for the expression of CD44, Foxp3, IFN γ , and IL-17A. Flow plots and bar graphs are gated on CD4⁺CD44⁺Foxp3⁻ cells. Flow plots depict cell number-controlled concatenated averages. *n* = 5 or 6 mice per group. Data were analyzed by using Student's *t* tests. ns, *P* > 0.05; **P* < 0.05; ***P* < 0.01; ****P* < 0.001; error bars depict SEM.

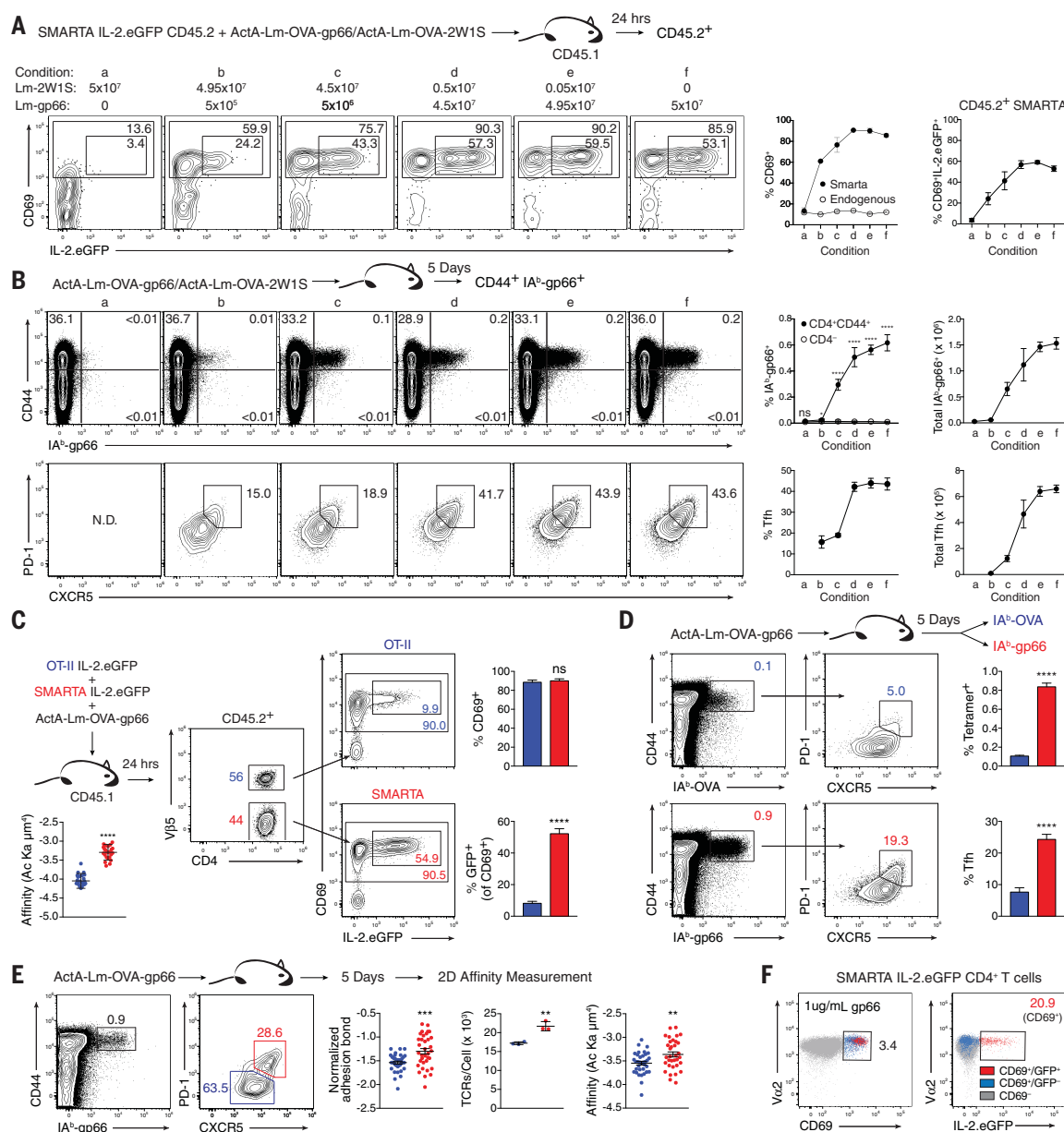


Fig. 7. IL-2 production and T_H differentiation correlate with TCR signal strength. (A) WT CD45.1⁺ recipient mice were infected with ActA-Lm-OVA-gp66 and/or ActA-Lm-OVA-2W1S at the indicated doses. After 24 hours, 10⁶ naive (GFP⁺CD44⁺CD62L⁺) SMARTA IL-2.eGFP CD4⁺ T cells were adoptively transferred into infected hosts. Splenic CD4⁺ T cells were harvested 15 hours after transfer and analyzed for expression of CD69 and IL-2.eGFP by flow cytometry. Values in the larger boxes of flow cytometric plots represent percentages of CD69⁺ cells, and values in the smaller boxes represent percentages IL-2.eGFP⁺ cells within the CD69⁺ fraction. *n* = 4 mice per group. Data are representative of two experiments. (B) WT mice were infected with ActA-Lm-OVA-gp66 and/or ActA-Lm-OVA-2W1S at the indicated doses. After 5 days, magnetically enriched endogenous splenic CD4⁺ T cells were analyzed by flow cytometry for binding of IA^b-gp66 tetramer and expression of CD44, CXCR5, and PD-1. *n* = 3 mice per group. Data are representative of two separate experiments. (C) 2D affinity measurements were performed on splenic TCR-transgenic CD4⁺ T cells via micropipette adhesion frequency assays with biotinylated p:MHC IA^b-gp66 and IA^b-OVA3C monomers. Log-normalized data are shown. WT CD45.1⁺ recipient mice were infected with ActA-Lm-OVA-gp66. After 24 hours, 0.5 × 10⁶ naive (GFP⁺CD44⁺CD62L⁺CD69⁺CD25⁺) SMARTA IL-2.eGFP and OTII IL-2.eGFP CD4⁺ T cells were pooled and adoptively transferred into infected hosts. Splenic CD4⁺ T cells were harvested 18 hours after transfer and analyzed for

expression of CD45.1, CD45.2, Vβ5, CD69, and IL-2.eGFP by flow cytometry. Values in the larger boxes of flow cytometric plots depicting CD69 and IL-2.eGFP represent percentages of CD69⁺ cells, and values in the smaller boxes represent the percentages of IL-2.eGFP⁺ cells within the CD69⁺ fraction. *n* = 3 mice per group. Data are representative of two experiments. Ac Ka, is the 2D affinity (see methods for details). (D) WT mice were infected with ActA-Lm-OVA-gp66. Five days after infection, magnetically enriched endogenous splenic CD4⁺ T cells were costained with IA^b-gp66 and IA^b-OVA3C tetramers and analyzed by flow cytometry for expression of CD44, CXCR5, and PD-1. Data are representative of four experiments. (E) WT mice were infected with 2.5 × 10⁷ CFU ActA-Lm-OVA-gp66. Enriched splenic CD4⁺ T cells harvested 5 days after infection were stained for IA^b-gp66, CD44, TCRβ, PD-1, and CXCR5. Log-normalized 2D affinity measurements were performed on FACS-purified IA^b-gp66 tetramer-positive splenic T_H and non-T_H cells pooled from three to five animals. TCRβ quantifications were performed on unsorted aliquots stained separately. Data from two experiments are shown. (F) Naive (GFP⁺CD44⁺CD62L⁺) SMARTA IL-2.eGFP CD4⁺ T cells were stimulated for 16 hours with irradiated CD4-depleted feeder cells and 1 μg/ml of gp66 and analyzed by flow cytometry for expression of CD69, Vα2, and IL-2.eGFP. Data are representative of two experiments. Data were analyzed by using Student's *t* tests. ns, *P* > 0.05; **P* < 0.05; ***P* < 0.01; ****P* < 0.001; *****P* < 0.0001; error bars depict SEM.

that is tightly associated with IL-2 production and T_{FH} cell differentiation. Although TCR affinity and antigen dose clearly contribute to the probability that a cell will attain this threshold, costimulation and cytokine signals can also contribute. It has been shown that transforming growth factor- β (TGF β) signaling can attenuate TCR signaling (34) and limit T cell responses to high-affinity antigens (35). Indeed, the addition of TGF β significantly reduced the mean expression of CD69 by activated naïve T cells, the proportion of CD69 $^{+}$ cells that produced IL-2, and the mean expression of IL-2, whereas TGF β blockade had the opposite effect (fig. S12). However, the percentage of cells that expressed CD69 was unaltered by either intervention. Thus, in addition to modulating TCR-independent signaling cascades that control effector T cell specification, TGF β may also influence IL-2 production by limiting TCR-signal strength without limiting the frequency of naïve T cells that receive activating TCR signals (36). In this regard, it is notable that the addition of IL-6 overrode the repressive effects of TGF β (T_{H17} cell conditions; Fig. 3A), resulting in significantly higher IL-2 expression. Indeed, this was greater than any other T effector-polarizing condition. Because the major effects of IL-6 are independent of TCR-signal strength and its actions contribute to both T_{FH} and T_{H17} cell development, clearly, TCR-independent factors that modulate IL-2 production may affect T_{FH} -non- T_{FH} cell developmental decisions. Furthermore, in view of the shared requirement for IL-6-induced Stat3 sig-

naling and high production of IL-21 by both T_{H17} and T_{FH} cells, these data suggest a considerable overlap in the developmental programming of these two subsets and, perhaps, shared regulation of the tightly syntenic *Il2* and *Il21* loci (Fig. 2A).

Discussion

The findings in this study provide new insights into the mechanics that control the early bifurcation of CD4 $^{+}$ T cells into T_{FH} and non- T_{FH} effectors, placing reciprocal production and utilization of IL-2 at the center of this key developmental decision. Because divergent IL-2 signaling and Bcl6 expression have been linked to effector versus central memory, respectively (37), these results may also have implications for alternate programming of CD4 $^{+}$ T cell memory. Our findings predict that IL-2 nonproducers are fated for effector memory, whereas IL-2 producers are fated for central memory.

It has been proposed that asymmetric cell division results in the partitioning of factors that guide the divergent development of progeny of activated naïve T cells (38). Although the observation herein that T_{FH} -non- T_{FH} cell fate determination is initially encoded well before cell division does not preclude a role for asymmetric cell division, it does suggest that signaling between T cells that receive differing activation signals likely plays a dominant role. It has been shown that homotypic T cell conjugation mediated by LFA-1-ICAM interactions between activated T cells facilitates directional, paracrine delivery

of IL-2 via multifocal synapses (39). The expression of *Icam1* was enhanced on IL-2 $^{+}$ cells in the current study (Figs. 1C and 4A). Because the kinetics of IL-2 production are within the average dwell time of T cells that form long-lived interactions on an activating dendritic cell (40–42), our findings suggest that T cell-T cell interactions that result in directional IL-2 signaling between IL-2 producers and nonproducers may occur on the same dendritic cell, although this will necessitate further study. The role of T_{reg} cells in buffering IL-2 availability to non-IL-2 producers, owing to the constitutive expression of the high-affinity IL-2 receptor and high-avidity LFA-1 by T_{reg} cells will also require additional inquiry.

Results in this report indicate that naïve CD4 $^{+}$ T cells that receive differing strengths of TCR signals—whether the result of intrinsic TCR affinity or expression differences or receipt of contemporaneous non-TCR signals that augment or repress TCR signal strength—stratify into those that exceed a threshold that predisposes to IL-2 production and early T_{FH} cell commitment and those that fail to express IL-2 yet are programmed to receive IL-2 signaling that reinforces non- T_{FH} effector commitment. However, although the exceedance of this threshold appears necessary, it is not always sufficient, because some cells that express comparable levels of CD69 do not express IL-2, implying the contribution of additional factors yet to be defined. Moreover, although in a primary response, IL-2 expression strongly correlates with the development of T_{FH} versus non- T_{FH} cells, this correlation

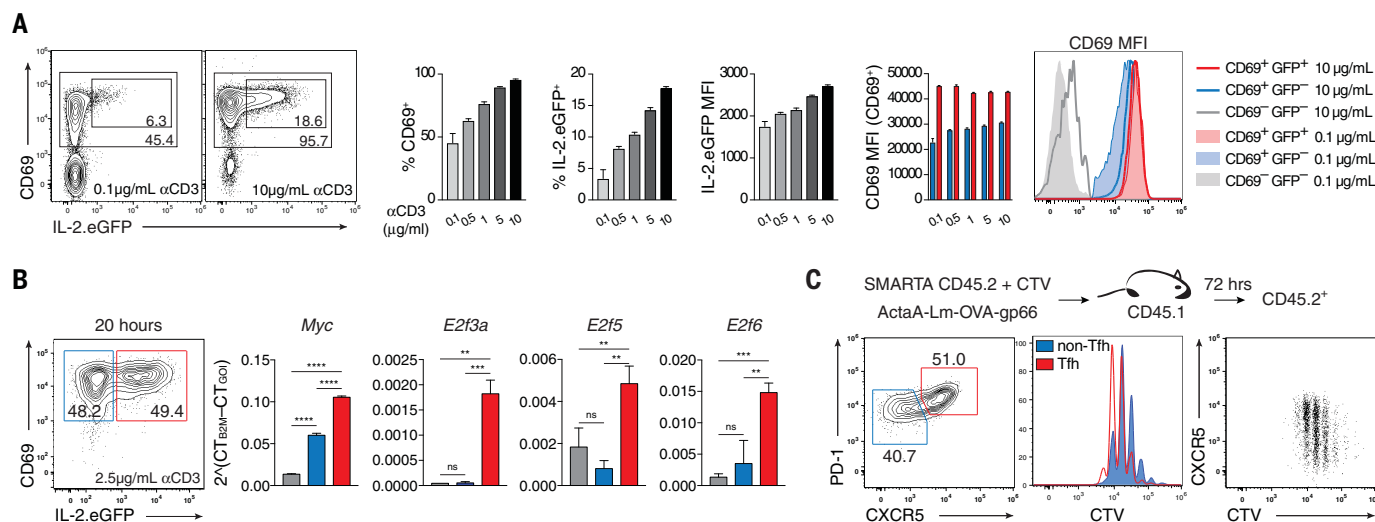


Fig. 8. IL-2 producers and T_{FH} exhibit enhanced cell-cycle progression.

(A) Naïve (GFP $^{-}$ CD44 $^{-}$ CD62L $^{+}$ CD69 $^{-}$ CD25 $^{-}$) IL-2.eGFP CD4 $^{+}$ T cells were stimulated for 18 hours with indicated concentrations of plate-bound anti-CD3 and 1 µg/ml of soluble anti-CD28. They were then analyzed for the expression of CD69 and IL-2.eGFP by flow cytometry. The MFI of CD69 expression within the CD69 $^{+}$ GFP $^{-}$ and CD69 $^{+}$ GFP $^{+}$ gates was quantitated for the indicated concentrations of anti-CD3 (right). Three technical replicates per condition are shown. This experiment was performed three times. (B) Naïve (GFP $^{-}$ CD44 $^{-}$ CD62L $^{+}$ CD69 $^{-}$ CD25 $^{-}$) IL-2.eGFP CD4 $^{+}$ T cells were stimulated in vitro with soluble anti-CD3 (2.5 µg/ml), soluble anti-CD28 (0.5 µg/ml), and irradiated

CD4-depleted feeder cells. qPCR was performed on CD69 $^{+}$ IL-2.eGFP $^{+}$ and IL-2.eGFP $^{-}$ CD4 $^{+}$ T cells sorted 20 hours after activation. Three technical replicates per condition are shown. Data are representative of two experiments and were analyzed by one-way ANOVA. (C) WT CD45.1 $^{+}$ recipient mice were infected with ActA-Lm-OVA-gp66. After 24 hours, 5×10^4 CTV-labeled naïve (GFP $^{-}$ CD44 $^{-}$ CD62L $^{+}$ CD69 $^{-}$ CD25 $^{-}$) SMARTA CD4 $^{+}$ T cells were adoptively transferred into infected hosts. Splenic CD4 $^{+}$ T cells harvested 3 days after transfer were analyzed for expression of CD44, PD-1, and CXCR5 by flow cytometry. $n = 4$ mice per experiment. This experiment was performed three times. ns, $P > 0.05$; ** $P < 0.01$; *** $P < 0.001$; **** $P < 0.0001$; error bars depict SEM.

is not fixed for subsequent responses (fig. S13). Thus, IL-2 expression by T_{FH} cell precursors does not ensure IL-2 expression by T_{FH} effectors in a recall response nor does lack of IL-2 expression by non- T_{FH} cell precursors preclude IL-2 expression by non- T_{FH} cell effectors. Nevertheless, the utility of IL-2 as an early marker for cells fated to these different effector programs is established herein. This will offer the opportunity to discover new factors that determine the bifurcation into T_{FH} and non- T_{FH} effectors, as exemplified by the finding of a possible Mxd-Myc-Max axis in controlling the early differential expression of Bcl6. We propose that this should provide a basis for strategies to modulate the balance of effector T cell responses for therapeutic ends.

Materials and methods

Mice

B6.Cg-Tg-*IL2*^{tm1(eGFP)^Wew} (IL-2.eGFP) and B6.IL-2.BAC-inThy1.1 (2BiT) were generated using strategies previously described (25) and bred at the University of Alabama at Birmingham (UAB) animal facility. B6N-Tyrc^{Brd}/BrdCrCl (albino B6) and B6-LY5.2/Cr (congenic B6 CD45.1) were purchased from Frederick Cancer Center and intercrossed to produce albino B6.CD45.1. C57BL/6 (WT B6), *Tcrb*^{-/-} (B6.129P2-*Tcrb*^{tm1Mom}/J), OT-II (B6.Cg-Tg(TcrTerb)425Cbn/J) mice and mice transgenic for constitutive eGFP expression (C57BL/6-Tg(CAG-EGFP)^{1310sb/LeySop}/J) were purchased from The Jackson Laboratory. SMARTA Tg [Tg(TcrLCMV)IAox] (43) on a B6 background were a generous gift from A. Zajac (Department of Microbiology, UAB). All intercrosses to generate additional strains, such as SMARTA IL-2.eGFP, SMARTA 2BiT, SMARTA IL-2.eGFP Thy1.1⁺, OT-II IL-2.eGFP, and 2BiT CD45.1 were generated by crosses in UAB's breeding facility. Animals were bred and maintained under specific pathogen-free conditions in accordance with institutional animal care and use committee regulations.

Tissue processing and flow cytometric analysis

Mice were sacrificed by isoflurane euthanasia before removal of spleen and/or lymph nodes. Secondary lymphoid tissues were disrupted by mashing with a syringe in complete RPMI-1640 over a 70- μ m filter. Surface staining was performed in PBS with 2% FBS and 0.1% sodium azide. T cells from 2BiT animals were directly stained for surface Thy1.1 (clone HIS5-1) without secondary stimulation. For identification of T_{FH} cells were incubated with biotinylated anti-CXCR5 for 1 hour at room temperature, then washed and incubated with streptavidin-APC or PE-Cy7 and additional surface markers for 20 min at 4°C. Intracellular staining for transcription factors was performed using either BD Fix/Perm or eBioscience Foxp3 staining kits. For ex vivo phospho-Stat staining, freshly harvested splenocytes were fixed for 10 min at 37°C in 4% PFA in PBS, stained with eFluor450- or PacBlue-conjugated anti-Thy1.1, refixed with 4% PFA in PBS and permeabilized in 90% MeOH for 30 min

on ice. Following this, cells were stained for phosphorylated Stat5 and additional markers at room temperature for 1 hour. Alternatively, cells were fixed in 4% PFA in PBS for 10 min at 37°C, permeabilized in 90% MeOH for 30 min on ice, and then stained for 1 hour at room temperature.

Absolute T and B cell numbers were calculated using PKH reference beads (Sigma-Aldrich) or concentration values (events per microliter) obtained on the Attune NxT. Absolute TCR β numbers were calculated using BD Quantibrite Beads Fluorescence Quantification Kits. Briefly, cells were stained at saturating concentrations of PE-labeled anti-TCR β (clone H57-597). A standard curve generated from PE Quantibrite Beads was then used to transform TCR β MFI measurements into absolute quantifications.

All flow cytometric data were acquired on an Attune NxT (Thermo Fisher Scientific), LSR II, or an Aria II (BD Immunocytometry Systems, San Jose, CA) and analyzed with FlowJo software (Tree Star, Eugene, OR).

T cell isolation

Naïve T cell isolation

Polyclonal CD62L^{hi}CD25^{lo}CD44^{lo}CD4⁺ and CD8⁺ T cells were purified from single-cell suspensions of secondary lymphoid tissues (spleen with or without axillary, brachial, cervical, mesenteric, inguinal, and medial iliac lymph nodes) in two stages. First, CD8⁺ or CD4⁺ T cells were isolated using Dynabeads (ThermoFisher 11445D), MACS Cell Separation (Miltenyi Biotec 130-104-454) or prepared by negative selection against CD8 or CD4, MHC class II, CD11b, B220, and CD25 (all Abs labeled with FITC) using anti-FITC BioMag particles (Polysciences, Warrington, PA). Second, cells were purified by sorting on a FACSaria II, gating on the CD4⁺CD25^{lo}CD62L^{hi}CD44^{lo} (and in some cases IL-2.Thy1.1⁺/IL-2.eGFP⁺) fraction. Naïve SMARTA TCR Tg cells were sorted directly as above from lymph node and splenic tissue.

Activated T cell isolation

Cells cultured in vitro were harvested at various time points, resuspended in labeling buffer (2% FBS in PBS), and FAC-sorted a second time as CD4⁺ or CD8 α ⁺ CD69⁺ and either IL-2.eGFP⁺/Thy1.1⁺ or as IL-2.eGFP⁺/Thy1.1⁻. SMARTA IL-2.eGFP T cells isolated ex vivo from acutely activated recipient mice were processed from tissue by negative selection with biotinylated antibodies to CD11b, CD11c, and B220, streptavidin-conjugated microbeads, and LS columns (Miltenyi Biotec). Column flow-through fractions were then stained for a congenic marker (Thy1.1, Thy1.2, or CD45.2) before sorting as above.

In vitro T cell activation

Sorted naïve T cells were activated in complete RPMI-1640 (RPMI medium containing 10% FBS, 100 IU/ml penicillin, 100 μ g/ml streptomycin, 1 mM sodium pyruvate, nonessential amino acids, 50 μ M β -mercaptoethanol and 2 mM l-glutamine) for 4 to 36 hours with anti-CD3 (2.5 μ g ml⁻¹) or 1 μ g ml⁻¹ LCMV glycoprotein pep-

tide 66-77, anti-CD28 (1 μ g ml⁻¹), and irradiated splenocytes at a 5:1 ratio of splenocytes to T cells under nonpolarizing conditions (i.e., without additional cytokines or antibodies). In some experiments, sorted naïve T cells were activated with a range of plate-bound anti-CD3 concentrations and 0.5 μ g/ml anti-CD28 or a range of soluble anti-CD3 concentrations and irradiated feeders at a CD4:feeder ratio of 1:5.

For restimulation of splenic T_{FH} and non- T_{FH} cells, magnetically enriched splenic CD4⁺ T cells were stained simultaneously with tetramer and biotin-labeled anti-CXCR5 (see table above) for 1 hour at room temperature. Cells were then washed and stained with fluorophore-labeled streptavidin and PD1 for 20 min at 4°C. Labeled cells were then incubated for 4 hours in complete RPMI with 2 μ g/ml anti-CD28 on flat-bottom 96-well plates precoated with 5 μ g/ml anti-CD3. Following restimulation, cells were stained for CD69, CD44, CD4, additional surface markers, and viability dye for 15 to 20 min at 4°C.

Adoptive transfer and Ab-mediated in vivo depletion

For adoptive transfer experiments examining IL-2.eGFP or IL-2.Thy1.1 expression at early time points, 1×10^6 to 2.5×10^6 naïve cells were injected i.v. into congenic recipient mice infected 24 hours before transfer unless otherwise indicated. For experiments involving cotransfer of SMARTA IL-2.eGFP and OT-II IL-2.eGFP donor cells, 5×10^5 sorted naïve cells of each donor strain were injected retro-orbitally (RO) into mice infected 24 hours before transfer. For adoptive transfer experiments examining T_{FH} differentiation three or more days after transfer, 5×10^4 sorted naïve donor cells were injected RO into congenic recipients infected 24 hours before transfer unless otherwise indicated. For cotransfer into TCR β KO recipients, 1×10^6 magnetically enriched bulk CD4⁺ T cells from wild-type B6 or transgenic eGFP and CD45.1 2BiT congenic mice were injected RO into TCR β -deficient mice followed by infection 1 day after transfer. For depletion of IL-2.Thy1.1 (2BiT) cells in vivo, mice were given a single intraperitoneal injection of 250 μ g of anti-Thy1.1 or isotype monoclonal antibody 24 hours before infection or immunization.

Infections and protein immunizations

Lm

Mice were immunized i.v. with 200 μ l of PBS containing live (dose as indicated) or heat-killed Actin A-deficient *Listeria monocytogenes* (ActA⁻ Lm; 2×10^9 to 2×10^{10}) (18). All Lm strains used were transformed by a plasmid containing OVA₂₅₀₋₃₈₇ and one of four different IA^b-specific "foreign" peptides: (i) a mutant epitope of I-Ea ("2WIS"); (ii) flagellin peptide 456-475 from *Clostridium* ("Cbir1"); (iii) glycoprotein 66-77 peptide of LCMV ("gp66"); or (iv) flagellin peptide 427-441 from *Salmonella typhimurium* ("FliC") all expressed under the control of the *hly* (listeriolysin O) promoter. All Lm strains were produced in the laboratory of S.-S. Way as previously described (44). Bacteria were grown in

brain-heart infusion (BHI) medium with 15 µg/ml chloramphenicol to an absorbance of >0.1 at 600 nm, and doses varied as indicated. The actual number of live bacteria injected was confirmed by dilution and growth on BHI agar plates containing chloramphenicol.

OVA/CFA

Mice were immunized i.p. with 100 µl of a 100-µg chicken egg ovalbumin emulsion in CFA.

OVA/Alum

Mice were injected i.p. with 200 µl of a 0.5-mg/ml emulsion of chicken egg ovalbumin in alum. The emulsion was prepared by mixing 1 mg/ml ovalbumin dissolved in water (Invivogen vac-pova) 1:1 with alum (FisherScientific Inject Alum 77161).

Citrobacter rodentium

Mice were orally gavaged with 1×10^9 to 2×10^9 CFU of *Citrobacter rodentium* strain DBS100 (ATCC 51459) or the bioluminescent ICC180 derivative (generously provided by G. Frankel and S. Wiles, Imperial College London). Mice infected with the ICC180 derivative were shaved and imaged with an IVIS 100 Imaging System (Xenogen, Inc.) as previously described (28).

RNA-seq and analysis

For sample preparation and hybridization, total RNA was isolated from purified naïve (CD4⁺ or CD8a⁺, CD25⁺CD69⁺CD44^{lo}CD62L⁺ IL-2.eGFP⁺) and activated (CD4⁺ or CD8a⁺, CD69⁺ IL-2.eGFP⁺ or IL-2.eGFP⁺) T cells with Qiazol and miRNeasy micro kits according to manufacturer's recommendations (Qiagen). Library preparation was performed using Illumina TruSeq technology. Samples were processed at UAB Hefflin Center for Genomic Science for Next Generation Sequencing (NGS) or La Jolla Institute (LJI) using the Illumina HiSeq 2000 Sequencing System. Reads were mapped to the mm10 genome using TopHat (version 2.0.12) (45). BAM files were sorted using SAMtools (version 0.1.19) (46), and reads were counted for each gene using HTSeq (version 0.6.1) (47) and NCBI *Mus musculus* Annotation Release 106 (GRCm38.p4). RNA expression was normalized using the rlog function from the DESeq2 R package (version 1.8.2) (48). Differential gene expression analysis was performed using DESeq2, and *P* values were corrected with the Benjamini-Hochberg procedure. Volcano plots were created using the ggrepel R package. To calculate gene set enrichment, a differential expression probability density function (PDF) was determined for each gene using Quantitative Set Analysis for Gene Expression (QUSAGE) (49). PDFs were combined for each gene set to calculate gene set activity after correcting for gene-gene correlation. Gene set PDFs were compared using Welch's *t* test, and *P* values were adjusted using the Benjamini-Hochberg procedure.

Statistical analysis

Experimental *P* values were calculated using unpaired Student's *t* tests, Welch's *t* tests, or

one-way or two-way ANOVA tests with Tukey's post hoc multiple comparisons analysis. A *P* value of <0.05 was considered significant. See figure legends for details.

REFERENCES AND NOTES

1. J. Zhu, H. Yamane, W. E. Paul, Differentiation of effector CD4 T cell populations. *Annu. Rev. Immunol.* **28**, 445–489 (2010). doi: [10.1146/annurev-immunol-030409-101212](https://doi.org/10.1146/annurev-immunol-030409-101212); pmid: 20192806
2. N. J. Tubo et al., Single naïve CD4⁺ T cells from a diverse repertoire produce different effector cell types during infection. *Cell* **153**, 785–796 (2013). doi: [10.1016/j.cell.2013.04.007](https://doi.org/10.1016/j.cell.2013.04.007); pmid: 23663778
3. R. P. Bucy et al., Single cell analysis of cytokine gene coexpression during CD4⁺ T-cell phenotype development. *Proc. Natl. Acad. Sci. U.S.A.* **92**, 7565–7569 (1995). doi: [10.1073/pnas.92.16.7565](https://doi.org/10.1073/pnas.92.16.7565); pmid: 7638231
4. R. J. Johnston et al., Bcl6 and Blimp-1 are reciprocal and antagonistic regulators of T follicular helper cell differentiation. *Science* **325**, 1006–1010 (2009). doi: [10.1126/science.1175870](https://doi.org/10.1126/science.1175870); pmid: 19608860
5. R. I. Nurieva et al., STAT5 protein negatively regulates T follicular helper (T_{FH}) cell generation and function. *J. Biol. Chem.* **287**, 11234–11239 (2012). doi: [10.1074/jbc.M111.324046](https://doi.org/10.1074/jbc.M111.324046); pmid: 22318729
6. A. Ballesteros-Tato et al., Interleukin-2 inhibits germinal center formation by limiting T follicular helper cell differentiation. *Immunity* **36**, 847–856 (2012). doi: [10.1016/j.immuni.2012.02.012](https://doi.org/10.1016/j.immuni.2012.02.012); pmid: 22464171
7. I. Bilic, W. Ellmeier, The role of BTB domain-containing zinc finger proteins in T cell development and function. *Immunol. Lett.* **108**, 1–9 (2007). doi: [10.1016/j.imlet.2006.09.007](https://doi.org/10.1016/j.imlet.2006.09.007); pmid: 17084908
8. J. G. Cyster, Chemokines, sphingosine-1-phosphate, and cell migration in secondary lymphoid organs. *Annu. Rev. Immunol.* **23**, 127–159 (2005). doi: [10.1146/annurev-immunol.23.021704.115628](https://doi.org/10.1146/annurev-immunol.23.021704.115628); pmid: 15771568
9. J.-Y. Lee et al., The transcription factor KLF2 restrains CD4⁺ T follicular helper cell differentiation. *Immunity* **42**, 252–264 (2015). doi: [10.1016/j.immuni.2015.01.013](https://doi.org/10.1016/j.immuni.2015.01.013); pmid: 25692701
10. J. P. Weber et al., ICOS maintains the T follicular helper cell phenotype by down-regulating Krüppel-like factor 2. *J. Exp. Med.* **212**, 217–233 (2015). doi: [10.1084/jem.20141432](https://doi.org/10.1084/jem.20141432); pmid: 25646266
11. W. Cui, S. M. Kaech, Generation of effector CD8⁺ T cells and their conversion to memory T cells. *Immunol. Rev.* **236**, 151–166 (2010). doi: [10.1111/j.1600-065X.2010.00926.x](https://doi.org/10.1111/j.1600-065X.2010.00926.x); pmid: 20636815
12. S. Crotty, Follicular helper CD4 T cells (T_{FH}). *Annu. Rev. Immunol.* **29**, 621–663 (2011). doi: [10.1146/annurev-immunol-031210-101400](https://doi.org/10.1146/annurev-immunol-031210-101400); pmid: 21314428
13. S. C. Lee, A. Bottaro, L. Chen, R. A. Insel, Mad1 is a transcriptional repressor of Bcl-6. *Mol. Immunol.* **43**, 1965–1971 (2006). doi: [10.1016/j.molimm.2005.11.017](https://doi.org/10.1016/j.molimm.2005.11.017); pmid: 16423395
14. E. L. Stone et al., ICOS coreceptor signaling inactivates the transcription factor FOXO1 to promote T_{FH} cell differentiation. *Immunity* **42**, 239–251 (2015). doi: [10.1016/j.immuni.2015.01.017](https://doi.org/10.1016/j.immuni.2015.01.017); pmid: 25692700
15. D. Gong, T. R. Malek, Cytokine-dependent Blimp-1 expression in activated T cells inhibits IL-2 production. *J. Immunol.* **178**, 242–252 (2007). doi: [10.4049/jimmunol.178.1.242](https://doi.org/10.4049/jimmunol.178.1.242); pmid: 17182561
16. G. A. Martins, L. Cimmino, J. Liao, E. Magnusdottir, K. Calame, Blimp-1 directly represses *Il2* and the *Il2* activator *Fos*, attenuating T cell proliferation and survival. *J. Exp. Med.* **205**, 1959–1965 (2008). doi: [10.1084/jem.20080526](https://doi.org/10.1084/jem.20080526); pmid: 18725523
17. A. Laurence et al., Interleukin-2 signaling via STAT3 constrains T helper 17 cell generation. *Immunity* **26**, 371–381 (2007). doi: [10.1016/j.immuni.2007.02.009](https://doi.org/10.1016/j.immuni.2007.02.009); pmid: 17363300
18. R. A. Brundage, G. A. Smith, A. Camilli, J. A. Theriot, D. A. Portnoy, Expression and phosphorylation of the *Listeria monocytogenes* ActA protein in mammalian cells. *Proc. Natl. Acad. Sci. U.S.A.* **90**, 11890–11894 (1993). doi: [10.1073/pnas.90.24.11890](https://doi.org/10.1073/pnas.90.24.11890); pmid: 8265643
19. M. M. Curtis et al., Fidelity of pathogen-specific CD4⁺ T cells to the Th1 lineage is controlled by exogenous cytokines, interferon-gamma expression, and pathogen lifestyle. *Cell Host Microbe* **8**, 163–173 (2010). doi: [10.1016/j.chom.2010.07.006](https://doi.org/10.1016/j.chom.2010.07.006); pmid: 20709293
20. Y. Lin, K. Wong, K. Calame, Repression of *c-myc* transcription by Blimp-1, an inducer of terminal B cell differentiation. *Science* **276**, 596–599 (1997). doi: [10.1126/science.276.5312.596](https://doi.org/10.1126/science.276.5312.596); pmid: 9110979
21. A. L. Shaffer et al., Blimp-1 orchestrates plasma cell differentiation by extinguishing the mature B cell gene expression program. *Immunity* **17**, 51–62 (2002). doi: [10.1016/S1074-7613\(02\)00335-7](https://doi.org/10.1016/S1074-7613(02)00335-7); pmid: 12150891
22. C. Grandori, S. M. Cowley, L. P. James, R. N. Eisenman, The Myc/Max/Mad network and the transcriptional control of cell behavior. *Annu. Rev. Cell Dev. Biol.* **16**, 653–699 (2000). doi: [10.1146/annurev.cellbio.16.1.653](https://doi.org/10.1146/annurev.cellbio.16.1.653); pmid: 11031250
23. G. C. Preston et al., Single cell tuning of Myc expression by antigen receptor signal strength and interleukin-2 in T lymphocytes. *EMBO J.* **34**, 2008–2024 (2015). doi: [10.15252/emboj.201490252](https://doi.org/10.15252/emboj.201490252); pmid: 26136212
24. S. Heinzl et al., A Myc-dependent division timer complements a cell-death timer to regulate T cell and B cell responses. *Nat. Immunol.* **18**, 96–103 (2017). doi: [10.1038/ni.3598](https://doi.org/10.1038/ni.3598); pmid: 27820810
25. L. E. Harrington, K. M. Janowski, J. R. Oliver, A. J. Zajac, C. T. Weaver, Memory CD4 T cells emerge from effector T-cell progenitors. *Nature* **452**, 356–360 (2008). doi: [10.1038/nature06672](https://doi.org/10.1038/nature06672); pmid: 18322463
26. M. Long, A. J. Adler, Cutting edge: Paracrine, but not autocrine, IL-2 signaling is sustained during early antiviral CD4 T cell response. *J. Immunol.* **177**, 4257–4261 (2006). doi: [10.1049/jimmunol.177.7.4257](https://doi.org/10.1049/jimmunol.177.7.4257); pmid: 16982857
27. B. T. Edelson, P. Cossart, E. R. Unanue, Cutting edge: Paradigm revisited: Antibody provides resistance to *Listeria* infection. *J. Immunol.* **163**, 4087–4090 (1999). pmid: 10510340
28. P. R. Mangan et al., Transforming growth factor-β induces development of the T_H17 lineage. *Nature* **441**, 231–234 (2006). doi: [10.1038/nature04754](https://doi.org/10.1038/nature04754); pmid: 16648837
29. R. Basu et al., Th22 cells are an important source of IL-22 for host protection against enteropathogenic bacteria. *Immunity* **37**, 1061–1075 (2012). doi: [10.1016/j.immuni.2012.08.024](https://doi.org/10.1016/j.immuni.2012.08.024); pmid: 23200827
30. D. J. Silberger, C. L. Zindl, C. T. Weaver, *Citrobacter rodentium*: A model enteropathogen for understanding the interplay of innate and adaptive components of type 3 immunity. *Mucosal Immunol.* **10**, 1108–1117 (2017). doi: [10.1038/mi.2017.47](https://doi.org/10.1038/mi.2017.47); pmid: 28612839
31. J. Huang et al., The kinetics of two-dimensional TCR and pMHC interactions determine T-cell responsiveness. *Nature* **464**, 932–936 (2010). doi: [10.1038/nature08944](https://doi.org/10.1038/nature08944); pmid: 20357766
32. B. D. Stadinski et al., Hydrophobic CDR3 residues promote the development of self-reactive T cells. *Nat. Immunol.* **17**, 946–955 (2016). doi: [10.1038/ni.3491](https://doi.org/10.1038/ni.3491); pmid: 27348411
33. Y. S. Choi et al., ICOS receptor instructs T follicular helper cell versus effector cell differentiation via induction of the transcriptional repressor Bcl6. *Immunity* **34**, 932–946 (2011). doi: [10.1016/j.immuni.2011.03.023](https://doi.org/10.1016/j.immuni.2011.03.023); pmid: 21636296
34. C.-H. Chen et al., Transforming growth factor β blocks Tec kinase phosphorylation, Ca²⁺ influx, and NFATc translocation causing inhibition of T cell differentiation. *J. Exp. Med.* **197**, 1689–1699 (2003). doi: [10.1084/jem.20021170](https://doi.org/10.1084/jem.20021170); pmid: 12810687
35. W. Z. Mehal, S. Z. Sheikh, L. Gorelik, R. A. Flavell, TGF-β signaling regulates CD8⁺ T cell responses to high- and low-affinity TCR interactions. *Int. Immunol.* **17**, 531–538 (2005). doi: [10.1093/intimm/dxh233](https://doi.org/10.1093/intimm/dxh233); pmid: 15824070
36. S. C. McKarns, R. H. Schwartz, N. E. Kaminski, Smad3 is essential for TGF-β1 to suppress IL-2 production and TCR-induced proliferation, but not IL-2-induced proliferation. *J. Immunol.* **172**, 4275–4284 (2004). doi: [10.4049/jimmunol.172.7.4275](https://doi.org/10.4049/jimmunol.172.7.4275); pmid: 15034041
37. M. Pepper, A. J. Pagán, B. Z. Igyártó, J. J. Taylor, M. K. Jenkins, Opposing signals from the Bcl6 transcription factor and the interleukin-2 receptor generate T helper 1 central and effector memory cells. *Immunity* **35**, 583–595 (2011). doi: [10.1016/j.immuni.2011.09.009](https://doi.org/10.1016/j.immuni.2011.09.009); pmid: 22018468
38. J. T. Chang et al., Asymmetric T lymphocyte division in the initiation of adaptive immune responses. *Science* **315**, 1687–1691 (2007). doi: [10.1126/science.1139393](https://doi.org/10.1126/science.1139393); pmid: 17332376
39. C. A. Sabatos et al., A synaptic basis for paracrine interleukin-2 signaling during homotypic T cell interaction. *Immunity* **29**, 238–248 (2008). doi: [10.1016/j.immuni.2008.05.017](https://doi.org/10.1016/j.immuni.2008.05.017); pmid: 18674934
40. S. Stoll, J. Delon, T. M. Brotz, R. N. Germain, Dynamic imaging of T cell-dendritic cell interactions in lymph nodes. *Science*

- 296, 1873–1876 (2002). doi: [10.1126/science.1071065](https://doi.org/10.1126/science.1071065); pmid: [12052961](https://pubmed.ncbi.nlm.nih.gov/12052961/)
41. G. Shakhar *et al.*, Stable T cell-dendritic cell interactions precede the development of both tolerance and immunity in vivo. *Nat. Immunol.* **6**, 707–714 (2005). doi: [10.1038/nri210](https://doi.org/10.1038/nri210); pmid: [15924144](https://pubmed.ncbi.nlm.nih.gov/15924144/)
 42. V. Hurez *et al.*, Restricted clonal expression of IL-2 by naive T cells reflects differential dynamic interactions with dendritic cells. *J. Exp. Med.* **198**, 123–132 (2003). doi: [10.1084/jem.20022230](https://doi.org/10.1084/jem.20022230); pmid: [12835480](https://pubmed.ncbi.nlm.nih.gov/12835480/)
 43. A. Oxenius, M. F. Bachmann, R. M. Zinkernagel, H. Hengartner, Virus-specific major MHC class II-restricted TCR-transgenic mice: Effects on humoral and cellular immune responses after viral infection. *Eur. J. Immunol.* **28**, 390–400 (1998). doi: [10.1002/\(SICI\)1521-4141\(199801\)28:01<390::AID-IMMU390>3.0.CO;2-O](https://doi.org/10.1002/(SICI)1521-4141(199801)28:01<390::AID-IMMU390>3.0.CO;2-O); pmid: [9485218](https://pubmed.ncbi.nlm.nih.gov/9485218/)
 44. J. M. Ertelt *et al.*, Selective priming and expansion of antigen-specific Foxp3⁺CD4⁺ T cells during *Listeria monocytogenes* infection. *J. Immunol.* **182**, 3032–3038 (2009). doi: [10.4049/jimmunol.0803402](https://doi.org/10.4049/jimmunol.0803402); pmid: [19234199](https://pubmed.ncbi.nlm.nih.gov/19234199/)
 45. D. Kim *et al.*, TopHat2: Accurate alignment of transcriptomes in the presence of insertions, deletions and gene fusions. *Genome Biol.* **14**, R36 (2013). doi: [10.1186/gb-2013-14-4-r36](https://doi.org/10.1186/gb-2013-14-4-r36); pmid: [23618408](https://pubmed.ncbi.nlm.nih.gov/23618408/)
 46. H. Li *et al.*, The Sequence Alignment/Map format and SAMtools. *Bioinformatics* **25**, 2078–2079 (2009). doi: [10.1093/bioinformatics/btp352](https://doi.org/10.1093/bioinformatics/btp352); pmid: [19505943](https://pubmed.ncbi.nlm.nih.gov/19505943/)
 47. S. Anders, P. T. Pyl, W. Huber, HTSeq—A Python framework to work with high-throughput sequencing data. *Bioinformatics* **31**, 166–169 (2015). doi: [10.1093/bioinformatics/btu638](https://doi.org/10.1093/bioinformatics/btu638); pmid: [25260700](https://pubmed.ncbi.nlm.nih.gov/25260700/)
 48. M. I. Love, W. Huber, S. Anders, Moderated estimation of fold change and dispersion for RNA-seq data with DESeq2. *Genome Biol.* **15**, 550 (2014). doi: [10.1186/s13059-014-0550-8](https://doi.org/10.1186/s13059-014-0550-8); pmid: [25516281](https://pubmed.ncbi.nlm.nih.gov/25516281/)
 49. G. Yaari, C. R. Bolen, J. Thakar, S. H. Kleinstein, Quantitative set analysis for gene expression: A method to quantify gene set differential expression including gene-gene correlations. *Nucleic Acids Res.* **41**, e170 (2013). doi: [10.1093/nar/gkt660](https://doi.org/10.1093/nar/gkt660); pmid: [23921631](https://pubmed.ncbi.nlm.nih.gov/23921631/)

ACKNOWLEDGMENTS

The authors thank members of the Weaver Lab, L. Harrington, H. Hu, S. Kaech, A. Weinmann, and A. Zajac for helpful discussions. We thank D. Wright and B. Dale for mouse breeding and genotyping. **Funding:** This work was supported by NIH grants R01 AI035783 and R01 DK113739 (C.T.W.), R01 AI10113 (B.D.E.), R01 AI107120 (J.J.M.), P30 DK04335 (J.J.M.), R21 AI124143 (J.J.M.), and DP1 AI131080 (S.S.W.). Trainee support was provided by NIH T32 AI007051 to C.J.W., D.D., D.P., and D.J.S. and by NIH F30 DK105680 (J.R.S.). Additional support was provided by UAB Institutional Funds (C.T.W.), March of Dimes Foundation (S.S.W.), HHMI Scholar's Program (S.S.W.), Burroughs Wellcome Fund (S.S.W.), and the Milton Fund (J.J.M.). D.D., S.W., J.R.S., and C.G.W. are members of the UAB Medical Scientist Training Program (MSTP), supported by NIH T32 GM008361. We acknowledge the UAB Epitope Recognition and Immunoreagent Core Facility for provision of some antibodies used in this study.

Author contributions: Author contributions are as follows: project

conception, experimental design, and data interpretation by D.D., C.J.W., and C.T.W.; reporter mouse design, construction, and validation by C.J.W., D.D., R.J.L., H.T., and C.T.W.; RNA-seq studies and data analysis by C.J.W., S.W., R.D.H., and B.T.W.; ChIP-PCR and ATAC-seq experiments and data analysis by D.P. and R.D.H.; in vivo *Listeria*, *Citrobacter*, and immunization data collection, analysis, and interpretation by C.J.W., D.D., D.J.S., C.G.W., J.R.S., and C.T.W.; confocal microscopy by C.L.Z.; TCR-affinity and stimulation-strength experiments and data interpretation by D.D., R.A., E.M.K., R.J.M., and B.D.E.; additional ex vivo experiments by D.D., C.J.W., C.G.W., and J.R.S.; design, construction, and validation of MHCII tetramers and data interpretation by J.J.M.; design, construction, and validation of ActA *Listeria* strains and data interpretation by S.S.W.; and manuscript preparation and editing by D.D., C.J.W., and C.T.W. **Competing interests:** The authors declare no competing interests. **Data and materials availability:** RNA-seq data are deposited in the NCBI Gene Expression Omnibus under accession number GSE116608. Any additional data needed to evaluate the conclusions in this paper are present either in the main text or the supplementary materials.

SUPPLEMENTARY MATERIALS

www.sciencemag.org/content/361/6407/eaao2933/suppl/DC1

Materials and Methods

Figs. S1 to S13

References (50–57)

4 July 2017; resubmitted 25 March 2018

Accepted 6 August 2018

10.1126/science.aao2933

RESEARCH ARTICLE SUMMARY

ORGANIC CHEMISTRY

Asymmetric phosphoric acid-catalyzed four-component Ugi reaction

Jian Zhang*, Peiyuan Yu*, Shao-Yu Li, He Sun, Shao-Hua Xiang, Jun (Joelle) Wang, Kendall N. Houk†, Bin Tan†

INTRODUCTION: The four-component Ugi reaction (Ugi-4CR) assembles peptide-like α -acylaminoamides through one-pot reaction of a carbonyl compound, an amine, an acid, and an isocyanide. Ugi-4CR is well suited for diversity-oriented synthesis applicable in drug discovery, as it facilitates rapid access to diverse libraries of biologically important molecules. The high step economy and atom efficiency of the reaction, as well as its convergent nature, foster its wide use in the synthesis of heterocyclic scaffolds, natural products, macrocycles, polymers, and other target molecules. Despite

these practical advantages, the long-standing stereochemical challenges of the Ugi reaction have yet to be fully addressed. Consequently, access to chiral Ugi products for drug candidate exploration is hindered.

RATIONALE: The chiral phosphoric acid (CPA) framework was targeted as a catalyst for asymmetric Ugi-4CR. The heightened acidity of CPAs over carboxylic acids is perceived to accelerate the kinetics of the enantioselective Ugi reaction so as to outcompete the background reaction. Also, self-assembled heterodimerization between

the CPA and carboxylic acid brings about a dual effect: enhanced acidity of the catalyst and nucleophilicity of the carboxylic acid. Both of these favor the catalytic enantioselective Ugi-4CR. A myriad of well-established or custom CPAs with well-defined chiral pockets could be readily applied, potentially leading to complete stereocontrol. A CPA that could suppress the Passerini and other side reactions would enable rapid imine formation and its preferential activation over the carbonyl group.

RESULTS: A catalytic asymmetric Ugi-4CR was accomplished with 1,1'-spirobiindane-7,7'-diol

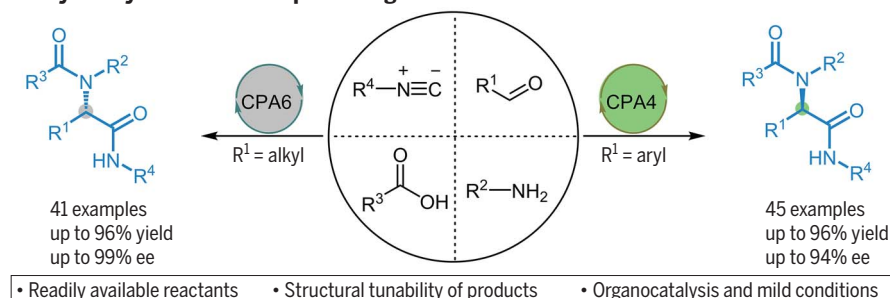
ON OUR WEBSITE

Read the full article at <http://dx.doi.org/10.1126/science.aas8707>

(SPINOL)-derived CPA4 and CPA6 as organocatalysts. The reaction exhibited broad substrate compatibility and good to excellent enantioselectivity [up to 99% enantiomeric excess (ee)]. Activation of the imine might be accomplished by CPA-carboxylic acid heterodimer catalysis via a bifunctional activation mode, which was supported by experiments (carboxylic acids with varying pK_a values and steric properties yielded products with a range of ee values) and density functional theory (DFT) calculations (lowest energy among all the considered activation modes). The calculated free energy profile for the catalytic Ugi reaction gave three CPA-combined key transition states, which highlighted the bifunctional property of the CPA. In the favored enantio-determining transition states, the aryl groups fit into the pocket formed by the two substituents (cyclohexyl rings) of the catalyst, revealing the importance of noncovalent interactions in controlling the stereochemical outcome of this reaction.

CONCLUSION: This operationally simple one-pot enantioselective Ugi-4CR harnesses inherent benefits of multicomponent reaction and organocatalysis to access up to 86 enantioenriched α -acylaminoamides, which are otherwise challenging to obtain via conventional methods, from four achiral building blocks in excellent yields and enantioselectivities. DFT calculations gave a detailed catalytic mechanism, especially with respect to activation modes and enantio-determining transition states. Because amide functionality constitutes the defining primary linkage in proteins, we foresee multiple uses of this asymmetric four-component Ugi protocol for the synthesis of chiral peptides and components of natural products. We also anticipate that this work will initiate the further development of asymmetric multicomponent chemistry. ■

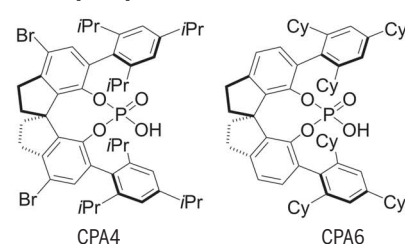
Catalytic asymmetric 4-component Ugi reaction



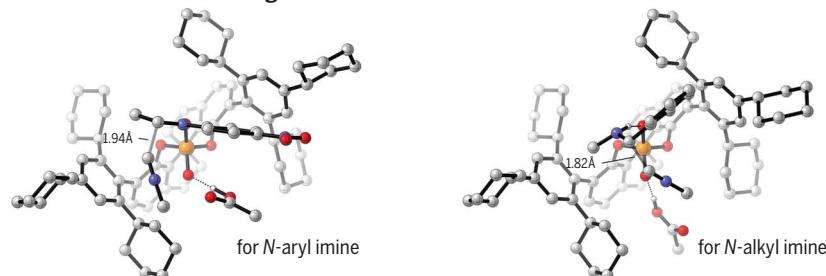
Key points in design

1. Tunable chiral pocket
2. Enhanced nucleophilicity
3. Enhanced acidity
4. Reactivity: imine > carbonyl

Chiral phosphoric acids



Favorable enantio-determining transition states



Design and exploration of catalytic asymmetric Ugi-4CR.

RESEARCH ARTICLE

ORGANIC CHEMISTRY

Asymmetric phosphoric acid-catalyzed four-component Ugi reaction

Jian Zhang^{1*}, Peiyuan Yu^{2*}, Shao-Yu Li¹, He Sun¹, Shao-Hua Xiang¹, Jun (Joelle) Wang¹, Kendall N. Houk^{2†}, Bin Tan^{1†}

The Ugi reaction constructs α -acylaminoamide compounds by combining an aldehyde or ketone, an amine, a carboxylic acid, and an isocyanide in a single flask. Its appealing features include inherent atom and step economy together with the potential to generate products of broad structural diversity. However, control of the stereochemistry in this reaction has proven to be a formidable challenge. We describe an efficient enantioselective four-component Ugi reaction catalyzed by a chiral phosphoric acid derivative that delivers more than 80 α -acylaminoamides in good to excellent enantiomeric excess. Experimental and computational studies establish the reaction mechanism and origins of stereoselectivity.

The prototypical four-component Ugi reaction (Ugi-4CR), first disclosed by Ugi in 1959 (1), assembles α -acylaminoamides through one-pot reaction of a carbonyl compound, an amine, an acid, and an isocyanide (Fig. 1A). The peptide-like moiety is abundant in biologically important molecules (Fig. 1B) (2–6) as well as natural products (Fig. 1C) (7). Although the precise mechanistic scenario may vary, the simplified contours involve preceding imine activation by a carboxylic acid for sequential nucleophilic addition of isocyanide and carboxylate trapping of the thus-formed nitrilium intermediate. Rearrangement via acyl group migration onto the nitrogen atom derived from the imine generates the final product (Fig. 1A) (8–11). The Ugi reaction is well suited for diversity-oriented synthesis applicable in drug discovery

(12–15). It has facilitated rapid access to diverse libraries of biologically important molecules because of its ease of synthetic operation (Fig. 1B) (2–6). In industrial applications, Dömling and co-workers reported an elegant two-step multicomponent synthesis of praziquantel, a drug to treat the parasitical disease schistosomiasis, via Ugi-cyclization cascade (Fig. 1D) (16). This strategy reduced the materials costs and offered a strategy for the synthesis of analogs to address plausible onset of resistance (17). In natural product studies (18), the convergent nature of the Ugi-4CR enabled one-step assembly of an intermediate containing more than half of the atoms in the final product from four building blocks in the total synthesis of ecteinascidin 743 (Fig. 1E) (19). The development of isocyanide-based multicomponent reactions (20, 21) in re-

cent decades reveals that the Ugi-4CR can also be applied to the synthesis of heterocyclic scaffolds (22–24), macrocycles (25, 26), polymers (27, 28), and other compounds.

Despite these practical advantages, the long-standing stereochemical challenges of the Ugi reaction have yet to be fully addressed (29). Whereas a single absolute configuration is strictly required of drug candidates, Ugi condensation products are often racemic. Conventionally, enantiomerically pure amino acids are used as chiral building blocks toward α -acylaminoamides (Fig. 2A). The lengthy route, limited choices of chiral amino acids, and inefficiency in generating structural diversity greatly restrict this protocol. Alternatively, enantiopure substrates could be used for chiral induction in a diastereoselective Ugi-4CR (Fig. 2B). However, this method suffers from poor or moderate diastereoselectivities (30–32) unless specialized amines are used. Catalytic enantioselective synthesis (Fig. 2C) offers flexibility in catalyst choice and facile delivery of distinct stereoisomers by inversion of the catalyst configuration. This approach would accommodate a broader substrate scope encompassing commercially available starting materials and would deliver products that cover substantial chemical space by modulating the components in each substrate quadrant. However, the advent of this approach is long overdue, probably impeded by several hurdles: the complexity of a four-component reaction system, the competition from the uncatalyzed background reaction, the difficulty in achieving stereocontrol of the α -addition of an isocyanide to the imine, and

¹Department of Chemistry, Shenzhen Grubbs Institute, Southern University of Science and Technology, Shenzhen 518055, China. ²Department of Chemistry and Biochemistry, University of California, Los Angeles, CA 90095, USA. *These authors contributed equally to this work.

†Corresponding author. Email: tanb@sustc.edu.cn (B.T.); houk@chem.ucla.edu (K.N.H.)

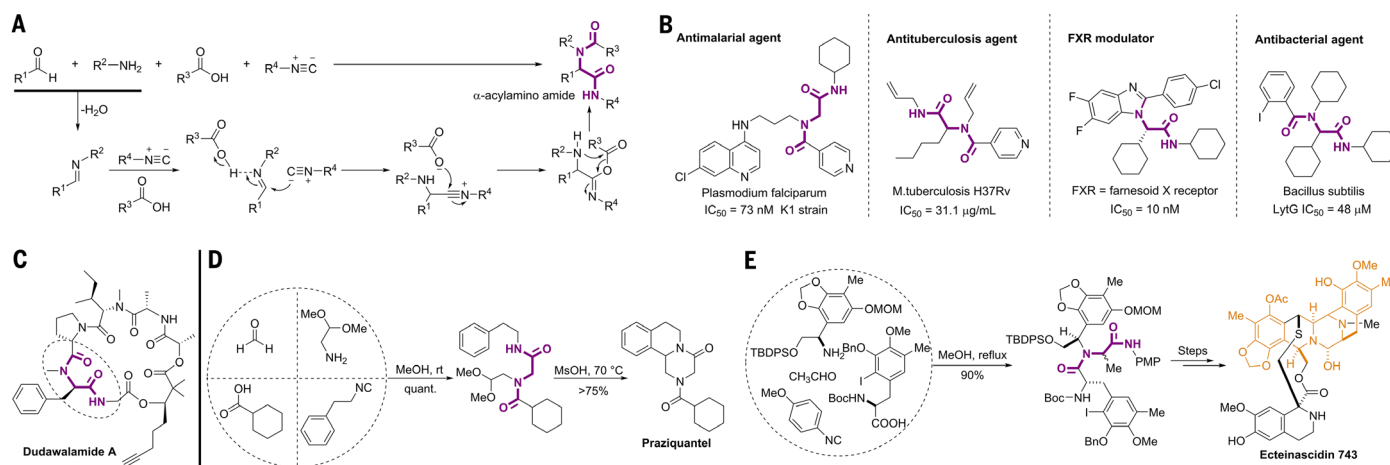


Fig. 1. The classic four-component Ugi reaction in chemistry. (A) The simplified mechanism for the reaction. (B) Selected examples of bioactive molecules prepared directly via Ugi-4CR or involving Ugi-4CR as the key step. (C) The recently identified natural product dudawalamide A bearing an α -acylaminoamide scaffold. (D) Two-step synthesis of the anti-schistosomiasis

drug praziquantel via Ugi-4CR. (E) Ugi-4CR as a key step in the total synthesis of ecteinascidin 743. Atoms in orange were incorporated by the Ugi reaction. Me, methyl; rt, room temperature; quant., quantitative; MsOH, methanesulfonic acid; MOM, methoxymethyl acetal; TBDPS, *t*-butyldiphenylsilyl; Bn, benzyl; Boc, *t*-butoxycarbonyl; PMP, 4-methoxyphenyl.

competition from the Passerini reaction or other side reactions.

We speculated that a mild reaction system with a chiral phosphoric acid (CPA) derivative as catalyst might meet the aforementioned challenges. This robust class of organocatalyst has been commonly used for asymmetric nucleophilic addition to imines after seminal reports by the groups of Akiyama and Terada (33, 34). The heightened acidity of chiral phosphoric acids over carboxylic acids is perceived to accelerate the kinetics of the desired reaction so as to out-compete the background reaction. Also, pioneering reports by List and co-workers suggested that the self-assembled heterodimerization between the CPA and the carboxylic acid brings about a dual effect: enhanced acidity of the catalyst and nucleophilicity of the carboxylic acid (35–37); both of these favor the catalytic enantioselective Ugi-4CR. A myriad of well-established or custom CPAs with well-defined chiral pockets can be readily applied (38–41), leading to complete stereocontrol in α -addition of the isocyanide to imine. Rapid imine formation or its preferential activation over the carbonyl group is viable with a CPA to suppress the Passerini and other side reactions. Elegant isocyanide-based Ugi-type two- or three-component reactions catalyzed by CPAs (42–44) as well as chiral carboxylic acid (45) have been reported. For example, Wang, Zhu, and co-workers achieved an important advance by using a CPA as a catalyst to accomplish the enantioselective Ugi four-center three-component reaction of 2-formylbenzoic acids, anilines, and isonitriles for the syntheses of isoindoline derivatives in high yields with 80 to 90% enantiomeric excess (ee) (44).

Catalyst optimization

After some initial trials (tables S1 to S4), we set out to optimize the model catalytic asymmetric Ugi-4CR between pentanal (**1a**), 4-nitroaniline (**2a**), 3-phenylpropanoic acid (**3a**), and cyclohexyl isocyanide (**4a**) in CH_2Cl_2 at room temperature with 5-Å molecular sieves as a dehydrating additive (Fig. 3). A strong background reaction was observed in the absence of catalyst under these reaction conditions, whereas moderate to good enantioselectivities were afforded with the addition of 5 mole percent (mol %) of Brønsted acid CPAs. 1,1'-Spirobiindane-7,7'-diol (SPINOL)-derived phosphoric acid **CPA6** with a bulky 2,4,6-tricyclohexylphenyl group at the 6,6'-position was found to be the best catalyst, providing the desired product **5** in 64% yield and 82% ee. Further investigations revealed that a 0.3 equivalent excess of **1a**, **2a**, and **4a** at -20°C and double the initial scale improved the chemical yield to 90%, with 92% ee (see table S11); the Passerini product was virtually absent according to ^1H nuclear magnetic resonance (NMR) analysis of the crude reaction mixture.

Asymmetric Ugi reaction with aliphatic aldehydes

With the optimal reaction conditions in hand, we explored the substrate scope with respect to aliphatic aldehydes, amines, carboxylic acids,

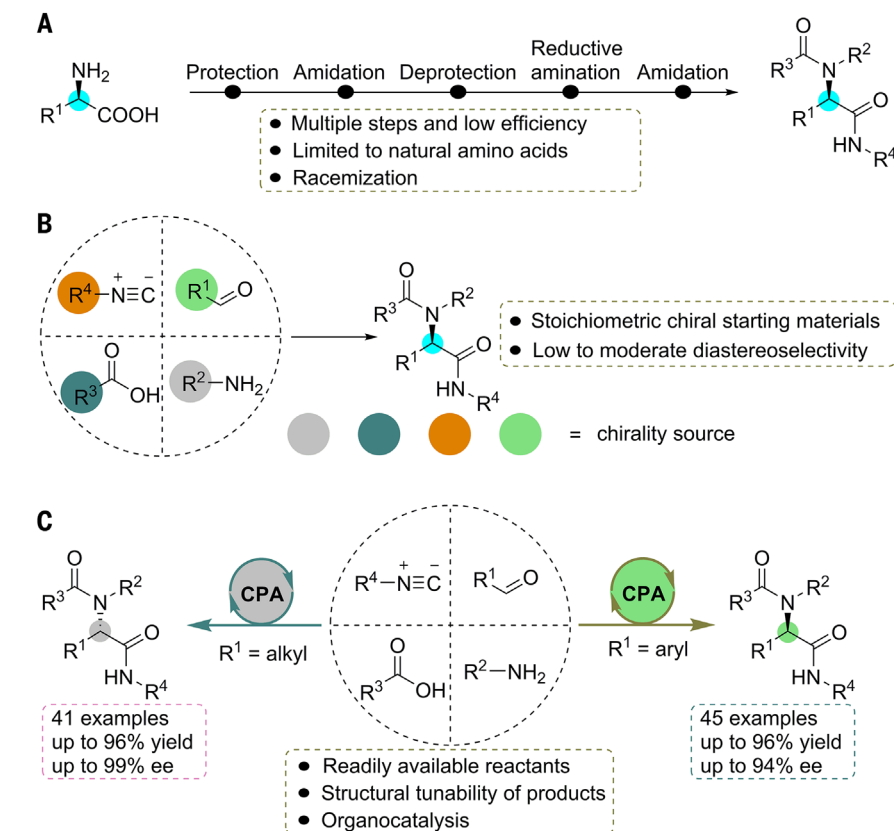


Fig. 2. Strategies for entry to enantioenriched α -acylaminoamides. (A) Asymmetry originates from natural amino acid. (B) Substrate-induced asymmetric Ugi-4CR. (C) Chiral catalyst-induced asymmetric Ugi-4CR. CPA, chiral phosphoric acid.

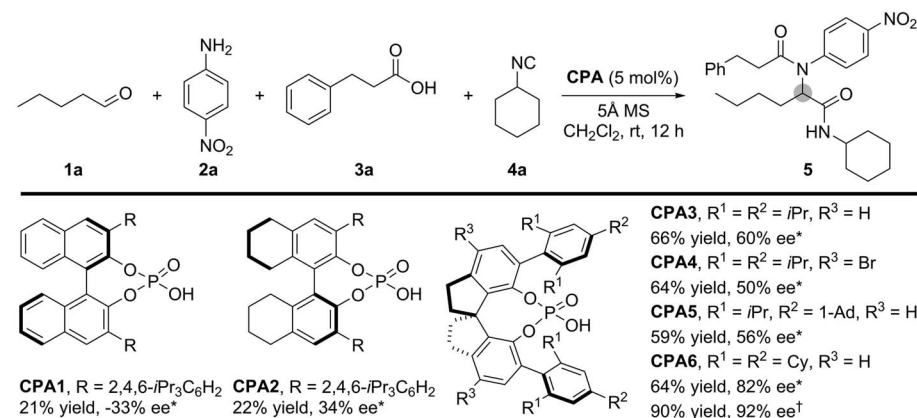


Fig. 3. Optimizing CPA structure in a model reaction. Notations for CPAs: *The reaction of **1a** (0.05 mmol), **2a** (0.05 mmol), **3a** (0.05 mmol), **4a** (0.055 mmol), and catalyst (5 mol %) was carried out in 1 ml of CH_2Cl_2 . †The reaction of **1a** (0.13 mmol), **2a** (0.13 mmol), **3a** (0.10 mmol), **4a** (0.13 mmol), and catalyst **CPA6** (5 mol %) was carried out in 2 ml of CH_2Cl_2 at -20°C . Isolated yields are shown. The ee values were determined by chiral HPLC analysis. Negative ee refers to inverted configuration of the more abundant product enantiomer. MS, molecular sieve; Ph, phenyl; *i*-Pr, isopropyl; 1-Ad, 1-adamantyl; Cy, cyclohexyl.

and isocyanides (Fig. 4). The reaction was applicable to a wide range of aliphatic aldehydes. The chain length of alkyl substituents had a negligible effect on the stereochemical outcome, providing corresponding products **6** to **9** in

92% ee. 3-Phenylpropanal possessing a β -aryl moiety furnished the desired product **10** in 91% yield and 90% ee. 3-Methylbutanal and 2-phenylacetaldehyde were also suitable substrates to afford **11** and **12**. A thioether (**13**)

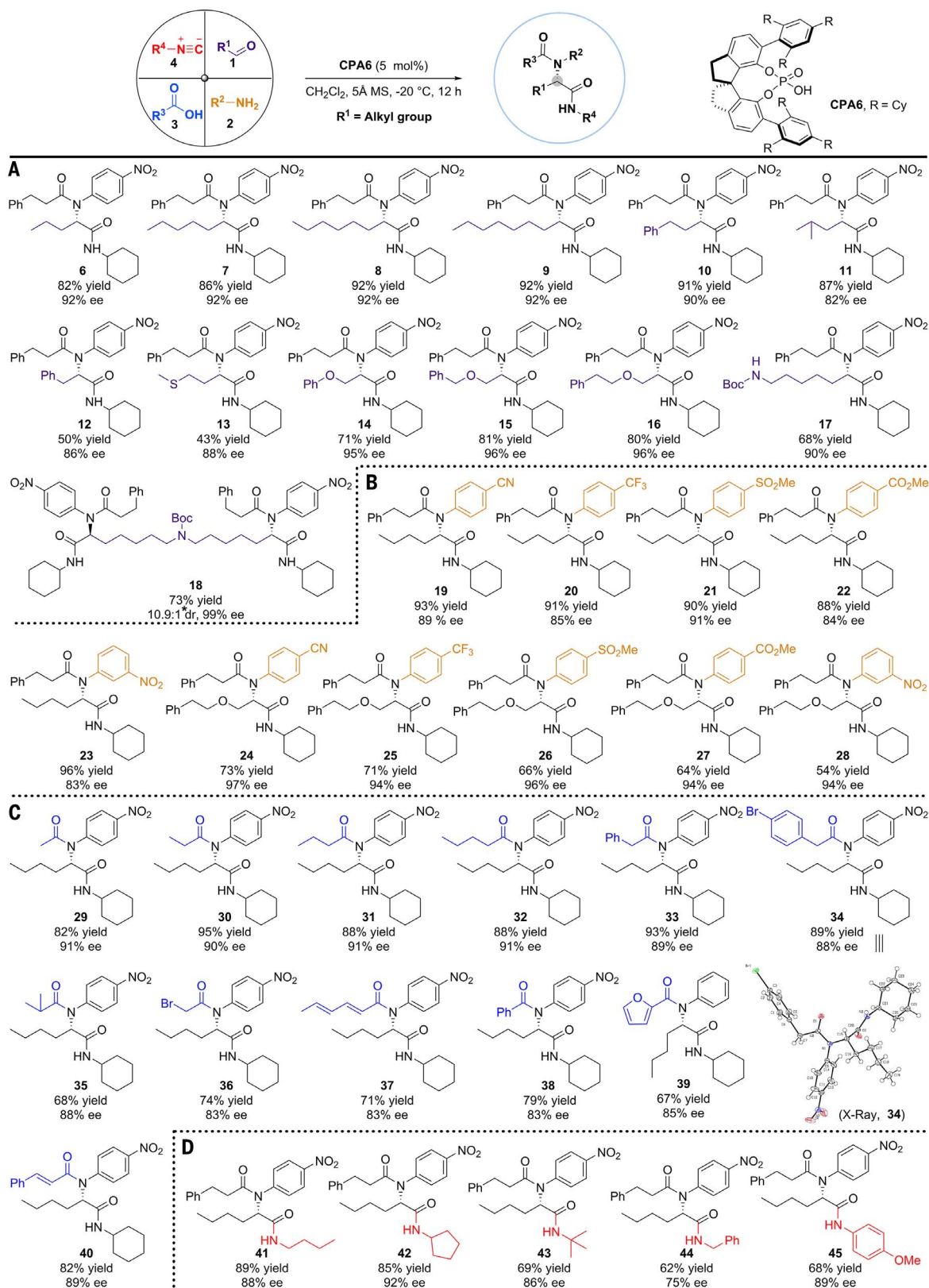


Fig. 4. Substrate scope of the enantioselective Ugi-4CR with aliphatic aldehydes. Colors in (A) to (D) correspond to component colors at upper left. **(A)** Scope of aldehydes. **(B)** Scope of amines. **(C)** Scope of acids. The absolute structure of **34** was defined by means of single-crystal x-ray diffraction with radiation wavelength of 0.71073 Å (Mo-Kα) at 100.0 K,

and the Flack *x* parameter was determined as 0.000(4). **(D)** Scope of isocyanides. Isolated yields are shown. The ee values were determined by chiral HPLC analysis. *The 10.9:1 dr for **18** was calculated on the basis of chiral HPLC analysis (the response factor was 1:1 for equimolar diastereoisomers calculated from the chiral HPLC trace).

substituent was well tolerated, and ether substituents (**14**, **15**, and **16**) afforded excellent enantioselectivities (95 to 96% ee) presumably due to the chelating effect as previously observed by Schreiber and colleagues (**46**). A symmetrical dialdehyde with a central *N*-*tert*-butoxycarbonyl group underwent a dual reaction at both carbonyls with a 10.9:1 diastereomeric ratio (dr) and 99% ee. Aside from 4-nitroaniline, amines with

varied functionalities reacted smoothly to give compounds **19** to **23**, and excellent enantioselectivities (94 to 97% ee) were achieved with chelating aldehydes (**24**–**28**). The generality of the acid component was broad, as products of linear alkyl carboxylic acids (**29**–**32**), benzyl carboxylic acids (**33** and **34**), α -branched isobutyric acid (**35**), α -halogenated acetic acid (**36**), alkenyl carboxylic acids (**37** and **40**), aromatic carboxyl-

ic acid (**38**), and heteroaromatic carboxylic acid (**39**) could all be generated with good enantioselectivities (83 to 91% ee). The absolute configuration of **34** was determined by x-ray crystallographic analysis after recrystallization, and those of other products in Fig. 4 were assigned by analogy. Although benzyl isocyanide formed **44** with moderate optical purity, primary, secondary, tertiary, and aromatic isocyanides

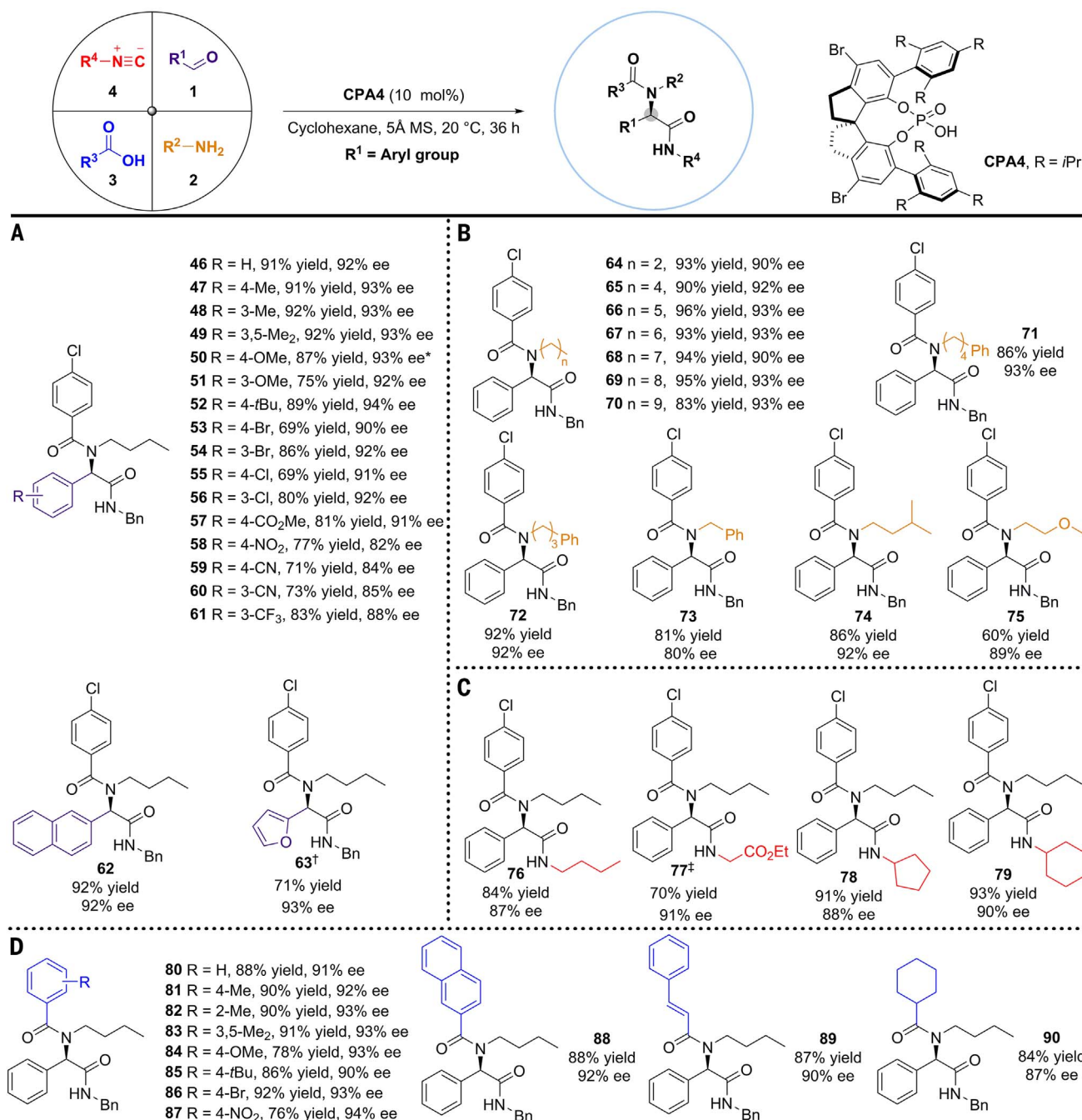


Fig. 5. Substrate scope of the enantioselective Ugi-4CR with aromatic aldehydes. Colors in (A) to (D) correspond to component colors at upper left. **(A)** Scope of aldehydes. **(B)** Scope of amines. **(C)** Scope of isocyanides. **(D)** Scope of acids. Isolated yields are shown.

The ee values were determined by chiral HPLC analysis. *For **50**, the reaction time was extended to 7 days. †For **63**, the reaction time was extended to 72 hours. ‡For **77**, 2.0 equiv of isocyanide was added to the reaction. *t*Bu, *tert*-butyl; Et, ethyl.

formed Ugi products (**41–43**, **45**) with good enantioselectivities, regardless of the extent of steric encumbrance.

Asymmetric Ugi reaction with aromatic aldehydes

We next examined the compatibility of our reaction protocol with aromatic aldehydes. Considering their distinct properties, we reoptimized the conditions (see tables S5 to S10, S12, and S13) with benzaldehyde (**1b**), butylamine (**2b**), 4-chlorobenzoic acid (**3b**), and benzyl isocyanide (**4b**) as model substrates. Product **46** was obtained in 95% yield and 74% ee with chiral phosphoric acid **CPA1** as catalyst in cyclohexane. We further varied the solvent, reaction temperature, and catalyst to identify the following optimal protocol: Reactants **1b** (0.13 mmol), **2b** (0.10 mmol), **3b** (0.10 mmol), and **4b** (0.13 mmol) were combined with a newly synthesized catalyst **CPA4** (10 mol %) in cyclohexane at 20°C for 36 hours to afford the expected Ugi product **46** in 91% isolated yield and 92% ee. To assess the substrate generality and limitations of these

conditions, we evaluated a number of aromatic aldehydes, amines, carboxylic acids, and isocyanides (Fig. 5). It was apparent that the positions and electronic properties of the substituents on the aromatic ring of the aldehydes exerted very limited influence on the stereoselectivity of the process (**47–57**); only slight decreases in enantioselectivity were observed for compounds **58** to **61** derived from aldehydes bearing strongly electron-withdrawing groups. The 2-naphthaldehyde and furfural were also applicable substrates for this transformation, affording **62** and **63** with 92% and 93% ee, respectively, although an extended reaction time was required for the latter. The reaction worked efficiently with different amines. Although benzyl amine delivered compound **73** in slightly compromised optical purity, all other linear amines of various chain length including an ether gave rise to products (**64–70**, **75**) in good enantiomeric excess. Similarly, 4-phenyl butylamine, 3-phenyl propylamine, and 3-methyl butanamine formed products **71**, **72**, and **74** in satisfactory enantiomeric excess. Also, replacing the benzyl isocyanide with other isocyanides produced cor-

responding Ugi products **76** to **79** without diminishing enantioselectivity (87 to 91% ee). Tolerance toward structural and electronic variations of the acids afforded access to a series of α -acylaminoamides with excellent optical purities. Products of aromatic acids bearing electron-donating (**81–85**), neutral (**80**), or electron-withdrawing (**86** and **87**) moieties at varying positions on the phenyl ring were formed in 90 to 94% ee. In addition, 2-naphthyl carboxylic acid and *trans*-cinnamic acid were suitable substrates, providing corresponding products (**88** and **89**) in good yield and enantioselectivity. Product **90** was assembled from aliphatic cyclohexanecarboxylic acid in 84% yield and 87% ee. The absolute configuration of **73** was assigned as (*R*) by comparing the high-performance liquid chromatography (HPLC) spectrum of the reaction product with the known configuration of (*S*)-**73** synthesized from protected L-phenylglycine (Fig. 6B). Those of other products were assigned analogously.

To further evaluate the practicality of the protocol, we performed a gram-scale reaction to prepare **46**. As shown in Fig. 6A, **46** was obtained

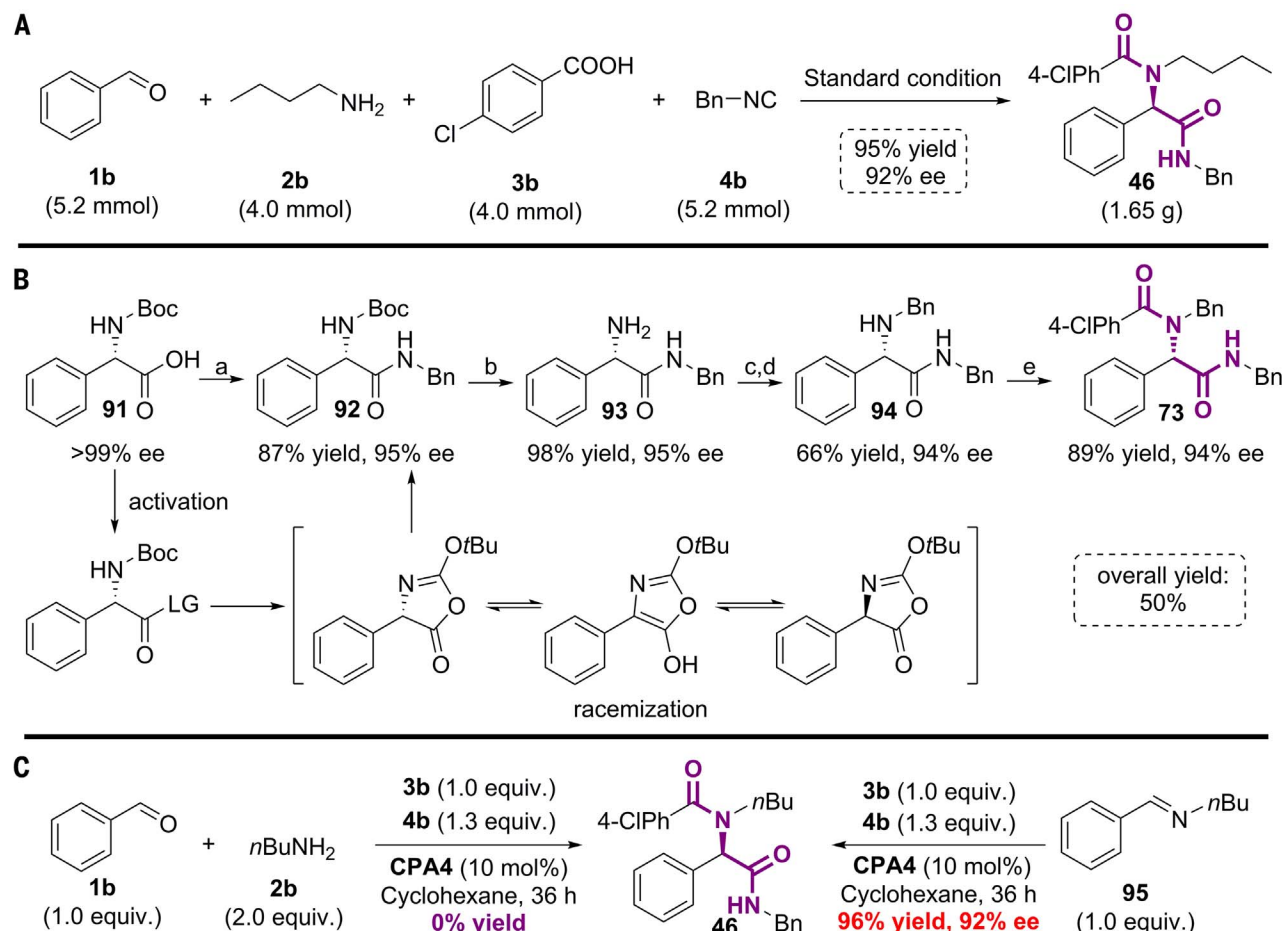


Fig. 6. Syntheses of (*R*)-46** and (*S*)-**73**, and control experiments.**

(A) Gram-scale synthesis of **46** via catalytic enantioselective Ugi-4CR.

(B) Synthesis of (*S*)-**73** from enantiopure amino acid source. Conditions: (a) benzylamine, *N,N*-diisopropylethylamine (DIEA), *O*-(benzotriazol-1-yl)-*N,N,N',N'*-tetramethyluronium tetrafluoroborate (TBTU), CH₂Cl₂, -20°C,

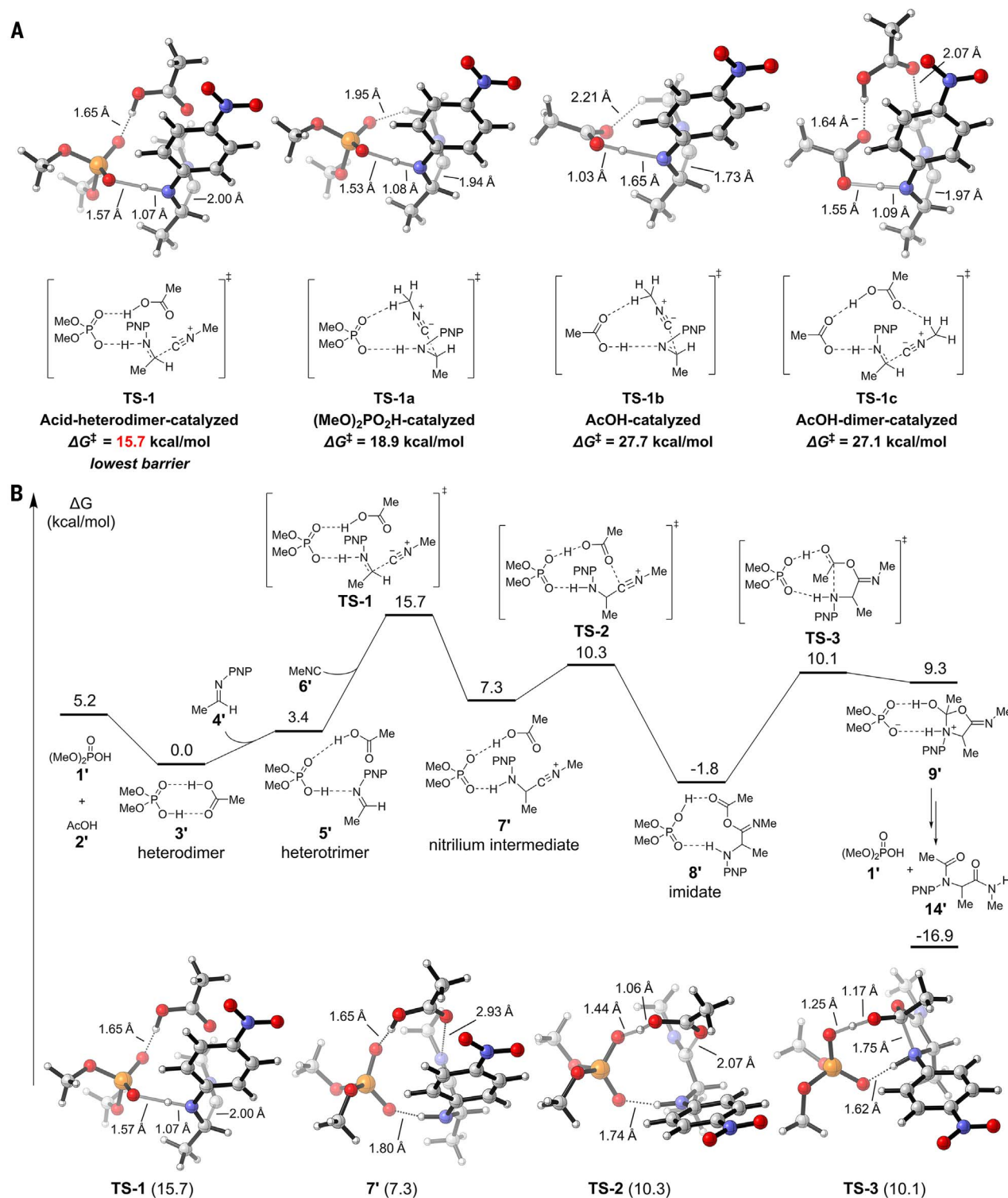
24 hours; (b) trifluoroacetic acid, CH₂Cl₂, rt, 10 hours; (c) benzaldehyde, MgSO₄, CH₂Cl₂, rt, 10 hours; (d) NaBH₄, MeOH/H₂O, rt, 4 hours; (e) *p*-chlorobenzoyl chloride, NEt₃, CH₂Cl₂, 0°C, 2 hours. **(C)** Control experiments. Isolated yields are shown. The ee values were determined by chiral HPLC analysis. LG, leaving group; *n*Bu, *n*-butyl.

with the same enantioselectivity but in higher yield. Our strategy is more efficient than the conventional method (Fig. 6B), which requires multiple steps and suffers from moderate overall yield (50%; Fig. 6B).

Mechanism studies

To gain mechanistic insights, we conducted control experiments and density functional theory (DFT) calculations. The reaction did not proceed in the presence of two equivalents of amine,

which implies that the active catalyst is the chiral phosphoric acid itself rather than phosphate or other deprotonated species. Also, the reaction outcome of mixing preformed imine **95** with carboxylic acid **3b** and isocyanide **4b** was similar



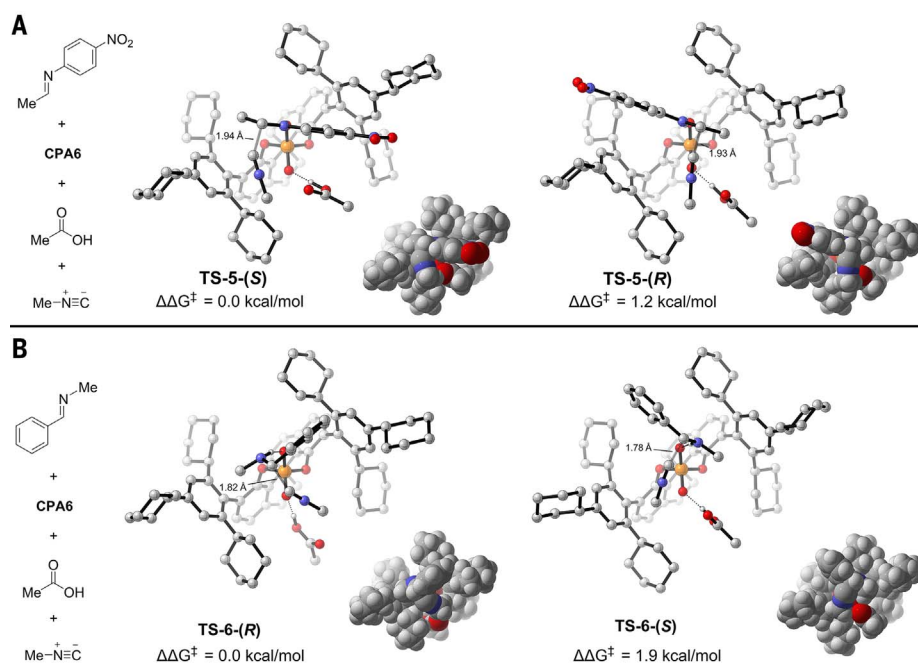


Fig. 8. Density functional theory calculations for enantioselectivity. (A) DFT-optimized enantio-determining transition state structures and their relative energies for *N*-aryl imine substrate. (B) DFT-optimized enantio-determining transition state structures and their relative energies for *N*-alkyl imine substrate.

to the four-component variant, suggesting earlier imine formation as well as the key intermediacy of *trans*-imine. Carboxylic acids with varying pK_a and steric properties gave products with a range of ee values—91% ee (**31**), 88% ee (**35**), and 83% ee (**38**) in Fig. 4 as well as 94% ee (**87**), 92% ee (**81**), and 87% ee (**90**) in Fig. 5—that hinted at the participation of this component in the enantio-determining step of the reaction mechanism, which could be the α -addition step of isocyanide to imine. Thus, we posited that lowest unoccupied molecular orbital (LUMO) activation of the imine might be accomplished by CPA-carboxylic acid heterodimer catalysis via a bifunctional activation mode (**41**). DFT calculations strongly support such a scenario, as transition state **TS-1** (Fig. 7A), resulting from **5'** (Fig. 7B), has the lowest energy among all the considered transition states. For the nucleophilic addition of the isocyanide to the *trans*-imine, four different modes (Fig. 7A) of catalysis were explored and compared. The chiral phosphoric acid is modeled with a dimethyl model catalyst. All these TS structures involve LUMO activation of the imine by the catalyst, as well as activation (directing) of the isocyanide via either electrostatic interaction (**TS-1**) or C-H...O hydrogen bonding (**TS-1a**–**TS-1c**). The acid-heterodimer catalysis via **TS-1** has the lowest energy barrier (15.7 kcal/mol). It features favorable electrostatic interactions between the positively charged nitrogen atom of the isocyanide and the carbonyl oxygen atom of the carboxylic acid.

In the calculated free energy profile for the reaction (Fig. 7B; see fig. S1 for full reaction pathway), the model phosphoric acid **1'** and

acetic acid **2'** form a relatively stable heterodimer **3'** (5.2 kcal/mol exergonic) as suggested by List and co-workers (**35**). Imine coordination at the Brønsted acid site of the phosphoric acid generates heterotrimer **5'**. The activated imine then undergoes a nucleophilic attack by isocyanide **6'** to form the nitrilium intermediate **7'**. Accompanying the proton delivery, the carboxylate attacks the nitrilium carbon via **TS-2** to form the imidate **8'** rapidly; the difference in energy between **TS-2** and **7'** is only 3 kcal/mol. Subsequently, phosphoric acid **1'** promotes a Mumm rearrangement to release the desired product **14'** and regenerate the catalyst. The overall rate-determining step is the nucleophilic addition of the isocyanide **6'** to the imine-catalyst complex **5'** via **TS-1**. The subsequent Mumm rearrangement catalyzed by phosphoric acid has a lower barrier (11.9 kcal/mol, via **TS-3**) than the first C-C bond-forming step (15.7 kcal/mol, via **TS-1**). For comparison, the Mumm rearrangement catalyzed by acetic acid has a much higher barrier (18.4 kcal/mol via **TS-3a**; fig. S2). This difference not only defines the rate-limiting step of the overall process, but also plays an important role in the stereochemical outcome of the reaction, as the enantioselectivity could be alternatively determined at the Mumm rearrangement step. For example, Zhu and co-workers attributed asymmetric induction in the Ugi variant they reported (**44**) to a dynamic kinetic resolution of the primary Ugi adduct, rather than to the C-C bond-forming process. Thus, the present work differs substantially from that previous work in the mode of selectivity.

Enantio-determining TS structures were also explored with catalyst **CPA6** (**CPA4** is used in

Fig. 5, but **CPA6** also works); the lowest-energy TSs for two different imine substrates are shown in Fig. 8. The favored transition states lead to (*S*)-product for *N*-aryl imine and to (*R*)-product for *N*-alkyl imine, in accord with the experimental observations. The difference is larger for **TS-6(R)** and **TS-6(S)** (1.9 kcal/mol at room temperature). Although no obvious steric clashes are detected in these transition states, the important factor is the orientation of the aryl groups of the substrates relative to the 2,4,6-tricyclohexyl group of the catalyst. In the favored TSs, the aryl groups fit into the pocket formed by the two cyclohexyl rings of the catalyst, whereas the aryl groups occupy the empty quadrant in the three-dimensional space left by the bulky substituents of the catalyst in the disfavored TSs. It is likely that the favorable noncovalent interactions between the aryl groups of the substrates and the cyclohexyl groups of the catalyst are responsible for the observed enantioselectivities. A general model for predicting the stereochemistry of phosphoric acid-catalyzed reactions of imines based primarily on steric effects (**47**, **48**) failed to predict the correct stereochemistry in this case, pointing to the importance of noncovalent interactions and their interplay with (and sometimes overriding of) steric effects in chiral phosphoric acid-catalyzed reactions (**49**, **50**). The bifunctional property of the chiral phosphoric acid plays a profound role in the reaction processes (fig. S1) with respect to generation of the heterodimer, activation of the imine for α -addition of isocyanide, control of the enantioselectivity, and promotion of the Mumm rearrangement.

Methods

^1H NMR, ^{13}C NMR, and ^{19}F NMR spectra of **46** to **90** were recorded at 80°C in DMSO-*d*₆ on a 400 MHz instrument with tetramethylsilane (TMS) as internal standard. ^1H NMR, ^{13}C NMR, ^{31}P NMR, and ^{19}F NMR spectra of other compounds were recorded at room temperature in CDCl₃ on a 400 MHz/500 MHz instrument with TMS as internal standard. Data for ^1H NMR are recorded as follows: chemical shift (ppm), multiplicity (s, singlet; d, doublet; t, triplet; q, quartet; m, multiplet), coupling constant (Hz), integration. Data for ^{13}C NMR are reported in terms of chemical shift (δ , ppm). High-resolution mass spectra (HRMS) were recorded on a LC-TOF spectrometer (Micromass). ESI-HRMS data were acquired using a Thermo LTQ Orbitrap XL Instrument equipped with an ESI source and controlled by Xcalibur software. Enantioselectivities were recorded on Shimadzu/Agilent HPLC, using a chiral stationary phase column (IC/ID, Daicel Co. CHIRALPAK). The chiral HPLC methods were calibrated with the corresponding racemic mixtures. Dichloromethane and cyclohexane were purchased from J&K. 5-Å molecular sieve was purchased from Acros. The silica gel (300–400 mesh) for flash column chromatography was purchased from Acela. Other chemicals were purchased from TCI, Energy, Adamas, Meryer, Acros, and Alfa Aesar, and used as received.

All calculations were performed with the Gaussian 09 package (51). Geometry optimizations were performed with B3LYP (52, 53) and the 6-31G(d) basis set. Normal vibrational mode analysis at the same level of theory confirmed that the optimized structures are minima (zero imaginary frequency) or saddle points (one imaginary frequency). Single-point energies and solvent effects in dichloromethane were computed with the dispersion-corrected density functional method B3LYP-D3 (54) with a Becke-Johnson (BJ) damping function (55) and the 6-311+G (d,p) basis set using the CPCM solvation model (56, 57). The relative energies with ZPE corrections and free energies (at 298.15 K) are in kcal/mol. Single-point energies were also evaluated within the CPCM model using the M06-2X (58), ω B97X-D (59), and B3LYP functionals to compare the stereoselectivities computed with or without dispersion corrections. DFT-optimized structures are illustrated using CYLView (60).

REFERENCES AND NOTES

1. I. Ugi, R. Meyr, U. Fetzter, C. Steinbrückner, Versuche mit isonitrilen. *Angew. Chem.* **71**, 386 (1959).
2. C. C. Musonda et al., Application of multi-component reactions to antimalarial drug discovery. Part 1: Parallel synthesis and antiparasmodal activity of new 4-aminoquinoline Ugi adducts. *Bioorg. Med. Chem. Lett.* **14**, 3901–3905 (2004). doi: [10.1016/j.bmcl.2004.05.063](#); pmid: [15225694](#)
3. A. Dömling, S. Achatz, B. Beck, Novel anti-tuberculosis agents from MCR libraries. *Bioorg. Med. Chem. Lett.* **17**, 5483–5486 (2007). doi: [10.1016/j.bmcl.2007.04.066](#); pmid: [17720495](#)
4. H. G. F. Richter et al., Discovery of novel and orally active FXR agonists for the potential treatment of dyslipidemia & diabetes. *Bioorg. Med. Chem. Lett.* **21**, 191–194 (2011). doi: [10.1016/j.bmcl.2010.11.039](#); pmid: [21134747](#)
5. H. G. F. Richter et al., Optimization of a novel class of benzimidazole-based farnesoid X receptor (FXR) agonists to improve physicochemical and ADME properties. *Bioorg. Med. Chem. Lett.* **21**, 1134–1140 (2011). doi: [10.1016/j.bmcl.2010.12.123](#); pmid: [21269824](#)
6. S. Nayyab et al., Diamide inhibitors of the bacillus subtilis N-acetylglucosaminidase LytG that exhibit antibacterial activity. *ACS Infect. Dis.* **3**, 421–427 (2017). doi: [10.1021/acsinfecdis.7b00005](#); pmid: [28448118](#)
7. J. Almaliti et al., Dudawalamides A-D, antiparasitic cyclic depsipeptides from the marine cyanobacterium moorea prodensis. *J. Nat. Prod.* **80**, 1827–1836 (2017). doi: [10.1021/acs.jnatprod.7b00034](#); pmid: [28535042](#)
8. G. Gokel, G. Lüdke, I. Ugi, in *Isonitrile Chemistry*, I. Ugi, Ed. (Academic Press, 1971), pp. 145–199.
9. N. Chéron, R. Ramozzi, L. El Kaim, L. Grimaud, P. Fleurat-Lessard, Challenging 50 years of established views on Ugi reaction: A theoretical approach. *J. Org. Chem.* **77**, 1361–1366 (2012). doi: [10.1021/jo2021554](#); pmid: [22225432](#)
10. C. Iacobucci, S. Reale, J.-F. Gal, F. De Angelis, Insight into the mechanisms of the multicomponent Ugi and Ugi-Smiles reactions by ESI-MS/(MS). *Eur. J. Org. Chem.* **2014**, 7087–7090 (2014). doi: [10.1002/ejoc.201403179](#)
11. G. A. Medeiros et al., Probing the mechanism of the Ugi four-component reaction with charge-tagged reagents by ESI-MS/(MS). *Chem. Commun.* **50**, 338–340 (2014). doi: [10.1039/C3CC47156J](#); pmid: [24244941](#)
12. I. Akratopoulou-Zanze, Isonitrile-based multicomponent reactions in drug discovery. *Curr. Opin. Chem. Biol.* **12**, 324–331 (2008). doi: [10.1016/j.cbpa.2008.02.004](#); pmid: [18312861](#)
13. M. Colombo, I. Peretto, Chemistry strategies in early drug discovery: An overview of recent trends. *Drug Discov. Today* **13**, 677–684 (2008). doi: [10.1016/j.drudis.2008.03.007](#); pmid: [18675762](#)
14. A. Dömling, W. Wang, K. Wang, Chemistry and biology of multicomponent reactions. *Chem. Rev.* **112**, 3083–3135 (2012). doi: [10.1021/cr100233r](#); pmid: [22435608](#)
15. P. Slobbe, E. Ruijter, R. V. A. Orru, Recent applications of multicomponent reactions in medicinal chemistry. *MedChemComm* **3**, 1189–1218 (2012). doi: [10.1039/c2md20089a](#)
16. H. Cao, H. Liu, A. Dömling, Efficient multicomponent reaction synthesis of the schistosomiasis drug praziquantel. *Chem. Eur. J.* **16**, 12296–12298 (2010). doi: [10.1002/chem.201002046](#); pmid: [20845417](#)
17. H. Liu, S. William, E. Herdtweck, S. Botros, A. Dömling, MCR synthesis of praziquantel derivatives. *Chem. Biol. Drug Des.* **79**, 470–477 (2012). doi: [10.1111/j.1747-0285.2011.01288.x](#); pmid: [22151001](#)
18. B. B. Touré, D. G. Hall, Natural product synthesis using multicomponent reaction strategies. *Chem. Rev.* **109**, 4439–4486 (2009). doi: [10.1021/cr800296p](#); pmid: [19480390](#)
19. A. Endo et al., Total synthesis of ecteinascidin 743. *J. Am. Chem. Soc.* **124**, 6552–6554 (2002). doi: [10.1021/ja026216d](#); pmid: [12047173](#)
20. A. Dömling, I. Ugi, Multicomponent reactions with isocyanides. *Angew. Chem. Int. Ed.* **39**, 3168–3210 (2000). doi: [10.1002/1521-3773\(20000915\)39:18<3168::AID-ANGE3168>3.0.CO;2-U](#); pmid: [11028061](#)
21. A. Dömling, Recent developments in isocyanide based multicomponent reactions in applied chemistry. *Chem. Rev.* **106**, 17–89 (2006). doi: [10.1021/cr0505728](#); pmid: [16402771](#)
22. J. Zhu, Recent developments in the isonitrile-based multicomponent synthesis of heterocycles. *Eur. J. Org. Chem.* **2003**, 1133–1144 (2003). doi: [10.1002/ejoc.200390167](#)
23. I. Akratopoulou-Zanze, S. W. Djuric, Recent advances in the development and applications of post-Ugi transformations. *Heterocycles* **73**, 125–147 (2007). doi: [10.3987/REV-07-SR\(U\)3](#)
24. U. K. Sharma, N. Sharma, D. D. Vachhani, E. V. Van der Eycken, Metal-mediated post-Ugi transformations for the construction of diverse heterocyclic scaffolds. *Chem. Soc. Rev.* **44**, 1836–1860 (2015). doi: [10.1039/C4CS00253A](#); pmid: [25652577](#)
25. L. A. Wessjohann, D. G. Rivera, O. E. Vercillo, Multiple multicomponent macrocyclizations (MiBs): A strategic development toward macrocycle diversity. *Chem. Rev.* **109**, 796–814 (2009). doi: [10.1021/cr8003407](#); pmid: [19166290](#)
26. L. A. Wessjohann, R. A. W. Neves Filho, A. R. Puentes, M. C. Morejon, in *Multicomponent Reactions in Organic Synthesis*, J. Zhu, Q. Wang, M.-X. Wang, Eds. (Wiley, 2015), pp. 231–264.
27. R. Kakuchi, Multicomponent reactions in polymer synthesis. *Angew. Chem. Int. Ed.* **53**, 46–48 (2014). doi: [10.1002/ange.201305538](#); pmid: [24302633](#)
28. A. Sehlinger, M. A. R. Meier, Passerini and Ugi multicomponent reactions in polymer science. *Adv. Polym. Sci.* **269**, 61–86 (2015). doi: [10.1007/12_2014_298](#)
29. Q. Wang, D.-X. Wang, M.-X. Wang, J. Zhu, Still unconquered: Enantioselective Passerini and Ugi multicomponent reactions. *Acc. Chem. Res.* **51**, 1290–1300 (2018). doi: [10.1021/acs.accounts.8b00105](#); pmid: [29708723](#)
30. L. Banfi, A. Basso, G. Guanti, R. Riva, in *Multicomponent Reactions*, J. Zhu, H. Bienaymé, Eds. (Wiley, 2005), pp. 1–32.
31. D. J. Ramón, M. Yus, Asymmetric multicomponent reactions (AMCRs): The new frontier. *Angew. Chem. Int. Ed.* **44**, 1602–1634 (2005). doi: [10.1002/anie.200406548](#); pmid: [15719349](#)
32. S. S. van Berkel, B. G. M. Bögers, M. A. Wijdevan, B. Westermann, F. P. J. T. Rutjes, Recent advances in asymmetric isocyanide-based multicomponent reactions. *Eur. J. Org. Chem.* **2012**, 3543–3559 (2012). doi: [10.1002/ejoc.201200030](#)
33. T. Akiyama, J. Itoh, K. Yokota, K. Fuchibe, Enantioselective Mannich-type reaction catalyzed by a chiral Brønsted acid. *Angew. Chem. Int. Ed.* **43**, 1566–1568 (2004). doi: [10.1002/anie.200353240](#); pmid: [15022235](#)
34. D. Uraguchi, M. Terada, Chiral Brønsted acid-catalyzed direct Mannich reactions via electrophilic activation. *J. Am. Chem. Soc.* **126**, 5356–5357 (2004). doi: [10.1021/ja0491533](#); pmid: [15113196](#)
35. M. R. Monaco et al., Activation of carboxylic acids in asymmetric organocatalysis. *Angew. Chem. Int. Ed.* **53**, 7063–7067 (2014). doi: [10.1002/anie.201400169](#); pmid: [24888674](#)
36. M. R. Monaco, S. Prévost, B. List, Organocatalytic asymmetric hydrolysis of epoxides. *Angew. Chem. Int. Ed.* **53**, 8142–8145 (2014). doi: [10.1002/anie.201400170](#); pmid: [24961995](#)
37. M. R. Monaco, G. Pupo, B. List, Phosphoric acid based heterodimers in asymmetric catalysis. *Synlett* **27**, 1027–1040 (2016). doi: [10.1055/s-0035-1561954](#)
38. T. Akiyama, Stronger Brønsted acids. *Chem. Rev.* **107**, 5744–5758 (2007). doi: [10.1021/cr068374j](#); pmid: [17983247](#)
39. D. Kampen, C. M. Reisinger, B. List, Chiral Brønsted acids for asymmetric organocatalysis. *Top. Curr. Chem.* **291**, 395–456 (2010). doi: [10.1007/978-3-642-02815-1_1](#); pmid: [21494945](#)
40. D. Parmar, E. Sugiono, S. Raja, M. Rueping, Complete field guide to asymmetric BINOL-phosphate derived Brønsted acid and metal catalysis: History and classification by mode of activation; Brønsted acidity, hydrogen bonding, ion pairing, and metal phosphates. *Chem. Rev.* **114**, 9047–9153 (2014). doi: [10.1021/cr5001496](#); pmid: [25203602](#)
41. T. Akiyama, K. Mori, Stronger Brønsted acids: Recent progress. *Chem. Rev.* **115**, 9277–9306 (2015). doi: [10.1021/acs.chemrev.5b00041](#); pmid: [26182163](#)
42. S. C. Pan, B. List, Catalytic three-component Ugi reaction. *Angew. Chem. Int. Ed.* **47**, 3622–3625 (2008). doi: [10.1002/anie.200800494](#); pmid: [18383491](#)
43. T. Yue, M.-X. Wang, D.-X. Wang, G. Masson, J. Zhu, Brønsted acid catalyzed enantioselective three-component reaction involving the α addition of isocyanides to imines. *Angew. Chem. Int. Ed.* **48**, 6717–6721 (2009). doi: [10.1002/anie.200902385](#); pmid: [19658144](#)
44. Y. Zhang et al., Chiral phosphoric acid catalyzed asymmetric Ugi reaction by dynamic kinetic resolution of the primary multicomponent adduct. *Angew. Chem. Int. Ed.* **55**, 5282–5285 (2016). doi: [10.1002/anie.201600751](#); pmid: [26997306](#)
45. T. Hashimoto, H. Kimura, Y. Kawamata, K. Maruoka, A catalytic asymmetric Ugi-type reaction with acyclic azomethine imines. *Angew. Chem. Int. Ed.* **51**, 7279–7281 (2012). doi: [10.1002/anie.201201905](#); pmid: [22692817](#)
46. P. R. Andreana, C. C. Liu, S. L. Schreiber, Stereochemical control of the Passerini reaction. *Org. Lett.* **6**, 4231–4233 (2004). doi: [10.1021/ol0482893](#); pmid: [15524450](#)
47. J. P. Reid, J. M. Goodman, Goldlocks catalysts: Computational insights into the role of the 3,3'-substituents on the selectivity of BINOL-derived phosphoric acid catalysts. *J. Am. Chem. Soc.* **138**, 7910–7917 (2016). doi: [10.1021/jacs.6b02825](#); pmid: [27227372](#)
48. J. P. Reid, L. Simón, J. M. Goodman, A practical guide for predicting the stereochemistry of bifunctional phosphoric acid catalyzed reactions of imines. *Acc. Chem. Res.* **49**, 1029–1041 (2016). doi: [10.1021/acs.accounts.6b00052](#); pmid: [27128106](#)
49. S. E. Wheeler, T. J. Seguin, Y. Guan, A. C. Doney, Noncovalent interactions in organocatalysis and the prospect of computational catalyst design. *Acc. Chem. Res.* **49**, 1061–1069 (2016). doi: [10.1021/acs.accounts.6b00096](#); pmid: [27110641](#)
50. R. Maji, P. A. Champagne, K. N. Houk, S. E. Wheeler, Activation mode and origin of selectivity in chiral phosphoric acid-catalyzed oxacycle formation by intramolecular oxetane desymmetrizations. *ACS Catal.* **7**, 7332–7339 (2017). doi: [10.1021/acscatal.7b02993](#)
51. Gaussian 09, rev. D.01 (Gaussian Inc., 2013).
52. A. D. Becke, Density-functional thermochemistry. III. The role of exact exchange. *J. Chem. Phys.* **98**, 5648–5652 (1993). doi: [10.1063/1.464913](#)
53. C. Lee, W. Yang, R. G. Parr, Development of the Colle-Salvetti correlation-energy formula into a functional of the electron density. *Phys. Rev. B* **37**, 785–789 (1988). doi: [10.1103/PhysRevB.37.785](#)
54. S. Grimme, J. Antony, S. Ehrlich, H. Krieg, A consistent and accurate ab initio parametrization of density functional dispersion correction (DFT-D) for the 94 elements H-Pu. *J. Chem. Phys.* **132**, 154104 (2010). doi: [10.1063/1.3382344](#); pmid: [20423165](#)
55. S. Grimme, S. Ehrlich, L. Goerigk, Effect of the damping function in dispersion corrected density functional theory. *J. Comput. Chem.* **32**, 1456–1465 (2011). doi: [10.1002/jcc.21759](#); pmid: [21370243](#)
56. V. Barone, M. Cossi, Quantum calculation of molecular energies and energy gradients in solution by a conductor solvent model. *J. Phys. Chem. A* **102**, 1995–2001 (1998). doi: [10.1021/jp9716997](#)
57. M. Cossi, N. Rega, G. Scalmani, V. Barone, Energies, structures, and electronic properties of molecules in solution with the C-PCM solvation model. *J. Comput. Chem.* **24**, 669–681 (2003). doi: [10.1002/jcc.10189](#); pmid: [12666158](#)
58. Y. Zhao, D. G. Truhlar, The M06 suite of density functionals for main group thermochemistry, thermochemical kinetics, noncovalent interactions, excited states, and transition elements: Two new functionals and systematic testing of four M06-class functionals and 12 other functionals. *Theor. Chem. Acc.* **120**, 215–241 (2008). doi: [10.1007/s00214-007-0310-x](#)

59. J.-D. Chai, M. Head-Gordon, Long-range corrected hybrid density functionals with damped atom-atom dispersion corrections. *Phys. Chem. Chem. Phys.* **10**, 6615–6620 (2008). doi: [10.1039/b810189b](https://doi.org/10.1039/b810189b); pmid: [18989472](https://pubmed.ncbi.nlm.nih.gov/18989472/)
60. C. Y. Legault, CYLView, 1.0b, Université de Sherbrook, 2009; www.cylview.org.

ACKNOWLEDGMENTS

Funding: Supported by the National Natural Science Foundation of China (Nos. 21572095, 21772081), Shenzhen special funds for the development of biomedicine, internet, new energy, and new material industries (JCYJ20170412151701379, KQJSCX20170328153203). B.T. thanks the Thousand Young Talents Program for financial support. P.Y. and K.N.H. acknowledge the computational resources provided by the Institute of Digital Research and Education (IDRE) at UCLA, and

by the Extreme Science and Engineering Discovery Environment (XSEDE), which is supported by the NSF (OCI-1053575).

Author contributions: B.T. conceived of and directed the project; J.Z. developed the catalytic asymmetric Ugi-4CR and conducted most of the experiments; S.-Y.L. and H.S. performed parts of substrate screening experiments; P.Y. conducted the DFT calculations and provided mechanism analysis; K.N.H. directed the DFT calculations and mechanism analysis; J.W. and S.-H.X. helped the direction of the project; and P.Y., S.-H.X., J.W., K.N.H., and B.T. co-wrote the manuscript. **Competing interests:** The authors declare no competing interests. **Data and materials availability:** The x-ray crystallographic coordinates for the structure of **34** are available free of charge from the Cambridge Crystallographic Data Centre under deposition number CCDC 1588496. Experimental procedures, characterization of new compounds,

and all other data supporting the findings are available in the supplementary materials.

SUPPLEMENTARY MATERIALS

www.sciencemag.org/content/361/6407/eaas8707/suppl/DC1
Materials and Methods
Supplementary Text
Tables S1 to S16
Figs. S1 to S5
NMR Spectra
References (61–63)
Movies S1 and S2

28 December 2017; resubmitted 25 May 2018

Accepted 16 July 2018

10.1126/science.aas8707

RESEARCH ARTICLE SUMMARY

NEUROSCIENCE

Recurrent cortical circuits implement concentration-invariant odor coding

Kevin A. Bolding and Kevin M. Franks*

INTRODUCTION: Objects can appear remarkably stable despite the often fickle cues they provide to our senses. For instance, a foraging mouse can identify and locate a piece of cheese several meters away entirely by smell, even though the concentration of airborne “cheese” molecules varies steeply over this distance. How the brain maintains perceptual stability across such widely ranging stimulus intensities remains a fundamental, unanswered question. The response properties of olfactory sensory neurons in the mouse’s nose may provide part of the answer. With each sniff, inhaled odorant molecules activate subsets of sensory neurons that each express a single type of odorant receptor. At low concentrations, when only a few odorant molecules are present, only those cells that express the most sensitive receptors for that particular odorant will be activated. However, many cells that express lower-affinity receptors will also be activated at higher concentrations, potentially degrading the odor representation. Crucially, the sensory neurons that express high-affinity receptors will always be activated earliest in the sniff, regardless of concentration. Could the mouse’s brain exploit this temporal structure to maintain stable odor representations despite changing odorant concentrations?

RATIONALE: To test this idea, we simultaneously recorded spiking activity from olfactory bulb (OB) mitral cells, which receive input from the olfactory sensory neurons, and from their cortical targets, principal neurons (PNs) in the piriform cortex (PCx), where odor identity is encoded. PNs form extensive, long-range “recurrent” excitatory synapses with each other in addition to forming excitatory synapses on PCx inhibitory interneurons. We

hypothesized that this architecture enables the earliest activated—and therefore most selective—PCx PNs to rapidly inhibit less selective PCx PNs, helping to maintain stimulus specificity across odorant concentrations. We directly tested this idea by selectively expressing tetanus toxin in PCx PNs, blocking their ability to excite other PCx neurons but leaving them responsive to OB inputs.

RESULTS: In control mice, OB responses to different odors were more correlated and

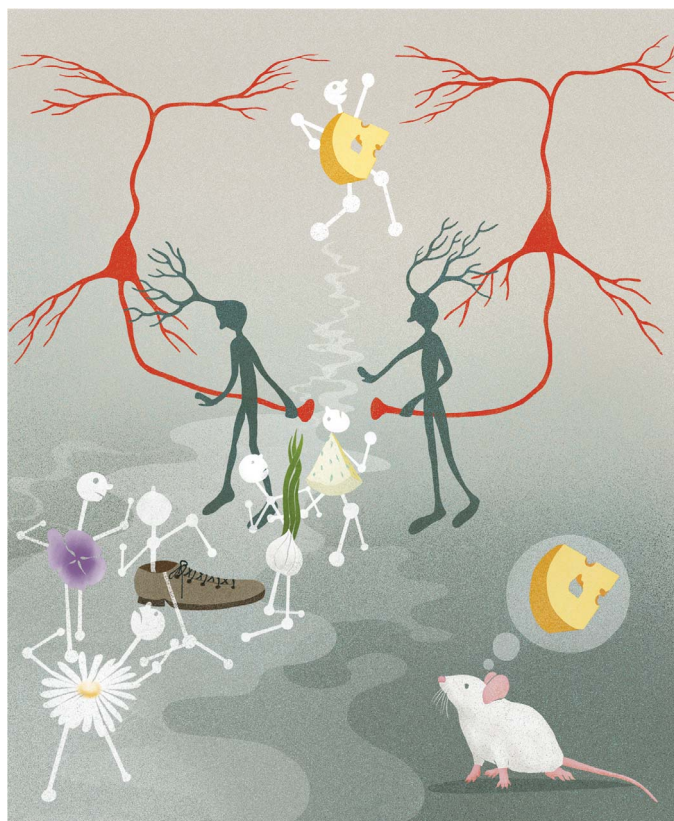
were more sensitive to differences in odor concentration than responses in PCx. Individual OB neurons fired bursts of action potentials, with odor-specific latencies and prolonged responses that were strongly concentration-dependent. By contrast, PCx PNs were briefly excited immediately after

ON OUR WEBSITE

Read the full article at <http://dx.doi.org/10.1126/science.aat6904>

inhalation and then rapidly truncated by strong and sustained suppression. To identify the source of this suppression, we recorded from feedforward and feedback inhibitory interneurons in PCx. Feedforward interneurons, which are excited exclusively by OB inputs, exhibited little odor-evoked activity. By contrast, feedback interneurons, which are excited by PCx PNs but not by OB, showed robust and sustained spiking that mirrored PN suppression, indicating that PCx itself controls the timing and strength of its own suppression. We eliminated this intracortical communication by silencing recurrent excitatory synapses in PCx with tetanus toxin. This amplified and prolonged PCx PN responses, rendered their responses steeply concentration-dependent, and abolished the ability to stably predict odor identity across concentrations from PCx spiking activity.

DISCUSSION: The PCx cells that respond earliest after inhalation represent the most odorant-specific and concentration-invariant features of the odor. The extensive, long-range recurrent circuitry broadcasts their activation across PCx, recruiting strong, sustained global inhibition that then suppresses subsequent cortical activity. Recurrent circuitry therefore effectively amplifies the impact of the earliest arriving OB inputs and discounts the impact of less-selective inputs that arrive later. Thus, the recurrent circuitry in the PCx acts as a precisely timed gate to ensure that only the most salient information is relayed further into the brain to guide the mouse’s behavior. ■



Whenever a mouse inhales, volatile molecules activate odorant receptors in the nose, evoking sequences of activity in the olfactory bulb. Bulb cells driven by the most specific receptors, which therefore best represent the odor stimulus (cheese), will always respond earliest. When this information is relayed to piriform cortex, activated principal neurons (red cells) recruit inhibitory neurons (green cells) that then suppress cortical responses to subsequent, less-specific olfactory bulb input (such as garlic, shoe, or flower), preserving the identity of the stimulus.

Department of Neurobiology, Duke University Medical School, Durham, NC, USA.
*Corresponding author. Email: franks@neuro.duke.edu
Cite this article as K. A. Bolding, K. M. Franks, *Science* 361, eaat6904 (2018). DOI: [10.1126/science.aat6904](https://doi.org/10.1126/science.aat6904)

RESEARCH ARTICLE

NEUROSCIENCE

Recurrent cortical circuits implement concentration-invariant odor coding

Kevin A. Bolding and Kevin M. Franks*

Animals rely on olfaction to find food, attract mates, and avoid predators. To support these behaviors, they must be able to identify odors across different odorant concentrations. The neural circuit operations that implement this concentration invariance remain unclear. We found that despite concentration-dependence in the olfactory bulb (OB), representations of odor identity were preserved downstream, in the piriform cortex (PCx). The OB cells responding earliest after inhalation drove robust responses in sparse subsets of PCx neurons. Recurrent collateral connections broadcast their activation across the PCx, recruiting global feedback inhibition that rapidly truncated and suppressed cortical activity for the remainder of the sniff, discounting the impact of slower, concentration-dependent OB inputs. Eliminating recurrent collateral output amplified PCx odor responses rendered the cortex steeply concentration-dependent and abolished concentration-invariant identity decoding.

Although the ability to reliably identify objects over a large range of stimulus intensities is a fundamental feature of all sensory systems, the neural mechanisms that implement intensity invariance remain poorly understood. At the earliest stages of processing, odor responses scale steeply with odorant concentration (1–4). However, psychophysical studies indicate that odors typically retain their perceptual identities, whereas concentration varies over several orders of magnitude (5–7). The olfactory system must therefore transform concentration-dependent odor responses encoded at early stages of processing into concentration-invariant representations of odor identity.

In the olfactory bulb (OB), odor-responsive mitral and tufted cells fire bursts of action potentials with odor-specific latencies that tile the ~500-ms respiration cycle (8–11). Odor information is then diffusely projected from the OB to the piriform cortex (PCx), so that individual PCx neurons can integrate inputs from different combinations of OB glomeruli, producing odor-specific ensembles of neurons distributed across the PCx whose concerted activity encodes odor identity (12–16). Theoretical studies have suggested that the PCx can form concentration-invariant odor representations by selectively responding to the earliest-active OB inputs while ignoring the contribution of inputs arriving later, which may reflect more spurious activation of lower-affinity receptors (17–22). Specifically, at low odorant concentrations, only those glomeruli innervated by receptors with the highest affinity will be activated; at higher concentrations, more glomeruli may be activated, but the highest affinity glomeruli will be most strongly activated, and the mitral and tufted cells

that innervate those glomeruli will therefore always be activated earliest in the sniff. A concentration-invariant odor representation could be formed if downstream areas selectively attended to the earliest OB inputs and discounted OB inputs that occur later in the sniff (23–25). How such a “temporal winner-take-all”-type filter would be implemented within the PCx is not known.

Concentration-invariance emerges in the PCx

To address this question, we simultaneously recorded spiking in populations of mitral cells and ipsilateral PCx principal cells in awake, head-fixed mice in response to different odorants presented at multiple concentrations (Fig. 1A). At low concentrations, odors activated small and specific subsets of cells in both the OB and PCx (Fig. 1B). Many OB cells that were not responsive at lower concentrations became responsive at higher concentrations, whereas responses were more stable across concentrations in the PCx (Fig. 1, B and C). We characterized the concentration-dependence of population responses by constructing trial-by-trial response vectors composed of spike counts for each cell in populations of OB and PCx cells (Materials and methods). We then projected these high-dimensional responses onto their three principal components (Fig. 1, D and E). We quantified the variance of responses to an odor at different concentrations ($\Delta \text{conc.}$) and compared these to the variance for repeated presentations of each odor at a single concentration (*repeat*) and for responses to different odors (Δodor): distances in PCA space for *repeat* and Δodor responses place upper and lower bounds, respectively, on the concentration-invariance of $\Delta \text{conc.}$ responses. Crucially, $\Delta \text{conc.}$ responses and Δodor responses were equally variable in the OB (Fig. 1D), whereas $\Delta \text{conc.}$ responses in the PCx were significantly less variable than Δodor re-

sponses (Fig. 1E), indicating that concentration-invariance emerges in the PCx. This result was robust when response distances were measured in all-neural space instead of PCA space (fig. S1). Given that PCx is driven directly by the OB, this result indicates that the PCx extracts and selectively represents the most concentration-invariant features of its OB inputs while discounting the impact of more concentration-dependent inputs.

We next examined response dynamics to understand how the PCx implements this filter. Over the course of a single sniff, odor-responsive mitral cells fired bursts of action potentials [full-width at half-maximum duration (mean \pm SD), 70.6 ± 49.3 ms; $n = 1830$ cell-odor pairs at $0.3\% \text{ v/v}$] with different latencies after inhalation onset. Spiking activity was more sparse in the PCx, with neurons typically responding more briefly (46.7 ± 27.0 ms; $n = 4197$ cell-odor pairs; $P = 5.06 \times 10^{-90}$, two-sample Kolmogorov-Smirnov test) shortly after inhalation (Fig. 2, A to C). Across the population, individual OB mitral cells responded with peak latencies that uniformly tiled the sniff cycle (Fig. 2D) (8–10), whereas >50% of PCx responses occurred within the first 60 ms after inhalation (Fig. 2E). In the OB, population activity—determined by averaging responses for all cell-odor pairs—showed a brief initial increase in spiking followed by a slower and sustained envelope of spiking activity (Fig. 2, C and F). However, in the PCx we only observed a transient increase in population spiking that was rapidly truncated and followed by suppression that sustained over the remainder of the sniff, despite continuing input from OB.

We then examined OB and PCx responses at different concentrations. OB spiking increased systematically with concentration, with sustained responses being especially concentration dependent (Fig. 2, G and H). Peak amplitude of the initial cortical population response increased as the ensemble of responsive PCx cells was activated more synchronously at higher concentrations; however, the ensembles themselves were largely concentration invariant (15). Beyond the initial phase, and for the remainder of the sniff, spiking in the PCx was more strongly suppressed at higher concentrations, despite receiving more input from OB. Thus, the PCx preserves odor representations across odorant concentrations by suppressing its response to later OB inputs that are especially concentration dependent.

Feedback inhibition truncates PCx odor responses

What is the source of this suppression? Principal neurons in the PCx receive inhibitory inputs from two general classes of γ -aminobutyric acid (GABA)-ergic interneurons. Feedforward interneurons reside in layer 1 and only get direct excitatory input from the OB (Fig. 3A). These neurons are well positioned to suppress responses to sustained OB input (26–29). However, PCx principal cells (both semilunar cells and pyramidal cells) extend long-range projections across the cortex, providing excitatory input onto other PCx pyramidal cells as well as onto feedback

Department of Neurobiology, Duke University Medical School, Durham, NC, USA.

*Corresponding author. Email: franks@neuro.duke.edu

interneurons that reside in deep layer 2 and layer 3 (26, 29–31). We took advantage of the laminar segregation of feedforward and feedback inhibitory interneurons and used an optical tagging approach to compare odor responses in these two distinct populations of interneurons. We recorded from neurons that were deep or superficial to the large population of glutamatergic principal cells in layer 2 in vesicular GABA transporter (VGAT)-ChR2-green fluorescent protein (GFP) mice, in which all GABAergic interneurons express channelrhodopsin-2 (ChR2) (32) (Fig. 3B). Light pulses evoked robust and sustained spiking in ~7% of cells (66 of 921 cells, $n = 15$ recordings), which is consistent with these cells being VGAT⁺ inhibitory interneurons, whereas spiking in the remaining cells was either significantly suppressed (639 of 921 cells) or unaffected (216 of 921 cells). We classified cells as layer 1 feedforward interneurons (FFIs) ($n = 13$ of 66 VGAT⁺ neurons) or layer

2/3 feedback interneurons (FBIs) ($n = 46$ of 66 VGAT⁺ neurons) according to their dorsoventral (DV) position relative to the dense population of VGAT⁺ principal cells in layer 2 (Fig. 3, C and D). Seven VGAT⁺ neurons could not be clearly classified as FFIs or FBIs and were excluded. Spike waveforms of FBIs were narrower than VGAT⁺ cells and more symmetrical than both VGAT⁺ and FFIs (Fig. 3C and fig. S2), which is consistent with a subset of these being fast-spiking interneurons. Spontaneous firing rates in FFIs and FBIs were significantly higher than those in VGAT⁺ cells (fig. S2).

In response to odors, we observed shortly after inhalation a large and rapid increase in FBI spiking that peaked just as spiking in principal cells was sharply suppressed and remained elevated for the duration of the sniff (Fig. 3, E to G). Odor-evoked spiking in FFIs increased slowly and only slightly after inhalation, suggesting that FFIs may

provide tonic inhibition driven by spontaneous OB input but do not play a major role in shaping phasic, odor-evoked cortical responses. This result is not entirely unexpected because although these cells do receive broadly tuned OB input, they are even more broadly self-inhibited (28). Moreover, spiking in FBIs, but not FFIs, increased systematically with concentration (Fig. 3, H and I), suggesting that they play the major role in normalizing PCx output, which is consistent with predictions from our recent modeling study (25). Thus, FBIs appear to play the dominant role in truncating and suppressing odor-evoked activity in the PCx. Because FBIs do not get OB input but instead are recruited by intracortical recurrent collateral connections, these data indicate that it is PCx activity itself that initiates its subsequent, rapid suppression, determining what OB information is transmitted and what information is effectively ignored.

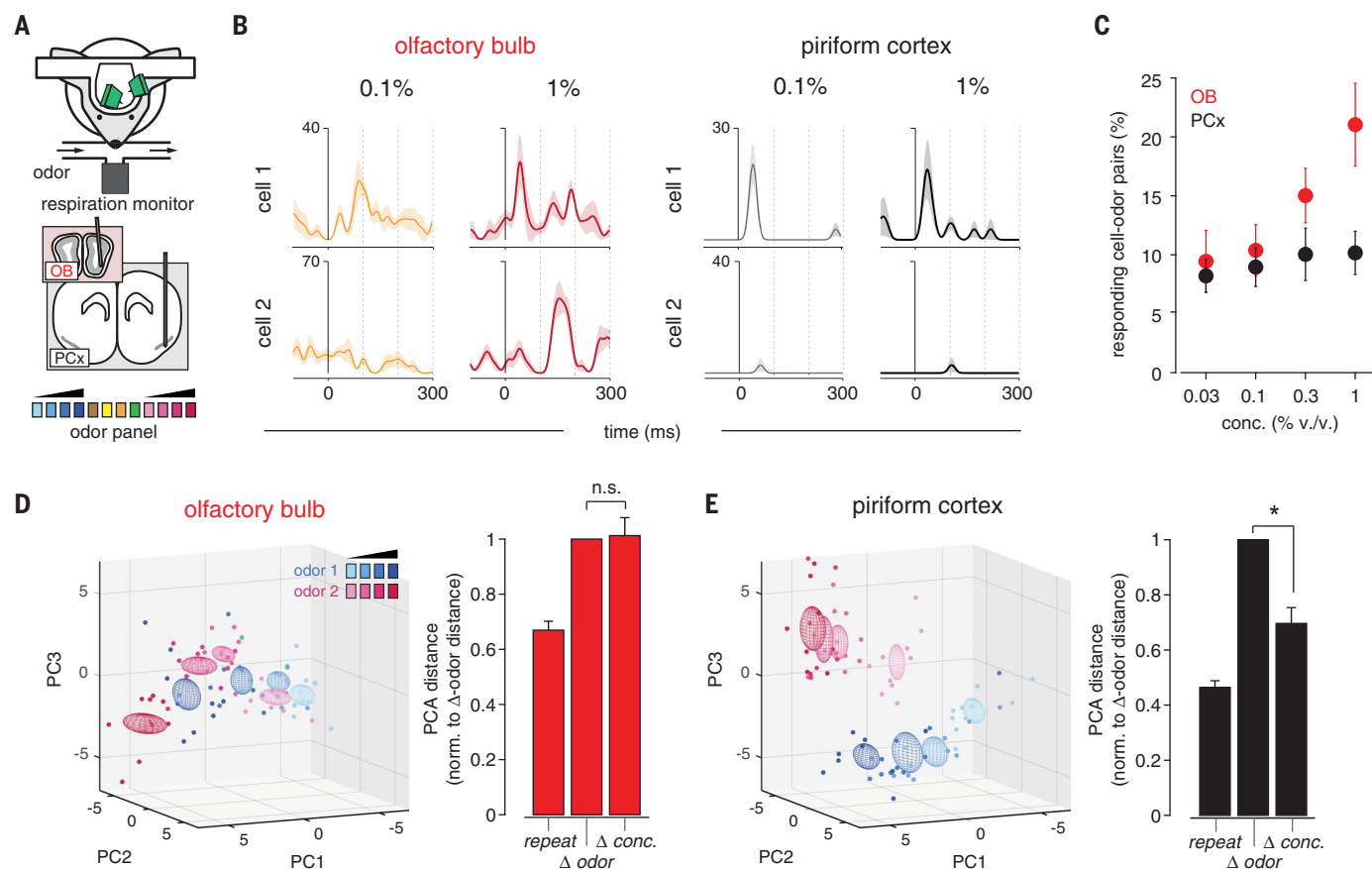


Fig. 1. Concentration-invariant odor representations emerge

in PCx. (A) Experimental schematic. Odor panel included four odors at a single concentration and two odors at four concentrations. **(B)** Example responses from simultaneously recorded pairs of (left) OB or (right) PCx cells to two odors at different concentrations. Responses are aligned to start of inhalation. **(C)** Percent of cells significantly activated by odors of increasing concentration ($P < 0.05$ rank-sum test, odor vs mineral oil) in the OB (red) or PCx (black, $n = 5$ simultaneous OB-PCx recordings, two odors, four concentrations). **(D)** (Left) PCA representation of OB pseudopopulation ($n = 94$ cells) response in a 330-ms window after inhalation to ethyl butyrate (blue) and hexanal (magenta) at different concentrations

(0.03 to 1%, different shades). Dots represent responses on individual trials; ellipsoids are mean ± 1 SD. (Right) Relative population response distances in neural activity space projected onto the first three principal components. Distances were computed for each stimulus between trials of the same odor and concentration (repeat, $n = 12$ stimuli), different odors (Δ odor, $n = 12$ stimuli), or same odor and different concentration (Δ conc., $n = 8$ stimuli), and normalized to the average Δ odor distance. OB responses to different concentrations were as dissimilar as responses to different odors (one-sample t test versus mean of 1, $P = 0.851$). **(E)** As in (D), but for PCx pseudopopulation ($n = 330$ cells). PCx responses to different concentrations were more clustered than responses to different odors ($P = 0.001$).

Strategy to eliminate recurrent excitation

Piriform pyramidal cells receive approximately 10 times more recurrent inputs than OB inputs, and recurrent connections are thought to provide

much of the excitatory drive onto odor-responsive cells (33, 34). However, because recurrent excitation also recruits FBIs, recurrent circuitry may actually exert a net inhibitory effect on PCx activity (25). We developed a cortical muting

strategy in order to distinguish between these alternatives. We selectively expressed tetanus toxin light chain (TeLC) in principal cells using cre-dependent adeno-associated viruses (AAVs) injected into the PCx of *emx1-cre* mice. TeLC

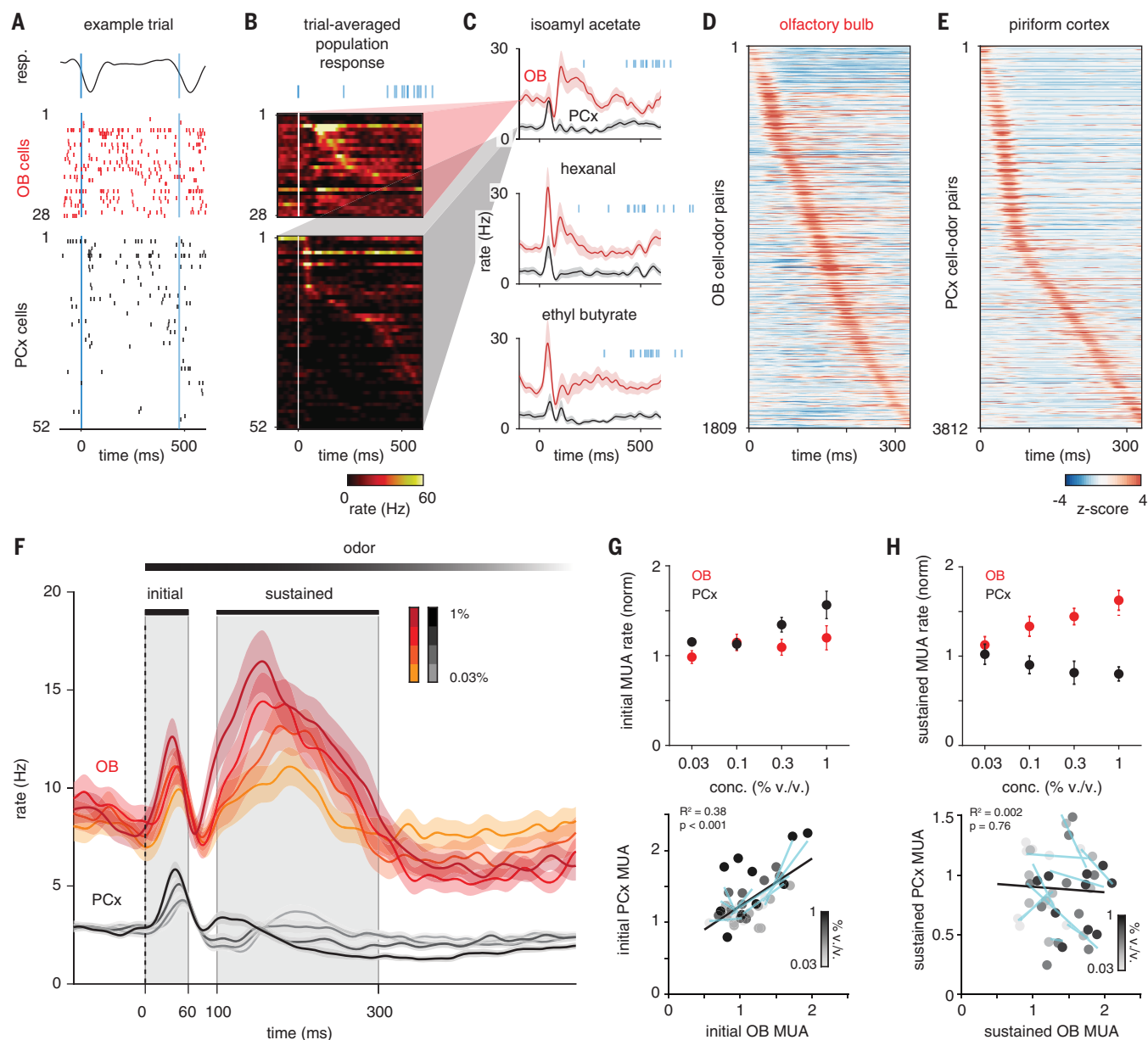


Fig. 2. PCx predominantly responds to early OB inputs. (A) Example single-trial response to isoamyl acetate (0.3% v/v) in populations of simultaneously recorded OB and PCx cells. Negative-going respiration signal (top) indicates inhalation. Bold blue line marks start of first inhalation after odor onset. Thin blue line marks second inhalation. Cells in each population are sorted by trial-averaged response peak latency. (B) Example trial-averaged peristimulus time histograms (PSTHs) for populations in (A). Blue lines indicate inhalation times on all 15 trials. (C) Average PSTHs for same OB and PCx populations responding to three odors. Shading is SEM across cells. (D) PSTHs for all OB cell-odor pairs sorted by latency to peak show uniform tiling of sniff cycle. (E) Same as (D) but for PCx. Majority of PCx responses occur within 60 ms after inhalation. (F) Average PSTHs for all

cell-odor responses at different concentrations (OB, $n = 188$; PCx, $n = 664$ cell-odor pairs; mean \pm SEM). Gray shading indicates initial (0 to 60 ms) and sustained (100 to 300 ms) analysis windows. Dashed line indicates inhalation onset. (G) Normalized multiunit activity (MUA) rates during initial phase ($n = 5$ experiments, two odors, four concentrations) in OB versus PCx. MUA is determined by recombining individual cell responses. (Top) Average OB (red) and PCx (black) response across recordings and odors. MUA was normalized to baseline activity 1 s before odor. (Bottom) Each point is the average response of one simultaneously recorded OB-PCx population response pair. Shading indicates concentration. Cyan lines are linear fits across concentrations for each OB-PCx population response pair. Black line is the linear fit to all data. (H) As in (G) but for the sustained phase.

expression should block transmitter release from PCx principal cells but should not alter their excitability. This strategy would allow us to record OB-driven spiking in the PCx, without affecting FFI, after blocking their ability to excite one another or recruit FBI (Fig. 4A). To validate this method, we first focally injected cocktails of two AAVs conditionally expressing Chr2 and either GFP or TeLC-GFP into a small region of the anterior PCx (Fig. 4B). We then isolated acute brain slices from these mice and obtained voltage-clamp recordings from uninfected cells. Brief light pulses above the recorded cell evoked large, monosynaptic responses in Chr2/GFP slices by activating recurrent excitatory inputs from other infected PCx neurons (31). However, light-evoked responses were almost completely abolished in Chr2/TeLC-GFP slices (Fig. 4C). Light drove robust spiking in Chr2/GFP and Chr2/GFP-TeLC-positive cells. In a separate set of control experiments, we expressed TeLC-GFP alone throughout the PCx. In current-clamp recordings, we verified that TeLC expression did not alter neural excitability (Fig. 4D). In voltage-clamp recordings, electrical stimulation of OB axons evoked equivalent monosynaptic excitatory postsynaptic currents (EPSCs) and disynaptic feedforward inhibitory postsynaptic currents (IPSCs) in TeLC-expressing cells, uninfected neighboring cells, and in cells from uninfected control slices, indicating that both OB input and FFI are unaffected by TeLC expression in the PCx (Fig. 4, E to G). Last, we examined responses to electrically stimulating recurrent axons in layers 2 and 3. Both EPSCs and disynaptic IPSCs were reduced in TeLC-infected slices. However, direct IPSCs, evoked by means of direct stimulation of FBIs after application of glutamate receptor antagonists, were equivalent, indicating that TeLC blocks transmitter release onto both other PCx principal cells and FBIs but does not block feedback inhibition (Fig. 4, H and I).

Recurrent excitation suppresses odor responses

To unilaterally eliminate recurrent circuitry, we injected AAV-DIO-TeLC-GFP at three different locations along the rostro-caudal axis, uniformly infecting ~60% of principal neurons across the PCx (Fig. 5, A and B, and fig. S3). We then recorded odor responses simultaneously in the PCx from infected and contralateral control hemispheres (Fig. 5C). Spontaneous firing rates in TeLC-infected (TeLC-PCx) and contralateral control hemispheres were similar. Population spiking was more strongly coupled to the respiration cycle in both TeLC-PCx and ipsilateral OB, indicating that cortical network activity normally desynchronizes spiking in both the PCx and OB (fig. S4). Despite eliminating much of its excitatory input, odor responses in TeLC-PCx were enhanced, increasing steeply after inhalation and remaining elevated for the duration of the sniff (Fig. 5, D to E). Spiking in simultaneously recorded contralateral control hemispheres was truncated shortly after inhalation and suppressed thereafter, as before. Two factors underlie this enhanced population response: first, a given odor

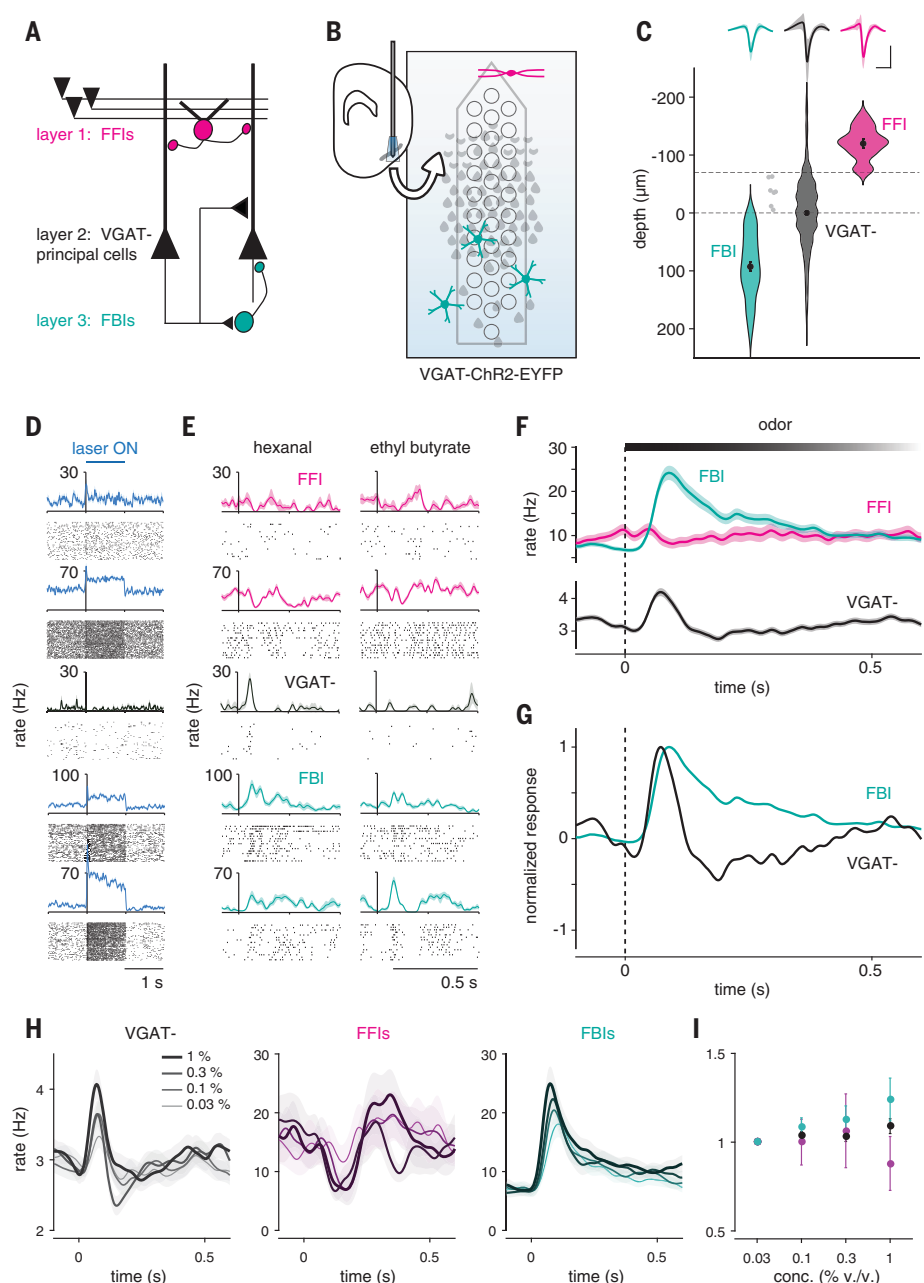


Fig. 3. Feedback inhibition shapes cortical odor responses. (A) Schematic of PCx circuit: FFIs in layer 1 receive OB input; principal cells in layer 2 provide recurrent excitatory input to other principal cells and to FBIs in layer 3. (B) Recording schematic. Light-responsive FFIs and FBIs in VGAT-ChR2 mice are differentiated by their depths relative to VGAT⁺ principal cells in layer 2, which are suppressed. (C) FFIs (magenta, $n = 13$), FBIs (teal, $n = 46$), and VGAT⁺ (black, $n = 855$) are classified by light-responsiveness and depth (dashed line). Dots with error bars are mean \pm SEM. Light gray indicates unclassified light-responsive cells. (Top) Average waveform of each cell type (mean \pm SEM). Scale bars, 0.5 ms, 0.1 mV. (D) Example light responses for one PC (black) and four cells classified as FFIs or FBIs (blue). (E) Example odor responses for cells in (D). (F) Average population PSTHs (mean \pm SEM) for each cell type. (G) Normalized PSTHs for FBIs and VGAT⁺ cells. (H) Average population PSTHs for (left) VGAT⁺, (middle) FFIs, and (right) FBIs responding to odors at increasing concentrations. (I) Normalized firing rates in response to increasing odor concentrations for each cell type (mean \pm SEM).

activated more and suppressed fewer cells across the population in TeLC-PCx; second, activated responses were larger and of longer duration in TeLC-PCx (fig. S5). We next examined how responses changed across concentrations after

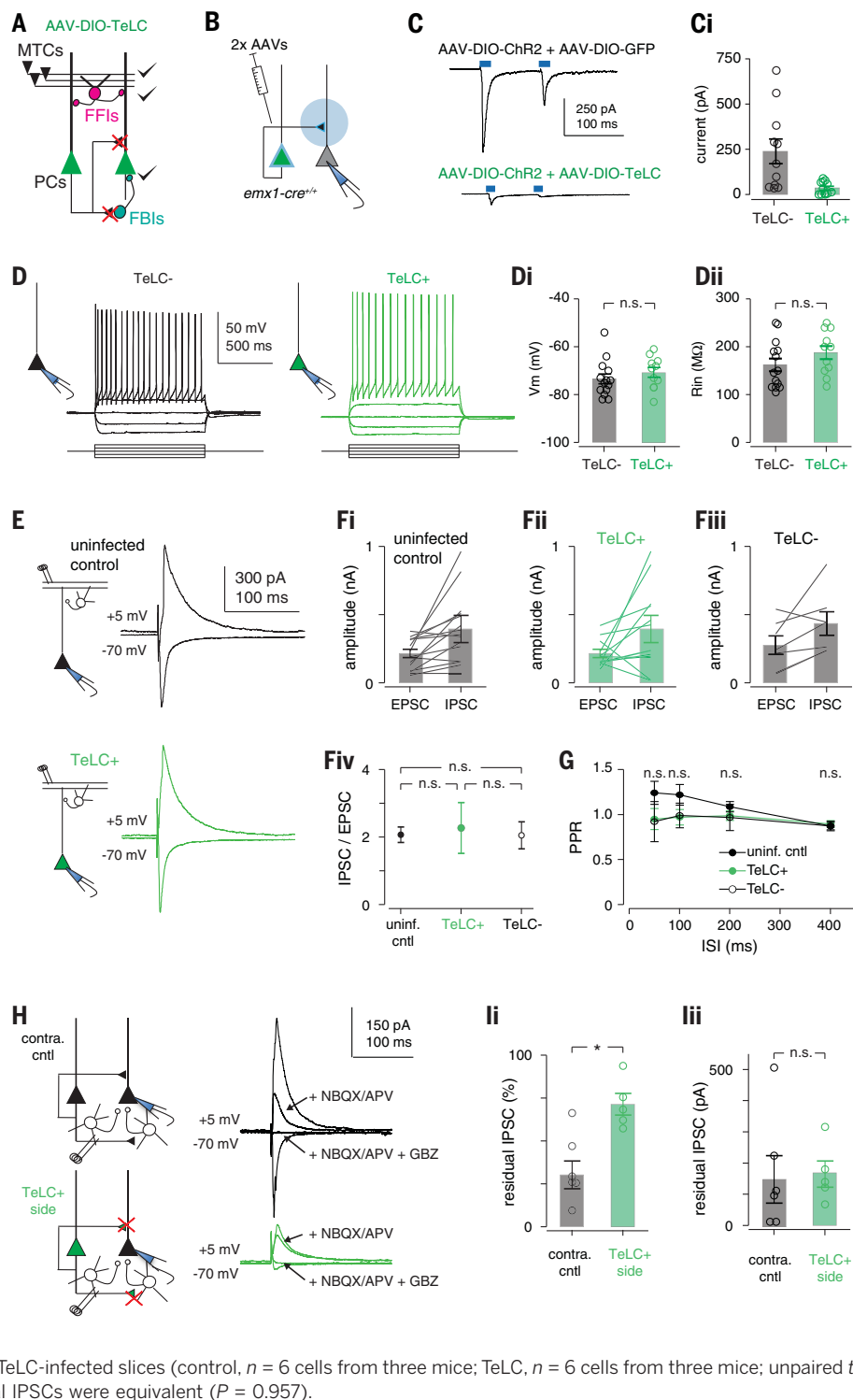
eliminating recurrent circuits. Gain control through divisive normalization is often thought to be implemented by feedforward inhibition (35). If FFIs control the gain of cortical odor responses, then PCx output should remain stable across

concentrations. However, response gain was markedly increased in TeLC-PCx, confirming the major role for feedback inhibition in controlling PCx output. Gain increased even though odor responses at the lowest concentrations were already considerably larger in TeLC-PCx (Fig. 5, F and G). PCx output remained constant across concentrations in contralateral control hemispheres.

But TeLC will block transmitter release from all synapses in infected cells, including centrifugal projections back to the OB, as well as to downstream target areas. Centrifugal inputs from PCx contact GABAergic OB neurons that can suppress mitral and tufted cell output (36–38), and this process would also be disrupted after TeLC infection (Fig. 6A). Indeed, we observed GFP

expression in OB ipsilateral to AAV injection (Fig. 6B). To determine whether the large, prolonged responses observed in TeLC-PCx were simply a consequence of enhanced OB input, we recorded OB responses ipsi- and contralateral to TeLC-PCx (Fig. 6C). Ipsilateral OB responses were larger than contralateral controls and increased more steeply at higher concentrations (Fig. 6, D

Fig. 4. TeLC expression selectively abolishes recurrent excitation. (A) Schematic of circuit changes after TeLC expression in PCx principal cells. (B) Focal coinfection in PCx with Chr2 and either GFP or TeLC-GFP, followed by whole-cell recordings from uninfected cells. (C) Light-evoked synaptic responses are abolished by TeLC. Example light-evoked response from non-Chr2-expressing neurons in (top) GFP- or (bottom) TeLC-GFP-infected PCx. *i* Light-evoked EPSC amplitudes in control and TeLC-expressing PCx (control: 239 ± 68 pA, $n = 11$ cells from two mice; TeLC 35 ± 10 pA, $n = 12$ cells from three mice; unpaired t test, $P = 0.0133$). (D) Example recordings from an (left) uninfected and (right) TeLC-infected neuron in the same slice in response to 50 pA current steps. (i) Resting membrane potentials (TeLC⁻, 73.4 ± 2.03 mV, $n = 14$ cells from three mice; TeLC⁺, 70.7 ± 2.01 mV, $n = 11$ cells from two mice; unpaired t test, $P = 0.335$) and (ii) input resistances (TeLC⁻, 162 ± 13.3 megohm; TeLC⁺, 188 ± 13.8 megohm; $P = 0.188$) were equivalent. (E) Synaptic inputs from OB are unaffected. Example recordings of EPSCs [membrane voltage (V_m), -70 mV] and disynaptic feedforward IPSCs (V_m , $+5$ mV) evoked by means of electrical stimulation of the lateral olfactory tract (LOT) in (top) an uninfected control slice or (bottom) a TeLC-infected neuron. Both EPSCs and IPSCs were blocked by 2,3-dihydroxy-6-nitro-7-sulfamoylbenzo[*f*]quinoxaline (NBQX) ($10 \mu\text{M}$) and D,L-2-amino-5-phosphonopentanoic acid (APV) ($50 \mu\text{M}$, not shown). (F) Summary of LOT-evoked EPSC and IPSC amplitudes from (i) uninfected control slices, (ii) TeLC⁺ neurons and (iii) TeLC⁻ neurons in TeLC-infected slices. (iv) EPSC/IPSC ratios were equivalent in all conditions; $P > 0.05$, unpaired t tests. (G) LOT EPSC paired-pulse ratios were not significantly altered after TeLC expression. n.s., not significant. (H) Example recordings showing recruitment of FBI is impaired, whereas FBI is unaffected. EPSCs and IPSCs were evoked by electrical stimulation of layer 2/3 $226 \pm 17 \mu\text{m}$ from recorded cell. EPSCs and IPSCs were attenuated in TeLC-infected slices. Blocking glutamate receptors with NBQX and APV eliminates the disynaptic component of IPSCs, with the residual IPSC evoked through direct stimulation of FBIs. The residual IPSC was fully blocked by gabazine (GBZ) ($10 \mu\text{M}$). (I) Summary of residual IPSC amplitudes. (i) The fractional size of residual IPSCs after NBQX/APV was substantially smaller in TeLC-infected slices (control, $n = 6$ cells from three mice; TeLC, $n = 6$ cells from three mice; unpaired t test, $P = 0.0055$), but (ii) the amplitudes of residual IPSCs were equivalent ($P = 0.957$).



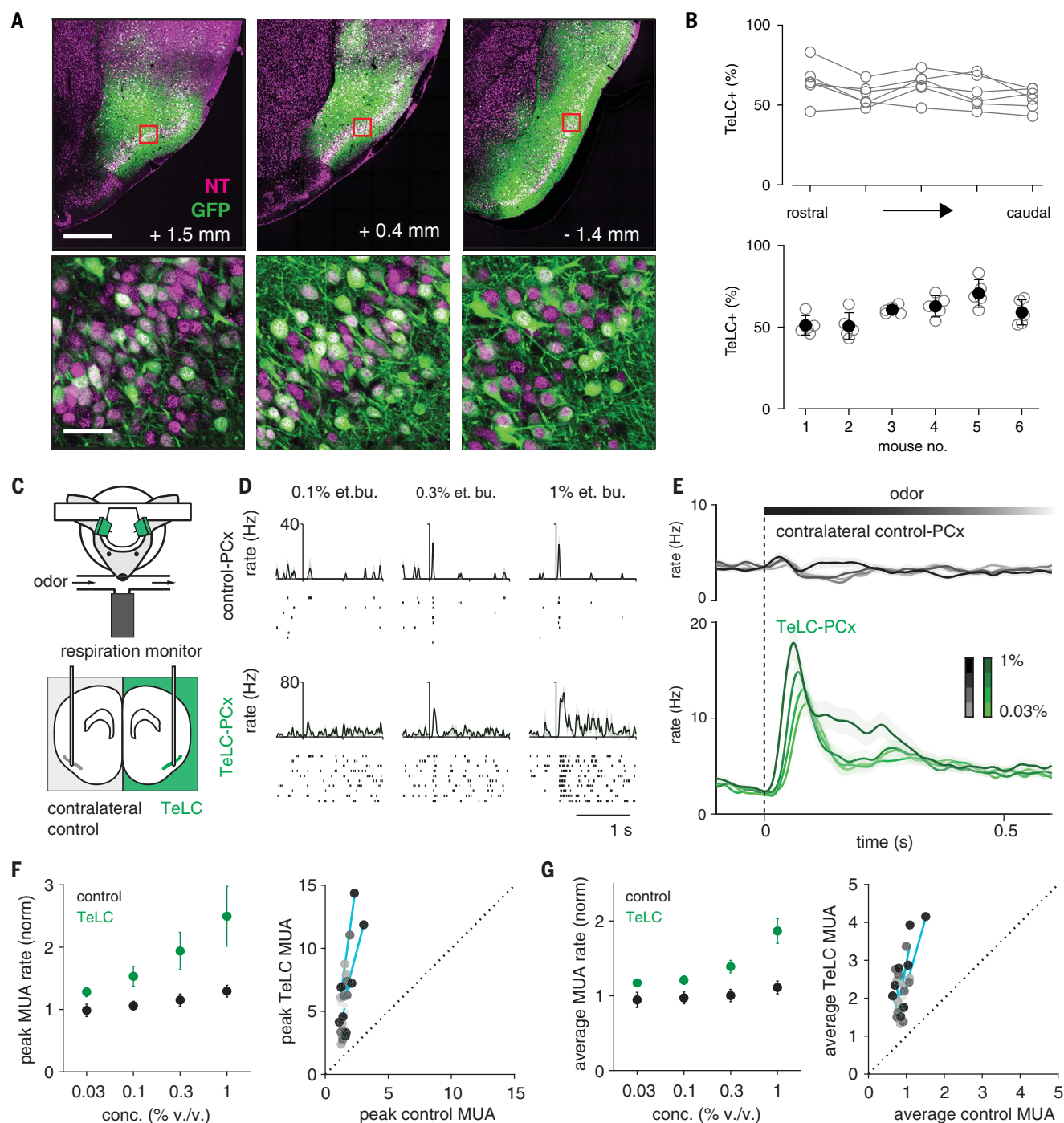
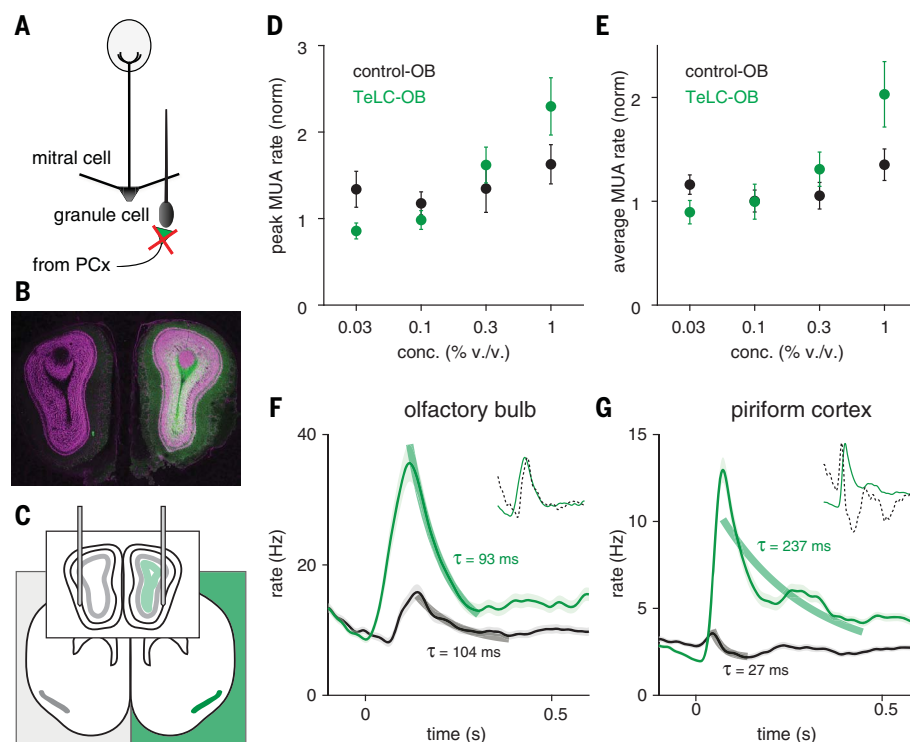


Fig. 5. Recurrent circuitry truncates and normalizes cortical output. (A) Extensive infection of layer 2 principal cells across PCx in an example mouse. GFP, green; NeuroTrace, magenta. Numbers indicate distance from bregma. Bottom row are the square sections from the top row. Scale bars, 500 μ m (top) and 50 μ m (bottom). (B) Percent cells expressing TeLC-GFP in six of seven mice used. Sections from one mouse were damaged, and infection could not be quantified. (Top) TeLC infection across rostral-caudal PCx. (Bottom) Low variation in TeLC expression across mice. (C) Experimental schematic. Simultaneous bilateral recordings from TeLC-infected and

contralateral control hemisphere with odor stimuli. (D and E) Example responses (D) and average population PSTHs (E) (mean \pm SEM; control, $n = 450$ cell-odor pairs; TeLC, $n = 388$ cell-odor pairs) (F) Normalized peaks in MUA rates ($n = 4$ experiments, two odors, four concentrations). (Left) Peak responses across recordings and odorant concentrations. (Right) Each point is average response of one simultaneously recorded TeLC-Control PCx pair normalized to mineral oil response. Shading indicates concentration. Cyan lines are linear fits for each experiment through all concentrations. (G) As in (F) but for average rate over the first 330 ms after inhalation.

Fig. 6. Centrifugal inputs from PCx control gain but not time course of OB responses.

(A) Schematic of circuit changes in OB after TeLC expression in ipsilateral PCx principal cells. (B) Centrifugal PCx fibers expressing TeLC in OB ipsilateral to PCx infection. GFP, green; NeuroTrace, magenta. (C) Experimental schematic. Simultaneous bilateral recordings from OB ipsilateral and contralateral to TeLC-infected PCx with odor stimuli. (D) Peaks in OB MUA rates averaged across population-odor pairs ($n = 3$ experiments, two odors, four concentrations). Odor responses are normalized to mineral oil responses. (E) As in (D) but for average rate over the first 330 ms after inhalation. (F) Average PSTH of all OB cell-odor pairs in control (black, $n = 406$) or TeLC (green, $n = 384$) side responding to odor (mean \pm SEM). Thick lines are exponential fits to decay from peak to minimum. (Inset) Rescaled control OB response (dotted line) overlaid on TeLC-OB response. Response dynamics are similar in control and TeLC hemisphere despite change in response gain. (G) Same as (F) but for PCx (control, $n = 1660$; TeLC, $n = 1532$). Here, decay constants differ by an order of magnitude between control and TeLC hemisphere.



to F). However, although both the amplitude and the gain of OB responses were larger after centrifugal inputs were blocked with TeLC, the time course of the response was unaffected. This contrasts with the markedly prolonged responses in TeLC-PCx (Fig. 6G), indicating that centrifugal inputs play an important role in modulating OB response amplitude and gain but suggesting that the rapid truncation and sustained suppression of PCx activity is predominantly an intracortical process.

PCx responds selectively to the earliest-activated OB inputs

To circumvent the contribution of centrifugal inputs and other intrabulbar processes that can normalize odor responses (39–41), and to isolate the intracortical processes that shape PCx odor responses, we used an optogenetic approach to stimulate OB directly. We presented 1-s light pulses above the OB of Thy1-ChR2-yellow fluorescent protein (YFP) mice, which express ChR2 in mitral and tufted cells (42) (Fig. 7A). We illuminated the dorsal surface of the OB while recording from mitral cells near the ventrolateral OB surface, providing a lower-bound estimate of the change in total OB output. Light pulses elicited an increase in OB spiking that scaled with light intensity and remained elevated for the duration of the stimulus (Fig. 7, B to E). This sustained OB activation only produced a large initial peak in PCx population spiking that rapidly returned to baseline for the remainder of the light pulse (Fig. 7C). Although initial peak spike rate in the PCx increased steeply at higher light intensities (Fig. 7D), sustained population activity was systematically suppressed at higher stimulation intensities (Fig. 7E). As the light pulse ended,

the sudden drop in input from the OB produced a transient dip in population PCx spiking, which quickly returned to baseline. Thus, PCx dynamically compensates for changes in excitatory drive with rapid recurrent inhibition that balances excitatory input and controls gain to stabilize total cortical output across input intensities. These experiments also demonstrate directly that PCx responds robustly to the earliest-activated OB inputs and then suppresses its output, discounting the impact of OB inputs that arrive later. To reveal the role of recurrent circuits in implementing this transformation, we repeated these experiments in Thy1-ChR2-YFP^{+/−}/emx1-Cre^{+/−} mice with unilateral TeLC expression (Fig. 7F). Direct OB stimulation now drove sustained spiking in TeLC-PCx that scaled with intensity (Fig. 7, G to J), whereas responses recorded in contralateral hemispheres were similar to what we observed in uninfected, control PCx.

Recurrent circuitry is required for concentration-invariant decoding

Next, we asked how eliminating recurrent connectivity alters population odor coding. We performed principal components analysis (PCA) on single-trial population response vectors from contralateral control or TeLC-PCx recordings and calculated the distances between responses in principal component space, as before. In contralateral PCx, Δ conc. responses were only slightly more variable than *repeat* responses to a single concentration and significantly less variable than Δ odor responses (Fig. 8A), which is consistent with results in unperturbed PCx (Fig. 1E). Δ conc. responses in TeLC-PCx were much more variable than *repeat* responses and as variable as Δ odor responses (Fig. 8B), which is equivalent to what

we observed in the OB under control conditions (Fig. 1E). Again, this result was also robust when computed in all-neural space (fig. S6). Last, we asked how and when odor information becomes available to a downstream observer and how this is altered when recurrent circuitry is removed. We trained and tested a linear classifier on three decoding tasks: classifying responses to different odorants, classifying responses to a single odorant at different concentrations, and generalizing for odor identity across odorant concentrations (Fig. 8, C to E). Input to the classifier consisted of spike counts for each neuron in an expanding series of 20 ms bins starting with inhalation onset (9). Decoding accuracy using responses recorded from the contralateral control hemisphere increased rapidly after inhalation and remained elevated for the duration of the sniff when classifying responses to different odorants or when generalizing for odor identity; concentration decoding was delayed and increased more slowly over the full sniff. These results are consistent with our previous findings in control mice (15).

Eliminating recurrent circuitry impaired classification of responses to different odorants, with decoding accuracy improving slowly but steadily over the duration of the sniff (Fig. 8C). This result suggests a more constructive role for recurrent circuitry in stabilizing or “completing” representations by using partial or incomplete input, although further work is required to demonstrate this effect unequivocally. Concentration decoding performance was equivalent in control and TeLC-PCx (Fig. 8D). This result may seem unexpected, given that TeLC-PCx responses are steeply concentration dependent. However, we have previously shown that spike time information is required for accurate concentration decoding

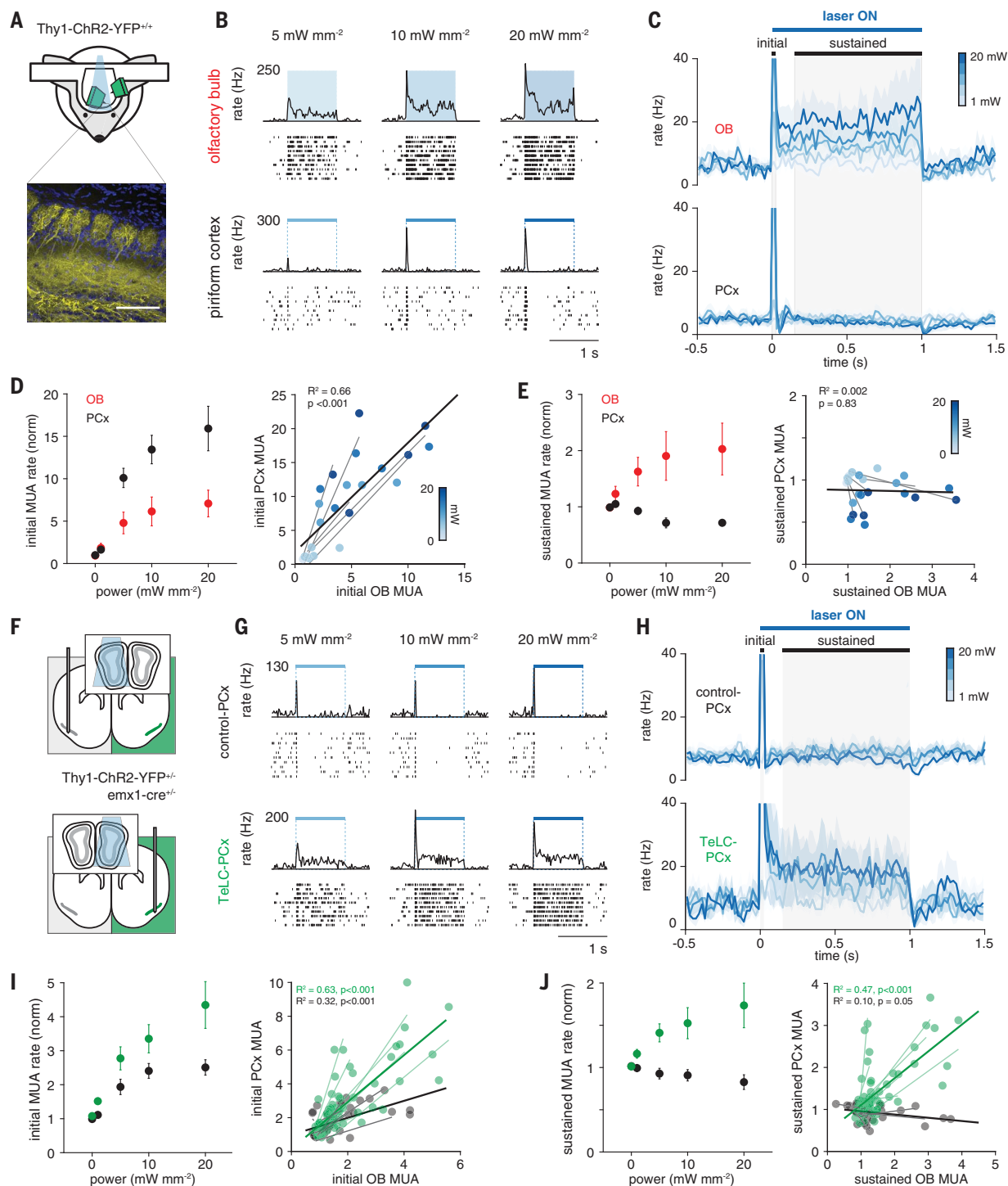


Fig. 7. PCx truncates sustained input from OB. (A) Simultaneous OB-PCx recordings with direct optical OB activation. (Top) Experimental schematic. (Bottom) ChR2 expression in mitral cells. Scale bar, 100 μ m. (B) Responses from example (top) OB and (bottom) PCx cells to 1-s light pulses over OB. (C) Average population PSTHs for responses from experiment in (B). Gray shading indicates initial and sustained analysis windows. (PCx time constants for 20 mW light pulses; decay from peak, 18.9 ± 2.0 ms; recovery from post-stimulus trough, 87.4 ± 46.3 ms; $n = 5$ population recordings.) (D) Normalized MUA rates during initial phase ($n = 5$ experiments) in OB versus PCx. (Left) Average OB (red) and PCx (black) responses across recordings. MUA was normalized to baseline activity 1 s before stimulation. (Right) Each point is the average response of one simultaneously recorded OB-PCx response pair.

Shading indicates light intensity. Light gray lines are linear fits for each OB-PCx population pair. Black line is the linear fit to all data. (E) As in (D) but for the sustained phase. (F) Experimental schematic. Simultaneous OB-PCx recordings from TeLC-infected or contralateral control hemisphere with optical OB activation. (G) Example responses from cells to 1-s light pulses over OB. (H) Average population PSTHs for responses from experiments in (G). (I) Normalized peak MUA rates during initial phase ($n = 13$ TeLC and 8 control experiments) in OB versus PCx. (Left) Average TeLC-PCx (green) and contralateral control PCx (black) MUA rates. (Right) Each point is the average response of one simultaneously recorded OB-PCx pair at one intensity. Light lines are linear fits for each TeLC (green) or control (gray) OB-PCx population pair. Solid lines are linear fits for all TeLC (green) and control (black) data. (J) As in (I) but for sustained rate.

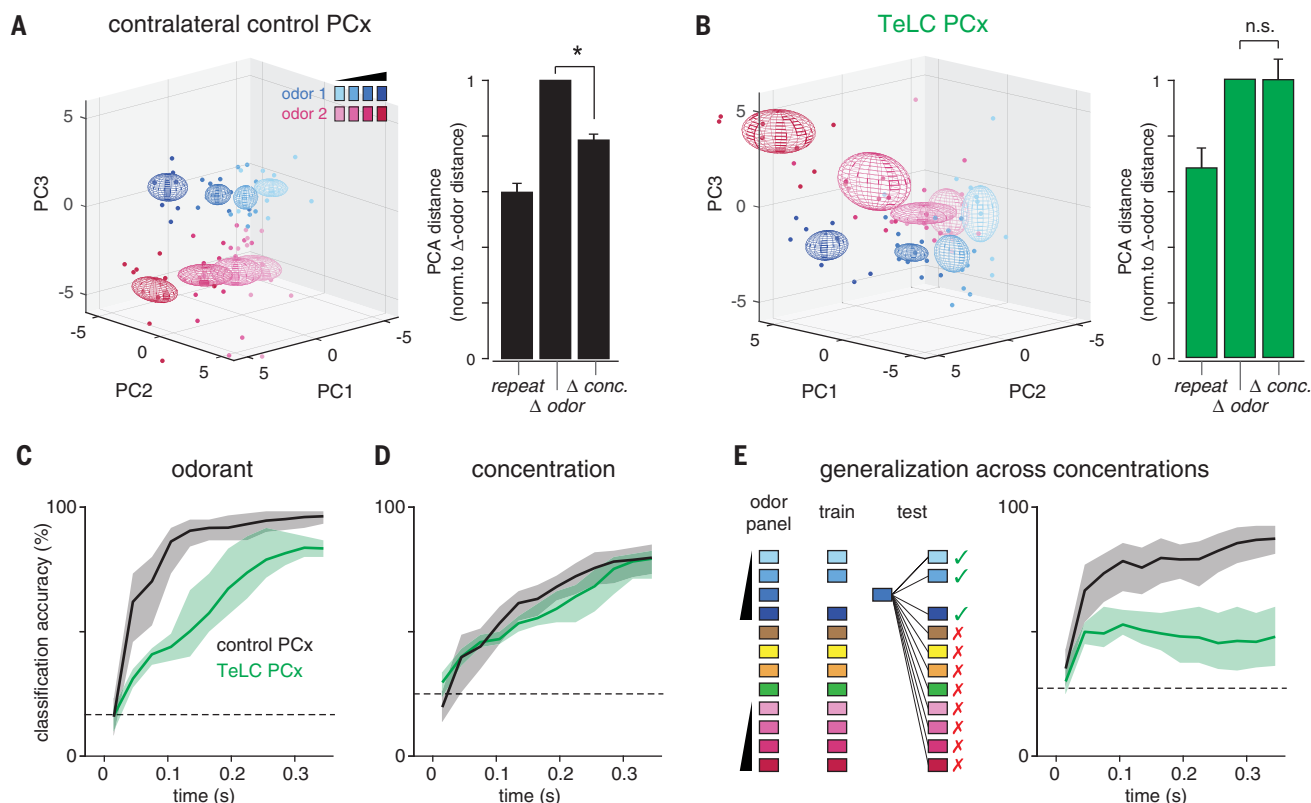


Fig. 8. Recurrent circuits implement concentration-invariant decoding. (A) (Left) PCA representation of pseudopopulation responses for contralateral control PCx hemispheres. (Right) Mean distance between population responses in PCA space normalized to Δ odor responses. Δ conc. responses were more similar than Δ odor responses in the control PCx (one-sample t test versus mean of 1, $P = 2.03 \times 10^{-5}$). (B) As in (A), but for TeLC-PCx. Δ conc. responses were no more similar than Δ odor responses ($P = 0.985$). (C) Linear classifier performance for odorant decoding (choose 1 of 6 odors) using TeLC-infected (green) or contralateral

control (black) PCx pseudopopulations. Classifier was trained and tested on spike counts in 20-ms bins in an expanding time window starting at odor inhalation. Pseudopopulation size in both conditions was held at 180 cells. Mean \pm 95% confidence intervals from 200 permutations. Dashed line is chance accuracy. (D) Same as (C) for classification of different concentrations of the same odorant (choose 1 of 4 dilutions). (E) Accuracy for generalization task in which classifier is trained and tested on different concentrations of odors. Loss of recurrent circuits severely impairs odor identity recognition across concentrations.

in PCx (15). If instead we discard temporal information by classifying using only total spike counts, then concentration decoding deteriorates in control but not TeLC-PCx, suggesting that recurrent circuits compensate for lower gain by helping maintain spike time precision. Eliminating recurrent circuits effectively abolished the ability to generalize for odor identity; decoding accuracy increased slightly immediately after inhalation, but there was no subsequent improvement and, if anything, a small decrease in decoding accuracy as the sniff progressed (Fig. 8E).

We interpret these results to indicate that cortical responses to different odors remain somewhat distinct across the entire sniff but that only the earliest PCx responses convey concentration-invariant, identity-specific odor information. In control hemispheres, the relative impact of these early cortical responses is amplified by broadcasting their activity across PCx via long-range recurrent collateral connections that recruit feedback inhibitory neurons and, consequently, rapidly and globally suppress subsequent cortical activity for the duration of the sniff. However, when recurrent output is blocked, the early responses

cannot suppress consequent activity, and so the PCx continues to be driven by OB inputs that convey decreasingly identity-specific and more concentration-dependent information as the sniff progresses (22). Ultimately, we want to know whether disrupting this circuitry abolishes concentration-invariant odor perception. However, TeLC expression in principal neurons blocks transmitter release from all their synapses, which eliminates PCx outputs and therefore precludes behavioral testing. Moreover, direct silencing of feedback interneurons will result in regenerative epileptogenic activity in this highly recurrent circuit. Therefore, development of optogenetic or chemogenetic effectors that can be efficiently targeted to defined subsets of synapses will be required to reveal the behavioral consequences of disrupting recurrent connectivity.

We revealed an essential role for recurrent feedback inhibition in preserving representations of odor identity across odorant concentrations. The combination of recurrent excitation and feedback inhibition implements a “temporal winner-take-all” filter to extract and selectively represent the most concentration-invariant fea-

tures of the odor stimulus. This process emphasizes the earliest and most odor-specific inputs to the PCx. Similar types of “first-spike” coding strategies have been identified in other sensory systems (43–47). Because sensory representations are topographically ordered in these neocortical sensory areas, local surround inhibition can implement this temporal filter (48, 49). However, odor ensembles are distributed across millimeters of PCx and lack any discernible topographic organization (13, 16). Consequently, diffuse, long-range recurrent collateral projections that recruit strong feedback inhibition ensure that recurrent inhibition is global in the PCx (31). This global inhibition truncates activity, sparsens responses, controls cortical gain, and supports concentration-invariant representations of odor identity. Thus, although recurrent circuitry in the PCx is typically thought to provide the excitatory substrate for odor learning, memory, and olfactory pattern completion (50, 51), recurrent excitation has a net-inhibitory impact on cortical activity. Strong and global feedback inhibition that sparsens and normalizes output has been identified at the equivalent stage of processing in invertebrate

olfactory systems; however, this is implemented by a single, globally connected interneuron (52, 53). The highly recurrent CA3 region of hippocampus exhibits a similar pattern of long-range recurrent collateral connectivity (54). Thus, recurrent excitation that is dominated by rapid, global feedback inhibition may reflect a canonical circuit motif for temporally filtering representations in associative cortex and related structures.

Materials and Methods

Subjects

All experimental protocols were approved by Duke University Institutional Animal Care and Use Committee. The methods for head-fixation, data acquisition, electrode placement, stimulus delivery, and analysis of single-unit and population odor responses are adapted from those described in detail previously (15). A portion of the data reported here (5 of 13 simultaneous OB and PCx recordings) were also described in that previous report. Mice were singly-housed on a normal light-dark cycle. For simultaneous OB/PCx recordings and Cre-dependent TeLC expression experiments, mice were adult (>P60, 20–24 g) offspring of *Emx1-cre* (+/+) breeding pairs obtained from The Jackson Laboratory (005628). Optogenetic experiments used adult *Thy1-ChR2-YFP* (+/+), line 18 (*Thy1-COP4/EYFP*, Jackson Laboratory, 007612) and *VGAT-ChR2-YFP* (+/-), line 8 (*Slc32a1-COP4*H134R/EYFP*, Jackson Laboratory, 014548). Adult offspring of *Emx1-cre* (+/+) mice crossed with *Thy1-ChR2-YFP* (+/+) mice were used for combined optogenetics and TeLC expression.

Adeno-associated viral vectors

All viruses were obtained from the vector core at the University of North Carolina-Chapel Hill (UNC Vector Core). AAV5-CBA-DIO-TeLC-GFP, AAV5-CBA-DIO-GFP, AAV5-eFla-DIO-ChR2-EYFP were used for in vitro slice physiology experiments. For in vivo experiments, AAV5-DIO-TeLC-GFP was expressed either under control of a CBA (6 of 7 mice) or synapsin (1 of 7 mice) promoter. Effects were similar and results were pooled. TeLC expression throughout PCx was achieved using 500 nL injections at three stereotaxic coordinates (AP, ML, DV: +1.8, 2.7, 3.85; +0.5, 3.5, 3.8; -1.5, 3.9, 4.2; DV measured from brain surface). Recordings were made ~14 days post-injection.

Immunohistochemistry

To confirm widespread expression of TeLC in PCx, after recordings, mice were perfused with PBS followed by PFA (4%) and the brains were postfixed overnight. Coronal sections (50 μ m) were taken through the A-P extent of PCx and permeabilized with Triton (0.1%). Brains were incubated overnight with a primary GFP antibody (Chicken Anti-GFP, Abcam, ab13970, 1:500) and then washed and stained overnight with a secondary antibody (Goat Anti-Chicken Alexa Fluor 488, Abcam, ab150169; 1:500) and counterstained (NeuroTrace 640/660, Invitrogen, N21483; 1:400). Slices were mounted and imaged on an upright Zeiss 780 confocal microscope. Quantitative analyses were performed using ImageJ.

In vitro electrophysiology and analysis

For experiments examining viability and excitability in TeLC-infected neurons (Fig. 4, D to G), viruses were injected as described above. For experiments validating that transmitter release was blocked in TeLC-infected neurons (Fig. 4, A to C), a single injection containing a cocktail of 150 nL AAV-EF1a-DIO-ChR2-EYFP and either 150 nL AAV-EF1a-DIO-ChR2-GFP or 150 nL AAV-CAG-DIO-GFP-TeLC was injected at a single site in anterior PCx. Fifteen \pm 2 days after virus injection, mice were anesthetized with isoflurane and decapitated. The cortex was quickly removed in ice-cold artificial CSF (aCSF). Parasagittal brain slices (300 μ m) were cut using a vibrating microtome (Leica) in a solution containing (in mM): 10 NaCl, 2.5 KCl, 0.5 CaCl₂, 7 MgSO₄, 1.25 NaH₂PO₄, 25 NaHCO₃, 10 glucose, and 195 sucrose, equilibrated with 95% O₂ and 5% CO₂. Slices were incubated at 34°C for 30 min in aCSF containing: 125 mM NaCl, 2.5 mM KCl, 1.25 mM NaH₂PO₄, 25 mM NaHCO₃, 25 mM glucose, 2 mM CaCl₂, 1 mM MgCl₂, 2 NaPyrivate. Slices were then maintained at room temperature until they were transferred to a recording chamber on an upright microscope (Olympus) equipped with a 40x objective.

For current clamp recordings, patch electrodes (3–6 megohm) contained: 130 Kmethysulfonate, 5 mM NaCl, 10 HEPES, 12 phosphocreatine, 3 MgATP, 0.2 NaGTP, 0.1 EGTA, 0.05 AlexaFluor 594 cadaverine. For voltage-clamp experiments, electrodes contained: 130 D-Gluconic acid, 130 CsOH, 5 mM NaCl, 10 HEPES, 12 phosphocreatine, 3 MgATP, 0.2 NaGTP, 10 EGTA, 0.05 AlexaFluor 594 cadaverine. Voltage- and current-clamp responses were recorded with a Multiclamp 700B amplifier, filtered at 2–4 kHz, and digitized at 10 kHz (Digidata 1440). Series resistance was typically ~10 megohm, always <20 megohm, and was compensated at 80%–95%. The bridge was balanced using the automated Multiclamp function in current clamp recordings. Data were collected and analyzed off-line using AxographX and IGOR Pro (Wavemetrics). Junction potentials were not corrected. Recordings targeted pyramidal cells, which were visualized (CoolLED) to ensure that cells had pyramidal cell morphologies.

For current clamp recordings to examine viability and excitability, TeLC- or GFP-infected neurons were targeted using 470 nm light (CoolLED). In current clamp recordings, a series of 1 s. current pulses were stepped in 50 pA increments. To examine synaptic properties, we first verified that fluorescent cells exhibited large photocurrents in both ChR2-YFP/GFP- and ChR2-YFP/GFP-TeLC-injected slices (not shown). We then recorded in voltage-clamp from uninfected cells adjacent to the infection site. Cells were held at either -70 mV or +5 mV to isolate excitatory or inhibitory synaptic currents, respectively. Brief (1 ms) 470 nm pulses were delivered through the objective every 10 s to activate ChR2⁺ axon terminals. A concentric bipolar electrode in the lateral olfactory tract was used to activate synaptic inputs from OB (Fig. 4, E and F). The bipolar electrode was placed at the layer 2/3 border $226 \pm 17 \mu$ m from the re-

corded cell to examine feedback inhibition (Fig. 4G). NBQX, D-APV, and gabazine were acquired from Tocris.

Head-fixation

Mice were habituated to head-fixation and tube restraint for 15–30 min on each of the two days prior to experiments. The head post was held in place by two clamps attached to ThorLabs posts. A hinged 50 ml Falcon tube on top of a heating pad (FHC) supported and restrained the body in the head-fixed apparatus.

Odor stimuli and delivery

Odor stimuli were prepared and delivered as described previously (15). Briefly, stimuli were monomolecular odorants diluted in mineral oil and included the following: hexanal (Aldrich 115606), ethyl butyrate (Aldrich E15701), ethyl acetate [Sigma-Aldrich (St. Louis, MO), 34858], 2-hexanone [Fluka (Mexico), 02473], isoamyl acetate [Tokyo Chemical Industry (Cambridge, MA), A0033], and ethyl tiglate [Alfa Aesar (Haverhill, MA), A12029]. Odor were delivered using a custom olfactometer controlled by MATLAB scripts. Normally a 1 LPM neutral air stream was directed to the mouse's nose. During a trial, air was directed through one of the odor vials and the odorized air stream directed to exhaust for an equilibration period of 4 s before rapid switching of a final valve triggered on exhalation re-directed odorized air to the nose and neutral air to exhaust. This was reversed after 1 s. Odors were presented every 10 s.

Data acquisition

Electrophysiological signals were acquired with 32-site polytrode acute probes (A1x32-Poly3-5mm-25s-177, Neuronexus) through an A32-OM32 adaptor (Neuronexus) connected to a Cereplex digital headstage (Blackrock Microsystems). A fiber-attached polytrode probe (A1x32-Poly3-5mm-25s-177-OA32LP, Neuronexus) was used for recordings from optogenetically identified GABAergic cells. Unfiltered signals were digitized at 30 kHz at the headstage and recorded by a Cerebus multichannel data acquisition system (BlackRock Microsystems). Experimental events and respiration signals were acquired at 2 kHz by analog inputs of the Cerebus system. Respiration was monitored with a microbridge mass airflow sensor (Honeywell AWM3300V) positioned directly opposite the animal's nose. Negative airflow corresponds to inhalation and negative changes in the voltage of the sensor output.

Electrode and optic fiber placement

The recording probe was positioned in the anterior piriform cortex using a Patchstar Micromanipulator (Scientifica). For piriform cortex recordings, the probe was positioned at 1.32 mm anterior and 3.8 mm lateral from bregma. Recordings were targeted 3.5–4 mm ventral from the brain surface at this position with adjustment according to the local field potential (LFP) and spiking activity monitored online. Electrode sites on the polytrode span 275 μ m along the dorsal-ventral

axis. The probe was lowered until a band of intense spiking activity covering 30–40% of electrode sites near the correct ventral coordinate was observed, reflecting the densely packed layer II of piriform cortex. For standard recordings, the probe was lowered to concentrate this activity at the center of the DV axis of the probe. For deep or superficial recordings, the probe was targeted such that strong activity was at the most ventral or most dorsal part of the probe respectively. For simultaneous ipsilateral olfactory bulb recordings, a micromanipulator holding the recording probe was set to a 10-degree angle in the coronal plane, targeting the ventrolateral mitral cell layer. The probe was initially positioned above the center of the olfactory bulb (4.85 AP, 0.6 ML) and then lowered along this angle through the dorsal mitral cell and granule layers until encountering a dense band of high-frequency activity signifying the targeted mitral cell layer, typically between 1.5 and 2.5 mm from the bulb surface. For experiments driving OB cells in Thy1-ChR2-YFP mice, an optic fiber was positioned <500 μ m above the dorsal surface of the bulb.

Spike sorting and waveform characteristics

Individual units were isolated using Spyking-Circus (<https://github.com/spyking-circus>) (55). Clusters with >1% of ISIs violating the refractory period (< 2 ms) or appearing otherwise contaminated were manually removed from the dataset. This criterion was relaxed to 2% in Thy1-ChR2-YFP recordings because these were short (<15 min) and had poorer overall sorting quality, and these results do not depend on unit isolation, but rather total population spiking activity. Pairs of units with similar waveforms and coordinated refractory periods in the cross-correlogram were combined into single clusters. Extracellular waveform features were characterized according to standard measures: peak-to-trough time and ratio and peak amplitude asymmetry (56). Unit position with respect to electrode sites was characterized as the average of all electrode site positions weighted by the wave amplitude on each electrode.

Spontaneous activity and respiration-locking

Spontaneous activity was assessed during inter-trial intervals at least 4 s after stimulus offset and 1 s preceding stimulus. The relationship of each unit's spiking to the ongoing respiratory oscillation was quantified using both phase concentration (κ) (57) and pairwise phase consistency (PPC) (58). Each spike was assigned a phase by interpolation between inhalation (0 degrees) and exhalation (180°). Each spike was then treated as a unit vector and PPC was taken as the average of the dot products of all pairs of spikes.

Individual and average cell-odor responses

We computed smoothed kernel density functions (KDF) with a 10 ms Gaussian kernel (using the psth routine from the Chronux toolbox (59) to

visualize trial-averaged firing rates as a function of time from inhalation onset and to define response latencies for each cell-odor pair. Multi-unit activity or population responses were constructed by averaging these KDFs across all cells and odors. Peak latency was defined as the maximum of the KDF within a 500-ms response window following inhalation. Response duration was the full-width at half-maximum of this peak.

Identifying VGAT+ interneurons

To assess odor responses in identified interneurons, 1-s light pulses were delivered just above the recording sites using a fiber-attached probe. Twenty pulses were delivered both before and after presentation of the full odor stimulation series. Cells were labeled as laser-responsive using a Wilcoxon rank-sum test comparing firing rates in the 1-s prior to and during laser stimulation.

Sparseness

Lifetime and population sparseness were calculated as described previously (15, 60).

Principal components analysis

Principal components were computed from pseudo-population response vectors using the Dimensionality Reduction Toolbox (<https://lvdmaaten.github.io/drtoolbox>). Responses were spike counts over the first 330 ms after inhalation on each trial for each cell. Responses were combined across all cells in TeLC or control conditions to form pseudo-population response vectors. To compute PC distance, 3-dimensional Euclidean distances were computed for each trial pair and the average trial-pair distance was computed for each stimulus. For example, the “same-odor, different concentration” distance for 1% ethyl butyrate is an average of ten 1% trials' distances from thirty trials of three other concentrations (300 distances). Summary statistics were computed on these average trial-pair distances.

Population decoding analysis

Odor classification accuracy based on population responses was measured using a Euclidean distance classifier with Leave-One-Out cross-validation. Responses to four distinct monomolecular odorants presented at 0.3% v/v and two more odorants presented in a concentration series at 0.03%, 0.1%, 0.3% and 1% v/v were used as the training and testing data. For generalization tasks, one concentration was left out during training and testing and the classifier prediction was recoded as ‘correct’ if the predicted odor was of the same identity as the presented odor. The feature vectors were spike counts in concatenated sets of 20 ms bins over the first 340 ms following inhalation.

Statistics

Statistics were computed in MATLAB. Paired *t* tests were used when comparing the same animals, cells, or cell-odor pairs across states. Unpaired *t* tests and two-sample Kolmogorov-Smirnov tests were used when comparing properties for distinct cell-odor pairs. Sample sizes

were large such that *t* tests were robust to non-normality. Results were equivalent with non-parametric tests. No formal a priori sample size calculation was performed, but our sample sizes are similar to those used in previous studies.

REFERENCES AND NOTES

- Y. Jiang *et al.*, Molecular profiling of activated olfactory neurons identifies odorant receptors for odors *in vivo*. *Nat. Neurosci.* **18**, 1446–1454 (2015). doi: [10.1038/nn.4104](https://doi.org/10.1038/nn.4104); pmid: [26322927](https://pubmed.ncbi.nlm.nih.gov/26322927/)
- B. D. Rubin, L. C. Katz, Optical imaging of odorant representations in the mammalian olfactory bulb. *Neuron* **23**, 499–511 (1999). doi: [10.1016/S0896-6273\(00\)80803-X](https://doi.org/10.1016/S0896-6273(00)80803-X); pmid: [10433262](https://pubmed.ncbi.nlm.nih.gov/10433262/)
- M. Meister, T. Bonhoeffer, Tuning and topography in an odor map on the rat olfactory bulb. *J. Neurosci.* **21**, 1351–1360 (2001). doi: [10.1523/JNEUROSCI.21-04-01351.2001](https://doi.org/10.1523/JNEUROSCI.21-04-01351.2001); pmid: [11160406](https://pubmed.ncbi.nlm.nih.gov/11160406/)
- T. Bozza, J. P. McGann, P. Mombaerts, M. Wachowiak, In vivo imaging of neuronal activity by targeted expression of a genetically encoded probe in the mouse. *Neuron* **42**, 9–21 (2004). doi: [10.1016/S0896-6273\(04\)00144-8](https://doi.org/10.1016/S0896-6273(04)00144-8); pmid: [15066261](https://pubmed.ncbi.nlm.nih.gov/15066261/)
- D. G. Laing, P. K. Legha, A. L. Jinks, I. Hutchinson, Relationship between molecular structure, concentration and odor qualities of oxygenated aliphatic molecules. *Chem. Senses* **28**, 57–69 (2003). doi: [10.1093/chemse/28.1.57](https://doi.org/10.1093/chemse/28.1.57); pmid: [12502524](https://pubmed.ncbi.nlm.nih.gov/12502524/)
- D. Krone, M. Mannel, E. Pauli, T. Hummel, Qualitative and quantitative olfactometric evaluation of different concentrations of ethanol peppermint oil solutions. *Phytother. Res.* **15**, 135–138 (2001). doi: [10.1002/ptr.716](https://doi.org/10.1002/ptr.716); pmid: [11268113](https://pubmed.ncbi.nlm.nih.gov/11268113/)
- R. Horma, L. B. Cohen, E. K. Kosmidis, S. L. Youngentob, Perceptual stability during dramatic changes in olfactory bulb activation maps and dramatic declines in activation amplitudes. *Eur. J. Neurosci.* **29**, 1027–1034 (2009). doi: [10.1111/j.1460-9568.2009.06644.x](https://doi.org/10.1111/j.1460-9568.2009.06644.x); pmid: [19291227](https://pubmed.ncbi.nlm.nih.gov/19291227/)
- B. Bathellier, D. L. Buhl, R. Accolla, A. Carleton, Dynamic ensemble odor coding in the mammalian olfactory bulb: Sensory information at different timescales. *Neuron* **57**, 586–598 (2008). doi: [10.1016/j.neuron.2008.02.011](https://doi.org/10.1016/j.neuron.2008.02.011); pmid: [18304487](https://pubmed.ncbi.nlm.nih.gov/18304487/)
- K. M. Curry, N. Uchida, Robust odor coding via inhalation-coupled transient activity in the mammalian olfactory bulb. *Neuron* **68**, 570–585 (2010). doi: [10.1016/j.neuron.2010.09.040](https://doi.org/10.1016/j.neuron.2010.09.040); pmid: [21040855](https://pubmed.ncbi.nlm.nih.gov/21040855/)
- R. Shusterman, M. C. Smeat, A. A. Koulakov, D. Rinberg, Precise olfactory responses tile the sniff cycle. *Nat. Neurosci.* **14**, 1039–1044 (2011). doi: [10.1038/nn.2877](https://doi.org/10.1038/nn.2877); pmid: [21765422](https://pubmed.ncbi.nlm.nih.gov/21765422/)
- I. Fukunaga, M. Berning, M. Kollo, A. Schmaltz, A. T. Schaefer, Two distinct channels of olfactory bulb output. *Neuron* **75**, 320–329 (2012). doi: [10.1016/j.jneuron.2012.05.017](https://doi.org/10.1016/j.jneuron.2012.05.017); pmid: [22841316](https://pubmed.ncbi.nlm.nih.gov/22841316/)
- K. R. Illig, L. B. Haberly, Odor-evoked activity is spatially distributed in piriform cortex. *J. Comp. Neurol.* **457**, 361–373 (2003). doi: [10.1002/cne.10557](https://doi.org/10.1002/cne.10557); pmid: [12561076](https://pubmed.ncbi.nlm.nih.gov/12561076/)
- D. D. Stettler, R. Axel, Representations of odor in the piriform cortex. *Neuron* **63**, 854–864 (2009). doi: [10.1016/j.jneuron.2009.09.005](https://doi.org/10.1016/j.jneuron.2009.09.005); pmid: [19778513](https://pubmed.ncbi.nlm.nih.gov/19778513/)
- K. Miura, Z. F. Mainen, N. Uchida, Odor representations in olfactory cortex: Distributed rate coding and decorrelated population activity. *Neuron* **74**, 1087–1098 (2012). doi: [10.1016/j.neuron.2012.04.021](https://doi.org/10.1016/j.neuron.2012.04.021); pmid: [22726838](https://pubmed.ncbi.nlm.nih.gov/22726838/)
- K. A. Bolding, K. M. Franks, Complementary codes for odor identity and intensity in olfactory cortex. *eLife* **6**, e22630 (2017). doi: [10.7554/eLife.22630](https://doi.org/10.7554/eLife.22630); pmid: [28379135](https://pubmed.ncbi.nlm.nih.gov/28379135/)
- B. Roland, T. Deneux, K. M. Franks, B. Bathellier, A. Fleischmann, Odor identity coding by distributed ensembles of neurons in the mouse olfactory cortex. *eLife* **6**, e26337 (2017). doi: [10.7554/eLife.26337](https://doi.org/10.7554/eLife.26337); pmid: [28489003](https://pubmed.ncbi.nlm.nih.gov/28489003/)
- H. Spors, A. Grinvald, Spatio-temporal dynamics of odor representations in the mammalian olfactory bulb. *Neuron* **34**, 301–315 (2002). doi: [10.1016/S0896-6273\(02\)00644-X](https://doi.org/10.1016/S0896-6273(02)00644-X); pmid: [11970871](https://pubmed.ncbi.nlm.nih.gov/11970871/)
- T. W. Margrie, A. T. Schaefer, Theta oscillation coupled spike latencies yield computational vigour in a mammalian sensory system. *J. Physiol.* **546**, 363–374 (2003). doi: [10.1113/jphysiol.2002.031245](https://doi.org/10.1113/jphysiol.2002.031245); pmid: [12527724](https://pubmed.ncbi.nlm.nih.gov/12527724/)
- J. Cang, J. S. Isaacson, In vivo whole-cell recording of odor-evoked synaptic transmission in the rat olfactory bulb.

- J. Neurosci.* **23**, 4108–4116 (2003). doi: [10.1523/JNEUROSCI.23-10-04108.2003](https://doi.org/10.1523/JNEUROSCI.23-10-04108.2003); pmid: [12764098](https://pubmed.ncbi.nlm.nih.gov/12764098/)
20. S. Junek, E. Kludt, F. Wolf, D. Schild, Olfactory coding with patterns of response latencies. *Neuron* **67**, 872–884 (2010). doi: [10.1016/j.neuron.2010.08.005](https://doi.org/10.1016/j.neuron.2010.08.005); pmid: [20826317](https://pubmed.ncbi.nlm.nih.gov/20826317/)
 21. C. D. Wilson, G. O. Serrano, A. A. Koulakov, D. Rinberg, A primacy code for odor identity. *Nat. Commun.* **8**, 1477 (2017). doi: [10.1038/s41467-017-01432-4](https://doi.org/10.1038/s41467-017-01432-4); pmid: [29133907](https://pubmed.ncbi.nlm.nih.gov/29133907/)
 22. E. M. Arnedo *et al.*, Stimulus dependent diversity and stereotypy in the output of an olfactory functional unit. *Nat. Commun.* **9**, 1347 (2018). doi: [10.1038/s41467-018-03837-1](https://doi.org/10.1038/s41467-018-03837-1); pmid: [29632302](https://pubmed.ncbi.nlm.nih.gov/29632302/)
 23. J. J. Hopfield, Pattern recognition computation using action potential timing for stimulus representation. *Nature* **376**, 33–36 (1995). doi: [10.1038/376033a0](https://doi.org/10.1038/376033a0); pmid: [7596429](https://pubmed.ncbi.nlm.nih.gov/7596429/)
 24. A. T. Schaefer, T. W. Margrie, Psychophysical properties of odor processing can be quantitatively described by relative action potential latency patterns in mitral and tufted cells. *Front. Syst. Neurosci.* **6**, 30 (2012). doi: [10.3389/fnsys.2012.00030](https://doi.org/10.3389/fnsys.2012.00030); pmid: [22582039](https://pubmed.ncbi.nlm.nih.gov/22582039/)
 25. M. Stern, K. A. Bolding, L. F. Abbott, K. M. Franks, A transformation from temporal to ensemble coding in a model of piriform cortex. *eLife* **7**, e34831 (2018). doi: [10.7554/eLife.34831](https://doi.org/10.7554/eLife.34831); pmid: [29595470](https://pubmed.ncbi.nlm.nih.gov/29595470/)
 26. N. Suzuki, J. M. Bekkers, Microcircuits mediating feedforward and feedback synaptic inhibition in the piriform cortex. *J. Neurosci.* **32**, 919–931 (2012). doi: [10.1523/JNEUROSCI.4112-11.2012](https://doi.org/10.1523/JNEUROSCI.4112-11.2012); pmid: [22262890](https://pubmed.ncbi.nlm.nih.gov/22262890/)
 27. V. M. Luna, N. E. Schoppa, GABAergic circuits control input-spike coupling in the piriform cortex. *J. Neurosci.* **28**, 8851–8859 (2008). doi: [10.1523/JNEUROSCI.2385-08.2008](https://doi.org/10.1523/JNEUROSCI.2385-08.2008); pmid: [18753387](https://pubmed.ncbi.nlm.nih.gov/18753387/)
 28. C. Poo, J. S. Isaacson, Odor representations in olfactory cortex: “Sparse” coding, global inhibition, and oscillations. *Neuron* **62**, 850–861 (2009). doi: [10.1016/j.neuron.2009.05.022](https://doi.org/10.1016/j.neuron.2009.05.022); pmid: [19555653](https://pubmed.ncbi.nlm.nih.gov/19555653/)
 29. C. C. A. Stokes, J. S. Isaacson, From dendrite to soma: Dynamic routing of inhibition by complementary interneuron microcircuits in olfactory cortex. *Neuron* **67**, 452–465 (2010). doi: [10.1016/j.neuron.2010.06.029](https://doi.org/10.1016/j.neuron.2010.06.029); pmid: [20696382](https://pubmed.ncbi.nlm.nih.gov/20696382/)
 30. D. M. G. Johnson, K. R. Illig, M. Behan, L. B. Haberly, New features of connectivity in piriform cortex visualized by intracellular injection of pyramidal cells suggest that “primary” olfactory cortex functions like “association” cortex in other sensory systems. *J. Neurosci.* **20**, 6974–6982 (2000). doi: [10.1523/JNEUROSCI.20-18-06974.2000](https://doi.org/10.1523/JNEUROSCI.20-18-06974.2000); pmid: [10995842](https://pubmed.ncbi.nlm.nih.gov/10995842/)
 31. K. M. Franks *et al.*, Recurrent circuitry dynamically shapes the activation of piriform cortex. *Neuron* **72**, 49–56 (2011). doi: [10.1016/j.neuron.2011.08.020](https://doi.org/10.1016/j.neuron.2011.08.020); pmid: [21982368](https://pubmed.ncbi.nlm.nih.gov/21982368/)
 32. R. Hu, J. Zhang, M. Luo, J. Hu, Response patterns of GABAergic neurons in the anterior piriform cortex of awake mice. *Cereb. Cortex* **27**, 3110–3124 (2017). pmid: [27252353](https://pubmed.ncbi.nlm.nih.gov/27252353/)
 33. I. G. Davison, M. D. Ehlers, Neural circuit mechanisms for pattern detection and feature combination in olfactory cortex. *Neuron* **70**, 82–94 (2011). doi: [10.1016/j.neuron.2011.02.047](https://doi.org/10.1016/j.neuron.2011.02.047); pmid: [21482358](https://pubmed.ncbi.nlm.nih.gov/21482358/)
 34. C. Poo, J. S. Isaacson, A major role for intracortical circuits in the strength and tuning of odor-evoked excitation in olfactory cortex. *Neuron* **72**, 41–48 (2011). doi: [10.1016/j.neuron.2011.08.015](https://doi.org/10.1016/j.neuron.2011.08.015); pmid: [21982367](https://pubmed.ncbi.nlm.nih.gov/21982367/)
 35. M. Carandini, D. J. Heeger, Normalization as a canonical neural computation. *Nat. Rev. Neurosci.* **13**, 51–62 (2011). doi: [10.1038/nrn3136](https://doi.org/10.1038/nrn3136); pmid: [22108672](https://pubmed.ncbi.nlm.nih.gov/22108672/)
 36. A. M. Boyd, J. F. Sturgill, C. Poo, J. S. Isaacson, Cortical feedback control of olfactory bulb circuits. *Neuron* **76**, 1161–1174 (2012). doi: [10.1016/j.neuron.2012.10.020](https://doi.org/10.1016/j.neuron.2012.10.020); pmid: [23259951](https://pubmed.ncbi.nlm.nih.gov/23259951/)
 37. F. Markopoulos, D. Rokni, D. H. Gire, V. N. Murthy, Functional properties of cortical feedback projections to the olfactory bulb. *Neuron* **76**, 1175–1188 (2012). doi: [10.1016/j.neuron.2012.10.028](https://doi.org/10.1016/j.neuron.2012.10.028); pmid: [23259952](https://pubmed.ncbi.nlm.nih.gov/23259952/)
 38. G. H. Otazu, H. Chae, M. B. Davis, D. F. Albeanu, Cortical Feedback Decorrelates Olfactory Bulb Output in Awake Mice. *Neuron* **86**, 1461–1477 (2015). doi: [10.1016/j.neuron.2015.05.023](https://doi.org/10.1016/j.neuron.2015.05.023); pmid: [26051422](https://pubmed.ncbi.nlm.nih.gov/26051422/)
 39. T. A. Cleland *et al.*, Sequential mechanisms underlying concentration invariance in biological olfaction. *Front. Neuroeng.* **4**, 21 (2012). pmid: [22287949](https://pubmed.ncbi.nlm.nih.gov/22287949/)
 40. P. Zhu, T. Frank, R. W. Friedrich, Equalization of odor representations by a network of electrically coupled inhibitory interneurons. *Nat. Neurosci.* **16**, 1678–1686 (2013). doi: [10.1038/nn.3528](https://doi.org/10.1038/nn.3528); pmid: [24077563](https://pubmed.ncbi.nlm.nih.gov/24077563/)
 41. A. Banerjee *et al.*, An interglomerular circuit gates glomerular output and implements gain control in the mouse olfactory bulb. *Neuron* **87**, 193–207 (2015). doi: [10.1016/j.neuron.2015.06.019](https://doi.org/10.1016/j.neuron.2015.06.019); pmid: [26139373](https://pubmed.ncbi.nlm.nih.gov/26139373/)
 42. B. R. Arenkiel *et al.*, In vivo light-induced activation of neural circuitry in transgenic mice expressing channelrhodopsin-2. *Neuron* **54**, 205–218 (2007). doi: [10.1016/j.neuron.2007.03.005](https://doi.org/10.1016/j.neuron.2007.03.005); pmid: [17442243](https://pubmed.ncbi.nlm.nih.gov/17442243/)
 43. T. Gollisch, M. Meister, Rapid neural coding in the retina with relative spike latencies. *Science* **319**, 1108–1111 (2008). doi: [10.1126/science.1149639](https://doi.org/10.1126/science.1149639); pmid: [18292344](https://pubmed.ncbi.nlm.nih.gov/18292344/)
 44. S. Thorpe, A. Delorme, R. Van Rullen, Spike-based strategies for rapid processing. *Neural Netw.* **14**, 715–725 (2001). doi: [10.1016/S0893-6080\(01\)00083-1](https://doi.org/10.1016/S0893-6080(01)00083-1); pmid: [11665765](https://pubmed.ncbi.nlm.nih.gov/11665765/)
 45. S. Panzeri, R. S. Petersen, S. R. Schultz, M. Lebedev, M. E. Diamond, The role of spike timing in the coding of stimulus location in rat somatosensory cortex. *Neuron* **29**, 769–777 (2001). doi: [10.1016/S0896-6273\(01\)00251-3](https://doi.org/10.1016/S0896-6273(01)00251-3); pmid: [11301035](https://pubmed.ncbi.nlm.nih.gov/11301035/)
 46. R. S. Johansson, I. Birznies, First spikes in ensembles of human tactile afferents code complex spatial fingertip events. *Nat. Neurosci.* **7**, 170–177 (2004). doi: [10.1038/nn1177](https://doi.org/10.1038/nn1177); pmid: [14730306](https://pubmed.ncbi.nlm.nih.gov/14730306/)
 47. P. Heil, First-spike latency of auditory neurons revisited. *Curr. Opin. Neurobiol.* **14**, 461–467 (2004). doi: [10.1016/j.conb.2004.07.002](https://doi.org/10.1016/j.conb.2004.07.002); pmid: [15321067](https://pubmed.ncbi.nlm.nih.gov/15321067/)
 48. O. Zohar, M. Shamir, A readout mechanism for latency codes. *Front. Comput. Neurosci.* **10**, 107 (2016). doi: [10.3389/fncom.2016.00107](https://doi.org/10.3389/fncom.2016.00107); pmid: [27812332](https://pubmed.ncbi.nlm.nih.gov/27812332/)
 49. Y. Chen, Mechanisms of winner-take-all and group selection in neuronal spiking networks. *Front. Comput. Neurosci.* **11**, 20 (2017). doi: [10.3389/fncom.2017.00020](https://doi.org/10.3389/fncom.2017.00020); pmid: [28484384](https://pubmed.ncbi.nlm.nih.gov/28484384/)
 50. L. B. Haberly, Parallel-distributed processing in olfactory cortex: New insights from morphological and physiological analysis of neuronal circuitry. *Chem. Senses* **26**, 551–576 (2001). doi: [10.1093/chemse/26.5.551](https://doi.org/10.1093/chemse/26.5.551); pmid: [11418502](https://pubmed.ncbi.nlm.nih.gov/11418502/)
 51. D. A. Wilson, R. M. Sullivan, Cortical processing of odor objects. *Neuron* **72**, 506–519 (2011). doi: [10.1016/j.neuron.2011.10.027](https://doi.org/10.1016/j.neuron.2011.10.027); pmid: [22099455](https://pubmed.ncbi.nlm.nih.gov/22099455/)
 52. M. Papadopolou, S. Cassenaer, T. Nowotny, G. Laurent, Normalization for sparse encoding of odors by a wide-field interneuron. *Science* **332**, 721–725 (2011). doi: [10.1126/science.1201835](https://doi.org/10.1126/science.1201835); pmid: [21551062](https://pubmed.ncbi.nlm.nih.gov/21551062/)
 53. A. C. Lin, A. M. Bygrave, A. de Calignon, T. Lee, G. Miesenböck, Sparse, decorrelated odor coding in the mushroom body enhances learned odor discrimination. *Nat. Neurosci.* **17**, 559–568 (2014). doi: [10.1038/nn.3660](https://doi.org/10.1038/nn.3660); pmid: [24561998](https://pubmed.ncbi.nlm.nih.gov/24561998/)
 54. S. J. Guzman, A. Schlögl, M. Frotscher, P. Jonas, Synaptic mechanisms of pattern completion in the hippocampal CA3 network. *Science* **353**, 1117–1123 (2016). doi: [10.1126/science.aaf1836](https://doi.org/10.1126/science.aaf1836); pmid: [27609885](https://pubmed.ncbi.nlm.nih.gov/27609885/)
 55. P. Yger *et al.*, A spike sorting toolbox for up to thousands of electrodes validated with ground truth recordings in vitro and in vivo. *eLife* **7**, e34518 (2018). doi: [10.7554/eLife.34518](https://doi.org/10.7554/eLife.34518); pmid: [29557782](https://pubmed.ncbi.nlm.nih.gov/29557782/)
 56. P. Barthó *et al.*, Characterization of neocortical principal cells and interneurons by network interactions and extracellular features. *J. Neurophysiol.* **92**, 600–608 (2004). doi: [10.1152/jn.01170.2003](https://doi.org/10.1152/jn.01170.2003); pmid: [15056678](https://pubmed.ncbi.nlm.nih.gov/15056678/)
 57. P. Berens, CircStat: A MATLAB toolbox for circular statistics. *J. Stat. Softw.* **31**, 1–21 (2009). doi: [10.18637/jss.v031.i10](https://doi.org/10.18637/jss.v031.i10)
 58. M. Vinck, M. van Wingerden, T. Womelsdorf, P. Fries, C. M. A. Pennartz, The pairwise phase consistency: A bias-free measure of rhythmic neuronal synchronization. *Neuroimage* **51**, 112–122 (2010). doi: [10.1016/j.neuroimage.2010.01.073](https://doi.org/10.1016/j.neuroimage.2010.01.073); pmid: [20114076](https://pubmed.ncbi.nlm.nih.gov/20114076/)
 59. H. Bokil, P. Andrews, J. E. Kulkarni, S. Mehta, P. P. Mitra, Chronux: A platform for analyzing neural signals. *J. Neurosci. Methods* **192**, 146–151 (2010). doi: [10.1016/j.jneumeth.2010.06.020](https://doi.org/10.1016/j.jneumeth.2010.06.020); pmid: [20637804](https://pubmed.ncbi.nlm.nih.gov/20637804/)
 60. W. E. Vinje, J. L. Gallant, Sparse coding and decorrelation in primary visual cortex during natural vision. *Science* **287**, 1273–1276 (2000). doi: [10.1126/science.287.5456.1273](https://doi.org/10.1126/science.287.5456.1273); pmid: [10678835](https://pubmed.ncbi.nlm.nih.gov/10678835/)

ACKNOWLEDGMENTS

We thank P. Lee, B. Ryu, and M. Dalgetty for technical assistance; A. West and F. Wang for GFP-TeLC AAVs; and A. Fleischmann, S. Lisberger, T. Margrie, R. Mooney, M. Scanziani, A. Schaefer, M. Tadross, and F. Wang for helpful comments on early versions of the manuscript. **Funding:** This work was supported by grants from the National Institute on Deafness and Other Communication Disorders (DC009839 and DC015525) and the Edward Mallinckrodt Jr. Foundation. **Author contributions:** Conceptualization, Methodology, investigation, formal analysis, writing of the original draft, review, and editing were performed by K.A.B. and K.M.F. Funding Acquisition, supervision, and project administration was performed by K.M.F. **Competing interests:** Authors declare no competing interests. **Data and materials availability:** Data have been deposited at the CRCNS (<https://crcns.org>) and can be accessed at <https://doi.org/10.6080/KOOC4SZB>. Materials are available from the authors upon reasonable request.

SUPPLEMENTARY MATERIALS

www.sciencemag.org/content/361/6407/eaat6904/suppl/DC1
Figs. S1 to S6

24 March 2018; accepted 3 August 2018
10.1126/science.aat6904

REPORT

ROBOTICS

A tailless aerial robotic flapper reveals that flies use torque coupling in rapid banked turns

Matěj Karásek^{1*}, Florian T. Muijres², Christophe De Wagter¹,
Bart D. W. Remes¹, Guido C. H. E. de Croon¹

Insects are among the most agile natural flyers. Hypotheses on their flight control cannot always be validated by experiments with animals or tethered robots. To this end, we developed a programmable and agile autonomous free-flying robot controlled through bio-inspired motion changes of its flapping wings. Despite being 55 times the size of a fruit fly, the robot can accurately mimic the rapid escape maneuvers of flies, including a correcting yaw rotation toward the escape heading. Because the robot's yaw control was turned off, we showed that these yaw rotations result from passive, translation-induced aerodynamic coupling between the yaw torque and the roll and pitch torques produced throughout the maneuver. The robot enables new methods for studying animal flight, and its flight characteristics allow for real-world flight missions.

Flying insects demonstrate extraordinary agility when they reject wind gusts (1), catch prey (2), or evade a human hand trying to swat them (3). Such aerobatic feats, enabled by unsteady aerodynamics (4, 5), require both quick and precise reactions of their neural sensory-motoric control system (6). Research into the underlying mechanisms typically involves in vivo observations of flight maneuvers, usually via high-speed cameras, and has yielded hypotheses on possible control strategies during maneuvers such as saccades (7), evasive maneuvers (3), or aerial tumble recovery (8). These hypotheses are currently being tested using theoretical modeling (8) or tethered, dynamically scaled robots (9). However, such tests are incomplete; existing theoretical models lack sufficient fidelity, and tethered robots cannot model the full movement dynamics experienced during free flight.

Lately, many bio-inspired robotic platforms have been developed that try to mimic the flapping flight of hummingbirds (10, 11), bats (12), beetles (13), and even flies (14). Unlike traditional fixed-wing and rotary-wing robots, which differ greatly from flying animals and thus experience different flight dynamics, flapping-wing vehicles could be used to test existing hypotheses on animal flight control through systematic and programmable experiments with known internal processes (15, 16). Nonetheless, because of technological challenges arising from stringent weight and size restrictions, most existing designs cannot

match the flight performance of their biological counterparts; they lack the necessary agility, sufficient power to take off, or sufficient energy to fly for more than a minute. The state-of-the-art Nano Hummingbird (10) and Robobee (14) come close in terms of performance and autonomous flight control, respectively. However, the Nano Hummingbird must be manually operated by a trained human pilot and thus cannot fly autonomously (10), whereas the fly-sized Robobee is tethered to an off-board power supply, which limits its maneuvering capabilities (14).

Here, we present a fully programmable autonomous and freely flying insect-inspired robot that is agile both around hover and in fast forward flight (Fig. 1). The robot is tailless, and thus, as in flies (5, 8), position and orientation in space are controlled solely through wing motion adjustments. When designing the robot, we built upon the reliable flapping mechanisms with flexible wings found in (17). Two wings on each side of the robot flap in counterphase and clap and peel with each other to enhance the produced thrust (movie S1), inspired by the clap-and-fling mechanism observed in nature during thrust-demanding tasks (4). The size, wing morphology, and wing kinematics of our robot do not mimic any specific natural flyer but were instead optimized for maximal power efficiency when driven by miniature brushless DC motors, an engineering alternative to the powerful animal flight muscles. The resulting 28.2-g robot has a wingspan of 33 cm (Fig. 1A); its 14-cm-long wings have a flapping frequency of approximately 17 Hz in hover. The power efficiency of our robot enables a flight endurance of 5 min in hover, or a flight range of more than 1 km, on a single battery charge. These performance characteristics allow for a wide

variety of (automated) experiments and even real-world missions.

To control its orientation, the robot produces torques around the three orthogonal body axes via bio-inspired adjustments of the wingbeat pattern (Fig. 1, H to J). As in fruit flies (5, 8), yaw torque is produced by changing the wing root angle such that the (wingbeat-average) thrust vectors of the left and right wing(s) are tilted in opposite directions (Fig. 1, E and H). Pitch torques are generated by adjusting the dihedral angle (center line of the flapping wings), which, as in fruit flies (5), shifts the wing thrust vectors relative to the center of mass (CoM) (Fig. 1, F and I). Roll torques are produced by generating a thrust difference between the left and right wing (pair). Flies have a coupled wingbeat actuation system and achieve this using asymmetric stroke amplitude adjustments (5), whereas our robot adjusts stroke frequencies (Fig. 1, G and J). Finally, symmetric flapping frequency variation is used for modulation of thrust magnitude. The resulting control torques and thrust have high magnitude (figs. S1 and S2), high bandwidth (fig. S3), and very little coupling (figs. S3 to S5) and are minimally sensitive to the vertical location of the CoM (fig. S5, E and F) (18).

Tailless flapping flight is unstable near hover (19), and thus the robot needs to actively stabilize its attitude (orientation in space). To this end, it carries a miniature 2.8-g autopilot (20) equipped with a programmable microcomputer and sensors for attitude estimation (18)—that is, a three-axis gyroscope and accelerometer (fig. S6). Attitude control (fig. S7) uses the estimated attitude as well as the body rotation rate signals from the gyroscopes (18) and is in many respects comparable to the haltere-based proportional-integral (PI) controller suggested to be used by fruit flies (5, 8). Apart from remotely piloted operation, the autopilot allows execution of preprogrammed control sequences triggered by the pilot.

Similar to many flying insects (3, 5), the robot can actively control four degrees of freedom (DOFs): roll, pitch, yaw, and thrust. To enable movement in a six-DOF space, translation control follows the helicopter model, whereby forward/backward flight speed is controlled via body pitch (Fig. 1C and movie S2) and sideways flight is achieved by rolling the body left or right (Fig. 1D and movie S3). The robot can perform stationary hovering flight and move in any direction with rapid, yet smooth and reproducible transitions (figs. S9 to S12 and movie S4). In forward flight, the highest power efficiency is achieved around 3 m/s; applying full power results in the maximal speed of 7 m/s. The maximal sideways speed is 4 m/s.

The key property of interest here is the robot's agility, which is exceptional for a flapping-wing robot and approaches that of rotorcraft robots (21). It can perform 360° roll and pitch flips, during which it reaches angular accelerations of up to about 5000° s⁻² (figs. S13 and S14 and movies S5 and S6). Its maximal thrust-to-weight ratio of 1.3 allows for quick climbs, although it remains inferior to the best natural fliers with thrust-to-weight ratios of ≥2 (3).

¹Micro Air Vehicle Laboratory, Control and Simulation, Delft University of Technology, Delft, Netherlands. ²Experimental Zoology Group, Wageningen University and Research, Wageningen, Netherlands.

*Corresponding author. Email: m.karasek@tudelft.nl

Despite the large variation in size, mass, wing kinematics, and wing morphology among flapping-wing fliers, they all experience the same type of passive aerodynamic damping, termed flapping countertorque and flapping counterforce (22), and thus their flight dynamics share similar characteristics (19). We can thus use the robot to study maneuver dynamics and control in a wide range of flying animals, from hummingbirds to tiny two-winged fruit flies. To demonstrate this potential for animal flight research, we programmed the robot to mimic the rapid banked turns observed in fruit flies when evading predators (movie S7) (3).

It has been hypothesized that these evasive maneuvers consist of two distinct phases (3, 5). The first phase is simply a feedforward program triggered by the visually detected threat, whereby the fly produces a combined roll and pitch rotation, with the ratio of pitch rate to roll rate (q/p) defining the turn angle. The second recovery phase is controlled using sensory feedback pro-

vided by the halteres. It has also been hypothesized that fruit flies do not control body yaw throughout the evasive maneuver, but instead control for the sideslip caused by the maneuver after the turn, possibly by using much slower visual feedback (3, 5, 9).

We tested these two hypotheses by reproducing a range of evasive maneuvers described in fruit flies. These maneuvers were preprogrammed and fully autonomous to ensure that the control inputs were always the same. The initial phase of a maneuver was controlled using an open-loop combination of pitch and roll torque commands (18). For the recovery phase, we used feedback control of roll and pitch, whereas yaw control was turned off.

In our first set of experiments, we performed two evasive maneuvers initiated with different q/p values (measured at the end of the open-loop phase), the first dominated by rolling ($q/p = 0.52$; Fig. 2A and fig. S15), and the second dominated by pitching ($q/p = 1.67$; Fig. 2C and fig. S16). Despite substantial differences between our four-

winged robot and the much smaller two-winged fruit fly, the robotic maneuvers resembled those observed in fruit flies remarkably well (Fig. 2, A to D, and movies S8 and S9). To enable quantitative comparison of the fruit fly and robot maneuvers, we normalized distances by wing length and time according to wingbeat-cycle period (flies) and half-wingbeat-cycle period (robot) (figs. S17 and S18) (18) and determined the Pearson correlation coefficient c_r and normalized root mean square error (RMSE) between the normalized robot and fruit fly data (table S5). For both maneuvers (Fig. 2, A to D), we found high correlations and low RMSE (table S5), further highlighting the similarity.

Detailed analysis of a 90° turn initiated with 94% of the maximal pitch torque and 74% of the maximal roll torque ($q/p = 0.54$) (Fig. 2, E to I, fig. S19, and movie S10) shows that at the apex of the turn, an extreme body attitude of ~100° in roll is reached, which is comparable to the equivalent attitudes observed in fruit flies (Fig. 2B) (3). In

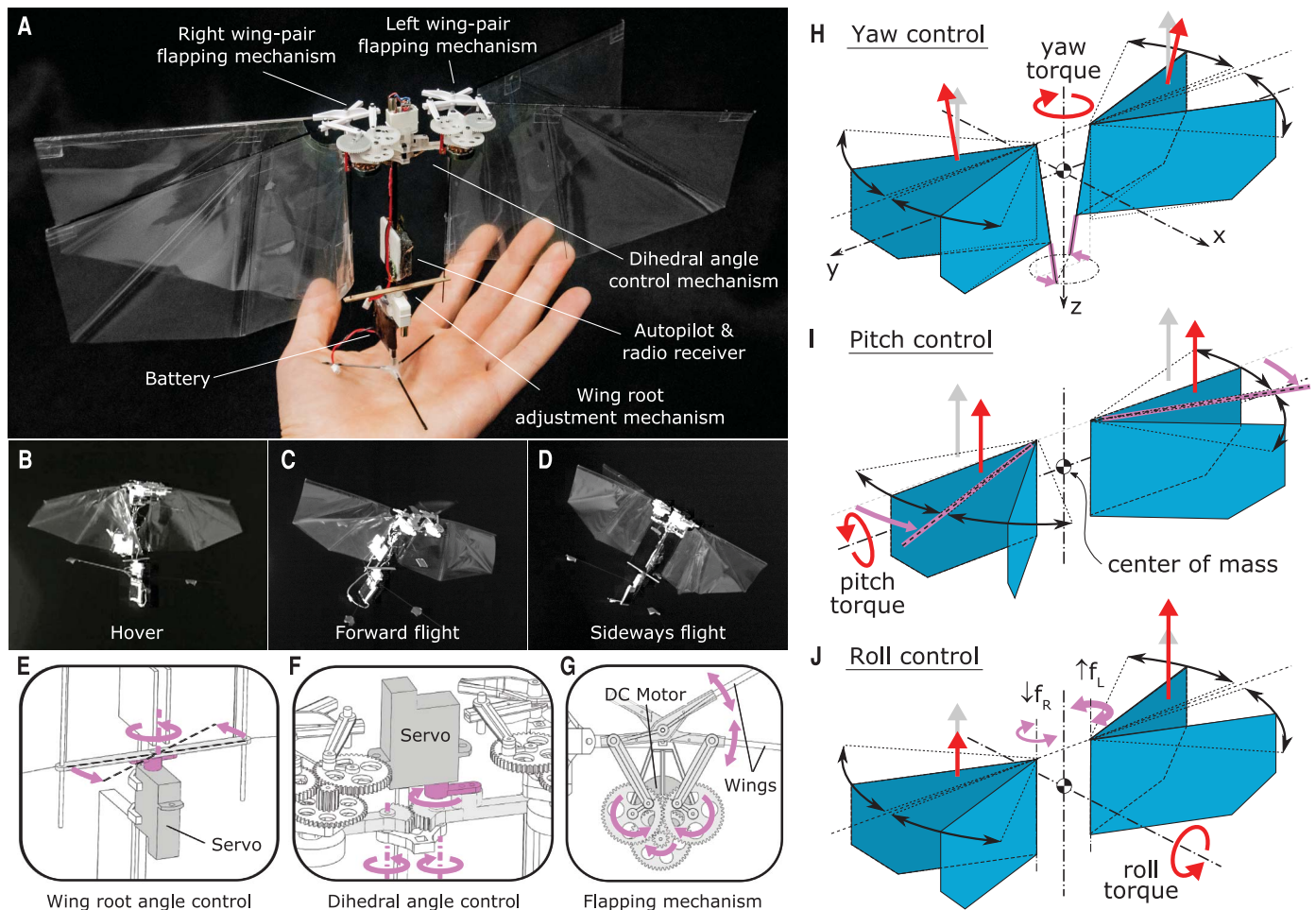


Fig. 1. An insect-inspired free-flying robotic platform is controlled through its two pairs of independently flapping wings. (A) Description of the robot's components. (B to D) High-speed camera frames capturing the robot in hover (B), forward flight (C), and sideways flight (D), from movies S1 to S3, respectively. (E to G) Details of the robot design: (E) the wing root adjustment mechanism for yaw torque control, (F) the dihedral control

mechanism for pitch torque control, and (G) the flapping mechanism (of the left wing pair), used for thrust and roll torque control. (H to J) Wing actuation and aerodynamic forces and torques during yaw control (H), pitch control (I), and roll control (J). Magenta arrows show actuation action, gray arrows show the nominal wingbeat-average aerodynamic thrust vectors, and red arrows show wingbeat-average thrust and torques after control actuation.

the subsequent feedback phase, the transition between the positive and negative acceleration peaks (difference of $9000^\circ \text{ s}^{-2}$) took fewer than three wingbeats ($\sim 0.18 \text{ s}$) while closely following the wing actuation that generates the body-accelerating torques (Fig. 2, G to I).

These results confirm that a rapid banked turn can be successfully achieved with an open-loop maneuver initiation and closed-loop recovery. Hence, they support the hypothesis that the recovery phase of the evasive maneuver in fruit flies

is also controlled using a PI-like roll and pitch control system, whereby halteres might provide the sensory input (3, 5).

To systematically test the relation between q/p and turn angle, we performed evasive maneuvers at five combinations of roll and pitch torque commands, varying q/p from ~ 0.3 to ~ 2.1 (Fig. 3 and figs. S20 and S21) (18). As shown in Fig. 3A, q/p had a clear effect on the flight trajectory, and in agreement with fruit flies, q/p was positively correlated with turn angle ($c_r = 0.95$;

Fig. 3F), whereby turns with dominant pitch rates resulted in larger turn angles.

In agreement with the fruit fly experiments (3), we also observed high yaw rates in the direction of the turn during the recovery phase (Fig. 3D). Because no yaw command was provided during the robot maneuvers, these yaw movements were thus passively induced (Fig. 1).

For the robot as well as the fruit flies, the observed yaw accelerations \dot{r} correlated strongly with the roll accelerations \dot{p} and, particularly for

Fig. 2. The robot mimics rapid banked turns observed in escaping fruit flies.

(A and C) Time sequences (top view) of a roll-dominated maneuver (pitch rate/roll rate ratio $q/p = 0.52$) and a pitch-dominated maneuver ($q/p = 1.67$), respectively. The start of the open-loop (OL) phase is marked with a green circle. (B and D) Time sequences (top view) of the equivalent fruit fly evasive maneuvers with the stimulus (green arrowhead) coming from the left and the front, respectively. (E to I) Detailed analysis of a roll-dominated maneuver ($q/p = 0.54$). (E) Time sequence with constant time interval of 0.125 s ; trajectory projections are shown by dotted lines. Wings are color-coded according to thrust command magnitude, as shown in the color bar. [(F) to (I)] Time histories of roll command (F), roll acceleration and flapping frequency of the right wing pair (G), pitch command (H), and pitch acceleration and dihedral angle (I). In (A) to (E), blue and magenta arrows represent velocity and acceleration vectors, respectively; vectors (arrow lengths) are relative to the black scale bars in (A) and (E) for the robot and in (B) for flies. The OL phase in (F) to (I) is highlighted by gray background.

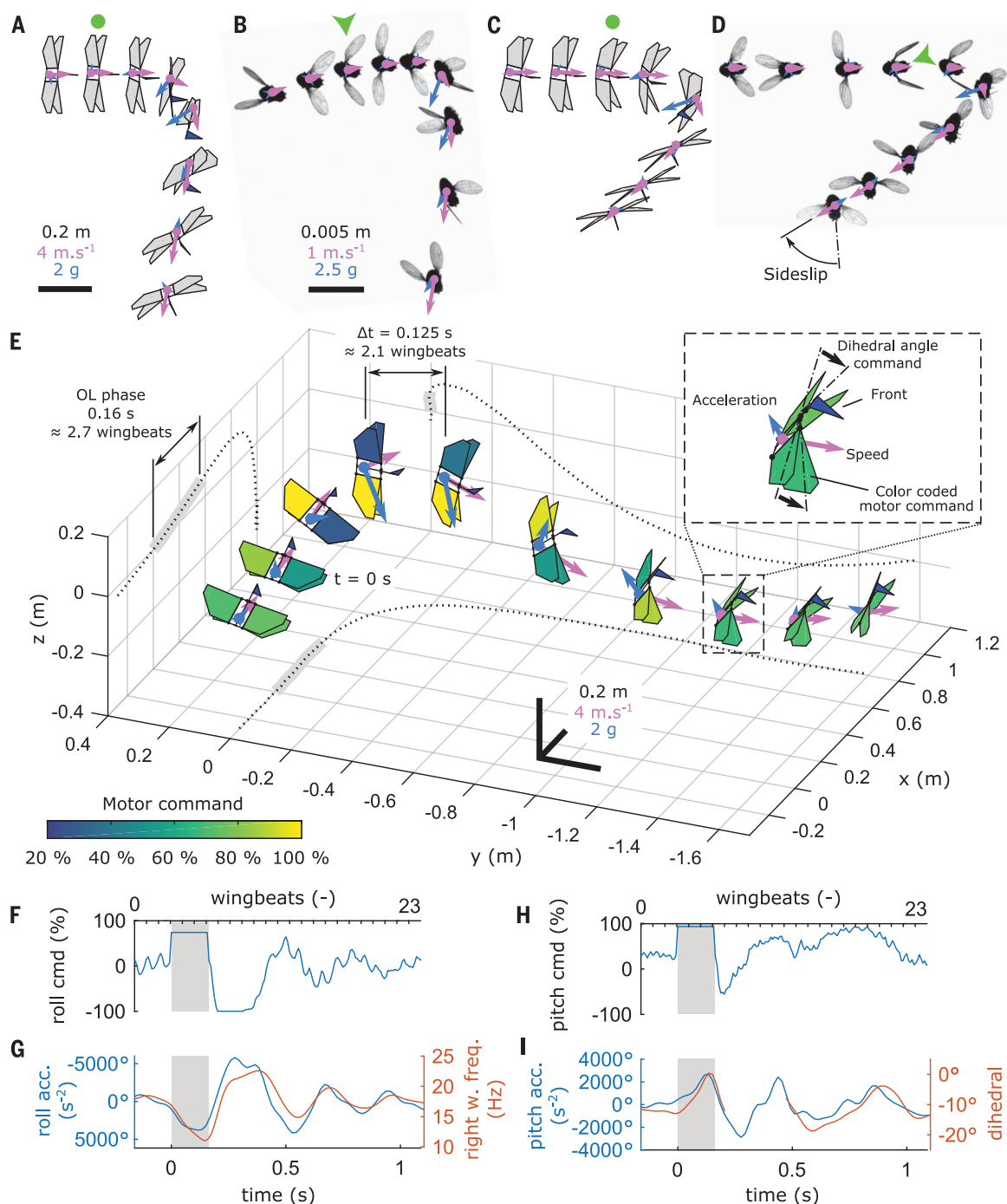
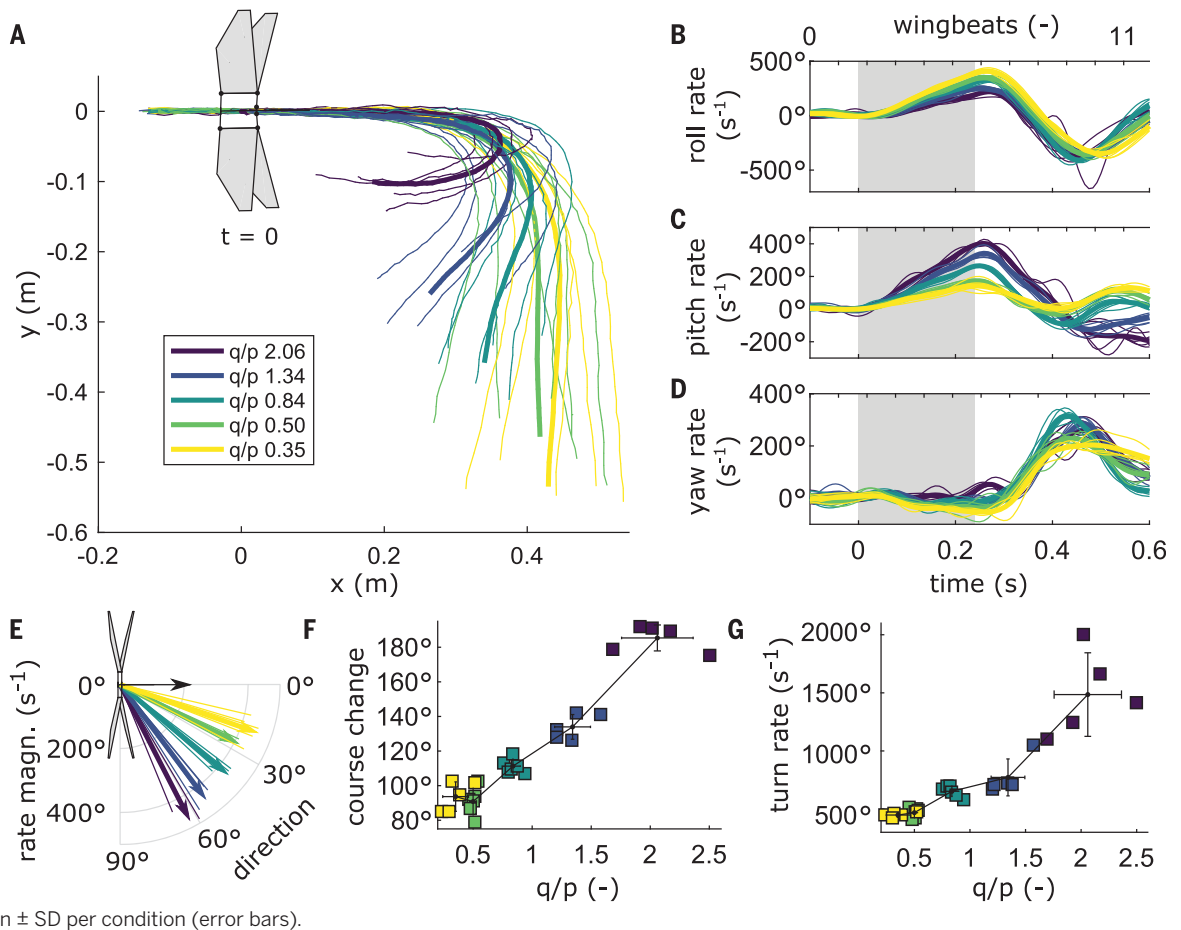


Fig. 3. The turn angle during the banked turn can be controlled by varying the ratio of pitch to roll torque commands. Results are color-coded [see key in (A)] according to the q/p ratio of the maneuver; thin lines are individual trials and thick lines are series averages.

(A) Top view of trajectories, aligned at the start of the OL phase ($t = 0$ s) where the robot is shown. (B to D) Time histories of angular rates during the maneuvers. The OL phase is highlighted by gray background. (E) Angular rate vector in the horizontal body plane, relative to the forward-directed black arrow. (F and G) Turn angle and turn rate versus q/p , respectively, for individual tests (squares) and mean \pm SD per condition (error bars).



the sharper turns (high q/p), also with the pitch accelerations \dot{q} (Fig. 4, A and B). Moreover, the largest yaw accelerations were observed in the recovery phase, where both the robot and the flies move at relatively high forward and sideways flight velocities (fig. S22).

On the basis of these observations, and thanks to the simple wing kinematics of the robot (where roll torque and pitch torque are each modulated by only one parameter), we were able to develop a functional aerodynamic yaw torque model that explains the observed yaw accelerations in the robot maneuvers (Fig. 4, D to H, and fig. S23) (18):

$$N = \frac{\dot{r}}{I_{zz}} = -b\Phi R[(f_L + f_R)Rr + (f_L - f_R)u + (f_L + f_R)\Gamma v] \quad (1)$$

where N is yaw torque; \dot{r} is yaw acceleration; I_{zz} is the moment of inertia around the vertical body axis; b is the linear damping coefficient due to flapping counterforce (22); Φ is flapping amplitude; R is wing length; f_L and f_R are flapping frequency of the left and the right wing, respectively; r is yaw rate; u and v are the forward and sideways velocity of the robot, respectively; and Γ is the wing dihedral angle.

The first term, $-b\Phi R(f_L + f_R)Rr$, represents the flapping counterforce (N_{FCF}), which is by def-

inition opposite to the direction of yaw rate (Fig. 4F) (22) and thus cannot explain the observed yaw accelerations. The two remaining terms are our addition to the passive yaw-torque system for flapping flight, which we call translation-induced coupled yaw torque (N_{TCT}), as it models the coupling effect of roll and pitch torque production on yaw torque in the presence of translating body motions ($N_{\text{TCT}} = N_{u\&roll} + N_{v\&pitch}$; Fig. 4, G and H). Thus, in the presence of a forward velocity u , the differential flapping frequency ($f_L - f_R$) used for roll torque production also results in a yaw torque ($N_{u\&roll}$; Fig. 4G). Similarly, in the presence of a sideways velocity v , the dihedral angle Γ used for pitch torque production equally generates a yaw torque ($N_{v\&pitch}$; Fig. 4H). In steady hover conditions, such coupling is negligible (fig. S4).

Despite its low complexity, this model accurately estimates the observed yaw acceleration in both roll-dominated and pitch-dominated banked turn maneuvers [Fig. 4, D and E; $c_r = 0.73 \pm 0.30$ (mean \pm SD) for the five sets of trials in fig. S24 and table S6]. Notably, the model predicts the same coupling effects when differential flapping amplitudes are used for roll torque production (eqs. S10 to S14 and fig. S23), which is what many biological fliers as well as other aerial robotic flappers use.

Because fruit fly wing motion patterns are highly complex, we were unable to adapt the model for fruit flies, where multiple degrees of freedom are involved in generating roll and pitch torques. For the fruit fly maneuvers, we estimated yaw accelerations resulting from translation-induced coupled yaw torque as the measured acceleration minus the accelerations caused by flapping counterforce (eq. S19). Relative to our initial yaw-pitch and yaw-roll correlations (Fig. 4B), these flapping counterforce-corrected yaw accelerations \dot{r}_{TCT} correlate even better with the product of roll acceleration and forward velocity, as well as with the product of pitch acceleration and sideways velocity (Fig. 4C); these findings suggest that translation-induced coupled yaw torque is also present in the fruit fly maneuvers.

Together with the high similarity between the turn dynamics of the robot and of the fruit flies (fig. S22), these results provide strong support for the hypothesis that fruit flies do not actively control yaw throughout evasive maneuvers (3, 5), but instead use the translation-induced coupled yaw torque (Eq. 1) to rotate their body in the direction of the banked turn. Given that many maneuvers of flying animals occur at nonzero translational velocities (2–4, 7, 22–24), the passive

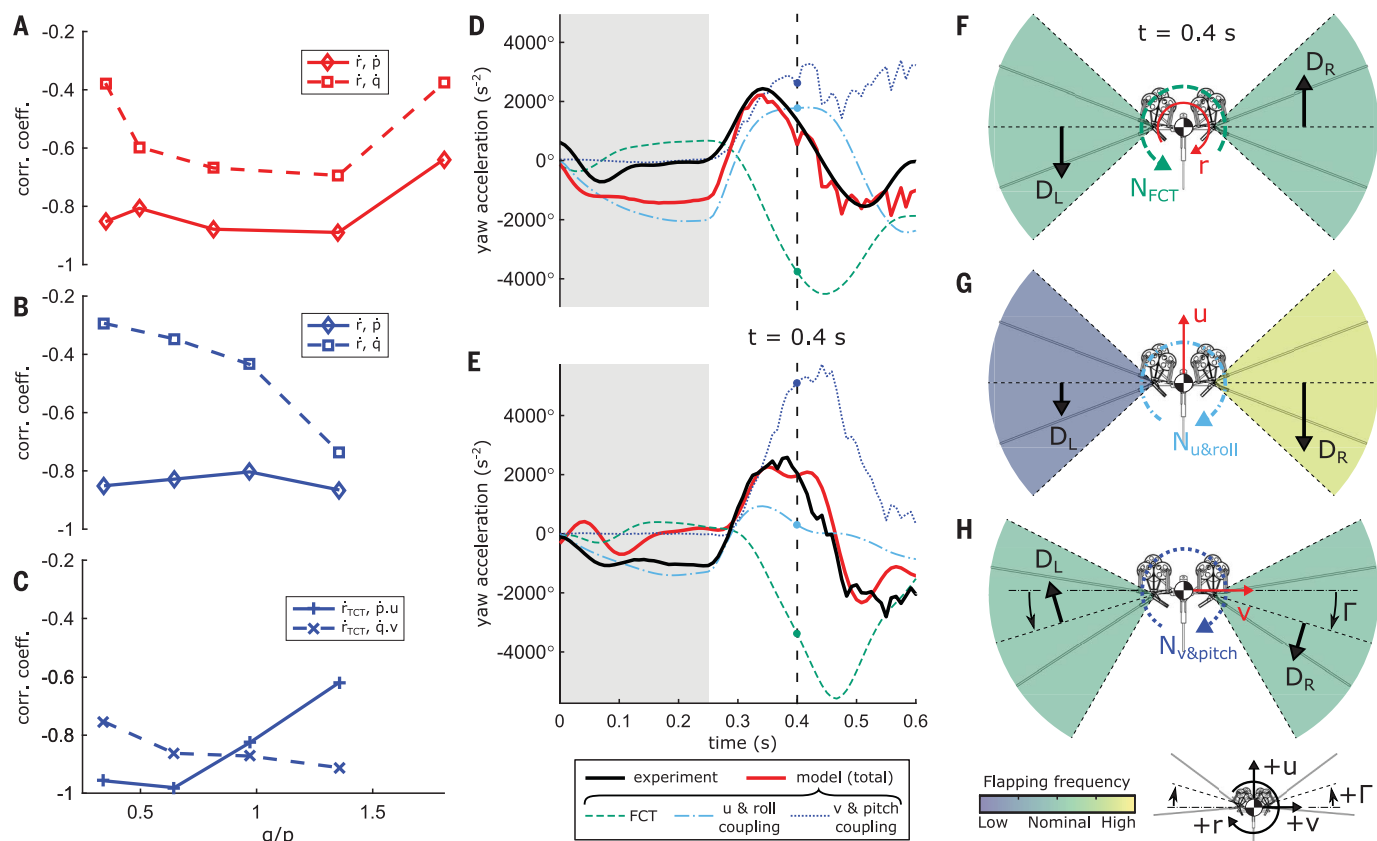


Fig. 4. The passive yaw accelerations during the recovery phase of banked turns originate from the coupling between the roll and pitch torque generation mechanisms and translational body motions.

(A and B) Correlation coefficient between the yaw acceleration and the roll (solid) and pitch (dashed) accelerations at various pitch-to-roll rate ratios q/p for rapid banked turns produced by the robot (A) and for evasive maneuvers produced by fruit flies (B). (C) Correlation coefficients for the same evasive maneuvers of fruit flies, after correcting for the flapping counter torque and including the translational body velocities. (D and E) Measured (black) and modeled (red) yaw accelerations during the

banked turn of the robot: (D) roll-dominated banked turn ($q/p = 0.50$), (E) pitch-dominated banked turn ($q/p = 1.34$). Line style of individual model components follows the legend below (E). (F to H) The three passive yaw torque-producing mechanisms at $t = 0.4$ s in (D) and (E) are flapping counter torque (F), torque due to forward motion with uneven left and right flapping frequencies (G), and torque due to sideways motion with nonzero dihedral angle (H). Color coding of the flapping frequency and the positive directions of all the coordinates are shown below (H). D_L and D_R are the wingbeat-average drag forces of the left and right wing pair, respectively, as defined by eq. S9.

torque coupling we have identified might be more widespread among natural flyers.

Despite the observed yaw accelerations, high sideslips remained at the end of the turns for both the robot and the flies (Fig. 2, A to D, and figs. S17, S18, and S22). In a separate set of robot experiments, we were able to completely remove this sideslip by producing feedforward maximum yaw torque throughout the recovery phase, but this body alignment did not increase the speed of the turn (figs. S25 and S26). Hence, producing such precisely timed and thus complex feedforward yaw command throughout the turn might not enable flies to increase evasive performance. This might be one of the reasons why flies prefer to rely on passive alignment throughout the turn and fully align their body actively only after the turn, possibly using a simpler feedback controller based on visual information (3, 5).

REFERENCES AND NOTES

1. J. T. Vance, I. Faruque, J. S. Humbert, *Bioinspir. Biomim.* **8**, 016004 (2013).

2. S. A. Combes, D. E. Rundle, J. M. Iwasaki, J. D. Crall, *J. Exp. Biol.* **215**, 903–913 (2012).
3. F. T. Muijres, M. J. Elzinga, J. M. Melis, M. H. Dickinson, *Science* **344**, 172–177 (2014).
4. D. D. Chin, D. Lentink, *J. Exp. Biol.* **219**, 920–932 (2016).
5. M. H. Dickinson, F. T. Muijres, *Philos. Trans. R. Soc. B* **371**, 20150388 (2016).
6. W. Shyy, C. K. Kang, P. Chirattananon, S. Ravi, H. Liu, *Proc. R. Soc. A* **472**, 20150712 (2016).
7. F. T. Muijres, M. J. Elzinga, N. A. Iwasaki, M. H. Dickinson, *J. Exp. Biol.* **218**, 864–875 (2015).
8. L. Ristroph et al., in *Natural Locomotion in Fluids and on Surfaces*, S. Childress, A. Hosoi, W. W. Schultz, J. Wang, Eds. (Springer, 2012), pp. 83–99.
9. M. J. Elzinga, W. B. Dickson, M. H. Dickinson, *J. R. Soc. Interface* **9**, 1685–1696 (2012).
10. M. Keenon, K. Klingebiel, H. Won, A. Andriukov, “Development of the Nano Hummingbird: A Tailless Flapping Wing Micro Air Vehicle.” Paper presented at the 50th AIAA Aerospace Sciences Meeting including the New Horizons Forum and Aerospace Exposition (2012).
11. A. Roshanbin, H. Altartouri, M. Karásek, A. Preumont, *Int. J. Micro Air Veh.* **9**, 270–282 (2017).
12. A. Ramezani, S.-J. Chung, S. Hutchinson, *Sci. Robot.* **2**, eaal2505 (2017).
13. H. V. Phan, T. Kang, H. C. Park, *Bioinspir. Biomim.* **12**, 36006 (2017).
14. K. Y. Ma, P. Chirattananon, S. B. Fuller, R. J. Wood, *Science* **340**, 603–607 (2013).
15. N. Franceschini, F. Ruffier, J. Serres, *Curr. Biol.* **17**, 329–335 (2007).
16. M. Kováč, *Soft Robot.* **1**, 28–37 (2014).
17. G. C. H. E. de Croon, M. Percin, B. D. W. Remes, R. Ruijsink, C. De Wagter, *The Delfly—Design, Aerodynamics, and Artificial Intelligence of a Flapping Wing Robot* (Springer, 2016).
18. See supplementary materials.
19. M. Sun, J. Wang, Y. Xiong, *Lixue Xuebao* **23**, 231–246 (2007).
20. B. D. W. Remes et al., in *IMAV 2014: International Micro Air Vehicle Conference and Competition 2014*, G. C. H. E. De Croon, E. Van Kampen, C. De Wagter, Eds. (Delft University of Technology, Delft, Netherlands, 2014), pp. 280–285.
21. S. Lupashin, A. Schöllig, M. Sherback, D. D’Andrea, in *2010 IEEE International Conference on Robotics and Automation (IEEE, 2010)*, pp. 1642–1648.
22. T. L. Hedrick, B. Cheng, X. Deng, *Science* **324**, 252–255 (2009).
23. I. G. Ros, L. C. Bassman, M. A. Badger, A. N. Pierson, A. A. Biewener, *Proc. Natl. Acad. Sci. U.S.A.* **108**, 19990–19995 (2011).
24. K. Ghose, T. K. Horiuchi, P. S. Krishnaprasad, C. F. Moss, *PLOS Biol.* **4**, e108 (2006).

ACKNOWLEDGMENTS

We greatly acknowledge the helpful comments on the manuscript from M. H. Dickinson, M. Kovac, J. L. van Leeuwen, H. Goosen, and B. van Oudheusden. We also thank everyone involved in the earlier stages of the Delfly project, from which we greatly benefited, and especially S. Tijmons for the useful discussions on the robot design and K. M. Kajak for his work on flight dynamics modeling. **Funding:** F.T.M. was supported by a grant from the

Netherlands Organization for Scientific Research, NWO-VENI-863-14-007. **Author contributions:** All authors contributed to the conception of the comparative study and to the analysis and interpretation of the results; M.K. designed and built the robot, performed the robot experiments, and processed the robotic data; F.T.M. provided the fruit fly data; The manuscript was primarily written by M.K., F.T.M., and G.d.C. All authors contributed critically to the drafts and gave final approval for publication. **Competing interests:** M.K. is the inventor on patent application

PCT/NL2018/050317 submitted by Delft University of Technology that covers the concept of the flapping wing robot. **Data and materials availability:** All data relevant to the manuscript are deposited as open access data in Dataverse NL: <https://hdl.handle.net/10411/ROXE/F>.

SUPPLEMENTARY MATERIALS

www.sciencemag.org/content/361/6407/1089/suppl/DC1
Materials and Methods

Supplementary Text
Figs. S1 to S26
Tables S1 to S6
Movies S1 to S10
References (25–29)

19 January 2018; resubmitted 4 May 2018
Accepted 20 July 2018
10.1126/science.aat0350

SOLAR CELLS

Organic and solution-processed tandem solar cells with 17.3% efficiency

Lingxian Meng¹, Yamin Zhang¹, Xiangjian Wan^{1*}, Chenxi Li¹, Xin Zhang¹, Yanbo Wang¹, Xin Ke¹, Zuo Xiao², Liming Ding^{2*}, Ruoxi Xia³, Hin-Lap Yip³, Yong Cao³, Yongsheng Chen^{1*}

Although organic photovoltaic (OPV) cells have many advantages, their performance still lags far behind that of other photovoltaic platforms. A fundamental reason for their low performance is the low charge mobility of organic materials, leading to a limit on the active-layer thickness and efficient light absorption. In this work, guided by a semi-empirical model analysis and using the tandem cell strategy to overcome such issues, and taking advantage of the high diversity and easily tunable band structure of organic materials, a record and certified 17.29% power conversion efficiency for a two-terminal monolithic solution-processed tandem OPV is achieved.

Organic photovoltaics (OPV) is considered to be a promising choice for next-generation technology platforms to address the increasing demands for renewable energy, owing to its many advantages such as low cost, flexibility, and large-area printing production (1–3). Indeed, there has been substantial improvement in the performance of OPV cells in the past decade, and the record power conversion efficiency (PCE) has been raised from ~5% to a current value of 14% (3, 4). However, the performance of OPV cells still lags far behind that of other photovoltaic platforms based mainly on inorganic materials (2, 5, 6). This has led to the impression that OPV cells have a lower performance limit than inorganic material-based devices. A fundamental reason for this is the low charge mobility of organic materials (7, 8), which limits the active-layer thickness of the devices and efficient sunlight absorption.

The tandem cell strategy is an effective way to simultaneously address these issues for OPV cells (9, 10), and furthermore, is probably well suited for OPV (11–15). First, the use of tandem cells would overcome the thickness constraint of single-junction cells due to the low mobility of organic materials because wide and efficient absorption could be achieved by stacking the active layers with complementary absorption in tandem cells. Moreover, tandem cells can take advantage of one of the most important features

of organic materials, i.e., their great diversity (16, 17). This is because in tandem cells, active organic materials in each subcell require different but matching band structures, and such materials could in principle be designed and obtained owing to the high diversity, easily tunable band structures, and advanced synthesis of currently available organic materials (18). In addition, benefiting from this, the thermalization and transmission loss can be reduced in the tandem cells (19). Indeed, tandem cells have also been pursued widely for OPV, and ~14% PCE has been achieved (11), which is about the same as that obtained for the record single-junction cell (4). The limited performance of organic tandem cells is primarily due to their limited sunlight absorption range owing to the lack of optimal low-bandgap materials for use in the rear subcell, as most such materials can only absorb photons with an energy of ~1.3 eV (~900 nm) (11, 14, 20) and thus are missing a large part of the entire sunlight spectrum absorption. Another important reason is the limited tandem cell current owing to the absorption overlapping and/or current mismatching of subcells. With the above analysis and guided by a semi-empirical analysis, we report a solution-processed two-terminal (2T) monolithic tandem OPV cell with a new record PCE of 17.36%.

On the basis of previous theoretical work (9, 21, 22) and state-of-the-art experimental results (3, 11, 14), we first have carried out a semi-empirical analysis for the possible but realistic PCE limit of 2T tandem OPV cells under Air Mass 1.5 Global (AM 1.5G) (details are provided in the supplementary materials and figs. S1 to S3). Briefly, in this model analysis, above the basic assumption for the Shockley-Queisser (SQ) limit analysis (21), the achievable PCEs ($= J_{sc} \times V_{oc} \times FF/P_{in}$ where J_{sc} is the short-circuit current density, V_{oc} is the open-circuit voltage, FF is the fill factor, and P_{in} is the power density of the incident light) are obtained using the following

approaches: (i) the J_{sc} is assumed to be half of the theoretical current in the entire absorption range multiplied by a given external quantum efficiency (EQE) value; (ii) the V_{oc} is the sum of each subcell's voltage, while the voltage of each subcell is determined by the equation $eV_{oc} = E_g - E_{loss}$ where $E_g (=1240/\lambda_{onset})$ is the optical energy gap of the active layers (23), E_{loss} is the energy loss, e is the elementary charge, and λ_{onset} is the absorption onset of the active layers; (iii) the FF is assumed to be the state-of-the-art value. Based on these considerations, figs. S2 and S3 give the predicted achievable PCEs of 2T tandem cells for absorption onset (λ_{onset}) from 900 to 1200 nm, EQE in the range of 65 to 85%, E_{loss} in the range of 0.4 to 0.8 eV, and FF in the range of 0.65 to 0.80. These ranges represent the most likely achievable ones based on the state-of-the-art results (3, 4, 24–27), particularly when considering the wide diversity of organic/polymeric materials, including the recent development of small molecules/oligomer acceptor-donor-acceptor (A-D-A)-type donors (14, 28, 29) and acceptors (3, 16). Extracted from these model results and as one example, Fig. 1A shows the achievable PCEs (14 to 28%) of the 2T tandem cells versus λ_{onset} (corresponding to E_g) of the rear-cell active layer, E_{loss} , and EQE, at a fixed FF of 0.75. Furthermore, as shown in Fig. 1B, a PCE of ~20% could be achieved if the $\lambda_{onset, rear cell}$ is ≤ 1100 nm with an average EQE of 75%, a FF of 0.75, and a typical E_{loss} of 0.6 eV, which is consistent with other theoretical analysis (16). From the model results shown in Fig. 1, C and D, and fig. S3, E_{loss} seems to have a bigger impact on the PCEs. Also, with E_{loss} increasing, the absorption onset of the rear cell ($\lambda_{onset, rear cell}$) with the maximum PCE has a tendency to blue-shift (Fig. 1, C and D) (details in the supplementary materials). These modeling results also indicate that the optimum $\lambda_{onset, rear cell}$, i.e., the E_g of the rear subcell active layer, is somewhat smaller than the optimum one from the SQ limit studies (of ~1127 nm) (9), probably owing to the large E_{loss} of OPV (30).

On the basis of the model analysis presented above, we discuss the screening of materials for use in tandem solar cells. For high-performance 2T tandem cells, various materials with wide and suitable bandgaps have been chosen for use in the front subcell (16). Critically, the first step is to choose suitable or optimal rear-subcell active materials with an infrared absorption onset up to 1050 to 1150 nm, based on the results shown in Fig. 1, B and C. This seemingly straightforward task has actually proved challenging, as a review of the literature (10, 20) and our previous work (14) indicates that donor materials reported to date with absorption onset around 1100 nm essentially all suffer from large E_{loss} , and only a few showed high J_{sc} suitable for rear cells (10). Adding to this challenge is that the performance of these materials should also have an optimal FF and EQE in their single-junction cell evaluation. Fortunately, recent emerging nonfullerene molecules offer another optimal choice of rear-cell active materials owing to the widely tunable band

¹State Key Laboratory and Institute of Elemento-Organic Chemistry, Centre of Nanoscale Science and Technology and Key Laboratory of Functional Polymer Materials, College of Chemistry, Nankai University, Tianjin, 300071, China. ²Center for Excellence in Nanoscience (CAS), Key Laboratory of Nanosystem and Hierarchical Fabrication (CAS), National Center for Nanoscience and Technology, Beijing 100190, China. ³Institute of Polymer Optoelectronic Materials and Devices, State Key Laboratory of Luminescent Materials and Devices, South China University of Technology, Guangzhou, 510640, China.

*Corresponding author. Email: yschen99@nankai.edu.cn (Y.C.); xjwan@nankai.edu.cn (X.W.); ding@nanoctr.cn (L.D.)

structure of these A-D-A structures (3, 16). After careful evaluation, we have found that the non-fullerene acceptor molecule CO₂8DFIC (also called O6T-4F, Fig. 2A) roughly meets these requirements (4, 31), as it has an infrared absorption onset of ~1050 nm (optical bandgap E_g 1.20 eV) and, when blended with PTB7-Th as donor and PC₇₁BM as the secondary acceptor (Fig. 2A and B) (4), a single-junction device based on it exhibited a high J_{sc} with an EQE >70% in the infrared absorption range, a FF of 69.7%, and a low E_{loss} of 0.51 eV.

Following the choice of rear-cell material, the next step is to find matching front subcell materials. From the above analysis, the maximum current achievable up to 1050 nm is ~31 mA/cm², assuming an EQE of 75% (fig. S1). With the requirement that both subcells must have the same current governed by the Kirchhoff's law to achieve optimal performance for a 2T tandem cell (22), the predicted best current of such a tandem cell should be ~15.5 mA/cm². A simple check of the

theoretical current versus wavelength plot (fig. S1) indicates that the absorption onset of the front cell should be at ~720 nm. On the basis of these analyses, the front-cell active layer was selected to use PBDB-T as the donor and F-M as the acceptor (Fig. 2A and figs. S4 to S7) (32), as this active-layer mixture exhibits not only an absorption onset close to 720 nm, but also an optimal current of ~16 mA/cm² and a high EQE (average ~70% in the range of 300 to 750 nm), FF (69.8%), etc. in their single-junction device evaluation discussed below.

The performance of the each subcell was first studied and optimized using the inverted structures (see supplementary materials for details). The current density–voltage (J - V) curves of the optimized single-junction devices are shown in Fig. 2C, with the performance parameters detailed in table S1. The single-junction device for the front cell based on the selected active material of PBDB-T:F-M has a high EQE response in the range of 300 to 750 nm (Fig. 2D), giving a current of

15.96 mA/cm², together with a high V_{oc} of ~0.94 V and a FF of 69.8%. The performance of this inverted device is slightly different from that of the regular device (32), and the E_{loss} for this single-junction cell is 0.71 eV. The optimal J_{sc} is close to the value predicted for the front subcell required in the best tandem cell (details in tables S2 to S6). However, the optimized single-junction devices using PTB7-Th:O6T-4F:PC₇₁BM for the rear unit gave a high current of 27.98 mA/cm² in the range from 300 to 1050 nm with a V_{oc} of 0.69 V, a FF of 69.7%, and a rather low E_{loss} of 0.51 eV, similar to that seen in the literature (4). Although the device showed a broad EQE response from 300 to 1050 nm (Fig. 2D), it has an integrated current of only 11.2 mA/cm² in the range of 720 to 1050 nm desired for the rear cell, lower than the best required current of 15.5 mA/cm² predicted above assuming a clear cut-off absorption for the rear subunit at 720 nm. The single-junction device using the pair of PTB7-Th:O6T-4F without PC₇₁BM

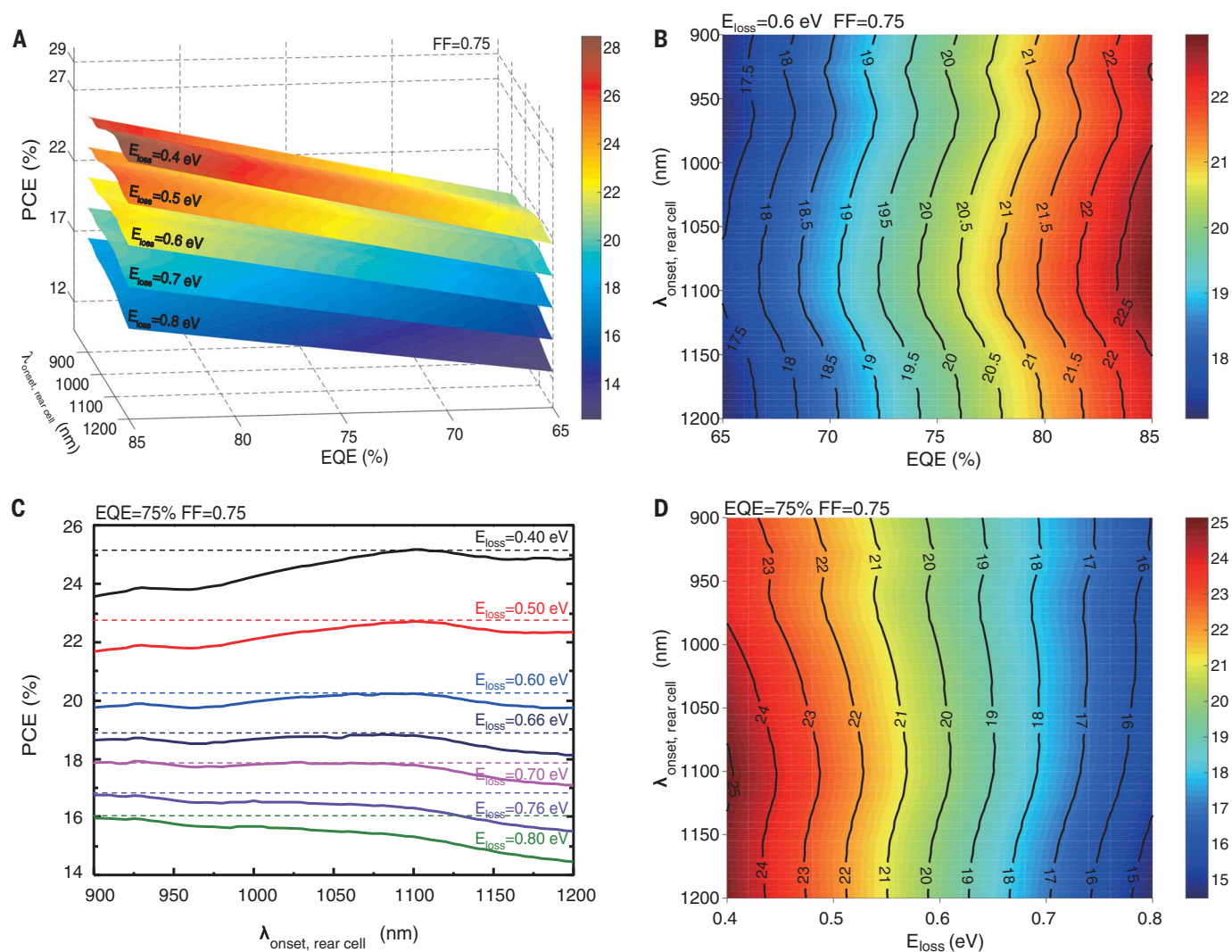


Fig. 1. Predicted PCEs of 2T tandem solar cells based on semi-empirical analysis under AM 1.5G. (A) PCEs versus EQE and $\lambda_{onset, rear cell}$, assuming E_{loss} of each subcell in the range of 0.4 to 0.8 eV and a fixed FF of 0.75. **(B)** PCEs versus EQE and $\lambda_{onset, rear cell}$, assuming E_{loss}

of 0.6 eV and FF of 0.75. **(C)** PCEs versus $\lambda_{onset, rear cell}$ with E_{loss} of 0.4, 0.5, 0.6, 0.66, 0.7, 0.76, and 0.8 eV, FF of 0.75, and EQE of 75%. **(D)** PCEs versus E_{loss} and $\lambda_{onset, rear cell}$ with assumed EQE of 75% and FF of 0.75.

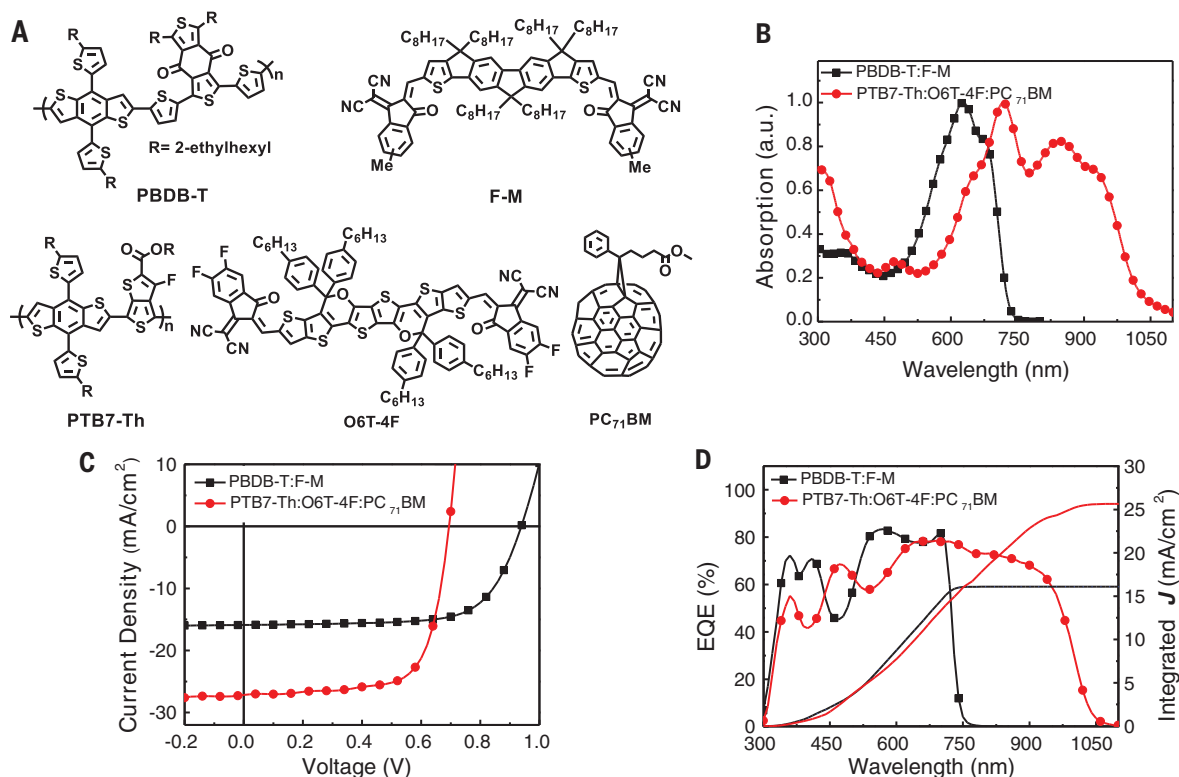


Fig. 2. Molecular structures and photovoltaic performance of the single-junction devices. (A) Molecular structures of PBDB-T, F-M, PTB7-Th, O6T-4F, and PC₇₁BM. (B) Normalized absorption spectra of PBDB-T:F-M and PTB7-Th:O6T-4F:PC₇₁BM films. (C) J-V curves and

(D) EQE curves of the single-junction devices based on PBDB-T:F-M and PTB7-Th:O6T-4F:PC₇₁BM with an architecture of ITO/ZnO/PFN-Br/active layer/M-PEDOT/Ag and ITO/ZnO/active layer/MoO₃/Ag.

was also tested, but it gave an even lower current (31), as discussed below and in table S1.

After subcell optimization, the inverted tandem cells were fabricated using solution processing, and the detailed optimal results are shown in tables S7 to S13. The tandem cell architecture and corresponding energy diagram are presented in Fig. 3, A and B.

Before the tandem cell optimization, optical simulation modeling using the transfer matrix method (33) was conducted to develop guidelines for the selection of optimal thicknesses of the subcells, because one of the biggest challenges in fabricating efficient 2T tandem cells is obtaining a high balanced J_{sc} . Figure 3C displays the simulation results of the dependence of tandem cell J_{sc} versus the thicknesses of the two active layers. On the basis of the optical simulation, the best J_{sc} would be achieved with thicknesses of the optimized front and rear subcell active layers of ~200 and ~120 nm, respectively. The detailed photovoltaic results for difference thicknesses of subcells are summarized in Table 1 and fig. S8 and discussed in the supplementary materials. The tandem cells all showed a V_{oc} of ~1.64 V, approximately equal to the sum of the individual V_{oc} 's of the subcells, indicating an optimal interconnecting layer with good ohmic contact (20), whereas the J_{sc} and FF depended on the thickness of the subcells. Overall, the devices all showed excellent performance

with PCEs above 15%. As shown in Fig. 3D and Table 1, the optimized 2T tandem cells gave a PCE of 17.36%, with a V_{oc} of 1.642 V, J_{sc} of 14.35 mA/cm², and FF of 73.7%, verified by the National Center of Supervision and Inspection on Solar Photovoltaic Products Quality of China (CPVT) with a measured PCE value of 17.29% (fig. S9). It is worth noting that the optimized tandem cell performance is well reproduced with a standard deviation (SD) of 0.29% of PCEs based on >50 devices with an average value of 16.89%, which is close to the best result (17.36%) (fig. S10).

The EQE of the tandem cell was measured following the protocol proposed in (34), and the results (Fig. 3E) show high values with an average of 72% in the absorption range from 300 to 1000 nm. The front cell showed a high EQE response in the range of 300 to 720 nm with a maximum EQE value of 76% at ~560 nm. The rear subcell absorbs mainly the low-energy photons (from ~720 to 1050 nm) with a strong EQE response of ~70% in the range of 740 to 940 nm, and the rear cell gave an integrated J_{sc} of 14.19 mA/cm², which closely matches the integrated J_{sc} (14.20 mA/cm²) of the front cell. The high and balanced J_{sc} of the two subcells is attributed to their complementary absorptions and high-efficiency photoresponse. The tandem cells without the secondary acceptor PC₇₁BM in the rear cell were also studied but gave PCEs below 16%, owing to the relatively low current and FF , which is probably caused by the

weaker absorption and lower EQE values in the range of 900 to 1050 nm (fig. S11). This is consistent with earlier results (4, 31) and probably due to the morphology difference in the active layer caused by adding PC₇₁BM (see details in the supplementary materials).

The optimal J_{sc} obtained was ~14.3 mA/cm², which is still less than 15.5 mA/cm² predicted for the best tandem cell with absorption onset up to 1050 nm. Clearly, an important reason for this is the effective absorption of only up to ~985 nm (Fig. 3E) versus the required best absorption of 1050 nm. Also the average (~72%) EQE is still lower than the 75% used in the analysis shown in Fig. 1B. Furthermore, the V_{oc} obtained for our tandem cell is ~1.64 V and nearly equal to the sum of the V_{oc} 's of the two subcells. However, it represents 73% of the theoretical value (35), corresponding to a substantial E_{loss} (0.71 and 0.51 eV, or an average of 0.61 eV) of the front and rear cells, respectively. Together with recent results showing E_{loss} for some OPV cells as small as 0.45 eV E_{loss} (26), considerable improvement is expected for reducing E_{loss} through methods such as morphological or interfacial engineering in addition to the optimization of materials (36–39). Considering the bigger impact of E_{loss} on the overall performance as discussed previously (23, 30), reducing E_{loss} should be a focus of future work. The tandem cell FF in this work is as high as 74%, also slightly higher than that of the

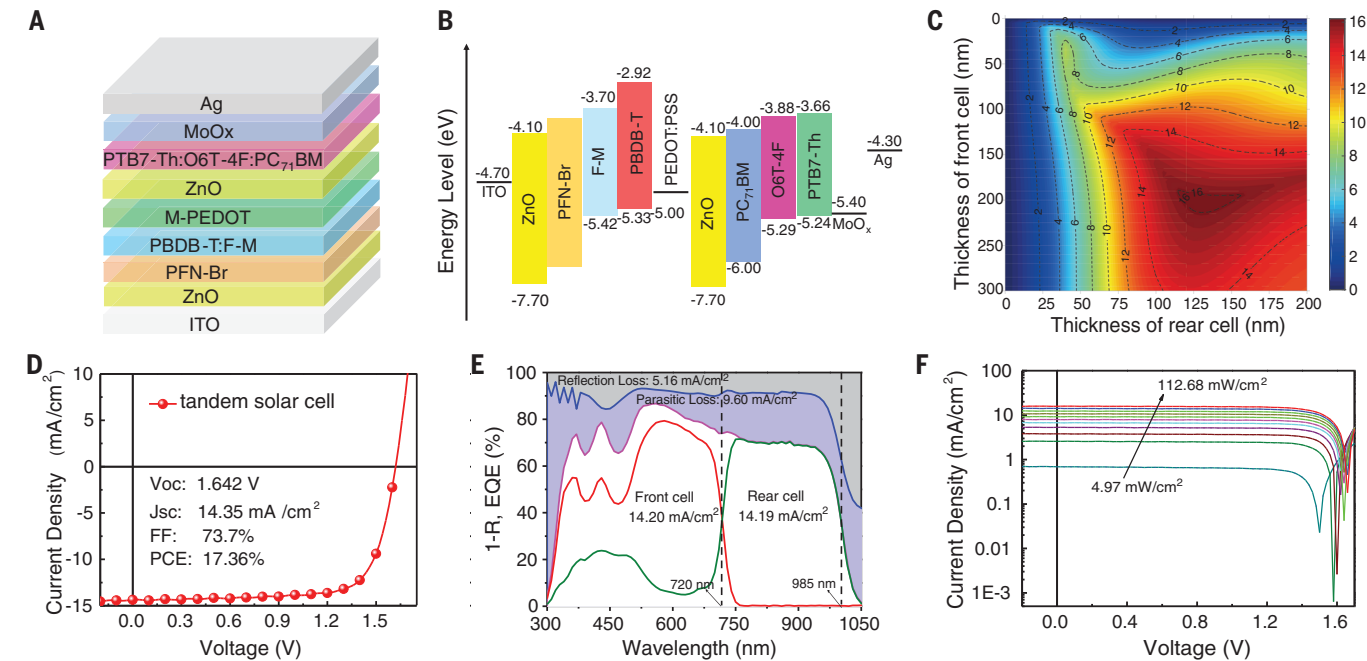


Fig. 3. Optical simulation and photovoltaic performance of the tandem cells. (A) Device architecture of the tandem cell. (B) Energy level diagram of the tandem solar cell. (C) Simulated current density generated in a tandem cell as a function of the thicknesses of the active layers. (D) J-V curve. (E) EQE and 1-reflectance (1-R) of the optimized tandem solar cell

and (F) J-V curve of the tandem cells under different light intensities, ranging from 4.97 to 112.68 mW/cm². The dashed vertical line at 720 nm in (E) is the cross point of the EQE plots of the two subcells, and the dashed vertical line at 985 nm indicates the effective absorption up position (assuming 50% EQE) of the rear subcell.

Table 1. 2T tandem cell performance with different thicknesses of the subcells. Results are shown as the mean \pm SD. Values in parentheses denote the best optimal results.

Thickness (nm)		V_{oc} (V)	J_{sc} (mA/cm ²)	FF (%)	PCE (%)
Front cell	Rear cell				
120	110	1.646 \pm 0.008 (1.646)	13.11 \pm 0.23 (13.32)	73.0 \pm 0.6 (73.2)	15.75 \pm 0.03 (16.05)*
135	110	1.634 \pm 0.005 (1.645)	13.76 \pm 0.27 (13.85)	71.2 \pm 1.1 (71.6)	16.01 \pm 0.35 (16.31)*
150	110	1.636 \pm 0.014 (1.642)	14.32 \pm 0.18 (14.35)	72.1 \pm 1.4 (73.7)	16.89 \pm 0.29 (17.36)†
165	110	1.630 \pm 0.012 (1.644)	14.21 \pm 0.18 (14.37)	68.3 \pm 1.2 (69.1)	15.82 \pm 0.29 (16.32)*
180	110	1.631 \pm 0.010 (1.636)	14.14 \pm 0.25 (14.34)	64.9 \pm 1.2 (65.9)	14.97 \pm 0.32 (15.46)*
150	125	1.635 \pm 0.007 (1.626)	14.08 \pm 0.21 (14.19)	69.9 \pm 1.1 (70.1)	16.09 \pm 0.20 (16.17)*
150	90	1.630 \pm 0.010 (1.636)	14.03 \pm 0.28 (14.00)	69.1 \pm 0.8 (69.6)	15.80 \pm 0.22 (15.94)*

*The average parameters were calculated from more than 20 devices. †The average parameters were calculated from 84 devices, and the area of the devices studied under the optimization condition is \sim 4 mm².

two subcells with a FF of \sim 70%, indicating that the reduced charge recombination in the tandem cell suppressed the carrier dynamics loss (19), but still lower than the best FF (80%) achieved (25) and theoretical values (85 to 94%) for devices with a bandgap between 1.0 and 3.0 eV (35). The performance of the optimized tandem cells was also measured under different illumination intensities, from 0.05 to 1.12 sun (Fig. 3F and fig. S12). The PCEs of the tandem cells remain above 15% when the light intensity varies from 4.97 to 112.68 mW/cm², and a PCE of 17.87% has been achieved at a light intensity of 25.99 mW/cm². In addition, the tandem cells show good stability behavior, with only a minor performance degradation of 4% after continuous testing for

166 days (fig. S13). Furthermore, we also fabricated tandem cells with large areas, and the preliminary results (table S14) show good performance even at sizes up to 100 mm². The much better PCE of 17.36% compared with the semi-empirical analysis provided, indicate that OPV tandem cells have a greater potential than previously thought, and a PCE $>$ 25% should be attainable with the already achieved best EQE of 80% (3), E_{loss} of 0.45 eV (26), and FF of 0.75 (25). Considering its other advantages, OPV should be competitive with other solar cell technologies for industry applications in the future if the issue of OPV stability can be addressed.

REFERENCES AND NOTES

1. M. C. Scharber, N. S. Saricicci, *Prog. Polym. Sci.* **38**, 1929–1940 (2013).
2. A. Polman, M. Knight, E. C. Garnett, B. Ehrler, W. C. Sinke, *Science* **352**, aad4424 (2016).
3. J. Hou, O. Inganäs, R. H. Friend, F. Gao, *Nat. Mater.* **17**, 119–128 (2018).
4. Z. Xiao, X. Jia, L. Ding, *Sci. Bull.* **62**, 1562–1564 (2017).
5. K. Yoshikawa et al., *Nat. Energy* **2**, 17032 (2017).
6. W. S. Yang et al., *Science* **348**, 1234–1237 (2015).
7. Q. Burlingame et al., *Nature* **554**, 77–80 (2018).
8. U. Würfel, D. Neher, A. Spies, S. Albrecht, *Nat. Commun.* **6**, 6951 (2015).
9. A. D. Vos, *J. Phys. D Appl. Phys.* **13**, 839–846 (1980).
10. G. Li, W.-H. Chang, Y. Yang, *Nat. Rev. Mater.* **2**, 17043 (2017).
11. Y. Cui et al., *J. Am. Chem. Soc.* **139**, 7302–7309 (2017).
12. W. Li, A. Furlan, K. H. Hendriks, M. M. Wien, R. A. Janssen, *J. Am. Chem. Soc.* **135**, 5529–5532 (2013).
13. N. Li, C. J. Brabec, *Energy Environ. Sci.* **8**, 2902–2909 (2015).

14. M. Li *et al.*, *Nat. Photonics* **11**, 85–90 (2017).
15. J. Y. Kim *et al.*, *Science* **317**, 222–225 (2007).
16. P. Cheng, G. Li, X. Zhan, Y. Yang, *Nat. Photonics* **12**, 131–142 (2018).
17. Y. J. Cheng, S. H. Yang, C. S. Hsu, *Chem. Rev.* **109**, 5868–5923 (2009).
18. Z. B. Henson, K. Müllen, G. C. Bazan, *Nat. Chem.* **4**, 699–704 (2012).
19. L. Zuo *et al.*, *Adv. Mater.* **30**, 1706816 (2018).
20. T. Ameri, N. Li, C. J. Brabec, *Energy Environ. Sci.* **6**, 2390–2413 (2013).
21. W. Shockley, H. J. Queisser, *J. Appl. Phys.* **32**, 510–519 (1961).
22. G. Dennler *et al.*, *Adv. Mater.* **20**, 579–583 (2008).
23. S. Matthew Menke, A. Niva, *Joule* **2**, 25–35 (2018).
24. Z. He *et al.*, *Nat. Photonics* **9**, 174–179 (2015).
25. X. Guo *et al.*, *Nat. Photonics* **7**, 825–833 (2013).
26. Z. Yao *et al.*, *J. Am. Chem. Soc.* **140**, 2054–2057 (2018).
27. J. Liu *et al.*, *Nat. Energy* **1**, 16089 (2016).
28. Q. Zhang *et al.*, *Nat. Photonics* **9**, 35–41 (2015).
29. Y. Chen, X. Wan, G. Long, *Acc. Chem. Res.* **46**, 2645–2655 (2013).
30. J. Benduhn *et al.*, *Nat. Energy* **2**, 17053 (2017).
31. Z. Xiao *et al.*, *Sci. Bull.* **62**, 1494–1496 (2017).
32. Y. Zhang *et al.*, *Adv. Mater.* **30**, 1707508 (2018).
33. G. F. Burkhard, E. T. Hoke, M. D. McGehee, *Adv. Mater.* **22**, 3293–3297 (2010).
34. R. Timmreck *et al.*, *Nat. Photonics* **9**, 478–479 (2015).
35. S. Rühle, *Sol. Energy* **130**, 139–147 (2016).
36. Y. Huang, E. J. Kramer, A. J. Heeger, G. C. Bazan, *Chem. Rev.* **114**, 7006–7043 (2014).
37. Z. A. Page, Y. Liu, V. V. Duzhko, T. P. Russell, T. Emrick, *Science* **346**, 441–444 (2014).
38. Z. Wu *et al.*, *J. Am. Chem. Soc.* **138**, 2004–2013 (2016).
39. H. Bin *et al.*, *Nat. Commun.* **7**, 13651 (2016).

ACKNOWLEDGMENTS

Funding: We gratefully acknowledge the financial support from MoST (2014CB643502, 2016YFA0200200, 2017YFA0206600), NSFC (51773095, 91633301) of China, and Tianjin City (17JCJC44500, 17JCZDJC31100). **Author contributions:** Y.C. and X.W. conceived and directed the study. L.M. fabricated and characterized the tandem cells, and Y.Z. fabricated and evaluated the

single-junction devices. O6T-4F was provided by L.D. and Z.X.; X.Z. and Y.W. synthesized the other materials. R.X. and H.Y. carried out the n , k measurement, and X.K. carried out the simulation of the tandem cell with different subcell thicknesses. The manuscript was mainly prepared by Y.C., L.M., X.W., and C. L., and all authors participated in the manuscript preparation and commented on the manuscript. **Competing interests:** The authors declare no competing interests; **Data and materials availability:** All data are available and presented in the main text and the supplementary materials. We have applied for a patent for this work.

SUPPLEMENTARY MATERIALS

www.sciencemag.org/content/361/6407/1094/suppl/DC1
Materials and Methods
Figs. S1 to S13
Tables S1 to S14
References (40–49)

23 March 2018; accepted 25 June 2018
Published online 9 August 2018
10.1126/science.aat2612

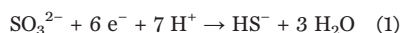
ENZYME DESIGN

A designed heme-[4Fe-4S] metalloenzyme catalyzes sulfite reduction like the native enzyme

Evan N. Mirts¹, Igor D. Petrik², Parisa Hosseinzadeh³, Mark J. Nilges⁴, Yi Lu^{1,2,3,5,6,7*}

Multielectron redox reactions often require multifactor metalloenzymes to facilitate coupled electron and proton movement, but it is challenging to design artificial enzymes to catalyze these important reactions, owing to their structural and functional complexity. We report a designed heteronuclear heme-[4Fe-4S] cofactor in cytochrome *c* peroxidase as a structural and functional model of the enzyme sulfite reductase. The initial model exhibits spectroscopic and ligand-binding properties of the native enzyme, and sulfite reduction activity was improved—through rational tuning of the secondary sphere interactions around the [4Fe-4S] and the substrate-binding sites—to be close to that of the native enzyme. By offering insight into the requirements for a demanding six-electron, seven-proton reaction that has so far eluded synthetic catalysts, this study provides strategies for designing highly functional multifactor artificial enzymes.

The presence of sulfite in the environment inhibits bioremediation of pervasive, toxic oxyanions such as (per)chlorate, arsenate, and nitrate (1) that are chemically challenging to reduce and have low binding affinity to transition metals. Bioinspired artificial catalysts have been developed to reduce nitrate and perchlorate (2), but sulfite reduction remains inaccessible to synthetic catalysts. As a result, complete oxyanion remediation has so far been accomplished only via biofilms undergoing anaerobic respiration (3, 4)



Sulfite reduction to sulfide (Eq. 1) is accomplished to completion by assimilatory sulfite reductase (SiR), which contains a structurally complex cofactor composed of a heme macrocycle (siroheme) and a cubane [4Fe-4S] cluster (5) bridged by a cysteine residue that serves as

both the proximal ligand to the siroheme and a ligand to one Fe atom of the [4Fe-4S] cluster (Fig. 1). The [4Fe-4S] cluster is proposed to act as a molecular battery that facilitates electron transfer to the heme, enabling sequential 2e⁻ reduction (6), even though the precise role it plays in catalysis and tuning siroheme reactivity is not understood. Two synthetic models of the heme-[4Fe-4S] cofactor have been reported but lacked activity (7, 8). These models did not include elements of the SiR substrate-binding pocket, which is rich in positively charged residues thought to facilitate binding and protonation of the substrate concurrent with electron transfer and proposed to be required for activity (9, 10). Designing artificial enzymes that include mononuclear or homonuclear metal-binding sites has been successful in generating catalysts (11–17); however, designed enzymes have rarely recapitulated the complex heteronuclear metal centers responsible for multi-electron, multiproton reactions. Here we report

success in replicating both structural and functional elements of SiR by designing a [4Fe-4S] cluster proximal to the heme center in cytochrome *c* peroxidase (CcP). By rationally building secondary sphere interactions in the metal- and substrate-binding sites, we increased the sulfite reductase activity of this artificial metalloenzyme to approach the activity of a native SiR.

We chose CcP, a native heme-binding protein, as a protein scaffold because of its small size and stability. Furthermore, we found that its active site contains a cavity on the heme proximal face large enough to host a [4Fe-4S] cluster (figs. S1 and S2). This heme proximal cavity was essential in discriminating among suitable hemoprotein scaffolds, as described in the supplementary materials (fig. S3). We then used the Rosetta matcher and enzyme design algorithms (11) to select residues to mutate to Cys to coordinate the [4Fe-4S], resulting in mutation of four residues (His, Thr, Tyr, and Leu) to Cys [His¹⁷⁵→Cys (H175C), T180C, W191C, and L232C] (Fig. 1) and two additional mutations for stability: M230A (M, Met; A, Ala), made to relieve steric clash, and D235V (D, Asp; V, Val), made to remove the nearby negative charge previously reported to interfere with Cys-heme coordination in CcP (18) (fig. S4). The computational model of this sextuple mutant CcP (called SiRCCcP.1) is a close structural match for the cofactor-binding site in native SiR (fig. S5) and was readily expressed in the cofactor-free apo form (figs. S6 and S7).

We incorporated an iron-sulfur cluster into apo-SiRCCcP.1 by in vitro reconstitution, and we

¹Center for Biophysics and Quantitative Biology, University of Illinois at Urbana-Champaign, Urbana, IL 61801, USA. ²Department of Chemistry, University of Illinois at Urbana-Champaign, Urbana, IL 61801, USA. ³Department of Biochemistry, University of Illinois at Urbana-Champaign, Urbana, IL 61801, USA. ⁴School of Chemical Sciences Electron Paramagnetic Resonance Lab, University of Illinois at Urbana-Champaign, Urbana, IL 61801, USA. ⁵Carl R. Woese Institute for Genomic Biology, University of Illinois at Urbana-Champaign, Urbana, IL 61801, USA. ⁶DOE Center for Advanced Bioenergy and Bioproducts Innovation, University of Illinois at Urbana-Champaign, Urbana, IL 61801, USA. ⁷Pacific Northwest National Laboratory, Richland, WA 99352, USA.

*Corresponding author. Email: yi-lu@illinois.edu

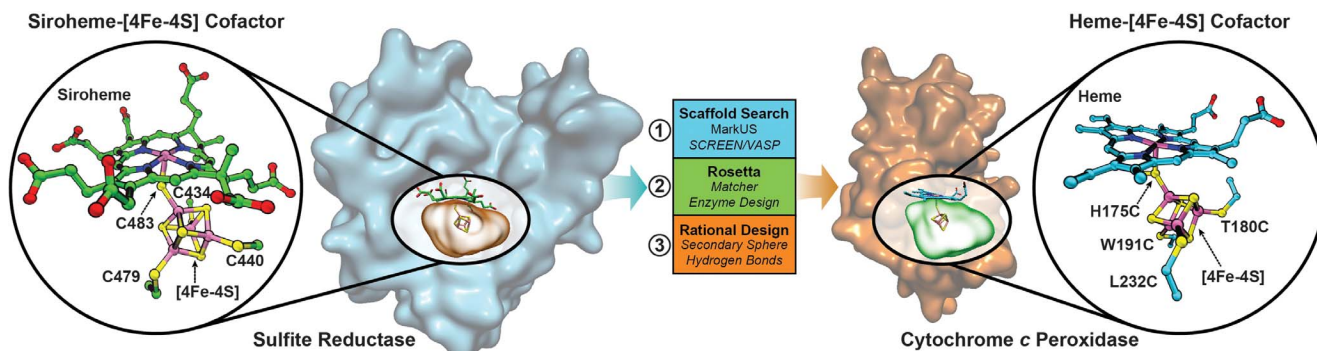


Fig. 1. Design of a [4Fe-4S] binding site in CcP to mimic the heme-[4Fe-4S] center in native SiR. From left to right: A search structure generated from the binding cavity of the [4Fe-4S] in the siroheme-[4Fe-4S] cofactor from the hemoprotein subunit of native *Escherichia coli* SiR [Protein Data Bank (PDB) ID 2GEP] (9) was used to search the PDB for suitable hemoprotein scaffolds. Yeast CcP was identified as a suitable

scaffold, and a binding site for a heme-[4Fe-4S] cofactor was designed by a combination of computational and rational design methods. The resulting computational model of the designed heme-[4Fe-4S] center in SiRCCcP.1 is shown on the right. Three Cys mutations (T180C, W191C, L232C) coordinate Fe atoms, and the H175C mutation acts as a bridging Cys ligand between the heme and [4Fe-4S] cofactors.

hereafter refer to this protein as FeS-SiRCcP.1. We characterized FeS-SiRCcP.1 by ultraviolet (UV)-visible absorption, electron paramagnetic resonance (EPR), and extended x-ray absorption fine structure (EXAFS) spectroscopies. These characterization methods of both the oxidized and reduced states indicate proper incorporation of a [4Fe-4S] cluster, as designed (19, 20) (Fig. 2, A and B, and figs. S8 to S11). Elemental analysis for Fe and S in FeS-SiRCcP.1 matched well with the Fe and S content expected at full [4Fe-4S] incorporation (4 Fe:14 S, accounting for inorganic S and all S atoms in Cys and Met residues) with a ratio of 4.00 Fe:14.01 S observed experimentally.

In addition to the [4Fe-4S], a heme cofactor is required to complete the SiR catalyst, and we found that heme-*b*, the native heme cofactor of

CcP, could be incorporated into FeS-SiRCcP.1 in vitro, similarly to native CcP. We call this double-cofactor form heme-FeS-SiRCcP.1 (Fig. 2C). Elemental analysis of heme-FeS-SiRCcP.1 yielded 5.54 Fe per heme, confirming that the [4Fe-4S] remains intact following heme reconstitution. Heme-FeS-SiRCcP.1 displayed key spectroscopic features and ligand-binding properties of thiol-ligated hemoproteins and even native SiR (Fig. 2, C and D, and figs. S12 to S14) (21–23). Notably, heme³⁺-FeS²⁺-SiRCcP.1 has low affinity for the cyanide anion (CN[−]), requiring ~2000 equivalents, whereas 1e[−] reduced heme²⁺-FeS²⁺-SiRCcP rapidly binds roughly one equivalent of CN[−] (Fig. 2C). This behavior has been reported for SiR (24) but not for most other hemoproteins, including CcP, which suggests that our designed SiRCcP.1 substantially alters the heme character of the

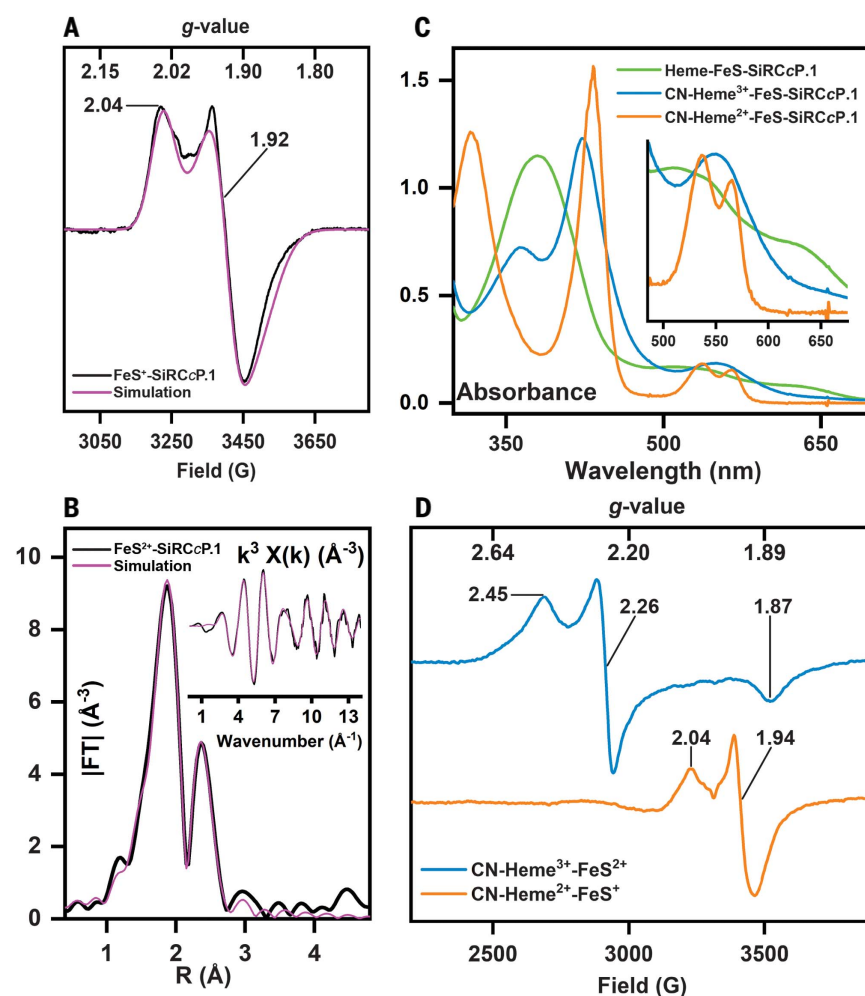
native scaffold protein without altering the heme chemical structure. The presence of the positively charged [4Fe-4S] could screen the increased negative charge in ferrous heme that tends to weaken the CN-Fe²⁺ interaction in hemoproteins, but we also observed higher CN[−] affinity in heme²⁺-SiRCcP.1 with no reconstituted [4Fe-4S]. Therefore, local electrostatic effects, perhaps related to removal of the proximal His-Asp-Trp peroxidase triad in SiRCcP.1 (fig. S2), or changes in heme conformation that affect σ acceptance and π back-donation must also play a role (25–27).

We measured the sulfite reductase activity of heme-FeS-SiRCcP.1 by the rate of oxidation of the electron mediator methyl viologen (MV⁺) in the presence of sodium sulfite using a protocol previously reported for native SiR (28). Heme-FeS-SiRCcP.1 oxidizes MV⁺ at a rate of 0.348

Fig. 2. Spectroscopic properties of SiRCcP.1 with [4Fe-4S], heme, and heme-[4Fe-4S] cofactors confirm binding of [4Fe-4S] and heme-[4Fe-4S] cofactors. (A) X-band EPR spectrum of FeS-SiRCcP.1 reduced with an excess of sodium dithionite (black) and simulated spectrum (magenta) indicating an $S = \frac{1}{2}$ species consistent with a [4Fe-4S]²⁺:

$g_x = 1.891$, $g_y = 1.919$, $g_z = 2.035$; linewidths (G) $A_x = 42$, $A_y = 27$, $A_z = 25$. The spectrum shown was measured at a frequency of 9.173 GHz and modulation amplitude of 10 Gauss; a microwave power of 10 mW, and a temperature of 15 K. No paramagnetic species at $g = 2$ are observed before reduction, suggesting a [4Fe-4S]²⁺ ($S = 0$) state as prepared (oxidized). A [3Fe-4S]⁺ species could be generated by reoxidation of the reduced species with an excess of potassium ferricyanide (fig. S10).

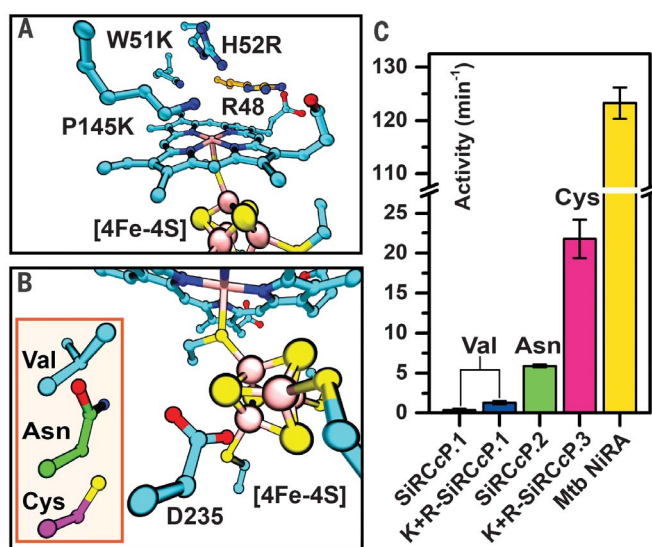
(B) Magnitude of the phase-uncorrected k^3 -weighted Fourier transform (FT) and EXAFS (inset) of the Fe K-edge spectra for FeS²⁺-SiRCcP.1 (black) and the best fit (magenta). The EXAFS spectrum is consistent with a symmetrical cubane structure (three scattering Fe atoms per absorber Fe and four scattering S atoms in the first coordination shell). Fitting parameters are provided in table S1, and the EXAFS of FeS²⁺-SiRCcP.1 are plotted in fig. S11. R, scattering shell distance. (C) UV-visible spectra of FeS-reconstituted SiRCcP.1 (FeS-SiRCcP.1) and heme-FeS-reconstituted SiRCcP.1 (heme-FeS-SiRCcP.1) in the presence and absence of potassium cyanide. As prepared, FeS-SiRCcP.1 has weak, broad absorption at 400 nm, which decreases upon reduction (fig. S9). Ferric heme-FeS-SiRCcP.1 has a blue-shifted Soret peak (378 nm) relative to that of native CcP (408 nm) and exhibits a Soret maximum and Q-bands (inset) consistent with penta-coordinate, thiolate-ligated high-spin ferriheme. The ferrous heme-FeS-SiRCcP.1 spectrum obtained by incubation with sodium dithionite (fig. S12) is distinct from the species obtained by photoreduction (fig. S13) and is identical to the spectrum of heme²⁺-FeS²⁺-SiRCcP.1 incubated with sulfite under nonturnover conditions (fig. S14), indicating sulfite-bound hexacoordinate ferroheme. The photoreduced spectrum (fig. S13) represents the ferrous pentacoordinate species. (D) X-band EPR spectra of



heme-FeS-SiRCcP.1 in the presence of cyanide. CN-heme³⁺-FeS²⁺-SiRCcP.1 is predominantly low-spin ferric heme ($g_x = 1.87$, $g_y = 2.26$, $g_z = 2.45$) with no visible [4Fe-4S] features. In the all-ferrous state, heme features disappear (presumably $S = 0$ ferrous heme) while the $S = \frac{1}{2}$ [4Fe-4S] feature reappears. Similar behavior has been reported for CN-bound SiR. EPR spectra were measured at 18 K with a microwave power of 10 mW at a frequency of 9.24 GHz.

Fig. 3. Sulfite reduction activity of SiRCcP mutants is modulated by substrate binding and [4Fe-4S] secondary sphere mutations.

(A) Computational model of the SiRCcP substrate-binding site with mutations W51K, H52R, and P145K (cyan) made to mimic native SiR residues K217, R153, and K215, respectively (fig. S15). The native CcP residue R48 (orange) is positioned similarly to R83 in native SiR. (B) Computational model of the mutations D235V (SiRCcP.1, cyan), D235N (SiRCcP.2, green), and D235C (SiRCcP.3, magenta) in SiRCcP. (C) Sulfite reduction activity of four SiRCcP mutants in comparison to a native sulfite reductase from *M. tuberculosis* (Mtb NiRA). “K+R” denotes the presence of the three mutations W51K, H52R, and P145K. Reported activities represent the average of triplicate measurements with standard error (see table S2).



(± 0.15) min^{-1} , whereas wild-type CcP displayed no measurable activity above background. Similarly, the rate by heme-FeS-SiRCcP.1 was nominally zero in the absence of sulfite. The initial design that incorporated the heme-[4Fe-4S] cofactor (SiRCcP.1), therefore, showed notable sulfite reduction activity compared with its native scaffold protein but far less than a native SiR, indicating that a heme-[4Fe-4S] cofactor alone is insufficient to promote rapid sulfite reduction. To improve activity, we sought to systematically examine the key features of native SiR active sites and determine which had the greatest impact on catalysis. Lys and Arg residues are conserved in SiR and are thought to be important for substrate binding and catalysis (9, 10) (fig. S15A). Therefore, we introduced analogous W51K, H52R, and P145K (K, Lys; R, Arg; P, Pro) mutations to SiRCcP.1, which, when combined with the native CcP residue Arg⁴⁸, form a positively charged cavity that resembles SiR (Fig. 3A and fig. S15B). The reductase activity of the resulting mutant, W51K/H52R/P145K-SiRCcP.1, is $1.26 \pm 0.20 \text{ min}^{-1}$, 5.3-fold greater than that of SiRCcP.1.

In proteins, [4Fe-4S] clusters are stabilized by backbone and amino acid side-chain interactions in the secondary coordination sphere (29, 30). The crystal structures of SiRs reveal several side-chain hydrogen bond donors to inorganic S atoms, such as the amino group of N481 (N, Asn) in *E. coli* SiR (fig. S16A). We sought to increase the activity of SiRCcP by adding similar stabilizing interactions to the [4Fe-4S] cluster secondary coordination sphere by mutating residue D235—whose functional group is oriented toward the [4Fe-4S] in SiRCcP in a position similar to N481 in SiR—to Asn and Cys based on important secondary sphere residues in various [4Fe-4S] centers (29). We found that the D235N mutation (called SiRCcP.2) (Fig. 3B and fig. S16B) increased activity to $5.91 \pm$

1.6 min^{-1} , 4.3-fold greater than that of W51K/H52R/P145K-SiRCcP.1 (a 17-fold increase over SiRCcP.1). We achieved an even greater increase in activity with the D235C mutant (called SiRCcP.3) (Fig. 3B), which, when combined with the substrate-binding site mutations given above (W51K/H52R/P145K-SiRCcP.3), exhibited sulfite reduction activity of $21.8 (\pm 2.4) \text{ min}^{-1}$, a 63-fold increase over that of SiRCcP.1 (fig. S17 and table S2). We compared these rates to a native dissimilatory SiR, NiRA from *Mycobacterium tuberculosis* (Mtb NiRA) (28), whose activity has been reported under comparable reaction conditions, and found that the activity of W51K/H52R/P145K-SiRCcP.3 is ~18% of a native SiR's activity (Fig. 3C and table S2). Assimilatory SiRs have been observed to reduce sulfite to sulfide with minimal side products, but dissimilatory SiRs typically achieve far less than 50% efficiency in vitro. We quantified sulfide as well as the side products trithionate ($\text{S}_3\text{O}_6^{2-}$) and thiosulfate ($\text{S}_2\text{O}_3^{2-}$) produced with sulfite as the substrate. Sulfide was quantified by methylene blue formation, and we found that ~10% of the products formed in the reaction were hydrogen sulfide (the six-electron reduction product), with the remainder being primarily the two- and four-electron-reduced side products in a distribution similar to native dissimilatory SiR. Together, these products account for more than 90% of the electron donors consumed (figs. S18 and S19). The product conversion efficiency of W51K/H52R/P145K-SiRCcP.3 is therefore similar to the efficiency of a natural dissimilatory SiR (31). SiRCcP is thus both a close structural model and a substantially active functional model of SiR capable of complete six-electron and seven-proton sulfite reduction.

Our progressive optimization of SiRCcP revealed structural features beyond the metallo-cofactor required for efficient multielectron

reduction of an oxyanion, including secondary sphere interactions such as hydrogen bonding to the [4Fe-4S] (through D235V/N/C mutations) and residues that may promote substrate binding and protonation (through W51K, H52R, and P145K mutations). Models that did not incorporate these features had diminished activity, and the necessity of these secondary interactions in our SiRCcP model has important implications for optimizing design strategies to achieve high activity in multielectron redox reactions with artificial enzymes, a process simplified and accelerated in this study by cavity-based scaffold selection. Furthermore, the SiRCcP enzyme is functional with the heme-*b* cofactor present in native CcP instead of the biologically distinct siroheme in SiR, suggesting that siroheme is not absolutely required for sulfite reduction. These insights, combined with the ability to recapitulate a complex multielectron, multiproton delivery system in a simple, stable scaffold, suggest a strategy to design highly active catalysts for other difficult oxyanion reduction and multielectron reactions that may be broadly applicable.

REFERENCES AND NOTES

- G. T. Townsend, J. M. Sulista, *Appl. Environ. Microbiol.* **63**, 3594–3599 (1997).
- C. L. Ford, Y. J. Park, E. M. Matson, Z. Gordon, A. R. Fout, *Science* **354**, 741–743 (2016).
- J. Chung, B. E. Rittmann, W. F. Wright, R. H. Bowman, *Biodegradation* **18**, 199–209 (2007).
- J. F. Stolz, R. S. Oremland, *FEMS Microbiol. Rev.* **23**, 615–627 (1999).
- B. R. Crane, L. M. Siegel, E. D. Getzoff, *Science* **270**, 59–67 (1995).
- M. Surduncan, S. V. Makarov, R. Silaghi-Dumitrescu, *Eur. J. Inorg. Chem.* **2014**, 5827–5837 (2014).
- L. Cai, R. H. Holm, *J. Am. Chem. Soc.* **116**, 7177–7188 (1994).
- C. Zhou, L. Cai, R. H. Holm, *Inorg. Chem.* **35**, 2767–2772 (1996).
- B. R. Crane, L. M. Siegel, E. D. Getzoff, *Biochemistry* **36**, 12120–12137 (1997).
- K. W. Smith, M. E. Stroupe, *Biochemistry* **51**, 9857–9868 (2012).
- J. B. Siegel *et al.*, *Science* **329**, 309–313 (2010).
- T. K. Hyster, L. Knörr, T. R. Ward, T. Rovis, *Science* **338**, 500–503 (2012).
- M. L. Zastrow, A. F. A. Peacock, J. A. Stuckey, V. L. Pecoraro, *Nat. Chem.* **4**, 118–123 (2012).
- I. D. Petrik, J. Liu, Y. Lu, *Curr. Opin. Chem. Biol.* **19**, 67–75 (2014).
- Y. Yu *et al.*, *J. Am. Chem. Soc.* **137**, 11570–11573 (2015).
- N. F. Polizzi *et al.*, *Nat. Chem.* **9**, 1157–1164 (2017).
- F. Schwoyer *et al.*, *Chem. Rev.* **118**, 142–231 (2018).
- J. A. Sigman, A. E. Pond, J. H. Dawson, Y. Lu, *Biochemistry* **38**, 11122–11129 (1999).
- D. C. Johnson, D. R. Dean, A. D. Smith, M. K. Johnson, *Annu. Rev. Biochem.* **74**, 247–281 (2005).
- S. E. Mulholland, B. R. Gibney, F. Rabanal, P. L. Dutton, *J. Am. Chem. Soc.* **120**, 10296–10302 (1998).
- P. A. Janick, L. M. Siegel, *Biochemistry* **21**, 3538–3547 (1982).
- A. Luthra, I. G. Denisov, S. G. Sligar, *Arch. Biochem. Biophys.* **507**, 26–35 (2011).
- P. A. Janick, L. M. Siegel, *Biochemistry* **22**, 504–515 (1983).
- R. J. Krueger, L. M. Siegel, *Biochemistry* **21**, 2905–2909 (1982).
- A. Boffi, A. Ilari, C. Spagnuolo, E. Chiancone, *Biochemistry* **35**, 8068–8074 (1996).
- K. S. Reddy *et al.*, *Biochemistry* **35**, 5562–5570 (1996).
- J. Li, B. C. Noll, C. E. Schulz, W. R. Scheidt, *Angew. Chem. Int. Ed.* **48**, 5010–5013 (2009).
- R. Schnell, T. Sandalova, U. Hellman, Y. Lindqvist, G. Schneider, *J. Biol. Chem.* **280**, 27319–27328 (2005).
- B. W. Beck, Q. Xie, T. Ichiiye, *Biophys. J.* **81**, 601–613 (2001).
- A. Dey *et al.*, *Science* **318**, 1464–1468 (2007).
- B. R. Crane, E. D. Getzoff, *Curr. Opin. Struct. Biol.* **6**, 744–756 (1996).

ACKNOWLEDGMENTS

We thank R. Schnell from Karolinska Institutet (Stockholm, Sweden) for providing plasmids used to express the native SiR from *M. tuberculosis* (Mtb NiRA), T. B. Rauchfuss and A. R. Fout for helpful discussions, and Y. Lee for assistance with collecting enzyme activity data. X-ray absorption studies were conducted at the Stanford Synchrotron Radiation Lightsource at the SLAC National Accelerator Laboratory, and we thank beamline scientists M. Latimer and E. Nelson for their assistance. All work reported here was conducted at the University of Illinois at Urbana-Champaign. **Funding:** The work described in this paper is supported by the U.S. National Institutes of Health (R01-GM062211 to Y.L. and predoctoral training grant 5T32-GM827625 to E.N.M.). This work is also partially funded by the U.S. Department of Energy's Center for Advanced Bioenergy and Bioproducts Innovation (Office of Science, Office of Biological and Environmental Research, under DE-SC0018420). Any opinions, findings, and conclusions or recommendations expressed in this publication are those of the author(s) and do not necessarily reflect the views of the U.S. Department of Energy. Use of the Stanford Synchrotron Radiation Lightsource, SLAC National Accelerator Laboratory, is supported by the U.S. Department of Energy, Office of Science, Office of Basic

Energy Sciences under contract DE-AC02-76SF00515. The SSRL Structural Molecular Biology Program is supported by the DOE Office of Biological and Environmental Research, and by the National Institutes of Health, National Institute of General Medical Sciences (including P41GM103393). The contents of this publication are solely the responsibility of the authors and do not necessarily represent the official views of NIGMS or NIH. **Author contributions:** E.N.M., P.H., and Y.L. conceptualized the project; E.N.M. and I.D.P. conducted computational investigations; E.N.M. and P.H. conducted experimental investigations and data analyses; E.N.M. and M.J.N. conducted EPR analyses; E.N.M. created data visualizations; Y.L. was responsible for project supervision, direction, resource acquisition, and data analyses and interpretation; E.N.M. drafted the original manuscript; and E.N.M., I.D.P., P.H., M.J.N., and Y.L. edited and reviewed the manuscript. **Competing interests:** E.N.M., P.H., and Y.L. are inventors on patent application 62/702,940, submitted by University of Illinois at Urbana-Champaign, that covers artificial metalloproteins as biocatalysts for sulfite reduction. I.D.P. is currently affiliated with the Bioinformatics Department, Ambry Genetics; P.H. is currently affiliated with the Department of Biochemistry and Institute for Protein Design, University of Washington; and Y.L. is also affiliated

with the Department of Bioengineering, Materials Science and Engineering, and Beckman Institute for Advanced Science and Technology, University of Illinois at Urbana-Champaign. **Data and materials availability:** All data are available in the main text or supplementary materials. All SiRCcP variants described in this Report (SiRCcP.1, SiRCcP.2, and SiRCcP.3 and their W51K/H52R/P145K variants, as described in the main text) are available from the University of Illinois at Urbana-Champaign under a material transfer agreement with the university.

SUPPLEMENTARY MATERIALS

www.sciencemag.org/content/361/6407/1098/suppl/DC1
Materials and Methods
Supplementary Text
Figs. S1 to S19
Tables S1 and S2
Listings S1 to S4
References (32–58)

11 April 2018; accepted 25 July 2018
10.1126/science.aat8474

METAMATERIALS

Quantum entanglement of the spin and orbital angular momentum of photons using metamaterials

Tomer Stav^{1*}, Arkady Faerman^{2*}, Elhanan Maguid², Dikla Oren¹, Vladimir Kleiner², Erez Hasman^{2†}, Mordechai Segev^{1*†}

Metamaterials constructed from deep subwavelength building blocks have been used to demonstrate phenomena ranging from negative refractive index and ϵ -near-zero to cloaking, emulations of general relativity, and superresolution imaging. More recently, metamaterials have been suggested as a new platform for quantum optics. We present the use of a dielectric metasurface to generate entanglement between the spin and orbital angular momentum of photons. We demonstrate the generation of the four Bell states on a single photon by using the geometric phase that arises from the photonic spin-orbit interaction and subsequently show nonlocal correlations between two photons that interacted with the metasurface. Our results show that metamaterials are suitable for the generation and manipulation of entangled photon states, introducing the area of quantum optics metamaterials.

Metamaterials are engineered structures, assembled from multiple elements of a scale smaller than the wavelength of incident light, with distinct electromagnetic response and functionalities such as negative refraction (1, 2), cloaking (3), and even near-zero permittivity and permeability (4, 5). Metasurfaces consist of a dense arrangement of dielectric or metallic subwavelength optical antennas (6–14). The light-matter interaction of an individual nanoantenna provides control over the local phase (15), enabling control over refraction and reflection. Accordingly, the light-scattering properties of the metasurface can be manipulated by tailoring the nanoantennas' material, size, and shaping the antenna resonance (9, 13, 14), or through their arrangement in space—for example, with geometric phase (6, 7, 12). These wavefront manipulations have been widely used with classical light. Recently, a metallic metasurface was used with quantum light (16) for detecting coherent perfect absorption of single photons. In this context, interesting ideas on how to utilize metamaterials for creating entanglement have been proposed (17). However, metamaterials have never been used to generate or manipulate entangled photon states, which are at the heart of the field of photonic quantum information.

By exploiting fundamental concepts in quantum physics, such as superposition and entanglement, quantum information offers ways of solving problems in reduced time-complexity (18–20). One of the many possible realizations of

quantum algorithms may be achieved by using single photons encoded with two qubits (21), whose relatively easy manipulation makes the construction of optical quantum processing units appealing. This is because photons can be controlled with the same optical devices used for classical light; they maintain their quantum coherence (quantum correlations) for extremely long times, unless absorbed (22–24). That is, they do not suffer from severe decoherence problems, as the alternative platforms to quantum information do. Indeed, recent advancements in on-chip quantum photonic circuits have shown the benefits of having integrated entangled photon sources (25, 26). Several experiments involving entangled photon states and metamaterials have

been performed (27, 28); however, thus far the entangled photon states were generated before the interaction with the metamaterial. Moreover, for experiments with quantum light, it is important to minimize the loss, whereas metallic metasurfaces inherently exhibit high loss (28). We used metasurfaces made of high-refractive index dielectrics, which do not involve any plasmonic decoherence or loss. Moreover, our dielectric metasurfaces are compatible with complementary metal-oxide semiconductor technology in the fabrication process, which is advantageous for future large-scale quantum computation devices. We rely on the recent realizations of Si-based metasurfaces with efficiencies close to 100% (14, 29), which makes them excellent candidates for quantum optics and quantum information applications.

We demonstrate that a dielectric metasurface can generate entanglement between the spin and the orbital angular momentum (OAM) of photons (Fig. 1). This is achieved by using the Pancharatnam-Berry phase, which provides a photonic spin-orbit interaction mechanism (30–32). We fabricated the Si-based geometric phase metasurface (GPM) depicted in Fig. 2A. In general, GPMs are designed for spin-controlled wave function shaping and are composed of anisotropic nanoantennas, designed to perform as nano half-waveplates, that generate a local geometric phase delay. The space-variant spin-dependent geometric phase $\phi_g(x, y) = -2\sigma_\pm\theta(x, y)$ corresponds to the orientation function $\theta(x, y)$ and defines the phase of the light passing through the metasurface at position (x, y) for the different spin states $\sigma_\pm = \pm 1$ (right- and left-handed circular polarizations). The angle $\theta(x, y)$ is the in-plane orientation of the nanoantennas. To design a GPM that entangles the photon's spin to its OAM, the nanoantenna orientations are chosen to be $\theta(r, \varphi) = \ell\varphi/2$, where φ is the azimuthal angle and ℓ is the winding number; in our case, $\ell = 1$. Therefore, the GPM adds or subtracts $\Delta\ell = 1$ —one

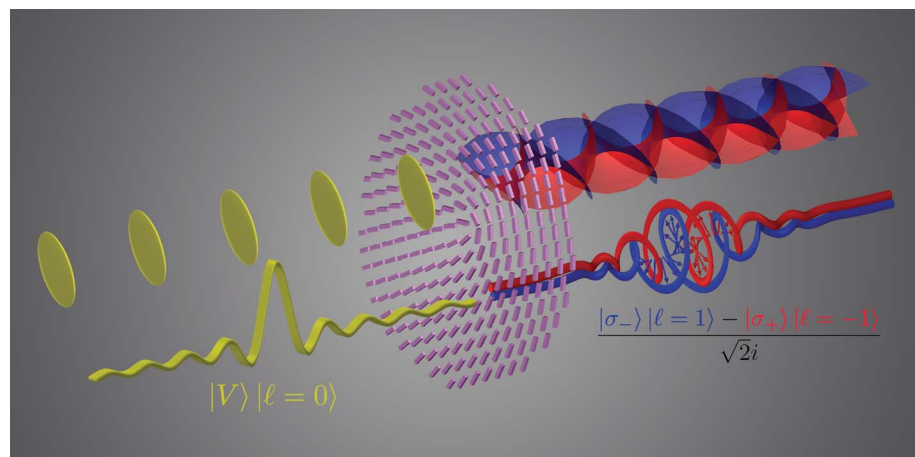


Fig. 1. Entanglement between spin and OAM on a single photon. A single photon vertically polarized is arriving from the left, as illustrated by the yellow wave packet representing the electric field amplitude. This photon carries zero OAM, as illustrated by the yellow flat phase fronts. The single photon passes through the metasurface nanoantennas (purple) and exits as a single-particle entangled state, depicted as a superposition of the red and blue electric field amplitudes, with the corresponding vortex phase fronts opposite to one another.

¹Physics Department and Solid State Institute, Technion, Haifa 32000, Israel. ²Micro and Nanooptics Laboratory, Faculty of Mechanical Engineering, and Russell Berrie Nanotechnology Institute, Technion, Haifa 32000, Israel.

*These authors contributed equally to this work.

†Corresponding author. Email: mehasman@technion.ac.il (E.H.); msegev@technion.ac.il (M.S.)

quanta of OAM, depending on the sign of the spin—and performs spin-flip $|\sigma_+\rangle \leftrightarrow |\sigma_-\rangle$. Such a metasurface performs the unitary transformation

$$|\sigma_\pm\rangle|\ell\rangle \xrightarrow{\text{GPM}} |\sigma_\mp\rangle|\ell \pm \Delta\ell\rangle \quad (1)$$

A single photon with zero OAM, polarized horizontally (H), incident upon the metasurface can be described by a superposition of spins (circular polarizations) as

$$|H\rangle|\ell=0\rangle = \frac{1}{\sqrt{2}}(|\sigma_+\rangle + |\sigma_-\rangle)|\ell=0\rangle \quad (2)$$

After passing through the metasurface, the state of the photon becomes (following Eq. 1)

$$\frac{1}{\sqrt{2}}(|\sigma_-\rangle|\ell=\Delta\ell\rangle + |\sigma_+\rangle|\ell=-\Delta\ell\rangle) \quad (3)$$

Similarly, an incident photon with zero OAM in the vertical polarization (V), described by $|V\rangle|\ell=0\rangle = \frac{1}{\sqrt{2i}}(|\sigma_+\rangle - |\sigma_-\rangle)|\ell=0\rangle$, is transformed by the metasurface into

$$\frac{1}{\sqrt{2i}}(|\sigma_-\rangle|\ell=\Delta\ell\rangle - |\sigma_+\rangle|\ell=-\Delta\ell\rangle) \quad (4)$$

The states described by Eqs. 3 and 4 are maximally entangled states encoded on a single photon. The entanglement here is between the spin and the OAM degrees of freedom. In a similar fashion, following Eqs. 3 and 4, if two indistinguishable photons in the state $|H\rangle|\ell=0\rangle \otimes |V\rangle|\ell=0\rangle$ are passed through the GPM, the result is the state

$$\frac{1}{\sqrt{2}}(|\sigma_+\rangle|\ell=-1\rangle \otimes |\sigma_+\rangle|\ell=-1\rangle - |\sigma_-\rangle|\ell=1\rangle \otimes |\sigma_-\rangle|\ell=1\rangle) \quad (5)$$

Both the spin and the OAM represent angular momentum, and only their sum is conserved (33). Nevertheless, for photons whose spatial wave function is paraxial, as in our case, the spin and the OAM are totally independent (32) and have Hilbert spaces of different dimensions. Furthermore, from expectation value perspective, the total

angular momentum is conserved; the incident state is of zero total angular momentum as well as the state emerging from the GPM.

The experimental setting shown in Fig. 2B is used to generate a single photon in the state $|H\rangle|\ell=0\rangle$. In the first set of experiments, the interaction with the metasurface results in a single

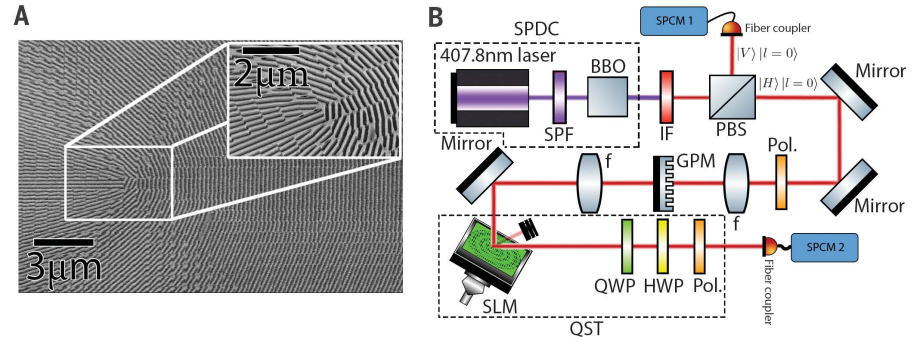


Fig. 2. Experimental setup used to generate and measure the entangled states. (A) Scanning electron microscope image of the Si-based GPM. Each building block in the GPM is composed of several nanorods filling an area of 700 by 700 nm². The nanorods are of 105 nm width and 300 nm depth, arranged 233 nm apart from each other. The metasurface diameter is 200 μm. (B) Schematic of the experimental setup. A 407.8-nm diode laser pumps a β-barium borate (BBO) crystal phase-matched for type-II collinear spontaneous parametric down-conversion (SPDC). The SPDC process produces two photons, one in vertical polarization (V) and the other in horizontal polarization (H), centered around the degenerate wavelength of $\lambda = 815.6$ nm. The pump field and photons produced at other wavelengths are filtered out by an interference filter (IF) filter. The pairs of photons produced by means of SPDC are spatially separated by using a polarizing beam splitter (PBS). The reflected photon acts as a trigger for the detection of the “signal photon” in H polarization (Eq. 2). The signal photon is passed through a linear polarizer (Pol.) and then through the GPM. In the measurement process, this single photon is reflected off a phase-only SLM that projects the state onto different OAM bases. Then the photons are projected on different polarization bases and measured in the SPCMs. Coincidence counts between the two SPCMs are used to measure different intensities for the QST.

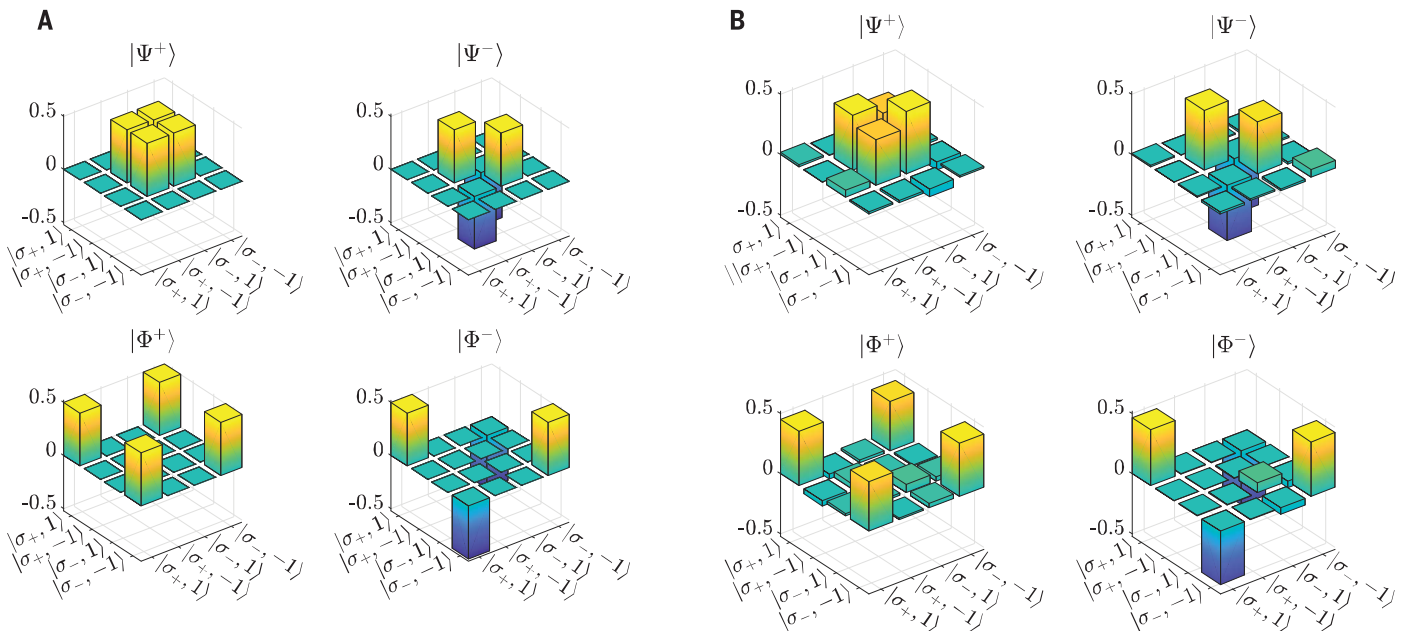


Fig. 3. Density matrices of the four Bell states. (A) Theoretical calculated density matrices for each Bell state. (B) Experimentally measured density matrices recovered for each Bell state by using QST. The

experimental results coincide with the theoretical results with higher than 90% fidelity. The results shown here are the real parts only because the imaginary part is identically zero both theoretically and experimentally.

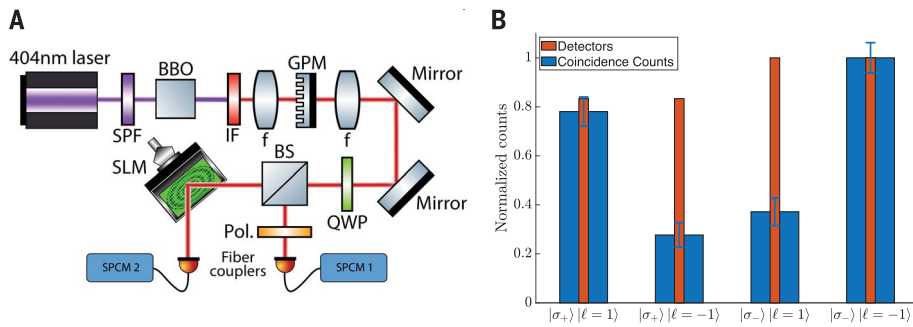


Fig. 4. Setup and measurements demonstrating nonlocal spin and OAM correlations on entangled biphoton states. (A) A 404-nm diode laser pumps a BBO crystal phase-matched for collinear type-II SPDC, which produces two photons in the degenerate wavelength of $\lambda = 808$ nm, filtered with an IF of $\Delta\lambda = 3$ nm. The pairs of photons are passed together through the GPM. After the interaction with the GPM, the photons pass through a QWP and into a BS. The reflected photons are projected on linear polarization states H and V, and the transmitted photons are projected on OAM states $\ell = \pm 1$. Coincidence counts between the two SPCMs are used to measure the nonlocal correlations between the two photons. (B) Coincidence counts measured between the two arms of the BS. The correlation between the linear polarization of one photon and the OAM of the second photon shows entanglement between the spin and OAM of two different photons. The uncorrelated terms are not zero because the metasurface we used was measured to have 72% conversion efficiency, decreasing the visibility in this case.

photon in an entangled state. In the second set of experiments, the metasurface generates entangled biphoton states. The experimental conversion efficiency of the metasurface was measured to be 72%.

To show entanglement, we performed full quantum state tomography (QST) on the state, and the density matrix is recovered (34). We used a spatial light modulator (SLM) to project the state onto different OAM basis elements, and a set of quarter-waveplate (QWP), half-waveplate (HWP) and a linear polarizer (Pol.) to project the state onto different elements of the polarization basis. The list of measurements is described in table S1. We used coincidence counts between the two detectors so that the single photon state is heralded. For integration time of 10 s, ~1000 coincidence counts were measured without any projections. From a total of 16 different measurements for each of the Bell states, we recovered the density matrix using a maximum likelihood estimation algorithm (35). Using this technique, we experimentally recovered the density matrices of the first two bell states $|\Psi^{\pm}\rangle = \frac{1}{\sqrt{2}}(|\sigma_{+}\rangle|\ell = -1\rangle \pm |\sigma_{-}\rangle|\ell = 1\rangle)$ with fidelity of 0.9250 and 0.9496 for $|\Psi^{+}\rangle$ and $|\Psi^{-}\rangle$, respectively (Fig. 3B), where we define the fidelity between the recovered ($\hat{\rho}$) and theoretical (ρ) density matrices by $F(\rho, \hat{\rho}) = \text{Tr}\left(\sqrt{\hat{\rho}^{1/2}\rho\hat{\rho}^{1/2}}\right)$.

By flipping the GPM (the winding number flips sign, and now $\ell = -1$), it performs the unitary transformation $|\sigma_{\pm}\rangle|\ell\rangle \xrightarrow{\text{GPM}} |\sigma_{\mp}\rangle|\ell \mp \Delta\ell\rangle$, which enables the generation of the remaining two bell states $|\Phi^{\pm}\rangle = \frac{1}{\sqrt{2}}(|\sigma_{+}\rangle|\ell = 1\rangle \pm |\sigma_{-}\rangle|\ell = -1\rangle)$. We performed QST on these states and measured density matrices with fidelity of 0.9274 and 0.9591 for $|\Phi^{+}\rangle$ and $|\Phi^{-}\rangle$, respectively (Fig. 3B). These

results are in very good agreement with theory (Fig. 3A). By introducing a HWP after the GPM, we can realize a SWAP gate on the spin qubit $|\sigma_{\pm}\rangle|\ell\rangle \xrightarrow{\text{SWAP}} |\sigma_{\mp}\rangle|\ell\rangle$, performing the transformation $|\Phi^{\pm}\rangle \xrightarrow{\text{SWAP}} |\Psi^{\pm}\rangle$. This SWAP gate does not affect the OAM qubit, which remains independent from the spin qubit (with fidelity 0.9276) (fig. S1).

Next, we demonstrate nonlocal spin and OAM correlations between two photons, using the experimental setting described in Fig. 4A. Coincidence counts between the two single-photon counting modules (SPCMs) measure correlations only half the times, when the two photons exit the beam splitter in different arms. The results displayed in Fig. 4B show that the emerging state manifests correlations between the spin of one photon and OAM of the other photon, which cannot be reproduced with classical light. The conclusion drawn from the single-photon state tomography (Fig. 3B) and the correlation measurements between two photons (Fig. 4B) is that the metasurface does not destroy the coherence of the wave function and generates entanglement between the spin and OAM at high fidelity.

Our demonstration of generating entangled photon states with metamaterials paves the way for nanophotonic quantum information applications. We anticipate that metasurfaces will become a standard tool in future quantum optics and will be used extensively in photonic quantum information systems—for example, for performing state tomography (36). These ideas can be extended to implement hyper-entangled state generation by using multifunctional or multispectral metasurfaces (29). The generation and control of quantum photon states via metamaterials leads to many new ideas and directions, ranging from using metasurfaces to entangle two photons of differ-

ent frequencies and OAMs to manipulating quantum states of photons emitted from quantum dots in an integrated fashion.

REFERENCES AND NOTES

1. J. B. Pendry, *Phys. Rev. Lett.* **85**, 3966–3969 (2000).
2. V. M. Shalae, *Nat. Photonics* **1**, 41–48 (2007).
3. D. Schurig et al., *Science* **314**, 977–980 (2006).
4. M. Silveirinha, N. Engheta, *Phys. Rev. Lett.* **97**, 157403 (2006).
5. I. Liberal, N. Engheta, *Nat. Photonics* **11**, 149–158 (2017).
6. Z. Bomzon, V. Kleiner, E. Hasman, *Opt. Lett.* **26**, 1424–1426 (2001).
7. Z. Bomzon, G. Biener, V. Kleiner, E. Hasman, *Opt. Lett.* **27**, 1141–1143 (2002).
8. A. V. Kildishev, A. Boltasseva, V. M. Shalae, *Science* **339**, 1232009 (2013).
9. A. Pors, O. Albrechtsen, I. P. Radko, S. I. Bozhevolnyi, *Sci. Rep.* **3**, 2155 (2013).
10. X. Yin, Z. Ye, J. Rho, Y. Wang, X. Zhang, *Science* **339**, 1405–1407 (2013).
11. N. Yu et al., *Science* **334**, 333–337 (2011).
12. D. Lin, P. Fan, E. Hasman, M. L. Brongersma, *Science* **345**, 298–302 (2014).
13. K. E. Chong et al., *Nano Lett.* **15**, 5369–5374 (2015).
14. A. Arbabi, Y. Horie, M. Bagheri, A. Faraon, *Nat. Nanotechnol.* **10**, 937–943 (2015).
15. A. I. Kuznetsov, A. E. Miroshnichenko, M. L. Brongersma, Y. S. Kivshar, B. Luk'yanchuk, *Science* **354**, aag2472 (2016).
16. T. Roger et al., *Nat. Commun.* **6**, 7031 (2015).
17. M. Siomau, A. A. Kamli, A. A. Moiseev, B. C. Sanders, *Phys. Rev. A* **85**, 050303 (2012).
18. L. K. Grover, *Proc. Twenty-eighth Annu. ACM Symp. Theory Comput.* **ACM**, 212–219 (1996).
19. P. W. Shor, *Proc. 35th Annu. Symp. Found. Comput. Sci. IEEE*, 124–134 (1994).
20. D. Deutsch, R. Jozsa, *Proc. R. Soc. Lond. A* **439**, 553–558 (1992).
21. B. G. Englert, C. Kurtsiefer, H. Weinfurter, *Phys. Rev. A* **63**, 032303 (2001).
22. A. Mair, A. Vaziri, G. Weihs, A. Zeilinger, *Nature* **412**, 313–316 (2001).
23. J. Leach et al., *Science* **329**, 662–665 (2010).
24. L. Shi, E. J. Galvez, R. R. Alfano, *Sci. Rep.* **6**, 37714 (2016).
25. J. W. Silverstone et al., *Nat. Photonics* **8**, 104–108 (2014).
26. M. Kues et al., *Nature* **546**, 622–626 (2017).
27. E. Altewischer, M. P. van Exter, J. P. Woerdman, *Nature* **418**, 304–306 (2002).
28. M. S. Tame et al., *Nat. Phys.* **9**, 329–340 (2013).
29. E. Maguid et al., *Light Sci. Appl.* **6**, e17027 (2017).
30. M. V. Berry, *Proc. R. Soc. London Ser. A* **392**, 45–57 (1984).
31. K. Y. Bliokh, F. J. Rodríguez-Fortuño, F. Nori, A. V. Zayats, *Nat. Photonics* **9**, 796–808 (2015).
32. K. Y. Bliokh, F. Nori, *Phys. Rep.* **592**, 1–38 (2015).
33. E. Nagali et al., *Phys. Rev. Lett.* **103**, 013601 (2009).
34. Materials and methods are available as supplementary materials.
35. D. F. V. James, P. G. Kwiat, W. J. Munro, A. G. White, *Phys. Rev. A* **64**, 052312 (2001).
36. K. Wang et al., *Science* **361**, 1104–1108 (2018).

ACKNOWLEDGMENTS

The authors thank the group of Y. Silberberg from Weizmann Institute of Science, Israel, for the use of their 404-nm laser. **Funding:** The authors gratefully acknowledge financial support from the U.S. Air Force Office of Scientific Research (FA9550-18-1-0208), through their program on photonic metamaterials, and the Israel Science Foundation (ISF). The fabrication was performed at the Micro-Nano Fabrication & Printing Unit (MNF&PU), Technion. **Author contributions:** All the authors contributed substantially to this work. **Competing interests:** The authors declare no competing interests. **Data and materials availability:** All data necessary to support this paper's conclusions are available in the supplementary materials.

SUPPLEMENTARY MATERIALS

www.sciencemag.org/content/361/6407/1101/suppl/DC1
Materials and Methods
Supplementary Text
Fig. S1
Table S1
References (37–39)

17 April 2018; accepted 17 July 2018
10.1126/science.aat9042

METAMATERIALS

Quantum metasurface for multiphoton interference and state reconstruction

Kai Wang¹, James G. Titchener^{1,2}, Sergey S. Kruk¹, Lei Xu^{1,3}, Hung-Pin Chung^{1,4}, Matthew Parry¹, Ivan I. Kravchenko⁵, Yen-Hung Chen^{4,6}, Alexander S. Solntsev^{1,7}, Yuri S. Kivshar¹, Dragomir N. Neshev¹, Andrey A. Sukhorukov^{1,*}

Metasurfaces based on resonant nanophotonic structures have enabled innovative types of flat-optics devices that often outperform the capabilities of bulk components, yet these advances remain largely unexplored for quantum applications. We show that nonclassical multiphoton interferences can be achieved at the subwavelength scale in all-dielectric metasurfaces. We simultaneously image multiple projections of quantum states with a single metasurface, enabling a robust reconstruction of amplitude, phase, coherence, and entanglement of multiphoton polarization-encoded states. One- and two-photon states are reconstructed through nonlocal photon correlation measurements with polarization-insensitive click detectors positioned after the metasurface, and the scalability to higher photon numbers is established theoretically. Our work illustrates the feasibility of ultrathin quantum metadevices for the manipulation and measurement of multiphoton quantum states, with applications in free-space quantum imaging and communications.

The field of nanostructured metasurfaces offers the possibility of replacing traditionally bulky imaging systems with flat optics devices (*1*), achieving high transmission based on all-dielectric platforms (*2–7*). The metasurfaces provide a freedom to tailor the light interference by coherently selecting and mixing different components on a subwavelength scale, enabling polarization-spatial conversion (*4*, *7–12*) and spin-orbital transformation (*13*). Such capabilities motivated multiple applications for the regime of classical light, yet the metasurfaces have the potential to emerge as essential components for quantum photonics (*14–17*).

The key manifestations of quantum light are associated with nonclassical multiphoton interference, which is an enabling phenomenon for the transformation and measurement of quantum states. Conventionally, manipulation of multiphoton states is performed through a sequence of beam-splitting optical elements, each realizing quantum interference (*18–20*). Recent advances in nanotechnology have enabled the integration

of beam-splitters and couplers on tailored plasmonic structures (*21*, *22*); however, material losses and complex photon-plasmon coupling interfaces restrict the platform scalability. We realize several multiphoton interferences in a single flat all-dielectric metasurface. The parallel quantum state transformations are encoded in multiple interleaved metagratings, taking advantage of the transverse spatial coherence of the photon wave functions extending across the beam cross section. In the classical context, the interleaving approach was effectively used for polarization-sensitive beam splitting (*8*, *9*, *11*, *12*), yet it requires nontrivial development for the application to multiphoton states.

We formulate and realize an application of the metasurface-based interferences for multiphoton quantum state measurement and reconstruction. We develop a metasurface that incorporates a set of $M/2$ interleaved metagratings [see part 3 of (*23*)], where M is an even number of diffracted beams forming imaging spots. Each metasurface is composed of nanoresonators with specially varying dimensions and orientations, according to the principle of geometric phase (*8*), to split specific elliptical polarization states (*7*), which would not be possible with conventional gratings [see parts 1 and 2 of (*23*)]. This performs quantum projections in a multiphoton Hilbert space to M imaging spots, which can be considered as output ports. Each port corresponds to a different elliptical polarization state (Fig. 1A), which is essential to minimize the error amplification in quantum state reconstruction (*24*). Then, by directly measuring all possible N -photon correlations, where N is the number of photons, from the M output beams, it becomes possible to reconstruct the initial N -photon density matrix, providing full infor-

mation on the multiphoton quantum entanglement. For example, in Fig. 1B, we show a sketch of three gratings (top) which realize an optimal set of projective bases shown as vectors on the Poincaré sphere (middle) for $M = 6$.

The photon correlations between M output ports can be obtained with simple polarization-insensitive single-photon click detectors. The metasurface can be potentially combined with single photon-sensitive electron-multiplying charge-coupled device (EMCCD) cameras (*25*, *26*) to determine the spatial correlations by processing multiple time-frame images of quantum states. We consider quantum states with a fixed photon number N , which is a widely used approach in photon detection (*27–30*). The N -fold correlation data, stored in an array with N dimensions, are obtained by averaging the coincidence events over multiple time frames. For example, in Fig. 1C, we sketch a case with $N = 2$ photons and $M = 6$. In each frame, two photons arrive at different combinations of spots. After summing up the coincidence events over multiple time frames, we obtain a correlation in two-dimensional space. Following the general measurement theory of (*30*), we establish that, for an indistinguishable detection of N -photon polarization states (i.e., the detectors cannot distinguish which is which of the N photons), the required number of output ports to perform the reconstruction scales linearly with the photon number as $M \geq N + 3$ (see Fig. 1B, bottom). For instance, with $M = 6$, up to $N = 3$ photon states can be measured.

The parallel realization of multiphoton interferences with a single metasurface offers practical advantages for quantum state measurements. Conventional quantum state tomography (*27*) methods based on reconfigurable setups can require extra time and potentially suffer from errors associated with the movement of bulk optical components (*27*) or tuning of optical interference elements (*31*). Moreover, the conventionally used sequential implementations of projective measurements present a fundamental limit for miniaturization while being inherently sensitive to fluctuations or misalignment between different elements, especially for higher-photon number states. The emerging methods based on static transformations implemented with bulk optical components (*19*) or integrated waveguides (*28–30*) still require multiple stages of interferences. By contrast, our quantum metasurface provides an ultimately robust and compact solution, the speed of which is limited only by the detectors.

We fabricate silicon-on-glass metasurfaces designed for $M = 6$ and 8 imaging spots using standard semiconductor fabrication technology [see parts 4 and 7 of (*23*) for details]. The experimentally determined polarization projective bases obtained through classical characterization are plotted on the Poincaré sphere in Fig. 2A for a metasurface with $M = 6$ that is used later for quantum experiments. The transfer matrix measurements confirm that the polarization projective bases are close to the optimal frame. The condition

¹Nonlinear Physics Centre, Research School of Physics and Engineering, The Australian National University, Canberra, ACT 2601, Australia. ²Quantum Technology Enterprise Centre, Quantum Engineering Technology Labs, H. H. Wills Physics Laboratory and Department of Electrical and Electronic Engineering, University of Bristol, Bristol BS8 1FD, UK. ³School of Engineering and Information Technology, University of New South Wales, Canberra, ACT 2600, Australia. ⁴Department of Optics and Photonics, National Central University, Jhongli 320, Taiwan. ⁵Center for Nanophase Materials Sciences, Oak Ridge National Laboratory, Oak Ridge, TN 37831, USA. ⁶Center for Astronautical Physics and Engineering, National Central University, Jhongli 320, Taiwan. ⁷School of Mathematical and Physical Sciences, University of Technology Sydney, Ultimo, NSW 2007, Australia.

*Corresponding author. Email: andrey.sukhorukov@anu.edu.au

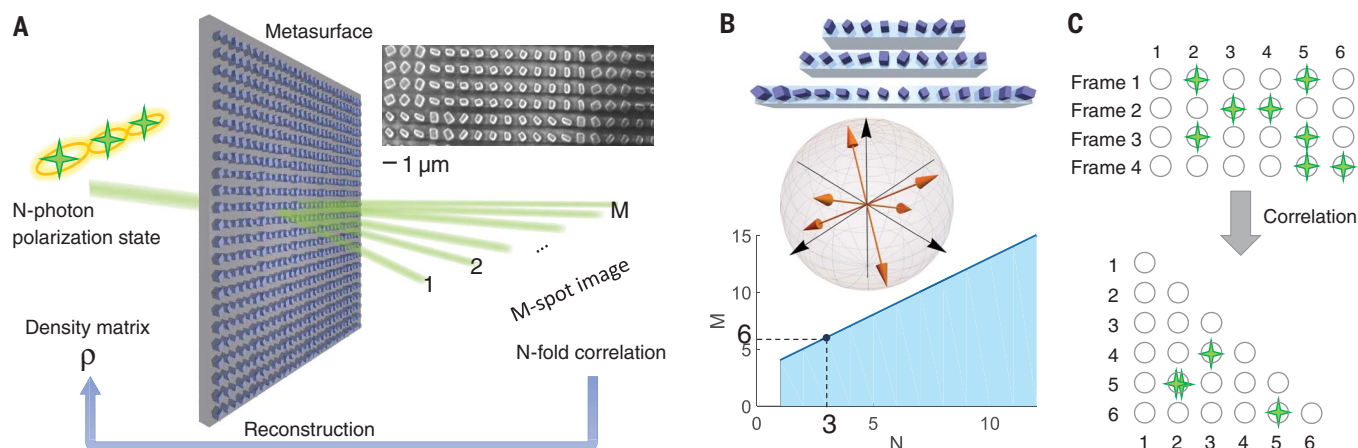
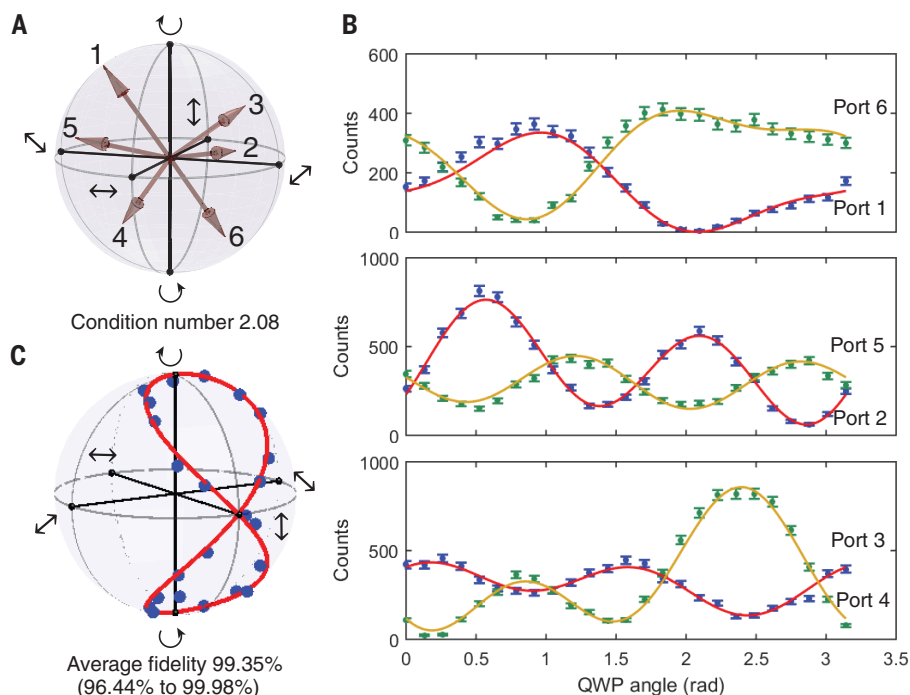


Fig. 1. Concept of quantum state imaging via nanostructured flat optics. (A) Sketch of a metasurface being used to image an input N -photon polarization state into an M -spot image. At the top right is a scanning electron microscopy image of the fabricated all-dielectric metasurface. Green crosses represent photons; purple blocks on the metasurface represent nanoresonators. (B) The top image is a sketch of three interleaved gratings for $M = 6$. The middle image shows, with orange arrows, the corresponding

projective bases as vectors on the Poincaré sphere; black arrows indicate the coordinate axes. Shown at the bottom are the minimum number of required spots to fully reconstruct the initial quantum state for different numbers of photons N , where optimal-frame choice of projective bases exists for $M = 6, 8, 12, 20, \dots$ (C) An example of correlation measurement with $N = 2$ and $M = 6$, with several time-frame measurements combined into a two-dimensional correlation image.

Fig. 2. Experimental measurement of heralded single-photon states with the metasurface. (A) Classically characterized projective bases of the metasurface for ports numbered 1 to 6. (B) Accumulated single-photon counts in each of $M = 6$ output ports versus the angle of a QWP realizing a photon state transformation before the metasurface. Experimental data are shown as dots, with error bars indicating shot noise. Solid lines represent theoretical predictions based on classically measured metasurface transfer matrix. rad, radians. (C) Comparison between the prepared (solid line) and reconstructed (dots) states based on the measurements presented in (B), plotted on a Poincaré sphere.



number, a measure of error amplification in the reconstruction [see part 1 of (23)], is 2.08, close to the fundamental theoretical minimum of $\sqrt{3} \approx 1.73$. The reconstruction is immune to fabrication imperfections because their effect is fully taken into consideration by performing an experimental metasurface characterization with classical light after the fabrication [see parts 6 and 10 of (23)].

First, we show that our metasurface enables accurate reconstruction of the quantum-polarization state of single photons. A heralded photon source is used at a wavelength of 1570.6 nm on the basis of spontaneous parametric down conversion (SPDC) in a nonlinear waveguide [see parts 5, 8, 9, and 11 of (23) for details]. The heralded single photons are initially linearly polarized. They are prepared in different polarization states by varying the

angle of a quarter-wave plate (QWP), then sent to the metasurface, and each diffracted photon beam is collected by a fiber-coupled interface to the single-photon detectors. By measuring the correlations with the master detector, we reconstruct the quantum-polarization state from the photon counts at the six ports. The results are shown in Fig. 2B, where the curves are theoretical predictions and dots are experimental

measurements. We observe that the measurement errors are dominated by the single-photon detection shot noise, which is proportional to the square root of the photon counts, as indicated by the error bars. We use the measured photon counts to reconstruct the input single-photon states by performing a maximum-likelihood estimation (27) and plot them on a Poincaré sphere in Fig. 2C. The reconstructed states present a

high average fidelity of 99.35% with respect to the prepared states.

Next, we realize two-photon interference, the setup of which is conceptually sketched in Fig. 3A. The SPDC source generates a photon pair with horizontal (H) and vertical (V) polarizations, with the path length difference between polarization components controllable by a delay line [see part 12 of (23) for details]. We measure the effect of

delay on the two-photon interference, analogous to the Hong-Ou-Mandel (HOM) experiment (32). In such a nontrivially generalized two-photon interference, we expect a dip or peak depending on the two-by-two transfer matrix $\mathbf{T}_{a,b} \propto [\mathbf{u}_a, \mathbf{u}_b]^\dagger$ from the two-dimensional polarization state vector to a chosen pair of ports, where \dagger denotes transpose conjugate and \mathbf{u}_a and \mathbf{u}_b are the projective bases of ports a and b , respectively. We

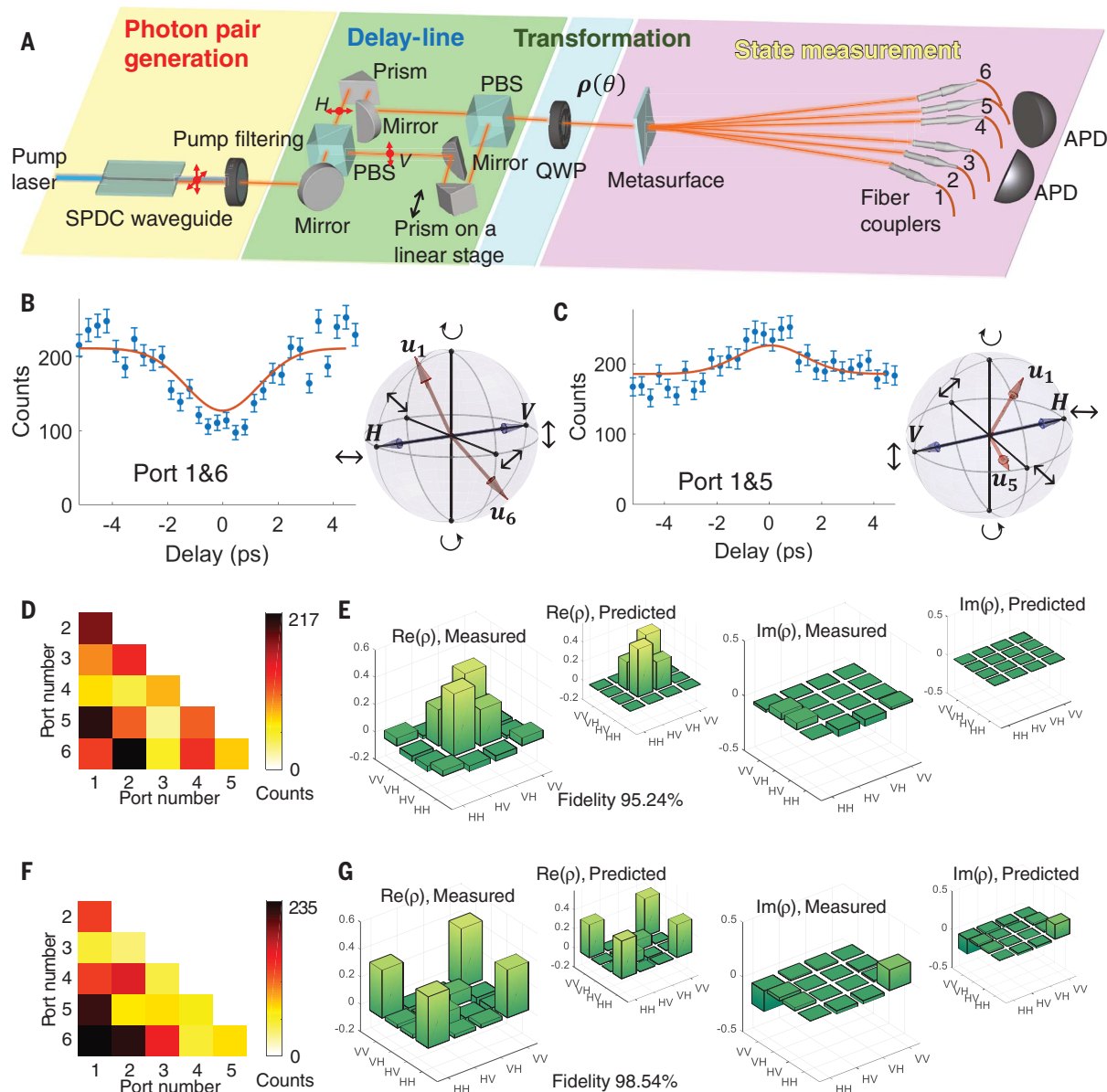


Fig. 3. Experimental two-photon interferences and state reconstruction with the metasurface. (A) Schematic of the setup, including photon-pair generation and pump filtering, a delay line with polarizing beam splitters (PBSs) to control the path difference between orthogonally polarized photons in a pair, state transformation with a QWP, and state measurement with the metasurface using avalanche photodiodes (APDs). (B and C) Quantum correlations between ports 1 and 6 (B) with close-to-orthogonal bases and ports 1 and 5 (C) with nonorthogonal bases, shown with dots and error bars

indicating shot noise. Solid curves represent theoretical predictions. Red arrows in the Poincaré spheres denote projective bases of different ports. Blue arrows indicate the polarization state of entangled photons, with one photon in H and the other in V polarization. (D and F) Representative twofold correlation measurements and (E and G) the corresponding reconstructed density matrices ρ labeled “Measured” alongside the theoretically predicted states labeled “Predicted” for QWP orientations $\theta = 0^\circ$ [(D) and (E)] and $\theta = 37.5^\circ$ [(F) and (G)].

note that $\mathbf{T}_{a,b}$ corresponds to an effective Hermitian Hamiltonian only if \mathbf{u}_a and \mathbf{u}_b are orthogonal, resulting in a conventional HOM dip, whereas otherwise, a HOM peak can appear analogous to a lossy beam splitter (22). Here we set the angle of the QWP at $\theta = 0^\circ$, which means that the photon pairs are in a state $\rho(\theta = 0^\circ)$, where one photon is H polarized and another is V polarized. As reflected in the Poincaré sphere of Fig. 3B—where the red arrows denote projective bases of the two ports (\mathbf{u}_a and \mathbf{u}_b) and the blue arrows represent the polarization of the photon pairs, one photon in H and the other in V polarization—we see that the state vector \mathbf{u}_1 points in the opposite direction of \mathbf{u}_6 . We find that, in this case, photons with cross-polarized entanglement in H-V basis will give rise to a dip in the interference pattern with the variation of path-length difference (see Fig. 3B, left). Such a behavior is directly caused by the coalescence nature of bosons. The situation is quite different if we measure such an interference between ports $a = 1$ and $b = 5$, because \mathbf{u}_1 and \mathbf{u}_5 are far from being orthogonal. This can be seen from the red arrows in the Poincaré sphere of Fig. 3C, where the angle between the two vectors representing \mathbf{u}_1 and \mathbf{u}_5 is much smaller than π . For entangled photons with H and V polarization in a pair, interference under the transfer matrix $\mathbf{T}_{1,5}$ leads to a peak instead of a dip when varying the path difference in the delay line. Indeed, in Fig. 3C (left) we observe a peak, which is related to the anticoalescence of bosons in transformations induced by non-Hermitian Hamiltonians, a nontrivial generalization of the HOM interference analogous to (22). For details of the theoretical predictions and experimental methods, see part 4 of (23).

As a following step, we measure all 15 twofold nonlocal correlations between the $M = 6$ outputs from the metasurface for a given input state where the time delay is fixed to zero. This provides us full information to accurately reconstruct the input two-photon density matrix. We use two single-photon detectors to map out all possible output combinations, although this could potentially be accomplished even more easily with an EMCCD camera. We show representative results for two different states $\rho(\theta = 0^\circ)$ and $\rho(\theta = 37.5^\circ)$ in Fig. 3, D and E, and Fig. 3, F and G, respectively. Note that $\rho(\theta = 0^\circ)$ is a state in which photon pairs have cross-polarized entanglement beyond the classical limit, yet it is not fully pure [see part 4 of (23)], providing a suitable test case for reconstruction of general mixed states. In Fig. 3D, we show the measured twofold correlations for the input state $\rho(\theta = 0^\circ)$, and the reconstructed density matrix is shown in Fig. 3E. That only the

bunched four central elements are nonzero confirms the cross-polarized property of our photon pairs in H-V basis. Moreover, the nonzero |HVH⟩ element implies the presence of two-photon entanglement. It is smaller compared to the diagonal element |HVHV⟩, indicating that the polarization state is not fully pure. Although $\rho(\theta = 0^\circ)$ only has nonzero elements in the real part of the density matrix, we also show the measurement and reconstruction of $\rho(\theta = 37.5^\circ)$, which contains nontrivial imaginary elements, in Fig. 3, F and G. In both cases, we achieve a very good agreement between the predicted and reconstructed density matrices, as evidenced by high fidelity exceeding 95%. The correlation counts are obtained by a Gaussian fitting to the correlation histogram to remove the background, which is less than 10% of the signal for all measurements shown in Fig. 3F; see details in part 12 of (23).

Our results illustrate the manifestation of multiphoton quantum interference on metasurfaces. We formulate a concept of parallel quantum state transformation with metasurfaces, enabling single- and multiphoton state measurements solely based on the interaction of light with sub-wavelength thin nanostructures and nonlocal correlation measurements without a requirement of photon number-resolvable detectors. This provides ultimate miniaturization and stability combined with high accuracy and robustness, as we demonstrate experimentally via reconstruction of one- and two-photon quantum-polarization states, including the amplitude, phase, coherence, and quantum entanglement. In general, our approach is particularly suitable for imaging-based measurements of multiphoton polarization states, where the metasurface can act as a quantum lens to transform the photons to a suitable format for the camera to recognize and retrieve more information. Furthermore, there is the potential to capture other degrees of freedom associated with spatially varying polarization states for the manipulation and measurement of high-dimensional quantum states of light, with applications including free-space communications and quantum imaging.

REFERENCES AND NOTES

- N. Yu, F. Capasso, *Nat. Mater.* **13**, 139–150 (2014).
- A. I. Kuznetsov, A. E. Miroshnichenko, M. L. Brongersma, Y. S. Kivshar, B. Luk'yanchuk, *Science* **354**, aag2472 (2016).
- M. Decker et al., *Adv. Opt. Mater.* **3**, 813–820 (2015).
- A. Arbabi, Y. Horie, M. Bagheri, A. Faraon, *Nat. Nanotechnol.* **10**, 937–943 (2015).
- S. Kruk et al., *APL Photonics* **1**, 030801 (2016).
- P. Genevet, F. Capasso, F. Aieta, M. Khorasaninejad, R. Devlin, *Optica* **4**, 139 (2017).
- J. P. Balthasar Mueller, N. A. Rubin, R. C. Devlin, B. Groever, F. Capasso, *Phys. Rev. Lett.* **118**, 113901 (2017).
- Z. Bomzon, V. Kleiner, E. Hasman, *Opt. Lett.* **26**, 1424–1426 (2001).
- A. Pors, M. G. Nielsen, S. I. Bozhevolnyi, *Optica* **2**, 716 (2015).
- J. P. Balthasar Mueller, K. Leosson, F. Capasso, *Optica* **3**, 42 (2016).
- E. Maguid et al., *Science* **352**, 1202–1206 (2016).
- F. Ding, A. Pors, Y. T. Chen, V. A. Zenin, S. I. Bozhevolnyi, *ACS Photonics* **4**, 943–949 (2017).
- R. C. Devlin, A. Ambrosio, N. A. Rubin, J. P. B. Mueller, F. Capasso, *Science* **358**, 896–901 (2017).
- P. K. Jha, X. Ni, C. Wu, Y. Wang, X. Zhang, *Phys. Rev. Lett.* **115**, 025501 (2015).
- T. Roger et al., *Nat. Commun.* **6**, 7031 (2015).
- A. Lyons et al., arXiv:1709.03428 [quant-ph] (11 September 2017).
- T. Stav et al., *Science* **361**, 1101–1104 (2018).
- J. W. Silverstone et al., *Nat. Photonics* **8**, 104–108 (2014).
- O. Bayraktar, M. Swillo, C. Canalias, G. Bjork, *Phys. Rev. A* **94**, 020105 (2016).
- J. S. Fakonas, A. Miskovets, H. A. Atwater, *New J. Phys.* **17**, 023002 (2015).
- G. Di Martino et al., *Phys. Rev. Appl.* **1**, 034004 (2014).
- B. Vest et al., *Science* **356**, 1373–1376 (2017).
- See supplementary materials.
- M. R. Foreman, A. Favaro, A. Aiello, *Phys. Rev. Lett.* **115**, 263901 (2015).
- M. P. Edgar et al., *Nat. Commun.* **3**, 984 (2012).
- M. Reichert, H. Defienne, J. W. Fleischer, *Sci. Rep.* **8**, 7925 (2018).
- D. F. V. James, P. G. Kwiat, W. J. Munro, A. G. White, *Phys. Rev. A* **64**, 052312 (2001).
- J. G. Titchener, A. S. Solntsev, A. A. Sukhorukov, *Opt. Lett.* **41**, 4079–4082 (2016).
- D. Oren, M. Mutfafi, Y. C. Eldar, M. Segev, *Optica* **4**, 993 (2017).
- J. G. Titchener et al., *npj Quantum Inf.* **4**, 19 (2018).
- P. J. Shadbolt et al., *Nat. Photonics* **6**, 45–49 (2012).
- C. K. Hong, Z. Y. Ou, L. Mandel, *Phys. Rev. Lett.* **59**, 2044–2046 (1987).

ACKNOWLEDGMENTS

We gratefully thank H. Bachor, M. Scully, I. Walmsley, and F. Setzpfandt for fruitful discussions; R. Schiek and Y. Zarate for help in developing ovens for waveguide temperature control; and M. Liu for advice on numerical simulations. **Funding:** This work was supported by the Australian Research Council (including projects DP160100619, DP150103733, and DE180100070) and the Ministry of Science and Technology (MOST), Taiwan, under contract 106-2221-E-008-068-MY3. A portion of this research was conducted at the Center for Nanophase Materials Sciences, which is a U.S. DOE Office of Science User Facility. **Author contributions:** K.W., D.N.N., and A.A.S. conceived and designed the research; K.W. and L.X. performed numerical modeling of metasurface design; S.S.K. and I.I.K. fabricated the dielectric metasurfaces; H.-P.C. and Y.-H.C. fabricated nonlinear waveguides; K.W., J.G.T., H.-P.C., M.P., and A.S.S. performed optical experimental measurements and data analysis; A.A.S., D.N.N., and Y.S.K. supervised the work; K.W., A.A.S., D.N.N., and Y.S.K. prepared the manuscript and supplementary materials in coordination with all authors. **Competing interests:** The authors declare no competing interests. **Data and materials availability:** All data needed to evaluate the conclusions in this study are presented in the paper or in the supplementary materials.

SUPPLEMENTARY MATERIALS

www.sciencemag.org/content/361/6407/1104/suppl/DC1
Materials and Methods
Figs. S1 to S11
References (33–37)

10 April 2018; accepted 17 July 2018
10.1126/science.aat8196

FOREST ECOLOGY

Classifying drivers of global forest loss

Philip G. Curtis^{1*}, Christy M. Slay¹, Nancy L. Harris²,
Alexandra Tyukavina³, Matthew C. Hansen³

Global maps of forest loss depict the scale and magnitude of forest disturbance, yet companies, governments, and nongovernmental organizations need to distinguish permanent conversion (i.e., deforestation) from temporary loss from forestry or wildfire. Using satellite imagery, we developed a forest loss classification model to determine a spatial attribution of forest disturbance to the dominant drivers of land cover and land use change over the period 2001 to 2015. Our results indicate that 27% of global forest loss can be attributed to deforestation through permanent land use change for commodity production. The remaining areas maintained the same land use over 15 years; in those areas, loss was attributed to forestry (26%), shifting agriculture (24%), and wildfire (23%). Despite corporate commitments, the rate of commodity-driven deforestation has not declined. To end deforestation, companies must eliminate 5 million hectares of conversion from supply chains each year.

Leaders of nearly 450 companies recently committed to zero deforestation in their supply chains by 2020 to meet consumer demand for deforestation-free products and to improve corporate social responsibility (1). Achieving these commitments requires transparency of complex supply chains for agricultural and forest products whose source locations are obscured by multiple aggregators and distributors (2). Large, multinational companies cannot determine the source of their supply beyond the location of their direct supplier, usually a distributor; this reduces the effectiveness of deforestation attribution and undermines a company's ability to take concrete action.

Companies, nongovernmental organizations, and governments are looking increasingly to data, maps, and tools to provide visibility on deforestation risk. Published maps of tree cover loss and gain derived from Landsat satellite observations (3) were a major step forward in consistent and transparent forest area change monitoring at a global scale. The launch of the online Global Forest Watch platform (4) extended the use and access of these data beyond the scientific community to include decision makers from governments, companies, and civil society organizations working to design and implement more effective forest policies.

However, the Hansen *et al.* dataset (3), updated annually on Global Forest Watch, does not distinguish permanent forest conversion associated with a change in land use [i.e., deforestation (5)] from other forms of forest dis-

turbance that may be associated with subsequent regrowth (i.e., forestry, shifting cultivation, wildfire). This not only limits its utility for corporate decision-makers but also generates confusion when global forest cover change statistics derived from satellite imagery are compared directly against global land use change statistics as reported by governments in their national inventories (6). Deforestation involves the abrupt transition from land with trees to land without trees with no subsequent regrowth; loss of forest cover can also be associated with events such as

wildfires, or with direct human-induced land use and land management practices such as clearcutting or selective logging, plantation forestry, smallholder agroforestry systems, or transitional subsistence farming due to shifting cultivation practices. As improvements in the spatial and temporal resolution of satellite imagery enable detection of smaller and more subtle changes to Earth's land surface relative to results from earlier monitoring efforts (7, 8), more nuance is required in the attribution of global forest change dynamics.

Using high-resolution Google Earth imagery to visually classify nearly 5000 training sample cells, we developed a decision-tree model that predicts the most likely cause of forest disturbance at any 10 km × 10 km grid cell around the world since the year 2000 (9). Categories were assigned according to dominant disturbance type (Fig. 1), with each representing a different forest and land use dynamic: (i) commodity-driven deforestation, defined by the long-term, permanent conversion of forest and shrubland to a nonforest land use such as agriculture (including oil palm), mining, or energy infrastructure; (ii) shifting agriculture, defined as small- to medium-scale forest and shrubland conversion for agriculture that is later abandoned and followed by subsequent forest regrowth; (iii) forestry, defined as large-scale forestry operations occurring within managed forests and tree plantations with evidence of forest regrowth in subsequent years; (iv) wildfire, defined as large-scale forest loss resulting from the burning of forest vegetation with no visible human conversion or agricultural activity afterward; and (v) urbanization, defined as forest and shrubland

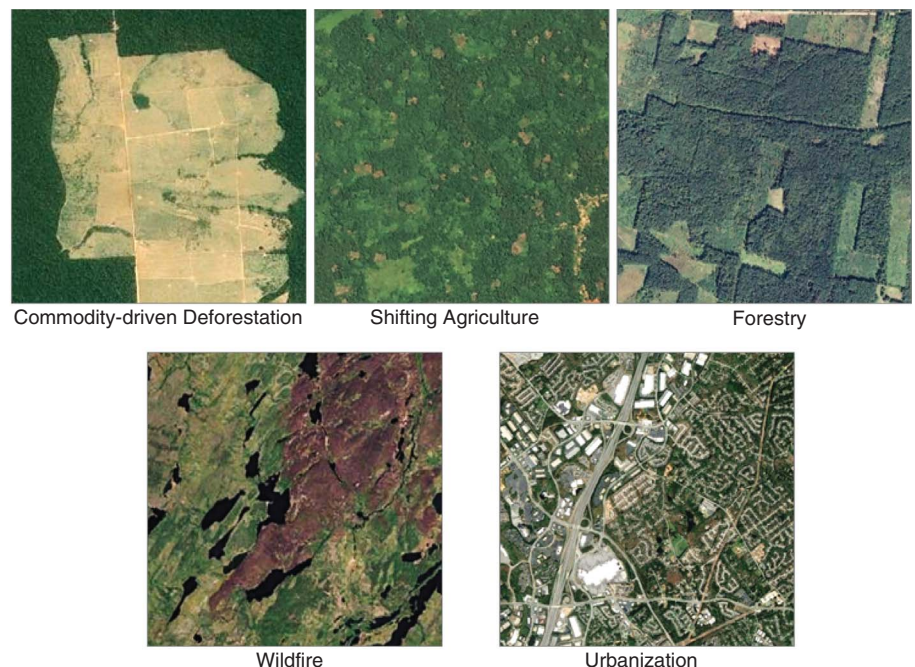


Fig. 1. Representative examples of Google Earth imagery used to train the forest loss classification model. See (9) for more examples of training imagery.

¹Sustainability Consortium, University of Arkansas, Fayetteville, AR 72701, USA. ²World Resources Institute, 10 G Street N.E., Washington, DC 20002, USA. ³Department of Geographical Sciences, University of Maryland, College Park, MD 20742, USA.

*Corresponding author. Email: philip.curtis@sustainabilityconsortium.org

conversion for the expansion and intensification of existing urban centers. Although urbanization is considered a form of deforestation, we included it as a separate class both to highlight the loss of forest in lands typically considered to be under urban use and because the set of actors responsible for clearing urban areas is distinct from those responsible for clearing forests for commodity production. We considered only direct drivers of forest disturbance, and we did not attempt to link these to underlying drivers such as demographic pressures or economic markets (10). A separate validation sample of 1565 randomly selected 10 × 10 grid cells was used to estimate map accuracy and proportions of the five disturbance types from the total forest disturbance area, both globally and by region.

Globally, 27 ± 5% of all forest disturbance between 2001 and 2015 was associated with commodity-driven deforestation (Table 1 and Fig. 2). The rate of deforestation remained steady across the 15-year period analyzed at approximately 5 Mha year⁻¹ (Fig. 3A) with a geographic shift away from Brazil toward tropical forests elsewhere in Latin America and Southeast Asia (Fig. 3B). Beyond deforestation, forestry represented 26 ± 4% of total forest disturbance (Table 1), followed by shifting agriculture (24 ± 3%) and wildfire (23 ± 4%). An additional 0.6 ± 0.3% of forest loss was attributed to the intensification and expansion of urban centers. The driver attribution model's overall accuracy was 89%, with individual class accuracies ranging from 55% (urbanization) to 94% (deforestation) (table S4).

Drivers of forest loss varied regionally (Fig. 2). In temperate and boreal forests, forestry and wildfire were the dominant disturbance factors; in tropical regions, shifting agriculture and commodity-driven deforestation were preeminent. In the Southeast Asian countries of Indonesia and Malaysia, we identified widespread deforestation for agricultural expansion through

visual evidence of oil palm plantations. Across Central and South America, forests were converted to row crop agriculture and cattle grazing lands. Shifting agriculture was the dominant driver in sub-Saharan Africa.

The forestry class in Fig. 2 explicitly maps sourcing regions for the global forest products industry. These are concentrated in North America, Europe, Russia, China, southern Brazil, Chile, South Africa, and Australia. Most forestry activities in South America, the United States, Europe, China, South Africa, and Australia showed signs of tree plantations, as evidenced by distinct rows of planted trees, whereas forestry activity in Canada and Russia contained predominantly large clearcuts without visibly distinct plantation rows (figs. S3 to S5). In Southeast Asia, most forestry activity took the form of low-intensity selective logging, especially on the island of Borneo. All forms of forestry were characterized by a dominant forest regrowth signal in the years following loss.

Wildfire was a dominant cause of forest disturbance in North America and Russia (Table 1 and Fig. 2). Wildfires in these regions were characterized by large areas of forest burned in a single year, then regenerating gradually over time (fig. S5). This driver was also differentiated from the others by the large disturbance size and low population density typically associated with wildfire events.

Other disturbances leading to forest loss (such as insect outbreaks, wind and ice storms, flooding, or rivers changing course) were not included in our model. However, only 1% of all model validation sample cells were attributed to a cause other than the five included in our analysis. We conclude that these other forms of disturbance are highly localized and temporally restricted phenomena.

Forest loss due to urbanization represented a small fraction (0.6 ± 0.3%) of total loss. More

than two-thirds of this loss occurred in the eastern United States, and the remainder was associated with expanding cities in China, Brazil, Indonesia, and Australia, as well as considerable low-density expansion across sub-Saharan Africa.

Regional class accuracies (tables S5 and S6) reflect the extent to which our model could distinguish differences in regional land use and land management patterns. Confusion among classes occurred when spatial land use patterns in a region were not sufficiently distinct from one another or when there were too few areas of a given class within a region to be adequately represented in a training sample. For example, forestry was associated with a distinct set of spatial patterns in North America, and thus the producer's accuracy (i.e., absence of errors of omission) was high (96%) for this class and region, whereas forestry in Southeast Asia showed less distinct patterns of tree harvesting and regrowth, resulting in a lower producer's accuracy (78%) for this class and region (table S6). Forest plantations in Southeast Asia contained patterns of loss and regrowth similar to those seen with the expansion of new agricultural oil palm plantations categorized within the commodity-driven deforestation class. This was particularly true for small-scale palm plantations that are planted and grown at roughly the same spatial and temporal scale as short-rotation wood fiber plantations (fig. S3). In sub-Saharan Africa, shifting agriculture is a widespread driver of forest disturbance (Fig. 2). Spatial patterns that distinguish this class include small size of clearings; the presence, timing, size, pattern, and location of human-induced fire; and the eventual regeneration of forest vegetation to a degraded secondary state. However, spatial patterns of commodity-driven deforestation in this region appear almost identical to shifting agriculture, but without the distinctive regrowth signal (fig. S6). The similarity in spatial patterns between

Table 1. Disaggregation of global and regional tree cover loss by driver for the period 2001 to 2015. Map-based estimates are based on Global Forest Watch data (3) and a driver of tree cover loss from the current study. Sample-based estimates are based on the validation sample of 1565 randomly selected 10 × 10 grid cells from the current study. Uncertainty of sample-based estimates represents a 95% confidence interval.												
Region	Map-based estimates							Sample-based estimates				
	Hansen et al. (3)		Current study: Driver of tree cover loss					Current study: Driver of tree cover loss				
	Tree cover loss (Mha, 2001–2015)	Tree cover loss (% of global total, 2001–2015)	Deforestation	Shifting agriculture	Forestry	Wildfire	Urbanization	Deforestation	Shifting agriculture	Forestry	Wildfire	Urbanization
North America	70	21%	1%	<1%	56%	40%	2%	2 ± 1%	1 ± 1%	48 ± 11%	48 ± 11%	1 ± 1%
Latin America	78	25%	56%	31%	13%	1%	<1%	64 ± 8%	24 ± 7%	9 ± 3%	<1 ± <1%	<1 ± <1%
Europe	15	5%	None	<1%	99%	1%	None	None	<1 ± <1%	95 ± 5%	5 ± 5%	None
Africa	39	13%	4%	92%	4%	<1%	<1%	2 ± 1%	93 ± 3%	4 ± 2%	<1 ± <1%	1 ± 2%
Russia/China/South Asia	64	20%	<1%	<1%	41%	58%	<1%	2 ± 2%	1 ± 1%	38 ± 12%	59 ± 12%	<1 ± <1%
Southeast Asia	39	13%	78%	9%	13%	<1%	<1%	61 ± 13%	20 ± 10%	14 ± 6%	2 ± 6%	<1 ± <1%
Australia/Oceania	10	3%	7%	10%	29%	53%	1%	8 ± 6%	10 ± 4%	19 ± 9%	62 ± 14%	1 ± <1%
Global	314	100%	25%	21%	31%	22%	<1%	27 ± 5%	24 ± 3%	26 ± 4%	23 ± 4%	1 ± <1%

these two classes resulted in low model accuracy for the commodity-driven deforestation class in Africa; much of the commodity-driven deforestation was misclassified as shifting agriculture (table S6). In northern forests, particularly Russia, there are locations where wildfires spread through previously logged areas or where logging occurred after a fire event (fig. S5). In these cases, attributing a single driver to such areas proved difficult because patterns indicative of multiple drivers were present in the same cell, albeit in different years within the time period analyzed (2001–2015).

The global scope of our analysis was designed to assist corporations in identifying wood fiber source regions and regions of deforestation due to commodity agriculture. Although we accurately mapped dominant classes of forest disturbance

globally, opportunities remain to disaggregate landscapes further at regional and local scales. For example, we did not map changes in forest condition through time in landscapes dominated by shifting agriculture; further differentiation of primary from secondary forest clearing within this land-use class could improve our understanding of the differences between deforestation and degradation impacts (11). Differentiating key drivers such as row crops from pasturelands in South America, or tree plantations from disturbed natural forests in Southeast Asia (12), would allow for more specific supply chain analyses to identify corporate risk and responsibility from commodity-driven deforestation.

Our methodology serves as a hybrid between the accuracy and statistically unbiased estimates achieved through a sample-based approach, as

avored by academic researchers (13, 14), and the spatial comprehensiveness of a wall-to-wall mapping approach (3) preferred by a wider variety of practitioners and forest stakeholders. The results identify where deforestation is occurring; perhaps as important, they show where forest loss is not deforestation. For most regions and drivers, the map output can be used directly to quantify the proportion of forest loss caused by each driver, because map-based estimates fall within the confidence intervals of sample-based estimates (table S7). Wildfire was associated with nearly one-fourth of the world's forest loss; this type of loss is not likely to be reduced easily through management intervention. In contrast, deforestation across Central and South America, Africa, and Southeast Asia should be the geographic focus of corporate

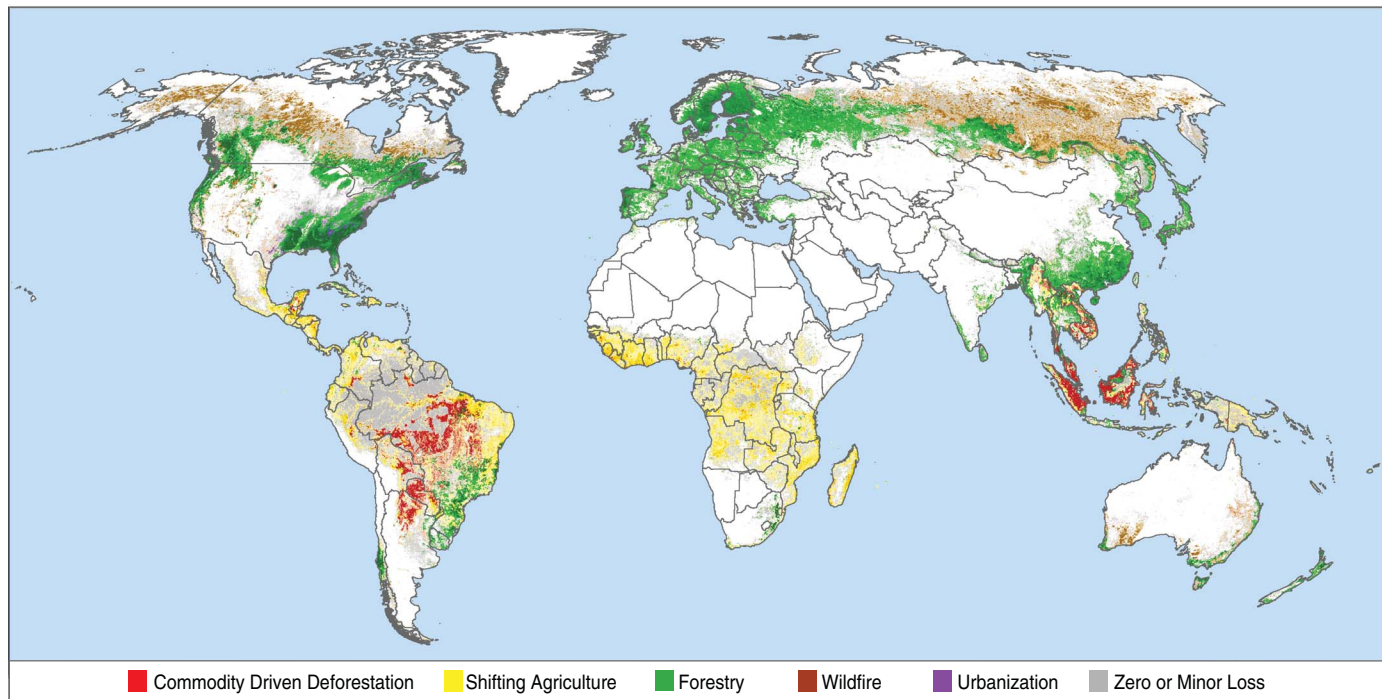


Fig. 2. Primary drivers of forest cover loss for the period 2001 to 2015. Darker color intensity indicates greater total quantity of forest cover loss.

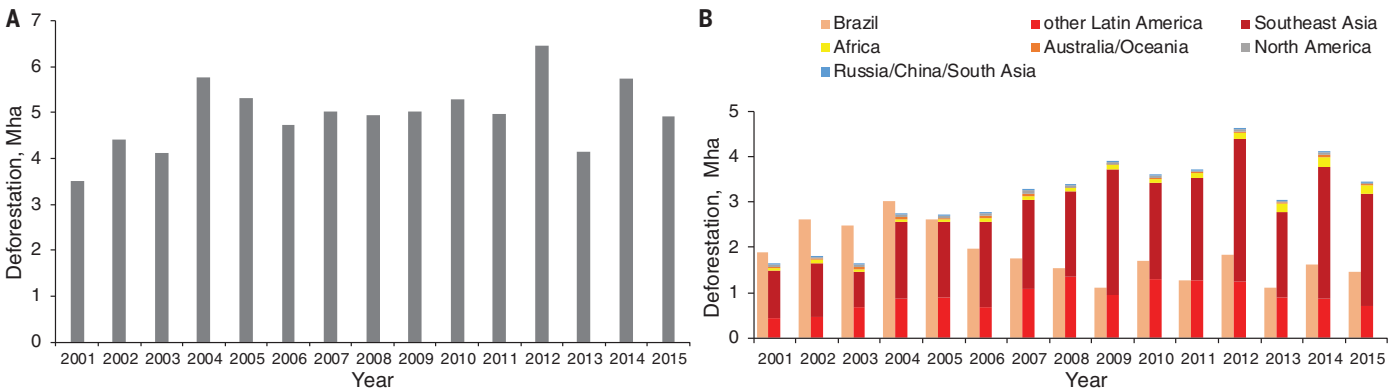


Fig. 3. Annual deforestation rates. (A) Annual worldwide tree cover loss from commodity-driven deforestation between 2001 and 2015. (B) Comparison of annual commodity-driven deforestation in Brazil and the rest of the world between 2001 and 2015.

efforts to eliminate deforestation from supply chains, as well as international policies designed to reduce greenhouse gas emissions from deforestation and forest degradation (15).

Our results indicate that policies designed to achieve zero-deforestation commitments are not being adopted or implemented at the pace needed to meet 2020 goals (Fig. 3). In regions dominated by forestry, felled trees enter wood and fiber supply chains including paper, packaging, and forest products. These areas should not be included in the monitoring of zero-deforestation commitments because they are not undergoing deforestation, as defined by a change in land use that prevents subsequent forest regrowth. Instead, companies and governments can use Fig. 2 as a wood fiber sourcing map to target priority areas for certification efforts and supply chain traceability. Identifying regions dominated by shifting agriculture may be important for identifying the extent to which this land use contributes to forest degradation, and for food supply chains where sourcing from smallholder farmers is often a priority, but where slash-and-burn practices may be leading to undesirable impacts and corporate risk. Finally, our analysis contributes to a more informed discussion about forest conservation, restoration, and management options globally by providing an enhanced experience for the more than 2 million users of the Global Forest Watch platform to understand

what is driving forest change around the world, thus preventing a common misperception that any tree cover loss shown on the map represents deforestation (16).

REFERENCES AND NOTES

1. S. Donofrio, P. Rothrock, J. Leonard, "Supply Change: Tracking Corporate Commitments to Deforestation-Free Supply Chains" (Forest Trends, 2017); www.forest-trends.org/documents/files/doc_5521.pdf#.
2. A. Sen, "Pathways to Deforestation-Free Food" (Oxfam, 2017); <https://policy-practice.oxfam.org.uk/publications/pathways-to-deforestation-free-food-developing-supply-chains-free-of-deforestation-620332>.
3. M. C. Hansen *et al.*, *Science* **342**, 850–853 (2013).
4. Global Forest Watch, <http://globalforestwatch.org>.
5. D. Schoene, W. Killmann, H. von Lüpke, M. L. Wilkie, "Definitional Issues Related to Reducing Emissions from Deforestation in Developing Countries" (Food and Agriculture Organization of the United Nations, 2007); www.fao.org/tempref/docrep/fao/009/j9345e/j9345e00.pdf.
6. N. Harris, R. Petersen, C. Davis, O. Payne, "Global Forest Watch and the Forest Resources Assessment, Explained in 5 Graphics" (World Resources Institute, 2016); www.wri.org/blog/2016/08/insider-global-forest-watch-and-forest-resources-assessment-explained-5-graphics.
7. R. S. DeFries *et al.*, *Proc. Natl. Acad. Sci. U.S.A.* **99**, 14256–14261 (2002).
8. M. C. Hansen, S. V. Stehman, P. V. Potapov, *Proc. Natl. Acad. Sci. U.S.A.* **107**, 8650–8655 (2010).
9. See supplementary materials.
10. H. J. Geist, E. F. Lambin, *Bioscience* **52**, 143–150 (2002).
11. G. Molinario, M. C. Hansen, P. V. Potapov, *Environ. Res. Lett.* **10**, 094009 (2015).
12. R. Tropek *et al.*, *Science* **344**, 981 (2014).
13. P. Olofsson *et al.*, *Remote Sens. Environ.* **148**, 42–57 (2014).
14. A. Tyukavina *et al.*, *Environ. Res. Lett.* **10**, 074002 (2015).
15. United Nations Framework Convention on Climate Change, "Warsaw Framework for REDD-Plus" (2013); http://unfccc.int/land_use_and_climate_change/redd/items/8180.php.
16. Huffington Post Canada, "Canada Largest Contributor to Deforestation Worldwide" (2014); www.huffingtonpost.ca/2014/09/05/canada-deforestation-worst-in-world_n_5773142.html.

ACKNOWLEDGMENTS

We thank M. Maier, A. Chao, M. Millstein, and J. Paltseva for their contributions to this project in its early stages of development; P. V. Potapov for the tree cover loss and gain data that were so integral to this project; the members of The Sustainability Consortium for their financial support; and L. Goldman for her cartographic assistance in creating figures for the paper and for calculating map-based summary statistics. **Funding:** This project was funded by The Sustainability Consortium. The World Resources Institute provided additional resources to the project. **Author contributions:** P.G.C.: conceptualization, formal analysis, methodology, validation, visualization, and writing; C.M.S.: conceptualization, funding acquisition, project administration, supervision, and writing; N.L.H.: methodology, resources, project administration, and writing; A.T.: methodology, validation, and writing; M.C.H.: writing. **Competing interests:** Authors declare no competing interests. **Data and materials availability:** All data are available in the main text or the supplementary materials.

SUPPLEMENTARY MATERIALS

www.sciencemag.org/content/361/6407/1108/suppl/DC1
Materials and Methods
Figs. S1 to S10
Tables S1 to S7
Data S1 to S4
References (17–30)

31 May 2018; accepted 14 August 2018
10.1126/science.aau3445

BOTANY

Glutamate triggers long-distance, calcium-based plant defense signaling

Masatsugu Toyota^{1,2,3*}, Dirk Spencer^{2†}, Satoe Sawai-Toyota^{2†}, Wang Jiaqi¹, Tong Zhang^{4,5§}, Abraham J. Koo^{4,5}, Gregg A. Howe^{6,7}, Simon Gilroy^{2*}

Animals require rapid, long-range molecular signaling networks to integrate sensing and response throughout their bodies. The amino acid glutamate acts as an excitatory neurotransmitter in the vertebrate central nervous system, facilitating long-range information exchange via activation of glutamate receptor channels. Similarly, plants sense local signals, such as herbivore attack, and transmit this information throughout the plant body to rapidly activate defense responses in undamaged parts. Here we show that glutamate is a wound signal in plants. Ion channels of the *GLUTAMATE RECEPTOR-LIKE* family act as sensors that convert this signal into an increase in intracellular calcium ion concentration that propagates to distant organs, where defense responses are then induced.

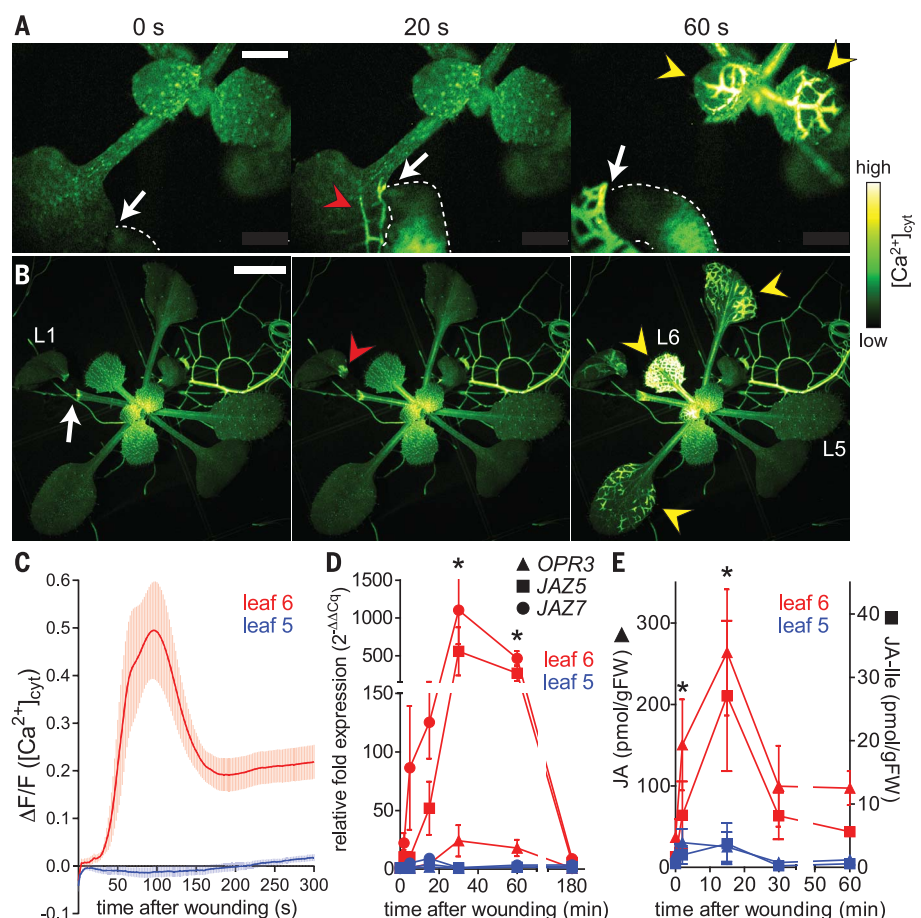
Plants respond within minutes to stresses such as wounding with both local and system-wide reactions that prime non-damaged regions to mount defenses. For herbivory, production of the defense hormone jasmonic acid (JA) and accumulation of toxic, repellent, or digestibility-reducing compounds all aid in deterring future attacks (1). Reactive oxygen species, electrical signals, and changes in cytosolic Ca^{2+} concentration ($[\text{Ca}^{2+}]_{\text{cyt}}$)

are thought to form signaling networks supporting both local and systemic defense responses [reviewed in (2)]. The electrical component is dependent on glutamate receptor-like (GLR) proteins (3–5), a family of cation-permeable ion channels that function in plant processes ranging from pathogen defense to root growth [reviewed in (6)]. Here we asked how GLRs are triggered by wounding and how subsequent Ca^{2+} -related signaling events operate to mediate systemic defense.

Caterpillar feeding on an *Arabidopsis* plant expressing the GCaMP3 fluorescent protein-based $[\text{Ca}^{2+}]_{\text{cyt}}$ sensor (7) revealed an increase in $[\text{Ca}^{2+}]_{\text{cyt}}$ at the herbivory site within 2 s that was transmitted over 1 to 2 min to distal leaves (Fig. 1A and movie S1). The spread was most evident in the vasculature, especially once the caterpillar severed a major vein. This $[\text{Ca}^{2+}]_{\text{cyt}}$ signal moved from older to younger leaves and vice versa (fig. S1 and movie S2). Wounding with scissors also caused a rapid $[\text{Ca}^{2+}]_{\text{cyt}}$ increase that propagated to distal leaves (Fig. 1B, fig. S2, and movie S3), indicating that herbivore chemical signals are not required. Mechanical wounding in leaf *n* [leaves numbered from oldest to youngest; fig. S3 (3)] led to $[\text{Ca}^{2+}]_{\text{cyt}}$ changes preferentially propagating to leaves $n \pm 3$ and $n \pm 5$ (table S1), paralleling previously defined patterns of wound-activated surface potential changes [WASPs (3)].

We wounded leaf 1 and monitored systemic responses in the “target” leaf 6 and “nontarget” leaf 5 to characterize this system. Upon wounding leaf 1, a $[\text{Ca}^{2+}]_{\text{cyt}}$ increase propagated at $1089 \pm 141 \mu\text{m/s}$ to leaf 6 (Fig. 1C and fig. S4), where a subsequent Ca^{2+} increase spread across the organ (movies S3 and S4), expression of defense marker genes increased (Fig. 1D and fig. S5), and JA and JA-Ile accumulated (Fig. 1E). The $[\text{Ca}^{2+}]_{\text{cyt}}$ increase velocity mirrors that of both WASPs (3) and a postulated systemic jasmonate production trigger (8, 9). Phloem can transport long-distance signals

Fig. 1. Wounding triggers long-distance transmission of $[\text{Ca}^{2+}]_{\text{cyt}}$ increases and systemic defense responses. (A) Caterpillar (dashed outline) feeding (white arrow) caused local $[\text{Ca}^{2+}]_{\text{cyt}}$ increases (red arrowhead) that propagated toward younger leaves (yellow arrowheads). (B) Cutting leaf 1 (L1, white arrow, 0 s) caused a local $[\text{Ca}^{2+}]_{\text{cyt}}$ increase (red arrowhead) that propagated toward target distal leaves (yellow arrowheads), e.g., leaf 6 (L6), but not to nontarget leaves such as L5. (C to E) $[\text{Ca}^{2+}]_{\text{cyt}}$ signature (C), defense gene induction (D), and JA and JA-Ile accumulation (E). *N* = 10 (C), *N* = 6 (D), and *N* = 3 (E) separate experiments. Error bars, mean \pm SE. **P* < 0.05 leaf 6 versus 5. Scale bars, 1 mm (A) or 5 mm (B).



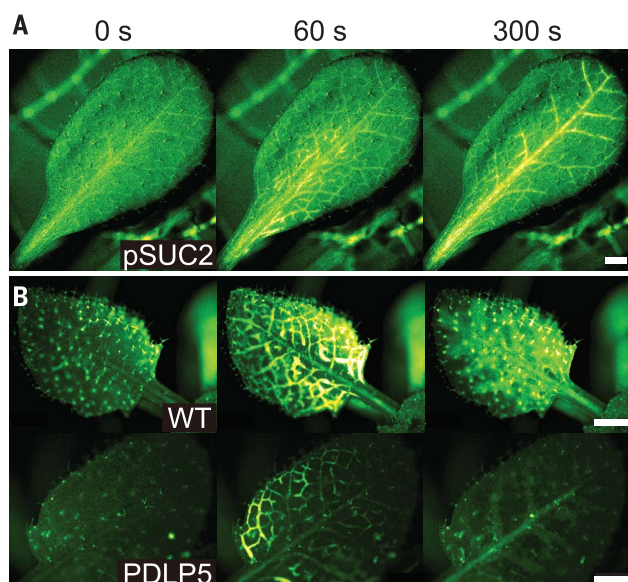


Fig. 2. Transmission of $[Ca^{2+}]_{cyt}$ increases through the phloem and plasmodesmata. (A) Phloem-specific Ca^{2+} imaging in target leaf 6 upon mechanical wounding of leaf 1 (0 s). (B) $[Ca^{2+}]_{cyt}$ increases in leaf 6 of wild-type (WT) and PDL5 overexpression (OE) lines after cutting leaf 1 (0 s). (C) $[Ca^{2+}]_{cyt}$ change in leaf 6 of wild-type and PDL5 OE and (D) defense gene induction in leaf 5 and 6 after cutting leaf 1 in PDL5 OE. The wild-type data from leaf 6 in Fig. 1, C and D, are reproduced (gray lines) to aid in comparison. Error bars, mean \pm SE. $N > 7$ separate experiments. * $P < 0.05$. Scale bars, 1 mm.

(10, 11); visualizing $[Ca^{2+}]_{cyt}$ in phloem and companion cells using the SUC2 promoter to selectively express GCaMP3 in these tissues revealed $[Ca^{2+}]_{cyt}$ phloem signal propagation at $996 \pm 207 \mu m/s$ (Fig. 2A, fig. S6, and movie S5). Pre-treating the petiole of the wounded leaf with the Ca^{2+} channel inhibitor La^{3+} prevented both export of the $[Ca^{2+}]_{cyt}$ increase (fig. S7) and systemic induction of wound-related marker genes (fig. S7D), suggesting that propagation of the $[Ca^{2+}]_{cyt}$ increase is required for induction of systemic responses.

The propagating $[Ca^{2+}]_{cyt}$ increase slowed when spreading across the target leaf (fig. S8 and movies S3 and S4). We hypothesized that this phase of transmission might be propagated through plasmodesmata [PD] (12)]. Overexpression of PLASMODESMATA-LOCATED PROTEIN 5 (PDL5) and knockout of PD-associated β -1,3-glucanase both impair PD conductance (13, 14); whereas neither of these disrupted the rapid leaf-to-leaf transmission of the $[Ca^{2+}]_{cyt}$ increase, both limited the subsequent spread in target leaves to regions adjacent to the vasculature (Fig. 2, B and C, fig. S9, and movie S6). Wound-induced systemic gene expression was also

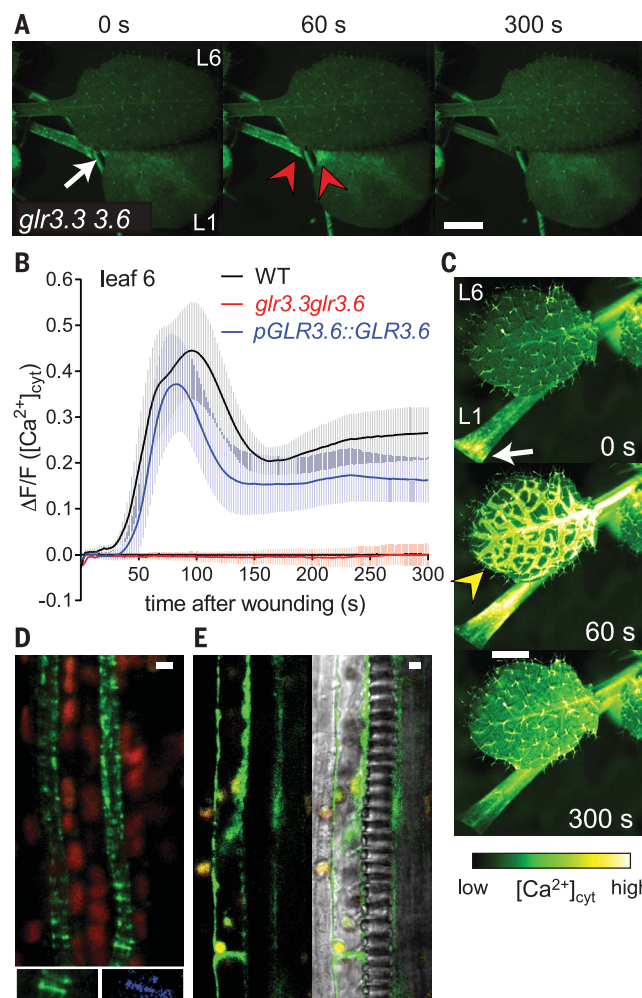


Fig. 3. GLR3.3 and GLR3.6 support long-distance transmission of $[Ca^{2+}]_{cyt}$ increases. (A) Cutting leaf 1 (L1; white arrow, 0 s) caused local $[Ca^{2+}]_{cyt}$ increases (red arrowheads) that were not propagated toward distal leaves in *glr3.3 glr3.6*. (B) $[Ca^{2+}]_{cyt}$ in the target leaf 6 (L6) of wild-type, *glr3.3 glr3.6* mutants, and its rescued line. Error bars, mean \pm SE. $N > 7$ separate experiments. Wild-type data from Fig. 1C are reproduced to aid in comparison. (C) Wound-induced $[Ca^{2+}]_{cyt}$ in L6 of *glr3.3 glr3.6 pGLR3.6::GLR3.6-EGFP* lines. (D) Localization of GLR3.3 and (E) GLR3.6 in longitudinal sections of leaf petioles (see also fig. S11 for transverse section). Green, GFP; red, autofluorescence; blue, callose (aniline blue staining) showing sieve plate. Scale bars, 2 mm (A), 5 μm [(D) and (E)].

¹Department of Biochemistry and Molecular Biology, Saitama University, Saitama 338-8570, Japan. ²Department of Botany, University of Wisconsin, Madison, WI, 53593, USA. ³JST, PRESTO, Saitama 332-0012, Japan. ⁴Department of Biochemistry, University of Missouri, Columbia, MO 65211, USA. ⁵Interdisciplinary Plant Group, University of Missouri, Columbia, MO 65211, USA. ⁶Department of Energy-PRL, Michigan State University, East Lansing, MI 48824, USA. ⁷Department of Biochemistry and Molecular Biology, and Plant Resilience Institute, Michigan State University, East Lansing, MI 48824, USA. *Corresponding author. Email: mtoyota@mail.saitama-u.ac.jp (M.T.); sgilroy@wisc.edu (S.G.) †Present address: Department of Biology, Stanford University, Stanford, CA 94305, USA. ‡Present address: Leica Microsystems, Tokyo 169-0075, Japan. §Present address: College of Agriculture, South China Agricultural University, Guangdong, China.

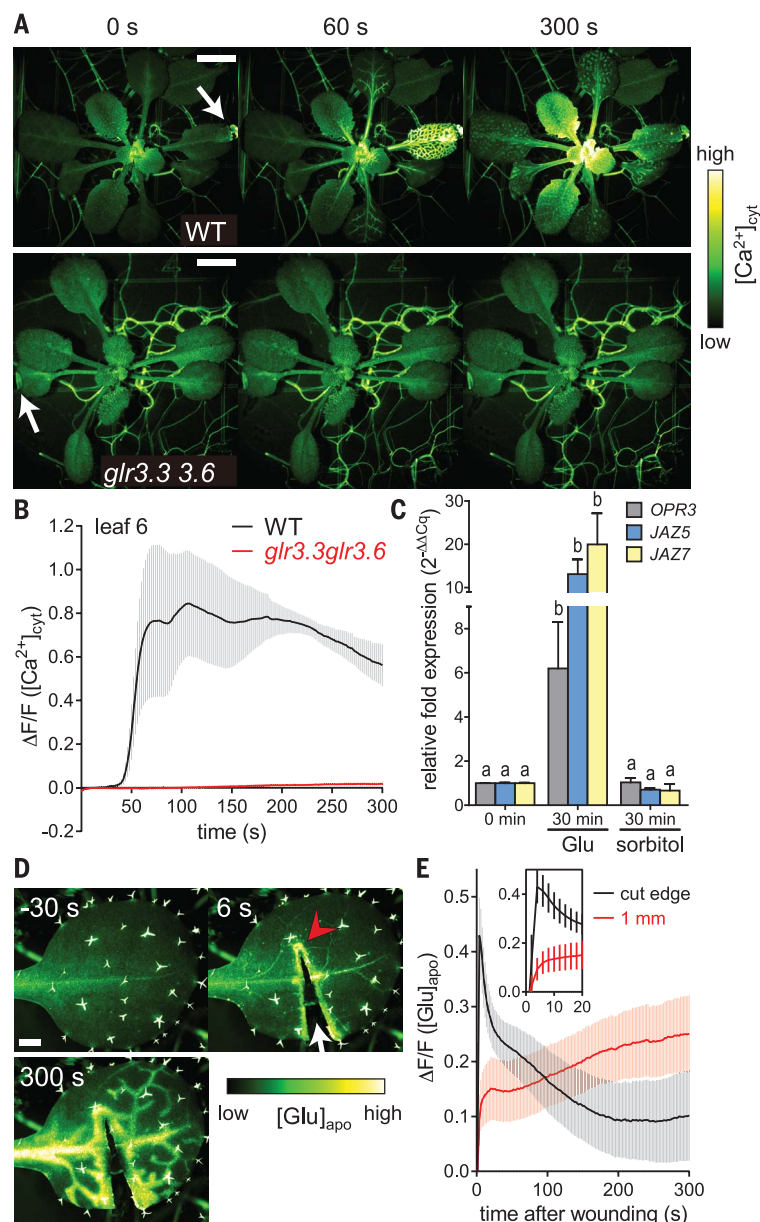


Fig. 4. Apoplastic Glu triggers systemic $[Ca^{2+}]_{cyt}$ changes and defense responses. (A) Application of 100 mM Glu (white arrow, 0 s) caused transmission of $[Ca^{2+}]_{cyt}$ increases to almost all leaves in wild type but not in the *glr3.3 glr3.6* mutants. (B and C) $[Ca^{2+}]_{cyt}$ (B) and defense gene induction (C) in leaf 6 after 100 mM Glu or sorbitol application to leaf 1. (D) $[Glu]_{apo}$ levels using iGluSnFR. Cutting leaf 1 (arrow, 0 s) caused an immediate increase in $[Glu]_{apo}$ at the wound, which gradually spread throughout the leaf. (E) iGluSnFR signals at the cut surface and 1 mm from the wound site (initial changes shown magnified in inset). Error bars, mean \pm SE. $N > 5$ (B), $N > 4$ (C), and $N = 11$ (E) separate experiments. Letters a, b denote statistical differences ($P < 0.05$). Scale bars, 5 mm (A) or 1 mm (D).

disrupted (Fig. 2D), reinforcing the likely role of PD in the spread of the $[Ca^{2+}]_{cyt}$ increase and triggering of the systemic response through target leaves.

Rapid propagation of systemic electrical signals depends upon GLR ion channel family members *GLR3.3* and *GLR3.6* (3–5); *glr3.3* and *glr3.6* single mutants showed altered kinetics of the propagating $[Ca^{2+}]_{cyt}$ signal, with *glr3.6* exhibiting the most severe reduction (fig. S10). Propagation was completely inhibited in the *glr3.3 glr3.6* double mutant (Fig. 3 and movie S7), but this response

was restored to nearly wild-type levels by driving *GLR3.6* expression in this line (Fig. 3, B and C, and movie S8), confirming the link between GLR function and propagation of the $[Ca^{2+}]_{cyt}$ increase.

GLR3.3 is ubiquitously expressed in roots, including the vasculature (15), and expressing *pGLR3.3::GLR3.3-EGFP* (enhanced green fluorescent protein) in the *glr3.3* background [*pGLR3.3::GLR3.3-EGFP* functionally rescues *glr3.3* knockout phenotypes (15)] showed that *GLR3.3* is localized to the phloem in leaves (Fig. 3D and fig. S11), consistent with a role of sieve tube Ca^{2+} channels

in wounding responses (16). By contrast, expressing *pGLR3.6::GLR3.6-EGFP* in the *glr3.6* mutant (where it also rescues the knockout phenotype; Fig. 3, B and C) showed localization to the contact cells of the xylem parenchyma (Fig. 3E and fig. S11). These same cells show expression of the lipoxygenase isoform (*LOX6*) responsible for wound-related systemic jasmonate production (17). The observation that the two GLRs supporting long-distance $[Ca^{2+}]_{cyt}$ signaling are expressed in distinct locations suggests either that there may be chemical or electrical coupling between these cell types, or that two parallel but independent pathways exist for the wound signal in phloem and xylem parenchyma.

The GLRs are gated by amino acids [reviewed in (6)]; application of 100 mM L-Glu, but not other amino acids or sorbitol (osmotic control), resulted in plant-wide *GLR3.3/GLR3.6*-dependent systemic $[Ca^{2+}]_{cyt}$ increases (Fig. 4, A and B, fig. S12, and movies S9 and S10) and defense gene induction (Fig. 4C and fig. S13). Applying less L-Glu restricted the extent of systemic $[Ca^{2+}]_{cyt}$ increase; e.g., applying 50 mM L-Glu mimicked Ca^{2+} increases observed with wounding (compare fig. S12, B and C, and table S1).

To determine whether apoplastic Glu concentration ($[Glu]_{apo}$) was increased by wounding, we targeted the GFP-based Glu sensor iGluSnFR (18) to the cell wall (fig. S14 and movie S11). Upon wounding, the iGluSnFR signal increased locally at the cut region (Fig. 4, D and E, and movie S12), mirroring $[Ca^{2+}]_{cyt}$ dynamics at this site (fig. S15A). In vivo calibrations (fig. S14, C to E) suggested that $[Glu]_{apo}$ reached ~ 50 mM at the damaged site, consistent with reports that resting $[Glu]_{apo}$ is ~ 1 mM (19) and that releasable symplastic $[Glu]$ in, e.g., the phloem is ~ 10 to 50 mM (20, 21). With greater leaf damage (hemostat crushing), Glu release to the apoplast was more extensive (fig. S15B and movie S13) and more distal leaves showed changes in $[Ca^{2+}]_{cyt}$ (table S1). Thus, the plant could tailor the extent of its systemic defense response to the severity of damage, possibly by adjusting $[Glu]_{apo}$ produced at the wound site(s).

Peptides, oligogalacturonides (OGs), adenosine 5'-triphosphate (ATP), and high mobility group (HMG) box domain-containing proteins have all been proposed as plant damage-associated molecular patterns (DAMPs), i.e., molecular elicitors of defense released upon wounding (22). We show here that Glu is also a DAMP, either leaking from damaged cells or actively released upon wounding. This Glu activates GLR ion channels, eliciting defense signal propagation through altered $[Ca^{2+}]_{cyt}$ with the vasculature as one key highway for transmission between organs. Despite links between the action of DAMPs to defense and Ca^{2+} signaling (22), application of neither OG nor the pathogen defense elicitor flg22 initiated systemic $[Ca^{2+}]_{cyt}$ increases (fig. S16), suggesting that Glu may be a critical signal in long-distance propagation of wound signaling events.

REFERENCES AND NOTES

- G. A. Howe, I. T. Major, A. J. Koo, *Annu. Rev. Plant Biol.* **69**, 387–415 (2018).
- W. G. Choi *et al.*, *Plant J.* **90**, 698–707 (2017).
- S. A. Mousavi, A. Chauvin, F. Pascaud, S. Kellenberger, E. E. Farmer, *Nature* **500**, 422–426 (2013).

4. V. Salvador-Recatalà, W. F. Tjallingii, E. E. Farmer, *New Phytol.* **203**, 674–684 (2014).
5. V. Salvador-Recatalà, *Plant Signal. Behav.* **11**, e1161879 (2016).
6. B. G. Forde, M. R. Roberts, *Fl000Prime Rep.* **6**, 37 (2014).
7. L. Tian *et al.*, *Nat. Methods* **6**, 875–881 (2009).
8. A. J. Koo, X. Gao, A. Daniel Jones, G. A. Howe, *Plant J.* **59**, 974–986 (2009).
9. G. Glauser *et al.*, *J. Biol. Chem.* **284**, 34506–34513 (2009).
10. W. J. Lucas *et al.*, *J. Integr. Plant Biol.* **55**, 294–388 (2013).
11. R. Hedrich, V. Salvador-Recatalà, I. Dreyer, *Trends Plant Sci.* **21**, 376–387 (2016).
12. J. Tilsner, W. Nicolas, A. Rosado, E. M. Bayer, *Annu. Rev. Plant Biol.* **67**, 337–364 (2016).
13. J. Y. Lee *et al.*, *Plant Cell* **23**, 3353–3373 (2011).
14. A. Levy, M. Erlanger, M. Rosenthal, B. L. Epel, *Plant J.* **49**, 669–682 (2007).
15. E. D. Vincill, A. E. Clarin, J. N. Molenda, E. P. Spalding, *Plant Cell* **25**, 1304–1313 (2013).
16. A. C. Furch *et al.*, *Plant Cell* **21**, 2118–2132 (2009).
17. E. E. Farmer, D. Gasperini, I. F. Acosta, *New Phytol.* **204**, 282–288 (2014).
18. J. S. Marvin *et al.*, *Nat. Methods* **10**, 162–170 (2013).
19. G. Lohaus, H. W. Heldt, *J. Exp. Bot.* **48**, 1779–1786 (1997).
20. E. Hunt *et al.*, *J. Exp. Bot.* **61**, 55–64 (2010).
21. J. Sandström, J. Pettersson, *J. Insect Physiol.* **40**, 947–955 (1994).
22. H. W. Choi, D. F. Klessig, *BMC Plant Biol.* **16**, 232 (2016).

ACKNOWLEDGMENTS

We thank E. Farmer, E. Spalding, J.-Y. Lee, and T. Kotake for mutant/transgenic lines and chemicals, and W. Wong and S. Swanson for critical reading of the manuscript. **Funding:** This research was supported by grants from JST PRESTO, KAKENHI (17H05007, 18H04775, 18H05491), NSF (MCB-1329273, IOS-1557439, IOS-1557899, IOS-1456864), DOE (DE-FG02-91ER20021), and NASA (NNX14AT25G).

Author contributions: M.T. and S.G. designed the study and wrote the manuscript. M.T., D.S., S.T., W.J., T.Z., A.K., and G.H. performed

experiments and analyzed data. All authors discussed the results and contributed to the manuscript. **Competing interests:** The authors declare no competing financial interests. **Data and materials availability:** All lines are available by contacting the corresponding author.

SUPPLEMENTARY MATERIALS

www.sciencemag.org/content/361/6407/1112/suppl/DC1
Materials and Methods

Figs. S1 to S16

Tables S1 and S2

Movies S1 to S13

References (23–35)

5 April 2018; accepted 27 July 2018

10.1126/science.aat7744

MIGRATION

A continental system for forecasting bird migration

Benjamin M. Van Doren^{1*} and Kyle G. Horton²

Billions of animals cross the globe each year during seasonal migrations, but efforts to monitor them are hampered by the unpredictability of their movements. We developed a bird migration forecast system at a continental scale by leveraging 23 years of spring observations to identify associations between atmospheric conditions and bird migration intensity. Our models explained up to 81% of variation in migration intensity across the United States at altitudes of 0 to 3000 meters, and performance remained high in forecasting events 1 to 7 days in advance (62 to 76% of variation was explained). Avian migratory movements across the United States likely exceed 500 million individuals per night during peak passage. Bird migration forecasts will reduce collisions with buildings, airplanes, and wind turbines; inform a variety of monitoring efforts; and engage the public.

Billions of birds migrate between distant breeding and wintering sites each year, through landscapes and airspaces increasingly transformed by humans. Hundreds of millions die annually from collisions with buildings, automobiles, and energy installations (1), and light pollution exacerbates these effects (2). Pulses of intense migration interspersed with periods of low activity characterize birds' movements aloft (3, 4), and efforts to reduce negative effects on migrants (e.g., turning off lights and wind turbines at strategic times) (5) would be most effective if they targeted the few nights with intense migratory pulses. However, bird movements are challenging to predict days or even hours in advance.

For decades, scientists have studied the drivers of avian migration. Winds, temperature, barometric pressure, and precipitation play key roles (6–8). However, such general relationships have not produced migration forecasts accurate at both broad continental extents and fine spatial and temporal resolutions (9, 10). Local topography, regional geography, and time of season modify relationships between conditions and migration intensity, and hundreds of species with diverse behaviors frequently pass over a single location during migration. The complex interactions between environmental conditions and animal behavior make predicting bird migration at the assemblage level a challenge.

One major difficulty has been amassing behavioral data that appropriately characterize bird migration at a continental scale. Radar, used globally as a tool to study animal migration (3, 11–14), offers a realistic solution to monitor hundreds of species (15). In the continental United States, the Next Generation Weather Radar (NEXRAD) network comprises 143 weather surveillance radars (16) and an archive with more than two decades of data. Although designed for meteorological applications, these radars measure energy reflected by a diversity of aerial targets, including birds. Only recently have advances in computational

methods [e.g., (17)] facilitated the use of the entire radar archive for longitudinal studies of bird migration at continental scales.

Using the NEXRAD archive, we quantified 23 years (1995 to 2017) of spring nocturnal bird migration across the United States (Fig. 1). We developed a classifier to eliminate radar scans contaminated with precipitation. We then trained gradient-boosted trees (18) to predict bird migration intensity from atmospheric conditions reported by the North American Regional Reanalysis (19). Our model used 12 predictors, including

winds, air temperature, barometric pressure, and relative humidity (fig. S1), which we used to predict a cube-root-transformed index of migration intensity (expressed in square centimeters per cubic kilometer). The cube-root transform reduces skewness but is less extreme than a log transformation, which would have given considerable weight to biologically unimportant differences between small values. We measured migration intensity in 100-m altitude bins up to 3 km to model the three-dimensional distribution of migrating birds over the continent. To express migration intensities in numbers of birds, we assumed a radar cross section per bird of 11 cm². The radar cross section is a measure of reflected energy; this value is typical of medium-sized songbirds and representative of migratory species (12).

Our migration forecast model explained 78.9% of variation in migration intensity over the United States (Figs. 2 and 3A). Performance was consistent across years (mean yearly coefficient of determination $R^2 = 0.781 \pm 0.010$ SD). We quantified the importance of each predictor by calculating gain, a measure of how much predictions improve by adding a given variable. Air temperature was most important, with an average gain more than three times that of the second-ranked predictor, date (fig. S2). High temperatures coincided with large migration pulses (Fig. 4 and figs. S3 and S4). As a predictor of bird migration, temperature likely plays a dual role as an index of spring phenology and a short-term signal for movement, as favorable

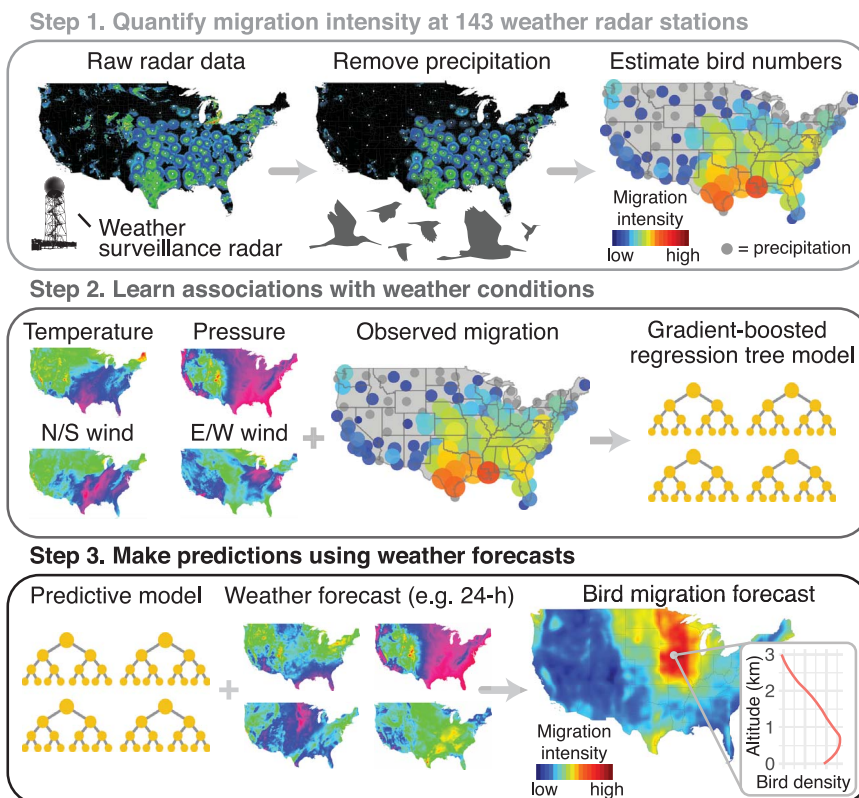


Fig. 1. Methodology for generating migration forecasts. We used weather surveillance radars to quantify 23 years of spring bird migration, modeled migration intensity as a function of observed atmospheric conditions, and used this model to forecast future migration events under predicted weather conditions.

¹Edward Grey Institute, Department of Zoology, University of Oxford, Oxford OX1 3PS, UK. ²Cornell Lab of Ornithology, Cornell University, Ithaca, NY 14850, USA.

*Corresponding author. Email: benjamin.vandoren@zoo.ox.ac.uk

southerly winds usually accompany warmer air masses. Other important predictors included altitude, longitude, surface pressure, latitude, and wind (fig. S2).

The model provides informative predictions several days in advance. We evaluated its utility as a true forecast system with archived weather forecasts from the North American Mesoscale Forecast System (NAM) and Global Forecast System (GFS). NAM has higher spatial resolution but is a shorter-range forecast (12-km grid, 3-day range) than GFS (0.5° grid, >7-day range). We made predictions up to 3 days in advance with NAM and up to 7 days in advance with GFS, expecting performance to degrade with time because of the decreasing accuracy of longer-range weather forecasts. Predictions on the basis of 24-hour NAM forecasts explained 75% of variation in migration

intensity, 3-day NAM forecasts explained 71%, and 7-day GFS forecasts explained 62% (fig. S5).

The model captures patterns of bird migration across the United States with high spatial accuracy, particularly in the central and eastern regions (fig. S6). We evaluated spatial accuracy over areas without radar coverage by iteratively removing the data from each radar station, retraining the model on the remaining data, and testing performance on the withheld station. Median R^2 for withheld stations was 0.72, and R^2 was 0.60 or higher for 75% of stations (fig. S7). Spatial variation in performance likely stems from local influences on migratory behavior (e.g., topography), which our model did not explicitly incorporate.

Previous research suggests that migration behavior and weather conditions in the days immediately preceding a migration event can predict

its intensity [e.g., (10)]. We found that including atmospheric data from the preceding night and 24-hour changes in conditions did improve performance, but not markedly. A model that included atmospheric conditions 24 hours before an event explained 80.1% of variation in migration intensity, and further including observed migration intensity from the previous night increased R^2 to 81.3%.

Finally, we used model predictions to estimate the total number of birds actively migrating each night across the United States. Summing predictions countrywide, we infer that nightly movements frequently exceed 200 million birds (Fig. 3B). Peak passage occurred in the first half of May, when the median predicted movement size was 422 million birds per night. Although our model tended to underpredict the largest observed movements (Fig. 3A), a conservative forecast system

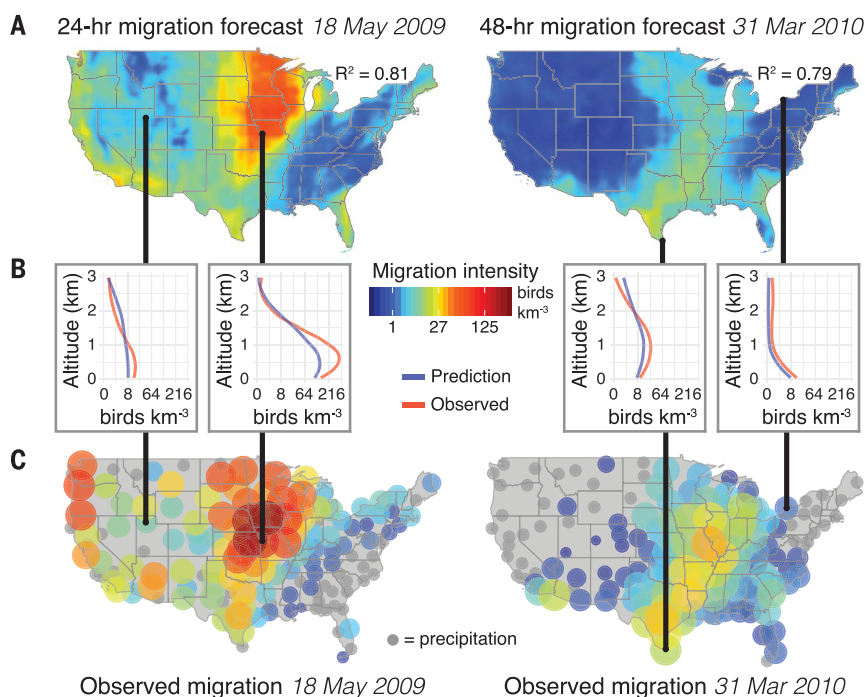


Fig. 2. Migration forecasts and corresponding observed migration.

(A) Countrywide migration forecast surfaces showing predicted mean migration intensity across altitudes. (B) Altitudinal profiles at four stations, showing predicted and observed intensity values. (C) Mean migration intensity observed at all radar stations. Gray circles indicate stations where migration intensity could not be measured because of precipitation.

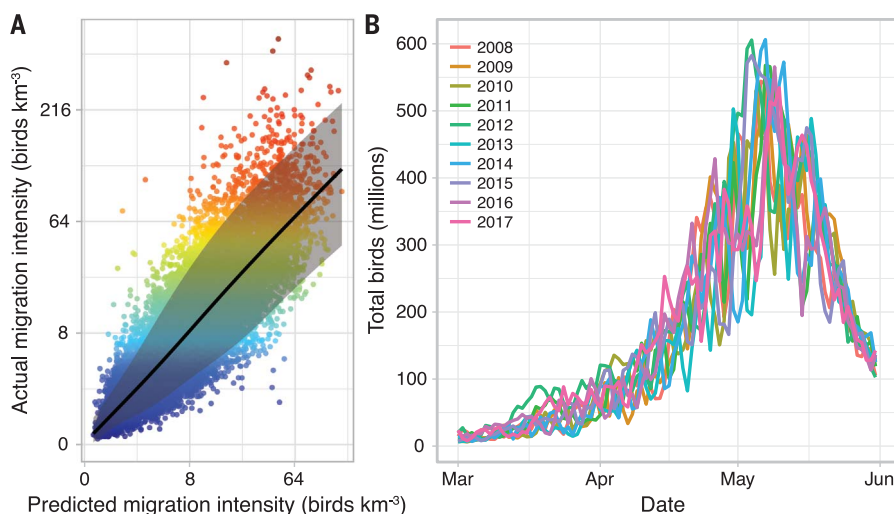
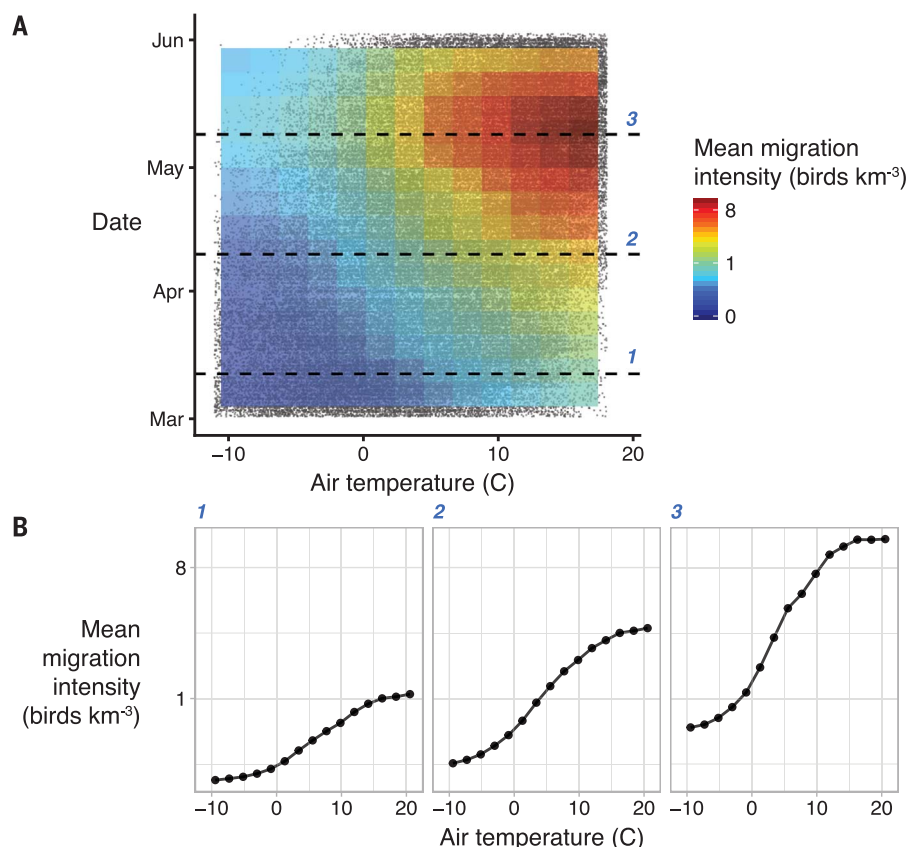


Fig. 3. Accuracy of forecasts and nightly continental predictions.

(A) Mean predicted and observed migration intensities for test data, with points colored by observed migration intensity (y axis). The scatterplot shows values after averaging across altitudes. Shading shows empirical 90% prediction intervals, which covered 90.5% of observed values. (B) Nightly peak migration magnitude estimated across the continental United States for 2008 to 2017. The size of migratory movements varied markedly from night to night during the peak of the migration season.

Fig. 4. Migration intensity predictions by air temperature and date.

(A) Heat map colors show migration intensity predictions for dates and air temperature values. Each data point on the scatterplot behind the heat map represents data for one night from one radar. Only well-supported predictions and corresponding data points are shown (the outer 10% of temperature and date values are excluded). Temperature values correspond to air temperatures at altitudes up to 3000 m. (B) Cross sections of model predictions for three spring dates. For a given date, the model predicts migration intensity to vary closely with temperature. Fewer observations correspond to cold temperatures later in the season.



decreases the risk of taking unneeded mitigation action. More accurately predicting the largest migration events may require explicit modeling of migrant flow across the continent, including responses to topographical features (20).

Migration forecasts will further ecological research while aiding monitoring and mortality mitigation efforts. Accurate predictions can inform decisions to temporarily shut down lights and wind turbines, halt gas flares, choose airplane flight paths, and take other actions to prevent human and avian mortality (10, 21). Global health workers monitoring avian-borne diseases can use migration forecasts to anticipate bird movements. Further integration of large citizen science datasets with radar observations will provide the means to study species-specific patterns of behavior at a large scale (22), and studying local variation in migratory behavior will lead to more accurate models of atmospheric bird distributions (23). Migration forecast systems have great potential to aid environmental monitoring and conservation efforts; fully realizing this potential will require the cooperation not just of scientists but also of governments and agencies that produce and disseminate radar products (21).

REFERENCES AND NOTES

1. S. R. Loss, T. Will, P. P. Marra, *Annu. Rev. Ecol. Evol. Syst.* **46**, 99–120 (2015).
2. J. D. McLaren *et al.*, *Ecol. Lett.* **21**, 356–364 (2018).
3. A. Farnsworth *et al.*, *Ecol. Appl.* **26**, 752–770 (2016).
4. B. Emi, F. Liechti, L. Underhill, B. Bruderer, *Ardea* **90**, 155–166 (2002).
5. B. M. Van Doren *et al.*, *Proc. Natl. Acad. Sci. USA* **114**, 11175–11180 (2017).
6. W. J. Richardson, *Oikos* **30**, 224–272 (1978).
7. F. Liechti, *J. Ornithol.* **147**, 202–211 (2006).
8. M. U. Kemp, J. Shamoun-Baranes, A. M. Dokter, E. van Loon, W. Bouten, *Ibis* **155**, 734–749 (2013).
9. S. A. Gauthreaux, *Direct Visual and Radar Methods for the Detection, Quantification, and Prediction of Bird Migration* (Department of Zoology, Clemson University, 1980).
10. J. Van Belle, J. Shamoun-Baranes, E. Van Loon, W. Bouten, *J. Appl. Ecol.* **44**, 864–874 (2007).
11. S. A. Gauthreaux, C. G. Belser, D. van Blaricom, in *Avian Migration*, P. Berthold, E. Gwinner, E. Sonnenschein, Eds. (Springer, 2003), pp. 335–346.
12. A. M. Dokter *et al.*, *J. R. Soc. Interface* **8**, 30–43 (2011).
13. G. Hu *et al.*, *Science* **354**, 1584–1587 (2016).
14. T. Alerstam, G. A. Gudmundsson, M. Green, A. Hedenström, *Science* **291**, 300–303 (2001).
15. J. F. Kelly, K. G. Horton, *Glob. Ecol. Biogeogr.* **25**, 1159–1165 (2016).
16. T. D. Crum, R. L. Alberty, *Bull. Am. Meteorol. Soc.* **74**, 1669–1687 (1993).
17. D. R. Sheldon, A. Farnsworth, J. Irvine, B. M. Van Doren, K. F. Webb, T. G. Dietterich, S. Kelling, in *Proceedings of the Twenty-Seventh AAAI Conference on Artificial Intelligence*, M. des Jardins, M. L. Littman, Eds. (Association for the Advancement of Artificial Intelligence, 2013), pp. 1334–1340.
18. T. Chen, C. Guestrin, in *Proceedings of the 22nd ACM SIGKDD International Conference on Knowledge Discovery and Data Mining* (Association for Computing Machinery, 2016), pp. 785–794.
19. F. Mesinger *et al.*, *Bull. Am. Meteorol. Soc.* **87**, 343–360 (2006).
20. A. Aurbach, B. Schmid, F. Liechti, N. Chokani, R. Abhari, *J. Theor. Biol.* **454**, 126–138 (2018).
21. S. Bauer *et al.*, *Bioscience* **67**, 912–918 (2017).
22. K. G. Horton *et al.*, *Ecol. Lett.* **21**, 1055–1064 (2018).
23. J. Shamoun-Baranes, H. van Gasteren, V. Ross-Smith, in *Aeroecology*, P. Chilson, W. F. Frick, J. Kelly, F. Liechti, Eds. (Springer, 2017), pp. 465–497.
24. B. M. Van Doren, K. G. Horton, Dataset for “A continental system for forecasting bird migration,” figshare (2018); <https://doi.org/10.6084/m9.figshare.6962810>.

ACKNOWLEDGMENTS

We thank A. Farnsworth, D. Sheldon, B. Sheldon, W. Hochachka, V. Melnikov, G. Hooker, J. Calvert, and three anonymous reviewers.

Funding: This work was funded by the Marshall Aid Commemoration Commission (B.M.V.D.) and by an Edward W. Rose postdoctoral fellowship, the Leon Levy Foundation, and NSF grants DBI-1661329 and DBI-1661259 (K.G.H.). **Author contributions:** B.M.V.D. conceived of the study, performed statistical analyses, and wrote the paper; K.G.H. performed radar analyses, shaped the study, and contributed writing. **Competing interests:** The authors declare no competing interests. **Data and materials availability:** Data and code are available from figshare (24).

SUPPLEMENTARY MATERIALS

www.sciencemag.org/content/361/6407/1115/suppl/DC1
Materials and Methods
Figs. S1 to S10
References (25–37)

2 April 2018; accepted 13 August 2018
10.1126/science.aat7526

PROTEIN TARGETING

An ER surface retrieval pathway safeguards the import of mitochondrial membrane proteins in yeast

Katja G. Hansen^{1*}, Naama Aviram^{2*†}, Janina Laborenz¹, Chen Bibi², Maren Meyer¹, Anne Spang³, Maya Schuldiner^{2‡}, Johannes M. Herrmann^{1‡}

The majority of organellar proteins are translated on cytosolic ribosomes and must be sorted correctly to function. Targeting routes have been identified for organelles such as peroxisomes and the endoplasmic reticulum (ER). However, little is known about the initial steps of targeting of mitochondrial proteins. In this study, we used a genome-wide screen in yeast and identified factors critical for the intracellular sorting of the mitochondrial inner membrane protein Oxa1. The screen uncovered an unexpected path, termed ER-SURF, for targeting of mitochondrial membrane proteins. This pathway retrieves mitochondrial proteins from the ER surface and reroutes them to mitochondria with the aid of the ER-localized chaperone Djpl. Hence, cells use the expanse of the ER surfaces as a fail-safe to maximize productive mitochondrial protein targeting.

Despite our detailed understanding of the translocation routes into mitochondria, little is known about cytosolic targeting of mitochondrial precursors (1, 2). To identify factors that take part in early targeting steps of mitochondrial membrane proteins, we designed a genetic screen in yeast, monitoring the cytosolic accumulation of nonimported mitochondrial precursors. To this end, we integrated the coding sequence of orotidine-phosphate decarboxylase (Ura3) into the C terminus of the nuclear encoded inner membrane protein Oxa1 while maintaining the endogenous flanking regions of the *OXA1* gene (Fig. 1A). The

corresponding Oxa1-Ura3 protein, expressed in the absence or presence of endogenous Oxa1, was efficiently targeted to mitochondria, integrated into the inner membrane, and fully functional (Fig. 1B and fig. S1, A to D). Owing to efficient targeting of Oxa1-Ura3 to mitochondria, Ura3 was sequestered from the cytosol, causing a severe growth defect on media lacking uracil. This effect was reverted when the presequence of Oxa1-Ura3 was deleted (Δ N-Oxa1-Ura3), causing its cytosolic accumulation and subsequent uracil-independent growth (Fig. 1C). Hence, a defect in mitochondrial targeting could be monitored by growth on medium lacking uracil.

Using automated mating approaches, the Oxa1-Ura3 construct was introduced into yeast libraries covering 4916 deletion mutants of nonessential genes as well as 1102 DAmP (decreased abundance by mRNA perturbation) mutants of essential genes (3) (Fig. 1D). Twelve mutants displayed particularly strong growth on uracil-deficient media, suggesting critical roles of corresponding proteins in preventing cytosolic accumulation of the Oxa1-Ura3 precursor (Fig. 1E). Whereas some of the identified factors were expected (e.g., Tim50, an essential subunit of the TIM23 translocase), several of the hits were nonmitochondrial proteins for which a role in mitochondrial protein import or precursor quality control was unknown. These include the uncharacterized proteins Yil029c, Ylr050c, and Ycr100c, which we named Ema17, Ema19, and Ema35, respectively (for efficient mitochondria targeting-associated proteins). These three components are predicted to be membrane proteins but were not previously found in mitochondria (4). Ema19 is embedded in the endoplasmic reticulum (ER) membrane and conserved among eukaryotes. Deletion mutants lacking Ema19 or Ema35 showed respiration problems at elevated temperatures (fig. S2, A to E).

One of the identified components was Djpl, an abundant yet poorly characterized member of the J-protein/Hsp40 cochaperone family (5). Oxa1-Ura3 growth assays with strains lacking

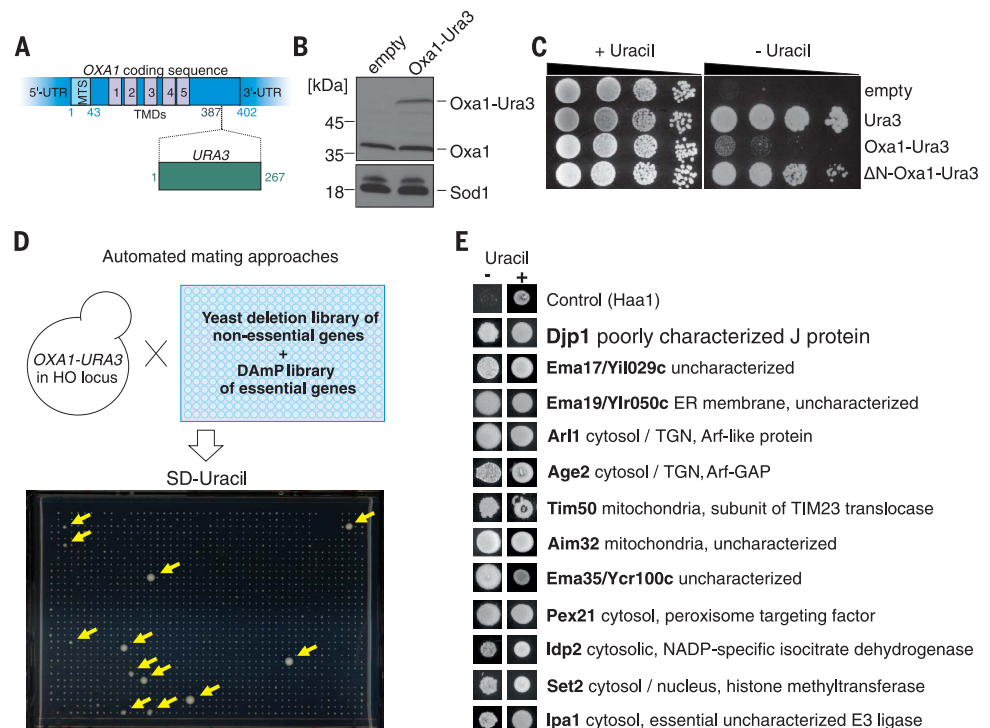
¹Division of Cell Biology, University of Kaiserslautern, Kaiserslautern, Germany. ²Department of Molecular Genetics, Weizmann Institute of Science, Rehovot, Israel. ³Biozentrum, University of Basel, Basel, Switzerland.

*These authors contributed equally to this work. †Present address: Laboratory of Bacteriology, The Rockefeller University, New York, NY, USA. ‡Corresponding author. Email: hannes.herrmann@biologie.uni-kl.de (J.M.H.); maya.schuldiner@weizmann.ac.il (M.S.)

Fig. 1. Genetic screen for mutants that accumulate Oxa1-Ura3 in the cytosol. (A) Structure of the Oxa1-Ura3 construct. TMD, transmembrane domain; MTS, mitochondrial targeting sequence; UTR, untranslated region.

(B) Immune blot of Oxa1-Ura3. (C) Growth of Δ ura3 mutants expressing the indicated constructs. (D) Representative array plate on uracil-deficient medium. Yellow arrows indicate mutants accumulating Oxa1-Ura3 in the cytosol. SD, synthetic dextrose medium.

(E) Proteins critical for the prevention of cytosolic accumulation of Oxa1-Ura3. TGN, trans-Golgi network; GAP, guanosine triphosphatase activating protein; NADP, nicotinamide adenine dinucleotide phosphate.



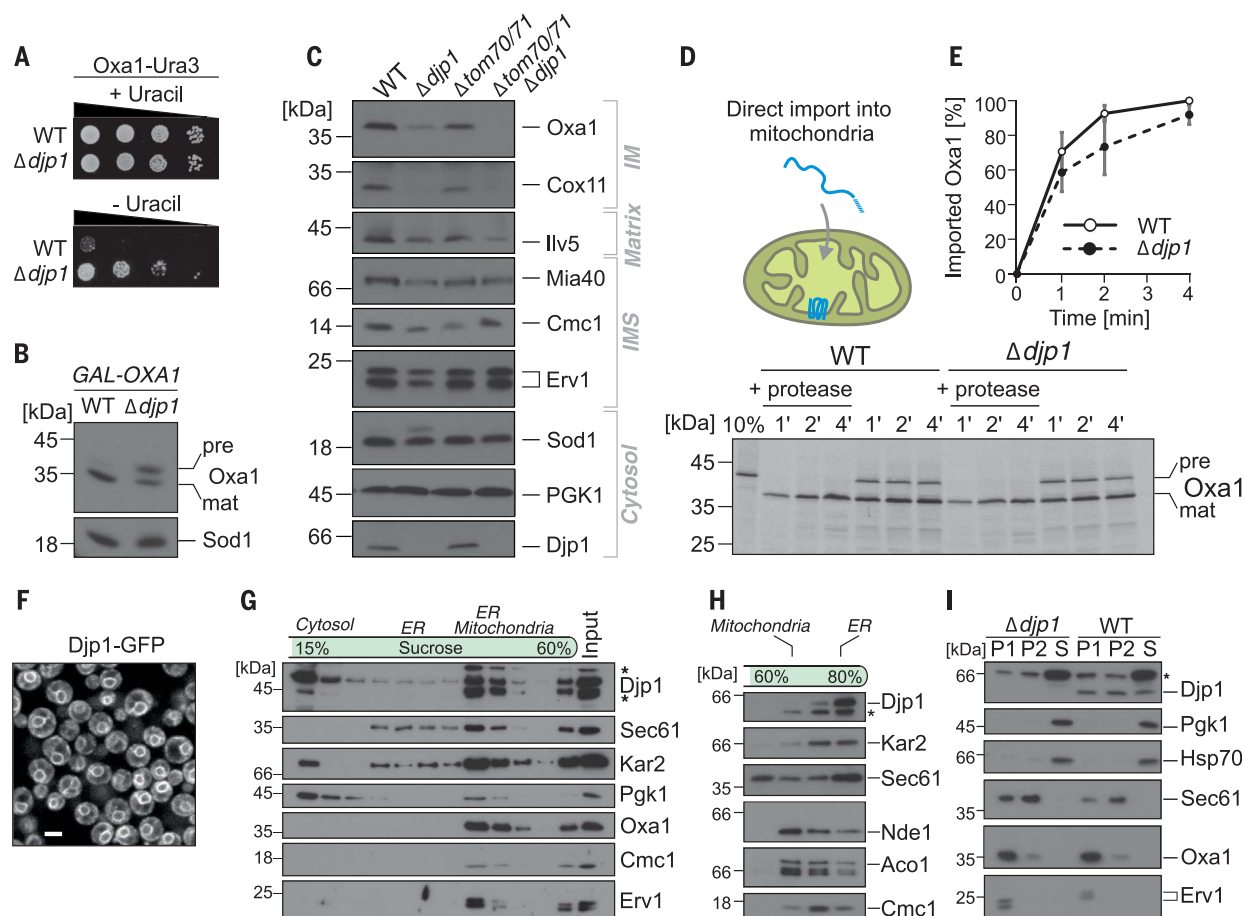


Fig. 2. Dj1 is critical for mitochondrial biogenesis. (A) Growth on synthetic medium with or without uracil. (B) Oxa1 was overexpressed in wild-type (WT) and $\Delta dj1$ using the GAL promoter. Cell extracts were analyzed by immune blot; pre, precursor; mat, mature. (C) Cellular extracts were analyzed by immune blotting. IMS, intermembrane space. (D and E) Radiolabeled Oxa1 precursor (pre) was incubated with WT or

$\Delta dj1$ mitochondria. Data shown are means \pm SD; $n = 4$ replicates. (F) Dj1-GFP shows a perinuclear staining typical for ER proteins. Scale bar, 5 μ m. (G to I) Cell extracts were separated on sucrose gradients or by differential centrifugation. A large fraction of Dj1 cofractionates with ER membranes. 12,000g and 30,000g pellets are labeled as P1 and P2, respectively. S, supernatant. Asterisks indicate cross-reactions of antibodies.

other J-proteins confirmed a specific role for Dj1 (fig. S3, A to E). Dj1 is involved in peroxisomal import and the biogenesis of the mitochondrial outer membrane protein Mim1; however, the mechanism of its function was not elucidated (6, 7). The robust growth of the Oxa1-Ura3-expressing $\Delta dj1$ mutant in the absence of uracil suggests that Dj1 plays a role in targeting or import of Oxa1 (Fig. 2A). Indeed, in $\Delta dj1$ cells we observed reduced levels of endogenous Oxa1 and a strong accumulation of the precursor when Oxa1 was overexpressed (Fig. 2, B and C, and fig. S4A). The relevance of Dj1 was not restricted to Oxa1. The steady-state levels of multiple mitochondrial proteins were considerably reduced in $\Delta dj1$ cells. Dj1 was particularly important in mutants lacking the mitochondrial preprotein receptors Tom70/71 (6) (Fig. 2C and fig. S4, B and C). However, in vitro, we did not observe a considerably reduced Oxa1 import efficiency of isolated $\Delta dj1$ mitochondria (Fig. 2, D and E). This suggests that Dj1 plays a role in Oxa1 targeting that is upstream of the translocation reaction.

Systematic localization studies previously identified Dj1 as an ER-associated protein (8), which we confirmed by fluorescence microscopy (Fig. 2F) and subcellular fractionation (Fig. 2, G to I). In addition, a fraction of Dj1 was present in the cytosol where it did not appear to interact with ribosomes (fig. S5A). We could not exclude that a small fraction of Dj1 may be bound to mitochondria. The ER-binding of Dj1 was very tight, nucleotide independent, and also observed in mutants lacking Ema19 or Ema35, although it appeared to be reduced in these mutants (fig. S5, B to E).

Why would an ER protein affect mitochondrial targeting? A fraction of Oxa1-green fluorescent protein (GFP) was ER-localized in $\Delta dj1$ but not in wild-type cells (Fig. 3A). This fraction considerably increased upon depletion of Cdc48, a component crucial for the proteasomal degradation of aberrant ER-associated proteins. Accordingly, Oxa1 lacking its mitochondrial presequence (AN-Oxa1) was partially glycosylated (fig. S6A). Glycosylated Oxa1 was also observed upon overexpression of Oxa1, particularly in $\Delta dj1$ cells. This suggests that in $\Delta dj1$ cells, a fraction

of Oxa1 that accumulates on the ER surface gets integrated into the membrane, glycosylated, and recognized as mislocalized.

Because Dj1 is present at different cellular locations, we tested whether the ER-bound Dj1 is critical for Oxa1 biogenesis: We expressed Dj1-GFP in the presence of GFP-binding chromobody traps that restricted Dj1 either to the ER (Erg11-binder) or to the vacuole (Vph1-binder) (Fig. 3B and fig. S6, B to D). The ER-tethered Dj1 version, but not that on the vacuolar membrane, fully promoted Oxa1 import into mitochondria (Fig. 3, C to E). In the absence of Dj1, Oxa1 may be inserted into the ER membrane, glycosylated, and recognized as aberrant and degraded (fig. S6E).

In vitro binding experiments showed that the ER surface binds Oxa1 precursor in a Dj1-mediated manner (Fig. 3F and fig. S7, A to D). It has previously been assumed that any targeting of mitochondrial proteins to the ER would be a dead end, resulting in recognition of mistargeting and degradation. However, our results suggest that the association with the ER surface could

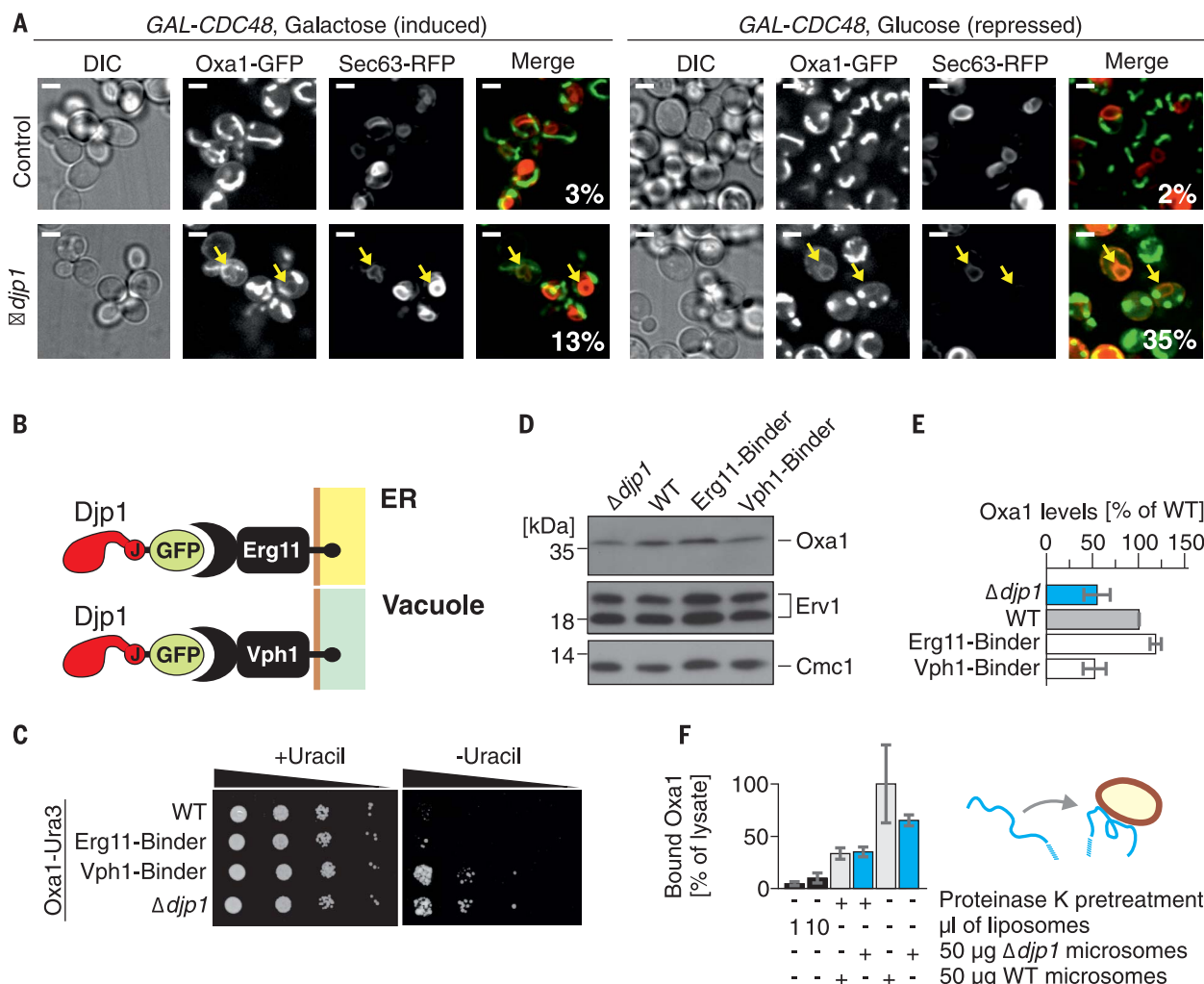


Fig. 3. Djpl prevents the accumulation of Oxa1 on the ER. (A) In the absence of Djpl, Oxa1 partially accumulated on the ER, especially upon depletion of Cdc48. Sec63-RFP served as an ER marker. The percentage of cells showing ER-localized Oxa1 is depicted. Scale bars, 5 μ m. RFP, red fluorescent protein; DIC, differential interference contrast. (B) Chromobody-based binders to trap Djpl on the ER or the

vacuole. (C to E) ER-localized Djpl promotes efficient import of Oxa1-Ura3 into mitochondria and leads to WT levels of Oxa1. Data shown are means \pm SD; $n = 3$. (F) Oxa1 precursor was incubated with liposomes or protease-treated and -untreated microsomes. Membranes were reisolated, and the associated Oxa1 was quantified. The bound Oxa1 was normalized to the WT microsome sample. Means \pm SE are shown; $n = 3$.

instead be an intermediate in productive protein targeting to mitochondria. To test whether the ER-localized Oxa1 is imported into mitochondria, we tethered Oxa1 mRNA to the ER surface such that all Oxa1 was translated on ER membranes (9). Under these conditions, Djpl became critical for respiration competence, indicating a crucial role in the productive Oxa1 transfer from the ER to mitochondria (fig. S7, E and F).

To investigate mitochondrial import of Oxa1 in a more physiological environment, we employed semi-intact cells with permeabilized plasma membranes (10) (Fig. 4A). The in vitro import into semi-intact cells was similar to the import into isolated mitochondria requiring mitochondrial membrane potential and mitochondrial translocases (fig. S8, A to C). However, in semi-intact cells, the mitochondrial import of Oxa1 and other mitochondrial membrane proteins was consid-

erably less efficient in the absence of Djpl (Fig. 4, B and C, and fig. S8, D to F). Preloading of $\Delta djp1$ semi-intact cells with purified Djpl restored their competence to import Oxa1 (fig. S8J). Oxa1 import was almost fully blocked in semi-intact $\Delta tom70/71/\Delta djp1$ cells, indicating that Djpl and Tom70 cooperate (fig. S8, A and B).

In vitro Djpl considerably stimulated the import of ER-bound mitochondrial precursors, including that of Oxa1. Hence, Djpl and other ER proteins maintained import-competent precursors (Fig. 4, D to G, and fig. S8G). Djpl was particularly critical for the microsome-to-mitochondria transfer of the very hydrophobic inner membrane protein Coq2 (fig. S8H), which showed a profound ER association in $\Delta djp1$ cells (fig. S8I). When we co-incubated wild-type and $\Delta djp1$ microsomes with low, rate-limiting amounts of mitochondria, a strong Djpl-dependent stimulation of the Oxa1

import was observed (Fig. 4, H and I, arrows). Thus, the ER supports import into mitochondria rather than competes with it. In this reaction, we observed a direct binding of Oxa1 precursors to Djpl, particularly when the mitochondrial membrane potential was depleted (Fig. 4J).

Taken together, Oxa1 precursor was found to absorb onto but not translocate into microsomes from where it was transferred to mitochondria in a Djpl-stimulated reaction (fig. S9, A to C). Soluble translocation intermediates of Oxa1 were not observed in this process, nor did mutation of the HPD motif in the J domain of Djpl compromise its function (fig. S9, D to G).

The early stages of mitochondrial preprotein targeting are poorly understood. Cytosolic chaperones (11, 12) and stabilizing factors called ubiquilins (13) associate with mitochondrial preproteins to prevent precursor-mediated proteotoxic

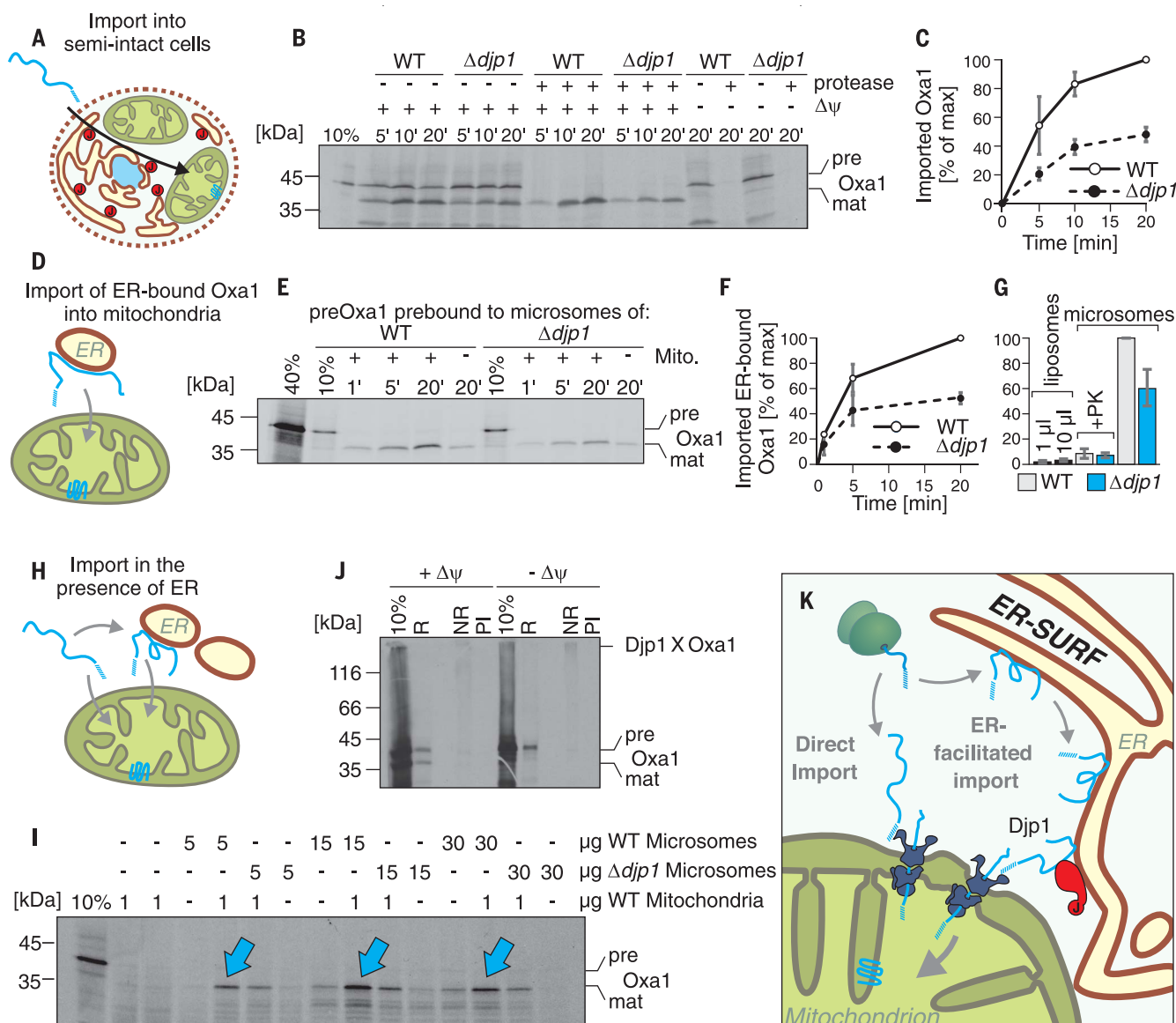


Fig. 4. The ER facilitates Oxa1 import in a Djp1-dependent process.

(A to C) Import of radiolabeled Oxa1 precursor into semi-intact cells. Amounts of protease-resistant mature Oxa1 were quantified. Data shown are means \pm SD; $n = 4$. **(D to G)** Djp1 promotes the import of ER-bound Oxa1. Quantification shows means \pm SD; $n = 3$. **(G)** Microsomes can transfer Oxa1 to mitochondria. Graph shows means \pm SE; $n = 3$. **(H and I)** Radiolabeled Oxa1 was incubated with WT and $\Delta djp1$ microsomes to which low (rate-limiting) amounts of WT mitochondria were added.

Nonimported Oxa1 was removed by protease. Arrows indicate Oxa1 import. **(J)** Radiolabeled Oxa1 precursor was incubated with semi-intact cells. After cross-linking with 400 μ M DSP, Djpl was immune-precipitated. NR, nonreducing; R, reducing (i.e., cross-links were broken); PI, preimmune serum. **(K)** Mitochondria can import Oxa1 precursor directly. However, in vivo, a fraction of Oxa1 associates with the ER surface. The ER-SURF pathway maintains the Oxa1 precursor in an import-competent state and facilitates its rerouting to mitochondria in a Djpl-dependent reaction.

stress (14, 15). Here we found that the ER surface can function as a capture net to salvage and redirect mitochondrial precursors and thus facilitate early targeting reactions by an import route that we termed the ER-SURF pathway (for ER surface-mediated protein targeting) (Fig. 4K). Our findings are consistent with a previous study that used a comprehensive proximity-based ribosome profiling approach showing that many mitochondrial membrane proteins are preferentially synthesized on the ER surface (2). The conservation and importance of Ema19 in this

pathway (fig. S8, K and L) suggests that this re-routing mechanism may be conserved among eukaryotes, including humans.

Hydrophobic mitochondrial proteins were previously observed on the ER, which was interpreted as mislocalization (16–19). However, our observations suggest that the ER surface can serve as a safeguard in targeting of mitochondrial precursor proteins, from where they are retrieved in a Djpl-mediated reaction. This ER-SURF targeting pathway could explain the difficulty in identifying targeting factors for mitochondrial proteins.

REFERENCES AND NOTES

1. A. Chacinska, C. M. Koehler, D. Milenkovic, T. Lithgow, N. Pfanner, *Cell* **138**, 628–644 (2009).
2. C. C. Williams, C. H. Jan, J. S. Weissman, *Science* **346**, 748–751 (2014).
3. M. Schuldiner *et al.*, *Cell* **123**, 507–519 (2005).
4. M. Morgenstern *et al.*, *Cell Reports* **19**, 2836–2852 (2017).
5. C. Sahi, E. A. Craig, *Proc. Natl. Acad. Sci. U.S.A.* **104**, 7163–7168 (2007).
6. D. Papic *et al.*, *Mol. Cell. Biol.* **33**, 4083–4094 (2013).
7. E. H. Hettema *et al.*, *J. Cell Biol.* **142**, 421–434 (1998).
8. J. L. Koh *et al.*, *G3* **5**, 1223–1232 (2015).
9. D. Zabezhinsky, B. Slobodin, D. Rapaport, J. E. Gerst, *Cell Reports* **15**, 540–549 (2016).

10. G. Schlenstedt, E. Hurt, V. Doye, P. A. Silver, *J. Cell Biol.* **123**, 785–798 (1993).
11. R. J. Deshaies, B. D. Koch, M. Werner-Washburne, E. A. Craig, R. Schekman, *Nature* **332**, 800–805 (1988).
12. J. C. Young, N. J. Hoogenraad, F. U. Hartl, *Cell* **112**, 41–50 (2003).
13. E. Itakura *et al.*, *Mol. Cell* **63**, 21–33 (2016).
14. L. Wrobel *et al.*, *Nature* **524**, 485–488 (2015).
15. H. Weidberg, A. Amon, *Science* **360**, eaan4146 (2018).
16. Y. C. Chen *et al.*, *EMBO J.* **33**, 1548–1564 (2014).
17. V. Okreglak, P. Walter, *Proc. Natl. Acad. Sci. U.S.A.* **111**, 8019–8024 (2014).
18. M. Gamerding, M. A. Hanebuth, T. Frickey, E. Deuerling, *Science* **348**, 201–207 (2015).
19. E. A. Costa, K. Subramanian, J. Nunnari, J. S. Weissman, *Science* **359**, 689–692 (2018).

ACKNOWLEDGMENTS

We thank F. Boos, M. Jung, E. Zalckvar, F. Wollweber, M. van der Laan, S. Lang, and S. Knaus for help with experiments and R. Erdmann, J. Gerst, S. Rospert, D. Rapoport, and R. Wedlich-Söldner for reagents. **Funding:** This study was supported by the Deutsche Forschungsgemeinschaft (DIP MitoBalance, SCHU2585/1-1, SFB1190, HE2803/8-2 to M.S. and J.M.H.), BioComp (to J.M.H.), and the Schweizerischer Nationalfond (310030B_163480 to A.S.). M.S. is an incumbent of the Dr. Gilbert Omenn and Martha Darling Professorial Chair in Molecular Genetics at the Weizmann Institute of Science. **Author contributions:** K.G.H., N.A., M.S., and J.M.H. conceived of the project. K.G.H., N.A., J.L., and M.M. designed, performed, and analyzed experiments. K.G.H. set up the Oxa1-Ura3 screen. K.G.H. and N.A. performed the synthetic genetic array analysis. N.A. and C.B. carried out microscopy experiments. K.G.H. performed biochemical experiments, to which

J.L. and M.M. also contributed. K.G.H., N.A., M.S., and J.M.H. analyzed data. K.G.H., M.S., and J.M.H. wrote the manuscript with contributions from all authors. **Competing interests:** None declared. **Data and materials availability:** All data needed to evaluate the conclusions in the paper are present in the paper or the supplementary materials.

SUPPLEMENTARY MATERIALS

www.sciencemag.org/content/361/6407/1118/suppl/DC1
Materials and Methods
Figs. S1 to S9
References (20–28)

20 December 2017; resubmitted 27 June 2018
Accepted 6 August 2018
10.1126/science.aar8174

BIOCHEMISTRY

Semisynthetic sensor proteins enable metabolic assays at the point of care

Qiuliayang Yu^{1,2}, Lin Xue¹, Julien Hiblot¹, Rudolf Griss², Sebastian Fabritz¹, Clothilde Roux³, Pierre-Alain Binz³, Dorothea Haas⁴, Jürgen G. Okun⁴, Kai Johnsson^{1,2*}

Monitoring metabolites at the point of care could improve the diagnosis and management of numerous diseases. Yet for most metabolites, such assays are not available. We introduce semisynthetic, light-emitting sensor proteins for use in paper-based metabolic assays. The metabolite is oxidized by nicotinamide adenine dinucleotide phosphate, and the sensor changes color in the presence of the reduced cofactor, enabling metabolite quantification with the use of a digital camera. The approach makes any metabolite that can be oxidized by the cofactor a candidate for quantitative point-of-care assays, as shown for phenylalanine, glucose, and glutamate. Phenylalanine blood levels of phenylketonuria patients were analyzed at the point of care within minutes with only 0.5 microliters of blood. Results were within 15% of those obtained with standard testing methods.

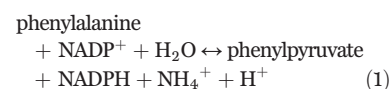
Diseases or injuries can result in large changes in metabolite blood concentrations. Examples include phenylalanine in phenylketonuria (PKU) (1), glutamate during ischemic strokes (2), galactose in galactosemia (3), leucine in maple syrup urine disease (4), and tyrosine in tyrosinemia (5). At present, these and numerous other medically relevant metabolites cannot be reliably quantified at the point of care (POC), hampering the diagnosis and management of the underlying medical conditions. To address this problem, we envisioned conducting paper-based enzymatic assays in which the metabolite is quantified through stoichiometric formation of the reduced redox cofactor nicotinamide adenine dinucleotide (NADH) or its phosphorylated form (NADPH). Such an approach would make all metabolites that can be specifically oxidized by the oxidized form of nicotinamide adenine dinucleotide (NAD⁺ and NADP⁺) accessible to POC analysis. Currently, NAD(P)H is measured by using a variety of different analytical methods (6–8), but the background and interference observed in whole-blood samples restrict the utility of these methods for quantitative POC assays. We therefore aimed at generating a biosensor that measures NADPH through a background-free bioluminescent output. Guided by our previous work on semisynthetic sensor proteins (9), we designed an NADPH sensor from the following three components: an NADPH-dependent receptor protein, the luciferase NanoLuc (NLuc) (10), and a fluorescently labeled ligand with

NADPH-dependent affinity for the receptor (Fig. 1A). The fluorescent ligand is covalently tethered to the receptor protein through the self-labeling protein SNAP-tag (11). In the presence of NADPH, the ligand binds to the receptor and brings the fluorophore close to the luciferase, thereby increasing bioluminescence resonance energy transfer (BRET). The NADPH concentration is given by the ratio of the emission intensities of NLuc and the fluorophore, which can be measured by a digital camera in paper-based assays (9).

We identified *Escherichia coli* dihydrofolate reductase (eDHFR) as a potential receptor protein because it has an NADPH-dependent affinity for its ligand trimethoprim (TMP) (12) and has been shown to bind to derivatized ligands (9). The affinity of eDHFR for a fluorescent TMP derivative [TMP-tetramethylrhodamine (TMR)] (Fig. 1B) increases by a factor of 23 in the presence of NADPH (Fig. 1C and table S1), but this modest cooperativity is not sufficient to generate an NADPH sensor (fig. S1). We hypothesized that the cooperativity of ligand binding could be increased through partial unfolding of the binding site that could be reversed by NADPH to induce the binding of the tethered ligand. We first analyzed a circularly permuted eDHFR (cpDHFR) in which new termini were created in a loop (between residues Asn²³ and Leu²⁴) that bridges the binding sites for NADPH and the ligand. The resulting cpDHFR showed increased cooperativity in ligand binding relative to the wild type: adding saturating concentrations of NADPH increased the affinity of cpDHFR for TMP-TMR by a factor of 150 (Fig. 1C and table S1). This cooperativity was further increased by inserting a circularly permuted variant of NLuc (cpNLuc) (13) in the same binding site loop of eDHFR (Fig. 1D): The affinity of the resulting protein chimera for TMP-TMR increased by a factor of 1400 upon the addition of saturating concentrations of NADPH (Fig. 1C and table S1). cpNLuc was used instead of regular NLuc because the

distance between the N and C termini of the latter (23 Å) was considered to be too large for the loop insertion. To create a functional sensor from the cpNLuc-inserted eDHFR, we fused it via a proline-30 (P30) linker to a SNAP-tag (11) (Fig. 1A) and labeled the SNAP-tag with a fluorescent TMP derivative [TMP-Cy3-benzylguanine (BG)] (Fig. 1B). The resulting BRET sensor displayed a 15-fold change in the emission ratio (NLuc/Cy3) when titrated with NADPH (Fig. 1E). The c_{50} of the sensor (the NADPH concentration resulting in 50% of the maximum sensor response) was measured to be 5.1 ± 0.4 nM (mean \pm SD). In addition, the sensor showed selectivity for NADPH over NADP⁺, NADH, and NAD⁺ by a factor of at least 8000 (Fig. 1F). Furthermore, by introducing point mutations in the NADPH binding site of the sensor, we generated a family of sensors with c_{50} values for NADPH ranging from 5 nM to 6 μ M (Fig. 1G). An important feature of the sensor is its large BRET ratio change. We attribute this large change to (i) the insertion of cpNLuc into the binding site loop of eDHFR, which brings the luciferase in close proximity to the fluorophore in the closed state of the sensor, and (ii) the P30 linker between the SNAP-tag and the engineered eDHFR, which separates the luciferase and the fluorophore in the open state of the sensor (14).

As the first application of our NADPH sensor, we developed a POC assay for PKU. PKU patients are classified according to their whole-blood phenylalanine levels before treatment: levels of 120 to 600 μ M denote mild hyperphenylalaninaemia; levels of 600 to 1200 μ M, mild PKU; and levels above 1200 μ M, classic PKU (1). Controlling phenylalanine blood levels is critical for pediatric and pregnant PKU patients (1, 15). For example, maternal phenylalanine levels above 360 μ M risk reducing the cognitive ability of the offspring (1). In order to avoid neuropsychological complications in pediatric PKU patients, target phenylalanine blood levels in the first decade of life are 120 to 360 μ M (1). Numerous assays for phenylalanine quantification at the POC have been proposed (16–18). However, none of these are simple and accurate enough to be suitable for patient self-testing. To quantify phenylalanine with our sensor, we envisioned using the following reaction for the sensing scheme (fig. S2):



The conversion of phenylalanine is quantitative under suitable reaction conditions (19). A candidate enzyme to catalyze the reaction is phenylalanine dehydrogenase (PDH) from *Rhodococcus* sp. M4, which has a high specific activity toward phenylalanine (19). As the enzyme is specific for NAD⁺ and NADH whereas our sensor binds NADPH, we engineered its cofactor specificity such that it accepts NADP⁺ instead of NAD⁺ (fig. S3). Current protocols measure phenylalanine levels in whole blood. To perform POC phenylalanine measurements that match this

¹Department of Chemical Biology, Max Planck Institute for Medical Research, 69120 Heidelberg, Germany. ²École Polytechnique Fédérale de Lausanne, Institute of Chemical Sciences and Engineering, NCCR in Chemical Biology, 1015 Lausanne, Switzerland. ³University Hospital of Lausanne, Service of Biomedicine, Clinical Chemistry Laboratory, 1011 Lausanne, Switzerland. ⁴University Children's Hospital Heidelberg, Center for Metabolic Diseases, Metabolic Laboratory, 69120 Heidelberg, Germany.

*Corresponding author. Email: johnsson@mr.mpg.de

standard, we designed an assay in which whole blood is diluted in a solution containing PDH, NADP⁺, and the luciferase substrate furimazine. We lyophilized the bioluminescent sensor onto test paper in the presence of a surfactant, resulting in the lysis of blood cells once they are applied to the paper (fig. S4) to release intracellular phenylalanine for analysis. A drop of the blood solution was added to the test paper containing the lyophilized sensor and analyzed by using a digital camera mounted on a cardboard box (Fig. 2A and movie S1). For the phenylalanine measurement, we chose a biosensor with a c_{50} of $1.01 \pm 0.06 \mu\text{M}$ for NADPH under the assay conditions (Fig. 2B and table S2). The threshold for abnormal phenylalanine concentrations is $120 \mu\text{M}$ (7). We therefore diluted blood samples by a factor of 50 to achieve maximal sensor response around this threshold. The dilution step and the analysis of samples as a thin film on the

paper reduce the matrix effect from the whole blood (9). The calibration of the test paper was performed with the whole blood spiked with defined concentrations of NADPH (Fig. 2B). In this way, the normal endogenous NADPH level ($20 \mu\text{M}$) in blood (20) represents the baseline, whereas the effect of interpatient variations in whole-blood NADPH levels was considered negligible (table S3). Phenylalanine concentrations were then calculated from the emission ratios of the test paper. The whole measurement takes less than 15 min and requires only $0.5 \mu\text{l}$ of whole blood. The ratiometric nature of the sensor facilitates the POC application, as neither the exact concentration of PDH, NADP⁺, or furimazine nor the precise volume of the drop applied to the paper should affect the result. The measured ratio is stable over minutes (fig. S5), indicating that neither sample evaporation nor cofactor degradation is substantial under these condi-

tions. Furthermore, the sensor lyophilized on the test paper proved stable at room temperature over a period of 42 days (fig. S6).

To validate our POC assay, we spiked whole blood with phenylalanine and analyzed the samples. The results showed excellent correlation with the values measured in parallel by liquid chromatography–mass spectrometry (LC-MS) (Fig. 2C). We furthermore measured the phenylalanine concentrations in 40 patient plasma samples. Again, the results showed very good correlation with two independent reference methods currently used in clinical laboratories (Fig. 2, D and E; fig. S7; and table S4). The test papers also demonstrated very good reproducibility, with an average coefficient of variation of $7\% \pm 4\%$ for technical triplicates. Lastly, we measured phenylalanine levels in venous blood samples freshly obtained from four different PKU patients (Fig. 2, F and G). Our results showed very good overlap

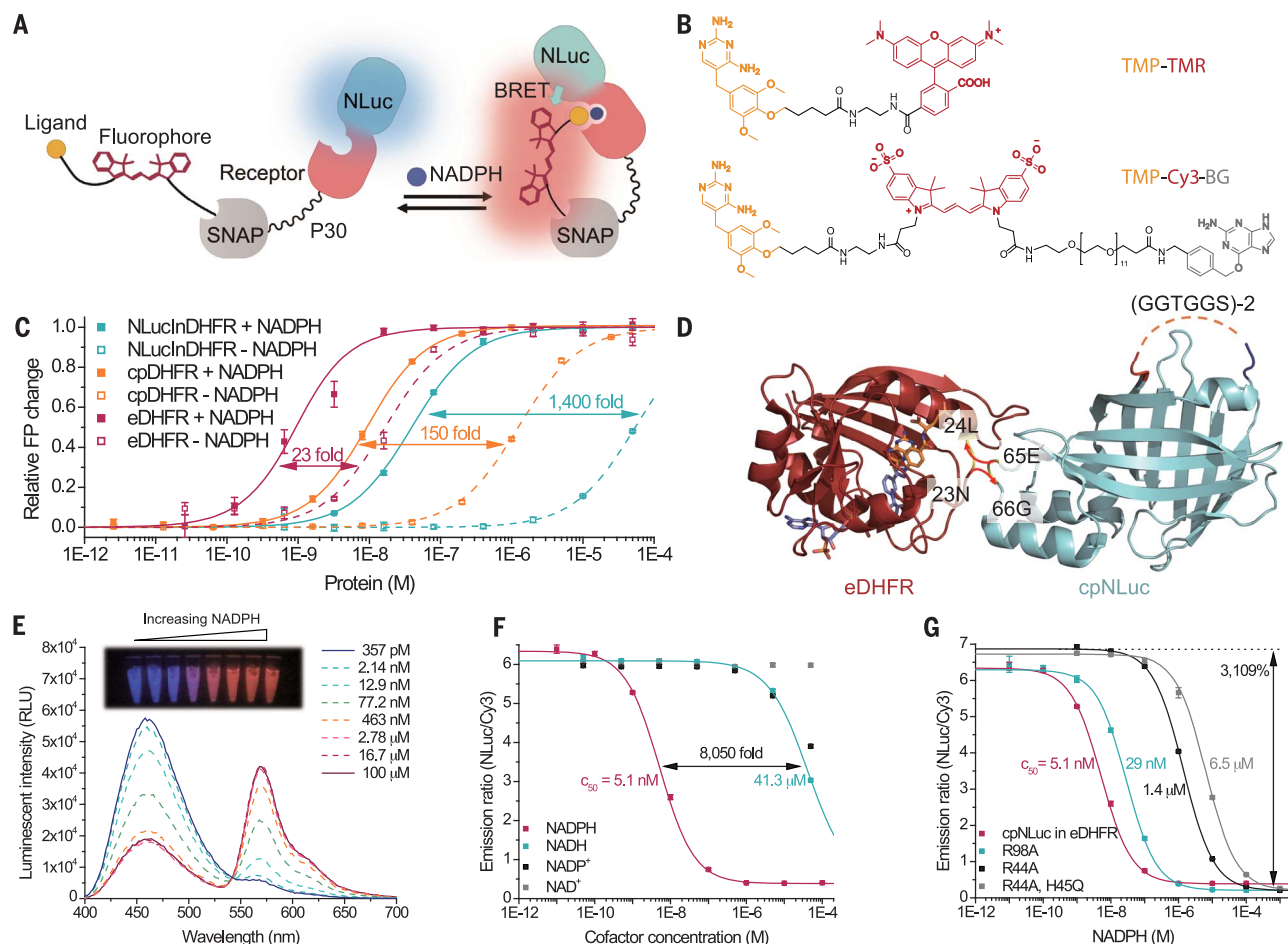


Fig. 1. Design of a BRET sensor for NADPH. (A) Design principle: A protein chimera between a receptor and a luciferase (NLuc) is tethered via a SNAP-tag to a ligand derivatized with a fluorophore. NADPH triggers ligand binding to the receptor, thereby increasing BRET. (B) Structure of TMP-TMR and TMP-Cy3-BG. BG (gray) tethers the probe to the SNAP-tag. (C) Affinity between engineered receptors and TMP-TMR as measured by fluorescence polarization (FP) in the presence or absence of $100 \mu\text{M}$ NADPH. NLucInDHFR stands for cpNLuc inserted in eDHFR; cpDHFR stands for cpDHFR with NLuc fused to its new N terminus; eDHFR stands for

wild-type eDHFR with NLuc fused to its N terminus. (D) Cartoon indicating the insertion of cpNLuc [Protein Data Bank (PDB) ID 5BOU] into eDHFR (PDB ID 4PDJ). The original N (blue) and C (red) termini of NLuc are linked by a (GGTGGG)₂ linker. E, Glu; G, Gly. (E) Emission spectra and photograph of the sensor in the presence of various concentrations of NADPH. RLU, relative light units. (F) Titration of the sensor with different cofactors. (G) NADPH titrations of sensors carrying mutations in the receptor protein. R, Arg; A, Ala; H, His; Q, Gln. Values in (C), (F), and (G) are given as means \pm SD for three independent measurements.

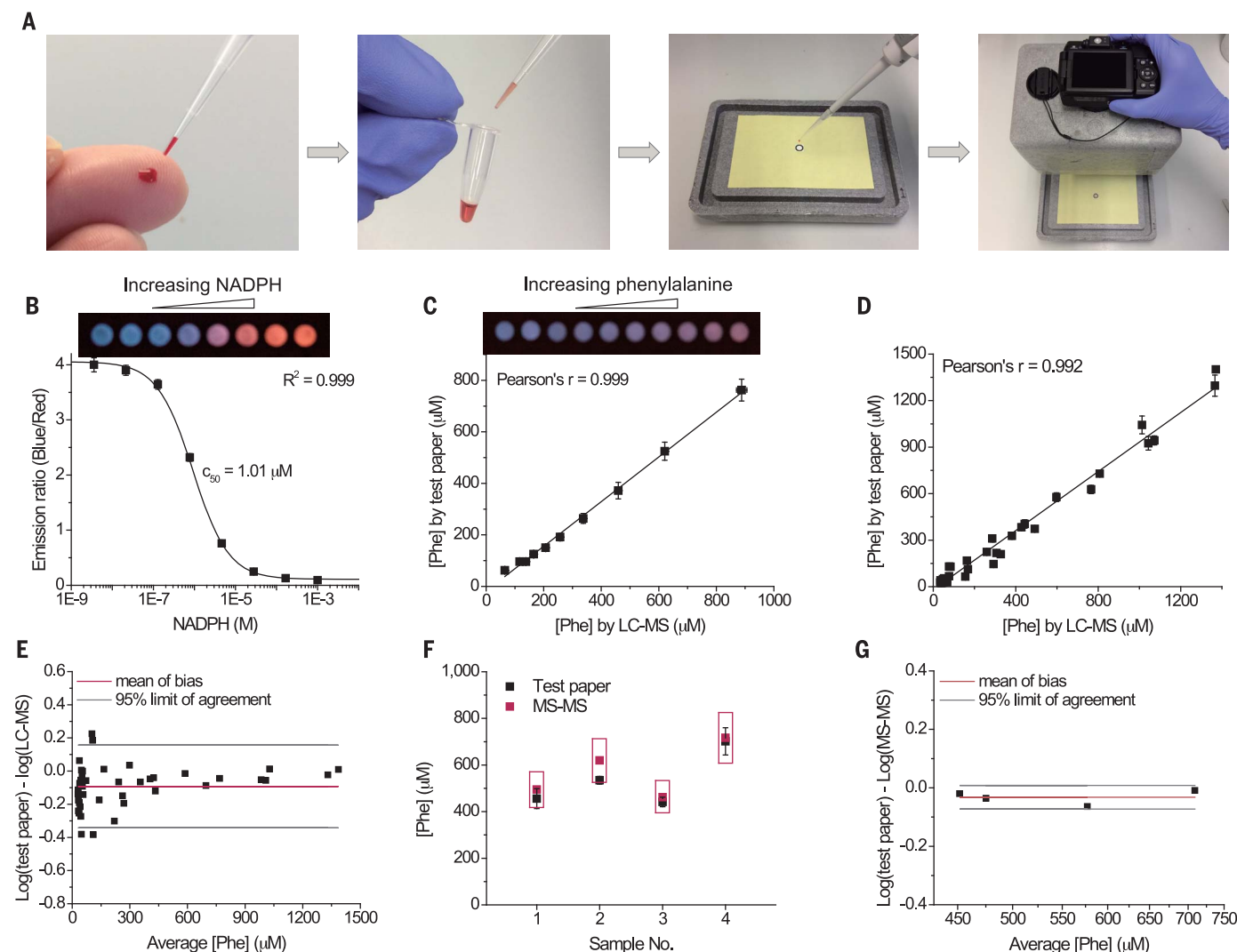


Fig. 2. Paper-based phenylalanine assay. (A) Procedure for measuring phenylalanine: 0.5 μ l of whole blood from a finger prick is diluted by a factor of 50 in reaction buffer. After a 10-min incubation period, 5 μ l of this mixture is added onto a test paper and subsequently analyzed with a digital camera. (B) Calibration of test paper by spiking whole-blood samples with NADPH. R^2 , coefficient of determination. (C) Quantification of phenylalanine spiked in whole blood. Test paper results are plotted against results obtained by LC-MS. r , correlation coefficient. (D) Quantification of phenylalanine in 40 patient plasma

samples. Test paper results are plotted against results obtained by LC-MS; the underlying data are listed in table S4. (E) Bland-Altman analysis for 40 patient plasma samples measured by test paper and LC-MS. (F) Comparison between test paper and MS-MS methods for measuring whole-blood samples from four patients. Red boxes represent MS-MS results \pm an allowable error of 15%. (G) Bland-Altman analysis for four patient whole-blood samples measured by test paper and MS-MS. Error bars represent SD for three independent measurements.

with MS-MS-based dried-blood-spot measurements performed in parallel, with an averaged total analytical error of $17\% \pm 4\%$. The average coefficient of variation for the test paper was $6\% \pm 3\%$. It is instructive to compare the performance of our test paper with that of a conventional NAD-dependent colorimetric assay using the same enzymatic reaction (21). When measuring whole-blood samples spiked with 200 μ M phenylalanine, the test paper showed a 232% ratio change, whereas the conventional assay showed only a 2% increase in absorbance over background (fig. S8). Furthermore, the sensor works in a “one-pot reaction” in solution, and it can be lyophilized together with the reaction

buffer, including the luciferase substrate, on the test paper (fig. S9). This setting allows all the steps of the assay, with the exception of the dilution step, to be performed on paper, further simplifying the procedure. We also demonstrated that a smartphone can be used as the camera (fig. S10), facilitating future POC applications. The simplicity of the assay procedure should eventually enable patient self-testing, even though some modifications of the assay would be needed. At present, our assay requires a 10- to 15-min incubation. A more immediate result could be achieved by increasing the activity of PDH. Furthermore, the user currently needs to dilute a defined volume of blood, and a more automated assay format

could be developed on the basis of microfluidics devices (7, 22). Finally, potential interferences with our assay by endogenous or exogenous substances will have to be kept in mind (table S3). For example, PKU patients receiving the antibiotic TMP would not be able to use the assay, as TMP directly binds to the sensor. Resolving these technical problems could put a much-needed tool in the hands of PKU patients.

In principle, any metabolite of clinical importance that can be oxidized with NAD(P)^+ could be analyzed with our paper-based assays at the POC. Using enzymatic reactions for glucose and glutamate (23, 24), we accurately analyzed commercial plasma samples spiked with various

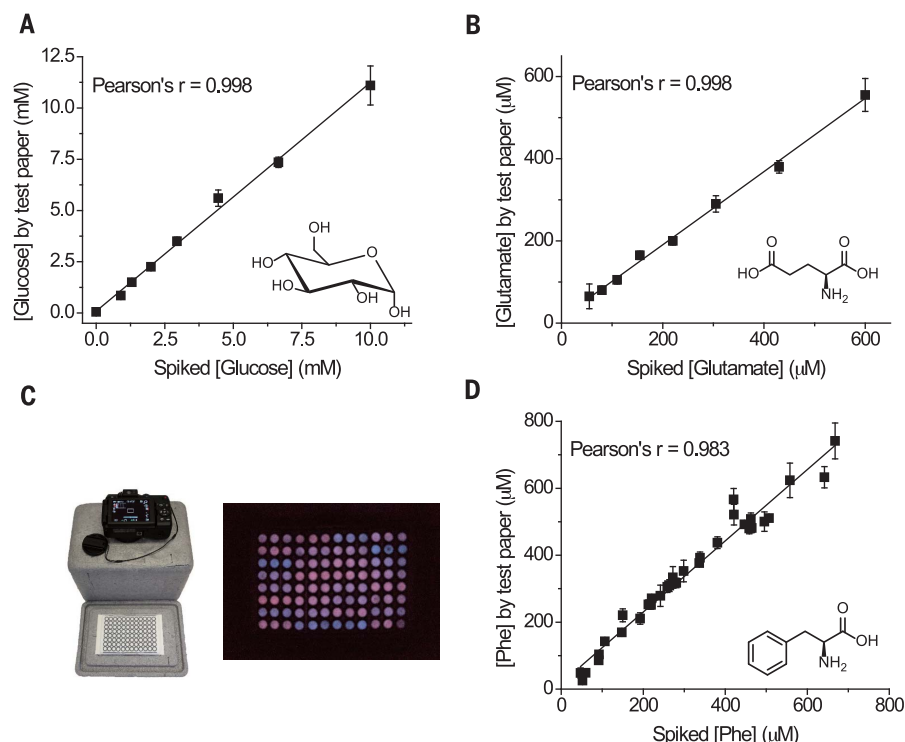


Fig. 3. Generalization of assay and scale-up. (A) Measurement of glucose spiked in plasma samples. (B) Measurement of glutamate spiked in plasma samples. (C) Photograph of test paper for analyzing 96 samples for phenylalanine in parallel (32 different blood samples measured in triplicates). (D) Quantification of phenylalanine for 32 blood samples in triplicates. Test paper results are plotted against concentrations of spiked phenylalanine. Error bars represent SD for three independent measurements. The y axis represents the measured analyte concentration after subtraction of the background concentration of the corresponding analyte in the sample.

glucose or glutamate concentrations (Fig. 3, A and B). As blood concentrations of glucose are in the millimolar range (25), in principle only 10 nl of capillary blood would be needed for such an assay.

Forty-two medically relevant metabolites that are potentially suitable for quantification in our assay are listed in table S5. These include carbohydrates such as galactose (26), alcohols such as ethanol (27), lipids such as triglycerides (28) and cholesterol (29), and other amino acids such as branched-chain amino acids (30). For analytes with lower concentrations, possible interpatient variations of the endogenous NADPH level would have to be considered (table S3). Such individual background corrections could be readily achieved by analyzing the sample in both the presence and absence of the analyte-converting enzyme (fig. S11). Furthermore, for some of these analytes,

only NAD-specific dehydrogenases have been described. However, as demonstrated for PDH and other dehydrogenases (31), the conserved nature of the NAD(P) binding sites of dehydrogenases should make it possible to engineer their cofactor specificities.

The use of a digital camera enables the simultaneous analysis of multiple metabolic assays for either the same or different analytes on a single piece of paper. As a proof-of-principle for neonatal PKU screening applications in resource-limited settings, we analyzed 96 whole-blood samples spiked with various concentrations of phenylalanine with one camera shot (Fig. 3, C and D). This experiment demonstrates the scalability of our metabolic assays.

In summary, we combined synthetic chemistry and protein engineering to create a biosensor

for the accurate quantification of metabolites in blood by a paper-based assay. The assay should enable the POC diagnosis and management of numerous diseases.

REFERENCES AND NOTES

- N. Blau, F. J. van Spronsen, H. L. Levy, *Lancet* **376**, 1417–1427 (2010).
- J. Castillo, A. Dávalos, M. Noya, *Lancet* **349**, 79–83 (1997).
- A. M. Bosch, *J. Inher. Metab. Dis.* **29**, 516–525 (2006).
- P. R. Blackburn et al., *Appl. Clin. Genet.* **10**, 57–66 (2017).
- N. Garcia Segarra et al., *J. Inher. Metab. Dis.* **33** (suppl. 3), 507–510 (2010).
- J. Zhang, Y. Xiang, M. Wang, A. Basu, Y. Lu, *Angew. Chem. Int. Ed.* **55**, 732–736 (2016).
- A. Koh et al., *Sci. Transl. Med.* **8**, 366ra165 (2016).
- R. Nagaraj et al., *Cell* **168**, 210–223.e11 (2017).
- R. Griss et al., *Nat. Chem. Biol.* **10**, 598–603 (2014).
- M. P. Hall et al., *ACS Chem. Biol.* **7**, 1848–1857 (2012).
- A. Keppler et al., *Nat. Biotechnol.* **21**, 86–89 (2003).
- D. J. Baker et al., *FEBS Lett.* **126**, 49–52 (1981).
- J. Hiblot et al., *Angew. Chem. Int. Ed.* **56**, 14556–14560 (2017).
- M. A. Brun et al., *J. Am. Chem. Soc.* **133**, 16235–16242 (2011).
- W. B. Hanley, *Am. J. Med.* **117**, 590–595 (2004).
- K. A. Yang et al., *Nat. Chem.* **6**, 1003–1008 (2014).
- G. Thiessen, R. Robinson, K. De Los Reyes, R. J. Monnat Jr., E. Fu, *Analyst* **140**, 609–615 (2015).
- R. Robinson, L. Wong, R. J. Monnat, E. Fu, *Micromachines* **7**, 28 (2016).
- N. M. Brunhuber, J. B. Thoden, J. S. Blanchard, J. L. Vanhoober, *Biochemistry* **39**, 9174–9187 (2000).
- T. C. Wagner, M. D. Scott, *Anal. Biochem.* **222**, 417–426 (1994).
- J. Dhondt, E. Paux, *Screening* **2**, 141–147 (1993).
- W. Du, L. Li, K. P. Nichols, R. F. Ismagilov, *Lab Chip* **9**, 2286–2292 (2009).
- M. W. Slein, in *Methods of Enzymatic Analysis*, H. U. Bergmeyer, Ed. (Academic Press, rev. ed., 1965), pp. 117–130.
- E. Bernt, H. U. Bergmeyer, in *Methods of Enzymatic Analysis*, H. U. Bergmeyer, Ed. (Academic Press, Engl. ed. 2, 1974), pp. 1704–1715.
- L. M. Welschen et al., *Diabetes Care* **28**, 1510–1517 (2005).
- G. Kurz, K. Wallenfels, in *Methods of Enzymatic Analysis*, H. U. Bergmeyer, Ed. (Academic Press, Engl. ed. 2, 1974), p. 1279.
- A. Poklis, M. A. Mackell, *Clin. Chem.* **28**, 2125–2127 (1982).
- P. Fossati, L. Prencipe, *Clin. Chem.* **28**, 2077–2080 (1982).
- E. Kim, M. Goldberg, *Clin. Chem.* **15**, 1171–1179 (1969).
- P. R. Beckett et al., *Anal. Biochem.* **240**, 48–53 (1996).
- N. S. Scrutton, A. Berry, R. N. Perham, *Nature* **343**, 38–43 (1990).

ACKNOWLEDGMENTS

We thank K. Schwarz for experimental assistance and M. C. Colombo for discussions. **Funding:** This work was supported by the Max Planck Society, the Swiss National Science Foundation, and École Polytechnique Fédérale de Lausanne. **Author contributions:** Q.Y. and K.J. conceived this study. Q.Y., L.X., J.H., R.G., S.F., C.R., P.-A.B., D.H., and J.G.O. performed experiments and contributed to data analysis. Q.Y., K.J., and L.X. wrote the manuscript. **Competing interests:** Q.Y. and K.J. are inventors on a patent application on the sensor filed by the Max Planck Society. **Data and materials availability:** All data are available in the main text or the supplementary materials.

SUPPLEMENTARY MATERIALS

www.sciencemag.org/content/361/6407/1122/suppl/DC1
Materials and Methods
Figs. S1 to S12
Tables S1 to S5
References (32–37)
Movie S1

5 April 2018; accepted 9 August 2018
10.1126/science.aat7992

MOLECULAR BIOLOGY

Ribonucleotide incorporation enables repair of chromosome breaks by nonhomologous end joining

John M. Pryor*, Michael P. Conlin, Juan Carvajal-Garcia, Megan E. Luedeman, Adam J. Luthman, George W. Small, Dale A. Ramsden†

The nonhomologous end-joining (NHEJ) pathway preserves genome stability by ligating the ends of broken chromosomes together. It employs end-processing enzymes, including polymerases, to prepare ends for ligation. We show that two such polymerases incorporate primarily ribonucleotides during NHEJ—an exception to the central dogma of molecular biology—both during repair of chromosome breaks made by Cas9 and during V(D)J recombination. Moreover, additions of ribonucleotides but not deoxynucleotides effectively promote ligation. Repair kinetics suggest that ribonucleotide-dependent first-strand ligation is followed by complementary strand repair with deoxynucleotides, then by replacement of ribonucleotides embedded in the first strand with deoxynucleotides. Our results indicate that as much as 65% of cellular NHEJ products have transiently embedded ribonucleotides, which promote flexibility in repair at the cost of more fragile intermediates.

Nonhomologous end joining (NHEJ) is the primary pathway for repairing chromosomal double-strand breaks (DSBs) in mammals and is required for genome stability in all cell types, as well as for the assembly of antigen-specific receptors by V(D)J recombination in lymphocytes (1). NHEJ employs specialized nucleases and polymerases, including the widely expressed polymerase μ (Pol μ) (encoded by *Polm*) and lymphocyte-specific terminal deoxynucleotidyl transferase (TdT), to modify broken end structures in preparation for ligation (2). Accordingly, the loss of Pol μ or TdT results in impaired immune responses (3–6). Loss of the more widely expressed Pol μ additionally interferes with cell growth (7, 8), hematopoiesis (7), and resistance to DNA damage (7–9). Pol μ and TdT notably favor deoxynucleotides over ribonucleotides by a factor of 1.4 to 11 (depending on the nucleotide base) (10). By comparison, other polymerases that maintain DNA genomes (including the closely related Pol λ and Pol β) typically incorporate deoxynucleotides several thousand times more efficiently than ribonucleotides (11–13). However, it is unknown whether ribonucleotide incorporation occurs during cellular NHEJ and, if ribonucleotide incorporation occurs, whether it substantially affects NHEJ function.

We initially investigated whether ribonucleotides are incorporated during NHEJ after introducing linear DNA substrates into transformed mouse embryonic fibroblasts (MEFs). We optimized this assay to allow for rapid harvesting of repair products, in anticipation that ribo-

nucleotides were only transiently present. Ribonucleotides embedded in NHEJ products were quantified by assessing the template lost in samples upon cleavage of ribonucleotide-containing strands (Fig. 1A and fig. S1, B and C) with validated quantitative polymerase chain reactions (qPCRs) (figs. S1A, S3A, and S4B). We determined that embedded ribonucleotides were present in 60% (SD, 4.2%) of NHEJ products (Fig. 1B) when products were assessed within the first minute after electroporation, and these ribonucleotides were dependent on either Pol μ or TdT (Fig. 1C and fig. S1, E and F).

Embedded ribonucleotides in NHEJ products decreased in frequency until they were almost

undetectable after 20 min (Fig. 1B, gray line). To determine whether this reduction was due to the replacement of incorporated ribonucleotides with deoxynucleotides [ribonucleotide excision repair (RER)], we employed CRISPR-Cas9 to generate a MEF variant deficient in *Rnaseh2a* (fig. S1G), which initiates RER (14). Levels of embedded ribonucleotides in *Rnaseh2a*-deficient cells were initially equivalent to those in wild-type cells; unlike those in wild-type cells, embedded ribonucleotides in *Rnaseh2a*-deficient cells were not completely removed and stabilized at levels approximately half those initially observed (Fig. 1B, orange line). Reexpression of RNaseH2A in the *Rnaseh2a*-deficient variant was sufficient to reduce embedded RNA in NHEJ products to the low levels observed in wild-type cells (fig. S1H).

The substrate used in the experiments described above had a single-nucleotide 3' overhang (3'G). Approximately half of repair products require ligation after the addition of a single complementary C, are dependent on both Ku and Pol μ (15), and can be identified by sensitivity to a restriction enzyme (NsiI) (+C product; Fig. 1D). Sequencing indicates that the remaining NsiI-resistant products have 1- to 5-base pair deletions of flanking sequence that are at best modestly affected by *Polm* deficiency (15). Embedded ribonucleotides were present in 91% (SD, 8%) of NsiI-sensitive products after 1 min (Fig. 1E). Similar results were observed when we used a different method to detect ribonucleotide-containing products (fig. S2A) and when we used a substrate with a different overhang template (C3') and a different Pol μ -dependent added nucleotide (G) (fig. S2B). We conclude that most Pol μ - and TdT-dependent NHEJ products contain embedded ribonucleotides and that the modest preference of Pol μ and TdT for the addition of deoxynucleotides in vitro (10) is overwhelmed by higher concentrations of ribonucleotides in cells (15).

Table 1. Stimulation of NHEJ repair pathway by a terminal ribonucleotide. To represent head-to-tail alignment of substrate ends, 3' overhang sequences for head ends are listed N3', and tail ends listed 3'N (for example, GAC3' and 3'AG align as in Fig. 3B). Underlined sequence letters correspond to the indicated terminal C. The relative joining efficiency is the joining efficiency for rC divided by the joining efficiency for dC, as measured by qPCR that amplifies all NHEJ products. Ligation stimulation = relative joining efficiency \times (% direct ligation of rC)/(% direct ligation of dC).

Substrate overhang sequences	Terminal C	Relative joining efficiency	% Direct ligation	Ligation stimulation
GC3' and 3'CG	dC	1	87 \pm 6	1
GC3' and 3'CG	(r)C	1.2 \pm 0.7	92 \pm 1	1.3
GAC3' and 3'AG	dC	1	19 \pm 8	1
GAC3' and 3'AG	(r)C	5.8 \pm 1.9	88 \pm 6	26
GAC3' and 3'AG	2'-Fluoro-C	5.4 \pm 3.9	88 \pm 1	25
GAC3' and 3'AG	Ara-C	1.1 \pm 0.6	<2*	<0.1*
GACGC3' and 3'GCAG	dC	1	32 \pm 3	1
GACGC3' and 3'GCAG	(r)C	6.3 \pm 3.1	88 \pm 3	17
TTTTTTTGC3' and 3'G	dC	1	4 \pm 1	1
TTTTTTTGC3' and 3'G	(r)C	3.0 \pm 0.9	64 \pm 5	48

*A direct ligation product was undetectable.

Lineberger Comprehensive Cancer Center, Department of Biochemistry and Biophysics and Curriculum in Genetics and Molecular Biology, University of North Carolina, Chapel Hill, NC 27599, USA.
*Present address: New England Biolabs, Ipswich, MA 01938, USA.
†Corresponding author. Email: dale_ramsden@med.unc.edu

As also informed by data in subsequent figures, we suggest that early products involve one ligated strand only. Subsequent repair of the complementary strand with deoxynucleotides accounts for the twofold dilution of products with embedded ribonucleotides that is independent of *Rnaseh2a* (Fig. 1B, orange line), whereas complete removal of ribonucleotides requires *Rnaseh2a*-dependent RER.

We determined whether ribonucleotides are similarly incorporated during repair by NHEJ of chromosomal breaks. We used a pre-B cell line that can be induced to arrest in G₁ phase and undergo V(D)J recombination at the immunoglobulin kappa locus (*Igk*) (Fig. 2A and fig. S3E) (15), because Pol μ is efficiently engaged by the 3' overhang intermediates in this process (5, 15–17). Embedded ribonucleotides were undetectable 24 hours after induction when cells were proficient in RER. By comparison, 35% of *Igk* recombination products had embedded ribonucleotides in an *Rnaseh2a*-deficient variant (Fig. 2B and fig. S3, A and B). This frequency is approximately half of the frequency for *Igk* products where Pol μ is active (5, 17), consistent with the model proposed above, where only the first strand of a chromosome DSB is repaired with ribonucleotides. Embedded ribonucleotides were again largely dependent on either Pol μ or TdT (Fig. 2B and fig. S3, C and D).

We sought to track polymerase-dependent ribonucleotide incorporation during chromosomal NHEJ earlier than was possible using the V(D)J recombination model and also to extend analysis to nonlymphoid cells. We directly introduced *Rosa26* locus-targeted Cas9 nuclease into *Rnaseh2a*-deficient MEFs, which allowed for rapid accumulation of repair products (fig. S4D) and thus assessment of ribonucleotides in these products immediately after they were generated. Sequencing of repair products from wild-type versus *Polm*^{-/-} MEFs confirms that Pol μ promotes repair accuracy (fig. S4A). However, the blunt ends generated by Cas9 engage Pol μ less frequently (in 16% of all repair) than V(D)J recombination intermediates, and the contribution of Pol μ is distributed over several mostly template-dependent products that cannot be easily distinguished from polymerase-independent repair products. We therefore expressed TdT in these cells (fig. S1F), as this generates a class of repair products—with the addition of two or more G's and no loss of flanking DNA (+GG products)—that are abundant (18% of NHEJ products) (table S1), unambiguously polymerase dependent, and that can be detected by a sensitive product-specific qPCR (Fig. 2, C and D, and fig. S4, B to D). Ribonucleotide incorporation by TdT does not differ significantly from that by Pol μ in cells (Figs. 1C and 2B) and in vitro (10), supporting the characterization of ribonucleotide incorporation by TdT during NHEJ as directly comparable to Pol μ -dependent repair. Embedded ribonucleotides were present in 84% and 77% of +GG NHEJ products 1 and 4 hours after the introduction of Cas9, respectively (Fig. 2D), and were reduced by a factor of two in these RER-deficient cells over the next 20 hours. This is consistent with strong

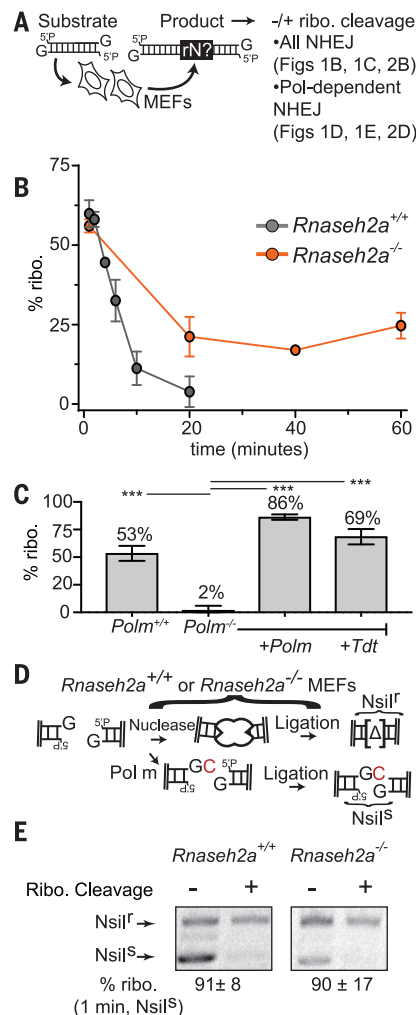


Fig. 1. Ribonucleotide incorporation during repair of extrachromosomal substrates.

(A) DNA fragments with 3'G overhangs at ends were introduced into MEFs, and the percentages of cellular NHEJ products with embedded ribonucleotides (% ribo.) were determined by comparing amplification efficiencies with and without prior cleavage at sites of ribonucleotide incorporation (see also fig. S1C). 5'P, 5'-phosphate. (B) Percentage of products with embedded ribonucleotides after the introduction of the substrate into *Rnaseh2a*^{+/+} or *Rnaseh2a*^{-/-} MEFs. Data points represent the mean for three transfections, and error bars represent SD. (C) Percentage of products with embedded ribonucleotides among products recovered after 1 min. Data points represent the mean for three transfections, and error bars represent SD. Means were compared in pairs with values for *Polm*^{-/-} by analysis of variance (ANOVA) (****P* < 0.001). (D and E) Digestion of amplified products with NsilI and electrophoresis distinguishes Pol μ -dependent +C products (products with the addition of a single complementary C) from products with deletions of flanking sequence (Δ). (E) The mean percentages \pm SD of products with embedded ribonucleotides among NsilI-susceptible (NsilI^s) products recovered after 1 min from three independent transfections are shown. NsilI^r, NsilI resistant.

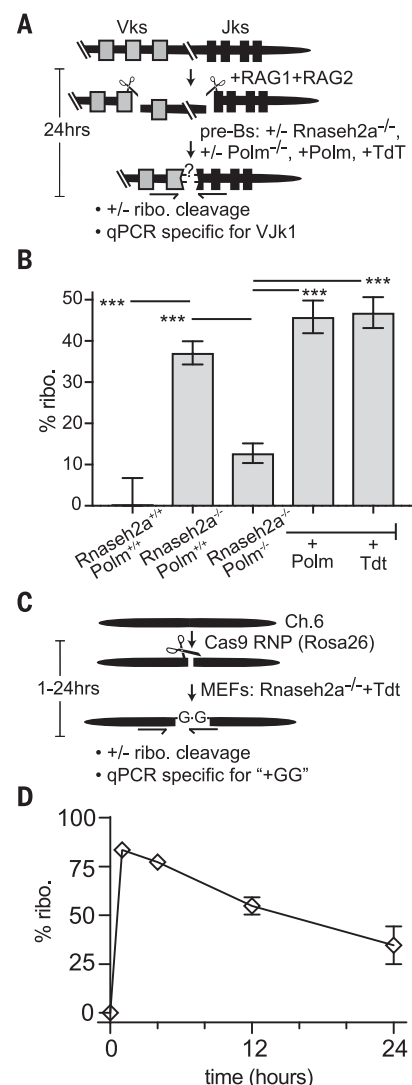


Fig. 2. Ribonucleotide incorporation during repair of chromosomal breaks.

(A and B) SP9 pre-B cells were induced for 24 hours, resulting in the expression of RAG1-RAG2 nuclease and the introduction of chromosome breaks adjacent to V_K (variable region) and J_K (joining region) coding segments (boxes). The percentage of products with embedded ribonucleotides in VJ_K coding junctions was measured as for Fig. 1A. (B) Data points represent the mean for five independent inductions, and error bars represent SD. Means were compared in pairs by ANOVA as noted (****P* < 0.001). (C and D) *Rosa26* locus-targeting Cas9 ribonucleoprotein was introduced into MEFs deficient in *Rnaseh2a* and expressing TdT. The percentage of products with embedded ribonucleotides was detected as for Fig. 1A by using a qPCR specific for the TdT-dependent +GG product (see also fig. S4). Ch. 6, chromosome 6. (D) Data points represent the mean for three independent transfections, and error bars represent SD.

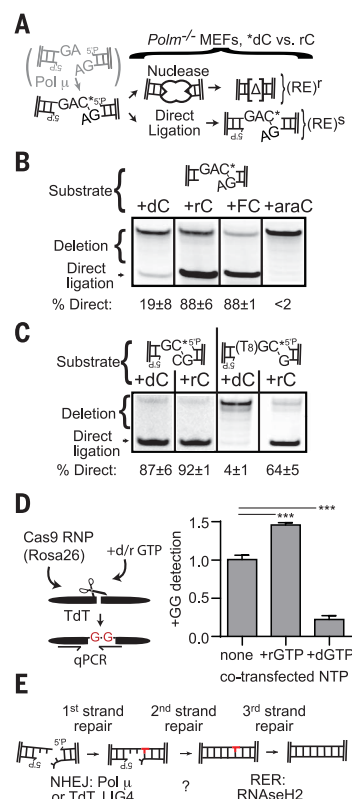


Fig. 3. Effect of ribonucleotide termini on the NHEJ ligation step. (A to C) Termini of NHEJ substrates were varied to be consistent with the polymerase-dependent addition of a ribonucleotide versus a deoxynucleotide and introduced into MEFs expressing neither Pol μ nor TdT. The sensitivity of amplified products to a diagnostic restriction enzyme (RE) was used to identify examples of direct head-to-tail ligation. (B and C) Substrates with the indicated terminal nucleotides were introduced into MEFs expressing neither Pol μ nor TdT. The mean percentage \pm SD of directly ligated products for three independent transfections is noted below. (D) dGTP, rGTP, or an equivalent amount of the relevant salt ("none") was added to Rosa26 Cas9–single guide RNA ribonucleoprotein (RNP) transfections performed as for Fig. 2, C and D, and genomic DNA was harvested after 1 hour. Data are the mean from four transfections, and error bars represent SD. Means were compared in pairs by ANOVA with values for no nucleotide triphosphate (NTP) addition ($***P < 0.001$). (E) Triple strand break repair model. Pol μ - or TdT-dependent ribonucleotide addition is noted in red.

favoring of ribonucleotide incorporation by these polymerases for first-strand repair, followed by repair of complementary strands with deoxynucleotides. As expected, levels of embedded ribonucleotides in repair products were much lower when cells were proficient in RER (23% after 1 hour) (fig. S4F) and undetectable at a nearby locus where breaks were not induced (whether cells were RER deficient or not) (fig. S4E).

We investigated the consequences of ribonucleotide addition for ligation, the next step of cellular NHEJ. We initially focused on a substrate with 3'GA overhangs, where 66% of NHEJ occurs by ligation after Pol μ -dependent addition of a single complementary C (fig. S5A). We made two variants of this substrate with a C already added: one where the added C was a ribonucleotide (+rC) and one where it was a deoxynucleotide (+dC) (Fig. 3A). We then introduced these two substrate variants into cells that express neither Pol μ nor TdT to isolate the effects of the different pre-added nucleotides on ligation and confirmed that repair under these conditions relies on the NHEJ-specific ligase (LIG4) (fig. S5B). Notably, only the +rC variant was able to efficiently promote direct ligation in cells, whereas the +dC variant was largely ineffective (the efficiency of direct ligation was reduced by a factor of >20) (Fig. 3B and Table 1). Direct ligation was also stimulated when the ribonucleotide 2'-OH was replaced with fluorine and blocked when the terminal nucleotide was replaced with a ribonucleotide stereoisomer, arabinofuranosylcytidine (Ara-C) (Fig. 3B and Table 1). Ara-C differs from rC only by the orientation of the 2'-OH and the favored sugar pucker (rC favors C3'-endo, and Ara-C favors C2'-endo), suggesting that a terminal C3'-endo nucleotide is required for the stimulation of ligation (fig. S5C). A terminal ribonucleotide also stimulated LIG4-dependent ligation in vitro, confirming that the effect on cellular NHEJ is specific to the ligation step. In contrast, T4 DNA ligase gained no benefit from a terminal ribonucleotide (fig. S5D). LIG4 may be alone among mammalian ligases in the ability to take advantage of added ribonucleotide termini, analogous to the in vitro activity of bacterial *Pseudomonas* LigD compared with that of other prokaryotic ligases (18).

We addressed whether end structure context affected whether ribonucleotide additions stimulated ligation. An added ribonucleotide was required for direct ligation in cells whenever the opposite strand was mostly mispaired or gapped (Fig. 3C and Table 1); in the context of mispaired or gapped end structures, Pol μ and TdT are distinctively active during NHEJ (15, 17). By comparison, direct ligation is similarly efficient for ribonucleotide and deoxynucleotide additions in contexts where other polymerases are more active—mostly complementary overhangs—both in cells (Fig. 3C and Table 1) and in vitro (10, 19). The class of end structures where Pol μ and TdT distinctively contribute to cellular NHEJ thus correlates well with the class of end structures where ribonucleotides are required for direct ligation. Moreover, deoxynucleotide additions in these contexts were associated with frequent deletion of both the added nucleotide and flanking DNA (fig. S5, E and F), and repair was less efficient (Table 1). Our results imply that ribonucleotide addition is required for the biological activity of Pol μ and TdT.

We sought to more directly address whether polymerase function during cellular NHEJ relies on ribonucleotide addition. We introduced

breaks in the chromosome with Cas9 and assessed whether the introduction of high concentrations of deoxynucleotide triphosphate affected the accumulation of the TdT-dependent repair products (+GG products) characterized in Fig. 2, C and D. The introduction of excess deoxyguanine triphosphate (dGTP) impaired the accumulation of these products by a factor of four relative to the accumulation in parallel experiments with unperturbed nucleotide pools. In contrast, the introduction of excess riboguanine triphosphate (rGTP) modestly stimulated +GG product recovery, consistent with the already high cellular rGTP pools in unperturbed cells (Fig. 3D). Similar results were also obtained by using two methods that more generally measure NHEJ-dependent short insertions and deletions (fig. S6, A and B). NHEJ was also impaired upon the introduction of Ara-GTP (fig. S6), in accordance with the inability of additions of this ribonucleotide stereoisomer to promote repair (Fig. 3B).

We show that Pol μ and TdT preferentially add ribonucleotides (Figs. 1 and 2) and contribute to the repair of a specific subset of end structures (15), that the same subset of end structures requires ribonucleotide additions for efficient LIG4-mediated repair (Fig. 3), and that only LIG4 may be able to take advantage of added nucleotides. Within all mammalian DNA metabolism, only the synthetic enzymes specific to NHEJ appear to cooperate in this unusual manner. Our results suggest that this reflects a coevolution of these enzymes to better repair damaged or mispaired ends, a central problem of this pathway.

Our results also have more general relevance. Ribonucleotides destabilize DNA genomes unless removed by RER (20, 21), and when incorporated during NHEJ, they pose special problems for the RER pathway. We show that safe accommodation of ribonucleotide-containing intermediates during NHEJ is most likely enabled by three sequential coupled strand break repair reactions (Fig. 3E), with each reaction coupled to the next: repair of the first strand with ribonucleotides, repair of the second strand with deoxynucleotides, and RNaseH2A-dependent excision of the ribonucleotides embedded during first-strand repair. This model explains the twofold dilution of embedded ribonucleotides that is independent of RER and RNaseH2A (Fig. 1B). Alternative models—where ribonucleotides are incorporated into both strands or where RNaseH2 incises the first strand before second-strand repair is complete—risk rebreakage of the chromosome. Additionally, the transient nature of intermediates with embedded ribonucleotides (for which the half-life is likely less than 5 min) (Fig. 1B) suggests that all three strand break repair reactions are joined together, possibly by physical interactions between pathway components.

Pol μ is widely expressed and participates in as little as 16% (e.g., fig. S4A) to as much as 66% (e.g., fig. S5A) of repair, depending on the end structure (15). In lymphocytes, either TdT or Pol μ is active in 65% of NHEJ events required

for V(D)J recombination (5, 17). The triple stand break repair model proposed here (Fig. 3E) is thus relevant to a large fraction of mammalian NHEJ and is a fundamental departure from the previously accepted model. It is probably relevant to NHEJ in other species (e.g., yeast and bacteria) (18, 22, 23) as well. Our work further indicates that ribonucleotide incorporation is required if mammalian Pol μ and TdT are to be effective in promoting long-term cellular proliferative capacity, the development of adaptive immunity, and radioresistance (3–9).

REFERENCES AND NOTES

1. G. E. Taccioli *et al.*, *Science* **260**, 207–210 (1993).
2. C. A. Waters, N. T. Strande, D. W. Wyatt, J. M. Pryor, D. A. Ramsden, *DNA Repair (Amst.)* **17**, 39–51 (2014).
3. T. Komori, A. Okada, V. Stewart, F. W. Alt, *Science* **261**, 1171–1175 (1993).
4. S. Gilfillan, A. Dierich, M. Lemeur, C. Benoist, D. Mathis, *Science* **261**, 1175–1178 (1993).
5. B. Bertocci, A. De Smet, C. Berek, J. C. Weill, C. A. Reynaud, *Immunity* **19**, 203–211 (2003).
6. J. P. Cabaniols, N. Fazilleau, A. Casrouge, P. Kourilsky, J. M. Kanellopoulos, *J. Exp. Med.* **194**, 1385–1390 (2001).
7. D. Lucas *et al.*, *PLoS Genet.* **5**, e1000389 (2009).
8. R. Chayot, A. Danckaert, B. Montagne, M. Ricchetti, *DNA Repair (Amst.)* **9**, 1187–1199 (2010).
9. J. Schimmel, H. Kool, R. van Schendel, M. Tijsterman, *EMBO J.* **36**, 3634–3649 (2017).
10. S. A. Nick McElhinny, D. A. Ramsden, *Mol. Cell. Biol.* **23**, 2309–2315 (2003).
11. N. A. Cavanaugh, W. A. Beard, S. H. Wilson, *J. Biol. Chem.* **285**, 24457–24465 (2010).
12. J. A. Brown *et al.*, *J. Mol. Biol.* **395**, 282–290 (2010).
13. R. A. Gosavi, A. F. Moon, T. A. Kunkel, L. C. Pedersen, K. Bebenek, *Nucleic Acids Res.* **40**, 7518–7527 (2012).
14. J. S. Williams, S. A. Lujan, T. A. Kunkel, *Nat. Rev. Mol. Cell Biol.* **17**, 350–363 (2016).
15. J. M. Pryor *et al.*, *Proc. Natl. Acad. Sci. U.S.A.* **112**, E4537–E4545 (2015).
16. M. S. Schlissel, *Mol. Cell. Biol.* **18**, 2029–2037 (1998).
17. S. A. Nick McElhinny *et al.*, *Mol. Cell* **19**, 357–366 (2005).
18. H. Zhu, S. Shuman, *J. Biol. Chem.* **283**, 8331–8339 (2008).
19. A. F. Moon *et al.*, *Nucleic Acids Res.* **45**, 9138–9148 (2017).
20. S. A. N. McElhinny *et al.*, *Nat. Chem. Biol.* **6**, 774–781 (2010).
21. M. A. M. Reijns *et al.*, *Cell* **149**, 1008–1022 (2012).
22. K. Bebenek, M. Garcia-Diaz, S. R. Patishall, T. A. Kunkel, *J. Biol. Chem.* **280**, 20051–20058 (2005).
23. M. Della *et al.*, *Science* **306**, 683–685 (2004).

ACKNOWLEDGMENTS

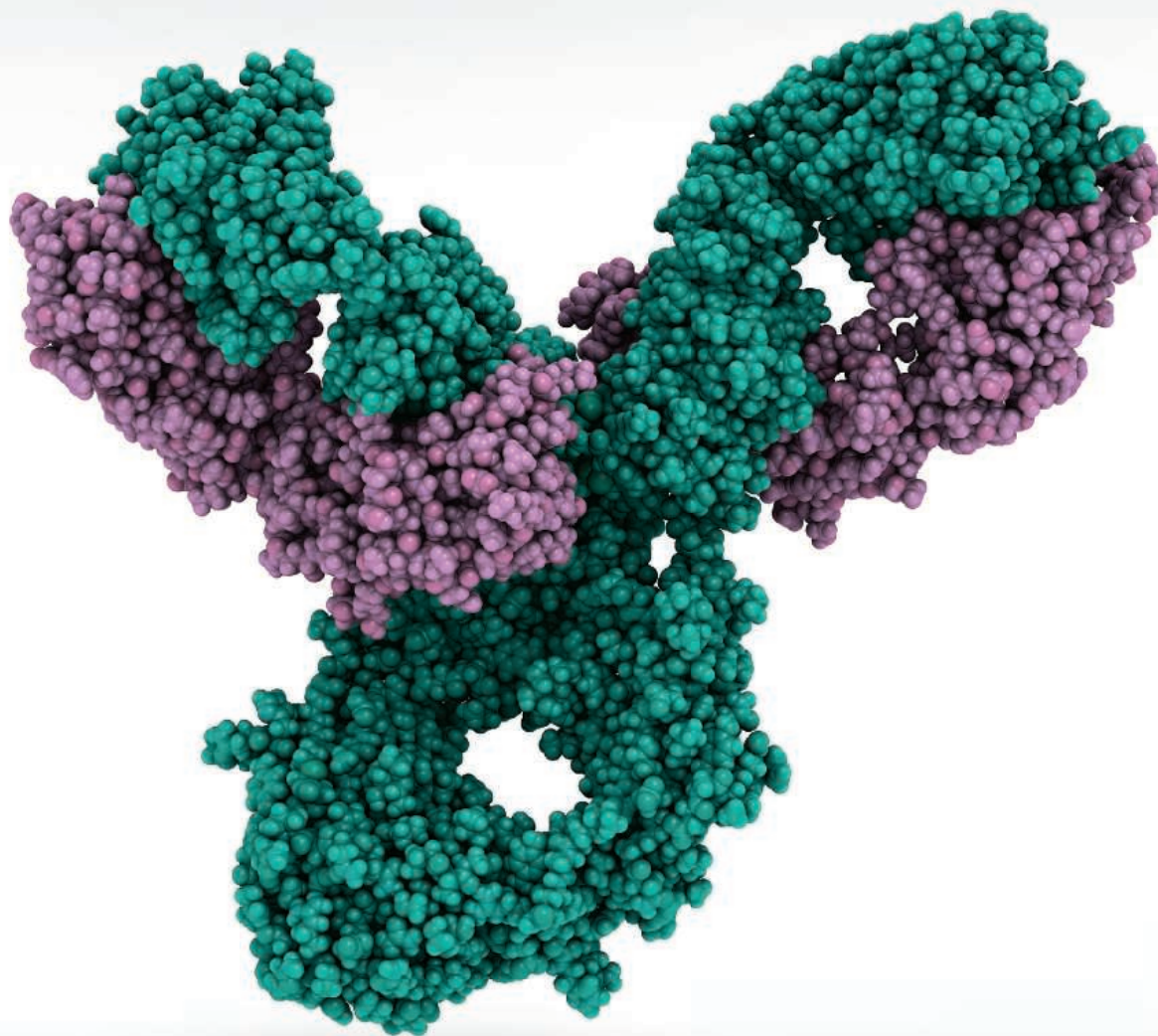
We thank S. N. McElhinny, J. Havener, T. Kunkel, R. S. Williams, Q. Zhang, and Ramsden lab members for help guiding the experiments described in this work; L. Blanco for providing MEFs; Y. Chang for providing SP9 cells; and E. Hendrickson for providing HCT116 cells. **Funding:** This work was supported by NCI R01CA097096 (D.A.R.), ACS PF-14-0438-01-DMC (J.M.P.), NCI F31CA203156 (M.P.C.), T32GM007092 (M.P.C. and M.E.L.), and T32GM119999 (A.J.L.). **Author contributions:** J.M.P., M.P.C., and D.A.R. authored the manuscript, designed experiments, and analyzed data. J.M.P., M.P.C., J.C.-G., M.E.L., A.J.L., and G.W.S. performed experiments. **Competing interests:** J.M.P. is currently an employee at New England Biolabs, a manufacturer and vendor of some of the molecular biology reagents used in this work. **Data and materials availability:** All materials and raw data are available upon request.

SUPPLEMENTARY MATERIALS

www.sciencemag.org/content/361/6407/1126/suppl/DC1
Materials and Methods
Figs. S1 to S6
Tables S1 and S2
References (24–27)

8 February 2018; resubmitted 31 May 2018
Accepted 20 July 2018
10.1126/science.aat2477

Publish your research
in ***Science Immunology***



Science Immunology publishes original, peer-reviewed, science-based research articles that report critical advances in all areas of immunological research, including important new tools and techniques.

For more information: ScienceImmunology.org

Science
Immunology
AAAS



2019 **MRS**® SPRING MEETING & EXHIBIT

April 22–26, 2019 | Phoenix, Arizona

CALL FOR PAPERS

Abstract Submission Opens
September 28, 2018

Abstract Submission Closes
October 31, 2018

Spring Meeting registrations include MRS Membership July 1, 2019 – June 30, 2020

BROADER IMPACT

- BI01 High Impact Practice—Increasing Ethnic and Gender Diversification in Engineering Education

CHARACTERIZATION, PROCESSING AND THEORY

- CP01 Advances in *In Situ* Experimentation Techniques Enabling Novel and Extreme Materials/Nanocomposite Design
- CP02 Design and *In Situ* TEM Characterization of Self-Assembling Colloidal Nanosystems
- CP03 Advances in *In Situ* Techniques for Diagnostics and Synthetic Design of Energy Materials
- CP04 Interfacial Science and Engineering—Mechanics, Thermodynamics, Kinetics and Chemistry
- CP05 Materials Evolution in Dry Friction—Microstructural, Chemical and Environmental Effects
- CP06 Smart Materials for Multifunctional Devices and Interfaces
- CP07 From Mechanical Metamaterials to Programmable Materials
- CP08 Additive Manufacturing of Metals
- CP09 Mathematical Aspects of Materials Science—Modeling, Analysis and Computations

ELECTRONICS AND PHOTONICS

Soft Organic and Biomolecular Electronics

- EP01 Liquid Crystalline Properties, Self-Assembly and Molecular Order in Organic Semiconductors
- EP02 Photonic Materials and Devices for Biointerfaces
- EP03 Materials Strategies and Device Fabrication for Biofriendly Electronics
- EP04 Soft and Stretchable Electronics—From Fundamentals to Applications
- EP05 Engineered Functional Multicellular Circuits, Devices and Systems
- EP06 Organic Electronics—Materials and Devices

Semiconductor Devices, Interconnects, Plasmonic and Thermoelectric Materials

- EP07 Next-Generation Interconnects—Materials, Processes and Integration
- EP08 Phase-Change Materials for Memories, Photonics, Neuromorphic and Emerging Application
- EP09 Devices and Materials to Extend the CMOS Roadmap for Logic and Memory Applications
- EP10 Heterovalent Integration of Semiconductors and Applications to Optical Devices
- EP11 Hybrid Materials and Devices for Enhanced Light-Matter Interactions
- EP12 Emerging Materials for Plasmonics, Metamaterials and Metasurfaces
- EP13 Thermoelectrics—Materials, Methods and Devices

ENERGY AND SUSTAINABILITY

Energy Storage

- ES01 Organic Materials in Electrochemical Energy Storage
- ES02 Next-Generation Intercalation Batteries
- ES03 Electrochemical Energy Materials Under Extreme Conditions
- ES04 Solid-State Electrochemical Energy Storage

Catalysis, Alternative Energy and Fuels

- ES05 Cooperative Catalysis for Energy and Environmental Applications
- ES06 Atomic-Level Understanding of Materials in Fuel Cells and Electrolyzers
- ES07 New Carbon for Energy—Materials, Chemistry and Applications
- ES08 Materials Challenges in Surfaces and Coatings for Solar Thermal Technologies
- ES10 Rational Designed Hierarchical Nanostructures for Photocatalytic System
- ES11 Advanced Low Temperature Water-Splitting for Renewable Hydrogen Production via Electrochemical and Photoelectrochemical Processes
- ES12 Redox-Active Oxides for Creating Renewable and Sustainable Energy Carriers

Water-Energy Materials and Sustainability

- ES09 Advanced Materials for the Water-Energy Nexus
- ES13 Materials Selection and Design—A Tool to Enable Sustainable Materials Development and a Reduced Materials Footprint

- ES14 Materials Circular Economy for Urban Sustainability

Photovoltaics and Energy Harvesting

- ES15 Fundamental Understanding of the Multifaceted Optoelectronic Properties of Halide Perovskites
- ES16 Perovskite Photovoltaics and Optoelectronics
- ES17 Perovskite-Based Light-Emission and Frontier Phenomena—Single Crystals, Thin Films and Nanocrystals
- ES18 Frontiers in Organic Photovoltaics
- ES19 Excitonic Materials and Quantum Dots for Energy Conversion
- ES20 Thin-Film Chalcogenide Semiconductor Photovoltaics
- ES21 Nanogenerators and Piezotronics

QUANTUM AND NANOMATERIALS

- QN01 2D Layered Materials Beyond Graphene—Theory, Discovery and Design
- QN02 Defects, Electronic and Magnetic Properties in Advanced 2D Materials Beyond Graphene
- QN03 2D Materials—Tunable Physical Properties, Heterostructures and Device Applications
- QN04 Nanoscale Heat Transport—Fundamentals
- QN05 Emerging Thermal Materials—From Nanoscale to Multiscale Thermal Transport, Energy Conversion, Storage and Thermal Management
- QN06 Emerging Materials for Quantum Information
- QN07 Emergent Phenomena in Oxide Quantum Materials
- QN08 Colloidal Nanoparticles—From Synthesis to Applications

SOFT MATERIALS AND BIOMATERIALS

- SM01 Materials for Biological and Medical Applications
- SM02 Progress in Supramolecular Nanotheranostics
- SM03 Growing Next-Generation Materials with Synthetic Biology
- SM04 Translational Materials in Medicine—Prosthetics, Sensors and Smart Scaffolds
- SM05 Supramolecular Biomaterials for Regenerative Medicine and Drug Delivery
- SM06 Nano- and Microgels
- SM07 Bioinspired Materials—From Basic Discovery to Biomimicry

www.mrs.org/spring2019

Meeting Chairs

Yuping Bao The University of Alabama
Bruce Dunn University of California, Los Angeles
Subodh Mhaisalkar Nanyang Technological University
Ruth Schwaiger Karlsruhe Institute of Technology—
 Institute for Applied Materials
Subhash L. Shinde University of Notre Dame

Don't Miss These Future MRS Meetings!

2019 MRS Fall Meeting & Exhibit
 December 1–6, 2019, Boston, Massachusetts

2020 MRS Spring Meeting & Exhibit
 April 13–17, 2020, Phoenix, Arizona



MATERIALS RESEARCH SOCIETY®
Advancing materials. Improving the quality of life.

506 Keystone Drive • Warrendale, PA 15086-7573
 Tel 724.779.3003 • Fax 724.779.8313 • info@mrs.org • www.mrs.org

Complex world, simple rules:

The School of Systems Science at Beijing Normal University

Muduo (traditional bell) at BNU

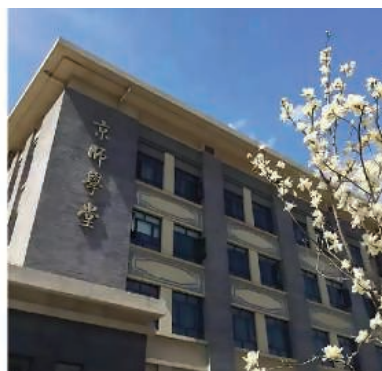
Founded in 1902, Beijing Normal University (BNU) is one of the top 10 universities in China, offering a strong emphasis on the humanities and sciences. The history of systems science studies at BNU began in 1979 with the establishment of the Institute of Nonequilibrium Systems. In 1985, the field of systems theory was founded, sparking a concerted effort by BNU to develop and grow systems science at the university. In the intervening three decades, BNU's systems science program has garnered support from many famous scholars—including world-renowned engineer Hsue-Shen Tsien and Nobel Prize-winning physical chemist Ilya Prigogine—and has grown into an internationally competitive program, providing students with a strong foundation in a broad range of systems-related disciplines.

The School of Systems Science

The School of Systems Science (SSS) was established in 2013, with the aim of creating a globally recognized institution for scientific research and training. The school strives to be a pioneer in building a solid base for systems science in China, while also offering a platform for interdisciplinary research and scientific innovation at BNU.

SSS is committed to discovering the “simple rules” that guide our exploration of this complex world, to expanding the frontiers of systems science research, to cultivating exceptional students and researchers, and to transforming academic progress in systems science into forces for social and economic change, all with the goal of deepening our understanding of nature and society.

“Systems science focuses on tackling the basic scientific problems underlying the nature and evolution of complex systems.”



Clockwise, from left: BNU's Jingshi Academic Hall, gate of the Zhuhai campus, and SSS logo and motto.

A broad research base

As a discipline, systems science focuses on tackling the basic scientific problems underlying the nature and evolution of complex systems. As the discipline has developed and matured over the past 30 years, researchers at BNU have attempted to reveal the general rules of complex systems through the study of their evolution. Areas of study include the emergent behavior of complex systems and the intelligent control of the nature and function of these systems. The direction and level of scientific research at SSS is on par with international systems science research and follows similar trends.

The work done at SSS spans an impressively broad range of topics, comprising six primary subfields: 1) fundamental theories of complex systems, 2) social and economic systems, 3) biological ecosystems and the self-organizing behavior of the brain and cognition, 4) multiagent systems and evolutionary algorithms, 5) information technology for artificial intelligence systems, and 6) the science of science. Research coming out of SSS has gained worldwide attention. Its groundbreaking work has aroused widespread interest both in the scientific community and in the public sphere in areas such as network reconstruction and control, the network structure of Chinese characters and related learning systems, the spiking neural

network model for understanding working memory, and a parameter-free model for human mobility. It should be noted that SSS is open to the pursuit of other fields of interdisciplinary research in the natural and social sciences beyond the six listed above.

With its drive to enhance our understanding of the richness and complexity of the world around us, SSS aims to train exceptional scientists with a solid academic foundation and strong interdisciplinary skills in systems science. These graduates will become proactive leaders with a strong sense of social responsibility and a comprehensive global vision. The school warmly welcomes applications and cooperation from top researchers from around the world.

Sponsored by

For more information, please contact us:

Website: <http://sss.bnu.edu.cn>

Email: sss@bnu.edu.cn

Address: School of Systems Science, Beijing Normal University, No. 19, Xijiekouwai St., Haidian District, Beijing, China 100875





2D Barcode Scanner

The DataPaq Mirage from Ziath is a camera-based, 2D barcode rack scanner that can be easily integrated with robotic liquid-handling systems as well as other laboratory automation solutions. It brings the benefits of a more sophisticated rack scanner to automation workflows for the

same price as an old flatbed scanner. Most camera-based scanners are too tall for use on liquid-handling workstations; but the patent-pending technology of DataPaq Mirage uses a mirror to give the scanner a more compact design. Its low profile allows samples in Society for Biomolecular Screening (SBS) format racks to be efficiently scanned and recorded at the point of processing.

Ziath

For info: +44-(0)-1223-855021
www.ziath.com

Antibody Arrays

With the RayBiotech Biotin Label-Based Antibody Array (L-Series), researchers can obtain a broad, panoramic view of protein expression. Up to 1,000 target proteins can be detected simultaneously, including cytokines, chemokines, adipokines, growth factors, proteases, soluble receptors, and adhesion molecules, among others, making this array ideally suited for biomarker discovery studies and exploratory screens. Through a simple labeling process, the sample proteins are directly conjugated to biotin, eliminating the need for a second antibody to develop the array signals. In this format, unintended antibody interactions are impossible, thus eliminating limitations on the size of the array panel.

RayBiotech

For info: 888-494-8555
www.raybiotech.com/l-series-label-based-antibody-arrays

Gas Analyzers

Hidden Analytical's HPR-20 range of application-specific compact benchtop gas analyzers for dynamic measurement of in-process gas composition features precision quadrupole mass spectrometers with standard mass-range options between 200 amu and 300 amu, with options from 20 amu to 1,000 amu available for specialized applications. The HPR-20 EGA system is configured for fast-response evolved gas analysis (EGA) at near-atmospheric pressures using bypass capillary sampling, with sample consumption rates typically from 1 mL/min to 15 mL/min. The HPR-20 TMS transient mass spectrometer system offers the optimum response time for fast-event studies. The system uses a direct-pulse ion-counting detector with a 7-decade dynamic range, from 1 to 10⁷ counts per second, and with the multichannel scalar option, provides a time resolution of just 50 ns. The HPR-20 R&D system is optimized for the researcher, including direct sampling options ranging from sample pressures up to 30 bar.

Hidden Analytical

For info: +44-(0)-1925-445-225
www.hiddenanalytical.com

Fluorescent ELISA Kits

CatchPoint SimpleStep ELISA (SSE) kits provide a simple, fast protocol with a single wash step and an assay time of 90 min or less. Their fluorescent substrate significantly improves linearity over an extended dynamic range when compared to horseradish peroxidase/TMB substrate, reducing the need for sample dilutions and allowing quantitation at lower protein concentrations, thus improving sensitivity. CatchPoint SSE kits are validated across a wide range of biological samples and optimized for Molecular Devices' microplate readers, delivering reproducible results across many different undiluted sample types on industry-leading instrumentation. The kits employ highly validated antibodies, most of which have been developed using Abcam's recombinant monoclonal antibody technology. Recombinant antibodies offer specificity and lot-to-lot reproducibility for consistent experimental results. CatchPoint SSE and SimpleStep colorimetric kits serve a variety of interests, including cancer, neuroscience, cardiovascular, and immunology research.

Abcam

For info: 888-772-2226
www.abcam.com/catchpoint-simplestep-elisa-kits

Quaternary Liquid Chromatograph

The Waters ACQUITY Arc Bio System is a versatile, quaternary liquid chromatograph specifically engineered to enable efficient transfer and improvement of bioseparation analytical methods regardless of the liquid chromatography (LC) platform on which the original method was developed. It is ideally suited to run reversed-phase, ion-exchange, size-exclusion, and hydrophobic-interaction LC methods with minimal carryover and maximum recovery of biomolecules. The system's flow paths are made of non-stainless steel and iron-free bioinert materials designed to minimize undesirable protein interactions and maximize system robustness under salt and pH extremes. What also sets the instrument apart is the unique Arc Multi-flow path technology, which delivers plug-and-play compatibility with HPLC or UHPLC methods through a selectable dwell volume, emulating the dwell volume of the original instrument. This feature minimizes the time required to redevelop methods from internal and external partners.

Waters

For info: 800-252-4752
www.waters.com/arcbio

High-Speed Spectrometer

The IRisF1 is a laser-based, infrared spectrometer that exploits the sensing performance of so-called "frequency combs" in the mid-infrared spectral region. As a result, the instrument offers high measurement speed (microsecond time resolution) with the high brightness of a laser-based instrument and a multicolor output. It is an alternative to Fourier transform infrared (FTIR) spectrometers that are often too slow for time-resolved applications. The IRisF1 enables high-throughput screening and analysis of strongly absorbing samples. For example, researchers can observe the folding or conformational changes of proteins in real time.

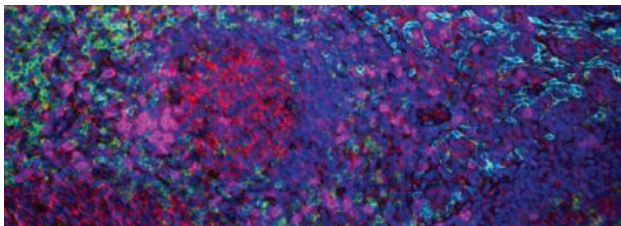
IRsweep

For info: +41-(0)-44-545-85-99
www.irsweep.com

Electronically submit your new product description or product literature information! Go to www.sciencemag.org/about/new-products-section for more information.

Newly offered instrumentation, apparatus, and laboratory materials of interest to researchers in all disciplines in academic, industrial, and governmental organizations are featured in this space. Emphasis is given to purpose, chief characteristics, and availability of products and materials. Endorsement by *Science* or AAAS of any products or materials mentioned is not implied. Additional information may be obtained from the manufacturer or supplier.

want new technologies?

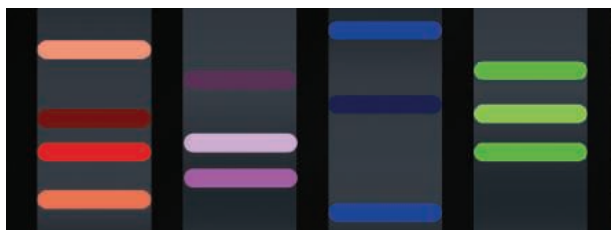
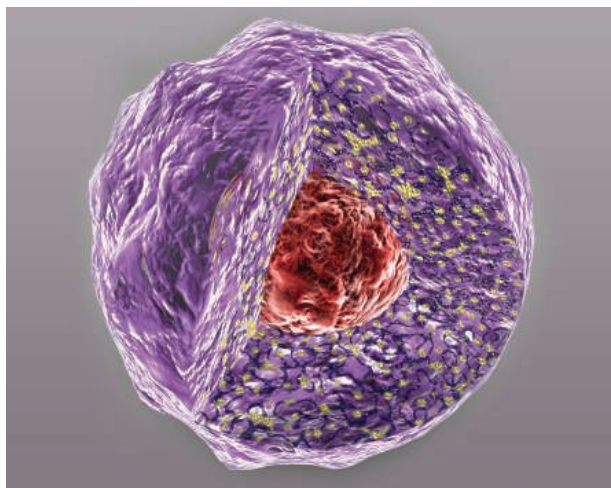


watch our webinars

Learn about the latest breakthroughs, new technologies, and ground-breaking research in a variety of fields. Our expert speakers explain their quality research to you and answer questions submitted by live viewers.

VIEW NOW!
webinar.
sciencemag.
org

antibodies
apoptosis
biomarkers
cancer
cytometry
data
diseases
DNA
epigenetics
genomics
immunotherapies
medicine
microbiomics
microfluidics
microscopy
neuroscience
proteomics
sequencing
toxicology
transcriptomics



Science
AAAS

Brought to you by the Science/AAAS
Custom Publishing Office

 @SciMagWebinars



Exceptional scientists wanted

Present your work to the world

Are you a representative of the upcoming generation of thought leaders in your field? Together we look forward to your application for the new Sartorius & Science Prize for Regenerative Medicine & Cell Therapy.

Apply now!

www.passionforscience.com/prize



The Sartorius & Science
Prize for Regenerative
Medicine & Cell Therapy

Awarded by



sartorius

Science

A novel target for accelerating drug development: Biomedical science training

Cherie Butts¹ and Avery August²

Demand for a qualified biomedical science workforce to tackle the challenges of making better medicines remains high; however, few scientists and clinicians learn about drug development during their training. To assist trainees with appreciating differences between basic science (understanding disease mechanisms) and applied science (drug development), Biogen and the Cornell Broadening Experiences in Scientific Training (BEST) program convened a conference in June 2018 at the Biogen headquarters in Cambridge, Massachusetts (#Biogen BESTDDConf2018).

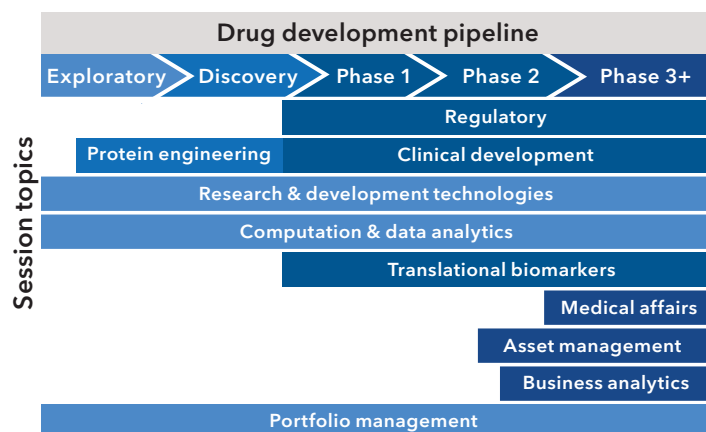


FIGURE 1.

Selection process

Participants were identified primarily from academic institutions with U.S. National Institutes of Health (NIH) BEST programs (www.nihbest.org; <https://commonfund.nih.gov/workforce>), as they are familiar with biopharma career pathways. Trainees* were exposed to key drug development questions, different roles in and out of the laboratory or clinic, and skills needed to be successful in biopharma. To ensure that information from the conference extended beyond those who attended, a requirement was that trainees share key concepts with others at their home institutions.

Unique approach

The average time for developing a new drug is approximately 12 years and costs over USD 1 billion, predominantly due to failures at each stage of drug development (1). An appropriately trained workforce is one mechanism for accelerating timelines and reducing the risk of failure. As many biomedical sciences training programs do not offer activities related to drug development, trainees must opt for additional specialized fellowships (ranging in duration from several weeks to a few years) or transition to industry with little knowledge of the skills necessary to be successful in this sector. As an initiative of Biogen's Portfolio Transformation, a short-term, intensive conference was developed to demystify drug development for academic trainees. The goal was to create a model for similar events across the country.

High-performing project teams are a hallmark of biopharma, but are less common in academia (2). Conference activities, therefore, focused on providing participants with a project-team experience that highlighted key drug development questions; stage-appropriate composition of project teams; the importance of team dynamics and of maximizing the strengths of each member; and how the biopharma ecosystem supports project teams.

Purposeful outcomes

Participants were introduced to the drug development process (from concept to approval), and sessions were led by individuals from across Biogen, who offered insight on their roles—including how they support project teams. The topics included asset management, biomarker development, business and data analytics, clinical development, medical affairs, portfolio management, protein engineering, and regulatory affairs and policy (Figure 1). In addition, participants served on teams that generated a business case and recommendations for progression of a mock project to the next drug development stage (Figure 2).

Refining and reframing

A new training model is needed to strengthen and refine the necessary skills for those who wish to translate new biomedical discoveries into beneficial drugs. More trainees with the right experience will increase the pace of drug development, reducing the burden of debilitating medical conditions on society. Such a reframing of the training experience will positively change the conduct of science and expand the ways that meaningful contributions to biomedical science are defined. This conference emphasizes the importance of experiential learning and serves as a model for such training.



FIGURE 2.

References

1. G. A. Van Norman, *JACC: Basic to Translational Science* **1**, 170-179 (2016).
2. J. R. Katzenbach, D. K. Smith, *Harvard Business Review* **71**, 111-120 (1993).

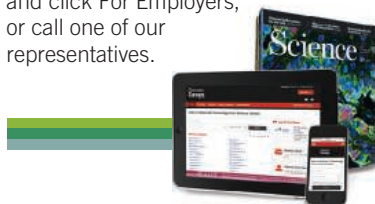
For additional information and to explore future opportunities with this drug development training model, please contact the authors: cherie.butts@biogen.com and averyaugust@cornell.edu.

¹Portfolio Transformation and Late-Stage Clinical Development, Biogen, Cambridge, MA; cherie.butts@biogen.com ²Cornell BEST Program and Department of Microbiology and Immunology, Cornell University, Ithaca, NY; averyaugust@cornell.edu

Science Careers

SCIENCE CAREERS ADVERTISING

For full advertising details,
go to ScienceCareers.org
and click For Employers,
or call one of our
representatives.



AMERICAS

+1 202 326-6577
+1 202 326-6578
advertise@sciencecareers.org

EUROPE, INDIA, AUSTRALIA, NEW ZEALAND, REST OF WORLD

+44 (0) 1223 326527
advertise@sciencecareers.org

CHINA, KOREA, SINGAPORE, TAIWAN, THAILAND

+86 131 4114 0012
advertise@sciencecareers.org

JAPAN

+81 3-6459-4174
advertise@sciencecareers.org

CUSTOMER SERVICE

AMERICAS

+1 202 326-6577

REST OF WORLD

+44 (0) 1223 326528

advertise@sciencecareers.org

All ads submitted for publication must comply with applicable U.S. and non-U.S. laws. *Science* reserves the right to refuse any advertisement at its sole discretion for any reason, including without limitation for offensive language or inappropriate content, and all advertising is subject to publisher approval. *Science* encourages our readers to alert us to any ads that they feel may be discriminatory or offensive.

ScienceCareers

FROM THE JOURNAL SCIENCE  AAAS

ScienceCareers.org



Department of Biological Engineering Faculty Position in Comparative Medicine

The MIT Department of Biological Engineering, in partnership with the MIT Division of Comparative Medicine, invites applications for a tenure-track faculty position at the Assistant Professor level, to begin July 2019 or thereafter. A more senior position may be considered in special cases. Teaching responsibilities will be in subjects within the Department's undergraduate and graduate curricula and compatible with his or her research expertise. Applicants should hold a DVM from an AVMA-accredited institute, or an MD, and/or a PhD in a discipline which applies molecular/cellular bioscience to the study of the microbial/host interface in health and disease with interests in microbial pathogenesis, microbiome bioinformatics, immunology, or pathobiology. The selected candidate will develop and sustain vigorous extramurally funded research programs, supervise graduate students, develop course materials and teach graduate-level subject(s). He or she may also teach undergraduate subjects.

To Apply:

Candidates must register with the BE search website at <http://be-fac-search.mit.edu>, and must submit application materials electronically to this website. Candidate applications should include a description of professional interests and goals in both teaching and research. Each application should include a curriculum vitae and the names and addresses of three or more references who will provide recommendation letters. References should submit their letters directly at the <http://be-fac-search.mit.edu> website.

Applications received by 1st December 2018 will be given priority.

Questions may be directed to: Prof. Douglas Lauffenburger, Head, Department of Biological Engineering, MIT 16-343, Cambridge MA 02139, lauffen@mit.edu

MIT is an Equal Opportunity/Affirmative Action employer

<http://web.mit.edu>



Department of Biological Engineering Faculty Position in Molecular/Cell Biophysics

The MIT Department of Biological Engineering invites applications for tenure-track faculty positions at the assistant professor level, to begin July 2019 or thereafter. Applicants should hold a Ph.D. in a science or engineering discipline related to biological engineering. A more senior faculty appointment may be considered in special cases. Candidates should aspire to direct a leading research program that fuses molecular/cellular bioscience with quantitative engineering analysis/synthesis approaches. Areas of high priority include molecular and cell biophysics, with applications in quantitative measurement and modeling of biological processes. Faculty duties include teaching at the graduate and undergraduate levels as well as oversight of research, conducting original scholarly research, and developing course materials at the graduate and undergraduate levels. Candidates should be capable of instructing in our core biological engineering educational curricula.

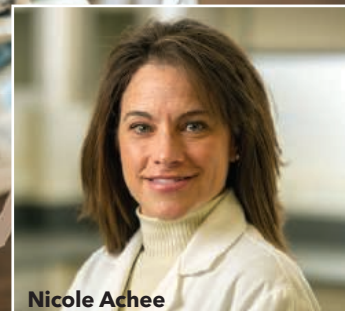
Candidates must register with the BE search website at <http://be-fac-search.mit.edu>, and must submit application materials electronically to this website. Candidate applications should include a description of professional interests and goals in both teaching and research. Each application should include a curriculum vitae and the names and addresses of three or more references who will provide recommendation letters. References should submit their letters directly at the <http://be-fac-search.mit.edu> website. Applications received by 1st December 2018 will be given priority.

Questions may be directed to: Prof. Douglas Lauffenburger, Head, Department of Biological Engineering, MIT 16-343, Cambridge MA 02139, lauffen@mit.edu

MIT is an Equal Opportunity/Affirmative Action employer

<http://web.mit.edu>

Beyond government grants: Widening your funding net



Nicole Achée

"Don't put all your eggs in one basket" is sound financial advice for both investors and researchers. Supplementing government grants with support from foundations, industry partners, and crowdfunding means that scientists must learn to navigate new fundraising systems. But they may also gain connections to broader, science-related communities. **By Chris Tachibana**

"Single-origin"—referring to a product that comes from one specific location, crop, or supplier—is now a trend for coffee and chocolate, but science funding is moving toward diversification. The reason? The proportion of U.S. R&D supported by federal funds fell from nearly 70% in 1973 to below 60% in 2016, according to a U.S. National Science Foundation report (1). Nonprofit and private organizations such as the Bill & Melinda Gates Foundation fill the funding gap for some researchers, while others explore options such as direct pitches to industry partners, investors, and crowdfunding donors.

Financial security is just one reason to diversify funding. Small awards from institutional sources, foundations, or crowdfunding can replace money lost to budget cuts. Supplemental funding can also support preliminary data collection for a larger proposal. Additionally, industry or investor partners may provide both funding and business mentoring for a scientist whose project has commercial potential. Or researchers can endorse open science while raising money on crowdfunding and science-challenge platforms. This article explores alternative funding resources that supplement or replace traditional government mechanisms.

Broadening your funding base

Nicole Achée, research associate professor in biological sciences, University of Notre Dame, Indiana, has a compelling reason to vary her funding sources. Her research goes "from lab to field," using laboratory assays to evaluate methods to control insects that carry diseases, then testing the effectiveness of those methods where disease occurs. In addition to support from the U.S. Department of Defense, the U.S. Agency for International Development, the U.S. National Institutes of Health,

and industry, Achée's team is receiving about USD 14 million from the Bill & Melinda Gates Foundation for work on *Aedes*-borne viruses such as dengue and Zika.

"The more diversified your funding," Achée says, "the more you have to be aware of what is due and when." Government funding is often timed to the fiscal year, she says, but foundations may have completely different schedules. A competent program manager to track paperwork and deadlines is critical.

To broaden a funding base, Achée advises following news from organizations that specialize in your field and regularly searching for novel funders that fit your research. Work with your institution's development and grants office to find opportunities with industry partners, private foundations, and nongovernmental organizations. Companies such as Instrumentl provide this service for a fee.

Once you have money from a donor organization, Achée says, you may be asked to serve on their committees and panels. "Say yes," she advises. "You'll be part of discussions that shape the research agenda, and you'll hear about upcoming funding calls." People you meet through these activities can lead to further connections. "It opens the door to larger networks of funding opportunities," she adds.

Researchers can also network through their own teams. A multidisciplinary, international group ensures diverse expertise and perspectives—and possibly funding as well, notes Achée. Some foundations give awards only to researchers based in certain countries, but these scientists can participate in global collaborations.

Thinking creatively about potential funders can pay off. An agricultural or brewing industry association might fund fungal genomics or chemical analysis of water or soil, for instance. The American Chemical Society (ACS) Petroleum Research Fund supports **Manny Curotto**, professor and chair of chemistry and physics at Arcadia University in Pennsylvania, in his fundamental research on quantum methods, a field that is relevant to energy storage.

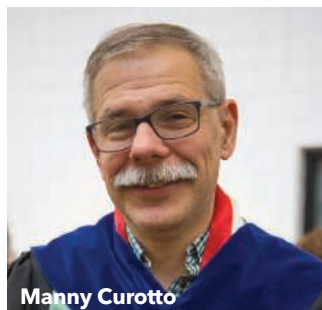
The fund gives nearly 200 grants a year, totaling USD 17 million in 2017, and is part of a larger ACS program **cont. >**

Upcoming features

Top Employers Survey—October 26 ■ Artificial Intelligence—November 30



Cindy Wu



Manny Curotto

Featured participants

Arcadia University
www.arcadia.edu

Biotechnology Innovation Organization
www.bio.org

Crowd.Science
crowd.science

Experiment
experiment.com

Royal Botanic Gardens, Kew
www.kew.org

Thinkable
www.thinkable.org

University of Notre Dame
www.nd.edu



Olwen Grace

supporting research and education. Curotto finds that the funding process and paperwork are similar to what is required for government grants, although if you're used to the submission system of a particular agency, he advises, expect to spend time learning the quirks of a new system.

Curotto tells early-career researchers at primarily undergraduate institutions to look into awards from the U.S. National Science Foundation, Camille & Henry Dreyfus Foundation, and Research Corporation for Science. "And don't give up," he says. Funding agencies want to see that recipients can manage a grant and deliver what they have proposed, so "it always looks better if you've had other grants." Internal institutional awards help researchers demonstrate competence in grant management, and can also aid them in getting preliminary data for external grants.

Fundraising through public engagement

Researchers with projects that appeal to the public can explore crowdfunding, which is asking for donations (or sometimes offering equity in a startup enterprise) through an online platform. Crowdfunding is best known for sites such as Kickstarter, where celebrities raise millions of dollars for humanitarian projects. However, scientists can select from research-specific platforms, including some in German, French, and Japanese. Researchers create a site on the platform describing their project in text, photos, and videos, then campaign for donations until their deadline is reached, usually a

few months later. Some platforms are all-or-nothing, with researchers receiving donations only if they reach a self-imposed goal; others send all money raised. Platform fees are usually a percentage of funds raised. Some, but not all, offer donor gifts such as a lab tour.

Experiment (formerly Microryza) is one of the first science-specific crowdfunding sites. Although one campaign driven by an exceptionally extensive network raised USD 2.6 million to study Batten disease, a fatal, inherited disorder of the nervous system, the average amount raised is about USD 4,100. **Cindy Wu**, Experiment cofounder, says that crowdfunding is an efficient way to raise seed funding, and emphasizes that the process is more transparent and less restricted than traditional mechanisms. "Grad students often tell me that Experiment gave them the freedom to work on their idea without tailoring it to a grant or foundation," she says. A 2018 National Bureau of Economic Research working paper shows that crowdfunding supports projects initiated by people who don't usually get grants. More than 60% of Experiment crowdfunders at educational institutions were students or postdocs.

Crowdfunding worked for **Olwen Grace**, a scientist at the Royal Botanic Gardens, Kew, United Kingdom. Like Achée's research, her study on the evolution of succulent plants spans both field and lab work. She needs a broad funding base to cover activities ranging from traveling for sample collection and habitat observation to analyzing data in her London laboratory.

In 2016, Grace ran a successful crowdfunding campaign to fund sequence analysis of plants related to *Aloe vera*. Because it often contributes ingredients to skin-care products, aloe is "a charismatic plant," says Grace, and her colleagues urged her to use it to crowdfund her work on desert plant evolution. Her campaign raised GBP 10,700, which Grace says could have come from a few small grants, "but this boost of a single grant from the crowdfunding campaign allowed us to do the work much faster."

Grace used the Crowd.Science (formerly Walacea) platform. **Natalie Jonk**, Crowd.Science cofounder, says crowdfunding has two parts. The first is creating a campaign page that's appealing to backers. The second, harder task is attracting people to that page by thinking carefully about outreach. "It's a bit of a chain reaction," she says, "building trust by getting your friends, family, and peers to promote you. People further down the chain like to see that a project has funding before they contribute."

Grace recalls that the effort of preparing the campaign video, researcher bios, and website was less stressful than grant writing. However, when the campaign was live, "it required constant attention," she says. Teamwork, including help from fundraising experts at the Royal Botanic Gardens, Kew, was crucial, especially for "passing the social media baton," to ensure that someone was always promoting the campaign online and monitoring responses.

An overarching goal of science crowdfunding is community building and raising public interest in research. Grace sends regular research reports to her backers. These are like grant progress reports, she says, but have "a lighter touch," and include explanations of techniques and results for nonscientists. Sometimes she has to report that "we're still working on it," but honest communication is the point. "The donors are expressing interest in our work, so the least we can do is show them what it looks like when we do our research," she adds.

Crowd.Science offers researchers who campaign on its platform the additional service of seeking support on their **cont.**>

UC San Diego

Biological Sciences

The Division of Biological Sciences at the University of California, San Diego (www.biology.ucsd.edu) invites applications from outstanding candidates for the following faculty positions. All candidates must have earned a Ph.D. or equivalent degree, and be committed to teaching at the undergraduate and graduate levels. In addition to excellence and creativity in research and scholarship, successful candidates must also demonstrate a commitment to equity and inclusion in higher education. We are especially interested in candidates who have created or contributed to programs that aim to increase access and success of underrepresented students and/or faculty in the sciences, and/or have detailed plans to accomplish such goals.

Computational & Theoretical Neuroscience: The Section of Neurobiology invites applications for a faculty position in Computational and Theoretical Neuroscience at the tenure-track Assistant, or tenured Associate or Full Professor level. Candidates who investigate the function and dynamics of neuronal circuits by the development of mathematical models, computer simulations, or novel approaches to data analysis and information processing are encouraged to apply. Solely theoretical research programs as well as those with a wet-lab component will be considered. The Neurobiology Section is a highly interactive group that seeks colleagues who complement existing strengths.

Host/Microbe Interactions: The Section of Molecular Biology invites applications for a faculty position in Host/Microbe Interactions at the tenure-track Assistant Professor level. We are broadly searching for applicants working towards a mechanistic understanding of microbiomes, host-microbe interactions, and/or microbe-microbe interactions. Research topics could include, but are not limited to, beneficial or antagonistic interactions of viruses, bacteria, archaea, protozoa, or fungi with each other or their hosts. This position will complement existing strengths in this area.

Microbial Ecology: The Section of Ecology, Behavior and Evolution invites applications for a faculty position in Microbial Ecology at the tenure-track Assistant Professor level. We are broadly searching for a microbial ecologist. Research topics could include, but are not limited to, soil microbial community structure and function, plant-microbe interactions, and the role of microbiomes in species interactions in nature. This position will complement existing strengths in this area.

Neural Circuits: The Section of Neurobiology invites applications for a faculty position in the broad area of Neural Circuit Studies at the tenure-track Assistant Professor level. Candidates should employ state-of-art technologies to address fundamental questions related to the development, function and disease of the nervous system. Our faculty are engaged in a number of areas of neuroscience research, including molecular/cellular/developmental neurobiology, neural circuit dissection, and neural systems and behavior. The new faculty member will have ample opportunities for rich intellectual interactions with highly supportive Section colleagues while developing his/her independent research program.

Plant Biology: The Section of Cell & Developmental Biology invites applications for a faculty position in Plant Biology at the tenure-track Assistant, or tenured Associate or Full Professor level. Candidates studying any plant species are welcome to apply. Research focused on mechanistic understanding is especially encouraged. This highly interactive group is looking for colleagues who will bring novel approaches, either technical or conceptual, to their study of plant biology.

Review of applications will commence on **October 26, 2018** and will continue until all positions are filled. Interested applicants must submit a cover letter, curriculum vitae, statement of research, statement of teaching, a statement describing their past experience and leadership in fostering equity and diversity and/or their potential to make future contributions, and 3-5 publications. Applicants at the Assistant Professor level need to submit 3-5 references, and applicants at the Associate or Full Professor level need to provide contact information for 3-5 references. Applications must be submitted through the University of California San Diego's Academic Personnel RECRUIT System at: <https://apol-recruit.ucsd.edu/apply>.

The Division of Biological Sciences at UC San Diego is a vibrant center of scientific discovery, innovation, and collaboration. Our large research base spans many areas of biology and has one of the most celebrated graduate programs in the country. We are committed to academic excellence and diversity within the faculty, staff, and student body.

UCSD is an Affirmative Action/Equal Opportunity Employer with a strong institutional commitment to excellence through diversity.
(<http://diversity.ucsd.edu/>)

faculty

behalf from philanthropists and businesses interested in their work. For example, outdoor equipment suppliers might support environmental projects. “Often scientists don’t think of business sponsors as an option, and they don’t know how to approach corporate marketing or social responsibility departments,” says Jonk. The success of this strategy varies, but she hopes that as the platform grows, their sponsor network will expand. “We’ve had about 5,000 people back projects, and Experiment has had more than 40,000,” she says. “When that figure is a million, we’ll have a community we can reach out to with projects we know are interesting to them.” Jonk’s vision is to tailor outreach to groups as large as hundreds of thousands of people who have backed similar projects.

The Experiment platform also offers possibilities beyond just crowdfunding. Campaigns may be eligible for challenge grants in which projects within a field such as botany or archaeology compete to attract the most donors for a bonus award. In honor of Earth Day 2018, the CAA Foundation, the philanthropic arm of the entertainment industry’s Creative Artists Agency, fully funded nine environmental projects on the Experiment site for a total gift of USD 25,000.

Attracting a global audience for foundations and other funders is the mission of Thinkable, founded by **Ben McNeil**, climate researcher at the University of New South Wales in Australia. Giving away money is harder than you might think, McNeil says. Established foundations have their own platforms and networks for attracting proposals, but smaller foundations, philanthropists, academic institutions, companies, and nonprofit organizations often need help promoting their awards. “Everyone is so consumed by information,” McNeil comments, “that funders need targeted, efficient channels to find their audience. We provide a community they can reach out to. We try to get funders’ causes and scientists’ research in front of as many eyeballs as possible.”

Thinkable’s services include hosting a funder’s campaign page and offering guidance about application forms and judging. The model has been compared to HeroX, which runs problem-solving challenges, except that Thinkable is focused on research, McNeil says. Thinkable helps scientists who are part of the platform’s community match their research to funding opportunities. And scientists who participate in contests inevitably raise the profile of their research, notes McNeil.

Thinkable users include companies that want maximum publicity for a science prize and universities holding a contest to motivate researchers to make and share videos showcasing their science. An example is the World Science Festival Brisbane’s annual Queensland Women in STEM Prize, for which each applicant supplies a page with a video, McNeil says. The award site gets more than 100,000 views, so “everyone who applies is a winner.”

McNeil’s ultimate goal aligns with science crowdfunding: opening science to the public and helping researchers connect with a broader audience. He is particularly motivated to support young scientists doing multidisciplinary, high-risk research.



Willie Reaves

Researchers whose projects have commercial potential can find another audience. McNeil observes, “In my view, the biggest source of potential new funding comes from industry groups looking to partner with researchers and startups around the world.” Global matching of researchers and industry partners is part of Thinkable’s services. Researchers can also pitch directly to industry funders and investors.

Biotech big leagues

Researchers with potentially marketable life science projects and business ambitions can get a four-day introduction to the biotechnology world at annual trade conferences hosted by the Biotechnology Innovation Organization (BIO).

A feature of the annual BIO International Convention, which boasted more than 18,000 attendees in 2018, and of the BIO World Congress on Industrial Biotechnology, is BIO’s One-on-One Partnering system. BIO’s director of partnering products and services, **Willie Reaves**, says the system is also available at other conferences, including regional biotech meetings. Participants in the system create a profile with text, images, and video, peruse profiles of industry R&D and business-development representatives from around the world, and then make appointments for 30-minute meetings during the conference they will be attending. At the BIO International Convention, meetings happen in 600 booths in a sportsfield-sized area, Reaves explains. Scientist-inventors may be represented by their institute’s technology transfer office, or they can attend themselves. The point of the meetings, he says, “is to spark conversations or follow up on a previous contact to discuss commercialization.” Scientists who are ready to launch a startup can request space from science parks and incubators in the partnering system. The atmosphere is intense—there were 3,900 partnering companies and 46,916 meetings at the 2018 conference, for example—but attendees who can handle that atmosphere can be productive. “One participant,” Reaves says, “said he made as many contacts that week as he did during the entire year.”

The BIO International Convention has an academic area for university researchers and people interested in partnering with them. Researchers who have advanced to the startup stage might participate in investor pitching at a startup stadium and get advice from industry and investor judges.

Government funding is still the cornerstone of research support, but scientists have other options. Success with these options requires identifying, interacting with, and participating in communities of foundations, investors, or citizens interested in your field. A critical element is to align your project with the funder’s scope, whether it is a foundation, industry, or individual donor. Reaves says that “specificity and targeting” are critical, and those who have tried the alternate-funding route advise being persistent to find the right fit.

References

1. U.S. National Science Foundation, National Science Board Science & Engineering Indicators 2018; available at www.nsf.gov/statistics/2018/nsb20181.

Chris Tachibana is a science writer based in Seattle, USA, and Copenhagen, Denmark.

PHOTO: WILLIE REAVES



Faculty Positions at the Sloan Kettering Institute Memorial Sloan Kettering Cancer Center

OPPORTUNITIES IN BIOMEDICAL RESEARCH

- Cancer Genetics
- Cell Signaling & Regulation
- Chemistry & Chemical Biology
- Computational Biology
- Developmental Biology
- Experimental Therapeutics
- Genome Integrity, Gene Expression, and Epigenetics
- Immunology
- Stem Cell Biology & Regenerative Medicine
- Structural Biology



JOIN OUR FACULTY

Successful candidates will hold an appointment in one of SKI's research programs.

Candidates may apply to up to two programs:

Cancer Biology & Genetics

Chair: Scott Lowe, PhD

Cell Biology

Chair: Kristian Helin, PhD

Chemical Biology

Chair: Derek Tan, PhD

Computational and Systems Biology

Chair: Dana Pe'er, PhD

Developmental Biology

Chair: Kathryn Anderson, PhD

Immunology

Chair: Alexander Rudensky, PhD

Molecular Biology

Chair: John Petrini, PhD

Molecular Pharmacology

Chair: David Scheinberg, MD, PhD

Structural Biology

Chair: Nikola Pavletich, PhD



RESEARCH AND TRAINING

- 130 research laboratories housed in state-of-the-art buildings
- Core facilities offering cutting-edge scientific services
- Over 800 pre- and post-doctoral trainees
- Appointments in the Gerstner Sloan Kettering Graduate School of Biomedical Sciences and the Weill Cornell Graduate School of Medical Sciences

Visit www.ski.edu to learn more.

Application deadline: **October 15, 2018**

Apply at: <https://facultysearch.ski.edu>





University of Pittsburgh

FACULTY POSITIONS Center for Vaccine Research

The Center for Vaccine Research (CVR) of the University of Pittsburgh invites outstanding scientists to apply for up to four tenure-track faculty positions at Assistant and Associate Professor levels. This interdepartmental center seeks to recruit faculty working on BSL-2, BSL-3 pathogens and/or select agents who are focusing on understanding the pathogenesis of infectious diseases with a view to translating this knowledge to the early stage development of creative interventions against clinically-relevant human and animal pathogens. Applicants with research interests in rational attenuation, predictive vaccinology, the novel delivery of biopharmaceuticals or who use platform-based approaches to mitigate emerging infectious diseases would be ideally aligned with the mission of CVR.

The University of Pittsburgh is currently ranked number three nationally for NIH funding. The center encompasses approximately 20,000 square feet of space, including the Regional Biocontainment Laboratory, and offers comprehensive accommodations for BSL-2, BSL-3 and BSL-3+ work. Biocontainment facilities include ten dedicated laboratories permitting *in vitro* work on select agents; an aerobiology core for computerized quantitative aerosol exposure in animal models; four fully equipped ABSL-3 facilities for *in vivo* infection and challenge studies; a necropsy suite and state-of-the-art multimodal whole animal imaging capabilities.

Applicants must hold a PhD (with or without DVM, MD) and postdoctoral research experience. Successful candidates are expected to have, or to establish independent, nationally and internationally recognized, externally funded research programs and contribute to teaching in graduate and/or professional curricula.

Salary, rank, and academic appointment will be commensurate with qualifications and experience. Competitive start-up, compensation and benefits packages are available.

Learn more about the work in the CVR by visiting our website: www.cvr.pitt.edu

Applicants should submit i) a cover letter ii) a statement of research accomplishments and plans iii) a curriculum vitae and iv) the names and contact information for at least three professional references to the **CVR Search Committee** c/o **W. Paul Duprex, PhD, Director Center for Vaccine Research** via **CVRInfo@pitt.edu** (subject line: CVR Faculty Search).

The University of Pittsburgh is an Affirmative Action/Equal Opportunity Employer and values equality of opportunity, human dignity and diversity.

EEO/AA/M/F/Vets/Disabled.

University of Pittsburgh • Center for Vaccine Research
9014 Biomedical Science Tower
3501 Fifth Avenue • Pittsburgh, PA 15261 • USA



Department of Genetics Yale University School of Medicine

Professor of Genetics and Director of the Center for Genomic Health

The Department of Genetics at Yale University School of Medicine is searching for a Professor of Genetics with an outstanding record of transformative scientific achievements in Human Genetics and Genomics. We expect that the candidate will lead a vigorous cross-disciplinary research program focused on identifying and characterizing genetic drivers of human disease. As a leader of human genetics both within the department and across the Yale School of Medicine, the successful candidate will have the opportunity to recruit other human geneticists to the Genetics Department and lead a new program in precision medicine as the Scientific Director of the Yale Center for Personalized Medicine and Genomic Health.

We are looking for a dynamic, internationally recognized scientist (Ph.D., M.D., or M.D./Ph.D.) with an outstanding research record of scientific discoveries, as well as a strong track record of training the best innovators in the field of human genetics and genomics.

To apply, please submit your CV to <http://apply.interfolio.com/45539> to the attention of **Antonio Giraldez**, Chair of Genetics. Applications will be reviewed until the position is filled. Inquiries should be addressed to neltja.brewster@yale.edu.

Tenure-Track Faculty Position (Assistant/Associate/Full Professor)

The Department of Genetics at Yale University School of Medicine invites applications for junior or senior tenure-track faculty positions. The search is open to investigators from all areas of biological and biomedical research. We are particularly interested in applicants working in one of the following areas: Developmental Biology, Imaging, Quantitative Biology, Computational Biology, Genomics, Systems Biology, and Genetics. Applications from investigators working at the interface of these areas will be strongly considered. The rank of the appointment will be commensurate with experience and the positions come with a substantial start-up package.

The Department of Genetics comprises an exceptional group of 31 primary basic science faculty with research interests including fundamental aspects of Developmental Biology, Genetics, Genomics and Epigenetics, using different model systems including flies, worms, fish and mouse, and humans (<https://medicine.yale.edu/genetics/>). The Department is closely associated with science initiatives at Yale including The Cancer Center, The Center for Neuroscience, The Stem Cell Center and the Yale Center for Genome Analysis.

Candidate must hold a Ph.D., M.D., or equivalent degree. Applicants should upload a cover letter, a curriculum vitae, a description of previous research (1 page), a concise statement of research plans (up to 2 pages), reprints of 2 publications, and the names of 3 references to the Interfolio website at: <https://apply.interfolio.com/52614>. Specific inquiries about the position may be sent to the attention of **Dr. Antonio Giraldez**, Chair of the Department of Genetics, at genetics.admin@yale.edu. Applications will begin to be evaluated on **November 1, 2018**.

Interviews will take place as part of a multidisciplinary symposium including candidates for different searches. Please reserve the dates of January 15, January 22 and February 11 (snow date) as potential dates for the symposium in case you are selected for an interview.

Yale University is an Affirmative Action/Equal Opportunity Employer. Yale values diversity among its students, staff, and faculty and strongly welcomes applications from women, persons with disabilities, protected veterans, and underrepresented minorities.



Faculty Positions in Integrative Biosciences



Wayne State University (WSU) is recruiting up to 15 faculty (open rank) for research and development programs as part of the continued expansion of a broad institutional initiative in Integrative Biosciences. This initiative leverages a new 200,000 sq. ft. Integrative Biosciences Center (IBio) that houses coordinated inter- and trans-disciplinary research teams, and a Clinical Research Center. Programmatic themes include a focus on pathophysiology and accumulated stressors affecting health in evolving urban environments with a strong emphasis on basic disease mechanisms, clinical translation and community health impact.

Ten faculty have been recruited to date as part of the IBio initiative and we are now entering the next phase of thematic-based, programmatic growth. Faculty recruitment (tenured, tenure-track, or research-track) will focus on six primary thematic areas: Behavioral Health (#043728); Bio & Systems Engineering (#043729); Environmental Sciences and Health (#043725); Health Disparities (#043726); Metabolic Diseases (Cardiovascular, Diabetes and Obesity) (#043727); and Translational Neurosciences (#043730). Each theme includes basic discovery-driven research as well as translational, community and implementation sciences cutting across departments, programs, centers, and colleges.

Faculty recruits (tenured or tenure-track) will integrate with departments and colleges or schools consistent with their areas of expertise and shared interests and engage in all aspects of our academic mission including research, education and service. Faculty are expected to either already have established extramural research funding and/or are on a clear path to secure and sustain extramural funding in support of their research programs.

Candidates must have a Ph.D., M.D., Pharm.D. and/or related degree(s) in disciplines aligning with the focus areas and possess a demonstrated track record of exceptional science, creative discovery and/or knowledge translation and application. We would be pleased to receive applications from groups of faculty from one or several institutions who may wish to work together. Qualified candidates should submit applications to the specific thematic position posting # identified above through the Wayne State University Online Hiring System https://jobs.wayne.edu/applicants/jsp/shared/Welcome_css.jsp. Applications should include a *curriculum vitae* and a brief narrative describing their research and how it relates to the Integrated Biosciences initiative (<http://www.IBio.wayne.edu>) with a cover letter addressed to the IBio Steering Committee Chair, Stephen M. Lanier, Ph.D. Vice President for Research. Review of applications for the next phase of recruitments will begin immediately with applications accepted through October 30, 2018. Competitive recruitment packages are available with salary and rank based on qualifications.

Wayne State University, which holds the highest Carnegie Foundation for the Advancement of Teaching designations in both research and community engagement, is a premier, public, urban, comprehensive research university located in the heart of Detroit where students from all backgrounds are offered a rich, high quality education. Our deep-rooted commitment to excellence, collaboration, integrity, diversity and inclusion creates exceptional opportunities for students and faculty in a diverse, global society. WSU encourages applications from women, people of color, and other underrepresented people. Wayne State is an Affirmative Action/Equal Opportunity Employer.

Founded in 1868, Wayne State University offers more than 370 academic programs through 13 schools and colleges to nearly 28,000 students. The campus in Midtown Detroit comprises 100 buildings over 200 acres including the School of Medicine, the Eugene Applebaum College of Pharmacy and Health Sciences and the College of Nursing. The university is home to the Perinatology Research Branch of the National Institutes of Health, the Karmanos Cancer Center, a National Cancer Institute-designated comprehensive cancer center, and a National Institute of Environmental Health Sciences Core Center - *Center for Urban Responses to Environmental Stressors (CURES)*.



Faculty Positions in Environmental Health Sciences



As part of a broad institutional initiative in integrative biosciences and environmental health sciences, Wayne State University (WSU) and the Institute of Environmental Health Sciences (IEHS) are recruiting up to three faculty positions (tenured or tenure-track, open rank). The program in environmental health sciences fosters interdisciplinary, integrative, and collaborative approaches to environmental disease prevention with primary areas for recruitment as follows.

- environmental epidemiology
- mechanisms underlying environmental exposure-mediated toxicities
- life-course factors affecting environmental health risk
- predictive modeling of toxicant exposure and health outcomes

WSU and the IEHS serve as headquarters for the Center for Urban Responses to Environmental Stressors (CURES), a National Institute of Environmental Health Sciences supported core center. CURES is situated in the heart of Detroit in the new Integrative Biosciences Center, a fulcrum for leading-edge technology platforms and specialized resources in support of advanced studies in precision environmental exposure science.

Through research, community engagement, and education, the CURES team of researchers and community partners seek to discover, investigate, and solve complex environmental health problems that affect humans exposed to chemical and non-chemical stressors in a dynamic urban environment. Successful faculty candidates will have a Ph.D., M.D., or equivalent degree in biomedical sciences relevant to environmental health sciences with evidence of peer recognition in the field, a commitment to excellence in research education and training, and the ability to engage with broader environmental science themes for the purpose of achieving transformative and translational research gains. Applicants are expected to have already established extramural research funding or to be on a clear path to secure extramural funding in support of their research programs. Faculty recruits will integrate with departments and colleges or schools consistent with their areas of expertise and shared interests and engage in all aspects of our academic mission, including research, training, instruction and service.

Competitive recruitment packages are available with salary and faculty rank based on qualifications. Applicants are encouraged to apply to posting #043725 through the WSU Online Hiring System <https://jobs.wayne.edu>. Applications will be accepted until positions are filled, but for full consideration this fall, application materials should be submitted by **November 30, 2018**. Applications should include a *curriculum vitae* and a brief narrative cover letter addressed to the Director of IEHS and the Vice President for Research, indicating the applicant's potential for research synergy within the CURES environmental health science programs and the broader institutional initiative in integrative biosciences.

Wayne State University is a premier, public, urban research university located in the heart of Detroit where students from all backgrounds are offered a rich, high quality education. Our deep-rooted commitment to excellence, collaboration, integrity, diversity and inclusion creates exceptional educational opportunities preparing students for success in a diverse, global society. WSU encourages applications from women, people of color and other underrepresented people. WSU is an affirmative action/equal opportunity employer.

Founded in 1868, Wayne State University offers a range of academic programs through 13 schools and colleges to nearly 28,000 students. The campus in Midtown Detroit comprises 100 buildings over 200 acres including the School of Medicine, the Eugene Applebaum College of Pharmacy and Health Sciences, and the College of Nursing. The University is home to the Perinatology Research Branch of the National Institutes of Health and the Karmanos Cancer Center, a National Cancer Institute-designated comprehensive cancer center. WSU holds designations for research and community engagement in the Carnegie Foundation for the Advancement of Teaching. WSU features a strong faculty mentoring program and offers rich opportunities for professional growth and career development.

DEPARTMENT OF MOLECULAR AND HUMAN GENETICS

TENURED/TENURE TRACK FACULTY POSITION in GENETICS/GENOMIC INSTABILITY

Among genetics departments at U.S. medical schools, the Department of Molecular and Human Genetics at Baylor College of Medicine (<https://www.bcm.edu/departments/molecular-and-human-genetics/>) ranks first in both number of grants and total funding from the National Institutes of Health. The Department of Molecular and Human Genetics provides a bridging environment for physicians and basic scientists, promoting a cross-species approach to functional genetics and a commitment to technology transfer. Activities within the Department include clinical genetics, basic and clinical research, a new joint venture diagnostic laboratory, long-standing association with a NIH large scale human genome sequencing centers, medical student teaching, a MS Genetic Counseling program, a Ph.D. graduate program, and residency/fellowship training in medical genetics.

The Department has over \$100 million in total research funding, 70 primary tenured and tenure-track research faculty members and a total of 140 primary faculty members, who are engaged in a variety of missions including basic and translational research, clinical diagnostic services, and prenatal, pediatric, and adult clinical care. To expand our translational impact, we established a uniquely structured and governed joint venture diagnostic laboratory, Baylor Genetics, and a Baylor College of Medicine/Chinese University of Hong Kong Center for Medical Genetics in Hong Kong that together will help to expand our clinical, diagnostic, and educational mission to a world-wide audience.

The Department's research interests include genomics, mammalian development, the metabolic and genetic bases for inherited human disease, gene therapy, gene structure and expression, mechanisms of DNA replication and repair, mutation, DNA recombination, genomic instability and cancer, cytogenetics, behavioral genetics, bioinformatics, and the biology of aging. Department research includes strengths in human, bacterial, mouse, yeast, Drosophila, worm and Dictyostelium genetics.

The Department is seeking an individual for faculty appointment at rank appropriate for achievement and experience. Appointment will be at the Assistant, Associate, or Full Professor level depending on experience. Successful candidates will have strong basic research programs related to genetic/genomic stability or instability, genome organization, genomics including but not limited to DNA replication, repair, mutation, genome rearrangements, DNA damage response, mechanisms of evolution, studied in any organism from bacteria to human. However, outstanding individuals in any area will be considered. Generous start-up support is available.

Curriculum vitae, a brief summary of research plans, letters of reference, along with the names, addresses, and phone numbers of at least three references to the following email address: mhgfacultyrecruits@bcm.edu

Department of Molecular and Human Genetics
Baylor College of Medicine
One Baylor College of Medicine, ABBR Room R830
Houston, TX 77030
Phone: 713-798-5443
Fax: 713-798-8515

Equal Opportunity, Affirmative Action and Equal Access Employer.



TENURE-TRACK ASSISTANT PROFESSOR PHYSICAL CHEMISTRY

Harvard University Faculty of Arts and Sciences
Department of Chemistry and Chemical Biology

Position Description: Candidates are invited to apply for a tenure-track assistant professorship in physical chemistry, broadly defined, including experimental and theoretical research in areas such as but not limited to atomic and molecular physics, biophysical chemistry, condensed matter, quantum science and ultrafast spectroscopy. The appointment is expected to begin on July 1, 2019. The tenure-track professor will be responsible for teaching at the undergraduate and graduate levels. We are seeking candidates who have an outstanding research record and a strong commitment to undergraduate and graduate teaching.

Basic Qualifications: Doctorate or terminal degree in chemistry or related discipline required by the time the appointment begins.

Additional Qualifications: Demonstrated experience in teaching is desired.

Special Instructions: Please submit the following materials through the ARIES portal (<http://academicpositions.harvard.edu/postings/8371>). Applications must be submitted no later than October 15, 2018.

1. Cover letter
2. Curriculum Vitae with publications list
3. Teaching statement (describing teaching approach and philosophy)
4. Outline of future research plans
5. Names and contact information of 3-5 references. Three letters of recommendation are required, and the application is complete only when all three letters have been received.
6. Selected publications

Contact Information: Susan M. Kinsella, Search Administrator, Department of Chemistry and Chemical Biology, Faculty of Arts and Sciences, Harvard University, 12 Oxford St., Cambridge, MA 02138. Phone: 617-496-4088. kinsella@chemistry.harvard.edu

Harvard is an Equal Opportunity Employer and all qualified applicants will receive consideration for employment without regard to race, color, religion, sex, national origin, disability status, protected veteran status, gender identity, sexual orientation, pregnancy and pregnancy-related conditions, or any other characteristic protected by law.



Duke UNIVERSITY

FACULTY POSITION IN REGENERATIVE BIOLOGY AND MEDICINE

Regeneration Next Initiative
Department of Pharmacology and Cancer Biology

Regeneration Next (RNI) is a campus-wide initiative to stimulate high impact research that crosses disciplinary boundaries in regenerative biology and medicine. The Department of Pharmacology and Cancer Biology is a collaborative basic science department broadly focused on cellular signaling and its impact on disease.

RNI is partnering with the Department of Pharmacology and Cancer Biology to hire a tenure-track faculty member at the rank of Assistant Professor. An appointment at the Associate or Full Professor level may be possible for exceptional senior applicants.

We invite applications from accomplished candidates with expertise in developmental and cell biology, stem cell biology, mechanisms of tissue regeneration, quantitative biology, imaging, signaling, chemical biology, or related areas. Candidates must have a PhD, MD, or equivalent degree. Women and underrepresented minority candidates are especially encouraged to apply.

Applicants should submit a curriculum vitae, a 3-page total summary of accomplishments and research plans, and at least 3 letters of recommendation by **November 1, 2018** to AcademicJobsOnline.org: <https://academicjobsonline.org/ajo/jobs/11605>. Questions may be directed to: Don Fox, Chair of the Search Committee (don.fox@duke.edu) or Ken Poss, Director, RNI (regeneration@duke.edu)

Duke University is an Affirmative Action/Equal Opportunity Employer committed to providing employment opportunity without regard to an individual's age, color, disability, genetic information, gender, gender identity, national origin, race, religion, sexual orientation, or veteran status.

Faculty Positions in Gene Regulation

The Cecil H. and Ida Green Center for Reproductive Biology Sciences, an endowed basic science research center within the Division of Basic Research in the Department of Obstetrics and Gynecology, is recruiting to fill newly created Tenure-track Assistant Professor Positions. We invite applications from outstanding candidates studying aspects of signaling, gene regulation, and genome function, especially in the areas of chromatin and transcription, epigenetics, nuclear endpoints of cellular signaling pathways, nuclear receptors, RNA biology, genome organization, and genome evolution. We are interested in a wide variety of model systems and experimental approaches, including biochemistry, molecular biology, structural biology, animal models, genetics, genomics, proteomics, bioinformatics, and computational biology. The Green Center's research programs focus on, but are not limited to, reproduction and development in a broad sense, as well as aspects of endocrinology, stem cells, cancer, metabolism, inflammation, immunity, and neurobiology.

- **Position 1: Signaling, chromatin, and gene regulation** – a broad search for candidates using a wide array of experimental approaches to address fundamental questions in nuclear signaling, chromatin, transcription, epigenetics, and RNA biology.
- **Position 2: Genomic, proteomic, bioinformatic, computational, and evolutionary approaches to understanding gene regulation** - a more focused search in research areas using state-of-the-art methodologies that will connect to broader "omic" initiatives on campus.
- **Position 3: Molecular biology of female reproductive systems** - a search for candidates using cell-based or physiological models in combination with molecular or genomic approaches to address fundamental questions concerning female reproductive biology.

The Green Center promotes and supports cutting-edge, integrative, and collaborative basic research in reproduction, development, and related areas of biology, as well as strong connections between basic and clinical research. This recruitment is part of a major university and department-supported renovation and rejuvenation of The Green Center over the past 8 years. Successful candidates will be housed in a newly renovated state-of-the-art research facility and provided a generous start-up package, and are expected to establish scientifically rigorous and externally funded research programs and participate in center, department, and university teaching and training programs. To learn more about The Green Center, visit: <https://www.utsouthwestern.edu/education/medical-school/departments/green-center/>.

Candidates must have a Ph.D. or M.D. or equivalent in a relevant field of study, postdoctoral or comparable experience, and a demonstrated record of research excellence. Applicants should send a letter of application, curriculum vitae, and a statement of planned research projects as pdf files to GreenCenter@UTSouthwestern.edu. Please indicate one of the three research areas listed above (Molecular biology of female reproduction; Gene regulation; Genomics) in the subject line of the email. Applicants should also arrange for three letters of reference to be sent directly to the above e-mail address. Collection and review of applications will commence **October 1, 2018** and will continue during the 2018–2019 academic year until the position is filled, but applicants are encouraged to submit their materials as soon as possible.

UT Southwestern is an Affirmative Action/Equal Opportunity Employer. Women, minorities, veterans, and individuals with disabilities are encouraged to apply.



Assistant Professor in Theoretical Quantum Condensed Matter Physics

The Department of Physics and Astronomy at the University of Pennsylvania seeks applications from outstanding candidates for an appointment as Assistant Professor in theoretical quantum condensed matter physics. Appointment at higher rank can be considered in exceptional cases. The successful candidate will develop an innovative research program on quantum phenomena in condensed matter that attracts the participation of students and creates collaborative links with other Penn scientists and engineers. The candidate should have a Ph.D. in physics along with post-doctoral experience and will be expected to teach, to attract external research funding and to contribute actively to the Laboratory for Research on the Structure of Matter. Applicants must apply online at <http://facultysearches.provost.upenn.edu/postings/1404>. Required application materials include: curriculum vitae with a list of publications, a research statement and a teaching statement. Applicants should submit the names and contact information for three individuals from whom we will request recommendation letters. Review of applications will begin no later than **November 1, 2018** and will continue until the position is filled. The Department of Physics and Astronomy is strongly committed to Penn's Action Plan for Faculty Diversity and Excellence and to creating a more diverse faculty (for more information see: <http://www.upenn.edu/almanac/volumes/v58/n02/diversityplan.html>).

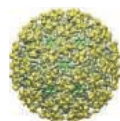
The University of Pennsylvania is an Equal Opportunity Employer. Minorities/Women/Individuals with disabilities/Protected Veterans are encouraged to apply.



Faculty Positions in Biochemistry & Molecular Biology The University of Texas Medical Branch

The University of Texas Medical Branch (UTMB Health), Galveston, Texas, seeks multiple outstanding faculty candidates for tenure-track/tenured positions at the rank of Assistant Professor in the broad fields of Biochemistry and Molecular Biology in the Department of Biochemistry and Molecular Biology (<http://www.bmb.utmb.edu>). The ideal candidate will have extensive experience in elucidating the mechanisms of important biomedical problems at a molecular / atomic level. The candidates should be energized by opportunities to interact with established biomedical researchers in a highly collaborative biomedical research community and to become outstanding mentors to students and postdoctoral fellows. Rich opportunities exist at UTMB for interactions and affiliations with centers of scientific excellence in structural biology and molecular biophysics, biodefense, molecular medicine, cancer biology, infectious diseases, environmental health, aging, and translational sciences (<http://www.utmb.edu/centers>). In addition to a highly collaborative environment, UTMB offers outstanding core services, including: next-generation sequencing, organic synthesis, mass spectrometry, optical microscopy, flow cytometry, protein expression and purification, molecular biology, solution biophysics, NMR, X-ray crystallography, cryo-electron microscopy, bioinformatics, and computational chemistry (see <http://www.utmb.edu/core>). Excellent opportunities for scientific interactions also exist through UTMB Health's participation in the Gulf Coast Consortia and the Keck Center for Interdisciplinary Bioscience (<http://www.gulfcoastconsortia.org>). We will accept and review applications immediately until December 1st, 2018.

A very attractive recruitment package of salary, start-up funding and newly renovated space will be offered. Interested applicants should submit a curriculum vitae, a summary of research accomplishments and future goals (max 3 pages), and contact information for three references to: **Mariano A. Garcia-Blanco M.D., Ph.D. at BMB.Recruting@utmb.edu**.



UTMB Health strives to provide equal opportunity employment without regard to race, color, national origin, sex, age, religion, disability, sexual orientation, gender identity or expression, genetic information or veteran status. As a Federal Contractor, UTMB Health takes affirmative action to hire and advance women, minorities, protected veterans and individuals with disabilities.



BAYLOR
UNIVERSITY

The Department of Biology in the College of Arts & Sciences (www.baylor.edu/artsandsciences/) at Baylor University seeks outstanding applicants for the following faculty positions:

- **Assistant Professor in Global Change Biology** (<https://www.baylor.edu/biology/globalchangebiology>) Search Committee Chair, Dr. Thad Scott at globalchange_biology@baylor.edu.
- **Assistant Professor in Mammalian Comparative Physiology** (<https://www.baylor.edu/biology/comparativemammalian>) Search Committee Chair, Dr. Stephen Trumble at mammalian_physiology@baylor.edu.
- **Associate to Full Professor in Cancer Biology/Immunology** (<https://www.baylor.edu/biology/cancerbiologyimmunology>) Search Committee Chair, Dr. Myeongwoo Lee at cancerbiology_immunology@baylor.edu.
- **Regular Lecturer in Biology** (<https://www.baylor.edu/biology/lecturerinbiology>) Search Committee Chair, Dr. Mark Taylor at biolecturersearch@baylor.edu.

The Department of Biology has over 20 graduate faculty and 10 undergraduate teaching faculty. We are seeking faculty candidates who will complement and expand existing research and teaching strengths in the areas of Ecology, Evolution, and Organismal (EEO) Biology, and Cell, Molecular, Health and Disease (CMHD) Biology. Our graduate programs are growing rapidly with significant investment from the university.

Review of application materials will begin on **October 1, 2018** and will be accepted until the positions are filled. Visit <https://jobs.baylor.edu/> for further details about these positions. Inquiries may be directed to the appropriate Search Committee Chairs listed above. To apply, submit all required materials (cover letter, CV, research and teaching statements, transcripts, and the names of references) as a single PDF file through the iApply application system at our Human Resources site: <https://jobs.baylor.edu/>. Finalists for these positions will be required to submit official transcripts for the doctoral degree in advance of a campus visit.

Baylor University is a private Christian university and a nationally ranked research institution, consistently listed with highest honors among *The Chronicle of Higher Education's* "Great Colleges to Work For." The University is recruiting new faculty with a deep commitment to excellence in teaching, research and scholarship. Baylor seeks faculty who share in our aspiration to become a tier one research institution while strengthening our distinctive Christian mission as described in our strategic vision, *Pro Futuris* (www.baylor.edu/profuturis/), and academic strategic plan, *Illuminate* (www.baylor.edu/illuminate). As the world's largest Baptist University, Baylor offers over 40 doctoral programs and has more than 17,000 students from all 50 states and more than 85 countries.

Baylor University is a private not-for-profit university affiliated with the Baptist General Convention of Texas. As an Affirmative Action/Equal Opportunity Employer, Baylor is committed to compliance with all applicable anti-discrimination laws, including those regarding age, race, color, sex, national origin, marital status, pregnancy status, military service, genetic information, and disability. As a religious educational institution, Baylor is lawfully permitted to consider an applicant's religion as a selection criterion. Baylor encourages women, minorities, veterans, and individuals with disabilities to apply.



**Research Plant Physiologist/Ecologist
USDA-ARS, Beltsville, Maryland**

Position Type: Full time, Permanent
Salary: \$81,548-\$126,062/ per year + benefits

We are seeking a highly motivated scientist to conduct research directed to increasing our understanding of mechanisms and diversity of plant responses to climate change factors; specifically, elevated carbon dioxide and/or high temperature and water stress at the biochemical, physiological and system levels; and to utilize this information to develop, test and modify models of crop and weed responses to climatic variability. The scientist will be a member of the Adaptive Crop Systems Laboratory (ACSL) at the USDA-ARS location in Beltsville, Maryland. ACSL scientists have an outstanding record of discovery and publication regarding climate change and rising levels of carbon dioxide in agriculture. This offers the incumbent unique opportunities to build upon these research areas and to collaborate with other ARS, university and private sector scientists as well. The successful candidate must be a U.S. citizen, hold a PhD in Botany or Plant Physiology, with 9 semester hours in ecology and 12 semester hours in physical and mathematical sciences. Experience is desired in defining research problems, developing and executing research plans and evaluation of results related to plant responses to climate change variables; the ability to use methodologies in developing testing and applying mathematical models of plant process and to simulate climate projections using field and enclosed facilities; and experience in publishing research in peer-reviewed scientific journals in plant physiology, ecology or physiological ecology.

This announcement will open September 17, 2018 and will close on September 28, 2018. U.S. Citizenship is required. USDA/ARS is an Equal Opportunity Provider and Employer. If you have any questions regarding the additional duties of this position please contact **Dr. V. R. Reddy** at vr.reddy@ars.usda.gov, (301)-504-5872 or **Dr. David Fleisher** at David.fleisher@ars.usda.gov, 301-504-7339. If you have any questions regarding the application process for this position please contact Elsa Ayala, Human Resources Specialist, at 301-504-1369 or elsa.ayala@ars.usda.gov. To view additional details about this position and complete application instructions, go to the USAJobs Web site: <https://www.usajobs.gov/> and refer to announcement number **ARS-D18E-0122**. Please note that the announcement number will not be accessible until September 17, 2018.

FACULTY POSITIONS AT THE ROCKEFELLER UNIVERSITY

The Rockefeller University seeks exceptional, creative scientists to join its faculty. We invite applications from outstanding junior candidates for tenure-track positions and also welcome applications from tenured scientists at an early stage of their career.

The University has a laboratory, rather than department-based organizational structure that fosters interdisciplinary research. We encourage applications in the following areas:

- **Biochemistry, Biophysics, Chemical Biology, and Structural Biology**
- **Cancer Biology**
- **Cell Biology**
- **Genetics and Genomics**
- **Immunology, Virology, and Microbiology**
- **Mechanisms of Human Disease**
- **Neurosciences and Behavior**
- **Organismal Biology and Evolution**
- **Physical, Mathematical, and Computational Biology**
- **Stem Cells, Development, Regeneration, and Aging**

The Rockefeller University provides strong support for the work of its faculty including competitive salary, a range of work-life employee benefits, start-up funds, renovated laboratory space and state-of-the-art core facilities. There are extensive opportunities for collaboration within the University and with neighboring institutions.

Visit <http://www.rockefeller.edu/facultysearch> to submit your application online and view further information about the positions.

Application deadline is October 1, 2018.

Address questions to
facultysearch@rockefeller.edu.



Rockefeller University is an equal opportunity employer and will consider all qualified applicants for employment without regard to race, color, religion, sex, sexual orientation, gender identity, national origin, disability or protected veteran status.



Faculty Position in Molecular Genetics Waksman Institute of Microbiology

The **Waksman Institute at Rutgers University** seeks an outstanding scientist to fill a new faculty position at the Assistant Professor level, with a tentative starting date of **September 1, 2019**. The academic appointment will be in the Division of Life Sciences within the School of Arts and Sciences at Rutgers.

We are seeking individuals with research interests that complement and expand our existing strengths, including genetics, developmental biology, neurobiology, reproductive biology, cell biology, gene regulation, genomics, and metabolomics. We are particularly interested in individuals who use invertebrate animal model systems (e.g., *Drosophila*, *C. elegans*). The candidate will teach and develop undergraduate and graduate courses in these areas, supervise students in the laboratory, and serve on departmental and university committees.

The Waksman Institute is home to over 15 faculty members who use a broad range of approaches and experimental systems in numerous well-funded research programs. The Institute is part of a vibrant and interactive life sciences community that includes the School of Arts and Sciences Division of Life Sciences, the Center for Advanced Biotechnology and Medicine, the Cancer Institute of New Jersey, the Human Genetics Institute of New Jersey, and the Robert Wood Johnson Medical School. A leading research university, Rutgers is a member of the AAU and the CIC. For more information, please visit our websites: <https://www.waksman.rutgers.edu>, <http://lifesci.rutgers.edu>, and <http://sas.rutgers.edu>.

Applicants must have a Ph.D. or equivalent degree. They should submit a CV, a detailed statement of research interests and plans, and full contact information for three individuals willing to provide confidential letters of reference. Applications must be submitted electronically at: <https://jobs.rutgers.edu/postings/72742>. All other inquiries may be made to Ms. Erin Sorge, esorge@waksman.rutgers.edu. **Review of applications will begin on or about October 15, 2018 and continue until the position is filled.**

Rutgers, the State University of New Jersey, is an Equal Opportunity/Affirmative Action Employer. For additional information please see the Non-Discrimination Statement at:
<http://uhr.rutgers.edu/non-discrimination-statement>.



ENDOWED CHAIR in Molecular Genetics Waksman Institute of Microbiology

The **Waksman Institute at Rutgers University** invites applications for a newly established endowed chair in Plant Molecular Genetics, with a tentative starting date of **September 1, 2019**. The academic appointment of the position is expected to be in the Department of Plant Biology, School of Environmental and Biological Sciences, Rutgers University.

We seek somebody that is already well funded in plant molecular genetics, using genomics, metabolomics, NGS and other omics technologies as applied to understanding basic biological processes and to applications, but could use the income from the endowed chair to take on novel innovative ideas that are not supported by conventional funding programs. The candidate will be expected to teach and develop undergraduate and graduate courses in these areas, supervise graduate students, and serve on departmental, college and university committees.

The Waksman Institute is home to over 15 faculty members who use a broad range of approaches and experimental systems in numerous well-funded research programs. The Institute is part of a vibrant and interactive life sciences community that includes the School of Environmental and Biological Sciences, School of Arts and Sciences Division of Life Sciences, the Center for Advanced Biotechnology and Medicine, the Cancer Institute of New Jersey, the Human Genetics Institute of New Jersey, and the Robert Wood Johnson Medical School. A leading research university, Rutgers is a member of the Association of American Universities (AAU).

Applicants must have a PhD or equivalent degree and be eligible for the rank of full Professor with tenure. They should submit a curriculum vitae, a statement of research accomplishments and plans, and full contact information for four individuals willing to provide confidential letters of reference at <http://jobs.rutgers.edu/postings/59059>. Direct all other inquiries to Ms. Erin Sorge, esorge@waksman.rutgers.edu. **Review of applications will begin October 15, 2018 and continue until the position is filled.**

Rutgers is an Equal Opportunity/Affirmative Action Employer. For additional information please see the Non-Discrimination Statement at: <http://uhr.rutgers.edu/non-discrimination-statement>.



Open Rank Faculty Position in Life Sciences University of California Los Angeles

Building on a successful multiyear initiative to hire leading research scientists with a strong commitment to promoting the success of underrepresented students, the Division of Life Sciences in the UCLA College of Letters and Sciences announces an open rank faculty position with Academic Senate appointment in one of the departments of Life Sciences (www.lifesciences.ucla.edu): Ecology and Evolutionary Biology; Integrative Biology and Physiology; Microbiology, Immunology, and Molecular Genetics; Molecular, Cell, and Developmental Biology; and Psychology. Candidates must have a PhD in a field relevant to one of the above departments, and have outstanding record of scholarly publications, research support, and a history of commitment to the mentorship of students from underrepresented and underserved populations. The successful candidate will be expected to continue their active research program and mentoring activities and to participate in campus-wide departmental programs that provide research and professional development opportunities for our diverse student body (such as, PEERS-Program for Excellence in Education & Research in Sciences, MARC-Maximizing Access to Research Careers, the Biomedical Research Minor, and others). Service and teaching expectations will not exceed those of any other faculty position. Faculty appointment will be made at a professorial rank commensurate with current academic standing. UCLA offers competitive salaries, research set-up funds, and recruitment allowances.

Application packages should be submitted online through <https://recruit.apo.ucla.edu/apply/JPF04028> and include the following documents: (1) curriculum vitae; (2) research statement; (3) statement of contributions to equity, diversity, and inclusion with particular attention to formal and informal mentoring activities and detailed plans for continuing such activities in the future; (4) teaching interests; and (5) cover letter that includes names of three referees who can be contacted for letters. Each of the five items should be submitted as a standalone document. Review of applications will begin on **October 15, 2018** and continue until the position is filled. Both inquiries about the position and nominations of potential candidates should be sent to search committee co-chairs: Professor Yuen Huo (huo@psych.ucla.edu) and Professor Jeff Long (jeffalong@ucla.edu).

Located in an urban setting, UCLA is California's largest university with a diverse student body of 38,000 undergraduate and graduate students, approximately 25% that come from underrepresented minority groups. UCLA College of Letters and Science is home to many innovative programs focused on student success in sciences and promotes excellence in STEM teaching through the Center for Education Innovation & Learning in the Sciences. Interdisciplinary programs in Life Sciences are enhanced by the Medical, Nursing, Dental and School of Public Health along with 7 other professional schools with renowned faculty offering more than 323 degree programs and majors. UCLA is home to a number of NIH, NSF, and HHMI funded training programs focused on increasing success for underrepresented students in science, medical and allied health fields, and currently serves as the coordinating center for NIH BUILD grants. As a campus with a continually growing diverse student body, we encourage applications from women, minorities, and individuals with a commitment to mentoring underrepresented groups in the sciences.

The University of California is an Equal Opportunity/Affirmative Action Employer. All qualified applicants will receive consideration for employment without regard to race, color, religion, sex, national origin, disability, age, sexual orientation, gender identity, or protected veteran status. For the complete University of California nondiscrimination and affirmative action policy see: UC Nondiscrimination & Affirmative Action Policy. (<http://policy.ucop.edu/doc/4000376/NondiscrimAffirmAct>).



WAYNE STATE UNIVERSITY

Assistant/Associate Professor Nanotechnology (Pharmaceutics) and Chemical Biology (Medicinal Chemistry)

The Department of Pharmaceutical Sciences in the Eugene Applebaum College of Pharmacy and Health Sciences invites applications for two 12-month tenure-track positions at the Assistant or Associate Professor level. Applicants are expected to have earned a PhD, MD/PhD, PharmD/PhD or equivalent degree in pharmaceutical sciences, medicinal chemistry or a related discipline. Preference will be afforded scientists with a record of high impact research in nanotechnology and pharmaceutical chemistry at the chemical biology interface, particularly in our strengths of drug discovery, delivery and development, metabolic disease, neurosciences and oncology. These Pharmaceutical Sciences faculty positions are part of a broader initiative in which the departments of Chemistry and Pharmacology are also expanding existing excellence in Chemical Biology. The finalists are expected to have or develop a vigorous externally funded research program and provide valued teaching in the PhD and PharmD programs. We offer an uncommonly collegial academic culture, competitive start-up and compensation package, generous benefits, excellent laboratory facilities and extensive research support. Submit applications via <http://jobs.wayne.edu> under Department H1822-Pharmaceutical Sciences posting #043817. Further details are available by contacting Dr. Aloke Dutta at adutta@wayne.edu or (313) 577-1064.

Wayne State University is a Carnegie Highest Research Activity (R1) institution and a premier public, urban research university in the heart of Detroit where students from all backgrounds enjoy a rich, high quality education. The College is located in midtown, one of the dynamic urban communities leading the Detroit renaissance. The cosmopolitan environment is rich in cultural offerings, strong schools and outstanding affordable housing, all within the beautiful Great Lakes region. Our deep-rooted commitment to excellence, collaboration, integrity, diversity and inclusion creates exceptional educational opportunities that prepare students for success in a diverse and global society. We encourage applications from women, people of color, and other underrepresented groups.

Wayne State is an Affirmative Action/Equal Opportunity Employer. All qualified applicants will receive consideration for employment without regard to race, color, religion, sex, national origin, age, disability, veteran status, or any other characteristic protected by law.

Application review will begin **October 21, 2018** with a target faculty start date in August 2019. The positions will remain open until filled.



Faculty Positions in Applied Physical Sciences Department of Applied Physical Sciences University of North Carolina at Chapel Hill

The Department of Applied Physical Sciences (APS) invites applications for two tenure-track assistant professor faculty positions and a senior endowed Kenan Distinguished Professorship. The goal of APS is to bridge fundamental research and training in the science and engineering of materials with translational impact on society's most challenging problems. APS partners with all STEM and Health Affairs departments toward multidisciplinary, team-based research, education, and entrepreneurship in a top 10 public research university. This hiring initiative continues an aggressive strategy to build a pre-eminent Department of Applied Physical Sciences, aiming for 20 new hires together with joint appointments from partnering departments. These new positions are intended to build upon existing strengths and aim for international prominence and leadership in the science and engineering of materials at the intersection of the physical, life, and energy sciences.

All candidates should have clear potential and commitment for research excellence, multidisciplinary collaboration, extramural funding from government, industry, or other sources, and translational impact in education and entrepreneurship. Excellence and commitment to education and mentorship at the graduate and undergraduate levels are essential qualities for these recruitments. The Department and University are broadly committed to equity and inclusion. It is part of our institutional mission to teach and engage a diverse community of undergraduate and graduate students, and postdoctoral scholars. We especially welcome applications from candidates who are committed to advancing these ideals. A PhD in a STEM field (science, technology, engineering or math) or related fields that contribute to applied physical sciences is required.

Applications will only be accepted online (<https://unc.peopleadmin.com/postings/147785>). Applicants should submit a curriculum vitae, a research statement, a statement on teaching and mentorship, and 1-2 representative publications (optional). Applicants are required to identify the names, titles, email addresses and phone numbers of four professional references when applying. Reference providers identified by the applicant will be contacted via email with instructions for uploading their letters of support. To assure full consideration, applications should be submitted and all letters received by **October 15, 2018**. Positions are open until filled. Questions should be directed to: **Chair, Applied Physical Sciences Search Committee, University of North Carolina at Chapel Hill, Chapel Hill, NC 27599-3050; apssearch@unc.edu.**

The University of North Carolina at Chapel Hill is an Equal Opportunity and Affirmative Action Employer. All qualified applicants will receive consideration for employment without regard to age, color, disability, gender, gender expression, gender identity, genetic information, national origin, race, religion, sex, sexual orientation, or status as a protected veteran.

Associate Scientist/Scientist Population Health Group, Sanford Research

The Population Health Group at Sanford Research invites applications for full-time faculty at the rank of Associate Scientist or Scientist within Sanford Research in Sioux Falls, SD, with commensurate rank of Associate Professor or Professor at the Sanford School of Medicine at the University of South Dakota. Sanford Research is the non-profit research branch under Sanford Health.

The Population Health Group is comprised of investigators focused on public health, epidemiology, and population health with a strong emphasis on American Indian and rural population health. Ideal candidates will have an existing research portfolio in population health, health disparities, or a similar field of study. Additionally, the candidate will become the Principal Investigator of a currently funded NIH Center for Biomedical Research Excellence (CoBRE) grant. The candidate will mentor junior faculty, oversee relevant scientific cores, and utilize the CoBRE and institutional resources to grow and sustain the Center, including recruitment of several new investigators during the tenure of the grant. This candidate would also have the opportunity to engage in translational health services research leveraging Sanford's integrated data warehouse (clinical and claims data) to inform healthcare delivery. Significant institutional support, including modern laboratory space and state-of-the-art facilities will be provided. A comprehensive benefits package will be tailored to the candidate's qualifications.

Qualifications

Applicants should hold a PhD, MD or MD/PhD degree and complement the existing strengths and interdisciplinary and collaborative nature of Sanford Research. Physician Scientists are encouraged to apply. Ideal candidates will have a strong record of independent investigator-initiated grant funding and ideally program grant funding in population health (or a similar field), managing large budgets, mentoring early-career investigators to funding success, and experience in developing collaborations with various communities and institutional partners.

Application

Sanford Health is an Equal Opportunity/Affirmative Action Employer. Applicants should submit a single PDF that includes: 1) detailed curriculum vitae, 2) description of research experience and future research plans with details on relevance of their research to population health (or related topic), and 3) three letters of recommendation. If any of the information above is missing, the submission will not be considered. Submit materials via email to: researchrecruitment@sanfordhealth.org

SANFORD[®]
HEALTH

019036-00774 8/18

Faculty Position in Cancer Biology/Genetics

The Life Sciences Institute (LSI) at the University of Michigan invites applications for an open rank faculty position in Cancer Biology/Genetics. Faculty will hold both a Research Professor appointment in the LSI as well as an Assistant, Associate, or Full Professor appointment in one of the University's schools and colleges.

The LSI is a scientific enterprise at the University of Michigan dedicated to fundamental discovery in the biological sciences in a state-of-the-art collaborative physical space (www.lsi.umich.edu).

Successful candidates will have experience in cancer biology/genetics, with specific research targets related to cancer metabolism, cancer genetics/genomics/epigenetics, chemical biology, tumor microenvironment, or tumor immunology.

Application materials are due on **Friday, September 28, 2018**. Interested applicants will submit a cover letter, curriculum vitae, a summary of future research plans (up to 4 pages), contact information for three references, and copies of up to three publications on our online application site (lsi.science/2018facultyposting). Individuals from groups historically under-represented in the sciences are strongly encouraged to apply.

The University of Michigan is an Equal Opportunity/Affirmative Action Employer.



**COLUMBIA UNIVERSITY
MEDICAL CENTER**

Assistant Professor Research Scholar

The Vagelos College of Physicians and Surgeons is seeking one or more outstanding scientists in the Biomedical Sciences for appointment as a Research Scholar. These assistant professor positions are limited to MD, PhD, or MD-PhD researchers who have, in general, 4 years or less of post-doctoral fellowship and who have demonstrated exceptional ability, creativity and productivity as reflected in first or senior authored publications in leading scientific journals. Applicants who do not meet these criteria should not apply.

There is no limitation regarding the field of research. Appropriate departmental affiliation will be decided after selection. Adequate start-up funds, space, and mentorship will be provided. Priority will be given to applicants outside Columbia University.

Applicants should provide 3 names of references and a proposed plan for their work over the next five years with the application. To apply please visit: <https://academicjobs.columbia.edu/applicants/Central?quickFind=66057> or search by requisition number 0008603

*Columbia University is an Equal Opportunity/Affirmative Action Employer
Race/Gender/ Disability/Veteran*

Williams

Ecologist Tenure -Track Faculty Position Biology Department

The Biology Department at Williams College, a premier liberal arts college with a long-standing tradition of excellence in the sciences, invites applications for a tenure-track position at the rank of Assistant Professor, to begin July 2019. We are especially interested in candidates who can contribute to the intellectual vibrancy and diversity of the academic community through their research, teaching, and service, and who are committed to working effectively with a diverse student population.

We seek a broadly trained ecologist whose research incorporates state-of-the-art methods and a strong field component to address questions of broad biological significance. The candidate should complement our existing faculty expertise by focusing on community or ecosystem or landscape level ecology. The successful candidate will teach in our introductory courses as well as upper-level courses in ecology, including courses on sustainability of natural or human dominated systems. Normally, faculty members teach one course and two associated laboratory sections (or the equivalent) each semester. This individual will advise undergraduates in research and have the opportunity to participate in interdisciplinary programs such as Environmental Studies.

A dynamic research program that is attractive to extramural funding agencies and involves talented undergraduates is expected. Start-up funds and internal funding for research are available. A Ph.D., postdoctoral experience, and a strong research record are required. We anticipate the appointment at the beginning assistant professor level, although a more senior appointment may be possible under special circumstances.

All applications should be submitted through Interfolio at <https://apply.interfolio.com/51768>. Email and paper applications will not be accepted. Through Interfolio submit: a letter of application addressed to Professor Steven Swoap (Chair, Biology Department), a curriculum vitae, concise statements of teaching and research plans, and three current letters of recommendation. Your cover letter should speak to your ability to work effectively with a student population that is broadly diverse with regard to gender, race, ethnicity, nationality, sexual orientation and religion. All offers of employment are contingent upon completion of a background check <http://faculty.williams.edu/prospective-faculty/background-check-policy/>. Application deadline is **October 12, 2018**. For more information on the Department of Biology, visit <https://biology.williams.edu/>.

Williams College is a coeducational liberal arts institution located in the Berkshire Hills of western Massachusetts. The college maintains the 2500-acre Hopkins Memorial Forest for teaching and research. The College has built its reputation on outstanding teaching and scholarship and on the academic excellence of its approximately 2,000 students. Please visit the Williams College website (<http://www.williams.edu>). Beyond meeting fully its legal obligations for non-discrimination, Williams College is committed to building a diverse and inclusive community where members from all backgrounds can live, learn, and thrive.

Williams

Metabolic Biochemist Tenure -Track Faculty Position Biology Department

The Biology Department at Williams College, a premier liberal arts college with a long-standing tradition of excellence in the sciences, invites applications for a tenure-track position at the rank of Assistant Professor, to begin July 2019. We are especially interested in candidates who can contribute to the intellectual vibrancy and diversity of the academic community through their research, teaching, and service, and who are committed to working effectively with a diverse student population.

We seek a Metabolic Biochemist whose research addresses questions of broad biological significance and incorporates state-of-the-art methods. The successful candidate will teach a course in metabolic biochemistry, along with introductory cell biology and upper level courses in the candidate's field of expertise. Normally, faculty members teach one course and two associated laboratory sections (or the equivalent) each semester. This individual will advise undergraduates in research and participate in interdisciplinary programs in Biochemistry & Molecular Biology, and/or Bioinformatics, Genomics & Proteomics.

A dynamic research program that is attractive to extramural funding agencies and involves talented undergraduates is expected. Start-up funds and internal funding for research are available. A Ph.D., postdoctoral experience, and a strong research record are required. We anticipate the appointment at the beginning assistant professor level, although a more senior appointment may be possible under special circumstances.

All applications should be submitted through Interfolio at <https://apply.interfolio.com/51770>. Email, fax, and paper applications will not be accepted. The application should include a cover letter addressed to Professor Steven Swoap (Chair, Biology Department), a curriculum vitae, concise statements of teaching and research plans, and three current letters of recommendation. Your cover letter should speak to your ability to work effectively with a student population that is broadly diverse with regard to gender, race, ethnicity, nationality, sexual orientation and religion. All offers of employment are contingent upon completion of a background check. Further information is available here: <http://faculty.williams.edu/prospective-faculty/background-check-policy/>. Application deadline is **October 12, 2018**. For more information on the Department of Biology, visit <https://biology.williams.edu/>.

Williams College is a coeducational liberal arts institution located in the Berkshire Hills of western Massachusetts. The College has built its reputation on outstanding teaching and scholarship and on the academic excellence of its approximately 2,000 students. Please visit the Williams College website (<http://www.williams.edu>). Beyond meeting fully its legal obligations for non-discrimination, Williams College is committed to building a diverse and inclusive community where members from all backgrounds can live, learn, and thrive.



TEXAS TECH UNIVERSITY

Tenured Faculty Positions in Chemistry and Biochemistry

The Department of Chemistry & Biochemistry at Texas Tech University invites applications for two senior tenured faculty positions at the Associate or Full Professor level. One position will be in the area of Biochemistry, broadly defined. The field for the second position is open; however, it is expected that the research interests will fit into one or more areas of excellence identified by the department, including (again, broadly defined) life sciences, computational chemistry, high-resolution chemical imaging, energy storage and conversion materials, and sustainable (green) catalysis. Applicants must be tenured at their current institution or have comparable experience, and must have a nationally recognized and externally-funded research program. Service duties include program-building, as well as commitment to extra-curricular activities. A demonstrated and ongoing commitment to serving diverse student populations and experience working with diverse student populations and first-generation students is highly desirable. Service to the department, college, and university is expected. Successful candidates for these positions will be part of a major expansion of the Department of Chemistry & Biochemistry, which is among the top academic units at Texas Tech in terms of research funding, publications and graduate education. Texas Tech University has a Carnegie R1: Highest Research Activity classification. It has an enrollment of more than 37,000 students, and is one of the major, state-supported, multidisciplinary universities in the Southwest. Texas Tech University recently surpassed the Hispanic student population threshold necessary for designation as a Hispanic Serving Institution (HSI).

All applications must be submitted online. Online application can be submitted at <http://www.texastech.edu/careers/>. Candidates for the Biochemistry position should apply to **requisition number 15017BR** or use the direct link <https://jobs.brassring.com/TGWebHost/jobdetails.aspx?partnerid=25898&siteid=5637&areq=15017BR>. Candidates for the Open position should apply to **requisition number 15086BR** or use the direct link <https://jobs.brassring.com/TGWebHost/jobdetails.aspx?partnerid=25898&siteid=5637&areq=15086BR>. Candidates may apply for both positions, if they are otherwise qualified. Applications must include a curriculum vitae, a statement of current and proposed research, and a teaching philosophy. Applicants must also arrange to have three confidential letters of recommendation sent on their behalf to **Faculty Search Committee, Department of Chemistry & Biochemistry, Texas Tech University, Box 41061, Lubbock, TX 79409-1061** (chemchair@ttu.edu). Evaluation of applications will begin on **October 31, 2018**, and continue until the position is filled.

As an Equal Employment Opportunity/Affirmative Action employer, Texas Tech University is dedicated to the goal of building a culturally diverse faculty committed to teaching and working in a multicultural environment. We actively encourage applications from all those who can contribute, through their research, teaching, and/or service, to the diversity and excellence of the academic community at Texas Tech University. The university welcomes applications from minorities, women, veterans, persons with disabilities, and dual-career couples.



UNIVERSITY OF
MARYLAND

TENURE-TRACK ASSISTANT PROFESSOR POSITION: ECOLOGY

The Department of Biology at the University of Maryland, College Park invites applications for an Assistant Professor of Ecology. We seek outstanding, innovative candidates with research interests that complement and integrate those of our existing faculty. We are especially interested in those with experimental, observational, analytical, and/or theoretical approaches that address major questions in Ecology. Possible areas of synergy include, but are not limited to: global change, biocomplexity, and/or effects of the environment and interspecific interactions on ecological processes.

Applicants must have a doctorate degree and should describe their ability to develop an outstanding research program that would lead to a robust and diverse portfolio of extramural funding. Postdoctoral experience is preferred. Applicants must provide evidence of their commitment to excellence in teaching and mentoring, including working with students and groups from underrepresented backgrounds. The University of Maryland and the Department of Biology are committed to increasing the diversity of the campus community. Candidates who have experience working with a diverse range of faculty, staff, and students, and who can contribute to our climate of inclusivity, are encouraged to identify their experience in these areas.

Application deadlines: Review of applications will begin **1 October 2018**.

Application materials: All applicants are required to use our official UMD jobs portal to apply: <https://ejobs.umd.edu/postings/62247>. You will upload PDF files containing a cover letter, curriculum vitae, separate statements of research and teaching interests, and will provide names and contact information for 3 references.

The University of Maryland, College Park is the flagship campus of the University of System of Maryland and is one of the most rapidly advancing public research universities in the country. The University sponsors the NSF-funded National Socio-Environmental Synthesis Center (SESYNC) in Annapolis. Our close proximity to Washington D.C., the Chesapeake Bay, and the Appalachian Mountains facilitates interactions with researchers at an extraordinary range of institutions and field stations (e.g., Smithsonian Institution, NIH, USDA, USGS Patuxent Research Center, USFWS, Smithsonian Environmental Research Center, Chesapeake Bay Foundation, University of Maryland Center for Environmental Studies). In addition, several major non-governmental organizations have their world headquarters in Washington, DC (e.g., Conservation International, The Nature Conservancy, World Wildlife Fund).

The University of Maryland, College Park, an Equal Opportunity/Affirmative Action Employer, complies with all applicable federal and state laws and regulations regarding nondiscrimination and affirmative action; all qualified applicants will receive consideration for employment. The University is committed to a policy of equal opportunity for all persons and does not discriminate on the basis of race, color, religion, sex, national origin, physical or mental disability, protected veteran status, age, gender identity or expression, sexual orientation, creed, marital status, political affiliation, personal appearance, or on the basis of rights secured by the First Amendment, in all aspects of employment, educational programs and activities, and admissions.

Assistant Scientist Cancer Biology Group, Sanford Research

The Cancer Biology Group at Sanford Research invites applications for full-time faculty at the rank of Assistant Scientist within Sanford Research in Sioux Falls, SD, with commensurate rank of Assistant Professor at the Sanford School of Medicine at the University of South Dakota. Sanford Research is the non-profit research branch under Sanford Health.

We seek outstanding scientists with research programs that span all areas of cancer research, especially those relevant to cancer immunology or immunotherapy. The successful candidate will have an opportunity to become a project leader on the NIH-funded Cancer Biology CoBRE. Significant institutional support, including modern laboratory space and state-of-the-art facilities will be provided. A comprehensive benefits package will be tailored to the candidate's qualifications.

Qualifications

Applicants should hold a PhD, MD or MD/PhD degree and complement the existing strengths and interdisciplinary and collaborative nature of Sanford Research. Physician Scientists are encouraged to apply. Candidates will be expected to develop independent research programs and secure extramural funding.

Application

Sanford Health is an Equal Opportunity/Affirmative Action Employer. Applicants should submit a single PDF that includes: 1) detailed curriculum vitae, 2) description of research experience and future research plans with details on relevance of their research to cancer biology and/or cancer immunology, and 3) three letters of recommendation. If any of the information above is missing, the submission will not be considered. Submit materials via email to: researchrecruitment@sanfordhealth.org

SANFORD[®]
HEALTH

019036-00762. 8/18

Assistant Professor, Tenure Track- Otorhinolaryngology- Head and Neck Surgery



Perelman
School of Medicine
UNIVERSITY OF PENNSYLVANIA

The Department of Otorhinolaryngology: Head and Neck Surgery at the **Perelman School of Medicine** at the **University of Pennsylvania** seeks candidates for an Assistant Professor position in the tenure track. The successful applicant will have experience in the field of genetics and biology of head and neck cancers with a focus on cancer etiology and/or cancer genomics, inflammation, and the development of novel therapeutic approaches towards treatment of head and neck cancers. Particular areas of interest include genetics, tumor immunology or virology, bioinformatics, and/or translational therapeutics.

Responsibilities include building an independent research program in basic and/or translational studies in head and neck cancer, training of graduate students and post-doctoral investigators, as well as to develop interactions with investigators within the greater cancer research environment at the Abramson Cancer Center and the Perelman School of Medicine at the University of Pennsylvania. In particular, the candidate should demonstrate the vision and potential or ability to interact with clinicians to foster translational

research programs. Candidates with a keen interest in building interdisciplinary programs through interactions across the basic and clinical departments within the Perelman School of Medicine, as well as other Health related schools at the University of Pennsylvania, are encouraged to apply. Key selection criteria will be research excellence and originality of science. Applicants must have an M.D. or Ph.D. or M.D./Ph.D. degree and have demonstrated excellent qualifications in research.

The Departments of Otorhinolaryngology-Head and Neck Surgery and Cancer Biology are among the leading departments in the nation, and is home to basic and translational scientists who conduct world-class research in broad areas of cancer, virology, and microbiome. The Perelman School of Medicine at the University of Pennsylvania provides an intellectually vibrant and collaborative interdisciplinary environment, with a wealth of cutting edge research resources. The successful applicant will have a secondary appointment in the Department of Cancer Biology.

The ideal candidate should have completed advanced postdoctoral training or be an early career investigator with an exceptional record of research achievement demonstrating a trajectory for success in academic medicine.

We seek candidates who embrace and reflect diversity in the broadest sense. The University of Pennsylvania is an EOE. Minorities / Women/ Individuals with disabilities/ Protected Veterans are encouraged to apply.

Apply for this position online at:

https://www.med.upenn.edu/apps/faculty_ad/index.php/g/d5040



PROGRAM IN
SYSTEMS BIOLOGY

Faculty Position

The Program in Systems Biology invites applications from outstanding candidates for a **tenure-track or senior tenured professor position**. Rank will be commensurate with ability and experience. The position will be highly competitive with regard to start-up funds, laboratory space and salary.

The candidate will be expected to develop and maintain an innovative, externally funded research program. We are seeking an energetic and collaborative individual who will develop a strong research program to tackle important problems in one of the following areas in systems biology: Network Biology, Single Cell Systems Biology, Genome Biology, Evolution, Variation, Immunology and Neurobiology. Exceptionally strong candidates in other areas will also be considered.

The Program in Systems Biology is housed in the new Albert Sherman Center that opened early in 2013. The Program has high-performance computing facilities, state-of-the-art laboratory space and equipment and a full-time administrator to support the research activities of its Faculty.

Applicants should submit a cover letter explaining their interest in the Program, a curriculum vitae that includes honors, publications, and a succinct research plan to <http://www.academicjobsonline.org> (Position ID# 11577). The position is open until filled. To expedite the review process, applicants should invite three individuals who are familiar with their work and potential for success to upload their recommendation letters at the same web address. Inquiries, but not application materials, may be directed to **Professors A.J. Marian Walhout** (marian.walhout@umassmed.edu) or **Job Dekker** (job.dekker@umassmed.edu).

UMass Medical School is committed to being an Equal Opportunity and Affirmative Action Employer and recognizes the power of a diverse community. We encourage applications from protected veterans, individuals with disabilities and those with varied experiences, perspectives and backgrounds to consider UMass Medical School as their employer of choice.

UT Southwestern Medical Center

TENURE-TRACK POSITIONS

The Department of Physiology invites outstanding scientists with Ph.D., M.D., or equivalent degrees to apply for tenure-track faculty positions at the level of Assistant Professor. Candidates who bring innovative approaches to the study of any under-explored/unexplored questions broadly related to physiology are encouraged to apply. The scientific excellence of the candidates is more important than the specific area of research. These positions are part of the continuing growth of the Department at one of the country's leading academic medical centers. They will be supported by significant laboratory space, competitive salaries, state-of-the-art core facilities and exceptional start-up packages. The University of Texas Southwestern Medical Center is the scientific home to six Nobel Prize laureates and many members of the National Academy of Sciences and Institute of Medicine. UT Southwestern conducts more than 3,500 research projects annually totaling more than \$417 million. Additional information about the Department of Physiology can be found at <http://www.utswmed.edu/education/medical-school/departments/physiology/index.html>.

Applicants should submit a CV, a brief statement of current and proposed research, and a summary of your two most significant publications describing the importance of the work (100-150 words each). Please arrange to have three letters of recommendation sent on his/her behalf. All items should be submitted to: <http://academicjobsonline.org/ajob/jobs/11597>. Completed applications will be reviewed starting **November 1, 2018**. You may email questions to ron.doris@utswmed.edu.

UT Southwestern Medical Center is an Equal Opportunity/Affirmative Action Employer: Women, minorities, veterans and individuals with disabilities are encouraged to apply.



Faculty Positions, Vollum Institute

Oregon Health & Science University
Portland, Oregon

The Vollum Institute (www.ohsu.edu/vollum) is undergoing an exciting phase of growth and announces multiple faculty openings for biomedical scientists. We are particularly interested in applicants whose research focuses on neuroscience-relevant topics such as **molecular and cellular neuroscience, molecular genetics, circuits and systems in model organisms, structural biology, and glial biology** to expand on our current research strengths.

Vollum appointments are full-time research positions within the Vollum Institute with minimal teaching or clinical requirements. Ample opportunities are available for collaboration with basic science and clinical departments within the School of Medicine, and additional research units at OHSU (www.ohsu.edu) such as the Oregon Hearing Research Center (auditory neuroscience) and the Jungers Center (disease-related neuroscience).

Applications will be accepted at junior and mid-career levels. We particularly encourage women scientists and those from diverse backgrounds to apply. Applicants should have a strong record of research success and an interest in training graduate students. We offer highly attractive start-up packages and the opportunity to work in an outstanding scientific environment that includes strong mentoring for junior scientists.

Candidates with a Ph.D. and/or M.D. and at least several years of postdoctoral experience should apply by submitting their curriculum vitae, a description of research plans and goals, and three letters of reference to <https://academicjobsonline.org/ajob/jobs/11555>. Applications must be received by **November 1, 2018**.

For questions contact Gary Westbrook, Search Chair, at volljob@ohsu.edu

OHSU is an equal opportunity/affirmative action employer committed to maintaining diversity in its faculty and addressing faculty family issues including dual career couples and single parents.



UNIVERSITY OF
SOUTH CAROLINA

The Department of Chemistry and Biochemistry at the University of South Carolina invites applications for a tenure-track Assistant Professor position in the area of Computational Polymer Chemistry, with a start date of August 16, 2019. Candidates should have a Ph.D. and postdoctoral experience in organic, polymer or computational chemistry, materials science, or polymer science and engineering or related discipline. The Department has vigorous research and comprehensive infrastructures in macro/supramolecular sciences. The successful candidate is expected to develop a highly recognized, externally funded research program focused on understanding and predicting the dynamic behavior of macromolecules in complex environments (interfaces, surfaces, etc.) of multiphase or heterogeneous systems, such as block copolymers, supramolecular polymers, biomacromolecules, polymer/particle mixtures and adaptive or responsive polymers. Candidates are expected to have expertise in macro/supramolecular modeling and method development for large-scale dynamic simulations and advanced data analysis. Candidates are also expected to strive for excellence in teaching of undergraduate general or organic chemistry, as well as more specialized and graduate courses. All applicants must fill out an application through the online employment system "USC Jobs" at <https://uscjobs.sc.edu/postings/40411>. Candidates should be prepared to upload a CV, a cover letter, research plans, and teaching interests. Three letters of recommendation are required to be submitted via the uscjobs system.

For full consideration, complete applications must be received no later than **November 1, 2018**.

The University of South Carolina is an Affirmative Action, Equal Opportunity Employer. Minorities and women are encouraged to apply. The University of South Carolina does not discriminate in educational or employment opportunities on the basis of race, color, religion, national origin, sex, sexual orientation, gender, age, disability, veteran status or genetics.



MULTIPLE FACULTY POSITIONS Department of Electrical and Systems Engineering

The School of Engineering and Applied Science at the University of Pennsylvania is growing its faculty by 33% over the next five years. As part of this initiative, the **Department of Electrical and Systems Engineering** is engaged in an aggressive, multi-year hiring effort for multiple tenure-track positions at all levels. Candidates must hold a Ph.D. in Electrical Engineering, Computer Engineering, Systems Engineering, or related area. The department seeks individuals with exceptional promise for, or proven record of, research achievement, who will take a position of international leadership in defining their field of study and excel in undergraduate and graduate education. Leadership in cross-disciplinary and multi-disciplinary collaborations is of particular interest. We are interested in candidates in all areas that enhance our research strengths in

1. **Nanodevices and nanosystems** (nanoelectronics, MEMS/NEMS, power electronics, nanophotonics, nanomagnetism, quantum devices, integrated devices and systems at nanoscale),
2. **Circuits and computer engineering** (analog, RF, mm-wave, digital circuits, emerging circuit design, computer engineering, IoT, embedded and cyber-physical systems), and
3. **Information and decision systems** (control, optimization, robotics, data science, network science, communications, information theory, signal processing).

Prospective candidates in all areas are strongly encouraged to address large-scale societal problems in energy, transportation, health, food and water, economic and financial networks, social networks, critical infrastructure, and national security. We are especially interested in candidates whose interests are aligned with the school's strategic plan, <https://www.seas.upenn.edu/about/penn-engineering-2020/>

Diversity candidates are strongly encouraged to apply. Interested persons should submit an online application at <https://www.es.eupenn.edu/faculty-staff/> and include curriculum vitae, statement of research and teaching interests, and at least three references. Review of applications will begin on **December 1, 2018**.

The University of Pennsylvania is an Equal Opportunity Employer. Minorities/Women/Individuals with Disabilities/Veterans are encouraged to apply.



University of
Massachusetts
UMASS Medical School

Program in Bioinformatics and Integrative Biology

The Program in Bioinformatics and Integrative Biology invites applications for tenure-track or senior tenured professor positions. We are seeking innovative, energetic and collaborative individuals who plan to develop strong computational research programs to tackle problems in one of the following areas: regulatory genomics, comparative genomics, systems biology, RNA biology, evolutionary biology, statistical genetics, or proteomics. Candidates in all computational biology areas, especially statisticians and computer scientists focused on biological questions, are strongly encouraged to apply. Wet bench research space can be arranged for individuals who are interested in performing experiments to augment their computational efforts. Salary and start-up package will be highly competitive and commensurate with the high level of accomplishment expected of successful applicants.

The Program in Bioinformatics and Integrative Biology is housed in the new state-of-the-art Albert Sherman building, where it is part of a vibrant and collaborative research community that includes the Program in Systems Biology and the RNA Therapeutics Institute. Other closely collaborating departments, including the Department of Molecular, Cell and Cancer Biology, Program in Molecular Medicine, and Department of Biochemistry and Molecular Pharmacology, are located in neighboring buildings. The Program is supported by high-performance computing facilities.

Applicants should submit a cover letter explaining their interest in the Program, a curriculum vitae that includes publications, honors, and a succinct research plan to <http://www.academicjobsonline.org/ajob/jobs/11580>. To expedite the review process, applicants should invite three individuals who are familiar with your work, and potential for success, to upload their recommendation letters at the same web address. Review of applications will begin on **October 1, 2018** and continue until positions are filled. Inquiries, but not application materials, may be directed to Professor Zhiping Weng at zhiping.weng@umassmed.edu. UMASS Medical School is located within a 10-minute drive from Worcester Polytechnic Institute (WPI). The two universities have numerous joint research and educational efforts in Bioinformatics and Systems Biology.

UMass Medical School is committed to being an Equal Opportunity and Affirmative Action Employer and recognizes the power of a diverse community. We encourage applications from protected veterans, individuals with disabilities, and those with varied experiences, perspectives, and backgrounds to consider UMass Medical School as their employer of choice.



W.M. Keck Science Department

Claremont McKenna College • Pitzer College • Scripps College

TENURE TRACK ASSISTANT PROFESSOR of PHYSICS – EXPERIMENTALIST

The W.M. Keck Science Department of Claremont McKenna College, Pitzer College, and Scripps College (three members of the 7-member Claremont Colleges Consortium) seeks to hire a table-top experimentalist at the Assistant Professor level starting July 1, 2019. Applicants from all areas of experimental physics, including interdisciplinary areas such as materials science, optics, biological physics, condensed matter, fluids, engineering, etc., are welcomed. Our integrative science department comprises scientists in biology, chemistry, environmental science, neuroscience, and physics (the physics discipline also oversees an active 3-2 pre-engineering program.) We are a vibrant community of teacher-scholars who value an interdisciplinary approach to teaching and research. We seek candidates who share our enthusiasm for both scientific research and undergraduate teaching, and who desire a liberal-arts college career that balances the two. In serving students of three distinct colleges, our faculty enjoy a richly diverse learning community. Candidates must have a Ph.D. in a relevant field (e.g., physics or engineering), postdoctoral or equivalent professional research experience, and the ability to teach a full spectrum of courses in physics. The desire and capacity to actively engage undergraduates in in-house laboratory research and to supervise senior-thesis research projects is essential. Located in the charming town of Claremont, The Claremont Colleges are situated in the Los Angeles basin, 35 miles east of downtown LA, and are within a one-hour drive of Caltech, UCLA, USC, UC Irvine, and UC Riverside.

Please apply online at: https://webapps.cmc.edu/jobs/faculty/faculty_opening_detail.php?PostingID=16044. Upload (i) a cover letter describing your background, experience, and, importantly, your interest in working in a liberal arts college environment, (ii) a c.v., (iii) a succinct statement outlining your research experience and plans, including how your research might engage undergraduates, (iv) a succinct statement outlining your teaching experience and interests, (v) a statement outlining your philosophy for fostering an inclusive educational environment for students of all socioeconomic backgrounds, and (vi) the names and e-mail addresses of four references, at least two of whom can address research and at least one of whom can address teaching. All named references will be automatically contacted and sent instructions for uploading their reference letters. However, it is incumbent upon candidates to follow up with their reference-letter writers to ensure letters have been sent. Review of applications will begin **October 1, 2018**, and the position will remain open until filled. Further inquiries may be directed to Professor Adam Landsberg at alandsberg@kecksci.claremont.edu (please put “Experimentalist” in the subject line).

The W.M. Keck Science Department of Claremont McKenna, Pitzer, and Scripps Colleges is an Equal Opportunity Employer. In a continuing effort to enrich its academic environment and provide equal educational and employment opportunities, the department actively encourage applications from women and from members of historically under-represented social groups in higher education.

Faculty Positions in Department of Molecular Biology

The Department of Molecular Biology and the Hamon Center for Regenerative Science and Medicine (CRSM) at the University of Texas Southwestern Medical Center invite applications for tenure track faculty positions at the level of Assistant Professor. We are seeking creative and interactive individuals with strong research programs focused on mechanistic aspects of gene regulation and cellular signaling, cell growth and differentiation, and stem cell biology, including the use of cellular and animal models to study development and disease. Attractive recruitment packages, state-of-the-art core facilities, and exceptional laboratory space are available. UT Southwestern has a vibrant graduate program and an atmosphere of collegiality and collaboration.

Appointment rank will be commensurate with academic accomplishments and experience.

Candidates should apply online at <https://jobs.utsouthwestern.edu/> (search for Job# 334883 or Job# 334889). Applicants should also submit a curriculum vitae containing a summary of past research accomplishments, a statement of future objectives, and names of three references via email to:

MolBioSearch@UTSouthwestern.edu
Department of Molecular Biology
Hamon Center for Regenerative Science and Medicine
University of Texas Southwestern Medical Center

UT Southwestern Medical Center is an Affirmative Action/Equal Opportunity Employer. Women, minorities, veterans and individuals with disabilities are encouraged to apply.

UT Southwestern
Medical Center

USC Stem Cell

Keck School of Medicine of USC

Department of Stem Cell Biology and Regenerative Medicine Assistant Professorship in Stem Cell Biology and Regenerative Medicine

The Department of Stem Cell Biology and Regenerative Medicine (stemcell.keck.usc.edu) is recruiting candidates exploring stem cells, development and regenerative processes through tissue engineering, modeling, and genetic, genomic and biochemical approaches. We are particularly interested in candidates with strong, complementary computational expertise. The department is housed in the Eli and Edythe Broad Center for Regenerative Medicine and Stem Cell Research within the Keck School of Medicine of USC.

Excellent resources and strong collaborative opportunities exist across USC campuses. In addition to our translational research mission, department members play a critical role in the university's educational mission. Successful applicants will receive a generous start-up package.

Online applications will be accepted; please apply to:
facultypositions.usc.edu/FAS/application_position?postingId=REQ20062328

Applications should include a letter of interest, curriculum vitae, brief 2–3 page outline of research past, present and future, and *four* letters of reference. The applicant is responsible for ensuring that the completed application is received before **October 12, 2018**.

USC strongly values diversity and is committed to equal opportunity in employment. Women and men, members of all racial and ethnic groups, people with disabilities, and veterans are encouraged to apply.



The **Department of Chemistry** at Boston University invites applications from outstanding candidates for an Assistant Professor tenure track position in the field of Synthetic Inorganic or Organometallic Chemistry, beginning July 1, 2019, subject to budget approval. Candidates with research focus broadly defined in the areas of metal complex synthesis, with applications in organometallic or coordination chemistry catalysis, small molecule conversion, solar fuels, recycling, or energy/sustainability are particularly encouraged to apply.

The successful applicant will benefit from the department's supportive and collegial environment, which includes close affiliations with Boston University's Materials Science & Engineering Division, the Photonics Center, the Biogeoscience Program, and the Institute for Sustainable Energy. Undergraduate teaching responsibilities will be in the areas of inorganic and general chemistry, with the opportunity to develop graduate courses in the candidate's area(s) of expertise. Boston University expects excellence in teaching and in research and is committed to building a culturally, racially, and ethnically diverse scholarly community. Applicants should apply by submitting a letter of interest, including teaching and research objectives, and a statement of their experiences in mentoring, diversity and inclusion, a current CV, and arrange to have three letters of reference submitted via **AcademicJobsOnline.org**, job reference #11560. Review of applications will begin on **October 8, 2018**.

We are an Equal Opportunity Employer and all qualified applicants will receive consideration for employment without regard to race, color, religion, sex, sexual orientation, gender identity, national origin, disability status, protected veteran status, or any other characteristic protected by law.

We are a VEVRAA Federal Contractor.



Molecular, Cellular, & Developmental Biology Faculty Search



UNIVERSITY OF MICHIGAN FACULTY POSITIONS IN MOLECULAR, CELLULAR, AND DEVELOPMENTAL BIOLOGY

The Department of Molecular, Cellular, and Developmental Biology (MCDB) in the College of Literature, Science and the Arts at the University of Michigan solicits applications for faculty positions at the assistant professor level, but appointment at a more senior level is possible for applicants with suitable experience. The faculty position will be tenured or tenure track with a university year appointment starting September 1, 2019 or January 1, 2020. Successful candidates will be expected to establish a vigorous, extramurally funded research program and to be involved in instruction of both undergraduate and graduate students.

We welcome applications from outstanding biologists in any area of research within the scope of the department, which includes studies of model organisms (plants, animals, and microbes) with a variety of approaches (genetics and genomics, biochemistry and structural biology, molecular biology, cell and developmental biology, and physiology). For further information about MCDB research areas, please visit www.lsa.umich.edu/mcdb.

All applications must be submitted on-line at <https://apps-prod.mcdb.lsa.umich.edu/search18/index.php>. You will be asked to upload the following materials: A cover letter, a *curriculum vitae*, a brief summary of recent research accomplishments and statement of future research plans, a statement of teaching interests and philosophy, and evidence of teaching excellence for those who have teaching experience. Candidates for appointment as an assistant professor should provide names and contact information for at least three references, as instructed in the on-line application form. To ensure full consideration, all materials should be received by **October 12, 2018**.

Women and underrepresented minorities are encouraged to apply. The University of Michigan is supportive of the needs of dual career couples and is an Equal Opportunity/Affirmative Action Employer.



UNIVERSITY of ROCHESTER MEDICAL CENTER

Assistant/Associate Professor Center for Biomedical Informatics (CBI) and Department of Microbiology and Immunology

The University of Rochester Medical Center (URMC) is expanding its research activities in the area of biomedical informatics. We are seeking investigators at the Assistant or Associate Professor level with independent and collaborative research programs. Six to ten faculty will be recruited into tenure track positions over the next three years.

We are searching for investigators with expertise in the broad areas of bioinformatics and systems biology as applied to a research program studying infectious disease. Successful candidates will hold appointments in the newly founded CBI and the Department of Microbiology and Immunology. Investigators with research experience in the following areas are highly encouraged to apply: Genome and transcriptome informatics, systems biology, population genomics, machine learning, data mining, computational modeling, multi-dimensional integration of clinical, genomic, microbiome, metabolome, gene expression and epigenetic data.

URMC offers attractive start-up packages and has a strong commitment to career development. The successful candidate is expected to develop a competitive research program, attract external funding, and participate in graduate education. Major recent institutional investments have created an outstanding research data-driven infrastructure, exemplified by the Health Sciences Center for Computational Innovation, and the recent \$50 million University investment to build the Goergen Institute for Data Science.

Applicants should submit a letter of application, CV, statement of research interests/plans, and arrange to have three letters of recommendation sent to: anne_reed@urmc.rochester.edu. Inquiries can be directed to Dirk Bohmann (dirk_bohmann@urmc.rochester.edu) or David Topham (david_topham@urmc.rochester.edu).

The University of Rochester is an Equal Opportunity Employer and has a strong commitment to diversity; it actively encourages applications from groups underrepresented in higher education.



WILMOT CANCER INSTITUTE

Cancer Biology Faculty Positions

The Wilmot Cancer Institute at the University of Rochester Medical Center is currently recruiting tenure-track faculty as part of a major expansion of its translational and basic science research base. The successful candidate(s) will join a growing multidisciplinary cancer research community with ongoing emphases in cancer cell metabolism, cancer stem cell biology, RNA biology, cancer (epi)d systems biology, microenvironment influences on tumor behavior/immunology, and therapeutic resistance.

The Wilmot Cancer Institute is the hub of cancer research at the University of Rochester, attracting more than \$20M in cancer-directed funding annually. Formal research programs exist in Cancer Biology, Tumor Microenvironment and Immunology, and Cancer Control and Survivorship. The Wilmot Cancer Institute and UR Medicine are the major providers of comprehensive, multidisciplinary cancer care in central New York State and the Finger Lakes region, with >6000 new patients every year and an extensive clinical trials program providing opportunity for innovative translational research.

Candidates holding a PhD and/or MD degree with a demonstrated track-record of research accomplishment in an area relevant to cancer biology/cancer genomics are invited to apply. Applicants making use of genomic/epigenomic approaches, tumor model systems and/or human specimens to address problems of translational relevance are strongly encouraged. New faculty will benefit from vibrant graduate/professional training programs and state of the art infrastructure and core facilities, as well as a strong Institutional commitment to career development. Appointments will be made at the Assistant Professor level although outstanding candidates at other levels will be considered, with commensurate expectations of research and funding accomplishment. Departmental affiliation will be determined according to best fit.

Interested applicants should submit a CV, statement of research interests/plans, pdfs of two key publications, and three letters of recommendation to the Search committee chair **Paula Vertino, PhD** c/o Elva Mikk at Elva_Mikk@urmc.rochester.edu. Review of applications will start **October 15, 2018**.

The University of Rochester is an Equal Opportunity Employer and has a strong commitment to diversity and actively encourages applications from candidates from groups underrepresented in higher education.



Faculty Positions in the Department of Physiology

The Department of Physiology at the Perelman School of Medicine at the University of Pennsylvania seeks highly qualified candidates for faculty positions in the tenure track at the Assistant, Associate, and full Professor ranks. Responsibilities include establishing and conducting an independent research program, plus teaching, supervising, and mentoring students. These positions require an M.D., Ph.D., or equivalent degree, plus demonstrated excellence in research. Candidates with experience in molecular, cellular, or organismal physiology will be considered. Investigators with research programs that leverage molecular and cellular insights to inform physiological, cell biological and pathophysiological functions are strongly encouraged to apply. We also seek researchers who develop and use novel and state-of-the-art biophysical, cell biological and physiological techniques. Research areas of interest include membrane protein structural biology, membrane transport physiology, signal transduction, organelle biology, molecular bases of disease, and metabolism. Other areas will also be considered, with the novelty, importance and potential impact of the research emphasized.

Assistant Professor: Applicants in the early stage of career development are encouraged to apply. Apply online: https://www.med.upenn.edu/apps/faculty_ad/index.php/g311/d5142

Associate or full Professor: Applicants are expected to have funding and an internationally recognized reputation of innovative research excellence and productivity. Apply online https://www.med.upenn.edu/apps/faculty_ad/index.php/g311/d5126

The Perelman School of Medicine, one of the top ranked medical schools in the country for NIH funding, is a highly collaborative environment with extensive core facilities. It is located on the campus of the University of Pennsylvania, a world-class institution with an easily walkable campus located near central Philadelphia.

We seek candidates who embrace and reflect diversity in the broadest sense. The University of Pennsylvania is an EOE. Minorities/Women/Individuals with disabilities/Protected Veterans are encouraged to apply.



THE OHIO STATE UNIVERSITY COLLEGE OF MEDICINE

Faculty Positions in Neuroscience

The Ohio State University (OSU), Wexner Medical Center

The Department of Neuroscience invites applications for tenure-track faculty positions at the rank of Assistant, Associate or Full Professor.

As part of an ongoing commitment to place OSU at the forefront of patient care, research and innovation, The College of Medicine is committing significant resources to build cutting-edge and internationally recognized basic and translational neuroscience programs. We have a goal that the Department of Neuroscience will become a Top 10 nationally-ranked department within 5 years.

Applicants who study the mechanisms underlying normal nervous system function and/or how these mechanisms and interactions are affected by disease or injury are encouraged to apply. Candidates with technical expertise in functional imaging, optogenetics, bioengineering, electrophysiology or -omics-based technologies (genomics, proteomics, metabolomics, connectomics, etc.) will be prioritized.

Newly recruited faculty will have the opportunity to be part of one or more established or rapidly growing research teams focused on neurotrauma (spinal cord and brain injury), neural regeneration or plasticity, neuroimmunology, neurodegeneration/cognitive impairment, pain, addiction, epilepsy and stroke/ischemic injury.

Candidates must hold a Ph.D. or equivalent and at least 3 years postdoctoral experience with a strong record of scholarly activity. Candidates for appointment as Associate or Full Professors should also be nationally or internationally recognized scholars with consistent externally funded research programs. Prospective candidates should send a statement of research interests, vita and a list of three references to recruitsneurosci@osumc.edu. Applications are being accepted now and formal review will begin **August 30, 2018**. The search will remain open until all positions are filled.

The Ohio State University is an Equal Opportunity, Affirmative Action Employer and as such, women and minorities are encouraged to apply. Unless confidentiality is requested in writing, information regarding the applicants must be released upon request.



Postdoctoral Fellow/Staff Scientist Positions in Cancer Epigenomics

The newly established Laboratory of Cancer Genomics in the Wilmot Cancer Institute at the University of Rochester Medical Center, led by Dr. Paula Vertino, is seeking productive and highly motivated individuals interested in cancer epigenetics/genomics. Current studies make use of molecular genetic and genomic approaches to understand epigenetic control of transcription and its role in phenotypic plasticity, intratumor heterogeneity and the emergence of invasive or drug resistant properties. Translational epigenomics studies in human cancers are focusing on defining epigenomic/genomic signatures associated with environmental exposures and patient outcomes with the goal of identifying novel routes for cancer therapy.

Applicants should hold a PhD in the biomedical sciences, computational biology or related discipline with experience in molecular/cancer biology, (epi)genetic/omics, and/or bioinformatics. Wet and/or 'dry' lab experience with epigenomics technology/data (WGBS, ChIP-seq, ATAC-seq, Pro-seq/RIP-seq), single-cell approaches, RNA biology, gene editing, or cancer models (3D culture, spheroid/organoid) are highly desirable, but applicants with a strong background in a related area, track-record of accomplishment, and desire to work in a multidisciplinary team of investigators focused on cancer epigenetics will be considered. Computational scientists (MS/PhD) with expertise in bioinformatics, systems biology and machine learning approaches are also encouraged to apply. Candidates should have excellent scientific writing and oral communication skills, as well as the ability to work effectively and collaboratively with others. Information about living/working at University of Rochester can be found at <https://www.rochester.edu/working/hr/relocation/>

Interested applicants should submit a cover letter, CV and contact information for three references to **Ms. Elva Mikk, Wilmot Cancer Institute, University of Rochester, 601 Elmwood Avenue Rochester, NY 14642**, or e-mail at: elva_mikk@urmc.rochester.edu



TENURE TRACK ASSISTANT PROFESSOR MICROBIAL BIOLOGY DEPARTMENT OF BIOLOGICAL SCIENCES, VANDERBILT UNIVERSITY VANDERBILT INSTITUTE FOR INFECTION, IMMUNOLOGY AND INFLAMMATION

The Vanderbilt University Department of Biological Sciences and the Vanderbilt Institute for Infection, Immunology and Inflammation invite applications for a tenure-track, faculty position in microbiology, including microbial ecology and the microbiome, at the Assistant Professor rank. The candidate will be expected to develop an independent laboratory research program using experimental and/or computational approaches complementing current departmental strengths in cell and molecular biology, chemical biology, evolution, genomics, host-microbe interactions, and neurobiology (<https://as.vanderbilt.edu/biosci/>). As a new faculty member, the candidate will play an integral role within the trans-institutional Vanderbilt Microbiome Initiative (<https://my.vanderbilt.edu/microbiome/>) and will benefit from collaborations with internationally recognized programs including the Vanderbilt Genetics Institute, the Vanderbilt Institute of Chemical Biology, or the Vanderbilt Institute for Global Health. Selection criteria are excellence in research and the ability to teach undergraduate and graduate students with a high level of effectiveness.

Applicants must have Ph.D. in hand by August 16, 2019. Applicants should submit a letter of interest, full curriculum vitae, and statements of research interests and teaching philosophy directly to <http://apply.interfolio.com/54094>. Applicants should arrange for four letters of recommendation to be sent to the same link. Completed applications must be received no later than October 24, 2018.

Vanderbilt University has a strong institutional commitment to recruiting and retaining an academically and culturally diverse community of faculty. Minorities, women, individuals with disabilities, and members of other underrepresented groups are encouraged to apply. Vanderbilt is an Equal Opportunity/Affirmative Action Employer.

Vanderbilt University is located in the heart of Music City, Nashville, TN, and ranks in the top 15 National Universities. Nashville is consistently rated as one of the best cities in which to live.



The Departments of Mathematics and Biology invite applications at the level of Associate or Full Professor for the Calabi-Simons Chair in Mathematics and Biology. This is a permanent endowed chair for which we are seeking an exceptional mathematical biologist or a mathematician with strong biological interests. The chair-holder will help build excellence in this field at Penn and provide leadership in enhancing interactions between the Mathematics and Biology departments. Responsibilities include teaching undergraduate and graduate courses in Mathematics and Biology and conducting research in the field. The Simons Foundation provides generous programmatic funds, which could support graduate students and postdoctoral fellows as well as seminars and conferences.

Applications should be submitted online through mathjobs.org and include the following items: a cover letter, a vision statement on building a program in mathematics+biology, curriculum vitae, research statement, and a publication list. **Review of applications will begin on October 15, 2018** and will continue until the position is filled. It is anticipated that the position will start **July 1, 2019**.

The Departments of Mathematics and Biology are strongly committed to Penn's Action Plan for Faculty Diversity and Excellence and to creating a more diverse faculty (for more information see: <http://www.upenn.edu/almanac/volumes/v58/n02/diversityplan.html>). The University of Pennsylvania is an EOE. Minorities/Women/Individuals with disabilities/Protected Veterans are encouraged to apply. Please address any questions to: personnel@math.upenn.edu.

UNIVERSITY
OF MIAMI



Open Rank Position in Ecology and Evolutionary Biology Department of Biology

The University of Miami's Department of Biology invites applications from outstanding scholars engaged in addressing fundamental questions in Ecology and/or Evolutionary Biology. We welcome applications from candidates at any career stage whose research will complement and grow the existing strengths of our department and who would be interested in contributing to cross-campus collaborations with other academic units at the University of Miami. Applicants working on any area of ecology or evolutionary biology are encouraged to apply, but we are especially interested in candidates whose work addresses at least one of the following themes using state-of-the-art approaches and techniques: Tropical Biology, Species Interactions (including symbiosis), Conservation Biology, Plant Biology, and/or Quantitative Biology (including Mathematical or Theoretical Biology). To be eligible for this open-rank position, successful candidates must hold a PhD, have postdoctoral experience, and have a strong track record of publications and funding commensurate with rank. The hire will be expected to develop a vigorous, externally funded research program and teach at the undergraduate and graduate levels. More information about the Department of Biology and the University of Miami can be found at <http://www.as.miami.edu/biology/>.

Applicants should submit a cover letter that includes a description of potential interactions they foresee with faculty in the Department of Biology or other units at the University of Miami, a curriculum vitae, two representative publications, a research statement, a teaching statement, and the names of three references online at <https://umiami.wd1.myworkdayjobs.com/UMFaculty>. Inquiries should be directed to the Search Chairs at eebfacultysearch@miami.edu. To receive full attention application materials must be received by **October 15, 2018**.

The University of Miami is an Equal Opportunity Employer, and Females/Minorities/Protected Veterans/Individuals with Disabilities are especially encouraged to apply. Applicants and employees are protected from discrimination based on certain categories protected by Federal law.



BIODISCOVERY INSTITUTE,
UNIVERSITY OF NORTH TEXAS
ASSISTANT/ASSOCIATE
PROFESSOR OF
MICROBIAL METABOLISM

The University of North Texas (UNT), Denton, Texas, invites applications from outstanding scientists for an assistant or associate professor position in the BioDiscovery Institute (BDI), one of four Institutes of Research Excellence. Candidates addressing important fundamental and applied questions in the synthesis and development of bio-based products for agriculture, materials engineering, bioenergy or health benefits are especially encouraged to apply. We are seeking individuals working at the forefront of microbial metabolism and metabolic engineering. The new hire will complement and interact with existing researchers in systems modeling of metabolism, plant biochemistry, and biotechnology. Newly renovated research space, competitive start-up packages, and state-of-the-art core facilities in genomics and metabolomics will support the new hire and colleagues in BDI.

The successful candidate will bring an internationally recognized research program, interact with diverse faculty, staff and students within BDI and across UNT, and contribute to graduate and/or undergraduate training. Applicants should have a Ph.D. in a biological, computational, chemical or engineering sciences discipline, a record of funding and publication in the target area, and a commitment to research excellence within an interdisciplinary environment. Applications should be made through the UNT Academic Resources website (<https://facultyjobs.unt.edu>) and should include a cover letter, curriculum vitae, two-page summary of research interests and accomplishments, one-page statement of teaching philosophy, and the names and contact information for three references. Questions may be directed to Brian G. Ayre (bgayre@unt.edu), Search Committee Chair, or Kent D. Chapman (chapman@unt.edu), BDI Director. Screening of applications will begin immediately and will continue until the positions are closed. For best consideration, apply by **October 15, 2018**.

The University of North Texas is an Equal Opportunity/Access/Affirmative Action/Pro Disabled and Veteran Institution committed to diversity in its employment and educational programs, thereby creating a welcoming environment for everyone.



Faculty position in Microbiology/Infectious Disease

Cummings School of Veterinary Medicine at Tufts University invites applications from experienced individuals to join the Department of Infectious Disease and Global Health (IDGH), with programs in infectious disease and international health, wildlife and conservation medicine.

The ideal candidate will have a DVM and/or PhD degree with substantial expertise and interest in teaching/directing the microbiology/infectious disease DVM degree course and participating in other graduate degree courses taught on campus. Applicants must have an established scientific research record and demonstrated grant-writing skills. Appointments will be considered at the assistant to full professor level, depending on experience and research record.

The candidate will help promote a team approach to problem solving through scientific research, teaching and service as a part of a strong faculty core in infectious disease with research interests spanning bacterial, viral, and parasite medicine in both animals and humans. Responsibilities will include teaching core and elective courses at the professional and graduate level; supervising, training and mentoring students; serving on faculty committees; and contributing to community service initiatives. Salary is commensurate with experience and includes a benefits package.

Specialized facilities available include the New England Regional Biosafety Laboratory, a BSL-3 biocontainment/Select Agent research space (<http://vetsites.tufts.edu/ne-rbl/>).

Please submit a letter of application stating your professional experience and goals along with your CV and 4 professional contact references electronically via Interfolio at <http://apply.interfolio.com/53633>. Questions about the position can be directed to Dr Saul Tzipori (saul.tzipori@tufts.edu).

Tufts University is an Equal Opportunity/ Affirmative Action Employer.



COLUMBIA UNIVERSITY

Vagelos College of Physicians and Surgeons

The Department of Surgery in the Vagelos College of Physicians and Surgeons and the Department of Biomedical Engineering in the School and Engineering and Applied Science are pleased to invite applications for a **tenure-track faculty position** at Columbia University in the City of New York. Applications at the level of Assistant, Associate or Full Professor will be considered. Candidates are sought in the broad area of Tissue Engineering and Regenerative Medicine. The selected candidate is expected to develop and lead an original externally funded research program, and to contribute to the research and educational missions of the Departments of Surgery and Biomedical Engineering. The University offers a rich environment for multidisciplinary research and encourages collaborations amongst clinical and basic science departments. This position seeks candidates who will develop research across the fields of tissue engineering, regenerative medicine, stem cell biology, and surgical disciplines. An ideal candidate will strengthen ties between the Departments of Surgery and Biomedical Engineering, building upon existing strengths in the use of cellular, tissue and whole organ engineering, and regenerative medicine to treat diseases of the cardiovascular, pulmonary and digestive systems. The University is especially interested in qualified candidates who can contribute, through their research, teaching, and service, to the diversity and excellence of the academic community. Requirements include MD, PhD or its professional equivalent in biomedical engineering or a related field, a record of pioneering research in the area of Tissue Engineering and Regenerative Medicine, and demonstrated abilities to attract extramural research funding and to teach effectively. Candidates should apply online and upload a curriculum vitae, statement of current and future research (1-2 pages), and contact information for three experts who can provide letters of recommendation.

Application link: academicjobs.columbia.edu/applicants/Central?quickFind=66483

The Department of Surgery and Department of Systems Biology in the Vagelos College of Physicians and Surgeons are pleased to invite applications for a **tenure-track faculty position** at Columbia University in the City of New York. Applications at the level of Assistant, Associate or Full Professor will be considered. Candidates are sought with specific research interests in applying systems biology approaches to questions in immunology of translational relevance to human diseases. Collaborations with groups studying the anatomy of the immune responses in mice and humans in health and disease are particularly encouraged. Columbia University Medical Center provides a highly interactive, collaborative environment for pursuing studies in systems biology. Candidates are expected to develop an independent peer-review funded research program. In addition to setting up a vibrant research program in systems immunology, the candidate is expected to participate in the training of graduate students and surgical residents, and participate in the teaching of graduate students. Candidate should also participate in both systems biology and immunology seminar series and serve as a member of the research committee in the Department of Surgery. PhD, MD or its professional equivalent required. Candidates should apply online and upload a curriculum vitae, statement of current and future research (1-2 pages), and contact information for three experts who can provide letters of recommendation.

Application link: academicjobs.columbia.edu/applicants/Central?quickFind=66484



FACULTY POSITION IN CANCER BIOLOGY

Department of Medicinal Chemistry and Molecular Pharmacology

The department of Medicinal Chemistry and Molecular Pharmacology (MCMP) (<http://www.mcmp.purdue.edu>) in conjunction with the NCI designated Purdue Center for Cancer Research (<https://www.cancerresearch.purdue.edu/>) invites applications for a **TENURED / TENURE-TRACK FACULTY POSITION** at all ranks. Preference will be given to qualified candidates with strong programs in **Translational Cancer Biology** focused on targeted therapies of signal transduction, epigenetics, immunotherapy and animal models of disease.

The department offers a unique multidisciplinary and collaborative environment with synergistic strengths in both chemistry and biology, spanning a wide range of topics including signal transduction, epigenetics, structural and computational biology, molecular pharmacology, systems biology, chemical biology, medicinal chemistry and drug discovery. In addition to the cancer center the MCMP department also contributes significantly to Purdue Institute for Integrative Neuroscience (<http://www.purdue.edu/discoverypark/pillars/integrative-neuroscience-center/index.php>), Purdue Institute for Inflammation, Immunology and Infectious Disease (<http://www.purdue.edu/discoverypark/pillars/pi4d/index.php>), and Purdue Institute for Drug Discovery (<http://www.purdue.edu/discoverypark/drug-discovery/>).

Purdue University is investing more than \$250 million in the life sciences over the next five years and offers state-of-the-art facilities for transgenic animals, imaging, genomics, bioinformatics, proteomic and metabolomics, NMR, X-ray crystallography, CryoEM, and chemical genomics. Faculty have the opportunity to train graduate students in the departmental and university-wide interdisciplinary programs. Highly competitive salary, start-up funds and laboratory space will be provided.

Candidates must have a Ph.D. degree or equivalent in Cell Biology, Biochemistry, Pharmacology or a relevant scientific discipline and relevant post-doctoral experience. The successful candidate will be expected to establish and/or maintain a strong extramurally-funded research program and will participate in undergraduate, professional, and graduate education/teaching.

Applications should consist of (1) a cover letter including the names and contact information of three references, (2) a curriculum vitae, (3) a statement of teaching philosophy and experience, and (4) a summary of planned and/or ongoing research. These materials should be submitted electronically to <https://bit.ly/2NmdVkv>. Please contact Barb Mullenberg at davidsba@purdue.edu if you have questions about uploading documents or the search. For technical assistance, please email careers@purdue.edu (<mailto:careers@purdue.edu>).

Review of applications will begin on **October 15, 2018** and will continue until the position is filled. Applications will be held in confidence until the interview phase of the process, and the applicants' permission to contact references prior to that time will be obtained. A background check will be required for employment in this position.

Purdue University's Department of Medicinal Chemistry and Molecular Pharmacology is committed to advancing diversity in all areas of faculty effort, including scholarship, instruction and engagement. Candidates should address at least one of these areas in their cover letter, indicating their past experiences, current interests or activities, and/or future goals to promote a climate that values diversity and inclusion.

Purdue University is an EOE/AA Employer. All individuals, including minorities, women, individuals with disabilities, and veterans are encouraged to apply.

POSITIONS OPEN

UNIVERSITY OF ILLINOIS AT CHICAGO, DEPARTMENT OF CHEMISTRY invites applications for a tenure-track assistant professor in inorganic chemistry emphasizing bioinorganic systems. Successful candidates will conduct rigorous and innovative research in bioinorganic chemistry broadly defined, including possible focus areas of inorganic spectroscopy, synthetic inorganic model chemistry, bio-mimetic and bio-inspired catalysis science, artificial metalloenzymes, and/or metal-based imaging and therapeutic agents. Candidates also are expected to contribute to teaching of inorganic chemistry to graduate and undergraduate students at UIC. A Ph.D. is required, and postdoctoral experience is highly recommended. This position is expected to start on August 16, 2019. Candidates should submit an online application including a cover letter, curriculum vitae, brief summary of past research accomplishments, proposals for a vibrant independent research program, and the names and email addresses of 3 references to website: <https://jobs.uic.edu/job-board/job-details?jobID=101540&job=assistant-professor-bioinorganic-chemistry> by **October 15, 2018**. Final authorization of the position is subject to availability of funding. *The University of Illinois at Chicago is an Affirmative Action, Equal Opportunity Employer, dedicated to the goal of building a culturally diverse and pluralistic faculty and staff committed to teaching and working in a multicultural environment. We strongly encourage applications from women, minorities, individuals with disabilities and covered veterans. The University of Illinois may conduct background checks on all job candidates upon acceptance of a contingent offer. Background checks will be performed in compliance with the Fair Credit Reporting Act.*

Professor and Director University of Minnesota Nuclear Magnetic Resonance Center

The University of Minnesota invites applicants to serve as Director of the University of Minnesota Nuclear Magnetic Resonance (NMR) Center (<http://www1.umn.edu/nmr/>). The Director is expected to provide overall academic leadership for the Center and represent the unit both inside and outside the University. The Center consists of several high-field spectrometers including a 900, 850, two 700 and two 600 MHz spectrometers equipped with cryogenic probes. In addition, two solid-state NMR spectrometers are equipped with MAS and static NMR probes. The Center Director is expected to maintain a creative and vibrant research program and be a leader in the community of scholars studying cellular biophysics. Preference will be given to scientists focusing on structural analysis of biomolecules and applications are encouraged from those studying macromolecular complexes, signaling systems or membrane proteins. The successful candidate will be tenured in the Department of Biochemistry, Molecular Biology and Biophysics of the Medical School.

Candidates must have a Ph.D. or equivalent degree in Biochemistry, Chemistry or a related field and be able to teach undergraduate and graduate level biophysics and biochemistry courses.

Applicants must apply online at email: **employment.umn.edu**. In the "Keywords" box enter 325629 and click "Search". Applicants should attach a cover letter, curriculum vitae, names and e-addresses of three references and a description of the proposed research. Review of complete applications will begin immediately and continue until the position is filled. More information concerning the Department and this position can be found at <http://www.cbs.umn.edu/bmbb>

The University of Minnesota provides equal access to and opportunity in its programs, facilities, and employment without regard to race, color, creed, religion, national origin, gender, age, marital status, disability, public assistance status, veteran status, sexual orientation, gender identity, or gender expression. The University supports the work-life balance of its faculty and especially encourages applications from women and members of under-represented groups.

POSITIONS OPEN



GEISEL SCHOOL OF MEDICINE AT DARTMOUTH SEEKS OUTSTANDING CANDIDATES FOR POSITION OF PROFESSOR AND CHAIR, DEPARTMENT OF MOLECULAR AND SYSTEMS BIOLOGY

Created in 2016, the Department of Molecular and Systems Biology encompasses a community of geneticists, cancer biologists, neurobiologists, physiologists, molecular pharmacologists, and data scientists committed to using interdisciplinary approaches to solve complex problems in biological systems. We seek an innovative scientist and scholar to lead this innovative department. Successful candidates will be recommended for appointment as Professor with tenure.

Candidates must possess a terminal degree (Ph.D, MD, or equivalent); a distinguished and active record of extramurally sponsored research; a history of excellent peer-reviewed scholarship; demonstrated expertise and commitment to graduate teaching; and a strong track record of leadership, mentoring/sponsorship, and personnel management, especially as it relates to oversight of multi-disciplinary and interdisciplinary research. The Chair will be committed to the principle that a diverse and inclusive community of students, staff, and faculty enhances our mission in providing exceptional education, advancing biomedical discovery, and fostering innovation to help tackle the most vexing challenges in biomedical science and health care.

Interested candidates should submit a cover letter; curriculum vitae; statement of research/scholarly accomplishments and interests; a narrative of administrative and leadership philosophy including a statement of past and proposed efforts to enhance diversity and inclusion; and names of three individuals who will be contacted, with permission of the candidate, following initial evaluations by the search committee to website: apply.interfolio.com/51278. Initial evaluation will begin September 30, 2018 and will continue until the position is filled. For information, contact Dr. Charles Barlowe, Chair of the Search Committee (Charles.Barlowe@Dartmouth.edu).

Dartmouth College is an Equal Opportunity/Affirmative Action employer with a strong commitment to diversity and inclusion. We prohibit discrimination on the basis of race, color, religion, sex, age, national origin, sexual orientation, gender identity or expression, disability, veteran status, marital status, or any other legally protected status. Applications by members of all underrepresented groups are encouraged.



SAINT LOUIS UNIVERSITY

FACULTY POSITIONS DEPARTMENT OF BIOCHEMISTRY AND MOLECULAR BIOLOGY SAINT LOUIS UNIVERSITY SCHOOL OF MEDICINE

Saint Louis University, a Catholic Jesuit institution dedicated to education, research, health care, and service, is seeking outstanding applicants for tenure-track faculty positions, open rank, in the Edward A. Doisy Department of Biochemistry and Molecular Biology (<http://biochem.slu.edu/>). We are specifically interested in research programs focused on the structural basis of biological mechanisms. Please submit a cover letter, curriculum vitae, description of future research plans with a detailed 3-year budget and addresses of three references to website: <http://jobs.slu.edu>.

Saint Louis University is an Affirmative Action, Equal Opportunity Employer, and encourages nominations and applications of women and minorities.

POSITIONS OPEN



UNIVERSITY OF ROCHESTER

The Department of Chemistry invites applications for a tenure track faculty position in the area of organic chemistry. Applications at the Assistant, Associate, and Full Professor levels will be considered, for positions starting July 2019 or later. Candidates are expected to establish an outstanding program of original research and be effective teachers at the graduate and undergraduate levels. Application materials should be submitted online at website: <http://www.rochester.edu/faculty-recruiting/positions>. Questions may be sent to e-mail: facrec@chem.rochester.edu. Review of completed applications will begin on **October 1, 2018**.

The University of Rochester has a strong commitment to diversity and actively encourages applications from candidates from groups underrepresented in higher education. The University is an Equal Opportunity Employer.

FACULTY POSITIONS IN MOLECULAR CARDIOVASCULAR BIOLOGY

Assistant, Associate or full Professor faculty positions are available for the Division of Molecular Cardiovascular Biology, within the Heart Institute, in the Department of Pediatrics at Cincinnati Children's Hospital Medical Center. These will be regular, tenure-track faculty appointments. The applicant should have a Ph.D., M.D. or M.D.-Ph.D. with a research program that investigates or can be applied to the investigation of the molecular biology of cardiac muscle, although applicants with a skeletal muscle research focus will also be considered. The successful applicant will receive a generous startup package and join a multi-disciplinary, world-renowned faculty performing cutting-edge heart and skeletal muscle research with a strong emphasis on disease mechanisms. Cincinnati Children's Hospital Medical Center was named the second best children's hospital in the United States in the 2018 *U.S. News & World Report* and is the second-highest ranking recipient of research grants from the NIH among pediatric institutions. The Heart Institute has brought together clinical care, research and education programs, all directed at providing comprehensive care for children with heart and muscle disease and developing novel therapeutic avenues for treatment (<https://www.cincinnatichildrens.org/research/divisions/h/heart>).

A letter of interest, accompanied by a complete curriculum vitae and the names of three references should be electronically sent to email: **Jeff.Molkentin@cchmc.org**

In consideration of our children the Medical Center is committed to a smoke-free workplace. Children's Hospital Medical Center conducts pre-employment drug screening as part of a comprehensive program to maintain a drug-free workplace. Equal Opportunity Employer M/F. Minorities are encouraged to apply.

University of Wisconsin-Milwaukee

The University of Wisconsin-Milwaukee seeking applicants for a tenure-track faculty position in Bioinorganic Chemistry. Preference will be given to applicants with primary interests in biomineralization, or to those having a strong background in synthesis and characterization of novel metal-containing biomimetic models. Review of applications will begin on **October 22, 2018**, and will continue until the position is filled. Visit website: jobs.uwm.edu/postings/27836 to see more details and to apply.

Post Your Jobs

- 1,877,103 unique job seekers
- 250,657 job applications in 2016

ScienceCareers





**University of Missouri
CELL BIOLOGY
Tenure Track Faculty Position
Assistant or Associate Professor
Division of Biological Sciences**

The Division of Biological Sciences at the University of Missouri (<http://biology.missouri.edu>) invites applications for a tenure-track position at the level of Assistant or Associate Professor. Candidates using innovative approaches to address important questions in cell biology are encouraged to apply. We seek an individual employing multiple approaches to investigate cellular processes involved in development, physiology or disease. We are particularly interested in individuals who are incorporating quantitative/computational approaches into their research. The successful candidate will establish and maintain a well-funded research program that complements our strengths in cell and molecular biology, genetics/genomics, evolution, and neurobiology. The position will provide excellent opportunities for multidisciplinary collaborations with basic and translational scientists across the University of Missouri campus.

The Division of Biological Sciences place a high value on diversity and inclusivity (<http://biology.missouri.edu/diversity-outreach/diversity-statement/>). We especially seek candidates with outstanding mentoring skills who welcome and appreciate the racial and cultural diversity of our academic community. We encourage applications from individuals who demonstrate a commitment towards inclusiveness and access to higher education for groups underrepresented in the sciences.

We offer a competitive salary and start-up package, a vibrant graduate program with institutional support for students, a highly interactive faculty and outstanding core facilities. Columbia, Missouri, is ranked among the top-ten college towns in the U.S.

The University of Missouri is fully committed to achieving the goal of a diverse and inclusive academic community of faculty, staff and students. We seek individuals who are committed to this goal and our core campus values of respect, responsibility, discovery and excellence.

Please apply on line at: <http://hrs.missouri.edu/find-a-job/academic>. Use the online application and be prepared to upload your CV cover letter, a description of research plans and teaching interests, a diversity statement addressing contributions to diversity through research, teaching, and service and names and contact information of three referees willing to write a letter if solicited. Applicants may contact the Chair of the Search Committee (bioscifacultysearch@missouri.edu) with any questions about the job duties. Contact Human Resource Services (muhrs@missouri.edu) for any questions about the application process.

Review of application materials will begin **October 26, 2018**. To ensure full consideration, applications should be complete by this date. The position will remain open until filled.

An Equal Opportunity/Access/Affirmative Action/Pro-disabled and Veteran Employer.

**Assistant Scientist in Biomedical Research,
Sanford Research**

Sanford Research invites applications for full-time faculty at the rank of Assistant Scientist within Sanford Research in Sioux Falls, SD, with commensurate rank of Assistant Professor at the Sanford School of Medicine at the University of South Dakota. Sanford Research is the non-profit research branch under Sanford Health.

We seek outstanding scientists with research programs that span areas of biomedical research including but not limited to: genetics and genomics, pediatrics and rare diseases, stem cell biology, diabetes, or environmental influences of diseases. The successful candidate will have an opportunity to become a project leader on the NIH-funded Center for Pediatric Research CoBRE which focuses on key regulators of cellular pliancy that contribute to the developmental origins of pediatric disorders. Significant institutional support, including modern laboratory space and state-of-the-art facilities will be provided. A comprehensive benefits package will be tailored to the candidate's qualifications.

Qualifications

Applicants should hold a PhD, MD or MD/PhD degree and complement the existing strengths and interdisciplinary and collaborative nature of Sanford Research. Physician Scientists are encouraged to apply. Candidates will be expected to develop independent research programs and secure extramural funding.

Application

Sanford Health is an Equal Opportunity/Affirmative Action Employer. Applicants should submit a single PDF that includes: 1) detailed curriculum vitae, 2) description of research experience and future research plans with details on relevance of their research to genetics and genomics, pediatrics and rare diseases, stem cell biology, diabetes, or environmental influences of diseases, and 3) three letters of recommendation. If any of the information above is missing, the submission will not be considered. Submit materials via email to: researchrecruitment@sanfordhealth.org

**SANFORD[®]
HEALTH**

019036-00761 8/18



Worcester Polytechnic Institute

**Tenure Track Assistant Professor
in Synthetic Chemistry**

As part of WPI's systems biology initiative, the Chemistry and Biochemistry Department invites applications for a tenure-track faculty position in chemical synthesis beginning in August 2019. Synthetic organic, synthetic inorganic, and/or biosynthetic chemists interested in biological problems are particularly encouraged to apply. Colleagues joining our research enterprise will benefit from an intimate, highly collaborative research environment with current strengths that include drug discovery, drug delivery, membrane biochemistry, and cell signaling. The successful applicant will develop a vigorous, externally funded, internationally highly regarded research program. A strong commitment to teaching in the undergraduate and graduate curricula is expected. Applicants for a senior position must have a strong record of high impact publications and funding.

WPI's reputation as a rigorous and innovative university rests on the shoulders of its faculty. A highly selective, private STEM focused university and one of the nation's first, WPI believes that when great minds work together, great advances follow. At WPI the boundaries to multidisciplinary collaboration are low; faculty members, students, and other partners work together on the real-world projects and purposeful research that are hallmarks of the WPI experience. We are most proud of a recent No. 1 ranking for "faculty who best combine research and teaching." (Wall Street Journal/Times Higher Ed, 2016). Located one hour west of Boston, the university's campus is in Worcester, Massachusetts, a thriving 21st century college city recognized as a growing hub of scientific and technological innovation.

To apply, visit: <http://apptkr.com/1281630>

WPI is an Equal Opportunity Employer

GREAT MINDS at WORK

Career Feature:

Artificial Intelligence

Issue date: November 30

Book ad by November 15

Ads accepted until November 21 if space allows



129,562

subscribers in print
every week

503,472

monthly unique browsers
on ScienceCareers.org

56 %

of our weekly readers
are Ph.D.s

To book your ad:
advertise@sciencecareers.org

The Americas

+ 202 326 6577

Europe

+44 (0) 1223 326527

Japan

+81 3 6459 4174

China/Korea/Singapore/ Taiwan

+86 131 4114 0012

Produced by the Science/AAAS
Custom Publishing Office.

Artificial Intelligence (AI) is impacting science in new and exciting ways as scientists are using it to better understand society to find solutions to problems across diverse disciplines. This feature will give an overview of AI, and explore the hotspots/centers of excellence and applications for AI. Typical career paths for those working in AI will be explored as well as the opportunities that exist for careers in AI.

Your organization can brand itself as a leader in AI by raising your visibility alongside relevant content while attracting potential candidates. Contact us for further details.

What makes *Science* the best choice for recruiting?

- Read and respected by 400,000 readers around the globe
- Your ad dollars support AAAS and its programs, which strengthens the global scientific community.

Why choose this AI Feature for your advertisement?

- Relevant ads lead off the career section with a special "AI" banner.

Expand your exposure by posting your print ad online:

- Link on the job board homepage directly to AI jobs
- Dedicated landing page for AI positions.



ScienceCareers
FROM THE JOURNAL SCIENCE AAAS

SCIENCECAREERS.ORG

FOR RECRUITMENT IN SCIENCE, THERE'S ONLY ONE SCIENCE.

Yale

YALE UNIVERSITY SCHOOL
OF MEDICINE

POSTDOCTORAL ASSOCIATE

Infectious Disease Pathogenesis/Immunology

Positions available to study the interactions between ticks, pathogens and the vertebrate host. The goal is to develop new strategies to prevent diverse tick-borne infections, such as Lyme disease, anaplasmosis, babesiosis and Powassan virus. An M.D. or Ph.D. in microbial pathogenesis, immunobiology, entomology, cell biology or molecular biology is necessary.

Send curriculum vitae and recent publications to: **Erol Fikrig M.D., Investigator, Howard Hughes Medical Institute, Yale University School of Medicine, Section of Infectious Diseases, P.O. Box 208022, New Haven, CT 06520-8022** or email: lynn.gambardella@yale.edu. Yale University is an Affirmative Action, Equal Opportunity Employer. Applications from women and minorities are encouraged.

Search more jobs online

Access hundreds of job postings
on ScienceCareers.org.

Expand your search today.



McGOVERN INSTITUTE
FOR BRAIN RESEARCH AT MIT

Call for Nominations: Scolnick Prize in Neuroscience

The McGovern Institute for Brain Research is accepting nominations for the 16th annual Edward M. Scolnick Prize in Neuroscience. The Prize recognizes an outstanding discovery or significant advance in the field of neuroscience. The prize is \$150,000. The recipient presents a public lecture at MIT, hosted by the McGovern Institute and followed by a dinner in Spring 2019.

Nomination Deadline: December 15, 2018

Nomination procedures: Candidates for the award must be nominated by individuals affiliated with universities, hospitals, medical schools, or research institutes, with a background in neuroscience. Self-nomination is not permitted. Each nomination should include:

- A biosketch or CV of the nominee;
- A letter of nomination with a summary and analysis of the major contributions of the nominee to the field of neuroscience.
- Up to two representative reprints will be accepted.

Selection Procedure:

- Members of the selection committee and faculty affiliated with MIT are not eligible.
- Announcement of the award recipient will be made in January 2018
- Recipient must attend all events to be awarded the prize.


Past Scolnick Prize Recipients:

Dr. Masakazu Konishi, Dr. Judith L. Rapoport, Dr. Michael E. Greenberg, Dr. David Julius, Dr. Michael Davis, Dr. Jeremy Nathans, Drs. Lily and Yuh-Nung Jan, Dr. Bruce McEwen, Dr. Roger Nicoll, Dr. Thomas Jessell, Dr. Huda Zoghbi, Dr. Charles Gilbert, Dr. Cornelia Bargmann, Dr. Catherine Dulac, Dr. David J. Anderson,

Send nomination packet to: gwolf@mit.edu or Attn: Scolnick Prize Nomination, McGovern Institute for Brain Research, Massachusetts Institute of Technology, 77 Massachusetts Avenue 46-3160, Cambridge, MA 02139.

For more information: <http://mcgovern.mit.edu>

ScienceCareers

FROM THE JOURNAL SCIENCE  AAAS

Follow us for jobs,
career advice & more!



@ScienceCareers



/ScienceCareers



Science Careers

ScienceCareers.org

SH

SERRA
HÜNTER
PROGRAMME

THE SERRA HÜNTER PROGRAMME

announces an opening of
122 academic positions at
the Catalan Public Universities

- serrahunter.gencat.cat/en
- The **deadline** for applications
is **september 16th 2018**



Generalitat de Catalunya
Government of Catalonia

Learning to lead

About a year ago, I took on the best imaginary job out there: CEO of CryoThaw, the finest company that never existed. I had come across a tweet announcing the 2017 Young Entrepreneurs Scheme competition, sponsored by the University of Nottingham with partners from the U.K. government and industry, in which teams form hypothetical startups based on feasible scientific ideas. As a graduate student unsure of my career plans, I was excited to explore outside academia. I also saw it as a way to develop my leadership skills. So, with the support of my supervisors and funders, I decided to give it a go. I recruited three other students, and we chose to focus on improving organ transplantation. I thought I had everything under control. I couldn't have been more wrong.

They say successful teams are part art, part science. Initially, we were neither. We were just four students with remarkably different personalities struggling to work toward a shared goal. I had allocated tasks based on each team member's skills, but I confused delegation with leadership and failed to motivate the team to work together. Our initial meetings went in circles—repetitive conversation with no clarity and a lot of time wasted rehashing previous decisions—and frequently ended in turmoil. As a result, the project started with frustration and animosity. The tension between being perceived as my teammates' competent CEO and who I actually was—their grad school buddy with no prior leadership experience or training—became intolerable. I considered opting out of the whole thing.

After a few weeks, a teammate confessed to me that he found our meetings stressful, too. I finally grasped that this culture was unsettling for everyone, not just me. "Oh boy, I suck!" I thought. Something needed to change.

I turned to my go-to tool for working through my thoughts and seeking clarity: I wrote in my notebook. I reflected on our performance and how each team member was an asset. I articulated examples where everyone, myself included, could do better. I thanked them for pushing me. When I saw that what I had written actually made sense, I decided that there was nothing to do but email it to my team as what I called an "open letter from your CEO." Maybe it would help us find a way forward, because otherwise we were going nowhere.

For a day, I could hardly bear to check my email. Then I cut myself some slack and decided I could feel proud of this appreciative, frank, vulnerable email. It felt like progress.



"Team chemistry took off as we spoke our minds, good and bad."

Soon, my teammates called and thanked me for what I had written. They were relieved to learn that they were not the only ones struggling. Ultimately, the email served as a bond. And it taught me that being a leader is all about authenticity.

From there, team chemistry took off as we spoke our minds, good and bad. I found my voice as a leader, fostering an environment where we acknowledged our individual strengths and weaknesses, and where I wasn't expected to have all the answers but could nevertheless provide guidance. We read and watched everything we could find about heart transplantation, learned from webinars about startups, networked with experienced entrepreneurs, contacted national health services for data, and arranged consultations with medical experts.

Then, one day, a teammate entered the meeting with his hands full of papers and his breath shallow with excitement. "This cryo-preservation thing is wicked!" he exclaimed. Soon after, we came up with CryoThaw Heart, a gold nanoparticle and laser-based approach to rapidly freeze and thaw hearts. We put together our business plan, pitched it, got selected for the finals—and won our division as well as the people's choice award.

Looking back, it wasn't just a matter of how successful we turned out to be; it was also how far from successful we were at first. Our initial failures made me realize how being a leader starts with being your better self. Heartbreak doesn't have to be the end of the world. In many ways, it can be a beginning. ■

Lucka Bibic is a Ph.D. candidate at the University of East Anglia in Norwich, U.K. Send your career story to SciCareerEditor@aaas.org.